Durham University

Durham E-Theses

A study of the physical properties of polymer monolayers spread at the air-water interface

Henderson, John A.

How to cite:

Henderson, John A. (1992) *A study of the physical properties of polymer monolayers spread at the air-water interface*, Durham theses, Durham University. Available at Durham E-Theses Online: http://etheses.dur.ac.uk/6132/

Use policy

The full-text may be used and/or reproduced, and given to third parties in any format or medium, without prior permission or charge, for personal research or study, educational, or not-for-profit purposes provided that:

- a full bibliographic reference is made to the original source
- a link is made to the metadata record in Durham E-Theses
- the full-text is not changed in any way

The full-text must not be sold in any format or medium without the formal permission of the copyright holders.

Please consult the full Durham E-Theses policy for further details.

Academic Support Office, The Palatine Centre, Durham University, Stockton Road, Durham, DH1 3LE
e-mail: e-theses.admin@durham.ac.uk Tel: +44 0191 334 6107
http://etheses.dur.ac.uk

A STUDY OF THE PHYSICAL PROPERTIES OF POLYMER MONOLAYERS SPREAD AT THE AIR-WATER INTERFACE

JOHN A. HENDERSON Ph.D. 1992

An account is given of the methods of anionic polymerisation and characterisation used to prepare polymer samples, and the experimental methods used to examine their interfacial properties, when spread as so-called Langmuir monolayers on water. Specifically, these are surface pressure - concentration isotherm studies, neutron reflectometry, ellipsometry of polarised light, and surface quasi-elastic light scattering.

Hydrogenous and deuterated analogues of three different groups of polymers have been synthesised. These are;

syndio, iso and atactic poly (methyl methacrylate) SYNDIO-, ISO-, and ATAPMMA;

poly (ethylene oxide), PEO;

0.85:0.15 diblock copolymers of poly(methyl methacrylate) with poly (4-vinyl pyridine), PMMA4VP.

The latter materials have been quaternised with hydrogenous and deuterated ethyl bromide to create partially poly-electrolyte materials, PMMA4VPQ.

Thermodynamic information obtained from surface pressure data regarding the interaction between polymer segments and the subphase in each case is related to structural and compositional changes in the film measured as a function of surface concentration by neutron reflectometry.

The trends described are supported by ellipsometric data, and preliminary experiments into the investigation of PMMA surface monolayer visco-elastic properties are described.

The copyright of this thesis rests with the author.
No quotation from it should be published without
his prior written consent and information derived
from it should be acknowledged.

A Study of the Physical Properties of Polymer Monolayers Spread at the Air - Water Interface

John A. Henderson

Graduate Society 1992

A thesis submitted to the University of Durham in partial fulfilment of the regulations for the Degree of Doctor of Philosophy.

No part of this work has been submitted previously for a degree at the University of Durham or any other university, and the contents represent the work of the author unless otherwise acknowledged.

2 DEC 1992

DEDICATION

This work is dedicated with love and gratitude to my mother and late father, and to Heather.

ACKNOWLEDGEMENTS

I would like to thank a great number of people who have contributed in many ways to this thesis. Firstly it gives me great pleasure to acknowledge the tireless enthusiasm of my supervisor Dr. Randal Richards, whose office door was always open and whose wallet was rarely closed, whether it be in the Wheatsheaf, the New Inn or the Club Sandwich.

Many of the experiments described herein would not have been possible without the matchless expertise of the instrumental scientists of the Rutherford Appleton Laboratories and the Institut Laue Langevin. In this context I gladly acknowledge the efforts of Jeff Penfold, Claire Shackleton, Archie Eaglesham and the late John Herdman at RAL, and Adrian Rennie and Manuel Cruz at ILL.

On many occasions I have had reason to be grateful to Dr. Bob Thomas and his research group at PCL Oxford, not least for the occasional chance of an uninterrupted night's sleep at ILL. In particular I would like to say a special thank you to the irrepressible Stuart Clarke.

I would also like to thank most of the above named people for their helpful contribution to data analysis methods and the generous provision of software and permission to alter it for my own purposes. In particular I should mention Jeff Penfold, Claire Shackleton, Adrian Rennie and Ellen Lee.

Professor John Earnshaw of Queen's University, Belfast has been a most obliging and encouraging advisor on the subject of surface light scattering, and again his most generous provision of analysis software is gratefully acknowledged.

Ellipsometry experiments were made possible through collaboration with Dr. Mannfred Stamm of the Max Planck Institute für Polymerforschung, Mainz, Germany, and through the patient guidance of Dr. Hubert Motschmann, whom I thank not only for his scientific expertise, but also for his excellent hospitality.

Sample characterisation was provided by the technical staff of

Strathclyde and Durham Universities, and I would like to thank Messrs. J. Carruthers and G. Forrest for GPC data, Mr. J. Ritchie, Dr. A. Kenwright and Mrs. J. Say for NMR spectroscopy, and Mrs. J. Dostal for elemental analyses. Thanks are also due to Messrs. G. Haswell and R. Hart for the construction of the vacuum synthesis line and glassware, and to Mr. B. Barker for modification of the reflectometry trough.

Financial support for this project was through a quota award from the SERC, and funding to enable participation at academic meetings was provided by the RSC Macro Group through a D.H. Richards Memorial bursary and the European Science Foundation.

I would like to thank my friends and colleagues at Strathclyde and Durham who have made my time studying with them such an enjoyable and enriching experience. I single out two people, Robin MacDonald, truly a big man, and John Holland, without whom the light scattering lab would have been a very dark place indeed. I would like to express further gratitude to John and Gwyn Holland whose hospitality helped greatly in the final preparation of this thesis.

Finally I would like to thank my family, and my fiancee Heather and her relatives for their support and patience in the last few eventful years in particular. I am very lucky to have you all.

CONTENTS

Preface - Units and Symbols

Throughout the text of this thesis, standard SI units have been used wherever appropriate. In several of the subject areas addressed however, it has become accepted practice to quote physical properties in non-SI units which are nevertheless more familiar or more convenient for discussion. Scattering length densities, for example are normally quoted in the unit of reciprocal square Ångstroms, $Å^{-2}$. Where such conventions exist, non-SI units may be used in the text. The following list provides conversions between these units and their SI equivalents.

1 Å = 10^{-10}m;

1 MHz = 10^{6}Hz = $10^{6}s^{-1}$

1 mm = 10^{-3}m

1 µl = 10^{-6}l = $10^{-9}m^{3}$

1 µm = 10^{-6}m

1 nm = 10^{-9}m

1 mW = 10^{-3}W = $10^{-3}Js^{-1}$

In an attempt to avoid the use of over cumbersome and unfamiliar notation in the theoretical sections of this thesis, the most generally accepted nomenclature in each of the subject areas addressed has been used. While this hopefully makes each section more easily read in itself, it inevitably leads to multiple and context sensitive definitions of characters and symbols. The list below attempts to define briefly the symbols used in the text, including a parenthesised indication of the context in which particular definitions are appropriate;

a = major semi-axis of an inclined ellipse (ellipsometry);

A = surface area (surface pressure theory);

A = amplitude of x direction vibration of electric field (ellipsometry);

A = amplitude factor (SQELS correlation function expression);

A_o = extrapolated surface area at zero surface pressure, or limiting area per

segment (surface pressure theory);

a = monomer length (surface pressure theory);

A_2 = second virial coefficient (polymer solution theory);

$A_{2,2}$ = two dimensional second virial coefficient(surface pressure theory);

α = azimuth of the electric field (ellipsometry);

B = amplitude of y direction vibration of electric field (ellipsometry);

B = instrumental background (SQELS correlation function expression);

b = bond coherent scattering length (neutron reflectivity);

b = minor semi-axis of an inclined ellipse (ellipsometry);

β = optical path length of beam in interfacial film (neutron reflectivity)

β = retardation of incident polarised beam at quarter wave plate (ellipsometry);

β = instrumental line broadening term (SQELS correlation function expression)

c = concentration (polymer solution theory)

c^* = concentration of transition from dilute to semi-dilute solution bahaviour, concentration of initial chain overlap (polymer solution theory);

χ = Flory-Huggins interaction parameter;

$D(\omega)$ = Lamb - Levich dispersion expression (SQELS);

d = dimensionality (polymer scaling theory);

d = film thickness (optical theory);

d = physical density (neutron reflectivity);

Δ = phase difference of x and y electric vibrations (ellipsometry);

$\delta\Delta$ = change in phase difference (ellipsometry);

Δf_s = line width of power spectrum (SQELS);

$\delta\theta$ = deviation from specular angle (SQELS);

$\delta\theta_n$ = angular separation from zero order of n^{th} order beam(SQELS);

$\delta\psi$ = change in amplitude attenuation;

E = electric field vector (electromagnetic theory of light);

E_p = parallel component of electric field (electromagnetic theory);

E_s = perpindicular component of electric field (electromagnetic theory);

ϵ_o = surface dilational modulus (SQELS);

ϵ' = surface dilational viscosity;

f = fractional coverage of surface (patchy film modelling in neutron reflectivity);

$F(\xi)$ = form factor (patchy film modelling in neutron reflectivity);

ϕ = volume fraction (surface pressure theory, also used in discussion of film compositions)

ϕ^* = polymer volume fraction of dilute - semi-dilute regime transition (two dimensional scaling theory);

ϕ^{**} = polymer volume fraction of semi-dilute - concentrated regime transition(two dimensional scaling theory);

$G(\tau)$ = measured auto-correlation function (SQELS);

g = gravitational acceleration = $9.81 ms^{-2}$;

$g(\tau)$ = correlation function in time domain (SQELS);

$g^{(1)}(\tau)$, $g^{(2)}(\tau)$ = first and second order correlation functions of scattered field (SQELS);

Γ = surface concentration (two dimensional scaling theory);

Γ = time damping constant (SQELS);

Γ^* = surface concentration of dilute - semi-dilute regime transition (two dimensional scaling theory);

Γ^{**} = surface concentration of semi-dilute - concentrated regime transition (two dimensional scaling theory);

γ = surface tension (surface pressure theory);

γ = surface tension modulus (SQELS);

γ_o = transverse shear modulus (SQELS);

γ' = transverse shear viscosity (SQELS);

h(Q), h'(Q) = modifying form factors in kinematic expressions for neutron reflectivity;

η = minor semi-axial direction of an inclined ellipse (ellipsometry);

η = dynamic viscosity (SQELS);

I = incident intensity of radiation (neutron reflectivity);

I_r = intensity of reference field (SQELS heterodyne beat spectroscopy);

I_s = intensity of scattered field (SQELS heterodyne beat spectroscopy);

K = scattering vector

K_B = Boltzmann Constant

k = neutron wave vector

λ = radiation wavelength (optical/neutron theory);

Λ = capillary ripplon wavelength (SQELS);

M_m = molecular weight of scattering species or monomer unit (neutron reflectivity);

M_n = number average molecular weight;

M_w = weight average molecular weight;

m = scattering mass per unit area (kinematic theory of neutron reflectivity);

N = degree of polymerisation (scaling theory);

N = atomic number density (neutron reflectivity);

N_{av} = Avogadro Number = 6.023×10^{23}

n = refractive index (optical or neutron);

ν = critical scaling exponent (scaling theory);

ν_θ = theta condition value of scaling exponent (scaling theory);

ν = kinematic viscosity = η/ρ

ω = flexibility parameter in Singer expression (surface pressure theory);

ω_o = flexibility with zero cohesion in Singer expression (surface pressure theory);

ω = vibrational frequency of electric field (optical theory);

ω = complex capillary ripplon frequency (SQELS);

ω_o = propogation frequency (SQELS);

$P(\omega)$ = Bouchiat and Meunier power spectrum (SQELS);

π = surface pressure;

Q = momentum transfer component normal to interface (neutron reflectivity);

Q = phase term in expression for correlation function (SQELS);

q = interfacial wavenumber = component of the scattering vector parallel to the liquid surface (SQELS);

R = reflected component of radiation (neutron reflectivity);

Re = Reynolds Number;

R_g = radius of gyration of polymer coil (scaling theory);

$r_{i,j}$ = Fresnel coefficient at the i,j^{th} interface (neutron reflectivity);

ρ = generalised Fresnel coefficient (optical theory);

ρ = scattering length density (neutron reflectivity);

ρ = physical density (sections other than neutron reflectivity);

$s(Q)$ = normalised form factor (kinematic theory of neutron reflectivity);

σ = adsorption cross-section (neutron reflectivity);

σ = standard deviation in the rate of change of the scattering length density (kinematic theory of neutron reflectivity);

$\langle\sigma\rangle$ = root mean square film thickness (kinematic theory of neutron reflectivity);

T = absolute temperature

T = transmitted component of radiation (neutron reflectivity);

t = time;

t = quarter wave plate thickness (ellipsometry);

τ = reduced temperature (surface pressure theory);

θ = temperature of theta or Flory condition behaviour (surface pressure theory);

θ = angle of radiation incidence (neutron reflectivity, ellipsometry, SQELS);

θ_c = critical angle of total reflection (optical/neutron reflectivity);

θ = phase term of electric vibration (optical theory);

θ = scattering angle (light scattering);

W = interchain cohesion (Singer expression for surface pressure);

ξ = island size (patchy monolayer film model for neutron reflectivity);

ξ = major semi-axial direction of an inclined ellipse (ellipsometry);

ψ = amplitude attenuation (ellipsometry);

ψ_θ = scaling exponent (scaling theory);

z = co-ordination number of monomer units in polymer chain (Singer expression for surface pressure);

$\langle z \rangle$ = n^{th} moment of scattering length density profile (kinematic theory of neutron reflectivity);

ζ = interfacial disturbance from the mean plane for a two dimensional wave (SQELS).

CHAPTER 1 - INTRODUCTION

The study of interfacial properties is of fundamental interest to physical science and also of increasing practical importance to industry. Interfacial properties are frequently very different from the bulk properties of the same material, and are found to have a profound influence on the behaviour of many diverse systems such as electronics components, solid powder and liquid flow systems, detergents, colloidal dispersions, biological systems, elastomers, adhesives, and ultra-thin coatings. The introduction of surface active materials at interfaces, be they protein chains at cell membranes, soap molecules adsorbed at the air - solution interface, or diblock copolymers providing adhesion between otherwise incompatible materials, greatly alters the properties at a given interface and hence a physical understanding of the way such materials act enables scientists and technologists to exploit them to greater effect in many applications.

One system in which the interfacial region to be studied is made convenient for examination by its very nature is the air - liquid interface. Apart from thermally induced surface ripples, in the absence of gross vibrations the air - liquid interface is a microscopically smooth and self levelling system. In addition, the air - liquid interface is of interest in many practical situations. Surfactant solutions, for example are well known to display surface excess adsorption at the solution - air interface. Other applications will be discussed later in this introduction.

The potential of polymeric materials as surface active agents has come to be increasingly recognised, as the nature of a long chain molecule provides wide opportunities for the introduction of amphiphilic properties at specified sites along the chain, leading to enhanced surface properties. Both soluble and insoluble polymeric materials are of interest in such applications and both will be considered in the bulk of this thesis.

Evidently there is a need to understand the fundamental physical science behind the many applications just described, and indeed a well established classical literature of experimental and theoretical considerations of air - liquid systems exists. However many of the classical techniques used provide only sketchy information about the actual structure of monolayer systems and it is only in recent times that more sophisticated non-invasive techniques employing radiation and light scattering type techniques have been developed successfully. The following sections provide an overview of the most commonly used classical techniques, followed by a fuller description of the more recent advances in experimental methods to non invasive techniques and the relevant theories on which they are based.

1.1 Classical Examination of Interfacial Monolayers

Several techniques have been commonly used for the study of monolayers at the liquid - gas interface. The most widely studied systems are water or aqueous solution systems at the interface with air, although organic liquid systems and liquid metals have been studied. The principle techniques used have been measurements of surface pressure, surface potential, surface viscosity and surface shear modulus values. The last three techniques will not be considered in any detail here but they have been achieved by adaption of three dimensional concepts to the two dimensional case, for example surface viscosities are measured by studying the flow of film through a capillary canal on the surface very much in the same way that bulk viscosities are measured by a capillary tube viscometer. By far the most standard technique is the measurement of the surface pressure in a film as it is compressed and that technique will now be considered.

1.1.1 Surface Pressure - Area (Concentration) Isotherm Measurement

The surface pressure at an interface is defined as the difference in surface tension between the clean substrate and the surface with a spread film.

$$\pi = \gamma_{sub} - \gamma_{film} \qquad 1.1$$

The measurement of π is conveniently achieved by the use of a Wilhelmy hanging plate type apparatus[1,2] where an inert metal or paper plate hangs vertically into the liquid suspended from a force balance. This basic design is usually adapted for continuous operation by attaching the plate to a displacement transducer where the movement of the plate (or the force required to maintain its stationary position) can be conveniently converted to an electrical output suitable for computer storage and manipulation.

The relative experimental simplicity, speed and ease of automation associated with surface pressure measurements make this a very attractive technique for the examination of interfacial monolayers. However traditional studies have always been rather limited by the lack of understanding of how the observed data relate to the structure of material in the layer. Many reports have been published in which the existence of various two dimensional phases and phase changes have been established. 2-D gaseous, liquid expanded and condensed, and solid films have all been observed, but with a very few exceptions interpretation has been very qualitative. Section 1.5 contains a fuller review of previous studies of monolayer systems.

1.1.2 Theoretical Description of Surface Pressure Phenomena

Apart from the pioneering efforts of Crisp,[3,4] the earliest attempt to develop a quantitative theory for the description of polymer monolayers according to the molecular interactions occurring at the interface was by Singer,[5] using the theory of polymer solutions developed by Huggins.[6] Using a two dimensional lattice model for the case of strong cohesive forces where the surface pressure exerted is less than that for a random coil, Singer derived the expression

$$\pi = \frac{NK_BT}{A_o}\left[\ln\left(\frac{A}{A - A_o} \right) + \left(\frac{N - 1}{N} \right) \frac{z}{2} \ln\left(1 - \frac{2A_o}{zA} \right) \right] \qquad 1.1$$

where N is degree of polymerisation, k_B is the Boltzmann constant, T is the temperature, A is the surface area for which the surface pressure equals π, A_o is the extrapolated area at zero pressure, and z is the co-ordination number of the monomer units in the chain (related to the degree of unfolding of the chain).

For any degree of polymerisation where z = 2, the chain is rigid and (1.1) reduces to

$$\pi = \frac{k_B T}{A_o} \ln\left(\frac{A}{A - A_o}\right) \qquad 1.2$$

For a fully flexible chain, z = 4. Davies[7] defined a flexibility parameter $\omega = z - 2$, such that

$$\omega = \omega_o \exp(-W/K_B T) \qquad 1.3$$

where W is the interchain cohesion from Van der Waal's forces between polymer segments and ω_o is the flexibility with zero cohesion. However, as pointed out by Kawai,[8] this theory makes no allowance for entropic effects on the chain flexibility caused by the strictures placed on chain configuration by the interface. Frisch and Simha[9,10] modified Singer's treatment to allow for chain looping and crossovers in pseudo two dimensional systems. Saraga and Prigogine[11] had proposed a treatment based on Flory's statistical analysis methods[12] which introduced another modifying term to account for cohesive enthalpic interactions. A variety of these and other theoretical treatments were developed to describe polymer monolayer behaviour but there seems to have been little inclination to apply them to experimental data.

In the past few years, there has been an important breakthrough in the understanding of the observed surface pressure data, with the development of two dimensional scaling theories analogous to those expounded for three dimensions by de Gennes. These theories have been derived in terms explicitly involving the dimensionality of the system and hence they have been extended to the two dimensional case.

1.1.3 Scaling Concepts

The scaling theories of P.G. de Gennes for polymer chains in three dimensional solutions are described in his book[13]. This describes the concepts of dilute and semi-dilute polymer solutions and the existence of a crossover between these regions at a concentration c^*, where chain overlap just begins to occur. For good solvents, c^* is expressed

$$c^* \cong N/R_g^3 = a^{-3}N^{1-3\nu} = a^{-3}N^{-4/5} \qquad 1.2$$

where N = degree of polymerisation, tending towards infinity,

R_g= radius of gyration,

a = monomer length,

ν = critical exponent

A corresponding polymer fraction ϕ^* may also be defined to scale according to

$$\phi^* \sim N^{-4/5} \qquad 1.3$$

In dilute solutions, that is for $c < c^*$, the solution is a system of separate coils behaving as hard spheres. In this region Flory - Huggins behaviour is observed and the equation of state 1.4 is observed

$$\pi/T = c^2/N + A_2c_2^2 + ... \qquad 1.4$$

where the second virial coefficient A_2 has the dependence

$$A_2 \cong R_g^3N^{-2} \sim N^{-1/5} \qquad 1.5$$

In the semi-dilute region where the polymer fraction ϕ is still low, such that $\phi^* < \phi < \phi^{**}$,(where ϕ^{**} is the polymer fraction at which transition to concentrated solution behaviour occurs) the chain overlaps necessitate the introduction of an excluded volume interaction term. The scaling law in this case is

$$\pi/T = c/N\, f_\pi(cR_g^3/N) = c/N\, f_\pi(c/c^*) \qquad 1.6$$

where f_π is a dimensionless function such that

$$\lim_{x\to\infty} f_\pi(x) = \text{const}\, x^m = \text{const}\, (\phi/\phi^*)^m$$

$$= \text{const}\, \phi^m N^{4m/5} \qquad 1.7$$

This gives

$$a^3\pi/T = \text{const}\ \phi^{m+1}\ N^{(4m/5)-1} \qquad 1.8$$

in the semi-dilute region. Since all thermodynamic properties are independent of degree of polymerisation in this region, m must equal 5/4 giving

$$a^3\pi/T = \text{const}\ \phi^{9/4} \qquad 1.9$$

This is in contrast to the mean field prediction which gives $\pi \sim \phi^2$.

1.1.4 Scaling Theory in Two Dimensions

The three dimensional theories outlined briefly above have been expressed in a uni-dimensional form by Daoud and Jannink[14] and des Cloizeaux[15]. These expressions may be applied to the two dimensional "solution" case encountered in polymer monolayers. In the dilute region the equation of state virial expression

$$\pi/\Gamma RT = (1/M_n + A_{2,2}\Gamma + ...) \qquad 1.10$$

is valid, where $A_{2,2}$ is the two dimensional second virial coefficient and Γ is the polymer surface concentration. The second virial coefficient can be defined generally in any dimensionality, d, as

$$A_{2,d} \sim N^{\nu d}\tau^{d(\nu-\nu_\theta)\psi_\theta} \qquad 1.11$$

where τ is the reduced temperature, ν, ν_θ, and ψ_θ are critical exponents for the good and theta 2-D solvent cases. Values for these exponents have been predicted by many theoretical methods. ϵ-expansion renormalisation group techniques give $\nu=0.77$[17,18], $\nu_\theta=0.505$[19] and $\psi_\theta=0.60$[20]. Thus

$$A_{2,2} \sim N^{1.34}\tau^{0.88} \qquad 1.12$$

Other theoretical predictions for the value of the ν exponent have been attempted widely. Mean field theory predicts that in the good solvent regime, $\nu=0.75$. Self avoiding walk calculations[21,22] suggest a similar value for short chains

(N < 18) whilst Monte Carlo simulations predict $\nu=0.753\pm0.004$[23]. The matrix transfer prediction is $\nu=0.7503\pm0.0002$[24].

There is much greater diversity in predictions of ν_θ, the value of ν in the θ condition. The mean field prediction is $\nu_\theta = 2/3$ and this considers only ternary interactions, whereas the collapsed chain value of 1/2 is obtained by ideal random walk treatment. Monte Carlo simulations have suggested values between 0.51[25] and 0.59[26]. An indefinitely growing self avoiding walk analysis prediction of 0.567 ± 0.003[27,28] has been obtained. Other predictions of 0.59 and 0.55 have been obtained by real space renormalisation[16,29,30] and transfer matrix[31] methods respectively. The variation in these values is reflected in the measured experimental values which are discussed in section 1.5.

The general n-dimensional definition of the crossover polymer concentration between dilute and semi-dilute behaviour is

$$c^* \sim N/R_{g,d}{}^d \sim N^{1-\nu d}\tau^{-d(\nu-\nu_\theta)\psi_\theta} \qquad 1.13$$

with

$$R_{g,d} \sim N^{\nu}\tau^{(\nu-\nu_\theta)/\psi_\theta} \qquad 1.14$$

the radius of gyration in the dimensional space of d. For d=2 one obtains

$$\Gamma^* \sim N^{-0.54}\tau^{-0.88} \qquad 1.15$$

An osmotic pressure expression was obtained by des Cloizeaux

$$\pi/T \sim c^{\nu d(\nu d-1)}\tau^{(\nu-\nu_\theta)d/\psi_\theta(\nu d-1)} \qquad 1.16$$

For d=2, the surface pressure expression is

$$\pi/T \sim \Gamma^{2.85}\tau^{1.64} \qquad 1.17$$

Considering the transition from semi-dilute to concentrated behaviour, Daoud and Jannink produced the following general expression for c^{**}

$$c^{**} \sim \tau^{(\nu_\theta d-1)/\psi_\theta} \qquad 1.18$$

Above c^{**} there is chain overlap but ,due to screening, θ conditions hold, corresponding to the semi-dilute region at θ conditions.

π is defined by

$$\pi/T \sim c^{\nu_\theta d/(\nu_\theta d-1)} \qquad 1.19$$

For d=2 then

$$\Gamma^{**} \sim \tau^{0.0167} \qquad 1.20$$

and

$$\pi/T \sim \Gamma^{101} \qquad 1.21$$

However this behaviour has never been observed, a fact which has been attributed to out of plane deformation of the monolayer before the concentrated regime can be attained.

1.1.5 Non-Perturbative Methods

The classical methods previously listed all necessitate some sort of perturbative contact with the surface under examination. For example, to measure the surface pressure requires the contact of a Wilhelmy hanging plate with the liquid surface. This can distort experimental measurements in some instances, yielding inconsistent results[32]. Non-perturbative methods involving the interaction of light and radiation sources with the surface have been developed to overcome this problem and provide more detailed information on the structure of surface monolayers. These include ellipsometry, surface light scattering, X-ray fluorescence microscopy, induced evanescent wave spectroscopy, and X-ray and neutron reflectometry. Of particular interest in the present context are neutron reflectometry, ellipsometry, and surface quasi-elastic light scattering.

1.2 Neutron Reflectometry

Neutron reflectometry has emerged in the last few years as a valuable tool for the investigation of the surface properties of many interfacial systems. In the relatively short period of time since the earliest pioneering work in the field, the suitability of the technique for the investigation of a broad range of surface science problems has been demonstrated by the successful development of the instrument CRISP at the Rutherford Appleton Laboratories, Oxford, UK and at present several other similar facilities have either opened or are planned in the foreseeable future.

The basis of the technique is the fact that the specular reflection of neutrons at an interface at small angles greater than the critical angle for total reflection is dependent on the density of material in the interfacial region and on the thickness of the interface. Reflectometry has been used to study a wide range of systems including multilayer structures of immiscible polymer blends and diblock copolymer spun cast films, interdiffusion properties of miscible polymer multilayers, the surface structure of biological materials, metal and semi-conductor substrate deposited solid films, surfactant and polymer solutions exhibiting surface excess adsorption at air-liquid, solid-liquid and liquid-liquid interfaces, and the properties of spread monolayers of surfactants and polymers.

A major attraction of neutron reflection is that, being a nuclear scattering phenomenon (unlike X-ray reflection which depends on electron densities) it is sensitive to certain isotopic substitutions in the material under examination. Of most common practical use in hydrocarbon systems, such as polymers, is hydrogen/deuterium substitution. ^{1}H and ^{2}H nuclei have very different coherent scattering lengths of different sign for neutrons, and hence materials which are otherwise chemically identical will, if one is hydrogenous and the other deuterated, have completely different scattering length densities (related to the

neutron refractive index). As this quantity appears explicitly in the mathematical functions used to describe the reflectivity, isotopic substitution may then be used to provide a second set of independent data for the same system. Given a suitable number of such contrast sets, it is possible to determine in favourable cases a unique solution for both the layer thickness and density profile, a result inaccessible by other methods.

Neutron reflectometry has been the major technique employed during this project and a fuller description of the technique, its development and the theory on which it is based is to be found in Chapter 2.

1.3 Ellipsometry[33]

Ellipsometry is a useful non-invasive technique for the investigation of the optical properties of surfaces and thin films. As polarised visible light is used as the incident radiation, the technique is non-destructive. Ellipsometry operates on the principle that when linearly or elliptically polarised light is reflected from a surface or interface, the components of its electric vector E undergo a relative phase change related to the layer thickness and refractive index. This results in a characteristic state of polarisation in the reflected beam which can be used to determine the thickness and composition of the film.

The classical description of electromagnetic radiation in terms of electric and magnetic field contributions are applied to the consideration of ellipsometric phenomena[34]. Polarised light is described in terms of two components of its electric field vector parallel or perpendicular to the plane of incidence, defined as the x-z plane. The interface between the two media is at z=0, and the angle between the electric field vector and the plane of incidence is the azimuth of the electric field, α.

The parallel and perpendicular components of the E field are then given by

$$E_x = E_p = E\cos\alpha \qquad 1.22(a)$$

$$E_y = E_s = E\sin\alpha \qquad 1.22(b)$$

For two arbitrary vibrations of similar frequency ω and amplitudes A and B in the directions of the co-ordinate axes then

$$E_x = A\cos(\omega t + \theta_x) \qquad 1.23(a)$$

and

$$E_y = B\cos(\omega t + \theta_y) \qquad 1.23(b)$$

If the two vibrations are in phase ($\theta_x = \theta_y$) or of opposite phase ($\theta_x = \theta_y \pm \pi$) the ratio of the above expressions is

$$E_y/E_x = \pm B/A \qquad 1.24$$

which is the equation of a straight line in the x-y plane, thus the light may be said to be linearly polarised.

If on the other hand there is an arbitrary phase difference between the two vibrations, then the equation of an ellipse is generated;

$$(E_x/A)^2+(E_y/B)^2-2(E_x/A)(E_y/B)\cos\Delta=\sin^2\Delta \qquad 1.25$$

where $\Delta = \theta_x - \theta_y$.

By redefinition of the co-ordinate system to axes ξ and η that lie along the major and minor axes of the ellipse described by the above equation

$$E_\xi = E_x\cos\chi + E_y\sin\chi \qquad 1.26(a)$$

$$E_\eta = -E_x\sin\chi + E_y\cos\chi \qquad 1.26(a)$$

where χ is the angle between the ξ-axis (the major semi-axis of the ellipse) and the x-axis (figure 1.4).

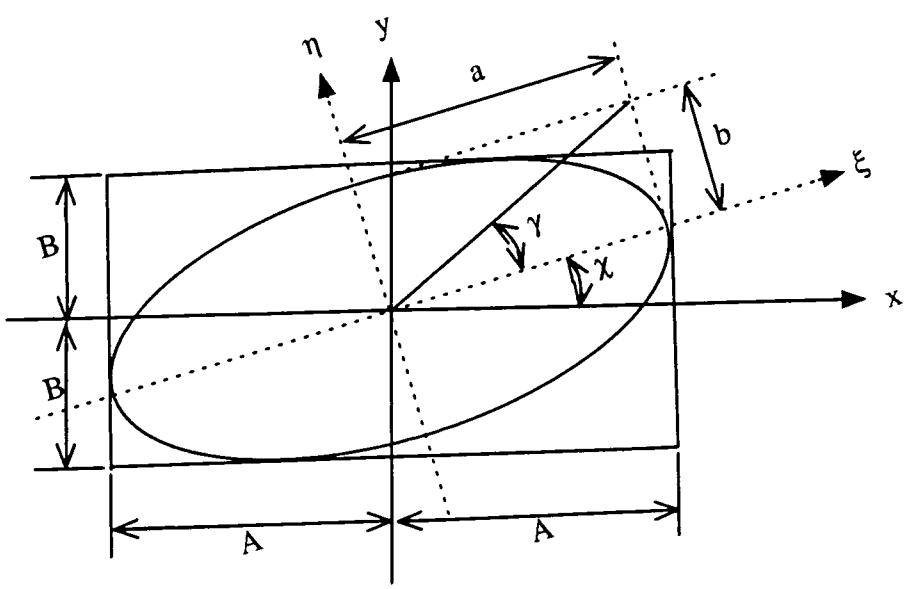

Figure 1.1 Characteristics of an inclined ellipse

The ellipse is now described by

$$E_\xi = a\cos(\omega t + \theta_o) \qquad 1.27(a)$$

$$E_\eta = \pm b\sin(\omega t + \theta_o) \qquad 1.27(b)$$

where a and b are the semi-axes of the ellipse, and the double sign in E_η takes account of positive and negative ellipticities.

Substituting the appropriate form of 1.22 into 1.26 and equating 1.26 and 1.27 gives on expansion

$$\tan 2\chi = \tan 2\psi \cos\Delta \qquad 1.28$$

$$\sin 2\gamma = \pm \sin 2\psi \sin\Delta \qquad 1.29$$

$$\tan\Delta = \pm \tan 2\gamma / \sin 2\chi \qquad 1.30$$

where

$$\tan\psi = B/A = |E_p|/|E_s| \qquad 1.31$$

and $$\tan\gamma = b/a \qquad 1.32$$

The quantities that characterise the orientation of polarisation at any stage then are the phase difference Δ and the amplitude attenuation ψ, and the relationships between these quantities and the disinclination of the ellipse from the x-y co-ordinate system are explicitly present in equations 1.28 to 1.30.

By comparison of the ratios of the incident (i) and reflected (r) p and s components of E on the reflection of polarised light at an interface, the fundamental relationship of ellipsometry is generated;

$$(E_p/E_s)_r/(E_p/E_s)_i = (E_r/E_i)_p/(E_r/E_i)_s$$

$$= R_p/R_s$$

$$= \rho_p/\rho_s$$

where ρ is the generalised Fresnel coefficient

$$= \tan\psi_r/\tan\psi_i . \exp(i(\Delta_r - \Delta_i))$$

$$= \tan\psi\, e^{i\Delta} \qquad 1.33$$

Specifically considering reflection from a thin film spread on water, denoting air by subscript 0, film by 1, and subphase by 2,

$$R_{p \text{ or } s} = (r_{01} + r_{12}e^{-i\beta})/(1 + r_{01}r_{12}e^{-i\beta}) \qquad 1.34$$

where $\beta = 4\pi n_1 d_1 \cos\phi_1/\lambda$.

β therefore contains terms in the refractive index, n_1, of the film, its thickness d_1, and also the incident light wavelength λ and angle ϕ_1. The terms r_{01} and r_{12} refer to the Fresnel coefficients of the appropriate interfaces and are either r_p or r_s coefficients depending on the form of equation 1.34.

Experimentally the changes in Δ and ψ for reflection from the clean water surface and the spread film are measured. The change in phase difference $\delta\Delta$ is defined as

$$\delta\Delta = \Delta - \Delta' \qquad 1.35$$

where Δ is the clean water value and Δ' the film value.

$\delta\Delta$ is found to be directly proportional to the film thickness, d_1.

For a non-absorbing substrate it is found that the equivalent amplitude attenuation difference

$$\delta\psi = \psi - \psi' \qquad 1.36$$

is essentially zero and so no sensitivity in this parameter is expected for monolayers spread on the surface of water.

1.4 Surface Quasi-Elastic Light Scattering[35]

Thermal excitations cause spontaneous propagation of low amplitude, high frequency transverse capillary waves at air - liquid interfaces. Fourier analysis of these thermal excitations results in a series of surface modes, the temporal evolution of which is reflected in the time domain spectrum of the scattered light. As the wave evolution is governed by interfacial visco-elastic properties, suitable fitting to an experimentally generated time spectrum of the scattered light yields information about the visco-elastic properties and processes occurring in the interfacial region of simple liquid and monolayer dosed systems. This is the basis of modern surface photon correlation type experiments.

1.4.1 Light Scattering from a Simple Liquid Interface

Considering the liquid - gas interface for a simple liquid as a Gibbs dividing surface, defined as the x - y plane, the interfacial disturbance from the mean plane of a two-dimensional wave propagating in the x direction (Figure 1.2) may be described by

$$\zeta(x,t) = \zeta_o \exp(i(qx + \omega t)) \qquad 1.37$$

where $q = 2\pi/\Lambda$ = interfacial wavenumber,

ω = wave frequency,

and Λ = wavelength of ripplon.

This behaves as a weak diffraction grating for light approaching in the x - z plane and there is a weak scattering effect upon some of the reflected light, which is scattered away from the specular angle θ by an amount $\delta\theta$. It is found that for small angles of scatter

$$q = 2k_o \sin(\delta\theta/2).\cos\theta \qquad 1.38$$

where $2k_o\sin(\delta\theta/2) = K$, the scattering vector.

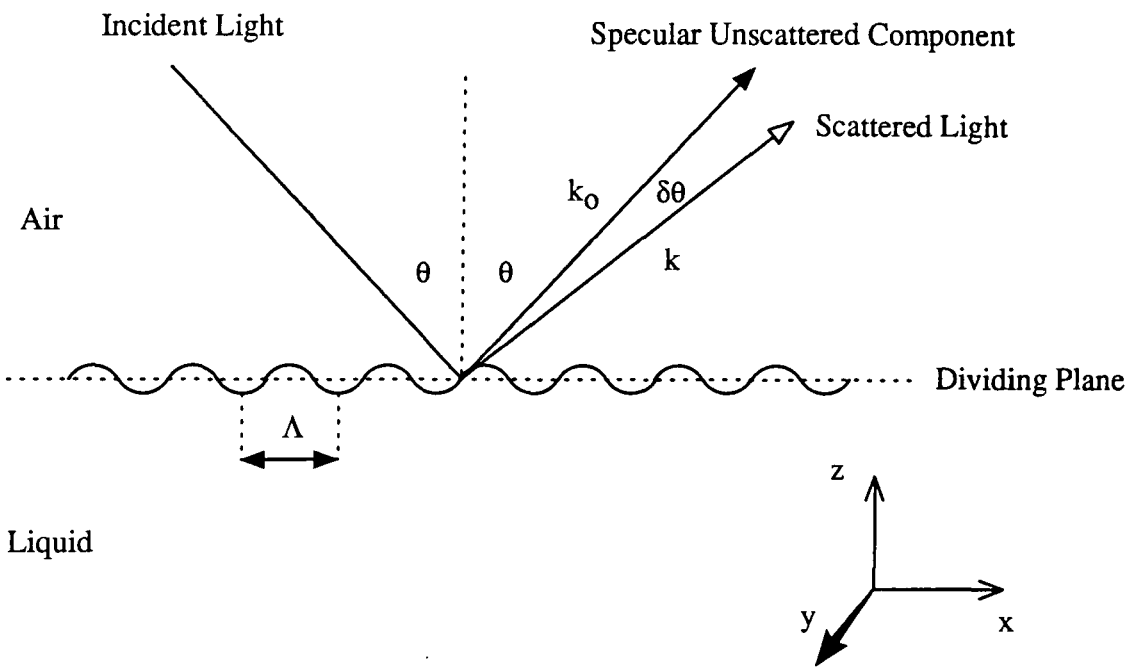

Figure 2.1 Light Scattered by Thermally Induced Ripples

1.4.2 The Dispersion Relationship for Capillary Waves

It is a matter of choice in studying light scattering events to examine either the spatial power spectrum of the scattered light as a function of real frequency or to measure the time domain correlation function which is the Fourier transform of the spatial power spectrum. Previous workers have increasingly favoured the latter method as methods of rapid photo-correlation detection have been developed to enable convenient time domain experiments to be carried out.

For the case of time domain spectral analysis of scattered light, a real ripplon wavenumber q is studied and the frequency ω is considered as complex;

$$\omega = \omega_0 + i\Gamma \qquad 1.39$$

where ω_0 is the propagation frequency and Γ is the time domain damping constant.

ω is related to q through a dispersion relationship which additionally introduces terms in the visco-elastic properties of the liquid at the interface. The classically accepted form of the dispersion expression $D(\omega)$ for simple liquid surfaces is that of Lamb[36] and Levich[37]

$$D(\omega) = (i\omega + 2\nu q^2)^2 + gq + \gamma q^3/\rho - 4\nu^2 q^3 (q^2 + i\omega/\nu)^{1/2} = 0 \qquad 1.40$$

where γ = surface tension,

ν = kinematic viscosity = η/ρ,

g = gravitational acceleration,

and ρ = density of the liquid.

For sufficiently short surface wavelengths, the gravitational term may be neglected, and by extraction of the following reduced variables

$$S = i\omega/2\nu q^2 \qquad 1.41$$

and

$$Y = \gamma/4\nu^2\rho q^2 = \gamma\rho/4\eta^2 q \qquad 1.42$$

the dispersion relationship may be rewritten

$$D(S) = (S + 1)^2 + Y - (2S + 1)^{1/2} = 0 \qquad 1.43$$

The reduced group Y represents the balance between driving forces and dissipative forces in wave propagation,

$$Y = \frac{\text{restoring force} \times \text{inertial force}}{(\text{damping force})^2} \qquad 1.44$$

Numerical solutions of 1.41 show that for $Y > 0.145$ the roots are complex conjugate, corresponding to propagating capillary modes. Below this value however damping dominates, two real roots are found, corresponding to overdamping of surface motions. This theoretical prediction has been borne out experimentally[38]. A first order approximation to the solution of 1.40 yields an expression for the wave frequency in the propagation mode,

$$\omega_o^2 = \gamma q^3/\rho \qquad 1.45$$

and a proportional dependence of the wave damping to the liquid viscosity,

$$\Gamma = 2\nu q^2 \qquad 1.46$$

ie $$\omega = \omega_o + i\Gamma = (\gamma q^3/\rho)^{1/2} + i2\nu q^2 \qquad 1.47$$

In the overdamped modes the damping constant are given by

$$\Gamma_1 = \nu q^2 \qquad 1.48$$

and $$\Gamma_2 = \gamma q/2\eta \qquad 1.49$$

These approximate solutions only agree with the exact solutions of 1.40 rather far from Y_{crit} (= 0.145), and higher order approximations have been derived, however the dispersion equation can be more conveniently solved using numerical methods.

It has been suggested[39,40] that specific surface visco-elastic properties, different from bulk fluid properties might affect surface wave propagation. Interfacial viscosities arising from various shear modes might be readily imagined, however the propagation of transverse capillary waves would be predominantly influenced by a surface viscosity governing response to an applied shear stress normal to the surface. This is the transverse shear viscosity and forms the imaginary part of the surface tension modulus, γ

$$\gamma = \gamma_o + i\omega\gamma' \qquad 1.50$$

where γ_o is the classical surface tension.

The effect of the complex term in 1.50 is to increase the dissipative influence in the balance of propagation and damping. Substituting 1.50 in 1.47 yields

$$\omega = [(\gamma_o + i\omega\gamma')q^3/\rho]^{1/2} + 2i\nu q^2$$

$$\approx (\gamma_o q^3/\rho)^{1/2} + i[2\nu q^2 + \gamma' q^3/2\rho] \qquad 1.51$$

This then predicts that the transition from propagating to overdamped modes will occur at a slightly lower value of q from that predicted in the absence of surface specific visco-elastic effects.

1.4.3 The Power Spectrum and the Correlation Function

The power spectrum describing the dependence of the scatter in the spatial dimension has been obtained by Bouchiat and Meunier[41];

$$P(\omega) = -k_BT/(\pi\omega).(\rho/4\eta^2q^3)Im\{1/D(S)\} \qquad 1.52$$

This spectrum is approximately Lorentzian in form and is characterised by a peak frequency f_s and linewidth (full width at half peak height) Δf_s which can be identified with ω_o and Γ by extraction from the dispersion equation D(S) present in 1.52.

The concept of photon correlation techniques is to measure the correlation function $g(\tau)$ in the time domain, which is simply the Fourier transform of $P(\omega)$, however in practice certain instrumental broadening factors have to be included in the expression for $g(\tau)$. These are discussed in section 1.4.7.

1.4.4 The Dispersion Relationship and Power Spectrum for a Monolayer Spread Liquid Surface

The presence of a monolayer on the surface of a liquid modifies the dispersion relationship $D(\omega)$ by introducing explicit terms in the physical properties of the monolayer. The modified form is[42,43]

$$D(\omega) = [\epsilon q^2+i\omega\eta(q+m)] \times [\gamma q^2+i\omega\eta(q+m)-\omega^2\rho/q] - [i\omega\eta(q-m)]^2 = 0 \qquad 1.53$$

where $m = (q^2 + i\omega\rho/\eta)^{1/2}$, $Re(m) > 0$, and $\epsilon = d\gamma/dln(A)$ is the dilational modulus of the monolayer, where A is the molecular area in the film.

The form of the power spectrum arising from capillary propagations governed by $D(\omega)$ in this case is[42]

$$P(\omega) = -k_BT/\pi\omega \,.\, Im[i\omega\eta(q + m) + \epsilon q^2) / D(\omega)] \qquad 1.54$$

Again this spectrum is approximately Lorentzian in form, although the

deviation from true Lorentzian form is well known[44,45].

1.4.5 Interfacial Viscolelastic Properties

As previously mentioned, for the case of a simple liquid film, it is the rheological properties of the fluid in the interfacial region which determine the propagation and/or damping of the temporal evolution of surface capillary modes. For monolayers on liquid surfaces the situation is complicated by the viscous effects of the film material.

In (x - z) plane hydrostatic compression of the film, K, and uniaxial in - plane strain, described by the shear modulus S, are summed in the dilational modulus ϵ,

$$\epsilon = K + S \qquad 1.55$$

In most cases S is negligible compared with K. Both the dilational modulus and the surface tension may be expanded to include complex viscous terms;

$$\gamma = \gamma_o + i\omega\gamma' \qquad 1.56$$

$$\epsilon = \epsilon_o + i\omega\epsilon' \qquad 1.57$$

γ_o and ϵ_o are elastic moduli describing the response of the system to transverse shear and dilation within the plane of the interface respectively. (1.56) is the same form as (1.50) for the case of a simple liquid. γ' and ϵ' are the surface viscous terms corresponding to these two perturbations, as distinct from the classical surface viscosity which refers to *in-plane* shear.

1.4.6 Experimental Considerations for Heterodyne Beat Spectroscopy

Due to the weak nature of surface scattering effects, modern SQELS

experiments are carried out using heterodyne mixing methods, where a reference beam of known q generated by a transmission diffraction grating is mixed with the detected scattered light. Given certain conditions the sensitivity of the technique is greatly increased by these means.

The measured auto-correlation function $G(\tau)$ obtained from a heterodyne mixture of scattered and reference fields of intensity I_s and I_r respectively is

$$G(\tau) = (I_s + I_r)^2 + I_s^2[g^{(2)}(\tau) - 1] + 2I_sI_rg^{(1)}(\tau) \qquad 1.58$$

where $g^{(1)}(\tau)$ and $g^{(2)}(\tau)$ are the first and second order correlation functions of the scattered field. Provided that I_r is sufficiently greater than I_s ($I_{r/Is} > 30$ is an accepted value) then the first order term $2I_sI_rg^{(1)}(\tau)$ dominates the expression for $G(\tau)$[46]. Earnshaw and co-workers[47,48] typically used an I_r/I_s ratio of 100 - 1000.

The accurate determination of the experimental q value is an important consideration in understanding the results of a scattering experiment. q is the component of the scattering vector *parallel* to the liquid surface and is given to a good approximation by

$$q = 4\pi/\lambda.\sin(\delta\theta_n/2).\cos\theta \qquad 1.59$$

where θ is the angle of incidence and $\delta\theta_n$ is the angular separation from the zero-order beam of the n^{th} diffracted beam.

1.4.7 Methods of Data Fitting

As previously alluded to, the measured correlation function is essentially the Fourier transform of the power spectrum of the thermally excited waves,

$$G(\tau) = g(\tau) = FT(P(\omega)) \qquad 1.60$$

In practice it is necessary to modify the form of the function used to fit $G(\tau)$ to include terms for instrumental broadening and background effects, and for the deviation of the spectrum from a true Lorentzian form. Earnshaw and

co-workers[47,49] employed the following expression

$$G(\tau) = B + A\cos(\omega_o\tau + \varphi)\exp(-\Gamma\tau) \times \exp(-\beta^2\tau^2/4) \qquad 1.61$$

where A is an amplitude factor, B represents the instrumental background (principally due to I_r), φ is a phase term accounting for non-Lorentzian behaviour and the Gaussian multiplicative term in β represents the instrumental line broadening. Earnshaw and McGivern found that this factor only affected the shape of the function significantly at q values greater than $700cm^{-1}$. 1.61 then is an expression containing explicitly the capillary wave frequency ω_o and the wave damping Γ. A best fit to the experimental data using a function of the form of 1.61 yields values of ω_o and Γ which may be related to the surface film visco-elastic properties via the dispersion equation.

In applying this method Earnshaw and co-workers advocated a non-weighted fitting procedure where the values of the function at all delay times $G(\tau_2)$ to $G(\tau_{128})$ (for a 128 channel correlator) were given equal importance. Additionally $G(\tau_1)$ was excluded to avoid dead-time effects in detection. Mann and Edwards[50] suggested a weighted fitting procedure to avoid bias in the fitted value of Γ but Earnshaw and McGivern argued that since the modulation of $G(\tau)$ represented a tiny perturbation on a large background that the statistical errors and hence the weights would be dependent predominantly on I_r and would thus be independent of τ.

Around the same time as Earnshaw and McGivern published the above analysis, Hård and Neuman[51] published critical comments on Earnshaw's treatment. Hård and Neuman attributed bias in the fitted parameters to the fitting procedures used to analyse $G(\tau)$, and criticised the full form of 1.61 as an over-complicated fitting expression which led to systematic over-estimates in experimental parameter values. In an attempt to resolve the issue of bias in data analysis Earnshaw and McGivern[52] responded with a consideration of various

alternative fitting procedures used to estimate interfacial parameters for free liquid films. Four models were compared with regard to the bias found in estimates of ω_o, Γ, γ_o and η generated from them. The four models used were;

a) a simple Fourier transform of a Lorentzian $P(\omega)$ as used in earlier studies[51,53] with a background addition

$$G(\tau) = B + A\cos(\omega_o\tau)\exp(-\Gamma\tau);$$

b) the Fourier transform of a modified Lorentzian $P(\omega)$ to include the phase term for non-Lorentzian behaviour

$$G(\tau) = B + A\cos(\omega_o\tau + \varphi)\exp(-\Gamma\tau);$$

c) the full form of 1.61 including the Gaussian instrumental broadening term;

d) an exact form of the Fourier transform of $P(\omega)$

$$f(\tau) = g(\tau)[1 + \lambda g(\tau)/g(0)]$$

where $g(\tau) = FT[P(\omega|\gamma,\eta)]$

and λ describes self-beat contributions due to inadequate heterodyne reference intensity.

Using the exhaustive model D to obtain non-biased values, Earnshaw and McGivern were able to demonstrate clearly that only the full form of 1.61 was capable of yielding non-biased estimates for the interfacial parameters for water over a range of q values from 300 to 1500cm^{-1}. Since that time however Earnshaw has advocated the use of the rigorous "direct" analysis method (method (d) above) in data interpretation.

1.5 Review of Studies of Monolayers and related topics

1.5.1 Surface Pressure Measurements

It has been noticed since ancient times that oils spread on water have intriguing properties[54]. The ancients attributed the multi-coloured swirling patterns observed to their gods, but it has only been in more recent times that a scientific interest has been taken in such phenomena. The earliest recorded observation of wave damping by oil on water was by Benjamin Franklin, who described in a letter to the Royal Society of London in 1765[55] how he had calmed an area of half an acre on a pond on Clapham Common. The pioneer of modern studies on monolayer systems however was Irving Langmuir who published details of his studies into the nature of monolayers of fatty acids, alcohols and esters on aqueous subphases in 1917.[56] Langmuir worked in conjunction with Katherine Blodgett, who developed the technique of lifting monolayers onto solid glass substrates for further examination or processing,[57] the so called Langmuir-Blodgett or L-B technique.

Since the time of Langmuir and Blodgett, an extensive body of work on the experimental study of monolayers and L-B films has been published.[58] The properties of spread films of many amphiphilic materials have been examined in great detail and the techniques of trough design and the preparation and lifting of L-B films have been greatly refined, principally in the introduction of convenient methods of automation of trough and dipping mechanisms and the automatic continuous recording of surface pressure data.

One group of materials to have received a considerable amount of attention has been polymeric films. The earliest attempts to investigate macromolecular films were on cellulose derivatives[59,60,61] and polyesters[62]. Even at this early stage the possibility of using monolayer techniques to study the surface

chemistry of natural macromolecules such as polypeptides and proteins was recognised[63-66] and a considerable concentration of effort has gone into this field since. A more systematic approach however has been the study of films of synthetic polymers. The earliest studies are described by Crisp.[3,4] Crisp later reviewed the field of research into macromolecular interfacial films towards the end of the nineteen fifties[67]. From around that time however there was something of a dearth of activity in the technique. This may have been for many reasons, however it seems that the limit of the technique had been reached in terms of theoretical understanding of the experimental results.

The classical interpretation of surface pressure data[3] has been to draw analogies with three dimensional phases. Depending on the rate of change of surface pressure with the decrease in area per molecule (reflecting the interactions between molecules in the layer; how far apart they are and how easily they can move for example) the film behaviour has been described as gaseous, liquid expanded or condensed, or solid. For non-polymeric materials such as long chain acids and surfactants the transitions between these phases are well observed. At very large areas per molecule very little or no surface pressure is discernible. As the film is compressed, at some point the molecules are brought closer together so that they begin to feel some influence from each other. The result is an increase in the surface pressure, corresponding to the transition to liquid film behaviour. Liquid films are divided into two categories, expanded and condensed. For an expanded type film the initial rise in the surface pressure is observed at a larger area per molecule than for a condensed film, and the rate of increase is generally more gradual. As the film is further compressed the molecules are eventually brought so close together that further compression becomes very difficult. The film becomes very stiff and the surface pressure rapidly increases in this solid phase and if the film is compressed beyond a certain point, catastrophic collapse occurs, accompanied by a sudden fall

in the surface pressure as molecules distort out of the plane of the layer. Alternatively, particularly for the more flexible, expanded type films, the surface pressure value may plateau in the high concentration (low area per molecule) region as molecules dip into the subphase or are excluded into bulk solution.

For surfactants it is relatively straightforward to rationalise these phase changes in terms of the orientation of the molecules and intermolecular distances, however for polymer films the macromolecular nature of the spread materials makes the situation rather less straightforward. The limiting area per molecule (extrapolated from the initial slope of the liquid region of the isotherm) has long been used to infer the nature of packing of molecules at the surface but the potential for statistical distributions of chain configurations, long recognised in three dimensional polymer solutions, makes the simple arguments employed in the description of fatty acid type films much less useful. There have been very few attempts to rationalise the measured behaviour of polymer films with their structure with the exception of Shuler and Zisman[68] who used surface pressure and physically induced wave damping techniques to argue for the existence of two distinct conformations of poly (ethylene oxide) associated with the presence of bound water molecules along the chain, depending on the degree to which the chain was compressed. Nevertheless, a great many polymer films have been studied and classified as either (liquid) expanded or condensed types. Among the former are poly (vinyl acetate),[4,69-73] poly (2-vinyl pyridine),[74] poly (ethylene oxide),[68] poly (propylene oxide) and poly (vinyl alkyl ethers)[75]. Among the latter are poly (methyl methacrylate),[76,77] and poly (vinyl benzoate).[78] Systematic trends in some homologous series of polymers have been noted. For example, in the poly (alkyl acrylates) a trend of increasingly expanded behaviour is observed with increasing alkyl group size from methyl to butyl.[3,4] A similar result was obtained for poly (alkyl methacrylates).[4]

Recent years have seen a revival in interest in monomolecular polymer film studies, primarily due to the development of new theoretical approaches to the prediction and interpretation of experimental results by Daoud and Jannink.[14] Briefly recapping, these predict that polymer films will observe three regions of behaviour depending on the segment density on the surface. In the dilute regime, where the surface concentration is less than a critical Γ^* value, the relationship between the surface pressure and the concentration should scale according to an exponent ν. In the semi-dilute regime, $\Gamma^* > \Gamma > \Gamma^{**}$, this exponent is altered to a function of ν, $y = 2\nu/(2\nu-1)$. Above Γ^{**}, a concentrated regime is predicted where an exponential dependence to the power 101 is predicted. This however is not observed experimentally due to the contribution of other effects such as broad looping out of the layer and ultimately collapse.

Many theoretical predictions for the value of the ν exponent have been made based on a variety of mathematical models for the system. These have been discussed in section 1.1. The ν exponent is of importance as it is characteristic of the thermodynamic state of the interaction between the polymer segments and the subphase. Theoretical predictions agree on a value of $\nu=0.77$ for the case of good 2-D solvent conditions, however there is a greater variety of predictions for the theta state. ν_θ is variously predicted between about 0.505 - 0.59, compared with a collapse value of 0.5. A value of around 0.56 is generally thought to be approximately correct.

The first attempts to apply these scaling concepts to experimental data was made by Ober and Vilanove[79] in 1977. In a study of poly (vinyl acetate) monolayers they were able to demonstrate deviations from the mean field type predictions previously developed, and so modified the two dimensional solution model by allowing a fraction of the monomer segments to exist away from the lattice defined by the interface.

In 1980, Vilanove and Rondelez[80] made use of the scaling laws to characterise polymer film thermodynamics for the first time from surface pressure data at rather higher surface concentrations, where experimental difficulties associated with the measurement of extremely low pressures were avoided. Previous equation of state methods required isolated chain conditions, but from the scaling relationships governing the semi-dilute regime, Vilanove and Rondelez were able to extract values for the characteristic scaling exponent ν governing the relationship between the radius of gyration and the degree of polymerisation. For poly (vinyl actetate) ν was equal to 0.79 and for poly (methyl methacrylate) the value was 0.56. The former value is that predicted for good, excluded volume type behaviour, while the latter tends towards the predictions for a theta type two dimensional solution. Additionally the authors were able to observe the transition between dilute and semi-dilute behaviour for PMMA, noting that when plotted on double logarithmic axes below Γ^* the data showed molecular weight dependence, but that above Γ^* the data for all molecular weights collapsed onto a single line, the slope of which was related to the scaling exponent by the relationship $y = 2\nu/(2\nu-1)$.

Takahashi, Yoshida and Kawaguchi[81,82] made use of the equation of state in the dilute regime to determine the theta temperature for poly (methyl acrylate) monolayers. By plotting $\pi/\Gamma RT$ as a function of Γ at $\Gamma < \Gamma^*$ and observing the initial slope at various temperatures they were able to extract the molecular weight from the extrapolation to zero concentration and the two dimensional second virial coefficient $A_{2,2}$ from the slope. This was found to reduce to zero at 18.2°C. The equivalent data in the semi-dilute regime was in complete agreement with the low concentration observations. At temperatures higher than the theta temperature, a slope of 2.85 corresponding to $\nu = 0.77$ was obtained, but at the theta temperature this slope became 35, for which $\nu = 0.51$, very close to the lowest theoretical prediction of $\nu = 0.505$. However in 1988 Vilanove, Poupinet and Rondelez[83]

contradicted these observations when they stated that they were unable to observe any theta state for poly (methyl acrylate) and indeed observed good solution conditions independent of temperature between 5 and 30°C.

In the same paper, Vilanove *et al* reconsidered the case of poly (methyl methacrylate) which they had previously observed to yield a v value of 0.56. In the later experiments over a range of temperatures from 1 to 35°C they found that for two widely different molecular weights, their data agreed on a value of $v = 0.53$ ($y \approx 16.5$). From the equation of state plot in the dilute regime they observed a *negative* slope for both polymers, corresponding to a negative second virial coefficient and less than theta conditions. This then was evidence for a v_θ value significantly higher than 0.505.

For lower molecular weight PMMA samples, Poupinet, Vilanove and Rondelez[84] observed a higher value of v, equal to 0.57, the difference being put down to the fact that the scaling predictions are made on the basis of infinite molecular weights. It is possible however that insufficient consideration of the stereotactic sequences in the earlier samples could have led to misleading results. Since very early work in the field,[76,77] the very different surface properties of spread films of syndiotactic and isotactic PMMA have been noted. Syndiotactic PMMA forms a liquid condensed type film but the isotactic polymer forms a liquid expanded type film. It is possible therefore that a degree of dissimilarity in the stereo sequences found in the various samples could have a significant effect on the structural properties of the film.

1.5.2 Charged Monolayers

Charge effects in ionised monolayers have been recognised for many years.[85] Davies[86] expressed the measured surface pressure π as a sum of

contributions from the equivalent uncharged film π_o and an electrical contribution π_e. Due to the fact that fully ionised poly-electrolyte materials are typically water soluble and unable to form stable films, most studies were confined to surfactants such as fatty acids.[87,88] Various methods have been attempted to avoid the problems associated with poly-electrolytes. The use of polyampholytes[89] for which the degree of ionisation can be controlled by adjusting the pH of the subphase, and random copolymers of charged and neutral monomers[90] have been reported, but a more recent approach is that of Bringuier *et al*[91] who studied diblock copolymers of an uncharged sequence, poly (methyl methacrylate) with the quaternary pyridinium bromide salt of poly (4-vinyl pyridine). By studying a range of polymer compositions and molecular weights, and comparing the surface pressures obtained from equivalent PMMA homopolymers (π_o) and PMMA-4VPQ diblock copolymers (π), they were able to demonstrate the existence of an electrical contribution π_e. They also demonstrated that on the addition of salt into the subphase water, the π_e contribution was diminished and at a salt solution concentration of greater than 0.1M, the electrical contribution disappeared entirely. Curiously however, the authors did not compare the behaviour of the quaternised diblock materials with their non-ionised PMMA-4VP equivalents, from which it would seem logical that another estimate of π_e could be made.

1.5.3 Ellipsometry

In 1964 Zaininger and Revesz[33] reported on the state of the art of ellipsometry as it stood at that time. The relevant optical theories were well understood and established, but experimental efforts had been exclusively in areas where highly favourable refractive index contrast conditions occurred. These tended to be studies of interfaces of solid materials, for example semi-conductors and

conductors,[92,93] liquid metal surfaces,[94] or examinations of the adsorption of materials onto solid substrates, for example water and organic liquids onto single crystal silicon and polystyrene onto chromium[95]. At that time ellipsometry was perceived as having most potential as an in situ probe for the examination of deposition, growth and dissolution processes of films from the liquid or gas phase. Some considerable effort had gone into the study of oxidation processes in metals but otherwise very little experimental progress appears to have been made.

By the later years of the 1960's Stromberg and co-workers had turned their attention towards the problem of polymer adsorption at solution-solid interfaces. Systems studied included the adsorption of polystyrene, poly(ethylene-o-phthalate) and various proteins onto chromium, gold, steel, or copper substrates.[96,97,98] McCrackin developed experimental methods for the study of these systems[99] and theoretical chain distribution models to try and rationalise experimental observations.[100]

In 1974 den Englesen and Konig demonstrated the applicability of ellipsometry for the study of monolayers spread on water by investigating spread films of a series of fatty acids and triglycerides[101] and light-absorbing biological type monolayers,[102] for example chlorophyll.

Some attempts were made to apply ellipsometry in the areas of surface active biological materials[103,104] and synthetic polymers[105,106] adsorbed from solution at the air-solution interface, long chain acid monolayers,[107] and interfacial effects in an organic liquid,[108] but in general the much smaller refractive index differences between the film and the subphase made the technique rather more difficult than was the case for solid substrates.

Nevertheless in 1988 Kawaguchi and co-workers published a pair of papers[109,110] describing ellipsometric measurements on spread monolayers of a series of polymers of expanded and condensed type, the former including

poly(ethylene oxide), and poly(vinyl acetate), and the latter poly(methyl methacrylate). These experiments demonstrated both the sensitivity and limitations of ellipsometry in the study of air-liquid interfacial films. Reference (109) used the experimental sensitivity in the phase retardation to estimate the film thickness, d as a function of surface concentration, and reference (110) claimed to calculate the refractive index of the film, n and hence the adsorbed amount. However the basis of independent determination of d and n by ellipsometry must be a sensitivity to *both* the measured parameters, the phase retardation and the amplitude attenuation. In reference (109), the authors admitted that the amplitude attenuation only exceeded experimental errors for high surface concentrations for two of the five polymers studied, poly tetrahydrofuran and poly (vinyl acetate). In all other cases the change in amplitude attenuation was essentially zero, therefore it is very difficult to justify the authors' claims to have calculated both d and n uniquely. It is perhaps more realistic to suggest that given a reasonable estimate in one parameter, ellipsometry may be used to determine the other.

In reference (110), the possible use of a Lorentz-Lorenz type relation was proposed for the estimation of n given that one knew the values of the refractive indices of polymer and subphase or air. Thus an estimate of d_1 and the adsorbed amount could be made by solving the Drude equation. The question of data analysis was addressed by Sauer *et al*[111]in a study of a polystyrene-poly(ethylene oxide) diblock copolymer and homo-poly(ethylene oxide). They used two approaches to data analysis, the Lorentz-Lorenz type macroscopic approach of weighted averaging of n to obtain d, and microscopic theories[93,107,112,113] which predict a linear dependence of the phase retardation on the fractional coverage of the surface. By neglecting PEO segment contributions, they constructed a model of the surface as partially covered with PS blobs which became squashed together on increasing the surface concentration.

The same group subsequently published a summary of their ellipsometric studies on polymeric monolayers including PEO, and PMMA.[114] In this case there was little to choose between the quality of data fitting obtained by use of a macroscopic or microscopic model, however Lorentz-Lorenz modelling using a weighted average refractive index between that of the polymer and the subphase was successfully used to fit the results, and the parameters obtained suggested that the films were well hydrated by the subphase.

1.5.4 Surface Quasi-Elastic Light Scattering

The experimental technique variously known as surface fluctuation spectroscopy, surface photon correlation spectroscopy or surface quasi-elastic light scattering has been greatly developed over the last fifteen years or so, although perhaps the earliest substantial review of the area was undertaken by Vrij.[115] Vrij acknowledged the earliest predictions of the presence of distinct *surface* scattering in addition to bulk scattering in colloidal solutions, caused by thermally induced surface corrugations, as described by Von Smoluchowski[116] and calculated by Mandlestam[117] to have an inverse square dependence on the light wavelength λ rather then the λ^{-4} dependence of bulk Rayleigh scattering. This prediction was quantitatively confirmed by Raman and Ramdas[118,119]. Vrij developed a theory for the scattering of light from soap films of a light beam polarised normal to the plane of incidence and presented some limited experimental results to support his interpretation of interfacial corrugations dependent on the balance of electrostatic and Wan der Waal's stabilizing forces in the films. The experimental data presented were rather preliminary in nature (one of the samples used being the laboratory cleaner Teepol!) and further experimental progress was hindered by the optical technology available at that time.

The development of laser optics increased the practicality of surface light scattering and in 1967 Katyl and Ingard[120] were first able to demonstrate spectral modification of light scattered by a liquid surface. Further experimental work at that time led to resolution of the spectral data in both the frequency and time domains[121,122], the existence of two distinct modes of capillary evolution, termed propagating and overdamped, was confirmed[113], and the validity of the dispersion relation was verified[123,124]. Systematic deviations from the previously expounded harmonic oscillator type spectrum were noted[125] and accounted for in an amended theory published in 1971.[126]

A major experimental advance in the detection of the small frequency shifts caused by surface fluctuations was the use of a diffraction grating by Hård *et al*[127] as a local oscillator for the generation of heterodyne beat signal enabling simultaneous detection of scattered and reference intensity at the same wavenumber value. The technique was developed for time domain surface correlation methods by Byrne and Earnshaw[128-130] and later Hård and Neuman[51] improved the experimental aspects of the technique by placing the grating before the liquid surface and re-focussing the diffraction spots on the surface. Thus local beam mixing was achieved by a method which minimises changes in experimental geometry and provides a convenient method for the selection of the wave number studied (according to the diffraction order selected for detection). In addition, problems caused by curvature in the liquid surface near the meniscus edges were minimised, surface cleaning by barrier sweeping was simplified, and the technique was rendered suitable for use at physically inaccessible surfaces. This method has been recognised as the preferred design and has been used subsequently with much success[131-133], including a reported method for ultra-fast data acquisition by Winch and Earnshaw[134,135].

Surface light scattering has now been applied to the study of both simple

liquids such as water[47,52,130,132], ethanol[47,131,132], glycerine[130], and anisole[132], and to liquids covered with monolayers of fatty acids[52,130,136-138], monoglycerides[133,139], and polymers[140-145].

In this last category Yu and co-workers have studied a range of materials including poly(vinyl acetate)[140,142,144,145], poly(ethylene oxide)[142-144], and poly(methyl methacrylate)[144]. Their studies have been carried out in the frequency domain, measuring the spectral peak frequency and line width as a function of surface concentration. They applied a form of direct data analysis in an attempt to overcome the familiar problem of trying to fit four viscoelastic parameters to two experimentally measurable quantities, by modelling a Lorentzian form from the dispersion relation for a selected set of film parameters until the observed frequency and line width were reproduced to within arbritrary limits. They were able to demonstrate that polymer monolayers demonstrated dynamic viscoelastic properties, and that condensed monolayers such as poly(methyl methacrylate) in particular possessed considerable longitudinal elasticity and viscosity, and that there was a significant difference between the static and dynamic surface pressures for this material.

References

1. Alexander,A.E., Hibbard, G.E., *Determination of Properties of Insoluble Monolayers at Mobile Interfaces*, in *Techniques of Chemistry*, Weissberger, A., Rossiter, T., Eds., Vol. 1, Part V, Interscience, New York.
2. Alexander,A.E., Hibbard, G.E., *Determination of Properties of Insoluble Monolayers at Mobile Interfaces*, in *Techniques of Chemistry*, Weissberger, A., Rossiter, T., Eds., Vol 1, Part IIIB, Interscience, New York.
3. Crisp, D.J., *J. Colloid Sci.*, **1**, 49, 1946.
4. Crisp, D.J., *J. Colloid Sci.*, **1**, 161, 1946.
5. Singer, S.J., *J. Chem. Phys.*, **16**, 872, 1948.
6. Huggins, M.L., *J. Phys. Chem.*, **46**, 151, 1942.
7. Davies, J.T., *J. Colloid Sci., Suppl.*, **No.1**, 9, 1955.
8. Kawai, T., *J. Polymer Sci.*, **35**, 401, 1959.
9. Frisch, H.L., Simha, R., *J. Chem. Phys.*, **24**, 652, 1956.
10. Frisch, H.L., Simha, R., *J. Chem. Phys.*, **27**, 702, 1957.
11. Saraga, L., Prigogine, I., *Mem. Serv. Chim. Etat. (Paris)*, **38**, 109, 1953.
12. Flory, P.J., *J. Chem. Phys.*, **13**, 453, 1945.
13. de Gennes, P.G., *Scaling Concepts in Polymer Physics*, Cornell Univ. Press, Ithaca, New York, 1979.
14. Daoud, M., Jannink, G., *J. Phys. (Paris)*, **37**, 973, 1976.
15. des Cloizeaux, J., *J. Phys. (Paris)*, **36**, 281, 1975.
16. Marqusee, J.A., Deutch, J.M., *J. Chem. Phys.*, **75**, 5179, 1981.
17. Le Guillou, J.C., Zinn-Justin, J., *Phys. Rev. Lett.*, **39**, 95, 1977.
18. Le Guillou, J.C., Zinn-Justin, J., *Phys. Rev. B*, **21**, 3976, 1980.
19. Stephen, M.J., McCauley, J., *Phys. Lett.*, **A44**, 89, 1973.
20. Stephen, M.J., *J. Phys. Lett.*, **A53**, 363, 1975.

21. Grassberger, P.Z., *Phys. B: Condens. Matter*, **48**, 255, 1982.

22. Djordjovic, L.V., Majid, I., Stanley, H.E., Dos Santos, R.J., *J. Phys. A: Math. Gen.*, **16**, L-519, 1983.

23. Havlin, S., Ben Avraham, D., *Phys. Rev. A.*, **27**, 2759, 1983.

24. Derrida, B., *J. Phys. A: Math. Gen.*, **14**, L-5, 1981.

25. Baumgartner, A., *J. Phys. (Les Ulis Fr.)*, **43**, 1407, 1982.

26. Birshtein, T.M., Buldyrev, S.V., Elyashevitch, A.M., *Polymer*, **26**, 1814, 1985.

27. Kremer, K., Lyklema, J.W., *J.Phys. A: Math. Gen.*, **18**, 1515, 1985.

28. Kremer, K., Lyklema, J.W., *Phys. Rev. Lett*, **54**, 267, 1985.

29. Dekeyser, R., Maritan, A., Stella, A.L., *J. Chem. Phys.*, **83**, 912, 1985.

30. Douglas, J.F., Cherayil, B.J., Freed, K.F., *Macromolecules*, **18**, 2455, 1985.

31. Derrida, B., Saleur, H., *J. Phys. A: Math. Gen.*, **18**, L-1075, 1985.

32. Mingins, J., Owens, N.F., *Thin Solid Films*, **152**, 9, 1987.

33. Zaininger, K.H., Revesz, A.G., *Ellipsometry - A valuable tool in surface research*, in *RCA Review*, Princetown, New Jersey, 1964.

34. Born, M., Wolf, E., *Principles of Optics*, Pergamon Press, Oxford, 1970.

35. Earnshaw, J.C., *Light Scattering at the Fluid Interface*, in *Fluid Interfacial Phenomena*, Croxton, C.A., Ed., John Wiley & Sons, 1986.

36. Lamb, H., p. 627 in *Hydrodynamics*, 6th Ed., New York, 1945.

37. Levich, V.G., p. 603 in *Physico chemical Hydrodynamics*, Prentice-Hall, Englewood Cliffs, New Jersey, 1962.

38. Huang, J.S., Webb, W.W., *Phys. Rev. Letts.*, **23**, 160, 1969.

39. Tejero, C.F., Rodriguez, M.J., Baus, M., *Phys. Letts.*, **98A**, 371, 1983.

40. Goodrich, F.C., *Proc. R. Soc.*, **A 374**, 341, 1981.

41. Bouchiat, M.A., Meunier, J., *J. Physique*, **32**, 561, 1971

42. Langevin, D., Meunier, J., Chatenay, D., *Surfactants in Solution*, Eds. Mittal, K.L., Lindman, B., Plenum, New York, **3**, 1991, 1984.

43. Lucassen-Reynders, E.H., Lucassen, J., *Adv. Colloid. Int. Sci.*, **114**, 330, 1969.

44. Wu, E.S., Webb, W.W., Phys. Rev., **A 8**, 2077, 1973.

45. Bouchiat, M.-A., Langevin, D., *C. R. Hebd. Séan. Acad. Sci.*, **B 272**, 1357, 1971.

46. Oliver, C.J., pp 151-223 in *Photon Correlation and Light Beating Spectroscopy*, eds. Cummins, H.Z., Pike E.R., Plenum, New York, 1974.

47. Earnshaw, J.C., McGivern, R.C., *J. Phys. D: Appl. Phys.*, **20**, 82, 1987.

48. Earnshaw, J.C., McGivern, R.C., Winch, P.J., *J. Phys. France*, **49**, 1271, 1988.

49. Crilly, J.F., Earnshaw, J.C., *J. Phys. D: Appl. Phys.*, **18**, 609, 1985.

50. Mann, J.A., Edwards, R.V., *Rev. Sci. Instrum.*, **55**, 727, 1984.

51. Hård, S., and Neuman, R.D., *J. Colloid. Int. Sci.*, **115**, 73, 1987.

52. Earnshaw, J.C., McGivern, R.C., *J. Colloid, Int. Sci.*, **123**, 36, 1988.

53. Hård, S., Neuman, R.D., *J. Colloid. Int. Sci.*, **83**, 315, 1981.

54. Adam, N.K., *The Physics and Chemistry of Surfaces*, Oxford University Press, London, 1941.

55. Franklin, B., *Philosophical Transactions of the Royal Society*, **64**, 445, 1774.

56. Langmuir, I. *J. Amer. Chem. Soc.*, **39**, 1848, 1917.

57. Blodgett, K.B., Physical Review, **55**, 391, 1939.

58. The following reviews contain many examples;

Harkins, W.D., *The Physical Chemistry of Surface Films*, Rheinhold, New York, 1952.

Gaines G.L. Jr., *Insoluble Monolayers at gas liquid interfaces*, Interscience New York, 1966.

Roberts G.G., *Advances in Physics*, **34**, 475, 1985.

Peterson I.R., *Journal of Molecular Electronics*, **3**, 103, 1987.

Langmuir-Blodgett Films 3, Vols I and II, Mobius, D., Ed., (Reprinted from *Thin Solid Films*, 159-160, 1989) Elsevier, London and New York.

59. Katz, J.R., Samwell, P.J.P., *Ann. Chem.*, **72**, 241, 1929.

60. Katz, J.R., Samwell, P.J.P., *Ann. Chem.*, **474**, 296, 1929.

61. Adam, N.K., *Trans. Faraday Soc.*, **29**, 90, 1933.

62. Harkins, W.D., Carman, E.F., Ries, H.E. Jr., *J. Chem. Phys.*, **3**, 692, 1935.

63. Gorter, E., Grendel, F., *Trans. Faraday Soc.*, **22**, 477, 1926.

64. Hughes, A. H., Rideal, E.K., *Proc. Roy. Soc. London*, **A137**, 62, 1932.

65. Mitchell, J.S., *Trans. Faraday Soc.*, **33**, 1129, 1937.

66. Schulman, J.H., Cockbain, E.G., *Trans. Faraday Soc.*, **35**,1266, 1937.

67. Crisp, D.J., *Surface Films of Polymers*, in *Surface Phenomena in Chemistry and Biology,* Eds. Danielli, J.F., Pankhurst, K.G.A., Riddiford, A.C., Pergamon Press, New York, 1958.

68. Shuler, R.L., Zisman, W.A., *J.Phys. Chem.*, **74**, 1523, 1970.

69. Benson, G.C., McIntosh,R.L., *J. Colloid Sci.*, **3**, 323, 1948.

70. Hotta, H., *J. Colloid Sci.*, **9**, 504, 1954.

71. Llopis, J., Rebello, D.V., *J. Colloid Sci.*, **11**, 543, 1956.

72. Schick, M.J., *J. Polymer Sci.*, **25**, 465, 1957.

73. Ries, H.E., Jr., Ahlbeck R.A., and Gabor, J., *J. Colloid Sci*, **14**, 354, 1959.

74. Miller, I.R., *J. Colloid Sci., Suppl., No.1*, **9**, 579, 1954.

75. Cockbain, E.G., Day, K.J., McMullen, A.J., *Proc. Intern. Congr. Surface Activity, 2nd, London*, **1**, 56, 1957.

76. Beredjick, N., Ries, H.E., Jr., *J.Polymer Sci.*, **62**, S64, 1962.

77. Beredjick, N., Ahlbeck, R.A., Kwei, T.K., Ries, H.E., Jr., *J. Polymer Sci.*, **46**, 268, 1960.

78. Beredjick, N., *Monomolecular Film Studies of Polymers*, in *Newer Methods of Polymer Synthesis and Characterization,* Ke, B., Ed., Interscience, New York, 1964.

79. Ober, R., Vilanove, R., *Colloid & Polym. Sci.*, **255**, 1067, 1977.

80. Vilanove, R., Rondelez, F., *Phys. Rev. Letts.*, **45**, 1502, 1980.

81. Takahashi, A., Yoshida, A., Kawaguchi, M., *Macromolecules*, **15**, 1196, 1982.

82. Kawaguchi, M., Yoshida, A., Takahashi, A., *Macromolecules*, **16**, 956, 1983.

83. Vilanove, R., Poupinet, D., Rondelez, F., *Macromolecules*, **21**, 2880, 1988.

84. Poupinet, D., Vilanove, R., Rondelez, F., *Macromolecules*, **22**, 2491, 1989.

85. Davies, J.T., Rideal, E.K., *Interfacial Phenomena*, Academic Press, New York, 1963.

86. Davies, J.T., *J. Colloid Sci.*, **11**, 377, 1956.

87. Gaines, G.L., *Insoluble Monolayers at Liquid-Gas Interfaces*, Interscience, New York, 1966.

88. Mingins, J., Taylor, J.A., Owens, N.F., Brooks, J.H., *Adv. Chem. Ser.* **144**, 28, 1975.

89. Davies, J.T., Llopis, J., *Proc. R. Soc. London Ser. A* **277**, 537, 1955.

90. Allan, A.J.G., Alexander, A.E., *Trans. Faraday Soc.* **50**, 863, 1954.

91. Bringuier, E., Vilanove, R., Gallot, Y. Selb, J., Rondelez, F., *J. Colloid. Int. Sci.* **104**, 95, 1985.

92. Archer, R.J., *J. Opt. Soc. Am.*, **52**, 970, 1962.

93. Bootsma, G.A., Meyer, F., *Surf. Sci.* **14**, 52, 1969.

94. Smith, T.J., *J. Opt. Soc. Am.*, **58**, 1069, 1968.

95. Stromberg, R.R., Tutas, D.J., Passaglia, E., *J. Phys. Chem.* **43**, 539, 1965.

96. Stromberg, R.R., Smith, L.E., *J. Phys. Chem*, **71**, 2470, 1967.

97. Peyser, P., Tutas, D.J., Stromberg, R.R., *J. Polym. Sci. A-1*, **5**, 651, 1967.

98. Stromberg, R.R., Smith, L.E., McCrackin, F.L., *Ellipsometry Techniques and their Application to Polymer Adsorption*, Nat. Bureau of Standards, 1970.

99. McCrackin, F.L., *J. Opt. Soc. Amer.* **60**, 56, 1970.

100. McCrackin, F.L., Colson, J., in *Ellipsometry in the measurement of Surfaces and Thin Films*, Eds. Passaglia, E., Stromberg, R.R., Kruger, J., *Nat. Bur. Stand. Misc. Publ.*, **256**, 61, 1964.

101. den Englesen, D., de Koning, R., *J. Chem. Soc. Farad. Trans. I*, **70**, 1603, 1974.

102. den Englesen, D., de Koning, R., *J. Chem. Soc. Farad. Trans. I*, **70**, 2100, 1974.

103. Benjamins, J., de Feitjer, J.A., Evans, M.T.A., Graham, D.E., Phillips, M.C., *Discuss. Farad. Soc.* **59**, 218, 1975.

104. de Feitjer, J.A., Benjamins, J., Veer, F.A., *Biopolymers*, **17**, 1759, 1978.

105. Graham, D.E., Phillips, M.C., *J. Colloid. Int. Sci.*, **70**, 415, 1979.

106. Kawaguchi, M., Oohira, M., Tajima, M., Takahashi, A., *Polym. J.* **12**, 849, 1980.

107. Rasing, T. Hsiung, H., Shen, Y.R., Kim, M.W., *Phys. Rev. A*, **37**, 2732, 1988.

108. Beagehole, D., *Phys. Rev. Lett.* **58**, 1434, 1987.

109. Kawaguchi, M., Tohyama, M., Mutoh, Y., Takahashi, A., *Langmuir*, **4**, 407, 1988.

110. Kawaguchi, M., Tohyama, M., Mutoh, Y., Takahashi, A., *Langmuir*, **4**, 411, 1988.

111. Sauer, B.B., Yu, H., Kim, M.W., *Langmuir*, **5**, 278, 1989.

112. Archer, R.J., in *Ellipsometry in the measurement of Surfaces and Thin Films*, Passaglia, E., Stromberg, R.R., Kruger, J., Eds., *Nat. Bur. Stand. Misc. Publ.*, **256**, 255, 1964.

113. Strachan, C.S., *Proc. Cambridge Philos. Soc.*, **29**, 116, 1933.

114. Kawaguchi, M., Nagata, K., *Macromolecules*, **23**, 3957, 1990.

115. Vrij, A., *J. Colloid. Sci.*, **19**, 1. 1964.

116. Von Smoluchowski, M., *Ann. Physik.*, **41**, 609, 1913.

117. Mandlestam, L., *Ann. Physik*, **41**, 609, 1913.

118. Raman, C.V., Ramdas, L.A., *Proc. Roy. Soc. London* A, **108**, 561, 1924.

119. Raman, C.V., Ramdas, L.A., *Proc. Roy. Soc. London* A, **109**, 150 & 272, 1925.

120. Katyl, R.H., Ingard, U., *Phys. Rev. Lett.*, **19**, 64, 1967.

121. Bouchiat, M.-A., Meunier, J., *C.R. Acad. Sci. Paris*, **266B**, 301, 1968.

122. Katyl, R.H., Ingard, U., *Phys. Rev. Lett.*, **20**, 248, 1968.

123. Katyl, R.H., Ingard, U., in *In Honor of P.M. Morse*, Feshbach, H., Ingard, U., Eds., MIT Press, Cambridge, Mass., 1969.

124. Cruchon, D., Meunier, J., Bouchiat, M.-A., *C.R. Acad. Sci. Paris*, **267B**, 32, 1968.

125. Cruchon, D., Meunier, J., Bouchiat, M.-A., *C.R. Acad. Sci. Paris*, **268B**, 422, 1969.

126. Bouchiat, M.-A., Langevin, D., *C.R. Acad. Sci. Paris*, **272B**, 1357, 1971.

127. Hård, S., Hamnerius, Y., Nilsson, O., *J. Appl. Phys.*, **47**, 3433, 1976.

128. Byrne, D., Earnshaw, J.C., in *Lasers in Chemistry*, West, M.A., Ed., Elsevier, Amsterdam, 1977.

129. Byrne, D., Earnshaw, J.C., *J. Phys. D: Appl. Phys.*, **10**, L207, 1977.

130. Byrne, D., Earnshaw, J.C., *J. Phys. D: Appl. Phys.*, **12**, 1133, 1979.

131. Shih, L.B., *Rev. Sci. Instrum.*, **55**, 716, 1984.

132. Sano, M., Kawaguchi, M., Chen, Y.-L., Skarlupka, R.J., Chang, T., Zografi, G., Yu, H., *Rev. Sci. Instrum.*, **57**, 1158, 1986.

133. Crilly, J.F., Earnshaw, J.C., *J. Physique*, **48**, 485, 1987.

134. Winch, P.J., Earnshaw, J.C., *J. Phys. E: Sci. Instrum.*, **21**, 287, 1988.

135. Earnshaw, J.C., McGivern, R.C., *J. Colloid Interface. Sci.*, **131**, 278, 1989.

136. Langevin, D., *J. Colloid Interface. Sci.*, **80**, 413, 1980.

137. Winch, P.J., Earnshaw, J.C., *J. Phys: Condens. Matter.*, **1**, 7187, 1989.

138. Earnshaw, J.C., Winch, P.J., *J. Phys: Condens. Matter.*, **2**, 8499, 1990.

139. Earnshaw, J.C., McGivern, R.C., Winch, P.J., *J. Phys. Fr.*, **49**, 1271, 1988.

140. Kawaguchi, M., Sano, M., Chen, Y.-L., Zografi, G., Yu, H., *Macromolecules*, **19**, 2606, 1986.

141. Sauer, B.B., Yu, H., Tien, C.-F., Hager, D.F., *Macromolecules*, **20**, 393, 1987.

142. Sauer, B.B., Kawaguchi, M., Yu, H., *Macromolecules*, **20**, 2732, 1987.

143. Sauer, B.B., Yu, H., *Macromolecules*, **22**, 786, 1989.

144. Kawaguchi, M., Sauer, B.B., Yu, H., *Macromolecules*, **22**, 1735, 1989.

145. Yoo, K.-H., Yu, H., *Macromolecules*, **22**, 4019, 1989.

CHAPTER 2 - NEUTRON REFLECTOMETRY

2.1 Introduction

Neutrons or X-rays may be used to investigate the density (composition) profile of solid thin films, adsorbed liquid surface films and spread monolayers in the direction normal to the plane of the layer by measuring the reflected intensity when an incident beam encounters the interface at angles greater than the critical (total reflection) angle. At this point the beam is partially reflected and partially propagated into the medium of the layer. Further successive reflections and refractions at compositional differences in the layer will lead to interferences in the reflected intensity which are characteristic of the layer composition.

It is shown in section 2.2 that standard mathematical methods used to describe the reflection of light may be applied to the description of neutron reflection at interfaces, and by these means one may obtain information about the interfacial layer thickness and density profile normal to the layer. These methods involve the generation of matrices including terms in the refractive indices of the materials at the interface. The neutron refractive index at the boundary between two media is defined as

$$n = k_1/k_0 \qquad 2.1$$

where k_1 and k_0 are the neutron wave vectors inside and outside the medium. This may be expressed

$$n = 1 - \lambda^2 Nb/2\pi + i\lambda N\sigma_a/4\pi \qquad 2.2$$

where λ = neutron wavelength,

N = atomic number density,

b = bound atom coherent scattering length,

and σ_a= adsorption cross- section.

From Snell's Law, n may be related to θ_c, the critical angle of total reflection, by

$$\cos \theta_c = n \qquad 2.3$$

and therefore at low angles expansion of the cosine gives

$$\theta_c/\lambda = (Nb/\pi)^{1/2} \qquad 2.4$$

For non-absorbing media the imaginary component of n in 2.2 is negligible, and so in the absence of magnetic interactions the neutron refractive index is simply related to the real part of equation 2.2. The quantity Nb is the scattering length density of the medium under consideration, and is hereafter referred to as ρ. For a given molecular species ρ may be calculated from the sum of the coherent scattering lengths of its constituent nuclei by the expression

$$\rho = \Sigma b_i d\, N_{av}/ M_m \qquad 2.5$$

where d = density

N_{av} = Avogadro's number

M_m = molecular weight of species (in the case of polymers usually one monomer unit).

The coherent scattering lengths of some common nuclei are shown in table 2.1[1]. From these values are calculated some values of ρ relevant to the

Nucleus	Coherent Scattering Length, $b/10^{-4}$Å
^{1}H	0.667
^{2}H	-0.374
^{12}C	0.665
^{14}N	0.937
^{16}O	0.580

Table 2.1 Coherent Scattering lengths of some common nuclei

reflectometry experiments described later in this thesis which are tabulated in table 2.2. Particularly noteworthy are the values for H_2O and D_2O which are of opposite

Molecule / unit	Σb_i / 10^{-4}Å	ρ / 10^{-6}Å^{-2}
H_2O	-1.68	-0.56
D_2O	1.92	6.35
air	-	0
methyl methacrylate	1.49	0.90
methyl methacrylate - d8	9.82	6.02
ethylene oxide	0.41	0.57
ethylene oxide - d4	4.58	6.32
4 - vinyl pyridine	2.97	1.32
ethyl 4 - vinyl pyridine	2.43	1.09
ethyl - d5 4 - vinyl pyridine	7.64	3.64
magnesium sulphate	3.11	4.15

Table 2.2 Scattering Length Densities for selected materials

sign (a negative value corresponding to a change of phase on scattering encounter). Thus it may be seen that a mixture of H_2O and D_2O in suitable proportions will produce water with scattering length density equal to zero, the value defined for air. This is in effect invisible to neutrons and is termed air contrast matched or null scattering water, abbreviated to acmw. Therefore it is possible to set up an experiment where the polymer is studied as a visible layer between air and an invisible subphase. The fitted solution to the obtained reflectivity then is only contributed to by the polymer and is a measure of the total adsorbed amount at the interface. In a similar fashion the reflectivity obtained from an interface consisting of a hydrogenous polymer on a deuterated subphase will be dominated by the subphase signal but will be depressed significantly by the presence of excess hydrogenous material at the interface.

In this way, it can be seen that, depending on the particular nature of any given interfacial system one can arrange various contrast conditions which yield complementary information about the layer structure, and, given sufficient simultaneous data sets, it is possible to calculate uniquely both the layer thickness and composition.

2.2 Specular Reflection at a Planar Interface

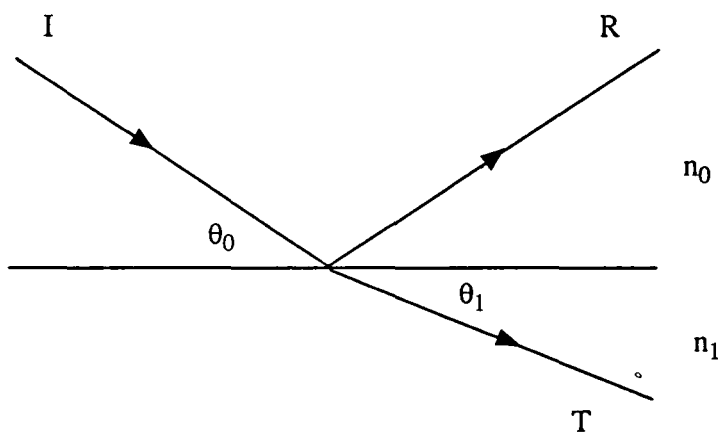

Figure 2.1 Reflection at a planar interface between regions of refractive index n_0 and n_1

The specular reflection from the interface of two bulk media R (Figure 2.1) is described by Fresnel's Law, which states that for incident angles greater than the critical angle for total reflection θ_c

$$R = \left| \frac{n_0 \sin\theta_0 - n_1 \sin\theta_1}{n_0 \sin\theta_0 + n_1 \sin\theta_1} \right|^2 \qquad 2.6$$

where the terms of 2.6 are as shown in Figure 2.1. For the region of total reflection

$$n_0 \cos\theta_0 = n_1 \cos\theta_1 \qquad 2.7$$

and so

$$n_1 \sin\theta_1 = (n_1^2 - n_0^2\cos^2\theta_0)^{1/2} \qquad 2.8$$

For $\theta > \theta_c$, $n_1^2 > n_0^2\cos^2\theta_0$ and $n_1\sin\theta_1$ is real but for $\theta < \theta_c$, $n_1^2 < n_0^2\cos^2\theta_0$ and therefore

$$n_1 \sin\theta_1 = -i(n_0^2\cos^2 - n_1^2)^{1/2} \qquad 2.9$$

is imaginary, corresponding to an evanescent induced wave in the plane of reflection. At the point of total reflection $n_1\sin\theta_1$ is zero and therefore

$$n_1^2 = n_0^2\cos^2\theta_0 \qquad 2.10$$

2.3 Representation of Optical Stratifications by Matrix Methods

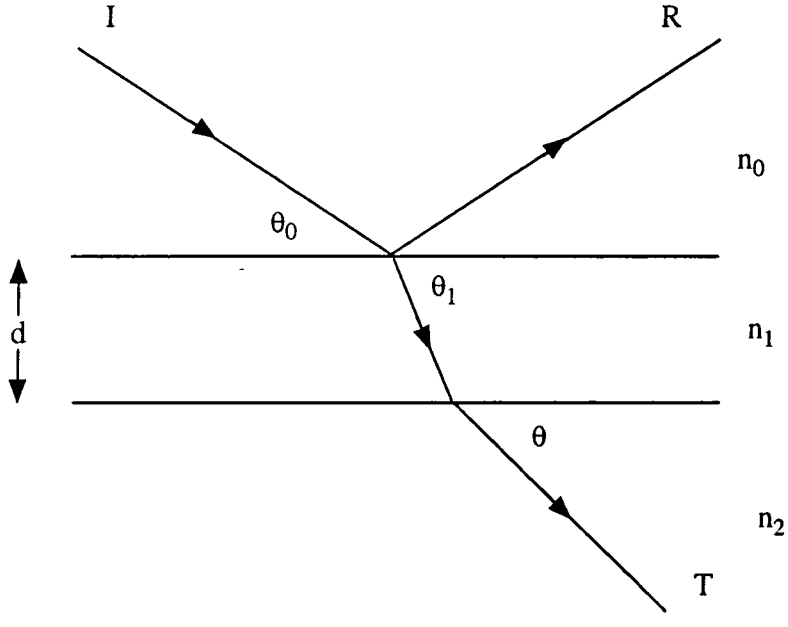

Figure 2.2 Reflection and transmission from a thin film of thickness d and refractive index n_1, at the boundary of media with refractive indices n_0 and n_2

The mathematical description of reflection and refraction from interfacial systems has been considered by several authors[2,3,4]. For a single film of thickness d at the interface of two bulk media, such as shown in figure 2.2, an exact

solution may be obtained for the reflectivity R such that

$$R = \left| \frac{r_{01} + r_{12}e^{2i\beta}}{1 + r_{01}r_{12}e^{2i\beta}} \right|^2 \qquad 2.11$$

where

$$r_{ij} = \frac{p_i - p_j}{p_i + p_j} \qquad 2.12$$

is the Fresnel coefficient at the ij interface, $p_j = n_j \sin\theta_j$ and $\beta = (2\pi/\lambda)n_1 d.\sin\theta_1$ is the optical path length of the beam in the film.

Similar exact solutions may be extracted for films of two or three such adjacent layers, but beyond this the complexity of the expressions involved becomes prohibitive and a general method must be invoked. The method described by Born and Wolf[2] was the earliest applied to the analysis of reflection data. This method uses the boundary condition that the wave functions and their gradients be continuous at each layer boundary, to define a characteristic matrix for each layer, such that for the j^{th} layer

For an n layer system a resultant matrix for the total reflectivity may be

$$M_j = \begin{bmatrix} \cos\beta_j & -(i/p_j)\sin\beta_j \\ -ip_j\sin\beta_j & \cos\beta_j \end{bmatrix} \qquad 2.13$$

obtained by multiplication of the individual layer matrices,

$$M_R = [M_1].[M_2]...[M_j]...[M_n] \qquad 2.14$$

such that

$$R = \left| \frac{(M_{11} + M_{12}p_s)p_a - (M_{21} + M_{22})p_s)}{(M_{11} + M_{12}p_s)p_a + (M_{21} + M_{22})p_s)} \right|^2 \qquad 2.15$$

The description of reflection may be extended to interfaces which are not perfectly smooth, by the application of a Debye-Waller factor for a Gaussian distribution of the interface[5] such that

$$I(\lambda) = I_o(\lambda)\exp(-q_0 q_1 <\sigma>^2) \qquad 2.16$$

where $I(\lambda)$ and $I_o(\lambda)$ are the reflected intensity with and without roughness, $<\sigma>$ is the root mean square thickness, $q_0 = 2k\sin\theta_0$, and $q_1 = 2k\sin\theta_1$. Such a method of treating surface roughness has been shown to be equivalent to the alternative Born and Wolf method of division of the interface into incremental layers of Gaussian density distribution which becomes unwieldy for more than a few layers. Thus the method of Abeles described by Heavens[3] has become favoured for the treatment of interfacial phenomena. In this case a characteristic matrix is defined in terms of Fresnel coefficients and phase factors from the relationship between electric vectors in successive layers such that

$$M_m = \begin{bmatrix} e^{i\beta_{m-1}} & r_m e^{i\beta_{m-1}} \\ r_m e^{-i\beta_{m-1}} & e^{-i\beta_{m-1}} \end{bmatrix} \qquad 2.17$$

For N layers, the elements of the resultant matrix M_{11}, M_{21} give

$$R = \frac{M_{21} M_{21}^*}{M_{11} M_{11}^*} \qquad 2.18$$

If roughness is to be modelled at each interface then the introduction of a Debye-Waller factor for the modification of the Fresnel coefficients of equations 2.13 and 2.15 of form

$$r_{ij} = \left(\frac{p_i - p_j}{p_i + p_j} \right) e^{-1/2.(q_i q_j <\sigma^2>)} \qquad 2.19$$

allows the exact calculation of a reflectivity profile.

2.4 Approximate Methods for the Description of Reflection

Lekner[4] has considered a number of approximate methods for the calculation of reflectivity. These are of some use in the description of the reflection of light but have not been applied to neutron reflection. As such they will not be considered further here. The most useful and illuminating approximate method is based on an analogy with weak elastic neutron scattering and was applied to reflectivity by Crowley[6], whose conclusions have since been developed elsewhere[7-10]. The kinematic or first Born approximation for weak elastic scattering yields the following expression for the differential scattering cross section

$$I(\kappa) = \langle|\hat{\rho}(\kappa)|^2\rangle \qquad 2.20$$

where $\hat{\rho}(\kappa)$ is the Fourier transform of $\rho(r)$ over the whole sample

$$\rho(\kappa) = \int_{-\infty}^{\infty} e^{i\kappa r}.\rho(r).dr \qquad 2.21$$

For a macroscopically flat surface the specular reflectivity can be derived from equation 2.20 as

$$R(Q) = \frac{16\pi^2}{Q^2} |\hat{\rho}(Q)|^2 \qquad 2.22$$

where Q is the momentum transfer component normal to the interface and $\hat{\rho}(Q)$ is the one dimensional Fourier transform of $\rho(z)$, the scattering length density profile in the direction normal to the interface. This may be expressed equivalently in terms of the Fourier transform of the derivative of the scattering length density profile, $\rho'(z) = d\rho/dz$, by

$$R(Q) = \frac{16\pi^2}{Q^4} \left|\hat{\rho}'(Q)\right|^2 \qquad 2.23$$

It is possible to derive useful expressions for a variety of commonly encountered interfacial scattering length density profiles. Firstly a slow continuous

change in scattering length density between the values for the two bulk media may be considered, such as the sigmoidal interface of figure 2.3(a). This is encountered for example in the interface of a liquid with its vapour. In this case

$$\hat{\rho}'(Q) = \int_{-\infty}^{\infty} e^{iQz} \cdot \frac{d\rho}{dz} \cdot dz \qquad 2.24$$

or

$$\hat{\rho}'(Q) = \int_{-\infty}^{\infty} e^{iQz} \cdot d\rho \qquad 2.25$$

When $Q = 0$, $\rho'(0) = -\Delta\rho_p$, where $\Delta\rho_p$ is the scattering length density difference between the two bulk media. The reflectivity may now be written in the form

$$R(Q) = R_p^{o}(Q).h'(Q) \qquad 2.26$$

where

$$R_p^{o} = \frac{16\pi^2}{Q^4} |\Delta\rho_p|^2 \qquad 2.27$$

is the kinematic expression for the reflectivity of a sharp interface with a step in scattering length density $\Delta\rho_p$, figure 2.3(b) and

$$h'(Q) = \left| \frac{\hat{\rho}'(Q)}{\hat{\rho}'(0)} \right| \qquad 2.28$$

is a normalised form factor which modifies R_p^{o} according to the shape and width of the interfacial region. When Q is much less than one, $h'(Q) \approx 1$ and the surface profile appears to be sharp. Total reflection occurs when Q is of the order of 10^{-2}Å^{-1}, and therefore the reflectivities from sharp or gradual interfaces will be indistinguishable in this region unless the variation is on a length scale greater than around 10Å. At greater Q values however $h'(Q)$ decreases rapidly and $R(Q)$ is depressed below the sharp interface value, $R(Q)$ being further depressed for a broader interfacial profile.

For small Qz, in the same manner as the Guinier approximation for small angle scattering, a Taylor expansion in powers of Qz may be made for e^{iQz}

which occurs in the expression for $h'(Q)$ and thus

$$h'(Q) \approx \exp(-Q^2\sigma^2), \quad Q\sigma < 1 \qquad 2.29$$

where σ is the standard deviation of $\rho'(z)$.

Another interfacial situation of importance in reflection from spread films is when the scattering length density is identical on either side of the interfacial layer, and in particular when the scattering length density is zero. This occurs when a monolayer is spread on air contrast matched water as described in the introduction to this chapter and is represented in figure 2.3(c). In this case the reflectivity may be expressed as

$$R(Q) = R_s^{\circ}(Q).h(Q) \qquad 2.30$$

where

$$R_s^{\circ}(Q) = \frac{16\pi^2}{Q^2} |m|^2 \qquad 2.31$$

$$h(Q) = \left| \frac{\hat{\rho}_s(Q)}{\hat{\rho}_s(0)} \right| \qquad 2.32$$

and

$$m = \int_{-\infty}^{\infty} \rho_s(z).dz \qquad 2.33$$

$R_s^{\circ}(Q)$ is the kinematic expression for the reflectivity of an infinitesimally thin film of scattering mass per unit area m, analogous to sheet scattering in small angle scattering. h(Q) is again a modulating normalised form factor which is approximately unity at low Q but decays at higher Q, causing the reflectivity to be depressed below R_s° according to the shape of the scattering length density profile. A similar Guinier type approximation may be made for h(Q) as for $h'(Q)$ previously, and therefore for this particular contrast case

$$R(Q).Q^2 = 16\pi^2 m^2 \exp(-Q^2\sigma^2) \qquad 2.34$$

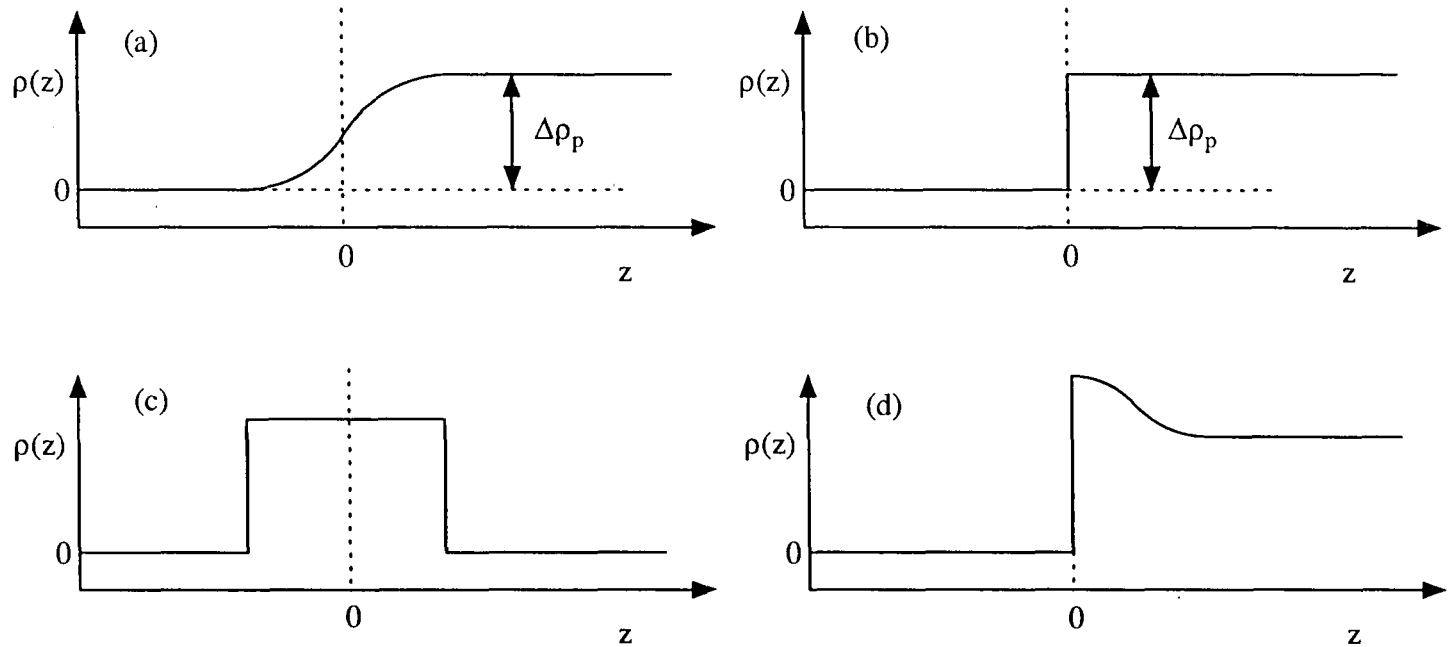

Figure 2.3 Scattering length density profiles considered in the kinematic approximation

Thus a plot of $\ln(R(Q).Q^2)$ against Q^2 should be a straight line whose intercept is proportional to m^2 and whose slope is proportional to σ^2.

For the general case of an absorbed or diffuse layer (figure 2.3(d)) the complicated scattering length density profile may be expressed

$$\rho(z) = \rho_s(z) + H(-z)\Delta\rho_p \qquad 2.35$$

where H(-z) is the Heaviside function. The Fourier transform of the Heaviside function is

$$\int_{-\infty}^{\infty} H(-z).e^{iQz}.dz = \pi\delta(Q) - iQ^{-1} \qquad 2.36$$

Using equations 2.30, 35 and 36 the reflectivity may be expressed by

$$R(Q) = R_0(Q) + R_1(Q)\Delta\rho_p + R_2(Q)\Delta\rho_p^2 \qquad 2.37$$

where

$$R_0(Q) = 16\pi^2/Q^2.m^2h(Q) \qquad 2.38$$

$$R_1(Q) = 32\pi^2/Q^3.S[\rho_s](Q) \qquad 2.39$$

and

$$R_2(Q) = 16\pi^2/Q^4 \qquad 2.40$$

$R_0(Q)$ is the reflectivity of the surface film alone and $R_2(Q)\Delta\rho_p^2$ is the reflectivity attributable to the sharp interface, denoted R_p^o. The linear term in $\Delta\rho_p$ in equation 2.37 describes the cross-interference between the scattering from the sharp interface and that from the adsorbed layer. $S[\rho_s](Q)$ is the sine transform of ρ_s which may be re-expressed in terms of a normalised form factor s(Q)

$$s(Q) = Q^{-1}S[\rho_s](Q)/\lim_{Q\to 0}(Q^{-1}S[\rho_s](Q)) \qquad 2.41$$

The denominator of s(Q) reduces to $\langle z\rangle m$, where $\langle z^n\rangle$ is the n^{th} moment of ρ_s and m is the total scattering length density as defined in 2.34. R_1 can now be re-expressed

$$R_1(Q) = -32\pi^2/Q^2.\langle z\rangle ms(Q) \qquad 2.42$$

If 2.38,39,40 and 2.42 are substituted into 2.36 and the resulting expression is divided by R_p^o so that the final term in 2.37 becomes unity, the following expression is obtained

$$\frac{R(Q)}{R_p^o(Q)} = \frac{m^2}{\Delta\rho_p^2} Q^2 h(Q) - \frac{2\langle z\rangle m}{\Delta\rho_p} Q^2 s(Q) + 1 \qquad 2.43$$

At Q = 0 therefore the limiting value of the ratio between the actual and sharp interface reflectivities is unity. Above Q = 0 the Q dependence is governed by the two terms in h(Q) and s(Q), which vary inversely with $\Delta\rho_p^2$ and $\Delta\rho_p$ respectively. At sufficiently large $\Delta\rho_p$ the s(Q) term dominates and the result is that the ratio is depressed below unity.

At low Q, Guinier approximations may be made for h(Q) as before and for $s(Q) \sim \exp(\langle z^3\rangle/3\langle z\rangle)$, and thus the measurement of the difference in reflectivity between the sharp subphase and film cases, ΔR, contains information about the film thickness (σ^2 or $\langle z^3\rangle/3\langle z\rangle$) and structure (m or $\langle z\rangle m$).

For a $\rho_s(z)$ profile which is a smooth function except for a step in scattering length density at the defined z = 0 plane described by

$$\Delta\rho_s = \rho_s(0_+) - \rho_s(0_-) \qquad 2.44$$

at sufficiently large Q the reflectivity is given by

$$R(Q) \approx 16\pi^2/Q^4.(\Delta\rho_s - \Delta\rho_p) \qquad 2.45$$

which may be compared with the expression for R_p^o and is analogous to a single sharp step of height $(\Delta\rho_s - \Delta\rho_p)$. Thus at large Q the measurement of ΔR should yield the scattering length density of the film at z = 0.

2.5 Inversion of Reflectivity Profiles

It would only be possible to demonstrate the uniqueness of a solution to a reflectivity profile beyond any doubt if one was able to directly invert the profile

in the momentum transfer dimension into the corresponding scattering length density profile in the z space dimension. The complexity of the relevant optical matrix expressions for the reflectivity makes this type of inversion practically impossible but the rather simpler relationships generated by the kinematic approximation make this a more useful approach towards the direct deduction of the scattering length density profile by use of Fourier transformations.

The form factors h(Q) and s(Q) defined above are related to the normalised Fourier transform of the surface scattering length density profile f(Q) by

$$h(Q) = |f(Q)|^2 \qquad 2.46$$

$$s(Q) = \mathrm{Im}\{f(Q)\}/\langle z\rangle Q \qquad 2.47$$

where

$$f(Q) = \hat{\rho}_s(Q) / \hat{\rho}_s(0) \qquad 2.48$$

If f(Q) could be measured, then by Fourier transformation the scattering length density profile $\rho_s(z)$ could be obtained by

$$\rho_s(z) = \frac{m}{2\pi} \int_{\infty}^{-\infty} e^{iQz} \,.\, f(Q) \,.\, dQ \qquad 2.49$$

However in equation 2.46 the phase $\psi(Q)$ of f(Q) is lost as is the real part of f(Q) in equation 2.47. Thus it is not possible to invert the reflectivity uniquely to the scattering length density profile in general. For the special case of a monotonic $\rho_s(z)$ which is zero on one side of the dividing plane, then a single profile does determine $\rho_s(z)$ uniquely. More generally, if one had access to a range of data obtained at different contrasts then h(Q) and s(Q) could be determined from 2.41 or one of its equivalents by virtue of their different dependences on $\Delta\rho_s$.

In addition to the above considerations other limitations exist which place severe restrictions on the applicability of such methods towards the interpretation of neutron reflection data. Firstly the kinematic approximation breaks down at low Q values where the region of total reflectivity is approached. Secondly

the neutron reflection experiment is subject to a considerable background due to isotropic incoherent scatter which places a limit on the upper Q value obtainable.

Instead of considering f(Q), it is useful to consider the Fourier transformation of $|\hat{\rho}(Q)|^2$ which gives the Patterson function for the scattering length density correlation, P(z), where P(z) is the average of the product of the scattering length densities at two points separated by a distance u normal to the surface,

$$P(z) = \int_{\infty}^{-\infty} \rho(z)\, \rho(z-u).du \qquad 2.50$$

According to equation 2.22 P(z) should be obtained by Fourier transforming the product of the reflectivity and $Q^2/16\pi^2$. An analogous Patterson function P′(z) for the gradient of the scattering length density profile ρ′(z), may be obtained if the reflectivity is multiplied by Q^4 instead of Q^2. The restrictions on Fourier transformation mentioned previously still apply to P(z) but it is useful to consider the form of the Patterson function P′(z) for a single uniform layer where the scattering length density of the film is intermediate with those of the two bulk media, such as is the case for a hydrogenous polymer spread as a monolayer on D_2O. In this case the scattering length density and scattering length density gradient profiles would be as shown in figures 2.4(a) and (b). ρ′(z), the scattering length density gradient, is zero except for the two delta functions at the two edges of the film separated by the distance d. The resultant P′(z) function is shown in figure 2.4(c). The Fourier transform of δ(0) is exp(0) and that of {δ(-d)+δ(+d)} is 2cos(Qa) and the following result is obtained

$$|\hat{\rho}(Q)|^2 = \Delta\rho_p^2 - 2\rho_d(\Delta\rho_p-\rho_d)(1-\cos(Qd))$$
$$= \Delta\rho_p^2 - 4\rho_d(\Delta\rho_p-\rho_d)\sin^2(Qd/2) \qquad 2.51$$

This function has the form shown in figure 2.4(d), with maximum at Q = 0, when the $\sin^2$ term disappears from 2.51, and a sharp minimum when the $\sin^2$

term is unity at $Q = \pi/d$ and so

$$|\hat{\rho}(Q)|^2 = \Delta\rho_p^2 - 4\rho_d(\Delta\rho_p - \rho_d)$$
$$= (2\rho_d - \Delta\rho_p)^2 \qquad 2.52$$

2.6 Patchy Film Modelling

For certain Langmuir monolayers there is some question as to whether the films are truly continuous on the surface or whether they are in fact distributed as islands of various density on the surface. It is of interest therefore to consider the effect of the presence of in plane scattering length density variations on the neutron reflectivity. Richardson and Roser[11] have recently presented a useful treatment based on the kinematic approximation, which provides a straightforward calculation for the reflectivity when the island size ξ is either smaller or larger than the coherence limit of the neutron experiment. In the former case the reflectivity is governed by the average scattering length density over the surface extent of the inhomogeneities but in the latter the reflectivity is affected by the contribution of off-specular scattering. The following summarises the pertinent results of this observation.

In a similar fashion to the expression for R_p^o, the reflectivity from a single sharp step function in scattering length density, the reflectivity for a single uniform monolayer film of thickness d with scattering length density ρ_F between air and subphase media with scattering length densities ρ_A and ρ_S respectively may be given in the kinematic approximation by

$$R(Q)_{mono} = (16\pi^2/Q^4).(\Delta\rho_{AF}^2 + \Delta\rho_{FS}^2 + 2\Delta\rho_{AF}\Delta\rho_{FS}\cos Qd) \qquad 2.53$$

where $\Delta\rho_{AF} = \rho_A - \rho_F$ and $\Delta\rho_{FS} = \rho_F - \rho_S$.

On the other hand if the film is divided into islands on the surface surrounded by air voids, then the reflectivity may be expressed as a weighted sum of

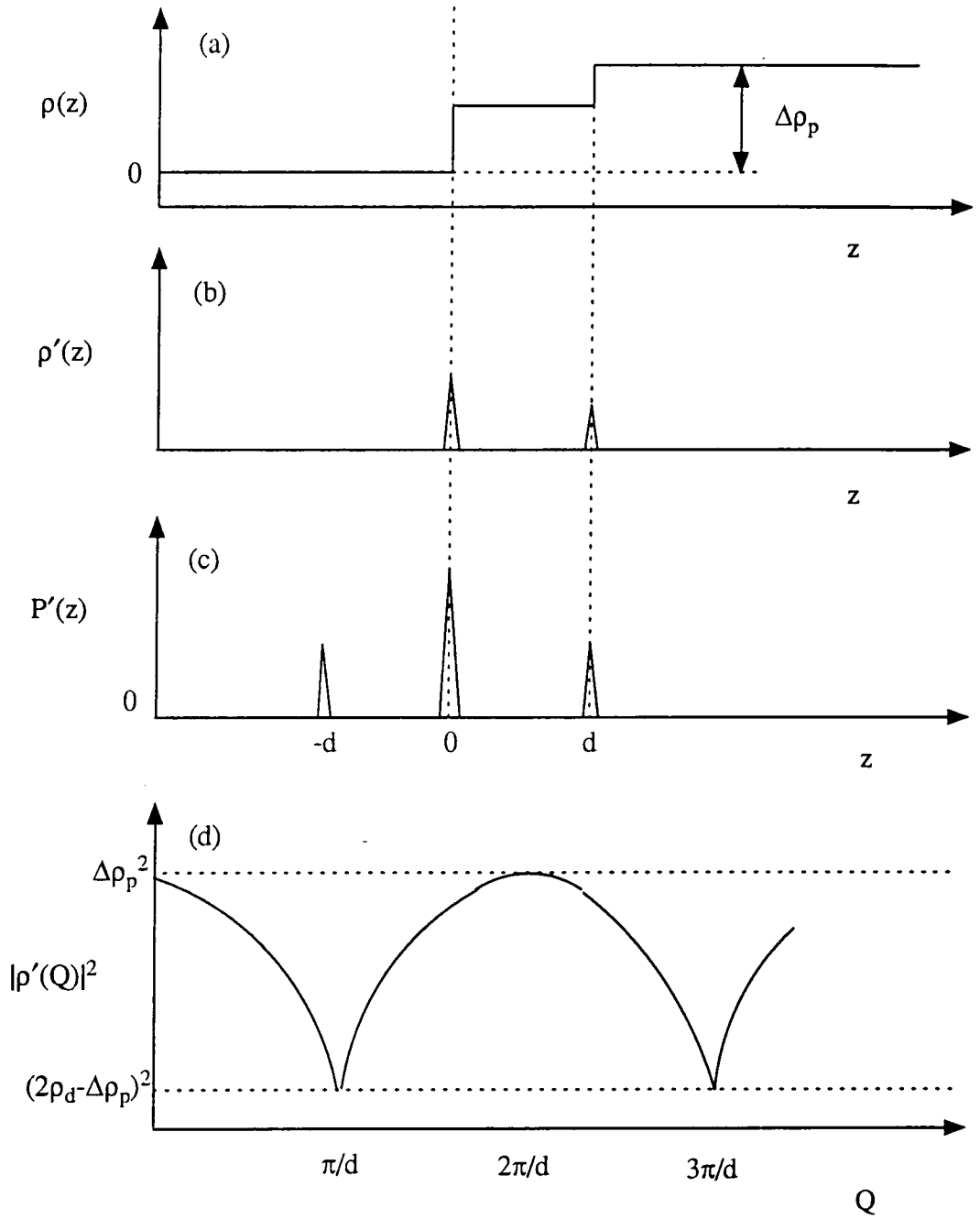

Figure 2.4 (a) Scattering Length Density Profile
(b) Scattering Length Density Gradient Profile
(c) Patterson Function for the Gradient
(d) Corresponding Form Factor Plot
for a film of ρ_d between ρ_a and ρ_s

the reflectivities observed in the limit of infinitely large or infinitely small islands (R_L and R_S);

$$R_{islands} = R_S + F(\xi).(R_L - R_S) \qquad 2.54$$

where $F(\xi)$ is a form factor dependent on the island size and instrumental resolution ΔQ_x

$$F(\xi) = (2/\pi).\tan^{-1}\xi\Delta Q_x \qquad 2.55$$

A coherence length for the neutron radiation in the experiment may be defined as the reciprocal of the resolution, ΔQ_x^{-1}. It may be seen that if the island size is very much smaller than the coherence length that $F(\xi) \approx 0$. If the island size is very much greater than ΔQ_x^{-1} however $F(\xi) \approx 1$. The crossover between the two cases occurs when the island size is of the same order as the coherence length.

R_S is determined by the kinematic expression for a monolayer with scattering length density averaged between that of the islands and the voids

$$R_S = (16\pi^2/Q^4).(\Delta\rho_{AF}^2 + \Delta\rho_{FS}^2 + 2\Delta\rho_{AF}\Delta\rho_{FS}\cos Qd) \qquad 2.56$$

where now $\Delta\rho_{AF} = \rho_A - f\rho_F$ and $\Delta\rho_{FS} = f\rho_F - \rho_S$, and f is the fractional coverage of the surface by islands.

R_L is the average of the reflectivities obtained from a fully covered monolayer with scattering length density ρ_F, equation 2.53, and the bare subphase

$$R_p^o = (16\pi^2/Q^4)\Delta\rho_{AF}^2 \qquad 2.57$$

where $\Delta\rho_{AF}$ is identical to $\Delta\rho_p$ in the terminology of section 2.5. R_L is then given by

$$R_L = f.R_{mono} + (1-f)R_p^o \qquad 2.58$$

Substituting appropriately into 2.58 yields

$$R_L = (16\pi^2/Q^4).[(\rho_A-\rho_S)^2+2f(\rho_A-\rho_F)(\rho_F-\rho_S)(\cos Qd-1) \qquad 2.59$$

For the case of a monolayer spread at the air/air contrast matched water interface, where $\rho_A = \rho_S = 0$, equations 2.56 and 2.59 simplify respectively to

$$R_S = (16\pi^2/Q^4).2\rho_F^2f^2(1-\cos Qd) \qquad 2.59$$

and

$$R_L = (16\pi^2/Q^4).2\rho_F^2f(1-\cos Qd) \qquad 2.60$$

For intermediate island sizes, the power dependence of the reflectivity on f will vary according to the island size/resolution factor by

$$Y = f^2(1-F(\xi)) + fF(\xi) \qquad 2.61$$

It can now be seen that from the reflection of a deuterated film spread on air contrast matched water it is possible to obtain uniquely the value of the layer thickness as this term is uncoupled in 2.59 and 2.60. It is also possible to determine the product of $\rho_F Y$ but not to determine either ρ_F or f individually as the two terms are expressed solely in that product.

In order to separate the two quantities, it is necessary to carry out a duplicate experiment at a different contrast where equations 2.56 and 2.59 apply and no product of $\rho_F^2 f^2$ or $\rho_F^2 f$ can be factorised out. If this is possible and values of ρ_F and f are obtained then in principle one can estimate the island size by

$$\xi = \Delta Q_x^{-1} \cdot \tan[(\pi/2).(Y-f^2)/(f-f^2)] \qquad 2.62$$

2.7 Review of Published Literature on Neutron Reflectometry

The earliest observation of the total reflection of slow neutrons was by Fermi and coworkers in the years after the Second World War[12]. In the intervening years between then and more recent times however there was very little attention paid towards applying neutron reflection to any practical purpose, but the development of neutron guide technology[13,14] utilising total external reflection encouraged Steyerl[15] and Handel[16] to point out the potential use of reflection as a surface probe.

A step nearer the modern neutron reflection experiment was made in 1976 when Hayter, Penfold and Williams[17] observed interference of reflected neutrons from magnetised metal films using the IN11 instrument on the high flux reactor of the Institut Laue Langevin, Grenoble, France. This was followed in 1981 by Hayter et al[18] which must be recognised as a watershed in the field of surface characterisation by neutron reflection, spelling out explicitly for the first time as it does a range of potential applications of interest to surface chemists which have since been fulfilled in very spectacular fashion. Hayter et al presented arguments and examples based on the optical matrix calculations for reflectivity from fatty acid multilayers, black films, and liquid-vapour interfaces and were able to present preliminary experimental data for films on solid glass substrates obtained on the adapted small angle scattering instrument D17 at the ILL.

The final element required to make neutron reflection a more generally feasible technique for surface analysis was the development of a dedicated reflection spectrometer. This was achieved in the instrument CRISP[19-22], operating as a time of flight, fixed angle reflectometer, off the pulsed spallation source ISIS at the Rutherford Appleton Laboratory, Chilton, Didcot, Oxfordshire. CRISP has since been used with much success for the study of a wide range of interfacial systems and

has prompted other neutron facilities to develop their own instrumentation, examples of both time of flight[23-26] and fixed wavelength[27-30] spectrometers existing. Following the development of successful experimental facilities, the experimental literature of neutron reflectometry has mushroomed in the last few years. Penfold and Thomas[9] and Russell[31] have published excellent reviews of the area, the latter also considering the related area of x-ray reflection which lies beyond the scope of this review.

The usefulness of neutron reflectometry in the characterisation of many interfacial systems has been demonstrated. Solid and liquid surfaces, solid-solid, liquid-solid, and liquid-liquid interfaces, magnetic, conducting and semi-conducting films, and biological membranes amongst others have all proved suitable for study.

Among solid surfaces to have received attention are chemical vapour deposited silicon oxide and silicon nitride layers on silicon[32,33], Langmuir-Blodgett films[34-35], and a variety of thin magnetic films, studied using spin polarised neutrons, for example ferromagnets[36] and superconductors[37,38]. A sizeable volume of work exists in these fields but will not be considered further in this review.

Polymer surfaces have also received much attention. Solution cast films[39] have been investigated and surface ordering in solution spun cast films of poly(styrene-d-methyl methacrylate) diblock copolymers has been reported[40]. The polymer-polymer interface has been studied for the cases of hydrogenous/deuterated bilayers of polystyrene[41], and for immiscible[42] and miscible[43,44] polymer pairs, while Jones and co-workers[45,46] have measured the surface segregation of deuterated polystyrene in blends with its hydrogenous analogue.

An area of important practical and industrial relevance to have been studied by reflectometry has been the surface chemistry of surfactants. Thomas and co-workers have been particularly prominent in this field, having studied surfactant

adsorption at the air-solution interface for decyltrimethylammoniumbromide[47], tetramethylammoniumdodecylsulphate[48], and sodium alkyl sulphates of various chain lengths[49]. Longer hydrocarbon chain, and therefore water insoluble, surfactants have also been studied by reflectometry when spread as Langmuir films[11,50,51], these materials being of interest as the precursors of Langmuir-Blodgett films. Finally Lee et al[52] have studied surfactant adsorption at the solution-quartz interface, utilizing the transparency of quartz to long wavelength neutrons to probe a physically inaccesible interface.

The experiments carried out on conventional surfactants have been echoed by studies of polymer solutions and monolayers. Rennie et al[53] have studied the adsorption from solution of poly(ethylene oxide) at the solution-quartz interface and the same polymer has been studied at the interface of its solution with air[54,55]. Cosgrove et al[56], Lee et al[57], and Russell and co-workers[58] have examined the adsorption of various polymers at solid quartz and mica interfaces from solution in organic solvents. Other studies have been reported of the air-liquid interfacial adsorption of polymers from solution in toluene, Sun et al[26] studying poly(dimethyl siloxane) and Dai et al[59] examining diblock copolymers of polyacetylene and polyisoprene.

Finally the case of insoluble Langmuir type monolayers of polymers has been considered. In some preliminary experiments[60], the sensitivity of the reflection technique to these films was demonstrated for a diblock copolymer of polystyrene and poly(ethylene oxide), but due to concerns over the uniformity of the spreading properties of the polymer the study was not continued. The purpose of the work described in this thesis was to increase the understanding of insoluble polymer monolayers by neutron reflectometry and part of that work concerning Langmuir films of poly(methyl methacrylate) has been recently published.[61].

References

1. Lovesey, S.W., *Theory of Neutron Scattering from Condensed Matter*, Vol I, International Series of Monographs on Physics, No. 72, Adair, R.K., Elliott, R.J., Krumhansl, J.A., Marshall, W., Wilkinson, D.H., Eds., Oxford Science Publ., 1986.
2. Born, M., Wolf, E., *Principles of Optics*, Pergamon Press, Oxford, 1970.
3. Heavens, O.S., *Optical Properties of Thin Films*, Butterworths, London, 1955.
4. J. Lekner, *Theory of Reflection*, Martinus Nijholf Dordrecht, 1987.
5. Névot L., Crocé, P., Phys. Appl. **15**, 761, 1980
6. Crowley, T.L., DPhil Thesis, Oxford University, 1984.
7. Crowley, T.L., Thomas, R.K., Willatt, A.J., private communication.
8. Crowley, T.L. Lee, E.M., Simister, E.A., Thomas, R.K., private communication.
9. Penfold J., Thomas, R.K., *J. Phys.: Condens. Matter*, **2**, 1369, 1990.
10. Crowley, T.L. Lee, E.M., Simister, E.A., Thomas, R.K., Penfold J., Rennie, A.R., *Colloids and Surfaces*, **52**, 85, 1990.
11. Richardson, R.M., Roser, S.J., *Langmuir*, 7, 1458, 1991.
12. Fermi, E., Zinn, W., *Phys. Rev.*, **70**, 103, 1946.
13. Fermi, E., Marshall, W., *Phys. Rev.*, **71**, 666, 1947.
14. Maier-Leibnitz, H., Springer, T., *Reactor Sci. Tech: J. Nucl. Energy A/B*, **17**, 217, 1963.
15. Alefeld, B., Christ, J., Kukla, D., Scherm, R., Schmatz, W., *Neutronenleiter*, Jül-294-NP (Jülich 1965).
16. Steyerl, A., *Z. Physik*, **253**, 169, 1972.
17. Handel, P.H., *Z. Physik*, **252**, 7, 1972.
18. Hayter, J.P., Penfold, J., Williams, W.G., *Nature*, **262**, 569, 1976.
19. Hayter, J.B., Highfield, R.R., Pullman, B.J., Thomas, R.K., McMullen, A.I.,

Penfold, J., *J. Chem. Soc., Farad. Trans.* I, **77**, 1437, 1981.

20. Penfold, J., Williams, W.G., Rutherford Appleton Laboratory Report RAL-85-045, 1985.
21. Penfold, J., Ward, R.C., Williams, W.G., Rutherford Appleton Laboratory Report RAL 87-014, 1987.
22. Penfold, J., Ward, R.C., Williams, W.G., *J. Phys. E: Sci. Instrum.*, **20**, 1411, 1987.
23. Felici, R., Penfold, J., Ward, R.C., Williams, W.G., *Appl. Phys. A.*, **45**, 169, 1988.
24. Felcher, G.P., Hilleke, R.D., Crawford, R.K., Haumann, J., Kleb, R., Ostroswki, G., *Rev. Sci. Instrum.* **58**, 609, 1987.
25. Los Alamos Report LA-11301-C, 1988.
26. Sun, X., Bouchard, E., Lapp, A., Farnoux, B., Daoud, M., Jannink, G., *Europhys. Letts.* **6**, 207, 1988.
27. Sun, X., Farnoux, B., des Cloizeaux, J., Jannink, G., *Physica B.*, **156 & 157**, 407, 1989.
28. Stamm, M., Reiter, G., Hüttenbach, S., *Physica B.*, **156 & 157**, 564, 1989.
29. Anastasiadis, S.H., Russell, T.P., Satija, S.K., Majkrzak, C.F., *J. Chem. Phys.*, **92**, 5677, 1990.
30. Anastasiadis, S.H., Russell, T.P., Satija, S.K., Majkrzak, C.F., *Phys. Rev. Lett.*, 62, 1852, 1989.
31. Russell, T.P., *Materials Sci. Rep.*, **5**, 171, 1990
32. Ashworth, C.D., Messoloras, S., Stewart, R.J., Wilkes, J.G., Baldwin, I.S., Penfold, J., *Phil. Mag. Lett.*, **60**, 37, 1989.
33. Ashworth, C.D., Messoloras, S., Stewart, R.J., Wilkes, J.G., Baldwin, I.S., Penfold, J., *J. Phys. D: Appl. Phys.*, **22**, 1862.
34. Highfield, R.R., Thomas, R.K., Cummins, P.G., Gregory, D.P., Mingins, J.,

Hayter, J.B., Scharpf, O., *Thin Solid Films*, **99**, 165, 1987.

35. Nicklow, R.M., Pomerantz, M., Segmuller, A., *Phys. Rev B*, **23**, 1081, 1981.
36. Buhaenko, M.R., Grundy, M.J., Richardson, R.M., Roser, S.J., *Thin Solid Films*, **159**, 253, 1988.
37. Felcher, G.P., *Phys. Rev. B*, **24**, 1995, 1981.
38. Felcher, G.P., Kampwirth, R.T., Gray, K.E., Felici, R., *Phys. Rev. Lett.*, **52**, 1537, 1984.
39. Felici, R., Penfold, J., Ward, R.C., Olsi, E., Matacotta, C., *Nature*, **329**, 523, 1987.
40. Stamm, M., Majkrzak, C.F., *Am. Chem. Soc. Polymer Prepr.* 1987.
41. Russell, T.P., Karim, A., Mansoor, A., Felcher, G.P., *Macromolecules*, **21**, 1890.
42. Fernandez, M.L., Higgins, J.S., Penfold, J., Ward, R.C., Shackleton, C., Walsh, D.J., *Polymer*, **29**, 1923, 1988.
43. Fernandez, M.L., Higgins, J.S., Penfold, J, Shackleton, C., Walsh, D.J., *Polymer*, **31**, 2146, 1990.
44. Fernandez, M.L., Higgins, J.S., 3rd Int. Conference on Diffusion of Polymers, York, UK, 13-15th Feb. 1991
45. Composto R.J., Stein R.S., Kramer, E.J., Jones, R.A.L., Mansour, A., Karim, A., Felcher, G.P., *Physica B*, **156 & 157**, 434, 1989.
46. Jones, R.A.L., Norton, L.J., Kramer, E.J., Composto, R.J., Stein, R.S., Russell, T.P., Mansour, A., Karim, A., Felcher, G.P., Rafailovich, M.H., Sokolov, J., Zhao, X., Schwarz, S.A., *Europhys. Lett.*, **12**, 41, 1990.
47. Lee, E.M., Thomas, R.K., Penfold, J., Ward, R.C., *J. Phys. Chem.*, **93**, 381, 1989.
48. Penfold, J., Lee, E.M., Thomas, R.K., *Mol. Phys.* **68**, 33, 1989.
49. Lee, E.M., Simister, E.A., Thomas, R.K., Penfold, J., *J. Physique Coll.* **50**, C7, Suppl.10 75, 1989.

50. Bradley, J.E., Lee, E.M., Thomas, R.K., Willatt, A.J., Gregory, D.P., Penfold, J., Ward, R.C., Waschkowski, W., *Langmuir*, **4**, 821, 1988.

51. Grundy, M.J., Richardson, R.M., Roser, S.J., Penfold, J., Ward, R.C., *Thin Solid Films*, **159**, 43, 1988.

52. Lee, E.M., Thomas, R.K., Rennie, A.R. Penfold, Cummins, P.G., Staples, E..J., *Chem. Phys. Lett.* **162**, 196, 1989.

53. Rennie, A.R., Lee, A.M., Thomas, R.K., in preparation.

54. Rennie, A.R. Crawford, R.J., Lee, E.M., Thomas, R.K., Crowley, T.L., Roberts, S., Qureshi, M.S., Richards, R.W., *Macromolecules*, **22**, 3466, 1989.

55. Thomas, R.K., private communication, 1991.

56. Cosgrove, T., Heath, T.G., Phipps, J.S., Richardson, R.M., *Macromolecules*, **24**, 94, 1991.

57. Lee, E.M., Simister, E.A., Thomas, R.K., *Langmuir*, **6**, 1031, 1990.

58. Satija, S.K., Majkrzak, C.F., Russell, T.P., Sinha, S.K., Sirota, E.B., Hughes, G.J., *Macromolecules*, **23**, 3860, 1990.

59. Dai, L., White, J.W., Kerr, J., Thomas, R.K., Penfold, J., Aldissi, M., *Synth. Met.*, **28**, D69, 1989.

60. Penfold, J., Richards, R.W., Qureshi, M.S., Thomas, R.K., unpublished results.

61. Henderson, J.A., Richards, R.W., Penfold, J., Shackleton, C., Thomas, R.K., *Polymer*, **32**, 3284, 1991.

CHAPTER 3 - EXPERIMENTAL

This chapter is divided into five sections. The first describes the synthetic methods used to prepare and characterise the polymer fractions studied, and the other four contain descriptions of the techniques and apparatus used to study the physical chemistry of monolayer systems of those polymers. Hydrogenous and deuterated analogues have been obtained successfully for several polymer systems. These systems (and the acronyms which will be used for them in general hereafter) are listed below;

1. syndiotactic, isotactic and atactic (polymethyl methacrylate), (SYNDIO-, ISO-, AND ATAPMMA);
2. poly (ethylene oxide), (PEO);
3. 85:15w/w diblock copolymers of poly (methyl methacrylate) with poly (4-vinyl pyridine), (PMMA4VP);
4. PMMA4VP polymers quaternised with ethyl bromide to give partial poly-electrolyte materials, (PMMA4VPQ)..

The letters H and D are used to indicate hydrogenous and deuterated materials respectively, thus for example ISODPMMA is a deuterated isotactic poly (methyl methacrylate), while DPMMA4VPQ(H) is a poly (methyl methacrylate)/poly (4-vinyl pyridine) copolymer with a deuterated PMMA block, quaternised with hyrogenous ethyl bromide. It should be noted that only hydrogenous 4-vinyl pyridine monomer was available, and hence no explicit specification of the isotopic nature of 4VP blocks is included in the code.

In addition to the samples prepared in the home laboratory the following materials have been used in this project;

free radically polymerised DPMMA (ATADPMMA) was generously donated by Dr. D. J. Walsh of Du Pont de Nemours Wilmington, Delaware, USA;

ATAHPMMA was fractionated from a broad distribution sample from the Rubber and Plastics Research Association, Shawsbury, UK;

isotactic hydrogenous and deuterated poly (methyl methacrylate) (ISOHPMMA and ISODPMMA) were purchased from Polymer Laboratories Ltd., Church Stretton, UK.

3.1 Synthesis and Characterisation

3.1.1 Anionic High Vacuum Polymerisation

Hydrogeneous and deuterated analogues of SYNDIOPMMA, PEO, and PMMA4VP were synthesised using high vacuum anionic polymerisation methods, as this technique is convenient for controlling the molecular weight, polydispersity and stereotacticity of polymers. The vacuum line consisted of a tubular glass main manifold fitted with three valved 'o'-ring/sleeve connections allowing the attachment of various sub-manifold combinations. Each sub-manifold had a further three outlets fitted with either 'o'-ring/sleeve or ball/socket type joints. All tap fittings, glassware, piston barrels etc were purchased from Young's Scientific Glassware, Acton, England, and were standardised around a nominal glassware diameter of 10mm. Fast screw PTT type tap fittings were used and all vacuum seals were of OS teflon type. Vacuum was achieved by a combination of an Edwards roughing rotary pump model E2195 with an Edwards backing diffusion pump model 63. Roughing on the rotary pump reduced the pressure from atmospheric to approximately $6x10^{-2}$ torr and, backing down from this value, typically the diffusion pump achieved a vacuum of around 10^{-6} to 10^{-7} bar. The combined rotary/diffusion pump system was purchased from Edwards High Vacuum, Crawley, Sussex.

In parallel with the vacuum line, an accompanying dry nitrogen line was attached at the sub-manifold connection points. This allowed convenient nitrogen purging of air or moisture sensitive materials whilst maintaining a high vacuum in the rest of the line. The combined vacuum/nitrogen line system is illustrated schematically in figure 3.1.

Preparation of Reagents

Anionic synthesis, although providing a convenient route to the preparation of well defined polymers, requires extremely rigorous preparation of glassware and reagents in terms of cleanliness, purity and dryness. The presence of even trace amounts of either moisture or polar impurities in starting materials can lead to premature termination of reaction or the complete failure of a polymerisation.

Methyl methacrylate (Aldrich, M5,590-9, 99%) is supplied containing 10ppm hydroquinone monomethyl ether as a polymerisation inhibitor during storage. This was removed by liquid-liquid extraction using repeated aqueous sodium hydroxide and water washes. The monomer was then dried over calcium chloride, distilled under reduced pressure under a dry nitrogen atmosphere, and finally stored under vacuum while standing over calcium hydride. 4-vinyl pyridine monomer (Aldrich, V320-4, 95%) is supplied containing 100ppm hydroquinone as inhibitor and this was removed in exactly the same fashion as for methyl methacrylate.

Ethylene oxide monomer is a highly volatile, poisonous liquid at room temperatures. As supplied (Fluka Chemika, 99.7% pure), it was immediately transferred (in acetone/dry ice cooled glassware) to a round bottomed flask containing calcium hydride and stored under vacuum. Immediately prior to polymerisation further more rigorous drying and purification was required. This is described in more detail in the description of the polymerisation procedure.

Tetrahydrofuran (BDH standard lab reagent stored over sodium) was dried over calcium chloride, refluxed for an hour over fresh lithium aluminium hydride, distilled under dry nitrogen, and stored under vacuum over freshly squeezed sodium wire and benzophenone, giving a deep blue/purple coloured solution. This

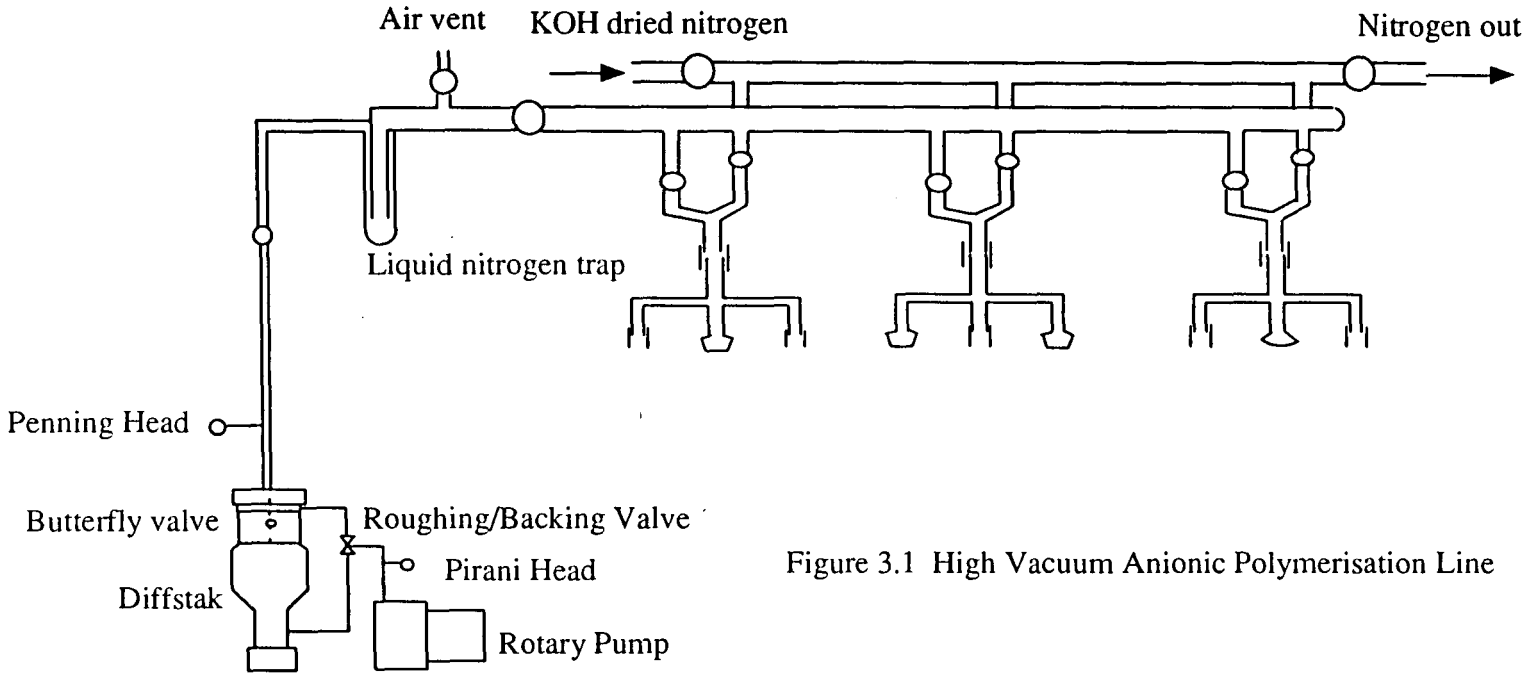

Figure 3.1 High Vacuum Anionic Polymerisation Line

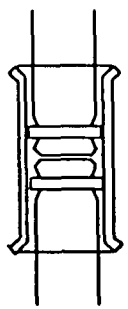

Figure 3.1(a) Sliding Glass joint

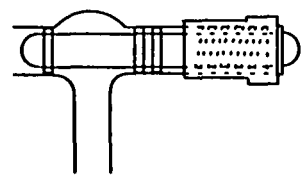

Figure 3.1(b) Young's PTT type Teflon Barrel Tap

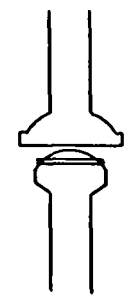

Figure 3.1(c) Ball and socket joint

was necessary to prevent the formation of peroxide radicals in the uninhibited tetrahydrofuran. Dimethyl formamide was distilled in a similar fashion, and was stored under vacuum over calcium hydride.

Reagents were stored on the vacuum line in ground glass B24 necked round bottomed flasks with the glass joint sealed with Apiezon N type high vacuum grease. Depending on the volume of reagent, the flask volume was chosen such that the flask was never more than half full.

Prior to use all reagents were degassed by means of freeze-thaw cycles on the vacuum line, that is to say, freezing the reagent by immersing the flask in liquid nitrogen, pumping down the frozen material, isolating the flask again, thawing the reagent, and stirring (by means of a magnetic stirrer placed in the flask) for several hours. The whole cycle was repeated many times, including one weekend of constant stirring, until the material was thoroughly degassed, indicated by no rapid rise in the measured pressure on opening the connection to the frozen material. The purpose of stirring is two-fold, firstly to facilitate the release of dissolved gases from the liquid, and secondly to ensure intimate mixing of the liquid and drying agent.

Preparation of Glassware

All glassware was washed with permanganic acid prior to its initial use, and between syntheses reaction flasks were washed repeatedly with chloroform and methanol. Immediately prior to distilling in reagents, the reaction flask (figure 3.2) was dried by flaming out with a gas/oxygen torch to remove water adsorbed on the glass surface and washed out with a living polystyryl-lithium solution. This solution consisted of a small amount of styrene monomer dissolved in benzene, initiated by injection of a few microlitres of 2.5M n-butyl lithium in hexanes (Aldrich, 23,070-7). This bright orange coloured solution was stored in the small side flask of

the reaction vessel.

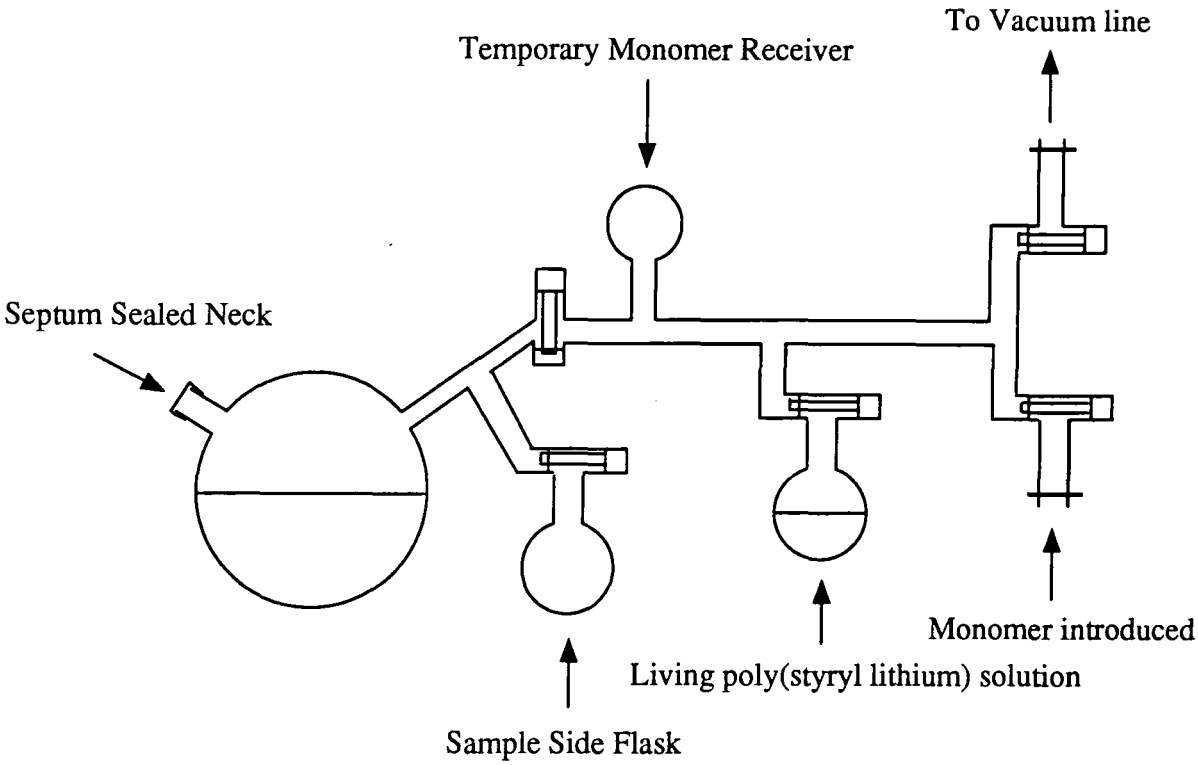

Figure 3.2 Anionic Polymerisation Reaction Vessel

Synthesis of Initiators

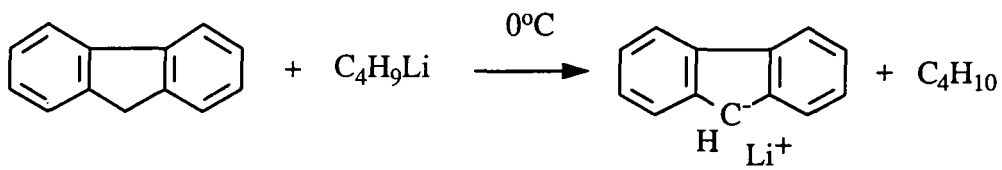

9-fluorenyl lithium was prepared by evacuating a simpler version of the reaction flask with a septum neck (figure 3.3) containing 2.2g fluorene (Aldrich, 12,833-3, 98%). Into this was distilled 50cm^3 THF and 4.8cm^3 of 2.5M n-butyl lithium in hexanes (Aldrich, 23,070-7) was added by injection through the rubber septum, producing an intense dark orange coloured solution as product. For storage

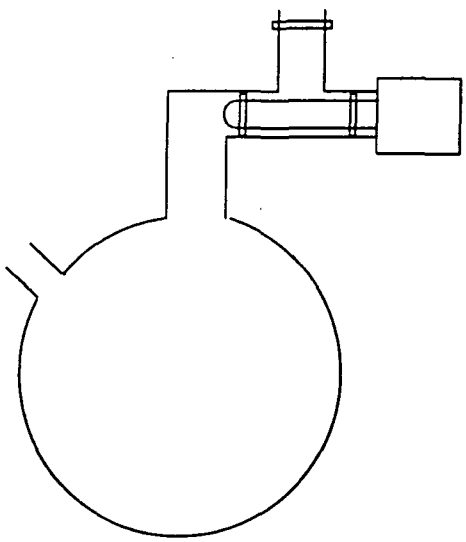

Figure 3.3 Simple Reaction Flask

purposes dry nitrogen was introduced into the flask. Initiator samples were withdrawn from the flask by use of a nitrogen purged Hamilton Gastight micro-syringe injected through the septum cap.

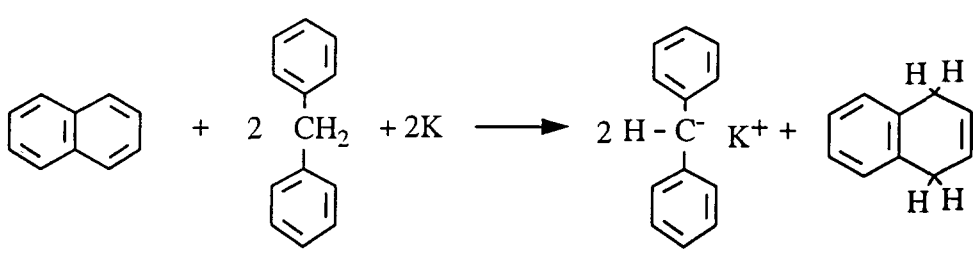

Diphenyl methyl potassium was synthesised by the following method. Dried distilled THF ($60cm^3$) and napthalene (Aldrich 14,714-1, 99%) were placed in the bottom of a $250cm^3$ flask, cooled to 273K in ice, under a dry nitrogen atmosphere. Potassium metal was added such that the mole ratio of napthalene to potassium was approximately 0.66:1. This ensures complete consumption of the napthalene. On addition of potassium a dark green colour appeared along with the evolution of heat. After refluxing for three hours with stirring until the potassium

was consumed, diphenyl methane (Aldrich, D20,931-7, 99%, mole ratio 0.66) in $40cm^3$ THF was added dropwise. After a further two hours the initiator was present as a dark red/purple solution. This was stored in a white natural rubber suba-sealed bottle under dry nitrogen.

Estimation of Initiator Concentration

For an initial estimate of the concentration of 9-fluorenyl lithium initiator, 0.5cm aliquots of the solution were quenched in distilled water to produce an equivalent amount of lithium hydroxide, which was titrated against standard 0.01M hydrochloric acid using phenolphthalein as the end point indicator. A generally more reliable method for both initiators however was to carry out several polymerisations with varying amounts of initiator and to calculate the required volume of initiator for any molecular weight from the molecular weights of the polymers so obtained. For 9-fluorenyl lithium therefore several PMMA samples were prepared, while for diphenyl methyl potassium a polystyrene sample was synthesised as this is considerably more convenient to prepare than poly (ethylene oxide).

Polymerisation

During polymerisation procedures the transfer of all reagents was achieved by molecular distillation under high vacuum with the receiver vessel immersed in liquid nitrogen.

Poly(methyl methacrylate)

Syndiotactic PMMA was prepared by distilling a known weight of monomer into a prepared reaction flask. THF was then distilled into the flask to make an approximately 10% v/v solution of monomer. The temperature of the liquid was allowed to rise to approximately 195K by immersion of the flask in a dry ice/acetone bath and the reaction was initiated by rapid injection of an appropriate volume of 9-fluorenyl lithium, according to the molecular weight required. Polymerisation was accompanied by a pale pink or purple colour in the solution. After one hour the reaction was terminated by the rapid injection of about $5cm^3$ methanol which had previously been degassed by bubbling with dry nitrogen. The product polymer was precipitated into ten volumes of rapidly stirred n-hexane and dried in a vacuum oven at 343K to constant mass. Deuterated PMMA was synthesised in exactly the same fashion as HPMMA.

Poly (ethylene oxide)

PEO was synthesised by a similar process to that used for PMMA. However the nature of the ethylene oxide monomer necessitated the introduction of some further preparatory measures before the reaction would proceed successfully.

Ethylene oxide monomer, prepared as previously described was dried more thoroughly immediately prior to reaction by exposure to the fresh surface of sodium metal. This was achieved by heating a small piece of sodium in a $250cm^3$ round bottomed flask fitted with a Young's tap under vacuum with a gas/oxygen torch flame until it boiled, coating the surface of the flask with fresh metal. Sufficient monomer for the reaction was distilled into the mirrored flask and shaken for an hour to ensure good contact with the surface. This process was repeated until

the mirror was not tarnished by contact with the monomer. This typically involved the use of four or five sodium mirrors. Only now was the dry monomer distilled into a weighed, flamed (simple type) reaction flask. The appropriate amount of THF was distilled into the flask and polymerisation initiated by the injection of a suitable amount of diphenylmethyl potassium at 195K (dry ice/acetone bath), resulting in a pale yellow solution. The reaction flask was left to rise slowly to room temperature overnight, during which time a deeper pink colour developed in the solution. The flask was then immersed in an oil bath at 348K for four days before the reaction was terminated by injection of 100µl of degassed glacial acetic acid. The polymer was precipitated into ten volumes of stirred n-hexane.

In the case of deuterated PEO one further pre-polymerisation step was introduced to remove impurities from the monomer which would otherwise provide potential terminating species. The sodium mirror dried monomer (MSD Isotopes) was distilled into a freshly flamed pre-polymerisation flask (figure 3.4). The

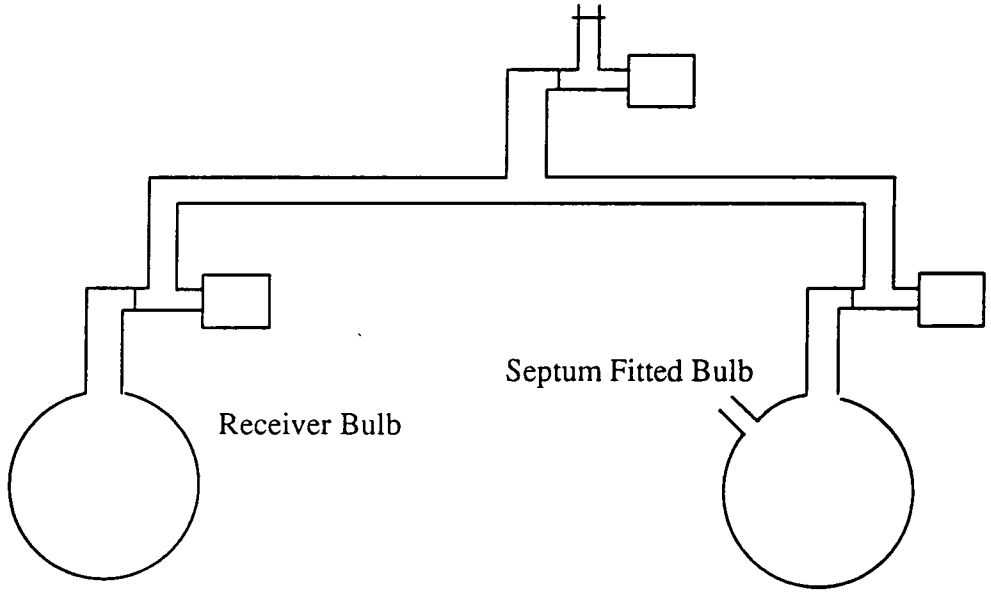

Figure 3.4 Pre-polymerisation Flask

monomer was distilled into the septum fitted arm, into which had been placed a few

crystals of 9-fluorenone (Aldrich, F150-6, 98%). Injection of about 15µl of 2.5M n-butyl lithium gave a bright yellow colour. The monomer was vacuum distilled rapidly into the receiver bulb of the pre-polymerisation vessel, leaving behind a residue of impurities. The purified monomer in the receiver was then transferred to a reaction flask for polymerisation by the same method as for hydrogenous ethylene oxide.

Poly (methyl methacrylate - 4-vinyl pyridine)

PMMA4VP diblock copolymers were also prepared in a fashion essentially similar to PMMA homopolymers. Diphenylmethyl potassium was used to initiate the reaction as this is a better initiatior for both blocks of the system than 9-fluorenyl lithium. Also a mixed solvent system of 85% THF/15% DMF v/v was used as 4VP chains of molecular weight greater than around 5000 are insoluble in THF alone. 4VP was chosen as the preferred block to start the reaction with, as chain branching is minimised by this route. A known weight of 4VP monomer was initiated by injection of diphenylmethyl potassium and after allowing the reaction to proceed at 195K for a few hours, a weighed amount of methyl methacrylate was added rapidly from the open side arm of the reaction vessel. After several more hours the reaction was terminated by addition of degassed methanol. The polymer was precipitated into ten volumes of n-hexane.

3.1.2 Quaternisation of PMMA4VP to PMMA4VPQ

PMMA4VP diblock copolymers have been quaternised with ethyl bromide to produce a block copolymer with a polyelectrolyte block by the following scheme:

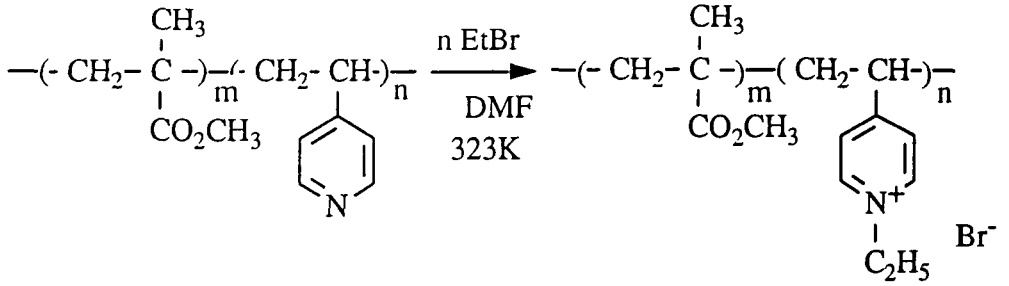

The reaction was carried out on the high vacuum line previously described as this provides a convenient means of transferring reagents under scrupulously anhydrous conditions. Dry distilled DMF was prepared as described in the previous section and stored on the line over calcium hydride. Ethyl bromide (Aldrich, 29,360-7, 99%) and deutero ethyl bromide (MSD Isotopes) were used as received without further purification, but were first dried and degassed by calcium hydride and freeze thaw cycles on the vacuum line.

Four syntheses were carried out using the four combinations of DPMMA4VP, HPMMA4VP, d_5-EtBr and EtBr to give the four products DPMMA4VPQ(D), DPMMA4VPQ(H), HPMMA4VPQ(D), and HPMMA4VPQ(H) where the bracketted letter indicates whether hydrogenous or deuterated ethyl bromide was used. A known weight of about 1g of the unquaternised polymer was put in a Young's tap fitted 50cm^3 reaction flask (no septum neck) with a magnetic follower and evacuated on the line. The polymer was dried by moderate heating of the flask by a hot air gun. To this was added around 10 - 15cm^3 DMF by vacuum distillation. After sufficient time had been allowed for the polymer to dissolve (at least 3 - 4 hours) the solution was frozen by liquid nitrogen immersion and an excess of ethyl bromide (around 0.5g) added by vacuum distillation. The mixture was stirred overnight in a water bath at 323K during which time a pale orange or pink colour developed. To this was added a small amount of AnalaR acetone and the product was precipitated into ten volumes of n-hexane. The resultant viscous

semi-solid material was washed free of residual DMF by re-dissolving in acetone and reprecipitation into hexane, followed by filtering at the pump and washing with more non-solvent. The product was dried to constant mass under vacuum and stored under dry nitrogen as a white powder.

3.1.3 Characterisation of Polymers

Molecular Weight Determination

The molecular weights of PMMA homopolymers and PMMA4VP diblock copolymers were obtained by size exclusion chromatography using two PL gel 10μm mixed columns with THF as solvent, and a Waters differential refractometer as detector. By this method were obtained values for the number average and weight average molecular weights relative to polystyrene standards.

Weight average molecular weights were obtained for PEO samples by static light scattering on a Chromatix KMX-6 photometer. By plotting the ratio of the solution concentration to the Rayleigh ratio (representing the excess scattering after the solvent contribution is subtracted) against the surface concentration, a Zimm plot is obtained. The linear extrapolation of this plot to zero concentration yields an intercept which is related to the weight average molecular weight by

$$M_w = 1 / (K_c.\text{Intercept})$$

where

$$K_c = 2\pi^2 n^2 (\delta n/\delta c)^2 (1+\cos^2\theta)/\lambda^4 N_{av}$$

and

n = refractive index of solvent

= 1.44 for chloroform at λ = 632.8nm

$\delta n/\delta c$ = specific refractive index increment

$= 0.0459$ for $PEO/CHCL_3$

N_{av} = Avogadro's number

θ = scattering angle, usually small enough that

$1 + \cos^2\theta \approx 2$.

Determination of Stereotactic Sequences in PMMA

The tacticities of poly (methyl methacrylate) samples were determined by 400 MHz ^1H and ^{13}C NMR on a Varian VXR-400(S) instrument. In the proton spectrum the methylene proton shift region at around 1-2ppm contains splittings which are characteristic of the tactic nature of the polymer. Two successive monomers in the chain form a statistical dyad, figure 3.5. For the case of a syndiotactic addition the dyad is termed racemo and the unit contains a twofold axis of symmetry. Thus the two methylene protons are chemically similar and there is only a sharp methylene singlet observed. For an isotactic addition or meso dyad on the other hand, there is a plane of symmetry but no twofold axis of symmetry. This means that the two methylene protons are no longer equivalent and a geminal coupling into two doublets split by approximately 15Hz should be observed. This analysis was pioneered by Bovey and Tiers[1] and has since been refined to enable the attribution of longer statistical sequences (triads, tetrads, etc)[2].

Similarly in the ^{13}C spectrum, the carbonyl signal at around 176-178ppm is subject to a slight change in shift according to the chain tactic sequences around it. Predicted assignments up to and including heptads have been calculated for a variety of statistical systems, and as the field strength and resolution of modern NMR technology has increased, experimental resolution of these signals has been achieved[3].

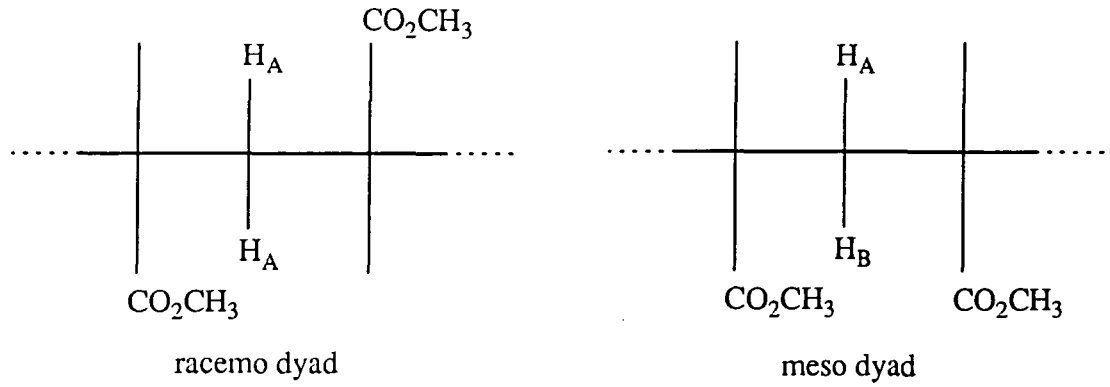

Figure 3.5 Dyad sequences of PMMA

Analysis of Composition of PMMA4VP Copolymers

The relative amounts of the two monomers in the PMMA4VP copolymers were obtained by microanalysis and UV-visible absorbance spectrophotometry. In the former instance, the single nitrogen atom of the pyridine ring in 4-vinyl pyridine provides a convenient measurement of the amount of that monomer. In the latter case 4VP displays a strong absorption band at 358nm associated with its conjugated ring system. By comparison of the relative intensities of this absorption for the copolymers and a poly(4-vinyl pyridine) homopolymer the fraction of the copolymer which is 4VP may be inferred.

Estimation of degree of Quaternisation in PMMA4VPQ Copolymers

The extent of quaternisation in PMMA4VPQ copolymers was obtained by elemental analysis for the bromine content in the molecule. The product was combusted in an oxygen atmosphere, then pure water was used to absorb HBr from the resultant gases. The acid was then estimated by titration with standard base, resulting in an equivalent Br content in the original material.

3.2 Surface Pressure - Concentration Studies

Surface pressure - surface concentration isotherms were obtained using a Teflon Langmuir trough purchased from Nima Technology Ltd, Coventry, UK. The trough was installed on a six by three foot by four inch thick optical vibration isolation table purchased from Ealing Electro-optics, Watford, UK. Temperature control was achieved by circulation of water through a network of tubes in the underside of the teflon trough base using a Neslab RTE-100 thermostat.

Surface pressure measurements were obtained by means of a 10mm wide, high grade filter paper Wilhelmy hanging plate sensor attached to a displacement transducer, the raw output from which was converted to a real time display of surface pressure against either surface concentration or area on a Dell System 220 PC by Nima's commercial software, written in Turbo Pascal. The Nima trough is shown in figure 3.6.

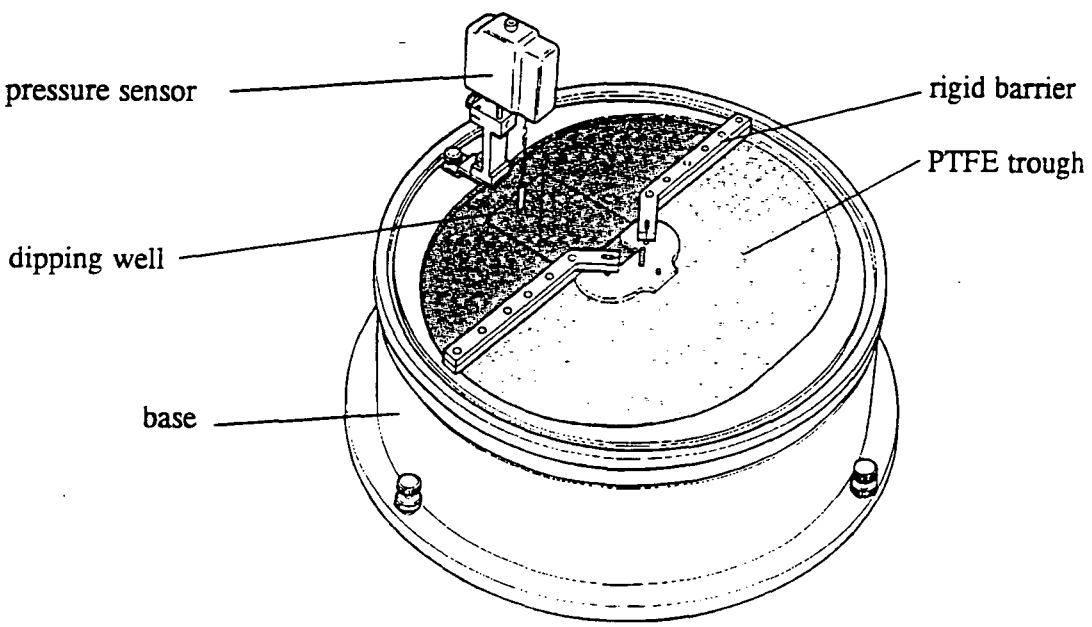

Figure 3.6 Nima Langmuir Trough

3.3 Neutron Reflectometry

Neutron reflection experiments were carried out on two instruments, one a time-of-flight, fixed geometry, dedicated reflectometer, and the other a fixed wavelength small angle neutron scattering spectrometer specially adapted for use as a reflectometer. These were respectively, CRISP, operating from the pulsed spallation source ISIS at the Rutherford Appleton Laboratory, Chilton, Didcot Oxfordshire, and D17 operating from the research nuclear reactor of the Institut Laue-Langevin, Grenoble, France. The data obtained from these instruments is equivalent in the same momentum transfer range, however the experimental methods used to obtain them are somewhat different and will be described in more detail below.

The same Langmuir trough was used for neutron reflection experiments on CRISP and D17. This was built to a design of reasonably standard type, but was slightly adjusted for the demands of reflection experiments. The reflectometry trough is illustrated in Figure 3.7. The active area of the trough surface was swept by two mobile, stepper motor driven parallel teflon barriers aligned in the long dimension of the trough. The outer aluminium casing of the trough contained a fused silica glass window at either end to allow the neutron incident and reflected beams to pass through and the trough was designed so that the barrier supports did not impede the pathway of the neutrons.

During neutron reflection experiments a known mass of sample was spread onto the surface from a volatile spreading solvent of known concentration onto a known area to obtain the initial concentration. Further increases in coverage were achieved either by the addition of more sample or slow compression of the barriers to a smaller area. After sample deposition or compression, around ten minutes were allowed to ellapse before data acquisition was commenced to allow

the spreading solvent to evaporate and the material in the layer to expand into the available area. Reflectometry experiments were carried out using ambient temperature conditions of approximately 298K.

3.3.1 CRISP

The Critical ReflectIon SPectrometer, CRISP at the Rutherford Appleton Laboratories, Chilton, Didcot, Oxfordshire, is a time-of-flight reflectometer for the study of critical reflection phenomena of a wide variety of surfaces. It operates in a fixed incident angle mode, which is usually, but not always, 1.5° to the horizontal. The normal momentum transfer range of 0.05 - 0.65Å^{-1} is achieved by use of a multi-wavelength, so called white neutron beam with wavelengths between 0.5 - 13Å. The instrument is operated from the N4 radial beamline of the spallation neutron source ISIS, and the raw neutron beam is cooled by a hydrogen moderator at 25K. Wavelength filtering is achieved by the use of a 50Hz wavelength limiting chopper at a distance of 6m from the source, where wavelengths of less than 0.5Å and greater than 13Å are rejected. From the pulsed beam any stray, out of sequence, contamination originating from pulses earlier than the primary reference pulse are rejected by nickel frame overlap filtering mirrors and the radiation is collimated by cadmium shielding into a beam size of typically 40mm width by 0.5 to 4mm height, depending on the requirements of the sample. The shielding components are held and adjusted by optical research quality micrometer positioning stages. At this point if it is necessary to measure at lower Q values (for example to probe to greater depths into the sample) it is possible to include a neutron reflecting, non-polarising supermirror which deflects the beamline from its standard 1.5° geometry to shallower incident angles. At an angle of approximately 0.4° the lowest Q value accessible is around 0.01Å^{-1}.

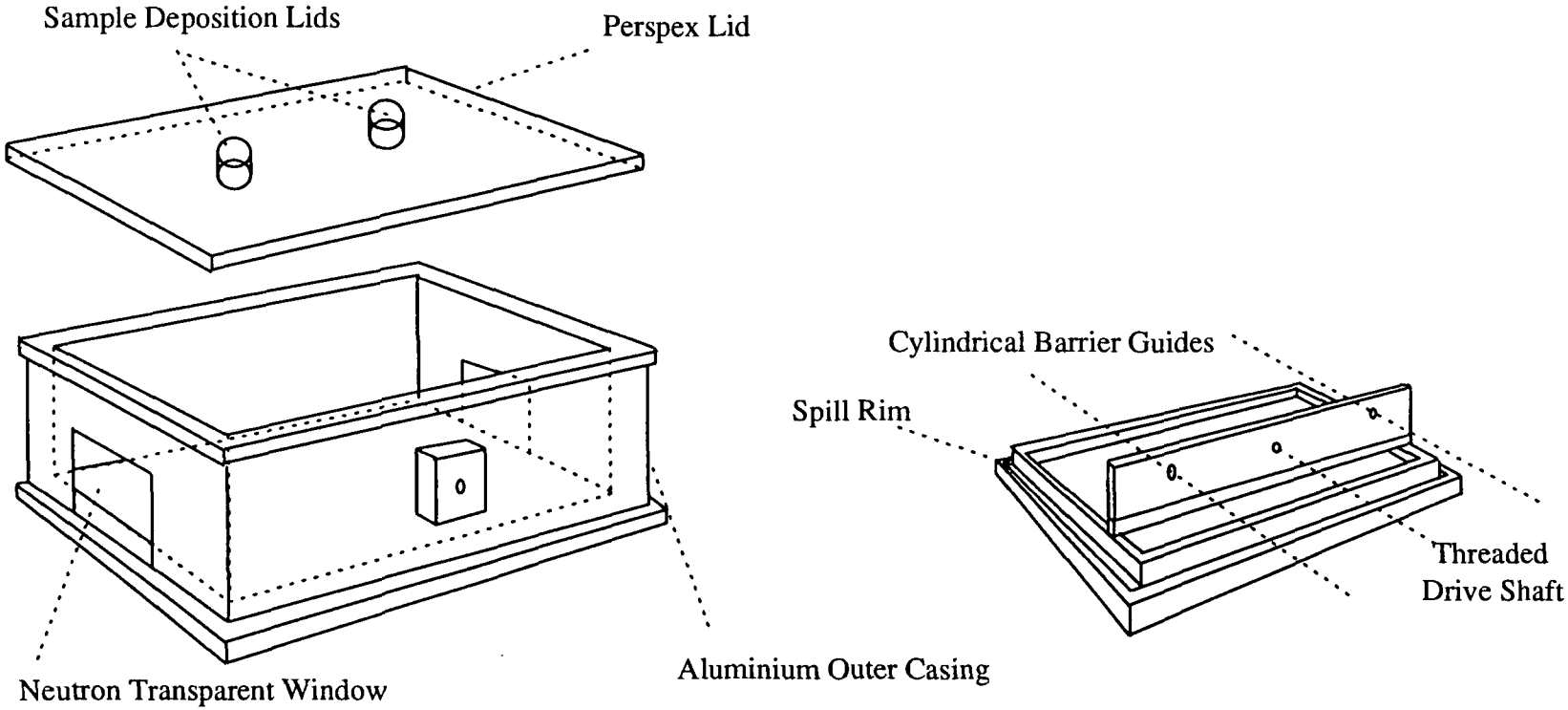

Figure 3.7 Langmuir Trough used for Neutron Reflection Experiments

(Single Barrier only shown for clarity)

The neutron radiation encounters the sample at a distance of 10.25 m from the source. The sample position is mounted on a massive concrete anti-vibration plinth and the sample itself is placed on a manual vertical height adjustment jack to allow efficient alignment of the system. The reflected signal is detected by a single He^3 gas detector which may be moved up or down according to the incident angle used. The sample to detector distance is 1.75m. Sample and detector alignment were achieved by the use of a laser beam which was manipulated by mirrors to be colinear with the path of the neutron beam.

The intensity of the reflected beam pulse was analysed as a function of the slightly different arrival times of reflected neutrons of different wavelengths at the detector, hence the term time of flight. This raw data was then converted to the corresponding reflectivity by ratioing the reflected intensity to the corresponding intensity in the incident pulse detected by a scintillation monitor mounted in the incident beamline. Momentum transfer values were calculated by rebinning the time analysed data packages into corresponding wavelength sets and combining these with the known incident angle. Data aquisition and treatment were carried out on a Vaxstation 3200 workstation. Typical data acquisition times were 2-4 hours in the standard 1.5° geometry and 10-30 minutes at the lower angles, depending on the proximity to total reflection in all cases. The CRISP reflectometer as used in non-polarising mode is illustrated in Figure 3.8.

3.3.2 D17

D17 at the Institut Laue Langevin is normally used as a small angle scattering spectrometer. The modified instrument as used as a reflectometer for liquid interfaces is described briefly below.

A curved guide from the reactor cold source conducts the incident

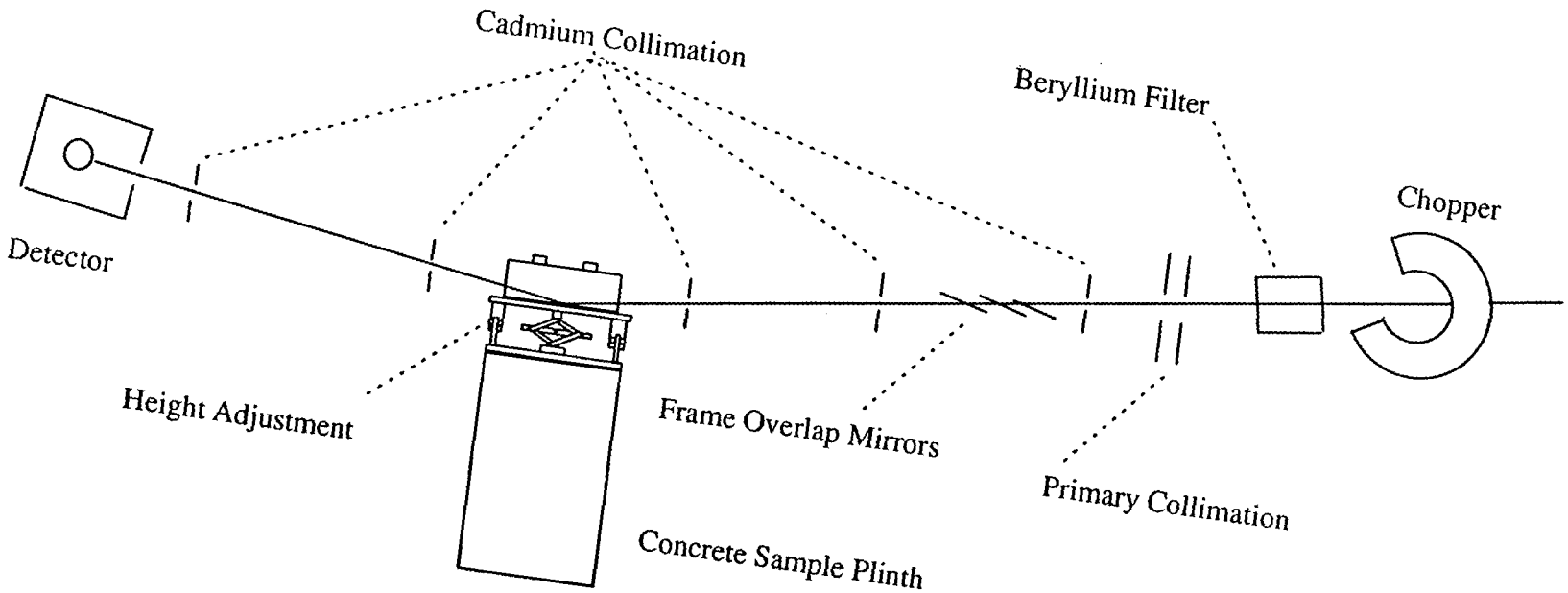

Figure 3.8 CRISP Critical Reflection Spectrometer

radiation to the instrument where primary collimation is carried out. A velocity selector with 5 or 10% resolution selects a single wavelength at any time but this may be conveniently altered between 8.7 and 30Å. The beam is collimated into a horizontal beam of cross-section approximately 30mm by 30mm. Shielding circular diaphragms are used to further reduce the beam diameter to 20mm and the beam passes down an evacuated guide tube towards the sample site. A rectangular beam of typically 20mm width by 0.5 to 2mm height is produced by micrometer - adjustable cadmium slits at the downstream end of the guide.

At the point normally used for the sample site during SANS experiments the beam is deflected downwards by a supermirror mounted in a goniometer cradle. The beam therefore is incident upon the sample at an angle twice the angle of the mirror to the horizontal. The range of incident angles on the sample was typically 0.4 to 1.0° giving an accessible Q range of approximately 0.01 to 0.1$Å^{-1}$. This was achieved by a combination of wavelength and angle changes and therefore it was necessary to alter the sample height frequently and reproducibly. This was achieved by mounting the sample on a jacking system powered by a stepper motor drive unit which could be driven a certain number of pulses either up or down. To exclude extraneous background vibrations the entire assembly was mounted on an aluminium supported base plate sitting on high density polyurethane foam blocks, essentially a large mass - flexible spring system. In later experiments, an active anti-vibration table was incorporated under the trough to further minimise background vibration. The sample area arrangement is shown in Figure 3.9.

The reflected specular peak (and any off-specular diffuse scattering) are detected by a BF_3 multi-detector situated at a distance of 2m from the sample. This consists of 128 horizontal x 128 vertical elements 5mm apart in both directions. The detector chamber was flushed with argon gas before and during use and the detector window covered by a thin aluminium sheet rather than using the detector evacuated.

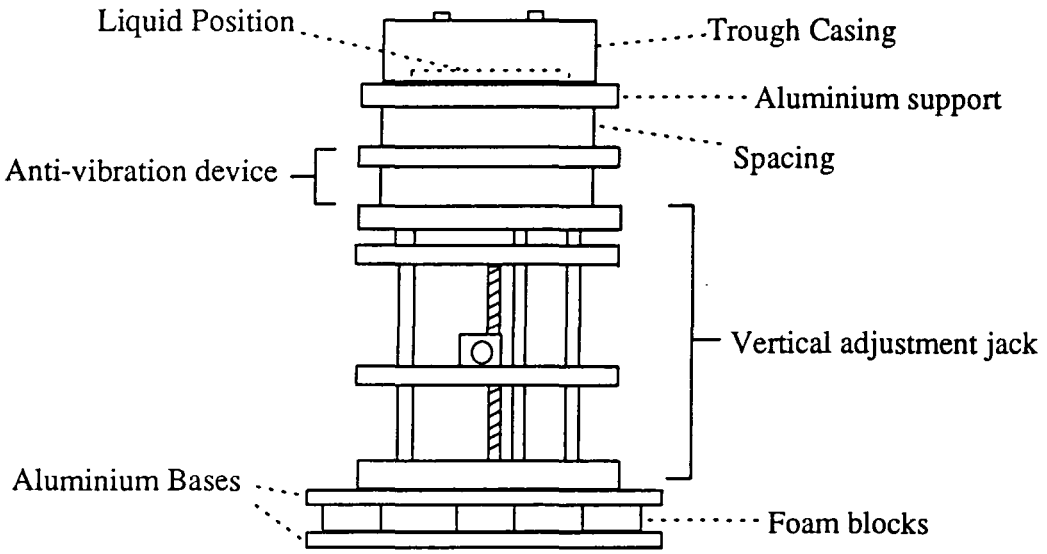

Figure 3.9 Sample Plinth at D17

This enabled measurement of low signal intensities, which would otherwise have been cut out by the more robust quartz window usually employed.

Sample alignment was carried out by the combined use of light from a high intensity lamp and a low power He/Ne laser, aligned to be colinear with the neutron path for rough alignment, and signal maximisation with neutrons for the precise optimisation of conditions. The micropositioning of the supermirror and the sample height, the acquisition of raw data, and the conversion of raw data to reflectivity values were controlled by the use of a Microvax II computer, using software developed by the scientific staff of the ILL. The collection time of each individual data point was governed by the magnitude of the reflected signal to the instrument background. Typically these ranged between 2 and 30 minutes. For a profile consisting of sixteen points evenly spaced in the Q interval of 0.01 to 0.1 $Å^{-1}$ the total profile acquisition time was roughly equivalent to a long run on CRISP. A schematic representation of the D17 instrument set up for an air-liquid interface

experiment is shown in Figure 3.10.

Exact angles and Q values could be calculated from the geometry of the instrument according to the detected peak maximum on the multi-detector. Reflectivity values were obtained by ratioing the combined integral counts for the detector cells corresponding to the reflected peak at a given angle and wavelength with the equivalent integrated count for a neutron beam reflected by the supermirror straight through the trough windows without encountering the liquid surface.

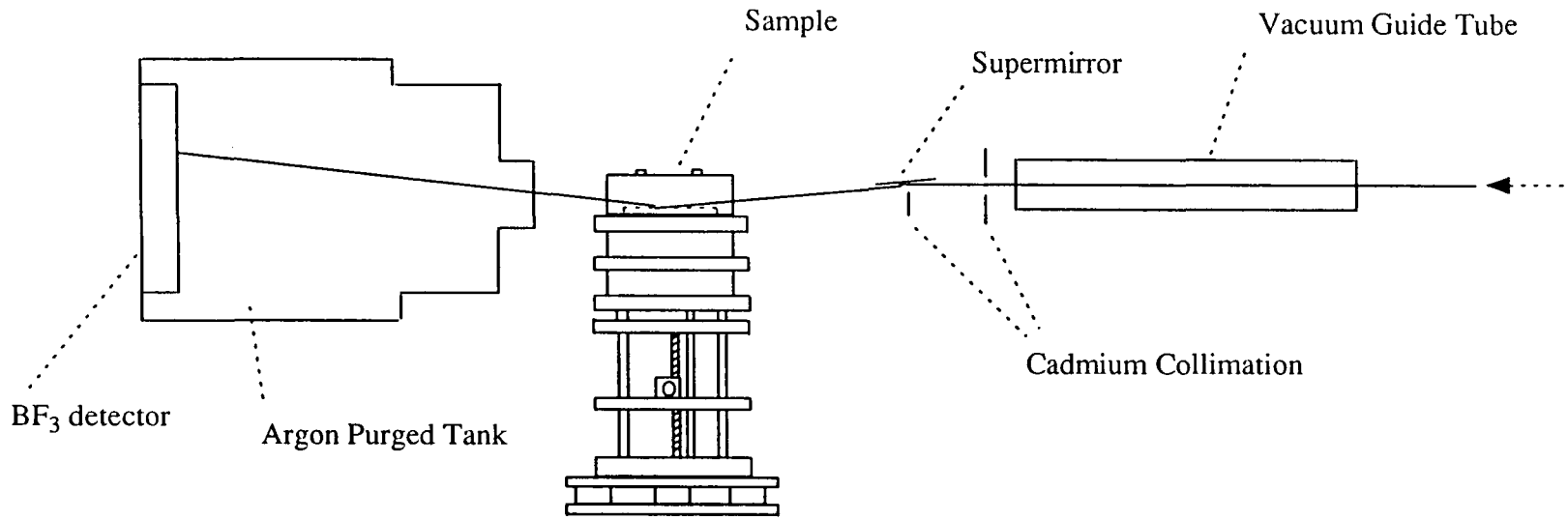

Figure 3.10 D17 modified for use as a Neutron Reflectometer

3.4 Ellipsometry

Ellipsometric studies were carried out on an ellipsometer designed and built at the Max-Planck Institut für Polymerforschung, Mainz, Germany. A schematic representation of the ellipsometer is shown in figure 3.11. The operation of the ellipsometer was based on the determination of the properties of elliptically polarised light incident on a surface such that on reflection the resultant beam was plane polarised and could therefore be extinguished by a plane polarising analyser.

The ellipsometer was mounted on an eight inch thick optical vibration isolation table in a black curtained booth. The incident and detection arms were pivoted from a solid metal plate bolted perpindicular to the surface of the optical table. The design was such as to allow these arms to be rotated through a range of angles and fixed precisely at a given position. The incident angle chosen was the Brewster angle of 64.4° as this gives maximum sensitivity in the measured parameters. The light source used was a 436nm Ar^+ ion laser, guided to the incident side of the polariser unit by a single mode optical fibre. A quartz quarter wave plate retarder (QWP) was incorporated in the incident beam line. This retarded the phase of the incident plane polarised beam as generated by the polariser anisotropically by the amount

$$\beta = 2\pi t(n_f - n_s)/\lambda$$

where

t = plate thickness

λ = wavelength

and n_f and n_s are the refractive indices in the fast and slow orthogonal axes of the QWP material.

The plate thickness was such that when the QWP was suitably aligned to the incident plane beam, one orthogonal component was retarded by $\pi/2$ (one quarter

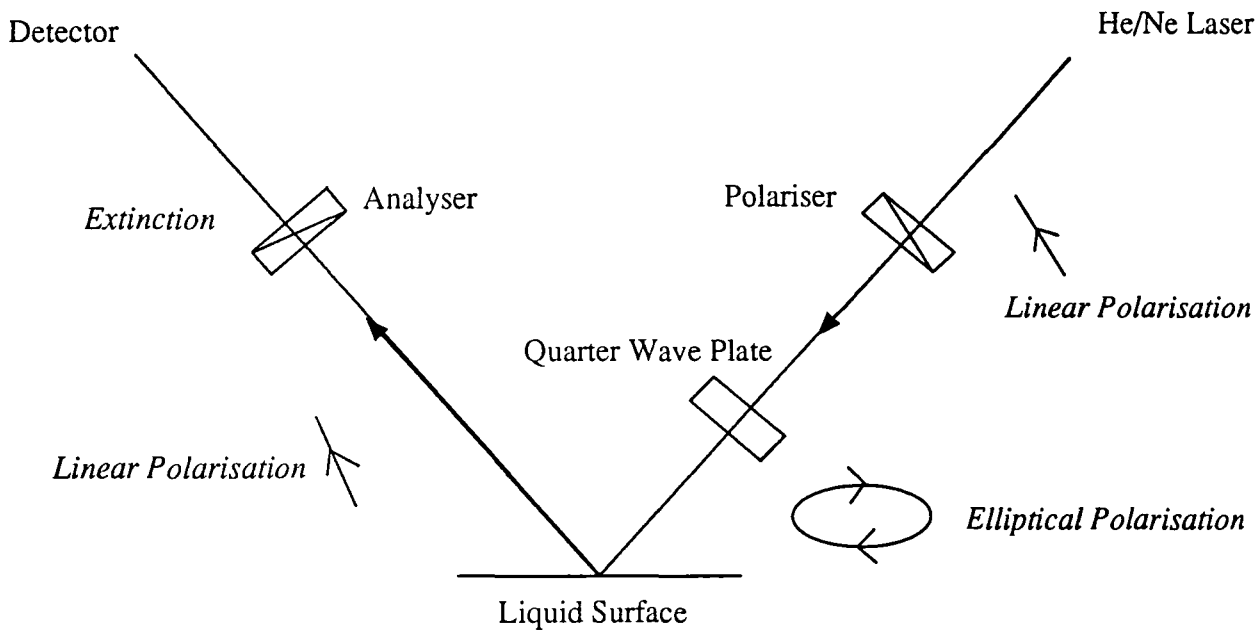

Figure 3.11 Schematic Representation of Ellipsometry Experiment

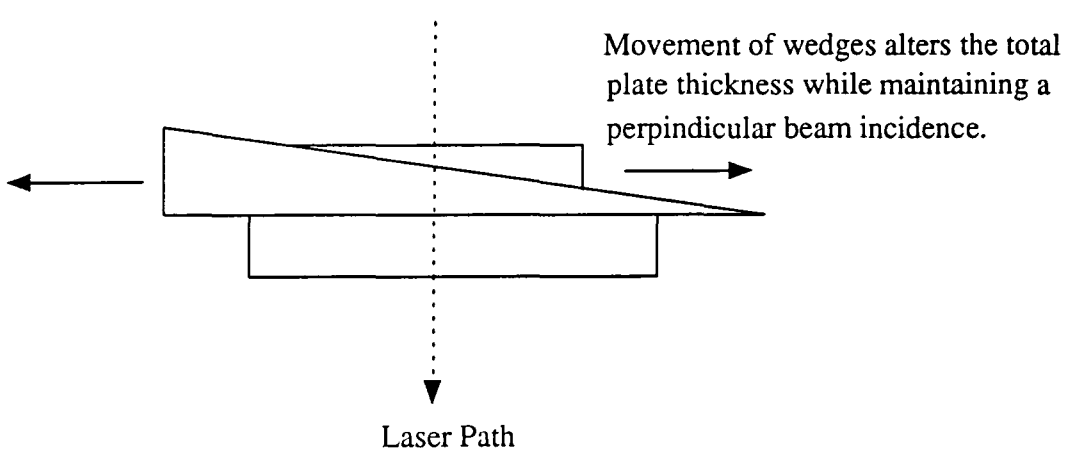

Figure 3.12 Quarter Wave Plate Assembly

wave) relative to the other. This resulted in an elliptically polarised beam incident on the surface. Exact quarter wave retardation was achieved by the use of three wedge shaped pieces of quartz which could be manipulated to produce precisely a given width of material, see figure 3.12.

The reflected signal was then minimised by the analyser (an identical component to the polariser). Analyser and polariser settings were adjusted in turn to give a plane polarised reflected signal, for which a single analyser setting gave total extinction. From the polariser, analyser and QWP settings the disinclination of the elliptically polarised incident field is obtained and hence the values of Δ and ψ, from the relationships

$$\tan\Delta = \sin\beta \tan(\pi/2 - 2P_o),$$

$$\cos 2L = -\cos\beta \cos 2P_o,$$

$$\tan\psi = \cot L \tan(-A_o)$$

where β = retardation of QWP,

P = polariser azimuth setting,

A = analyser azimuth setting,

and subscript o represents the extinction setting.

The polariser and analyser units and the detected light intensity were controlled and recorded by a Digital Research VAX computer using custom written FORTRAN software, and the polariser and analyser movements were performed with high reproducibility by stepper motor units driven by step commands from the computer. The error in the measured angles was estimated at $\pm 0.003^\circ$ by triplicate measurements.

A classical rectangular design of Langmuir type trough was used to contain sample films for ellipsometric study. A single barrier driven by an electric stepping motor via a high gearing system swept the water surface. The liquid containing body of the trough and barrier were constructed of teflon and the whole

was protected by a perspex outer box. The lid of this box however was partially withdrawn to provide just enough clearance for the entrance and exit of the light beam. Temperature was maintained at a steady 298±0.1K by a Lauda water circulator, which fed a network of channels on the underside of the teflon body of the trough. The trough was placed in the sample area of the ellipsometer on an optical quality fine screwed lab jack mounted on a three legged 30cm square marble optical bed. This allowed the sample height to be conveniently altered with minimal vibration.

Surface pressure measurements were obtained in situ simultaneously with the ellipsometric studies by a Wilhelmy hanging plate sensor connected via a displacement transducer to a PC. Custom written Turbo Basic software controlled the barrier movement and displayed surface pressure data in real time as a function of trough area.

3.5 Surface Quasi-Elastic Light Scattering

Surface Quasi-Elastic Light Scattering (SQELS) experiments were carried out on a spectrometer designed and built in the home laboratory at Durham. The apparatus is shown in figure 3.13. The instrument was constructed from standard components purchased from Ealing Electro-optics, Watford, UK, and standardised around the range of components fitting their table mounting triangular optical benches. The SQELS instrument was constructed around the Nima film balance used for surface pressure studies and mounted on the optical vibration isolation table on which the trough was placed. The apparatus took the form of two parallel 1.5m lengths of triangular optical track fixed equi-distantly either side of the Nima trough, one to guide and manipulate the incident beam onto the liquid surface, and the other to collect the reflected light and guide it to a detector. All component mountings were capable of three axis precision translation to ensure exact beam guidance.

The light source used was a Hughes 10mW nominal power rating He/Ne laser, model No. 3225H-PC, whose radiation was polarised normal to the plane of incidence. After passing through lens l_1 the focussed beam was split into several orders of diffraction maxima by a transmission diffraction grating, G, purchased from Data Sites Ltd, UK. This consisted of a series of 10 micron silvered lines with an inter-line separation of 100 microns. Thus the transmission from the grating was approximately 90 per cent. The split beam was incident upon lens l_2 which was positioned so that the combined effect of l_1 and l_2 was to image the laser source from the exit of the laser tube as a focussed spot at the entrance of the photo multiplier detector. The beam was guided onto the liquid surface by a "periscope" arrangement of $\lambda/10$ research quality mirrors which first diverted the beam vertically and then simultaneously turned it to 90° from the direction of the optical track and

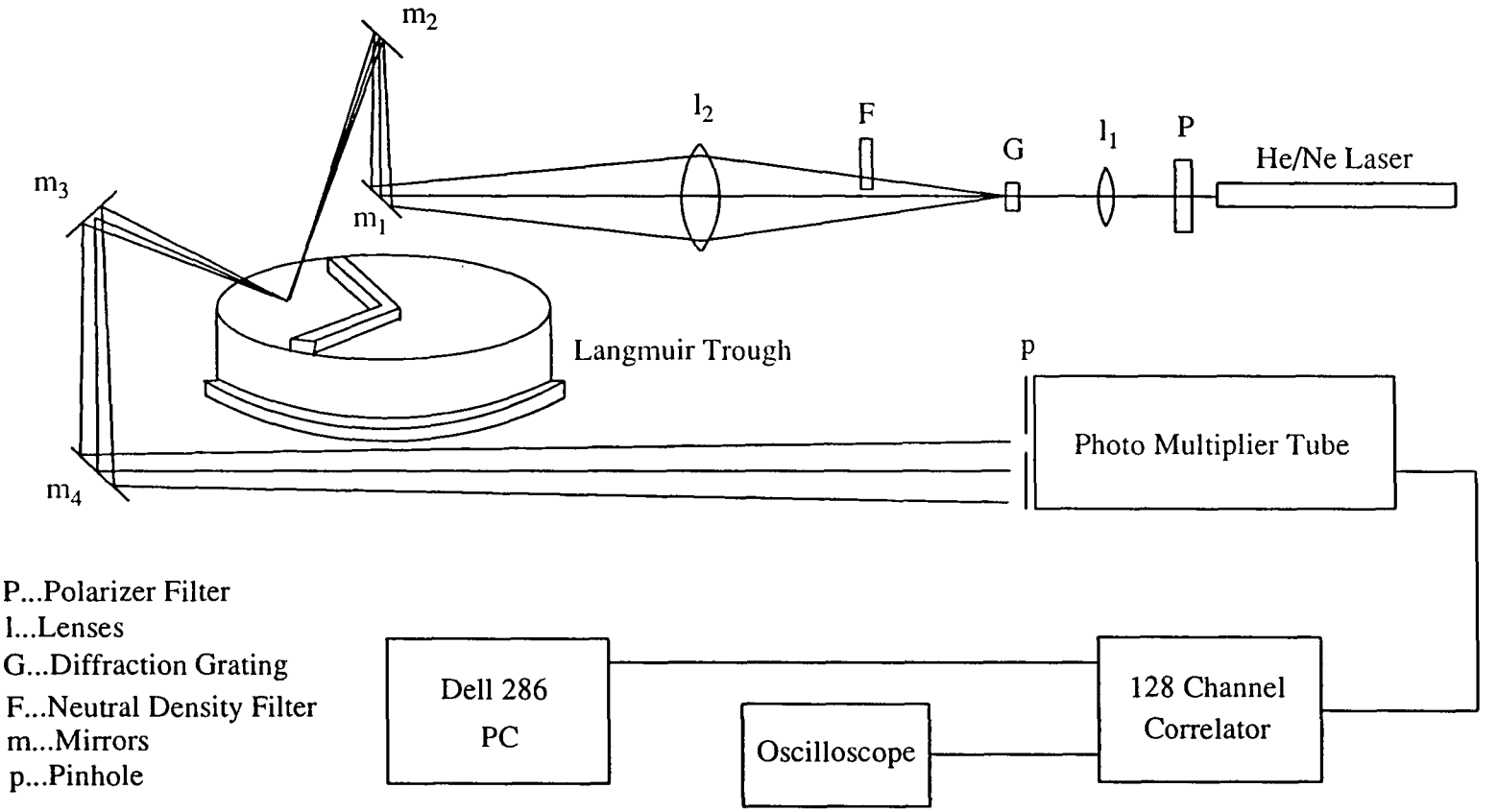

Figure 3.13 Surface Quasi-Elastic Light Scattering Apparatus

downwards onto the liquid at an incident angle of 55.0°. The combination of lenses and distances between l_1,l_2 and G was adjusted so that the divergent diffraction orders were reconverged as a single spot of approximate diameter 2.5mm on the liquid surface. This was conveniently obtained with focal length lengths of 100mm for l_1 and 300mm for l_2.

After encountering the surface, the reflected beam was collected by a second periscope of mirrors and guided horizontally to a photo multiplier tube detector at a distance of approximately 2.25m from the sample surface. The reflected beam fell as a horizontal series of spots, with the brightest central spot being the specular reflection from the main undiffracted spot and the others the specular reference spots from the diffraction orders. These then provided local heterodyne mixing beat signals for the scattered intensity from the main spot falling on the detector pinhole at the same angle. Thus by tilting mirror m_4 slightly, a given diffraction order (and hence scattering vector value) could be selected by directing it into the 1.5mm pinhole of the photo multiplier. A 5% transmission neutral density filter was used to attenuate the diffraction orders down to an intensity where the heterodyne beating effect was maximised.

The output from the PMT was fed to a 128 channel autocorrelator (Malvern model K7025) with channel widths of about 5-10μs, the measured signal being displayed as it was obtained on an oscilloscope. Operation of the correlator and storage of the data in ASCII file format was controlled through a Dell PC using GW-Basic software.

References

1. Bovey, F.A., Tiers, G.V.D., *J. Polym. Sci.*, **44**, 173, 1960.
2. Bovey, F.A., *Chain Microstructure of Macromolecules* in *Nuclear Magnetic Resonance Spectroscopy*, 2nd Ed., Bovey, F.A., Jelinski, L., Mirau, P.A. co-authors, Academic Press, New York, 1989.
3. Hatada, K., Kitayama, T., Koichi, U., *Prog. Polym. Sci.*, **13**, 189, 1988.

CHAPTER 4 - POLY(METHYL METHACRYLATE)

Summary

Several fractions of syndiotactic poly (methyl methacrylate) have been synthesised. The analysis of these fractions and those of atactic and isotactic PMMA samples with respect to molecular weight and tacticity is described. The results of examination of selected fractions of each tacticity by surface pressure, neutron reflection, ellipsometry and SQELS techniques are reported and comparisons between the behaviour of the various materials are made.

Syndiotactic and atactic PMMA are classically defined as liquid condensed in type while isotactic PMMA is liquid expanded, a surface pressure being detected at much larger areas per molecule. Analysis of the surface pressure data by scaling theory shows that SYNDIO and ATAPMMA exhibit behaviour associated with less than or near theta conditions whereas ISOPMMA exhibits good 2-D solution behaviour.

Correspondingly neutron reflection indicates that SYNDIO and ATAPMMA monolayers are rather similar in structure, but that ISOPMMA contains a rather higher proportion of air in the film. Optical matrix fitting suggests that the films may contain >50% air in some cases and only around 5-10% water and so the use of an alternative patchy film model has been assessed. The usefulness of kinematic approximate expressions has been demonstrated both as an alternative to matrix methods for the determination of film parameters and also as a clear way of determining the uniqueness of the model fitted to the data.

4.1 Synthesis and Characterisation

Various fractions of syndiotactic PMMA were synthesised by the anionic high vacuum route previously described. A summary of the molecular weights values obtained by Gel Permeation Chromatography for these polymers and for the samples of atactic and isotactic PMMA used later are is given in table 4.1.

Sample Code	$M_n/10^3$	$M_w/10^3$	M_w/M_n
001	75.1	184.7	2.46
002	151.0	267.0	1.77
003	30.8	67.4	2.19
004	13.3	22.3	1.68
005	17.7	47.7	2.70
006	17.6	45.4	2.59
007	24.2	56.4	2.33
008	26.6	71.8	2.70
009	50.1	69.3	1.38
011	47.3	101.3	2.14
012	119.3	335.9	2.81
013	8.9	21.1	2.37
014	29.9	46.2	1.55
ATAHPMMA	130.4	144.9	1.11
ATADPMMA	1706	4800	2.81
ISOHPMMA	10.4	51.1	4.94
ISODPMMA	9.5	134.2	14.2

Table 4.1 Molecular Weights of PMMA Samples

From the above samples the fractions coded 002 and 012 were selected for further study, along with ISOHPMMA, ISODPMMA, ATAHPMMA and ATADPMMA. Hereafter these fractions are referred to as SYNDIOHPMMA and SYNDIODPMMA respectively.

The stereotactic sequences in the polymer chains were estimated by 400MHz ^{13}C NMR, by ratioing the integral intensity of carbonyl resonance signals

in the 176 - 178 ppm region, which are sensitive to the statistical distribution of the tacticity of neighbouring chain sequences. It should be noted that the finely separated lines do not originate from conventional proton neighbour splitting but are in fact due to the slight shift changes caused by the differing stereo-sequences around the carbon atoms. Typical expansions of the relevant region in the spectra for syndio and isotactic polymers are shown in figure 4.1. From the weighted average of the various contributions it is possible to calculate the probability of racemo (syndiotactic) or meso (isotactic) dyads along the chain. These values are summarised in table 4.2.

Shift	176.6	176.8 - 177.2	177.7-177.9	178.0-178.2	Proportion in molecule	
Attributable to	mmmm	rmrr/mmrr + mmrm/rmrm	rrr	mrrr		
Polymer	Relative Integral Intensity				P_r	P_s
SYNDIOHPMMA	0	0.32	0.56	0.12	0.85	0.15
SYNDIODPMMA	0	0.24	0.60	0.16	0.87	0.13
ATAHPMMA	0	0.42	0.36	0.22	0.79	0.21
ISOHPMMA	0.84	0	0.16	0	0.16	0.84
ISODPMMA	1.00	0	0	0	0	1.00

Table 4.2 Stereotacticity of PMMA by ^{13}C NMR

Additional evidence for the tacticity of the polymers is obtained from the ^{1}H NMR spectra which may be compared in figure 4.2. In a similar fashion to the ^{13}C spectra, signals in the shift range 1.0 - 2.0 ppm are attributable to methylene protons experiencing various neighbouring statistical sequences. In the meso dyad there is a plane of symmetry but no twofold axis of symmetry whereas in the racemo dyad there is a two fold axis of symmetry. Thus for a racemo dyad the two methylene protons are equivalent, and there should be a sharp methylene singlet peak in the 1ppm region. The non-equivalence of the meso dyad protons however leads to a splitting pattern of two doublets split by the geminal coupling of around

15Hz. This pattern is indeed seen in the spectra of SYNDIOHPMMA and ISOHPMMA, other signals being due to a variety of longer range tactic sequences reflecting the occasional occurrence of tactic defects along the chain backbone.

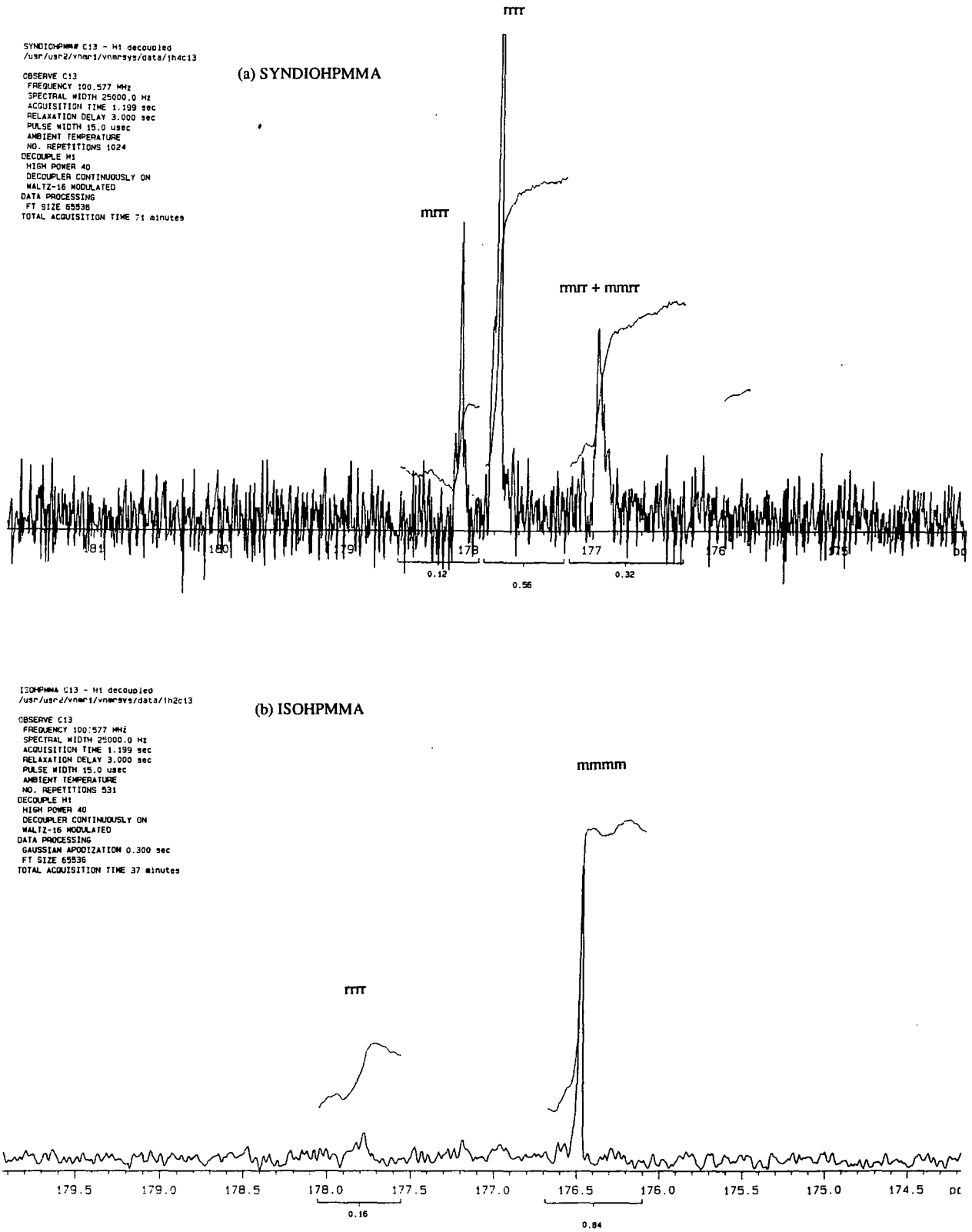

Figure 4.1 ^{13}C NMR Spectra for PMMA

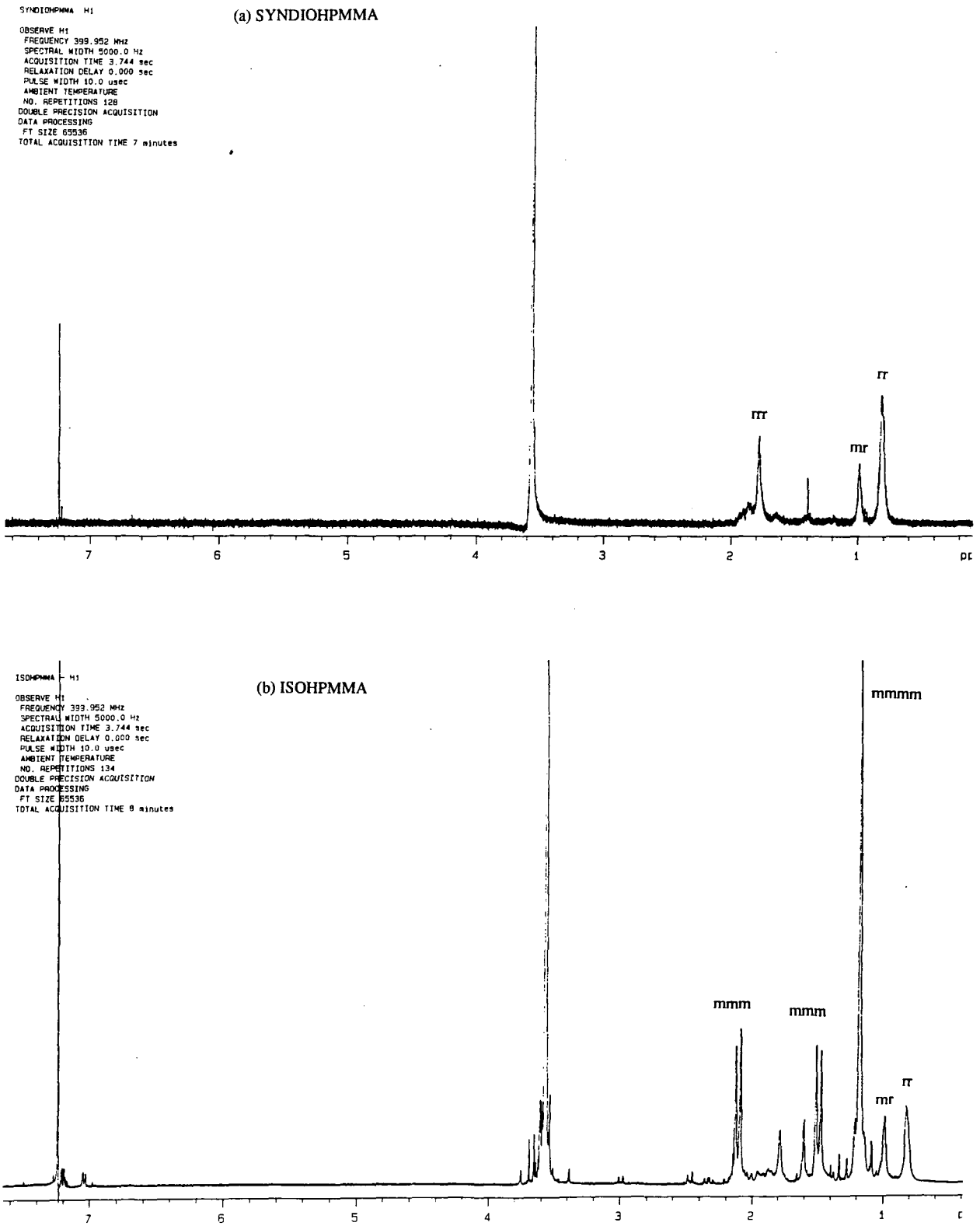

Figure 4.2 ^{1}H NMR Spectra for PMMA

4.2 Surface Pressure - Concentration Isotherm Studies

Surface pressure - concentration isotherms have been obtained for each pair of hydrogenous and deuterated polymers SYNDIO-, ISO- and ATACTIC PMMA, figures 4.3-5. The data were recorded at 298K, although no temperature dependence was observed in data measured at temperatures between 285K and 298K. (Jaffe and co-workers[1,2] published results to support a temperature transition in the form of the PMMA isotherm, but Rondelez and co-workers[3] argued strongly that the surface pressure of atactic PMMA was temperature independent, any apparent effects being due to surface contamination due to leaching out from the trough or other difficulties associated with measurements at high temperature). Repeated runs under identical conditions were used to assess the uncertainty in the measured values.

An estimate of the reproducibility of the data may be obtained by the comparison of two typical replica data sets for SYNDIOHPMMA and ISOHPMMA, figure 4.6(a) and (b).At low surface concentrations there is very good agreement between the two sets in both cases, but as the surface coverage is increased there is a greater spread in the data. This is due partially to increased fractional error in the surface coverage since a slight error in the volume spread becomes more apparent as the area defined by the barriers becomes smaller, and partially to factors associated with the high compression of the film. At high surface concentrations the film becomes stiffer and eventually local deformation can lead to collapse of the film. This is not uniformly reproducible and can be prompted by faults in the monolayer such as surface contamination. Rigorous surface cleaning by aspiration minimises this problem but it is still present to some extent. However since the theories used to rationalise the data consider the semi-dilute region and this region is well within the reproducible part of the isotherm, high coverage effects are not a major factor.

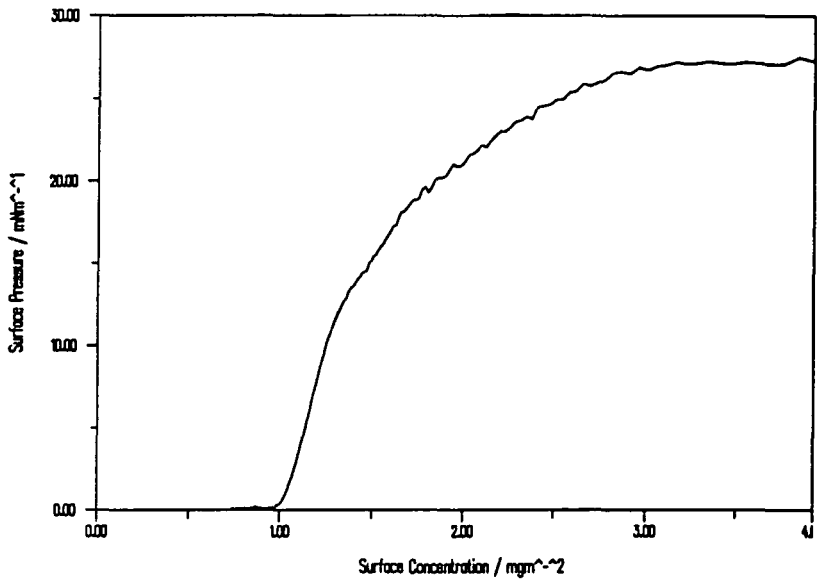

Figure 4.3(a) Surface Pressure - Surface Concentration Isotherm for SYNDIOHPMMA

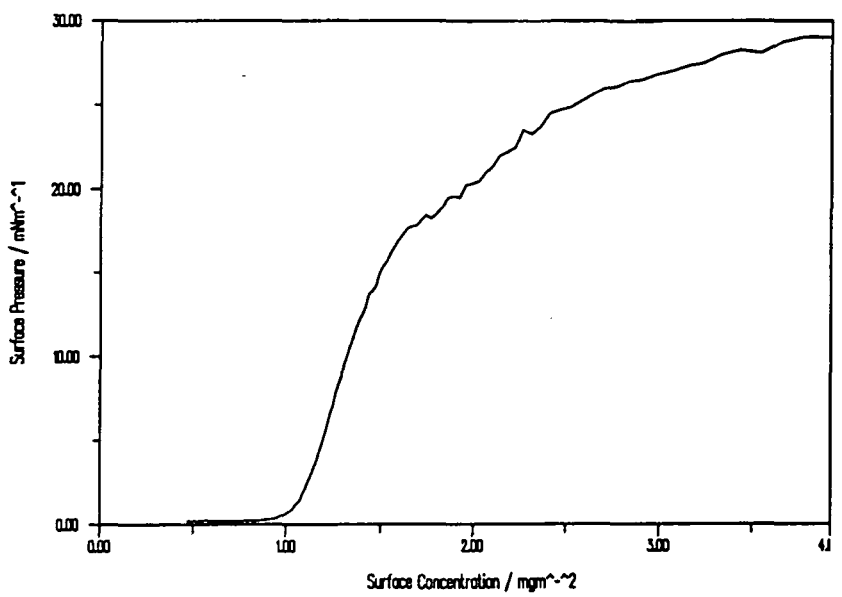

Figure 4.3(b) Surface Pressure - Surface Concentration Isotherm for SYNDIODPMMA

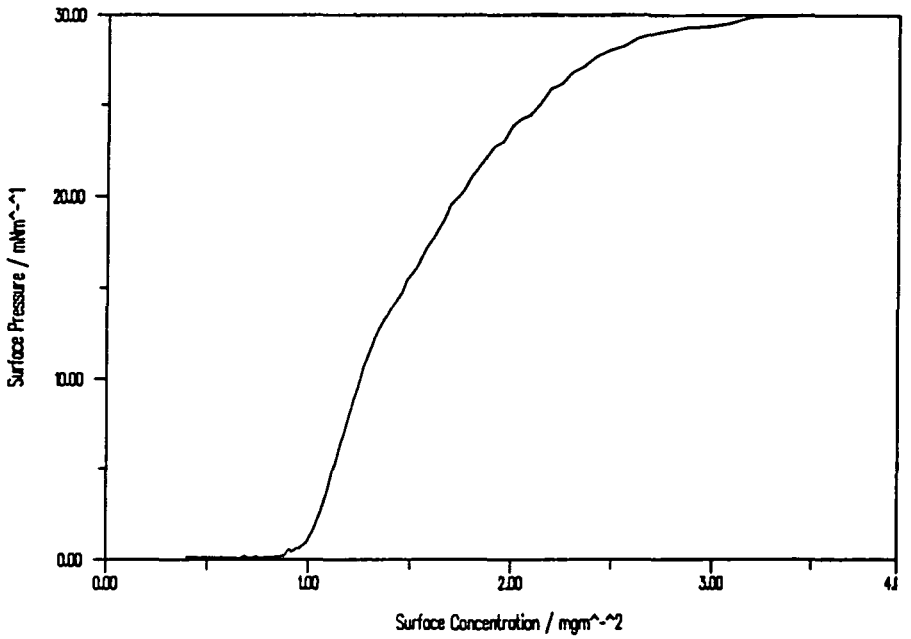

Figure 4.4 (a) Surface Pressure - Surface Concentration Isotherm for ATAHPMMA

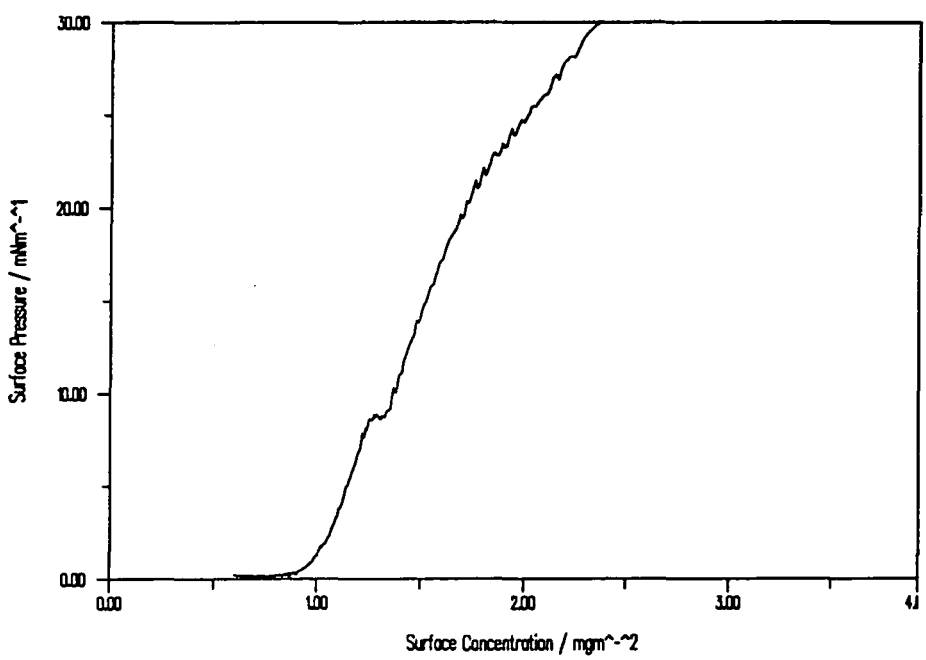

Figure 4.4(b) Surface Pressure - Surface Concentration Isotherm for ATADPMMA

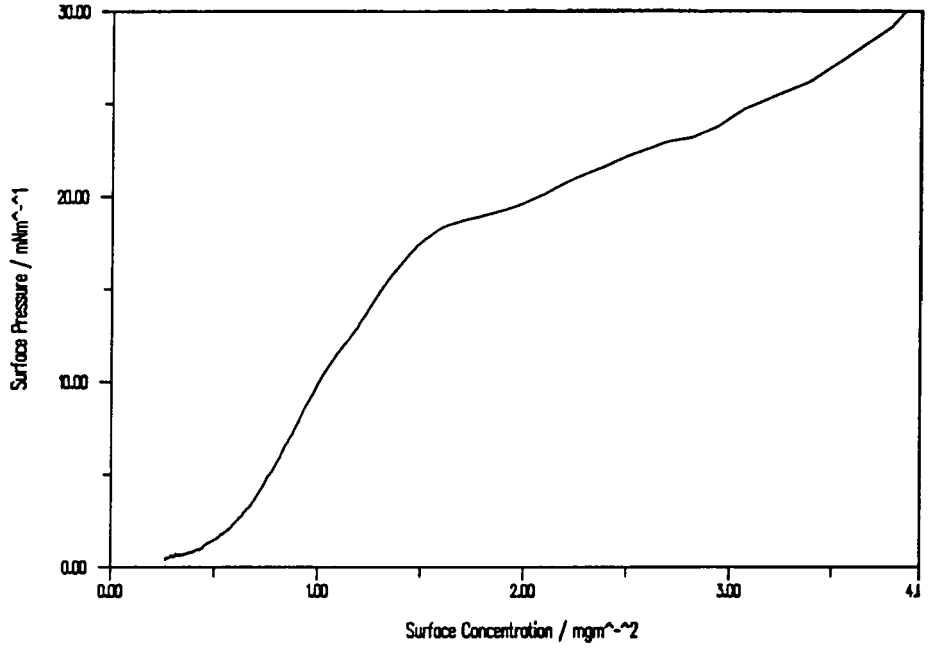

Figure 4.5(a) Surface Pressure - Surface Concentration Isotherm for ISOHPMMA

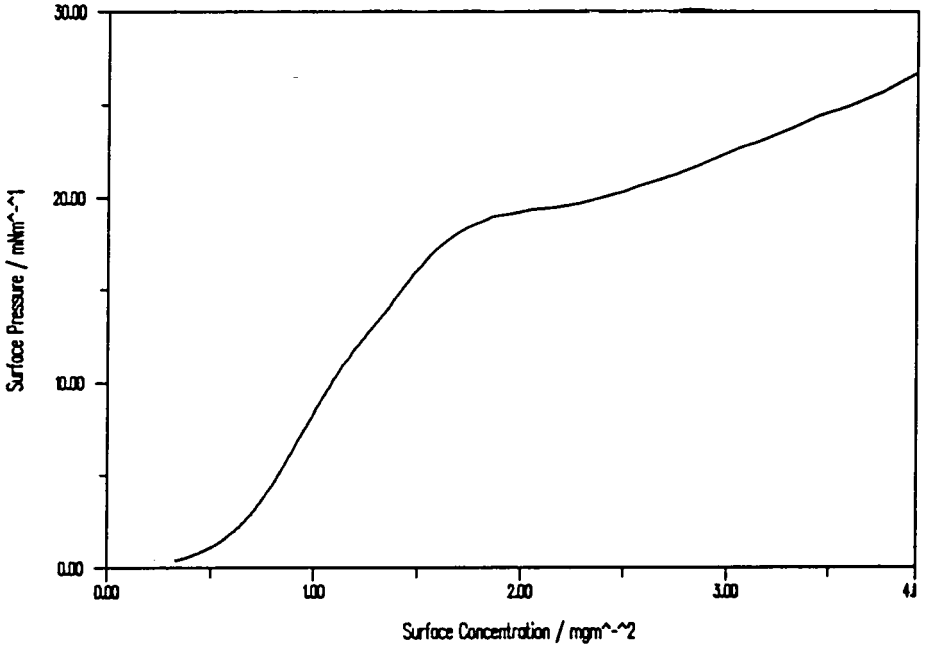

Figure 4.5(b) Surface Pressure - Surface Concentration Isotherm for ISODPMMA

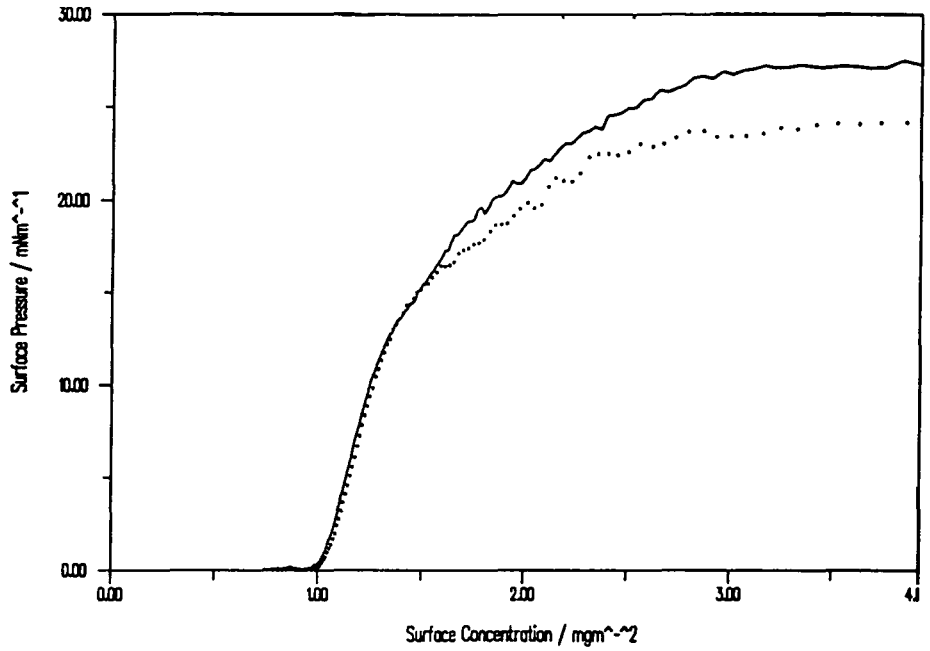

Figure 4.6(a) Repeated Surface Pressure Isotherms for SYNDIOHPMMA

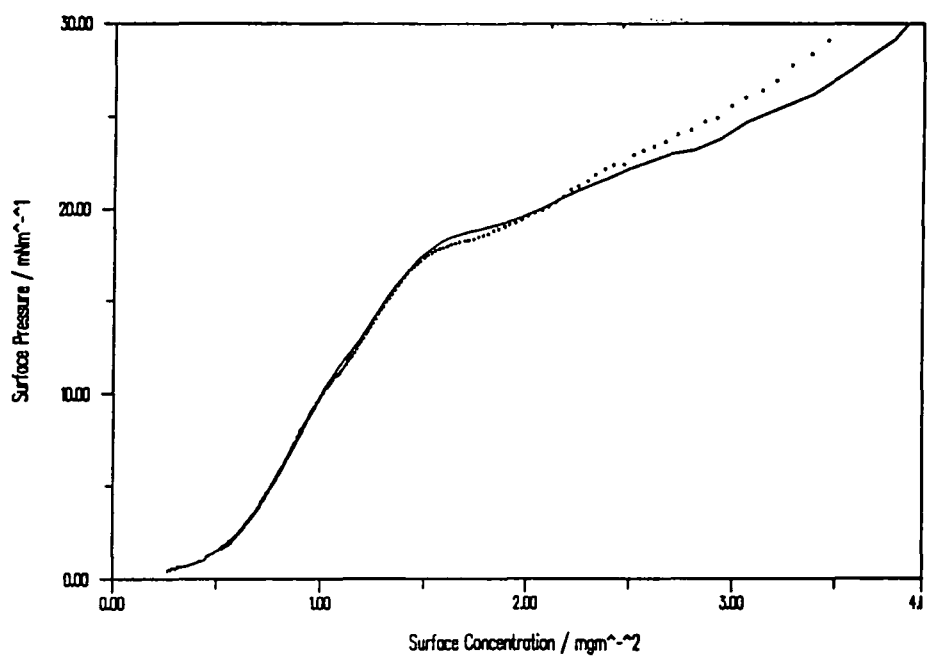

Figure 4.6(b) Repeated Surface Pressure Isotherms for ISOHPMMA

It is important for neutron reflection work to ascertain that the hydrogenous and deuterated films behave in a similar fashion, as the reflected signals from each are analysed together to characterise the layer. Comparison of figures 4.3-5 suggests that the three pairs of polymers behaved in a reasonably self-consistent fashion.

Comparing the behaviour of the various tactic forms, on initial inspection it is evident that the isotherms of syndio and atactic PMMA are reasonably similar in shape to each other, and both rather different to that of ISOPMMA. In the light of the tactic information obtained from NMR this is to be expected as the atactic material is much more like the syndiotactic than the isotactic. The shape of the syndiotactic isotherm is that classically defined as liquid condensed; the surface pressure is first observed at a low area per segment (high surface concentration) and rises rather steeply in the first instance. ISOPMMA on the other hand behaves as a liquid expanded type film with a more gradual rise in pressure from a much smaller onset concentration. One quantity classically used to describe the isotherm is the limiting area per molecule, which is obtained by the extrapolation of the steep rise in surface pressure back to zero concentration. In the case of macromolecular films the equivalent quantity is a limiting area per monomer unit which may be obtained from the limiting surface concentration and the monomer molecular weight. Limiting surface concentrations and corresponding limiting areas per monomer unit of surface pressure onset for PMMA are shown in table 4.3. The values suggest that the average segment adopts a more extended conformation in ISOPMMA than SYNDIOPMMA for which much closer approach is possible before interactions between segments are sensed.

In order to define further the behaviour of the layers, it is desirable to re-present the surface pressure data logarithmically in order to obtain values for the critical scaling exponent v, described in Chapter 1. Figures 4.7-9 show the data of

Polymer	Γ_{lim}	apm_{lim}
SYNDIOHPMMA	1.05	15.8
SYNDIODPMMA	1.05	17.1
ATAHPMMA	0.95	17.5
ATADPMMA	0.95	18.9
ISOHPMMA	0.5	33.2
ISODPMMA	0.5	35.9

Table 4.3 Limiting Surface Concentrations and areas per monomer for PMMA

figures 4.3-5 plotted on a double logarithmic scale in the semi-dilute region (where a linear dependence is observed). From a least squares fitting analysis of the straight line of best fit in this region, the slope y may be obtained and the value of ν from the simple relationship, $y = 2\nu/(2\nu-1)$. The values so obtained are shown in table 4.4. In addition an estimate may be obtained of the values of Γ^* and Γ^{**}, the critical concentrations of the transitions from dilute to semi-dilute and semi-dilute to concentrated behaviour by the points where the linearity of the double logarithmic plots is lost. These values are listed in the final columns of table 4.4.

Polymer	Slope	ν	Γ^*/mgm^{-2}	Γ^{**}/mgm^{-2}
SYNDIOHPMMA	26.2	0.52	0.91	1.10
SYNDIODPMMA	12.3	0.54	0.90	1.17
ATAHPMMA	12.3	0.54	0.83	1.12
ATADPMMA	11.7	0.55	0.83	1.15
ISOHPMMA	2.8	0.77	0.45	1.12
ISODPMMA	2.8	0.77	0.35	1.07

Table 4.4 Critical Scaling Exponents and Surface Concentrations for PMMA

The values of the critical exponent ν in table 4.4 demonstrate clearly that the various forms of PMMA exist in very different thermodynamic conditions when

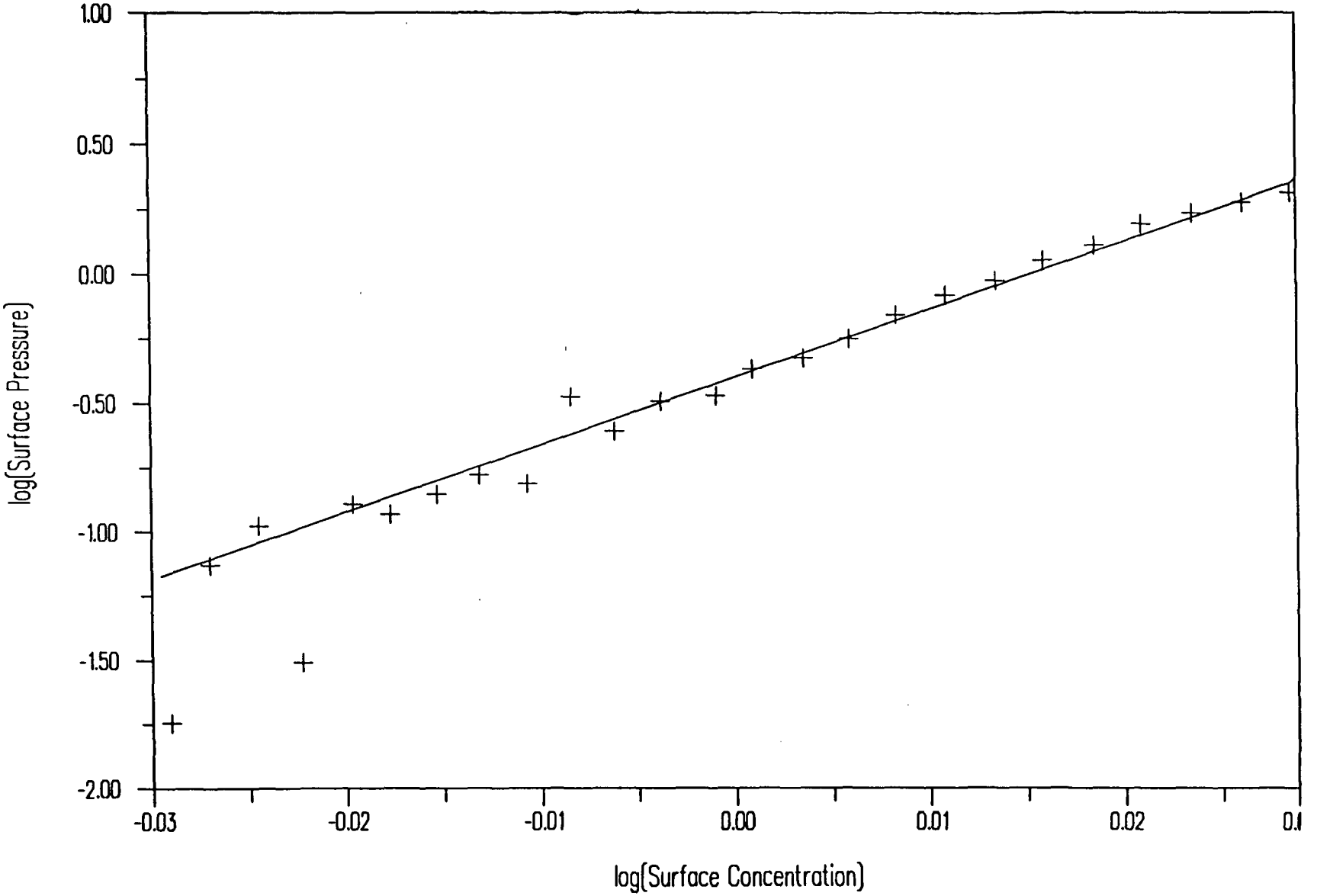

Figure 4.7 Double Logarithmic Plot of Surface Pressure Isotherm for SYNDIOHPMMA

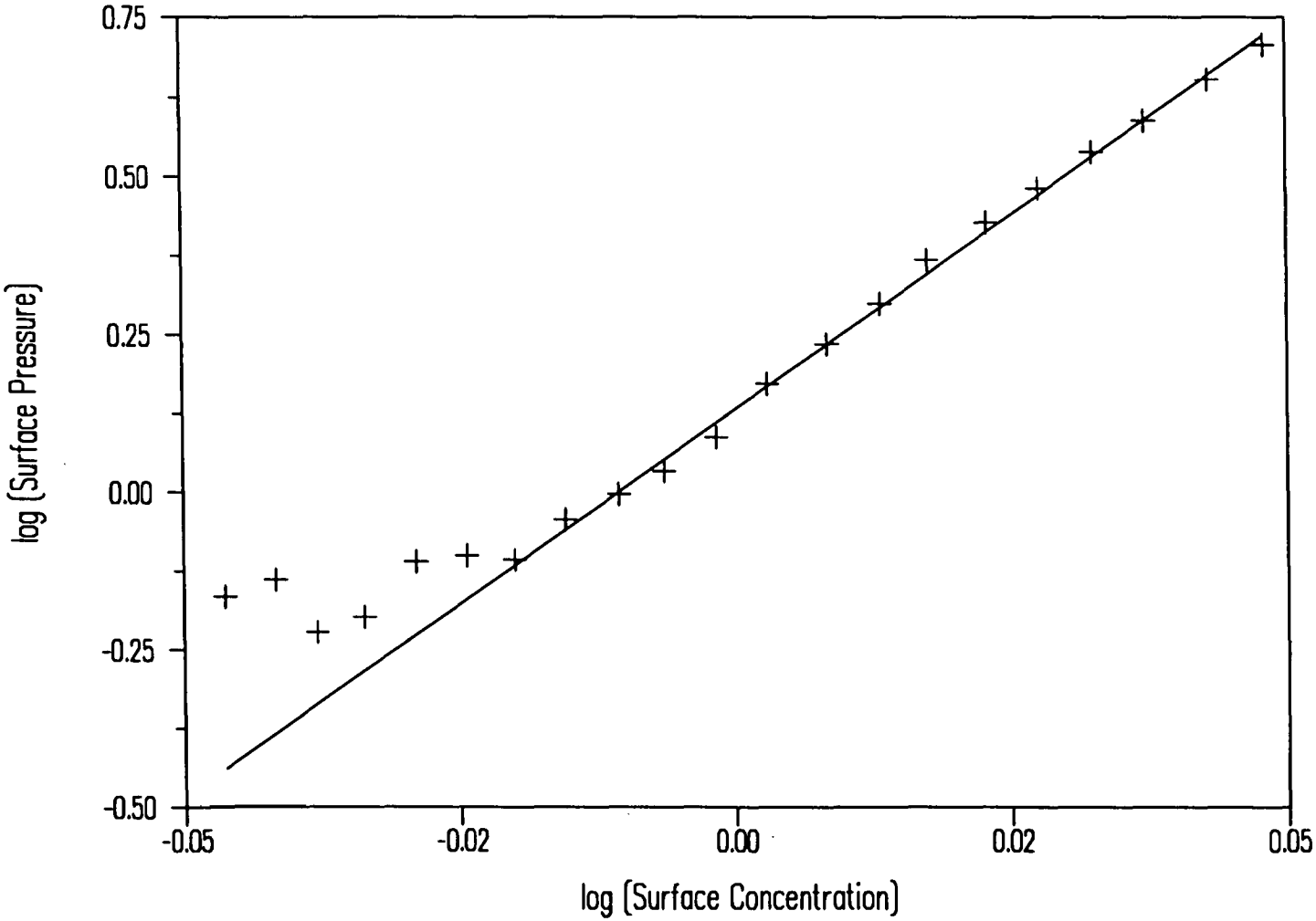

Figure 4.8 Double Logarithmic Plot of Surface Pressure Isotherm for ATAHPMMA

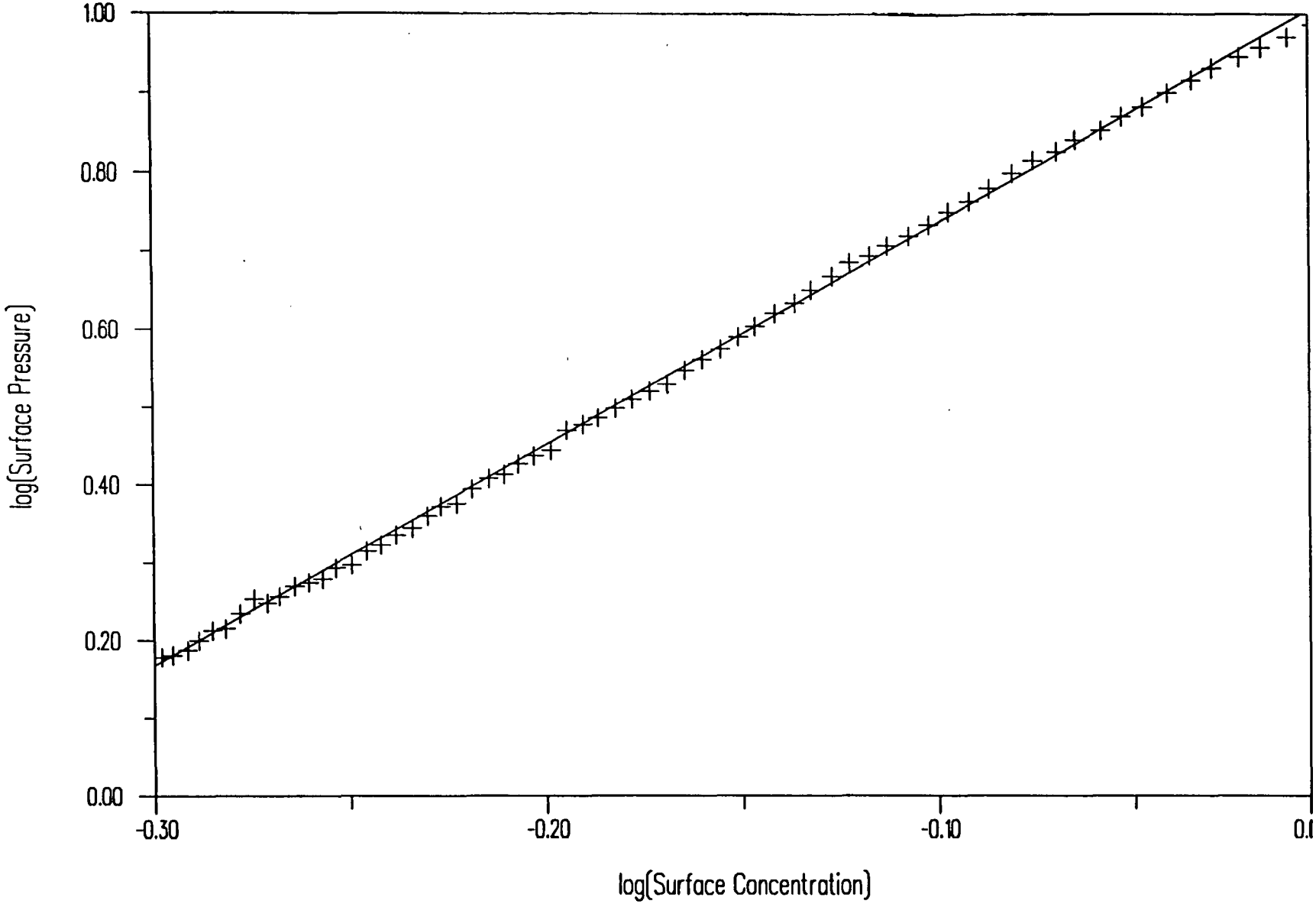

Figure 4.9 Double Logarithmic Plot of Surface Pressure Isotherm for ISOHPMMA

spread as monolayers. The value of 0.52 for SYNDIOPMMA suggests a less than theta condition, since at collapse $\nu = 0.5$. The value for ATAPMMA is slightly different from this, a value of 0.55 indicating a closer approximation to the theta condition where unperturbed two dimensional chain dimensions are expected. ISOPMMA on the other hand displays unambiguously the behaviour associated with good solvent conditions, with a ν value of 0.77, in agreement with the predicted value.

A further indication of the thermodynamic state of the layer may be obtained by consideration of the dilute regime. By presenting the data as π/Γ v Γ, the equation of state theory predicts that at extremely low surface concentrations, an extrapolation of the data back to zero concentration will yield values for the two dimensional second virial coefficient, $A_{2,2}$, and the molecular weight of the polymer. Unfortunately under the conditions in which the trough was operated there proved to be a considerable amount of noise compared to the extremely low measured signal corresponding to the change in surface pressure. As most vibrations associated with nearby instrumentation and human movement were damped by the optical table, the main source of fluctuation was airborne, which although reduced by the trough casing, cannot be elimated entirely without access to much more thorough draught elimination than was readily available. Therefore there is some considerable scatter on the data in the low surface pressure regime, figures 4.10-12. As a consequence it has proved difficult to obtain any meaningful molecular weight and second virial coeffiecient values in this region, however comparing the slopes of these plots it is evident that there is a large positive slope for ISOPMMA whereas SYNDIOPMMA and ATAPMMA both have small negative slopes. This indicates a positive $A_{2,2}$ value for ISOPMMA and a negative value for the other cases, confirming that ISOPMMA is in good solvent conditions where chain-solvent interactions are favourable but the other forms are in less that theta conditions with unfavourable

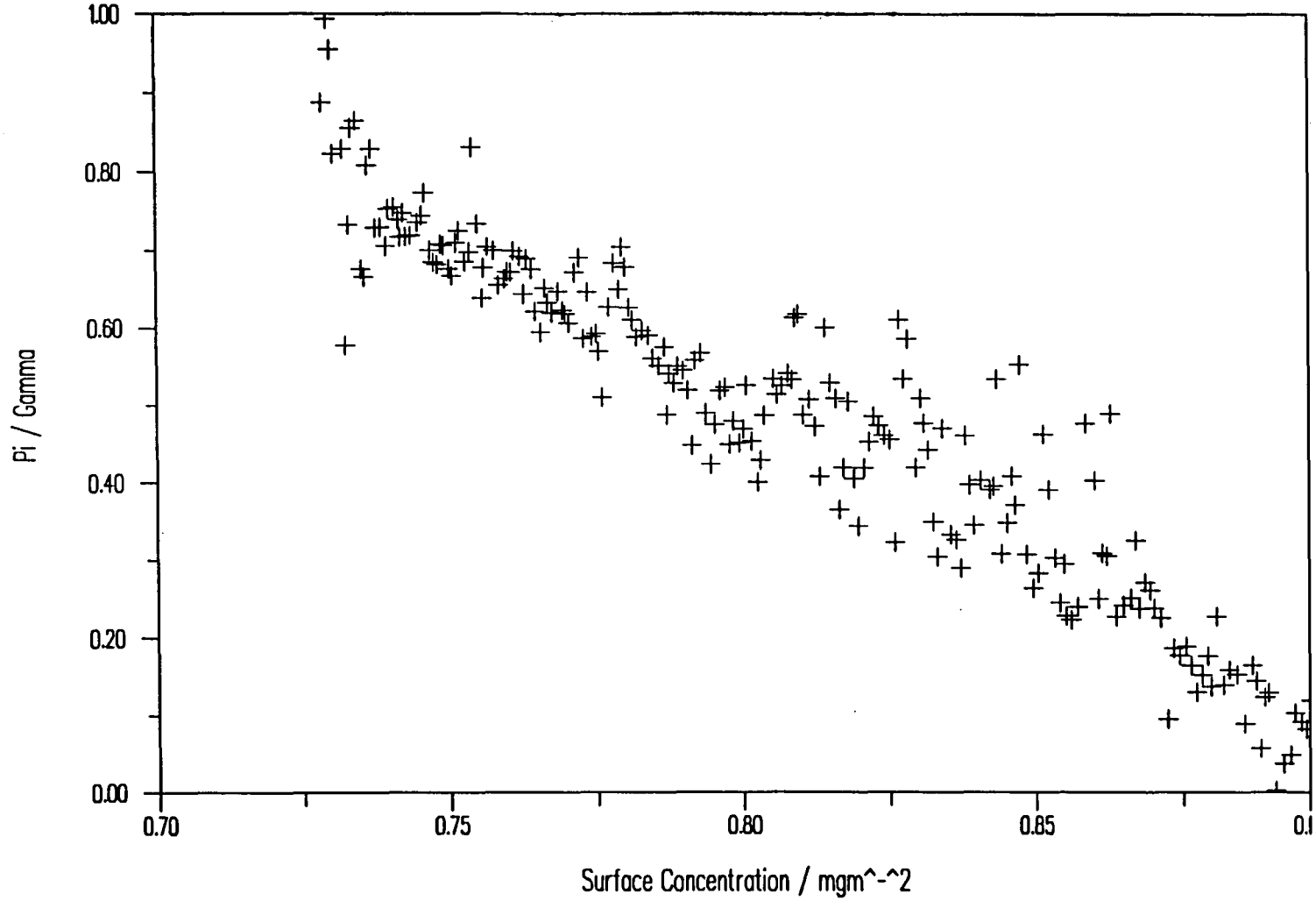

Figure 4.10(a) Surface Pressure / Surface Concentration against Surface Concentration for SYNDIOHPMMA

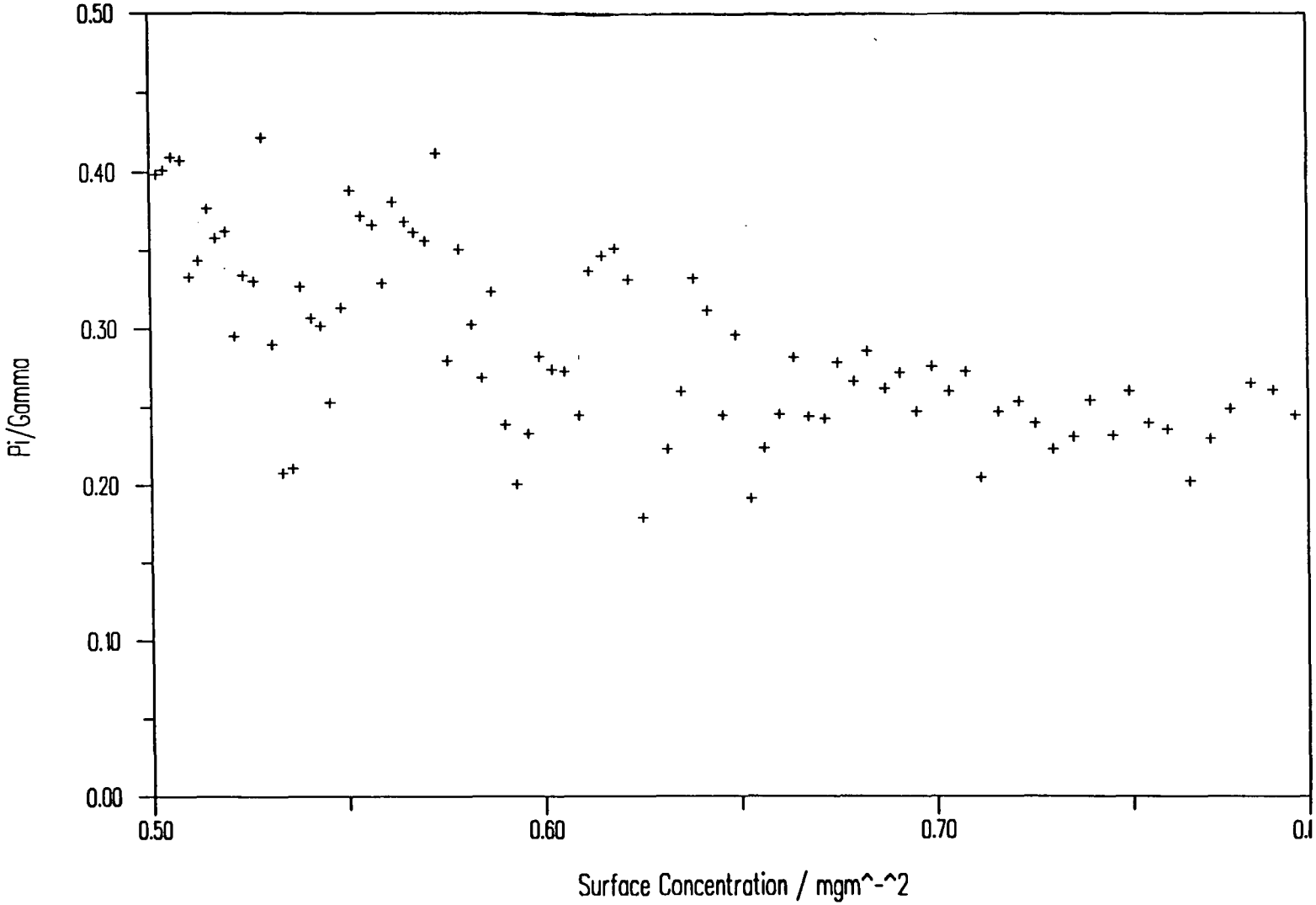

Figure 4.10(b) Surface Pressure / Surface Concentration v Surface Concentration for SYNDIODPMMA

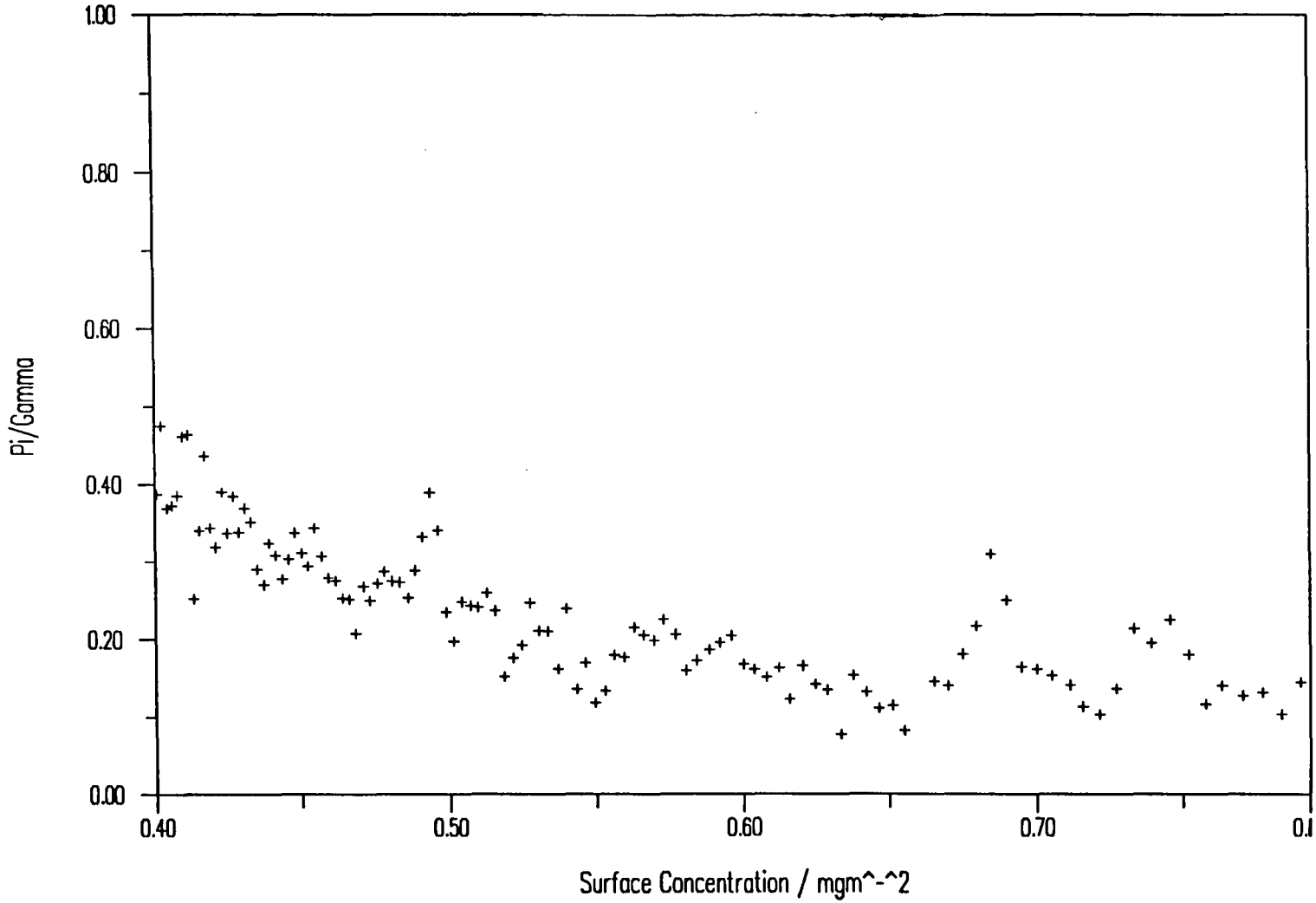

Figure 4.11(a) Surface Pressure / Surface Concentration v Surface Concentration for ATAHPMMA

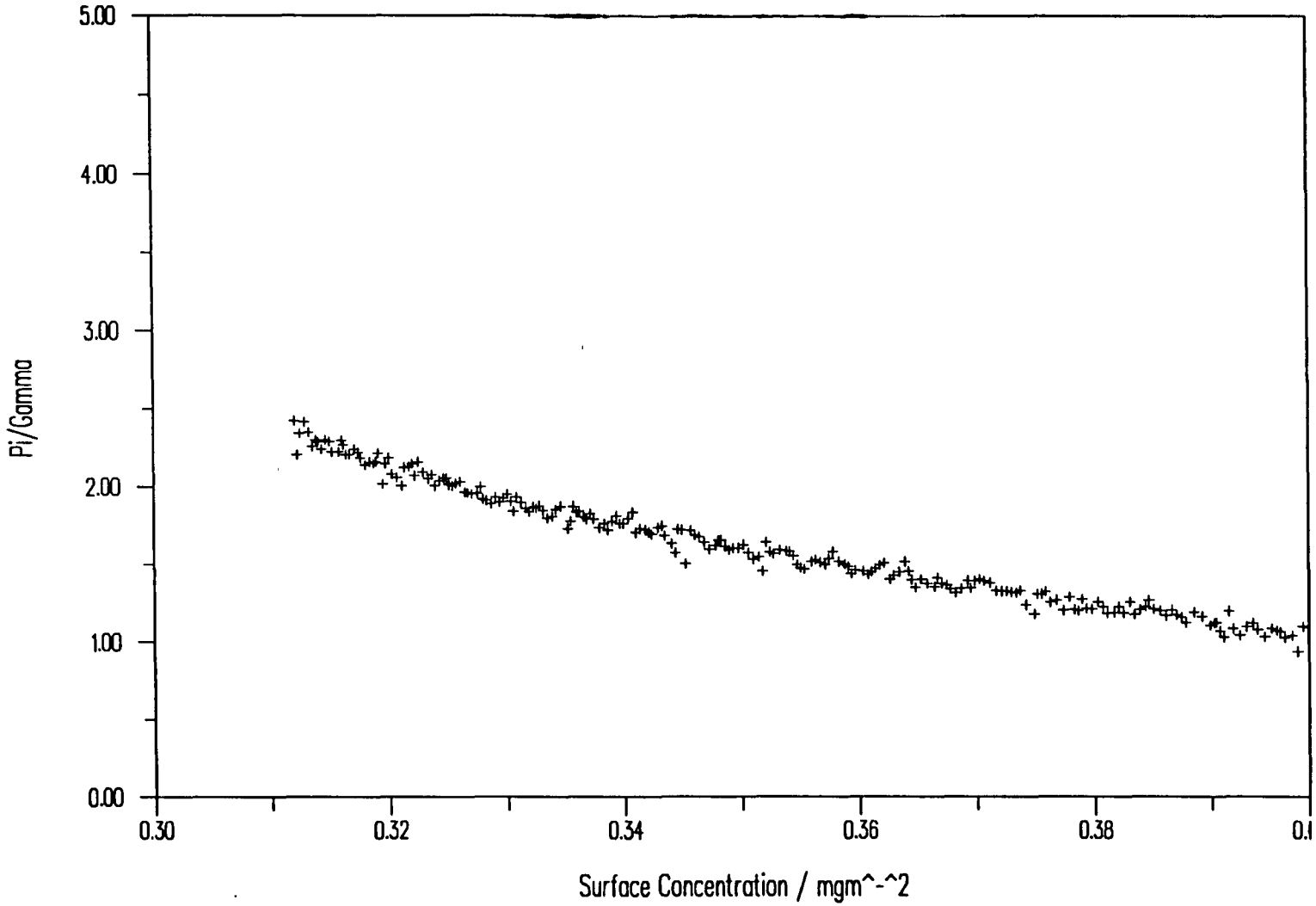

Figure 4.11(b) Surface Pressure / Surface Concentration v Surface Concentration for ATADPMMA

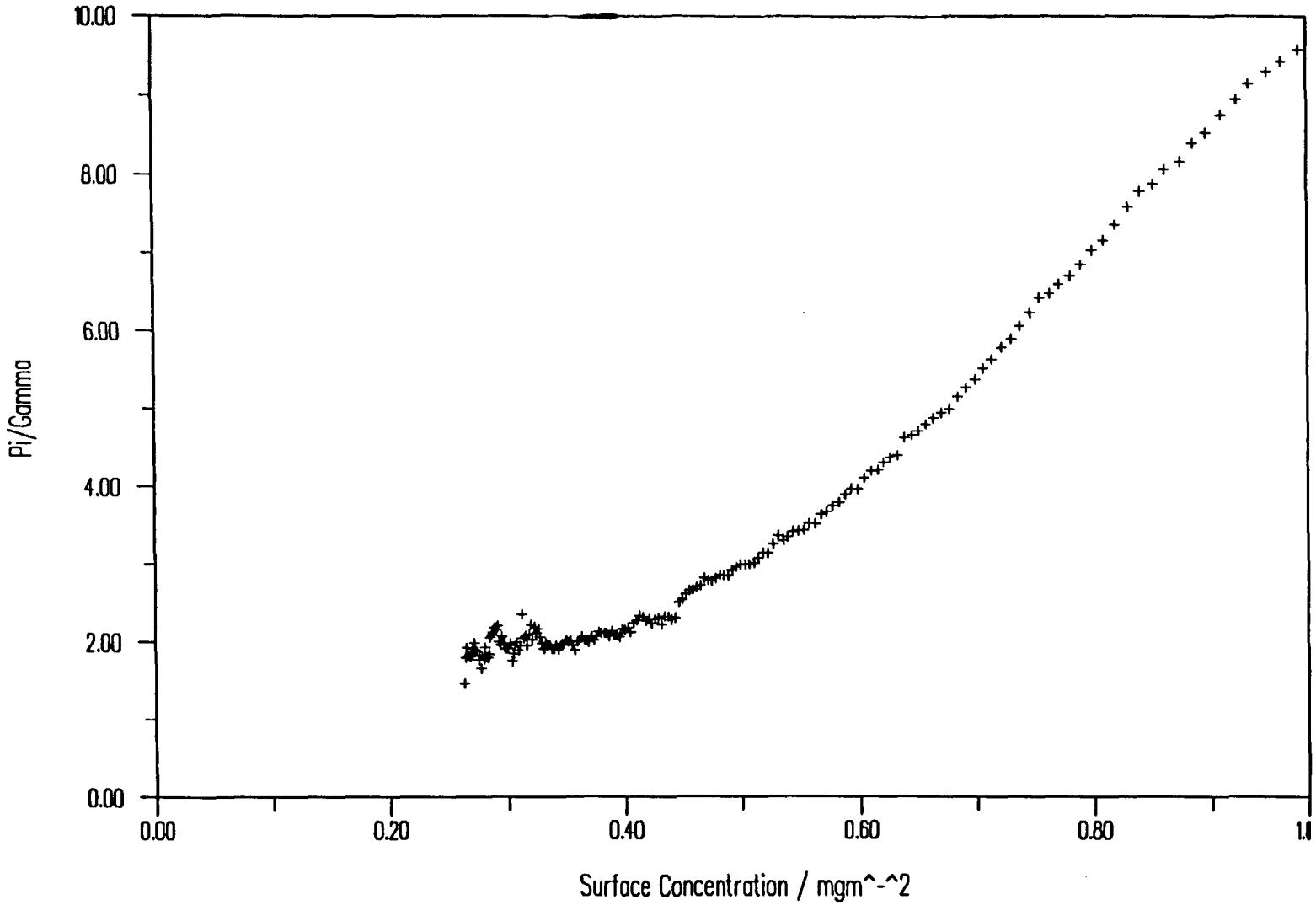

Figure 4.12(a) Surface Pressure / Surface Concentration v Surface Concentration for ISOHPMMA

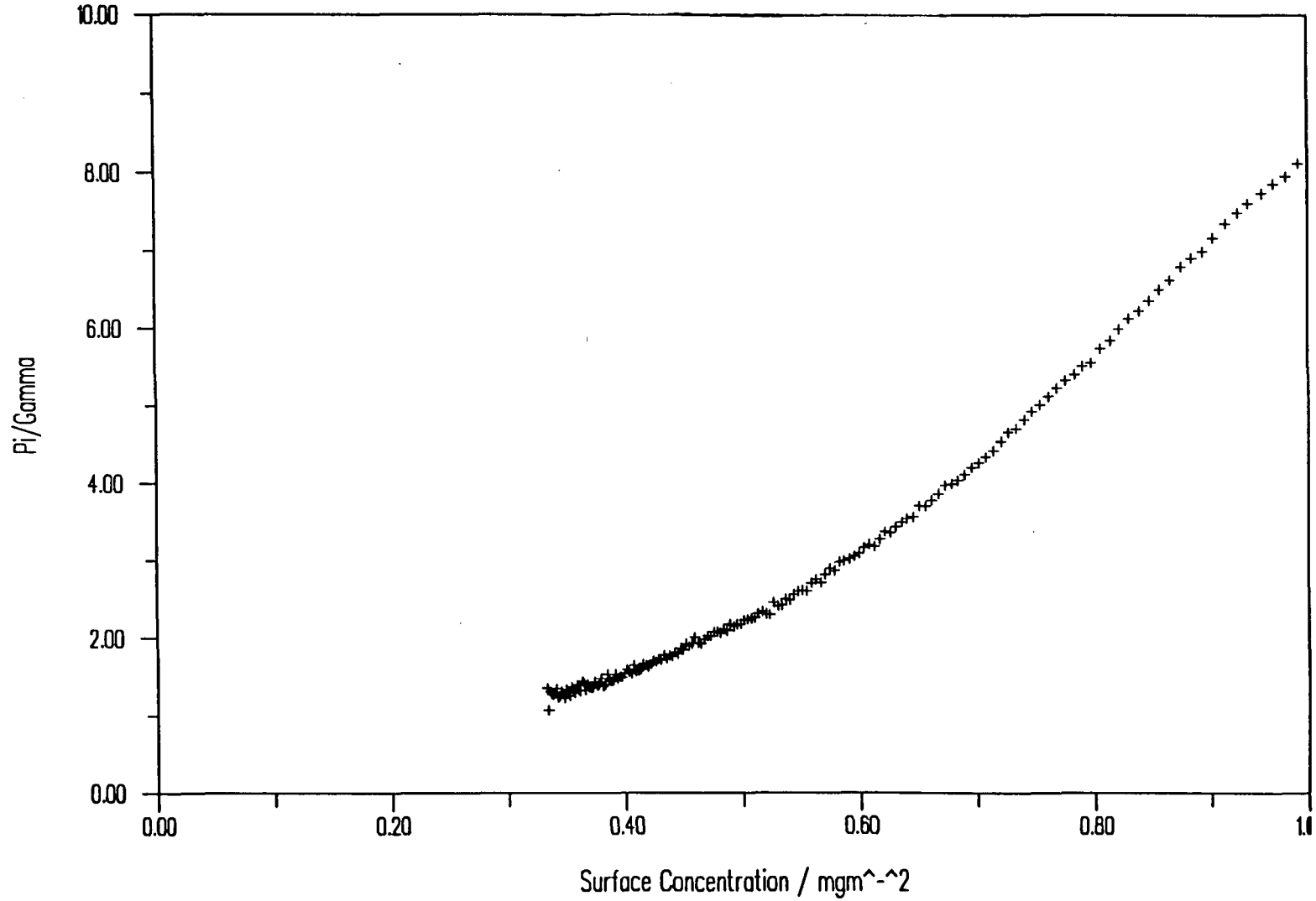

Figure 4.12(b) Surface Pressure / Surface Concentration v Surface Concentration for ISODPMMA

chain-solvent interactions. This incidentally suggests that a higher value of around 0.56-0.57 is indeed the correct theta value for the critical v exponent as there is a finite negative slope to the data for ATAPMMA.

The effect of the rate of compression (barrier speed) on the shape of the isotherm has also been considered. It is difficult to illustrate the effect of barrier speed clearly, but in general terms there is little effect in the low concentration regime where the isotherm is well reproduced. The main occurence of irreproducibility was at higher concentrations where overcompression of a monolayer can lead to surface pressure overshoot on the one hand or premature collapse on the other. To some extent these mechanisms are also governed by defects in the surface as previously discussed and it is difficult to isolate the effect of barrier speed alone. A qualitative rationalisation of the effect of overcompression may be obtained by considering the mobility of chains in the layer and consequently the time taken for them to respond to the perturbation of compression. It is to be expected that at low surface coverages the layer will be relatively flexible and the chains less constrained and thus able to respond to compression with a relaxation time that is very small compared to the barrier speed. At higher concentrations the mobility of the chains is limited increasingly by their closer proximity to one another and consequently the relaxation time increases relative to the barrier speed. In a recent letter[4] Kato has proposed the use of constant strain rate rather than constant barrier speed for the measurement of surface pressures for insoluble monolayers, governed by the critical parameter, the so called Deborah number, where

$$\text{Deborah Number} = \frac{\text{Time of Relaxation}}{\text{Time of Observation}}$$

Such a method might clarify behaviour in the concentrated regime to some extent, however to extend measurements to high surface concentrations

requires prohibitively long measurement times and, as previously observed, the time of relaxation in the dilute and semi-dilute regimes are such that if a reasonably slow rate of compression of around 20 cm^2 min^{-1} is used, then the data obtained are reproducible and unaffected by the rate of compression.

An associated phenomenon observed at high surface concentrations is a slow decay in the surface pressure if the barriers are closed to a given value and held there. In this case there is a very marked difference between the behaviour observed for SYNDIO and ISOPMMA. Figure 4.13 shows a multiple plot of surface pressure as a function of time after an initial compression to a given surface pressure for SYNDIOPMMA. For a low initial surface pressure such as 5mNm^{-1} there is a more or less constant surface pressure recorded over a two hour period, but as the initial surface pressure is increased a significant drop in surface pressure after the barriers were stopped is observed. From an initial surface pressure of 20mNm^{-1} for example the surface pressure drops to a steady value of 14mNm^{-2} after two hours. This trend is consistent with a film possessing the properties of increasing stiffness with increased compression but which then has the ability to relax in a manner which reduces the perturbation on the system. This effect it should be noted is distinct from that which might be seen in the event of barrier leakage. In that case surface pressure would decay in a rather more drastic fashion and the recording of consistent surface pressure - surface area data would become impossible.

The relaxation phenomenon observed for ISOPMMA is dramatically different to that obtained for the syndiotactic polymer, see figure 4.14. In this case holding barrier position from a low or moderate surface pressure leads to a surface pressure decay that is larger and more sustained with time than for SYNDIOPMMA. As surface pressure is increased, as one might expect, the effect becomes greater. However once compressed to an initial surface pressure of 20mNm^{-2}, a quite remarkable transition occurs. In this instance the surface pressure measured with

time is virtually unchanging, indicative of a film that is incapable of relaxation. This observation will be discussed later in conjunction with evidence obtained from neutron reflectometry.

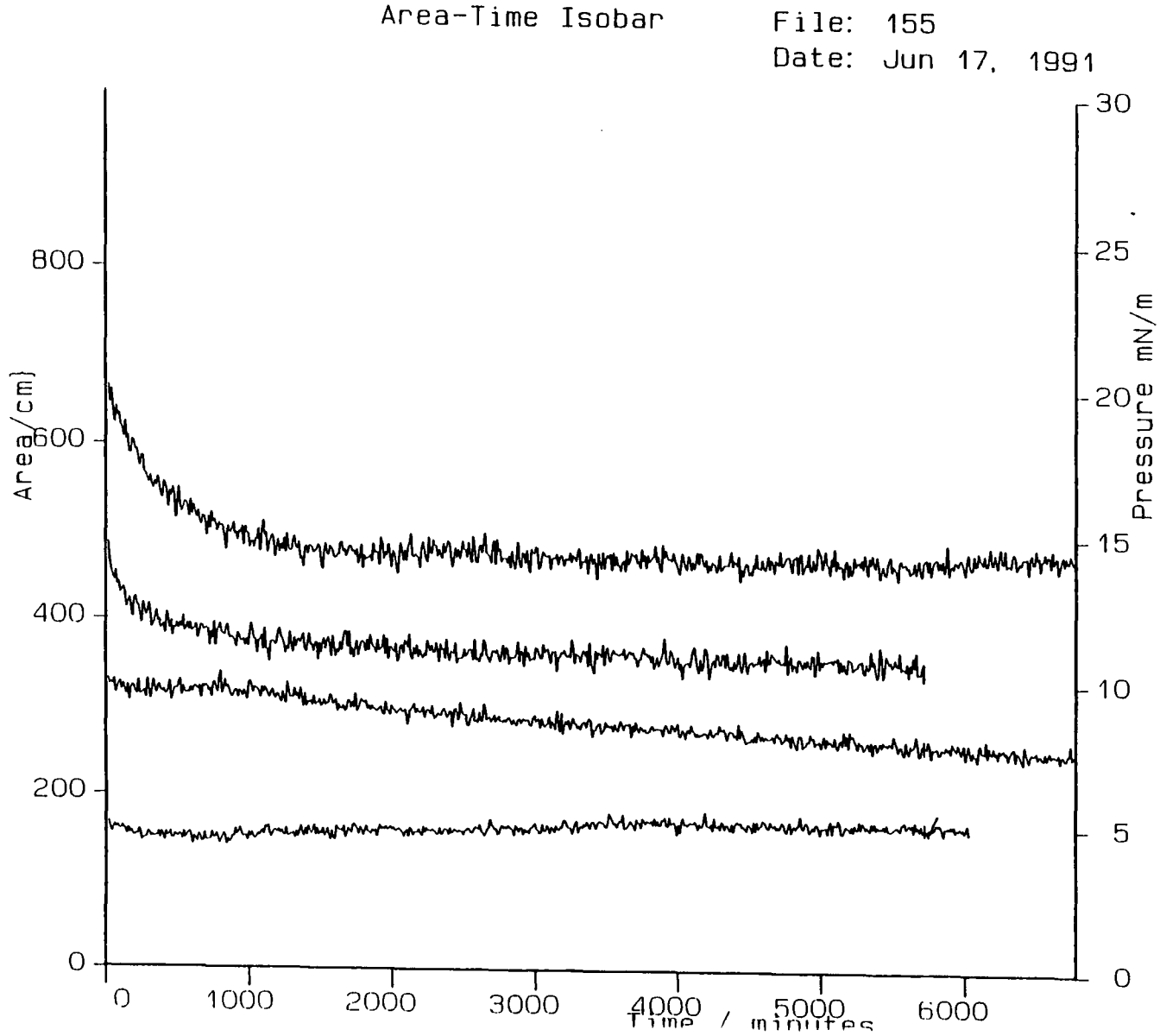

Figure 4.13 Surface Pressure v Time for SYNDIOPMMA monolayers with stationary barriers after initial compression

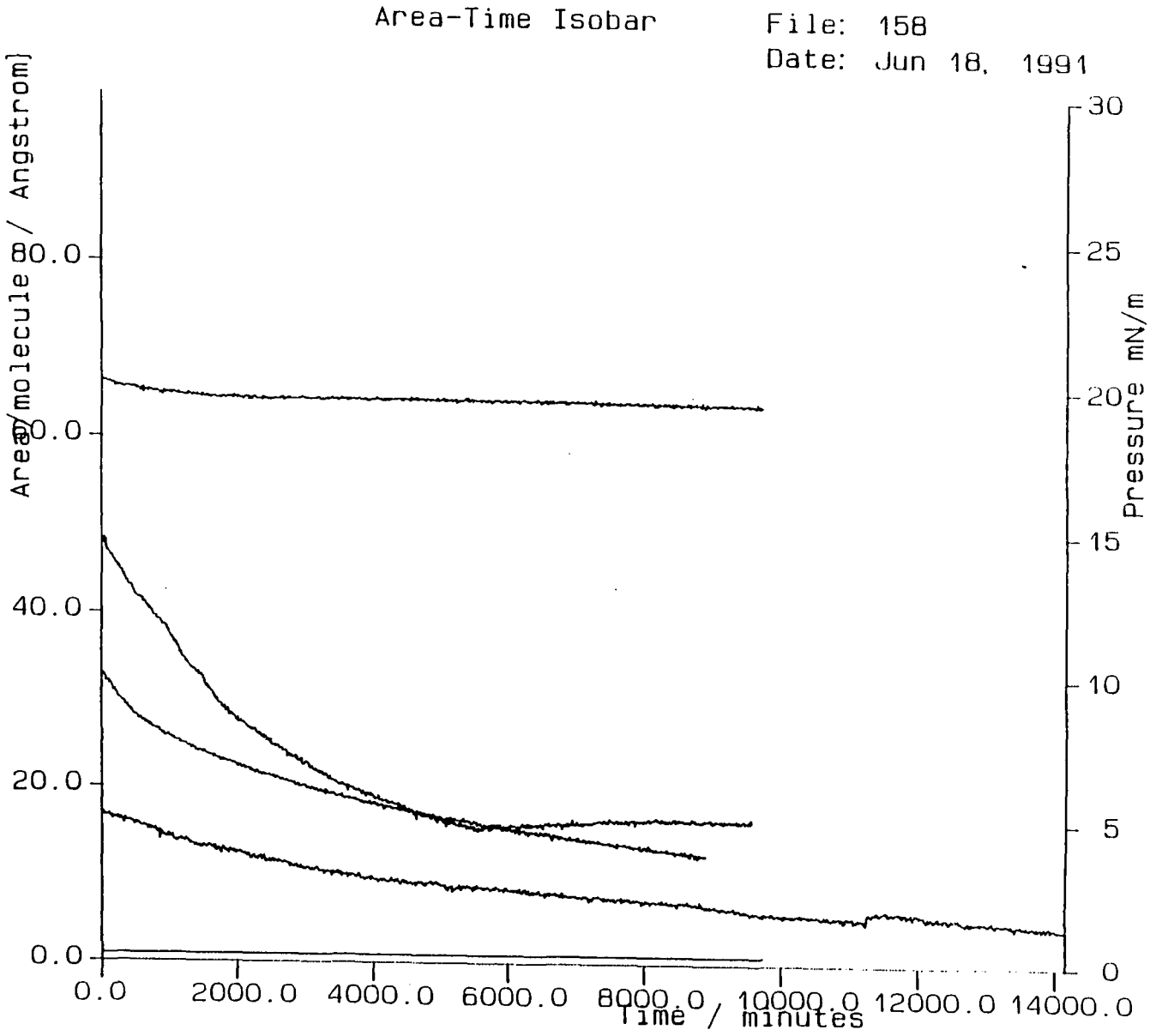

Figure 4.14 Surface Pressure v Time for ISOPMMA monolayers with stationary barriers after initial compression

4.3 Neutron Reflectometry

Neutron reflectometry has been used to study all three tactic forms of PMMA at the air-water interface. The bulk of the work has been carried out on CRISP but D17 has been used to probe for longer range effects for the case of ISOPMMA.

Experiments have been carried out using two sets of contrast conditions. These were the deuterated polymer spread on water contrast matched to air (acmw) which gives a direct measure of the amount of material spread on the surface, and the hydrogenous polymer spread on D_2O which is more sensitive to the intrusion of water into the layer.

Neutron reflectivity profiles obtained on CRISP for SYNDIODPMMA on acmw over a range of surface concentrations are illustrated in figure 4.15. The reflectivity is presented renormalised to the incident monitor counts as a function of the perpindicular component of the momentum transfer vector, Q, and error bars, which are generally within the points except near the high Q background, are omitted for clarity. The theory of reflection predicts a strong inverse dependence of reflectivity on Q, namely that it should decrease with Q^4. This is indeed seen in the experimental data which is consequently presented on a logarithmic y scale to clarify the effect of surface concentration. The general shape of a reflectivity profile is governed by this decline until the instrumental background signal is reached. This background is predominantly governed by isotropic incoherent scattering and is dependent on the particular contrast used. Since the ^1H nucleus has a larger incoherent scattering cross section then ^2H, a higher background is obtained for systems containing a larger amount of hydrogen. Thus the background for air contrast matched subphase systems is slightly higher (at around $9x10^{-6}$-$1.1x10^{-5}$)

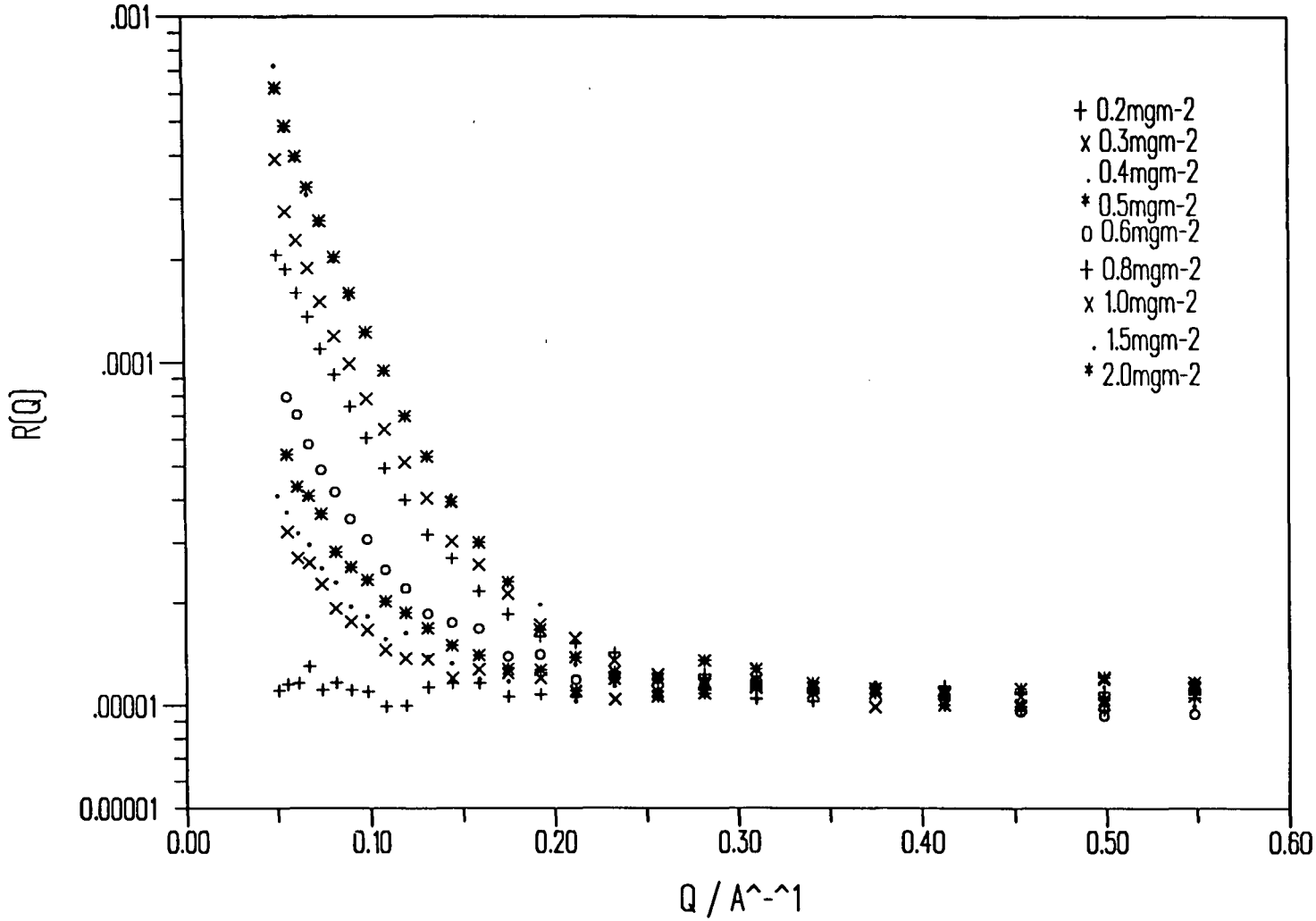

Figure 4.15 Neutron Reflectivity Profiles for SYNDIODPMMA on air contrast matched water

than for a D_2O system (around $3x10^{-6}$). Generally this background level is reached by a Q value of around 0.3-0.35Å^{-1}.

The change in the shape of the reflectivity profile can be ascribed to increased (nuclear) density, which causes the reflectivity to rise, and the layer thickness, which tends to affect the slope of the profile and increase the reflectivity according to the total scattering length density. The experimental reflectivity rises with increasing surface concentration indicating a rise in deuterated material at the interface. Since the subphase is air contrast matched and does not contribute to the reflectivity, non-linear least squares fitting of the relevant optical matrix expressions gives rise to values for the layer thickness and scattering length density which may be use to calculate the polymer density (surface concentration) in the interfacial region.

Experimental reflectivity profiles for SYNDIOHPMMA/D_2O at the same surface concentrations are shown in figure 4.16. In this case the effect of increasing the surface concentration of polymer is to increase the amount of hydrogenous material at the interface. Consequently the reflectivity profile is depressed slightly from the reflectivity obtained from pure D_2O. The layer scattering length density fitted in this case is contributed to by the polymer and the subphase material.

Equivalent reflectivity profiles for ATAPMMA and ISOPMMA at the same contrasts are illustrated in figures 4.17-20. The same general features are observed, but it should be noted that at similar surface concentrations there is less effect on the reflectivity profile for the the isotactic film than the syndiotactic.

A simple model has been used as a first approximation, namely a single solid slab. The Rutherford Appleton Laboratory GENIE suite program L_MULFIT and the program DRYDOC by A.R. Rennie have been used to fit the data by non-linear least squares analysis according to Abelès method. By scanning a fixed

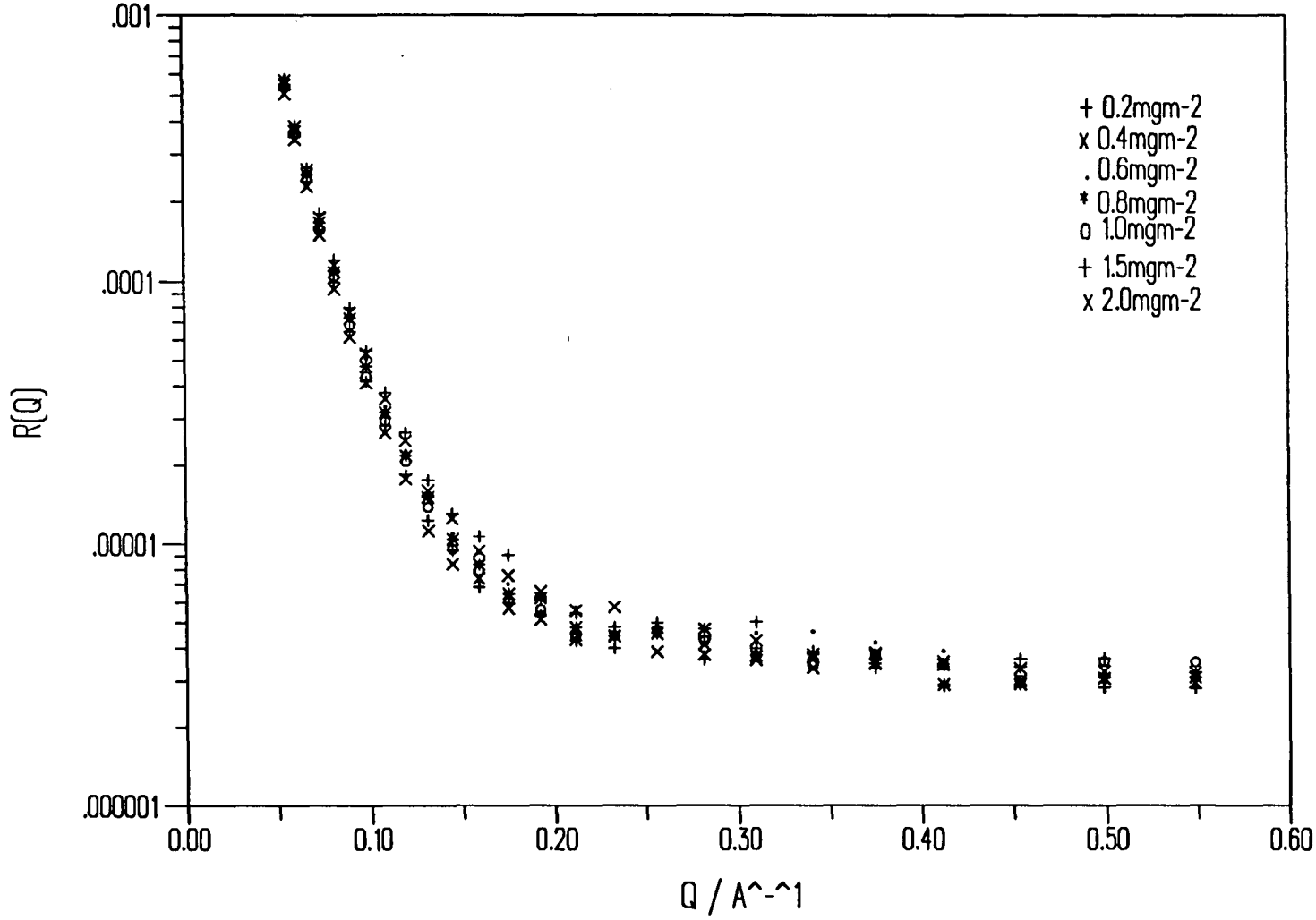

Figure 4.16 Neutron Reflectivity Profiles for SYNDIOHPMMA on D_2O

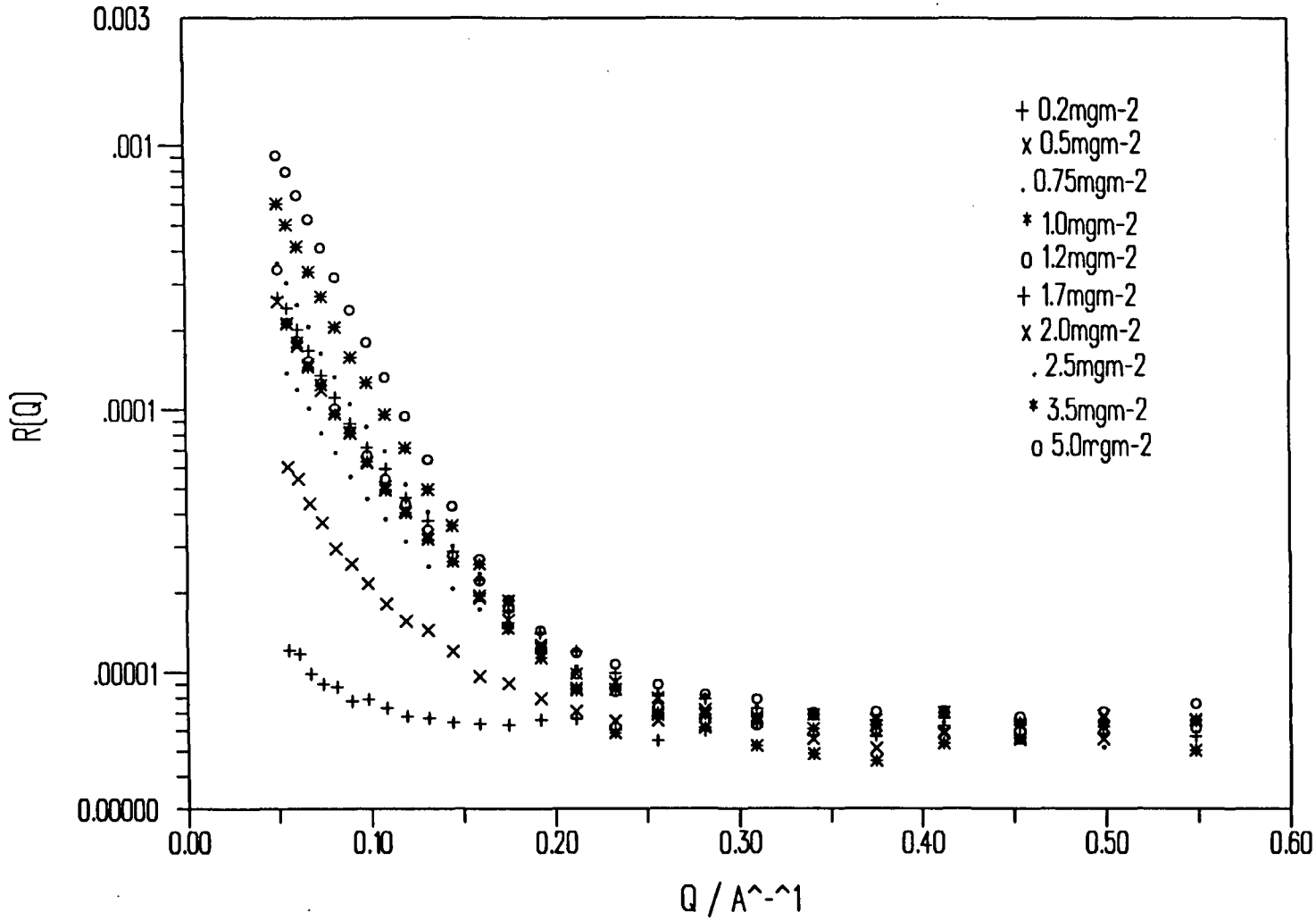

Figure 4.17 Neutron Reflectivity Profiles for ATADPMMA on acmw

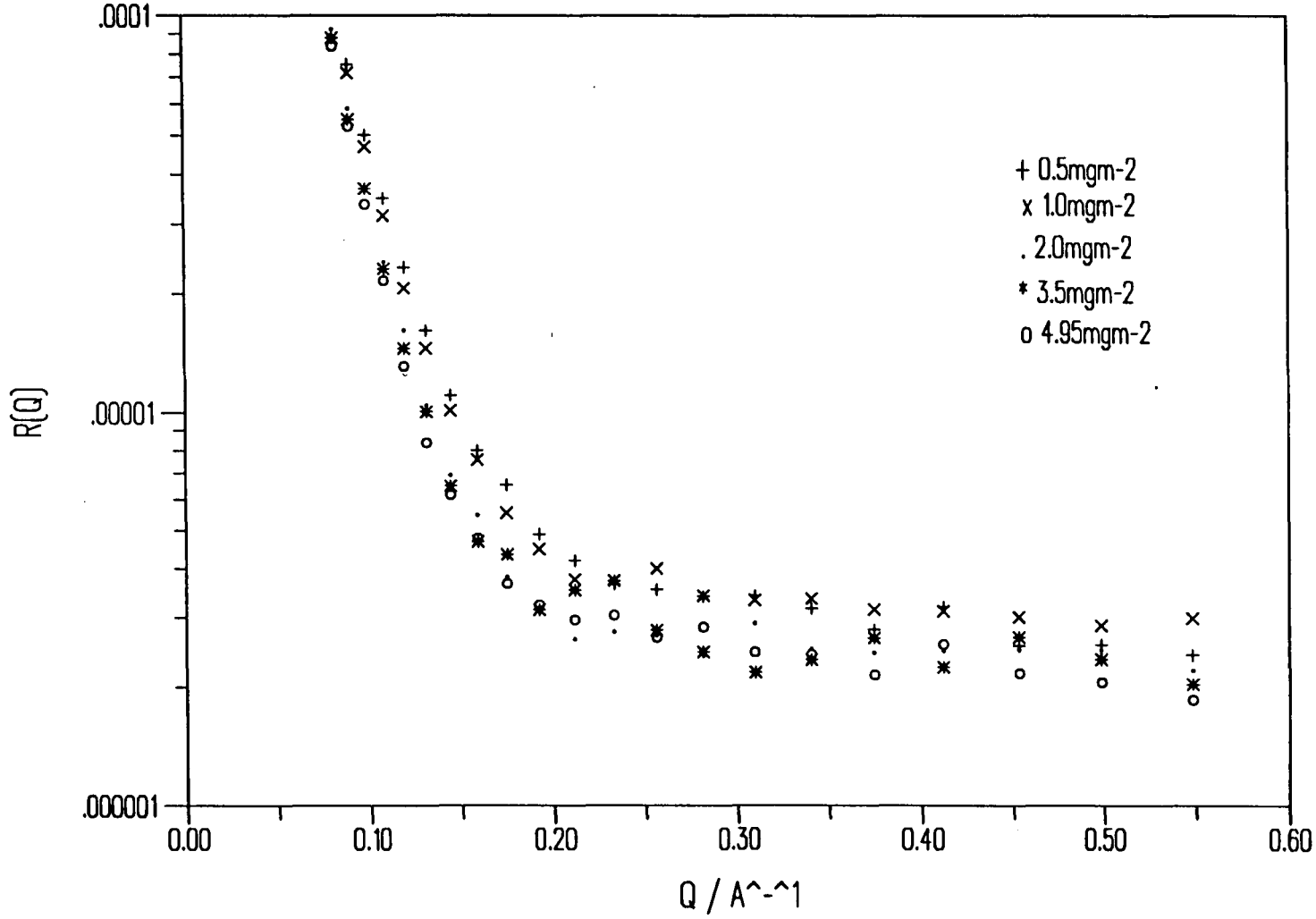

Figure 4.18 Neutron Reflectivity Profiles for ATAHPMMA on D_2O

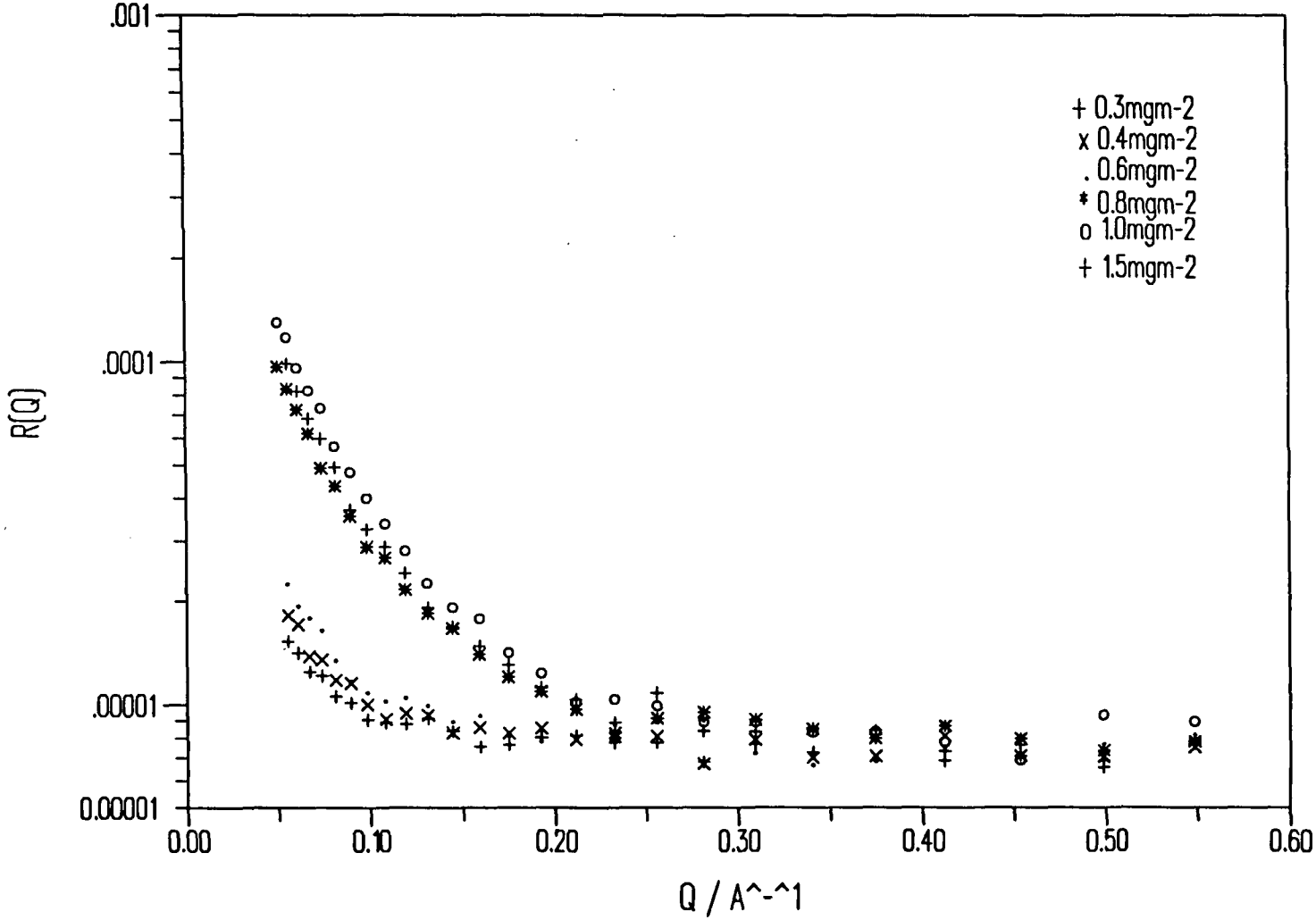

Figure 4.19 Neutron Reflectivity Profiles for ISODPMMA on air contrast matched water

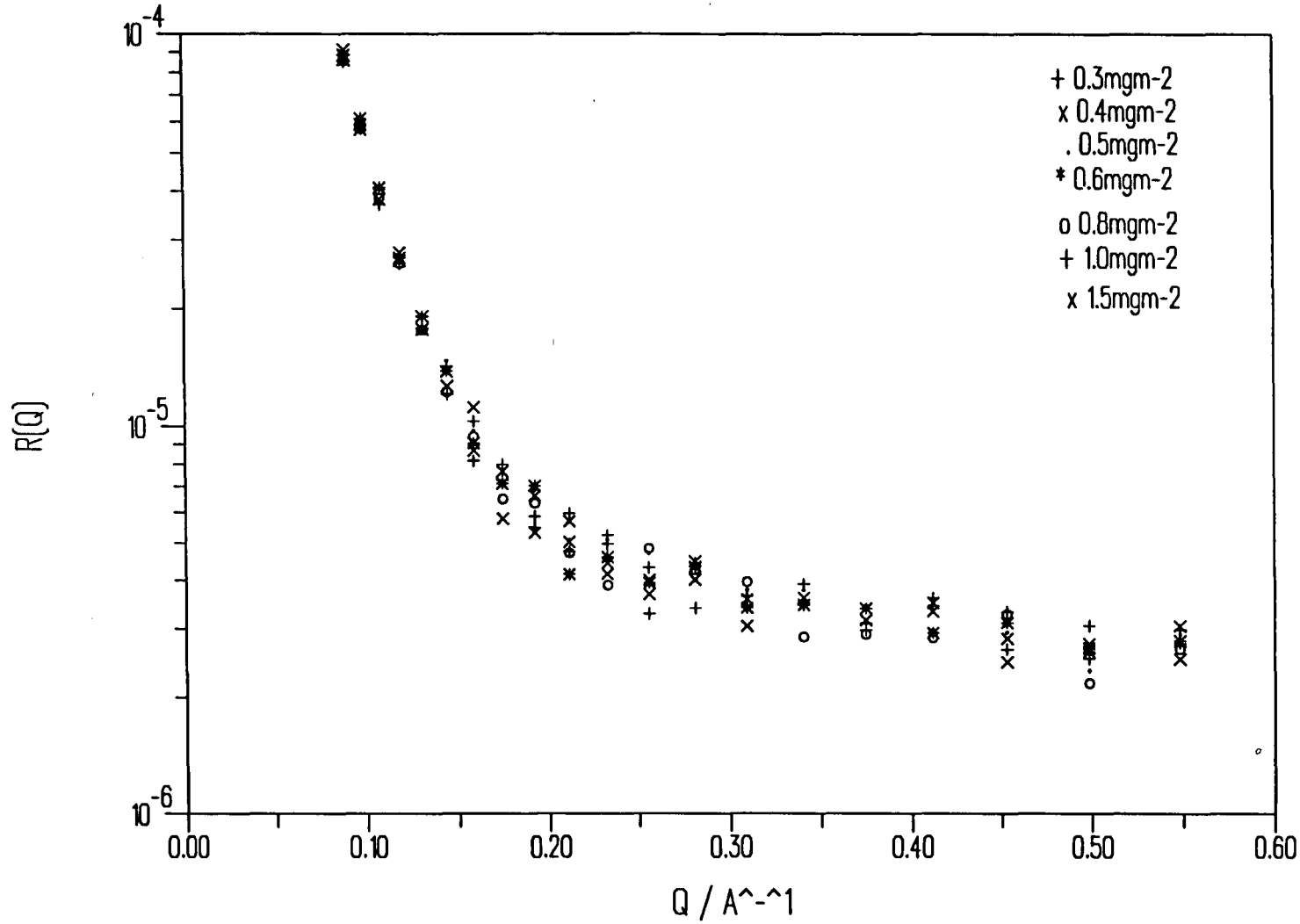

Figure 4.20 Neutron Reflectivity Profiles for ISOHPMMA on D2O

layer thickness in the fit and allowing the scattering length density to float for each thickness to obtain a minimum in the residual error for the fit, values of layer thickness and scattering length density have been obtained for each surface concentration and for both contrasts for each polymer. These values are summarised in table 4.5.

A measure of the uncertainty associated with the fits may be made by considering the behaviour of the residual of the fit (the sum of the squares of the difference in the data and fitted function values) when one of the fitting parameters, for example the layer thickness, is held constant and the other, the scattering length density, allowed to float to minimise the residual. By plotting the value of the residual as a function of the fixed layer thickness when the scattering length density is the only floating variable, the depth and breadth of the curve so obtained reflects the quality of the best fit to the data. Figures 4.21 and 4.22 show some typical residual curves superimposed on one another, and figures 4.23 and 4.24 show the corresponding reflectivity profiles and curves of best fit.

The value of the residual is somewhat dependent on the individual features of the profile (for example scatter in the points at high Q due to shorter run times can arbritarily increase the value), but the features observed in the examples were typical. At very low surface concentrations both residual curves, the D/acmw curve in particular, tended to become very broad and shallow and the positions of their minima were rather far apart. The reflectivities in this case were, on the one hand only just above background, and on the other only slightly different from that obtained for clean D_2O. There is a considerable correlation between the values of d and ρ so and so their individual values can only be determined with a fairly large uncertainty. As the surface concentration is increased however the minima become both better defined and closer together. Thus at moderate surface concentrations both the thickness and scattering length density can be determined with reasonable

Syndiotactic						
Γ/mg m^{-2}	D/acmw			H/D_2O		
	d/Å	$\rho/10^{-6}$Å^{-2}	residual/10^{-2}	d/Å	$\rho/10^{-6}$Å^{-2}	residual/10^{-2}
0.2	-	-	-	22	0.58	1.010
0.3	20	1.07	0.4083	-	-	-
0.4	19	1.25	0.3785	22	0.72	0.4037
0.5	18	1.70	0.3963	-	-	-
0.6	12	3.12	0.4780	21	0.84	0.8693
0.8	16	3.82	0.5581	21	0.93	0.9636
1.0	19	3.99	0.4407	21	1.09	0.5741
1.5	23	4.50	0.5700	21	1.09	0.7322
2.0	23	4.54	0.7937	22	1.26	0.7961
Atactic						
0.2	18	0.64	0.3809	-	-	-
0.5	16	2.15	0.4655	19	0.90	0.6167
0.75	15	3.57	0.2646	-	-	-
1.0	18	3.76	0.5988	17	1.31	0.6141
1.2	17	4.04	0.4162	-	-	-
1.7	17	4.15	0.3895	-	-	-
2.0	17	3.91	0.5004	17	1.85	1.007
2.1	20	4.47	0.6753	-	-	-
2.5	19	4.22	0.5447	-	-	-
3.5	23	4.59	0.6466	19	1.75	1.336
4.95	25	5.31	0.7751	20	1.69	0.9333
Isotactic						
0.2	36	0.22	0.5466	21	0.54	0.7558
0.3	11	1.12	0.4829	20	0.55	0.7085
0.4	14	1.05	0.4861	19	0.53	0.4610
0.5	24	0.64	0.5521	20	0.52	0.6287
0.6	-	-	-	19	0.52	0.8549
0.8	15	2.67	0.4861	18	0.75	0.9730
1.0	15	3.18	0.5123	17	0.84	0.7418
1.5	17	2.60	0.7477	17	0.87	0.8323

Table 4.5 Residual Minimum fitted values for PMMA on water

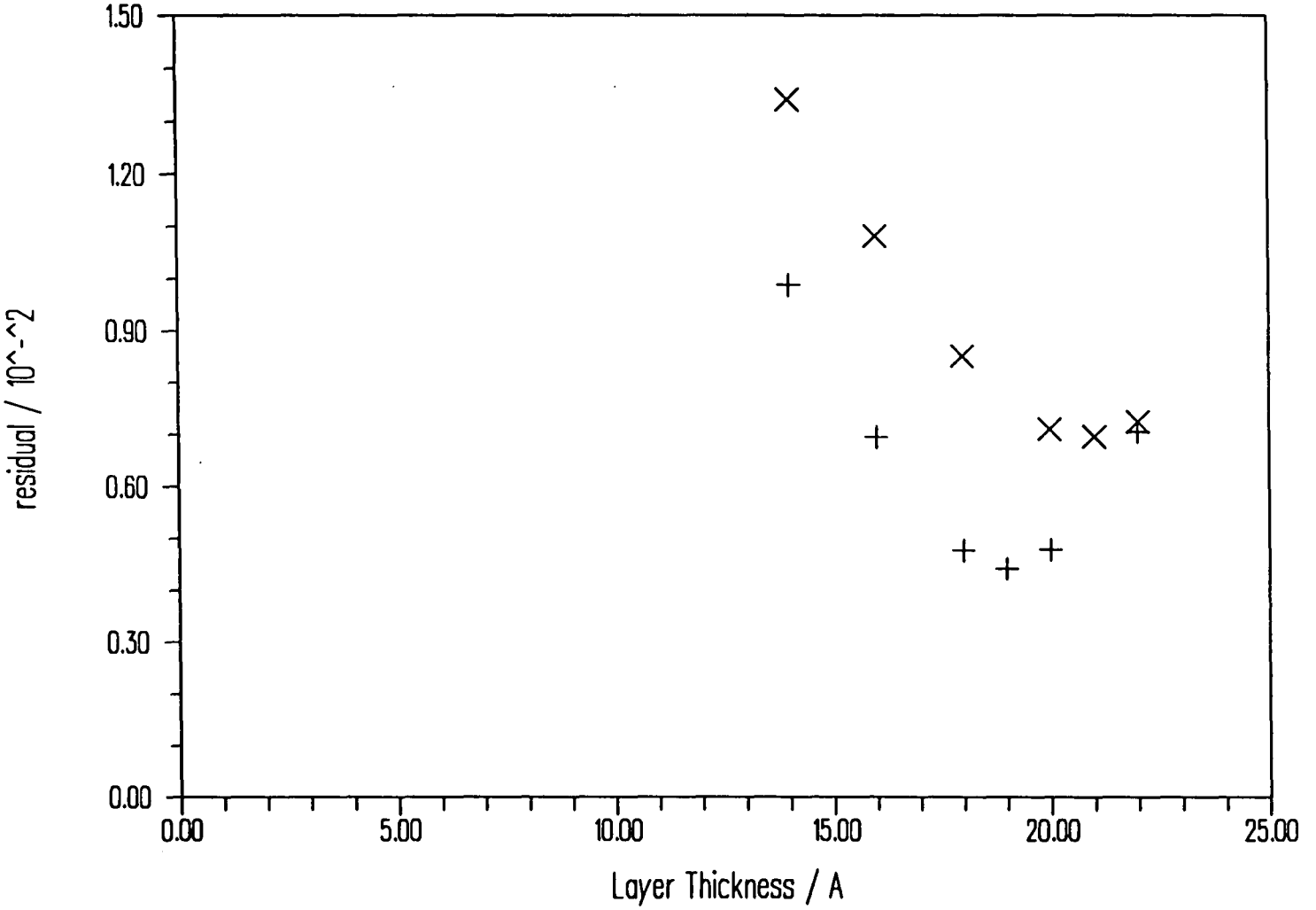

Figure 4.21 Residual of fit as a function of fixed layer thickness for SYNDIOPMMA at $\Gamma = 1.0 mg^{-2}$, + = D/acmw, x = H/D_2O

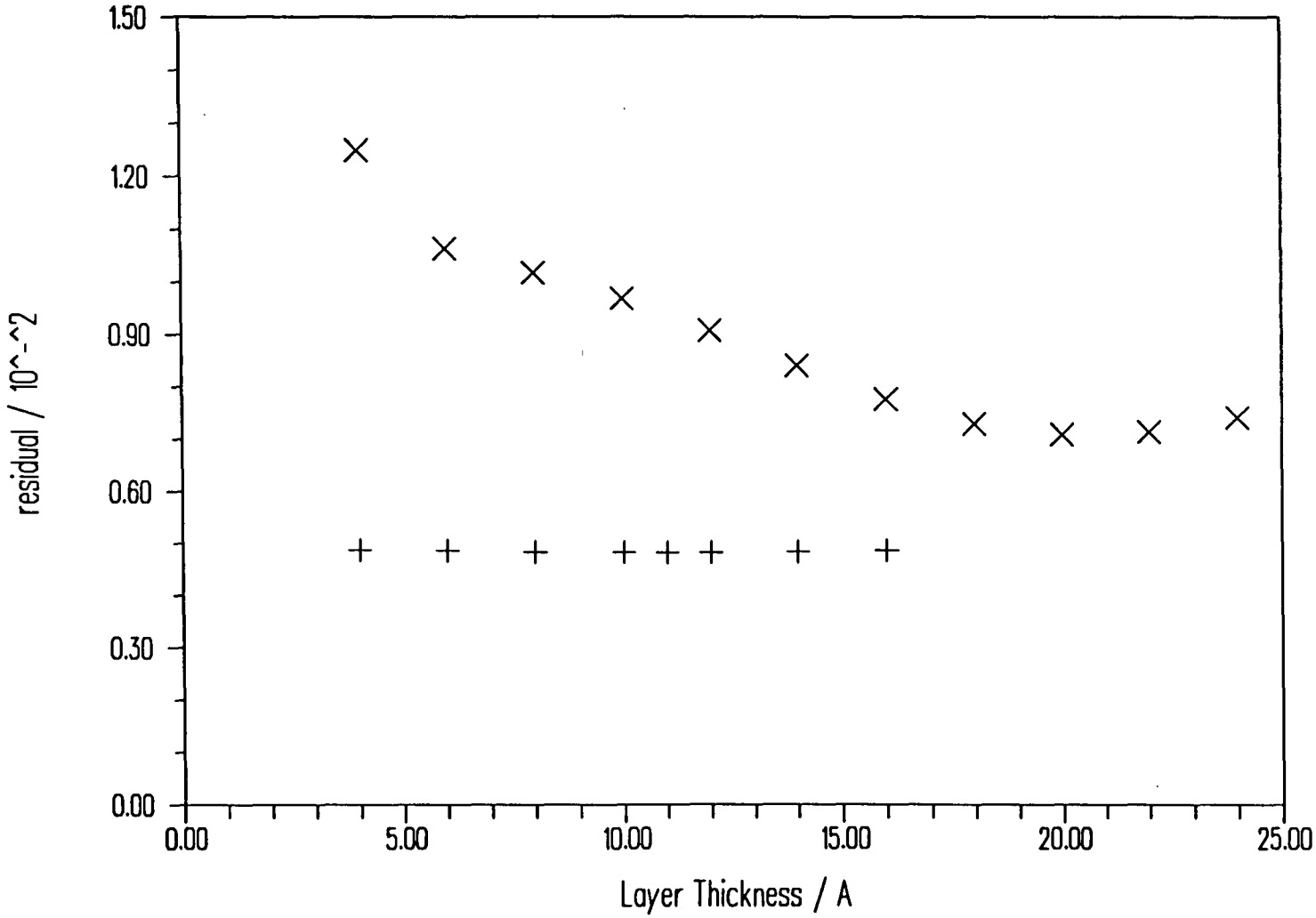

Figure 4.22 Residual Plot for ISOPMMA at $\Gamma = 0.3 mgm^{-2}$

+ = D/acmw, x = H/D_2O

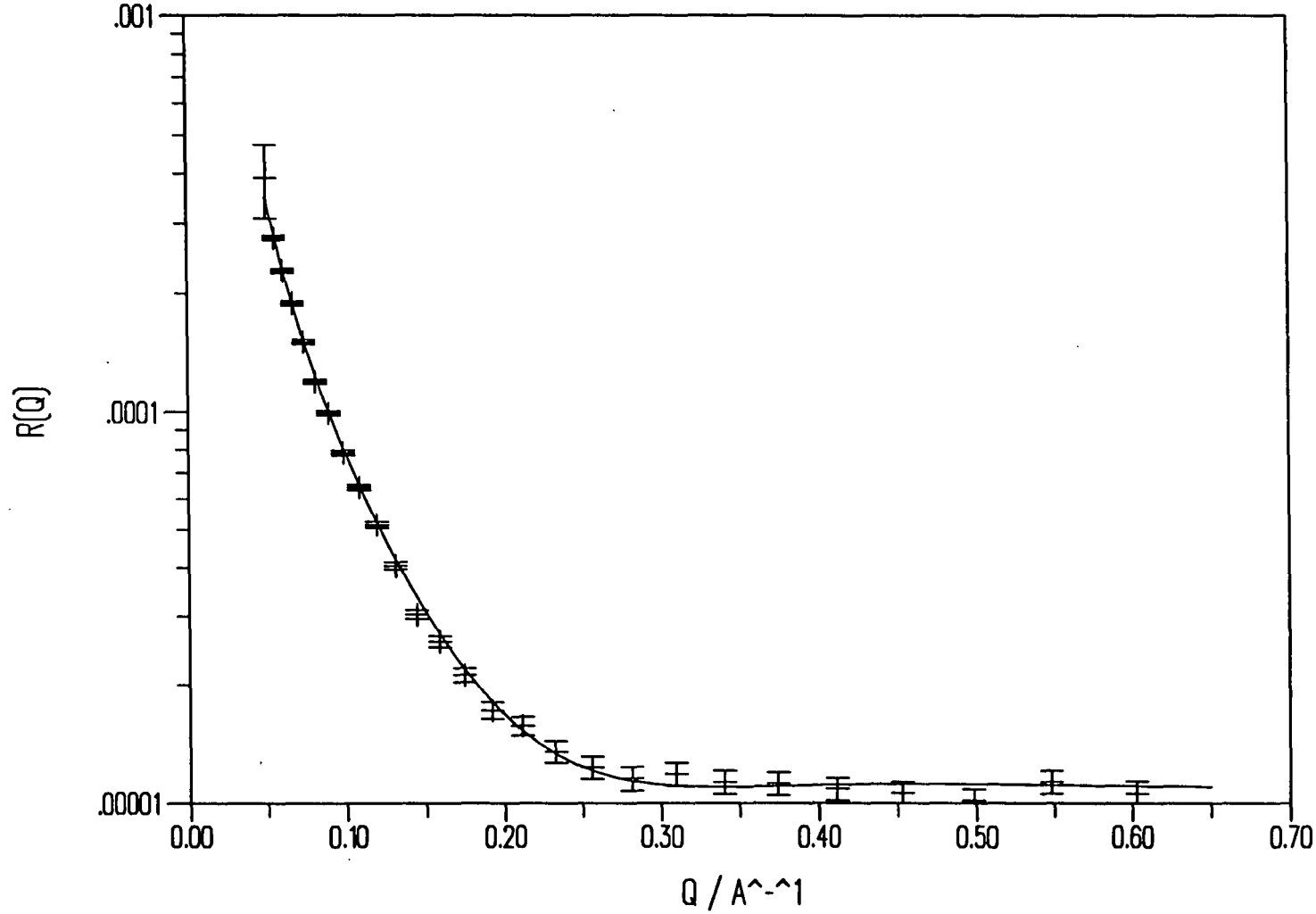

Figure 4.23(a) Fitted Reflectivity Profile for SYNDIODPMMA on acmw , $\Gamma = 1.0 mgm^{-2}$

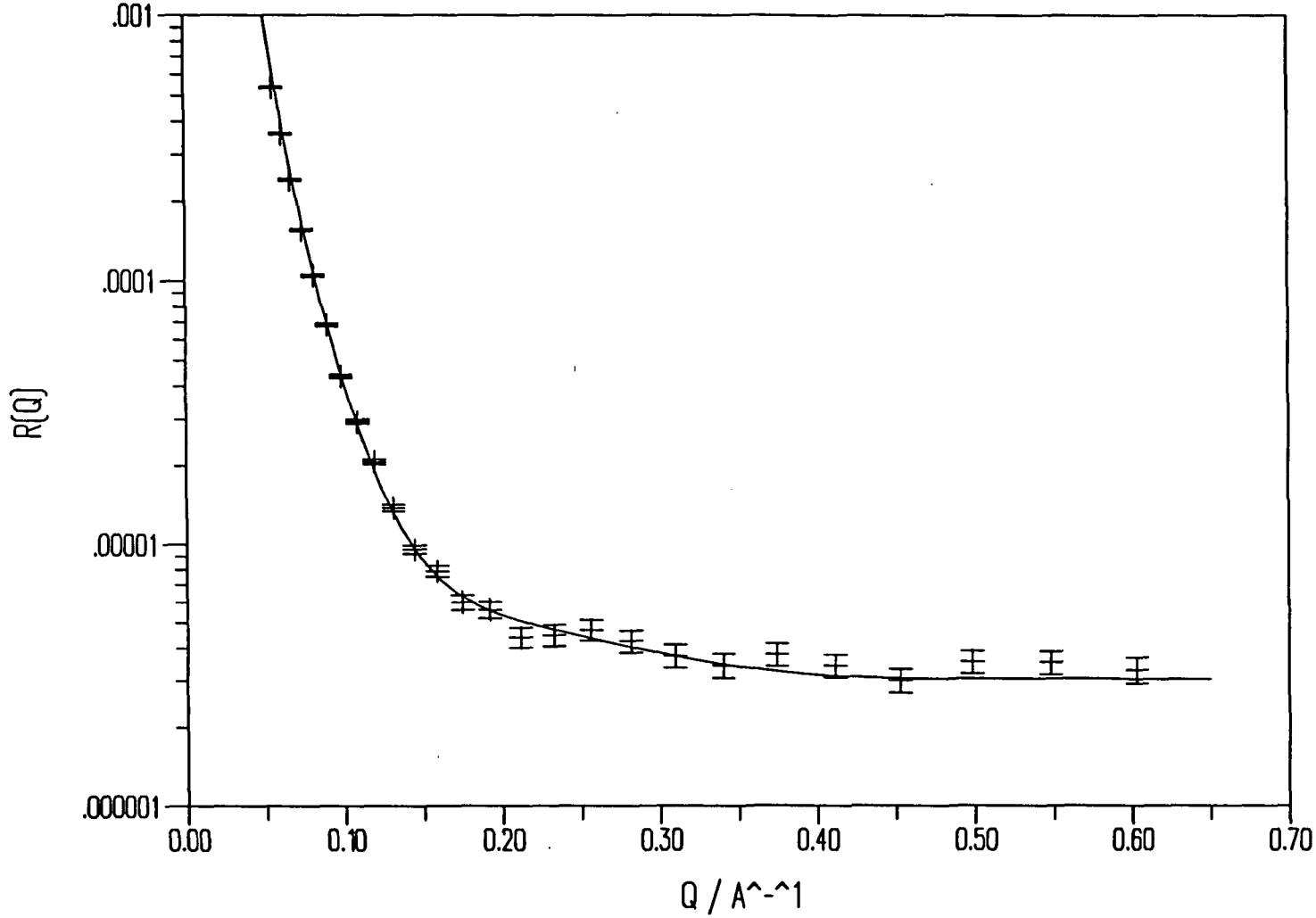

Figure 4.23(b) Fitted Reflectivity Profile for SYNDIOHPMMA on D_2O, Γ = 1.0mgm^{-2}

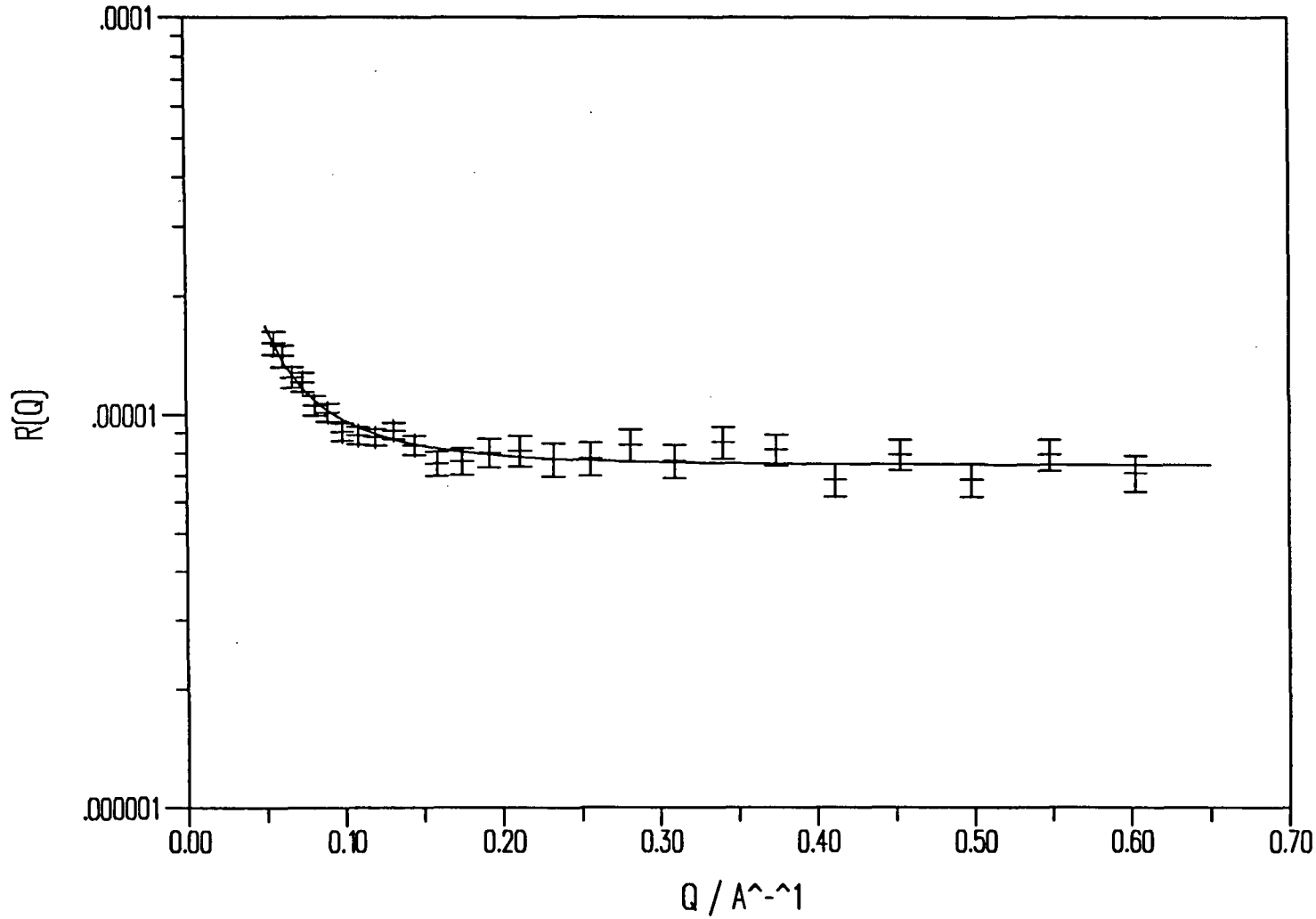

Figure 4.24(a) Fitted Reflectivity Profile for ISODPMMA on acmw, $\Gamma = 0.3 mgm^{-2}$

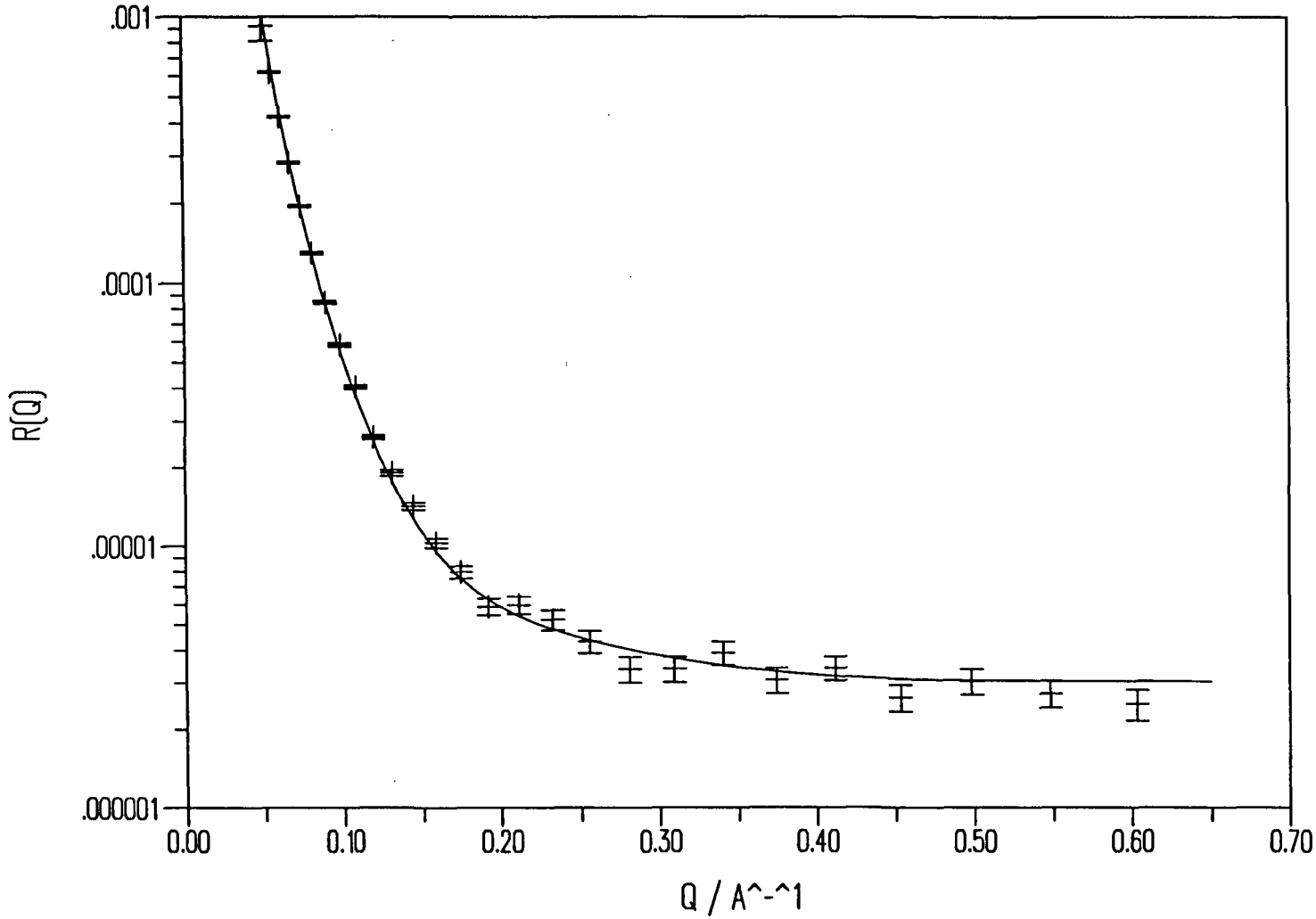

Figure 4.24(b) Fitted Reflectivity Profile for ISOHPMMA on D_2O, $\Gamma = 0.3 mgm^{-2}$

confidence.

From these observations it seems reasonable to estimate an error on the fitted values of the layer thickness and scattering length density according to the differences between the minima, and in the absence of any better estimate, to fix the layer thickness at an intermediate value between the two minima. Using these figures as a basis for refitting the scattering length density the values obtained are shown in table 4.6 and illustrated graphically in figures 4.25-30.

The use of different contrast systems may be used to estimate the volume fraction composition of the surface layer in terms of the various components that could be present in it. For a single layer system one can describe the composition in terms of volume fractions of polymer, air, and subphase (water) in the interfacial region. The contributions to the measured scattering length density may be expressed by an appropriately weighted sum of the individual scattering length densities of these species such that

$$\rho_{layer} = \phi_p\rho_p + \phi_a\rho_a + \phi_s\rho_s$$

where ϕ = volume fraction of species

ρ = scattering length density of species

p = polymer

a = air

s = subphase.

Remembering that the value of the scattering length density of air is zero, this simplifies to

$$\rho_{layer} = \phi_p\rho_p + \phi_s\rho_s$$

For any contrast ρ_p and ρ_s are known and ρ_{layer} may be measured by a reflectometry experiment. Therefore by studying at two different contrasts, ϕ_p and ϕ_s may be obtained by simultaneous equations and $\phi_a$obtained by the difference

$$\phi_a = 1 - (\phi_p + \phi_s)$$

Syndiotactic					
Γ/mg m^{-2}	D/acmw			H/D_2O	
	d/Å	$\rho/10^{-6}$Å^{-2}	residual/10^{-2}	$\rho/10^{-6}$Å^{-2}	residual/10^{-2}
0.4	20	1.20	0.3815	0.75	0.6147
0.6	16	2.44	0.5698	0.98	1.315
0.8	18	3.50	0.6464	1.02	1.090
1.0	20	3.86	0.4774	1.12	0.7096
1.5	22	4.60	0.6136	1.15	1.031
2.0	23	4.54	0.7937	1.22	0.8610
Atactic					
0.5	17	2.05	0.4752	0.97	0.6508
1.0	18	3.76	0.5988	1.24	0.6544
2.0	17	3.91	0.5004	1.85	1.007
3.5	21	4.75	0.9873	1.59	1.467
4.95	22	5.54	1.203	1.59	1.122
Isotactic					
0.2	29	0.25	0.5530	0.44	0.9450
0.3	16	0.80	0.4871	0.63	0.7769
0.4	16	0.93	0.4890	0.59	0.5070
0.5	22	0.68	0.5534	0.49	0.6492
0.8	16	2.53	0.4874	0.82	0.9975
1.0	15	3.18	0.5123	0.84	0.7418
1.5	17	2.60	0.7477	0.87	0.8323

Table 4.6 Optimum Fitting parameters for PMMA on water

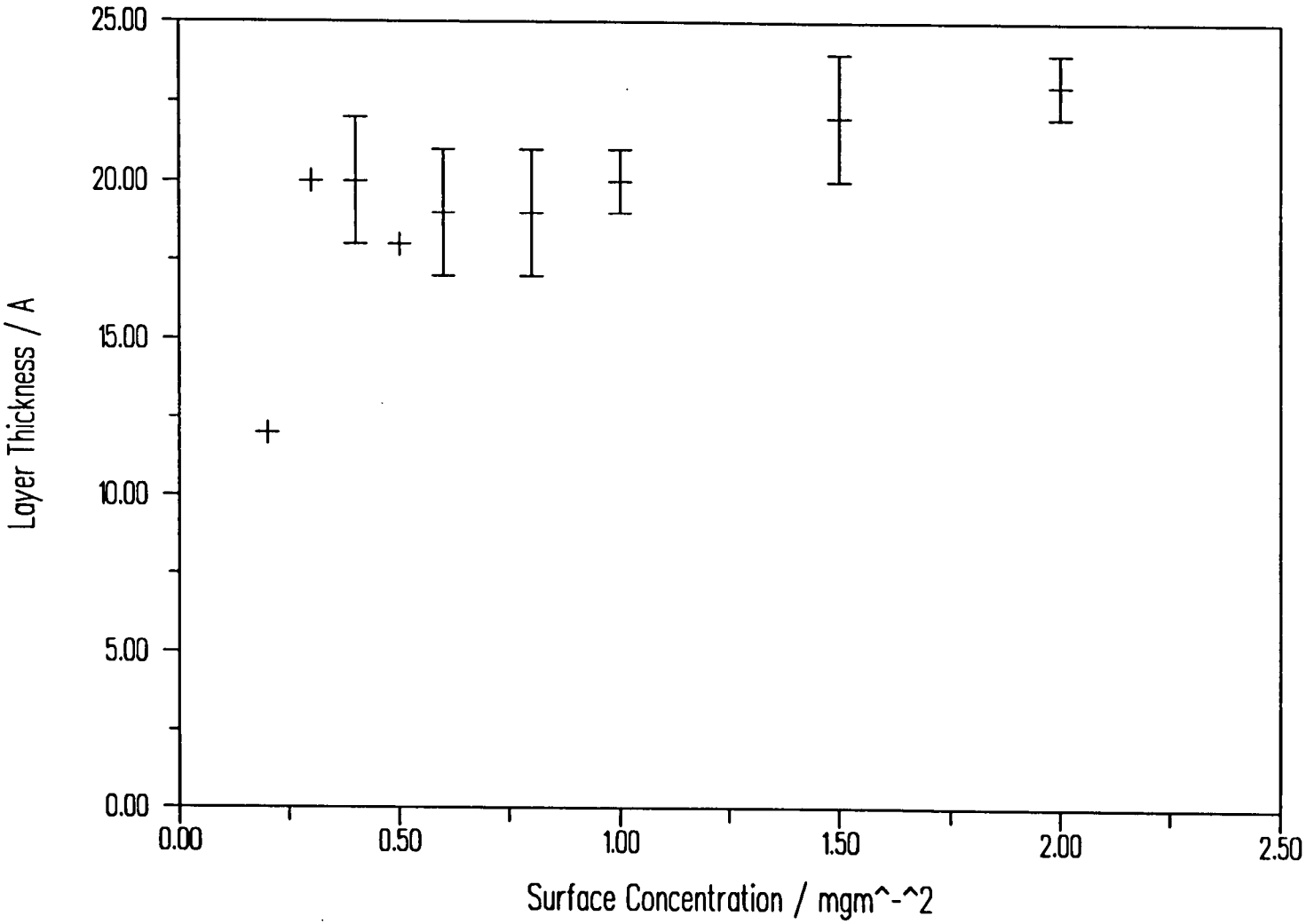

Figure 4.25 Variation of Layer Thickness with Surface Concentration for SYNDIOPMMA

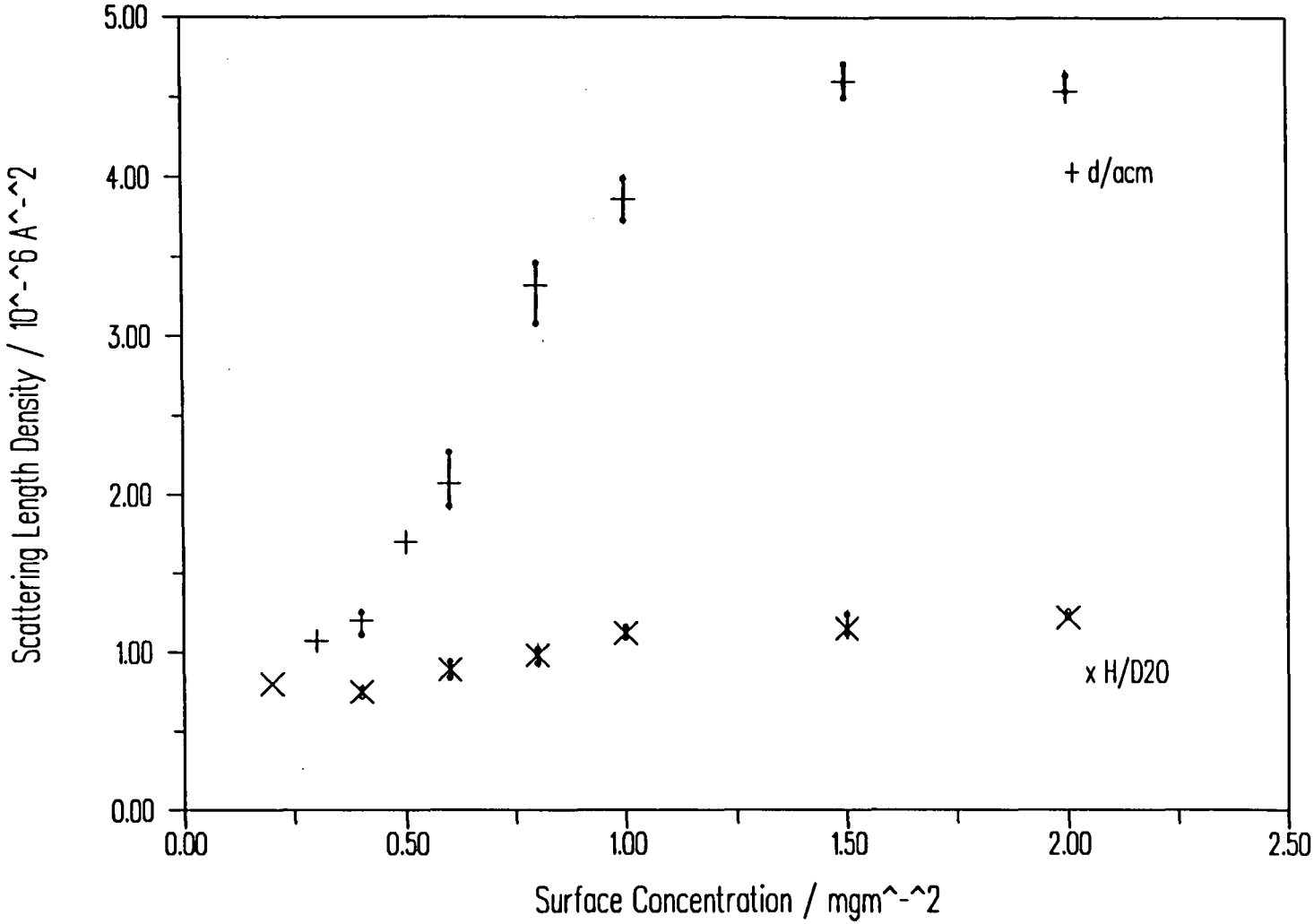

Figure 4.26 Variation in Scattering Length Density with Surface Concentration for syndio-PMMA

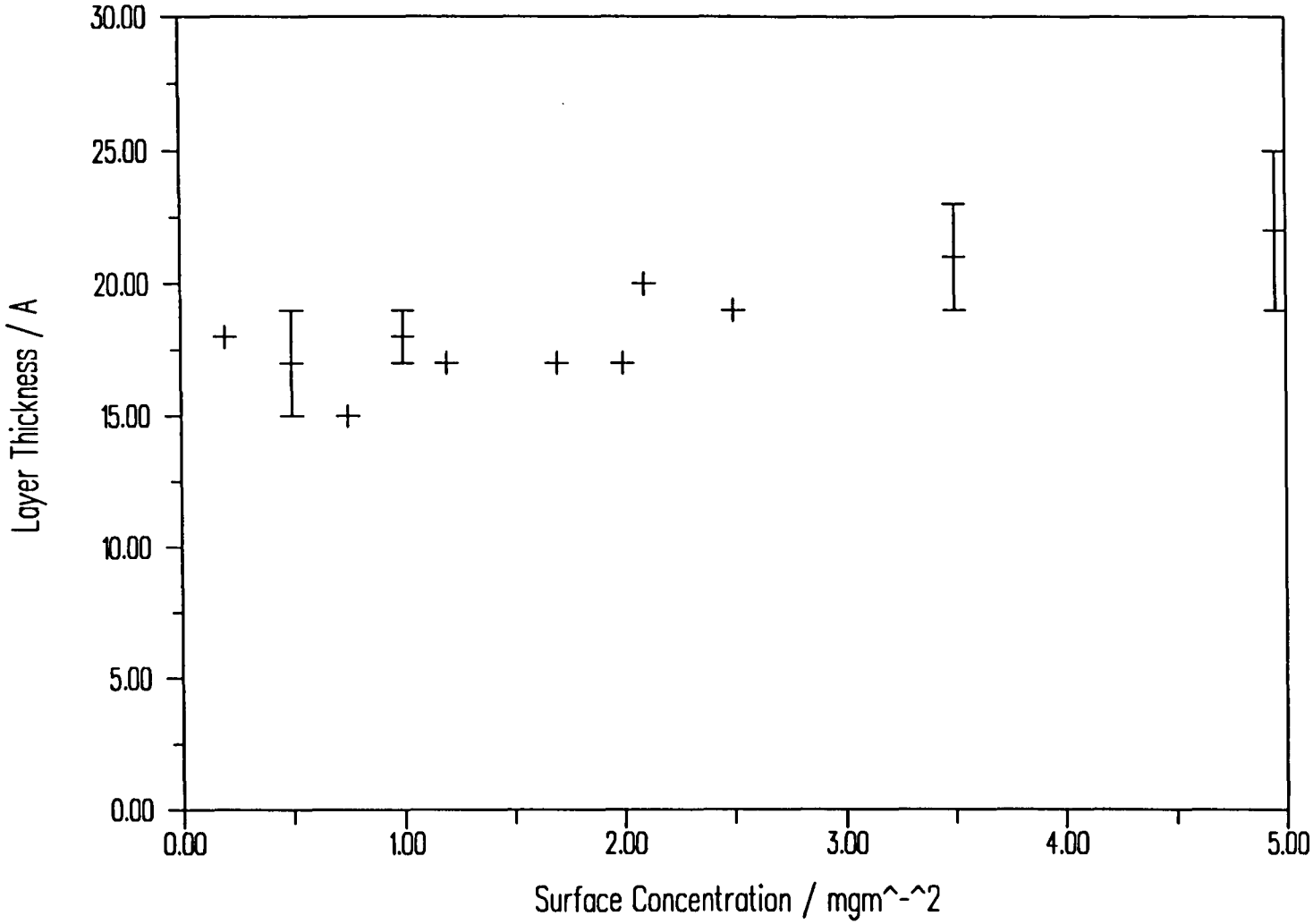

Figure 4.27 Variation in Layer Thickness with Scattering Length Density for ata-PMMA

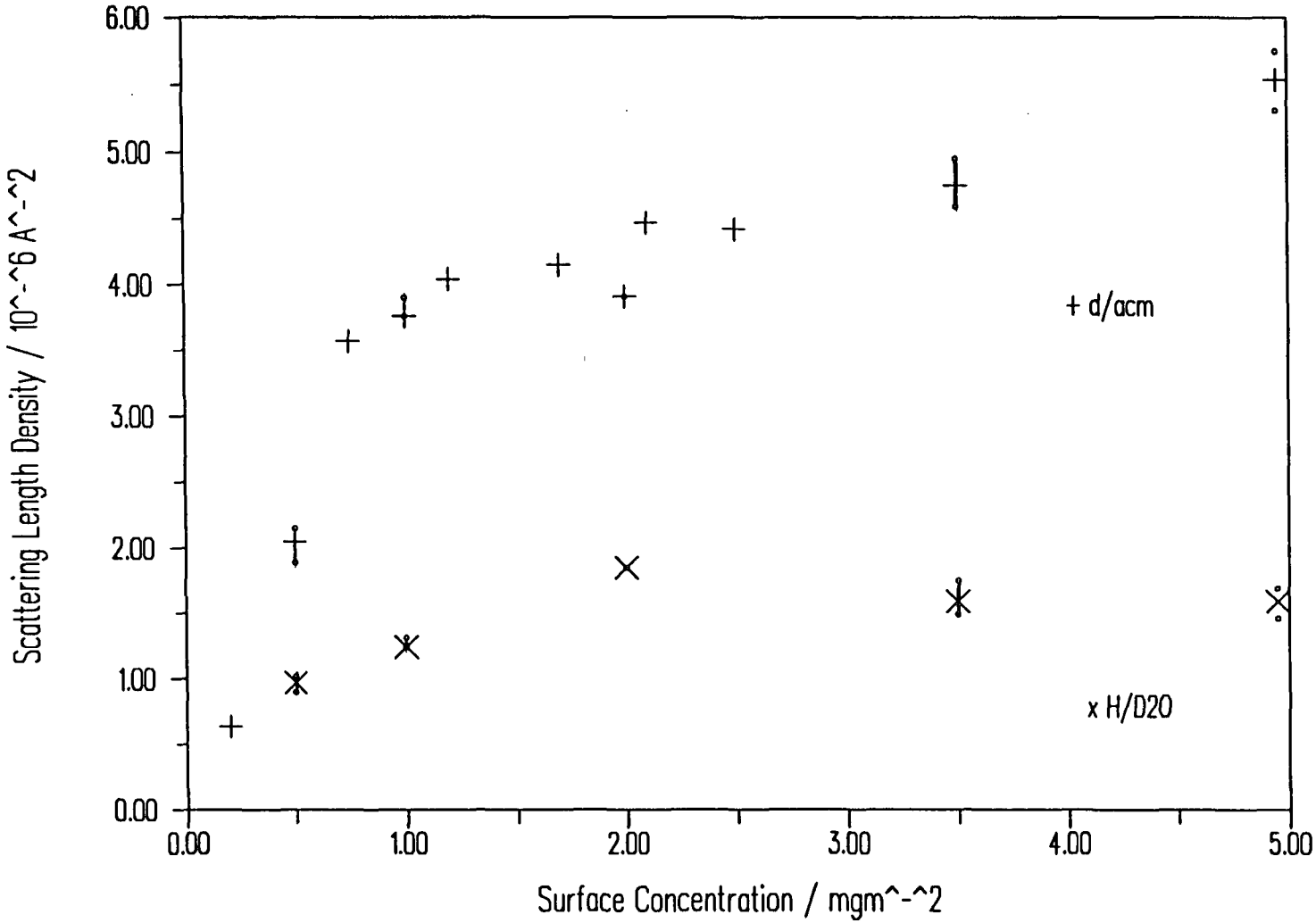

Figure 4.28 Variation in Scattering Length Density with Surface Concentration for ata-PMMA

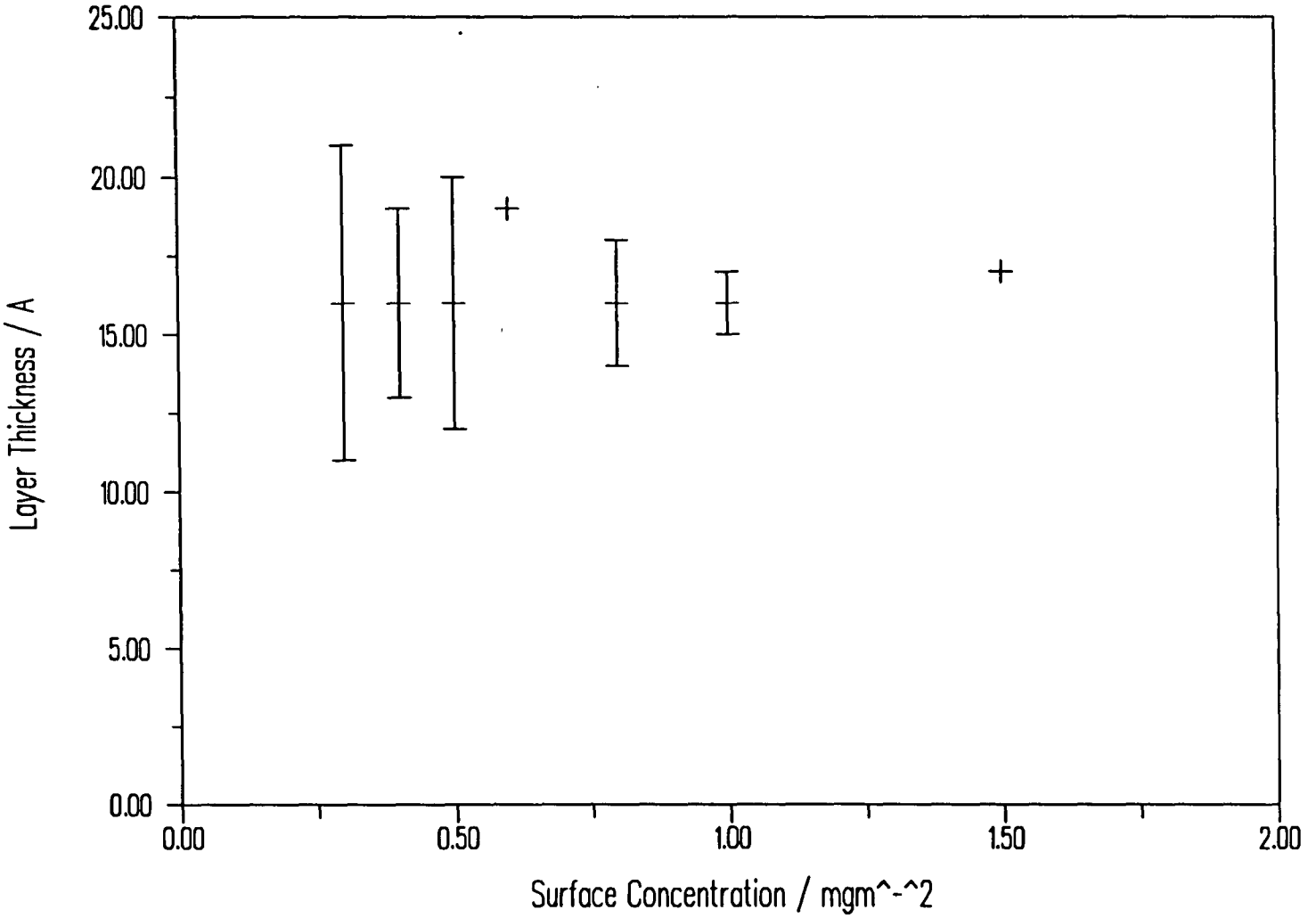

Figure 4.29 Variation in Layer Thickness with Surface Concentration for iso-PMMA

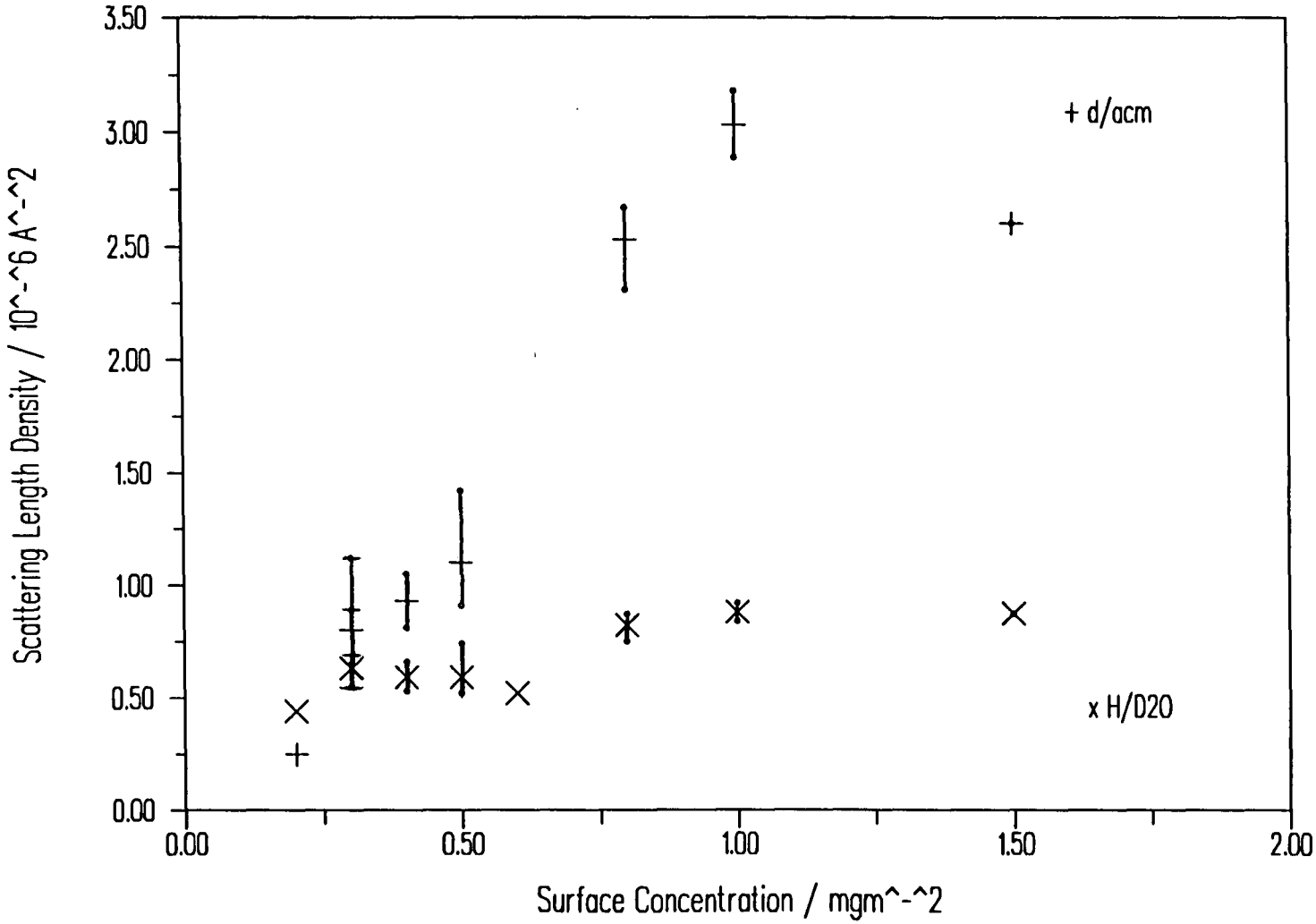

Figure 4.30 Variation in Scattering Length Density with Surface Concentration for iso-PMMA

Applying this method to the data of table 4.6, the volume fraction values obtained for the three polymer tacticities are shown in table 4.7.

The volume fraction composition for each tacticity are presented graphically as a function of surface concentration in figures 4.31-33, where errors are estimated by the considerations of the residual minima discussed above.

A comparison of the trends in the layer thickness and composition curves suggests that,as one might expect, the syndiotactic polymer has very different properties from the isotactic and that the atactic polymer lies in an intermediate position, but is somewhat similar to the syndiotactic. The layer thickness for SYNDIOPMMA is approximately constant at around 19-20Å, rising slightly to 23Å at the higher surface concentrations. An isolated measurement on ATAPMMA at a much greater surface concentration ($5mgm^{-2}$) indicated a very similar thickness value suggesting that very little multi-layer type deformation occurred in the film, however due to the factors concerning reproducibility of very high surface coverage data too much emphasis should not be placed on this point. There is a rather larger uncertainty in the low coverage values than those obtained at higher surface concentrations and this probably accounts for the scatter in the thickness values obtained from measurements on one contrast at low surface concentrations. The layer thickness obtained for ISOPMMA seems to be more or less constant at a value of 16-17Å whatever the surface concentration.

Again, comparing the film composition data for the various tacticities, some marked differences are apparent. The same general pattern of increasing polymer content with surface concentration is observed in all cases, however for SYNDIOPMMA the volume fraction of polymer increases to a limiting value of around 0.8, much higher than for ISOPMMA which reaches a limit of around 50% polymer in the layer. The increase is at the expense of air, the volume fraction of which decreases in a more or less direct correspondence with the increase in

SYNDIOTACTIC			
Γ/mg m^{-2}	Volume Fraction		
	polymer	water	air
0.3	0.18	-	-
0.4	0.20	0.09	0.71
0.5	0.28	-	-
0.6	0.41	0.10	0.49
0.8	0.58	0.08	0.34
1.0	0.64	0.09	0.27
1.5	0.76	0.07	0.17
2.0	0.75	0.09	0.16
ATACTIC			
0.2	0.11	-	-
0.5	0.34	0.10	0.56
0.75	0.59	-	-
1.0	0.62	0.11	0.27
1.2	0.67	-	-
1.7	0.69	-	-
2.0	0.65	0.20	0.15
2.1	0.74	-	-
2.5	0.70	-	-
3.5	0.79	0.14	0.07
5.0	0.92	0.12	-0.04
ISOTACTIC			
0.3	0.13	0.08	0.79
0.4	0.15	0.07	0.78
0.5	0.11	0.06	0.83
0.8	0.42	0.07	0.51
1.0	0.50	0.07	0.43
1.5	0.43	0.08	0.49

Table 4.7 Volume Fraction Composition Variation for PMMA on Water

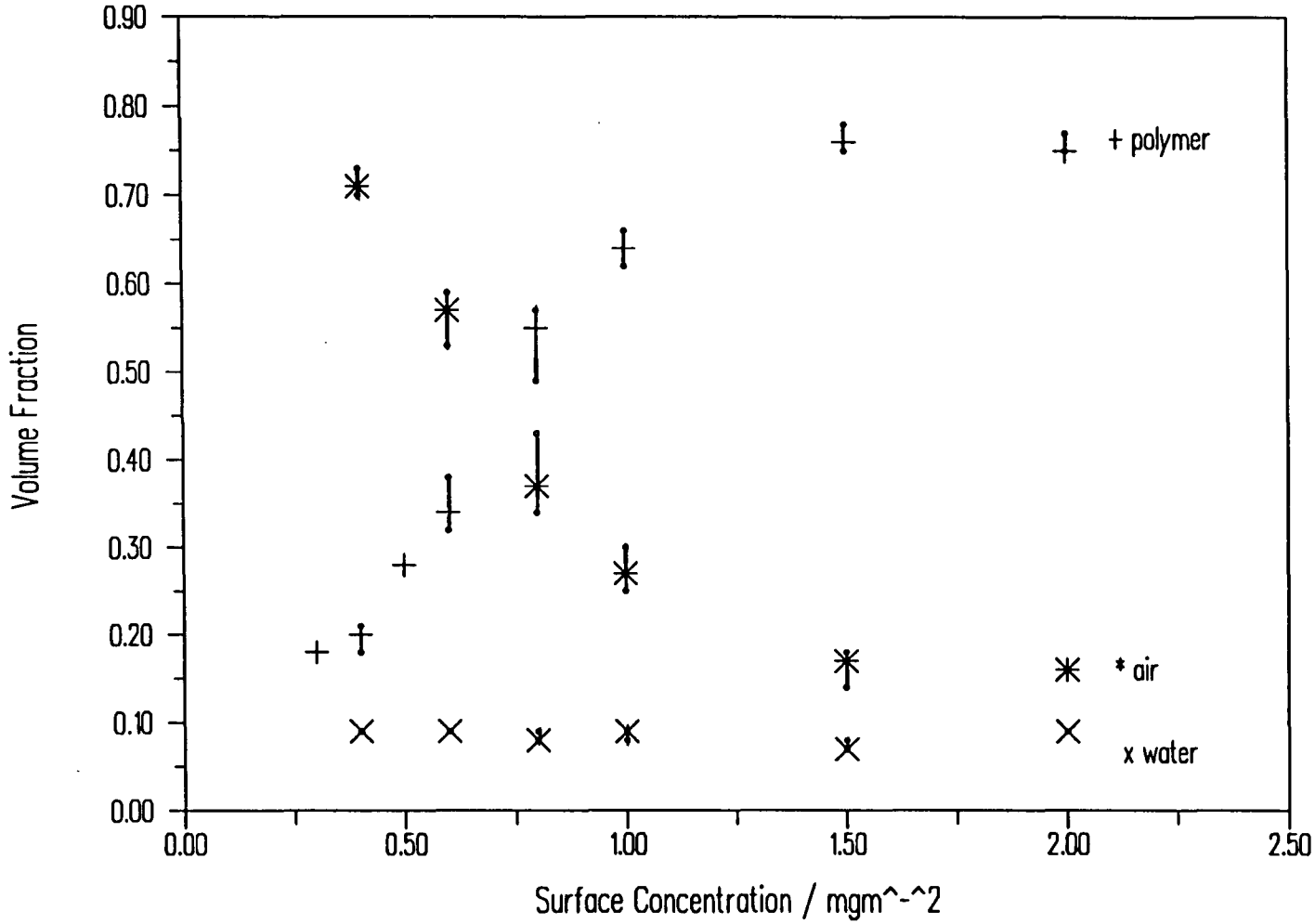

Figure 4.31 Variation in Layer Composition with Surface Concentration for syndio-PMMA

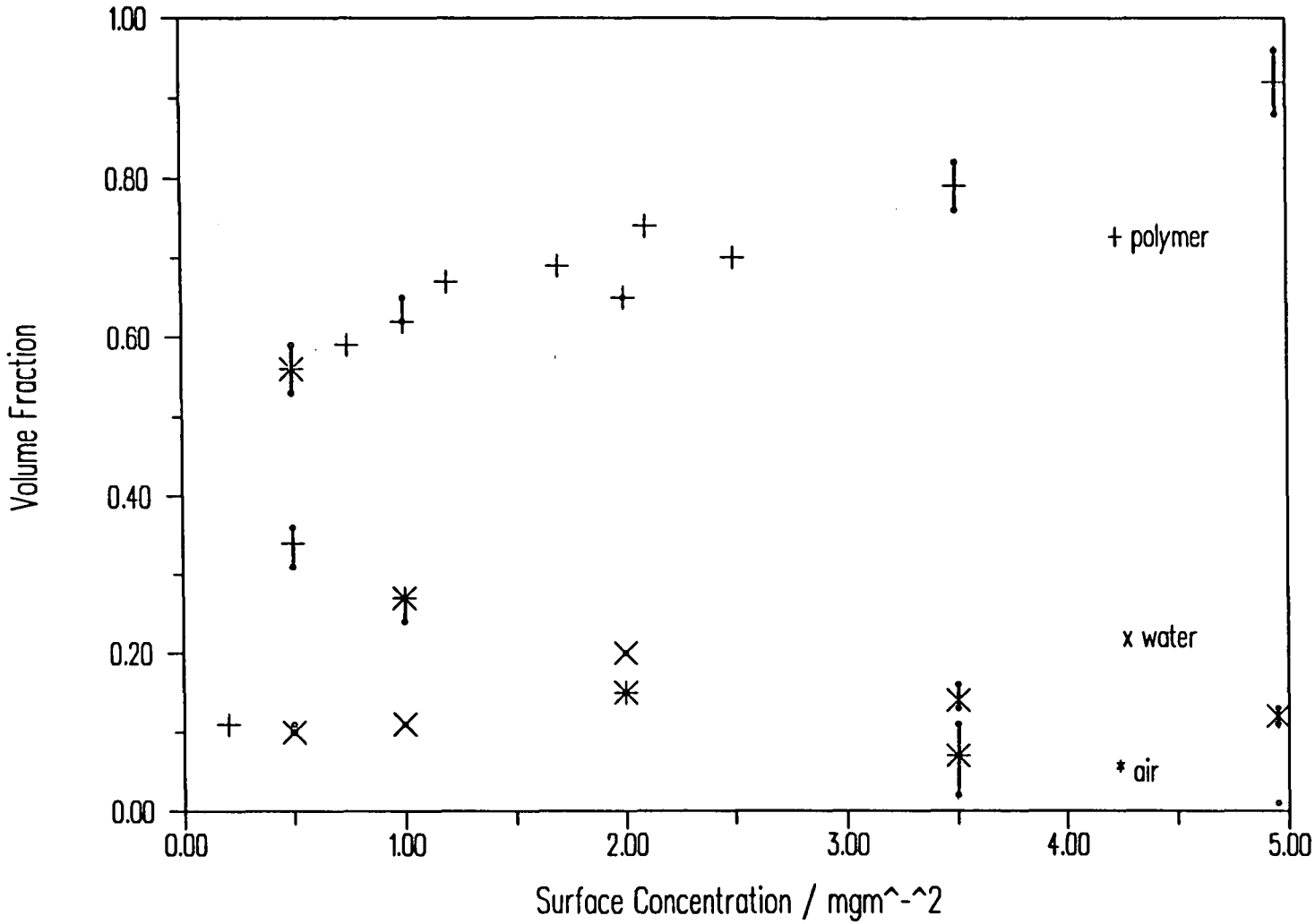

Figure 4.32 Variation of Layer Composition with Surface Concentration for ata-PMMA

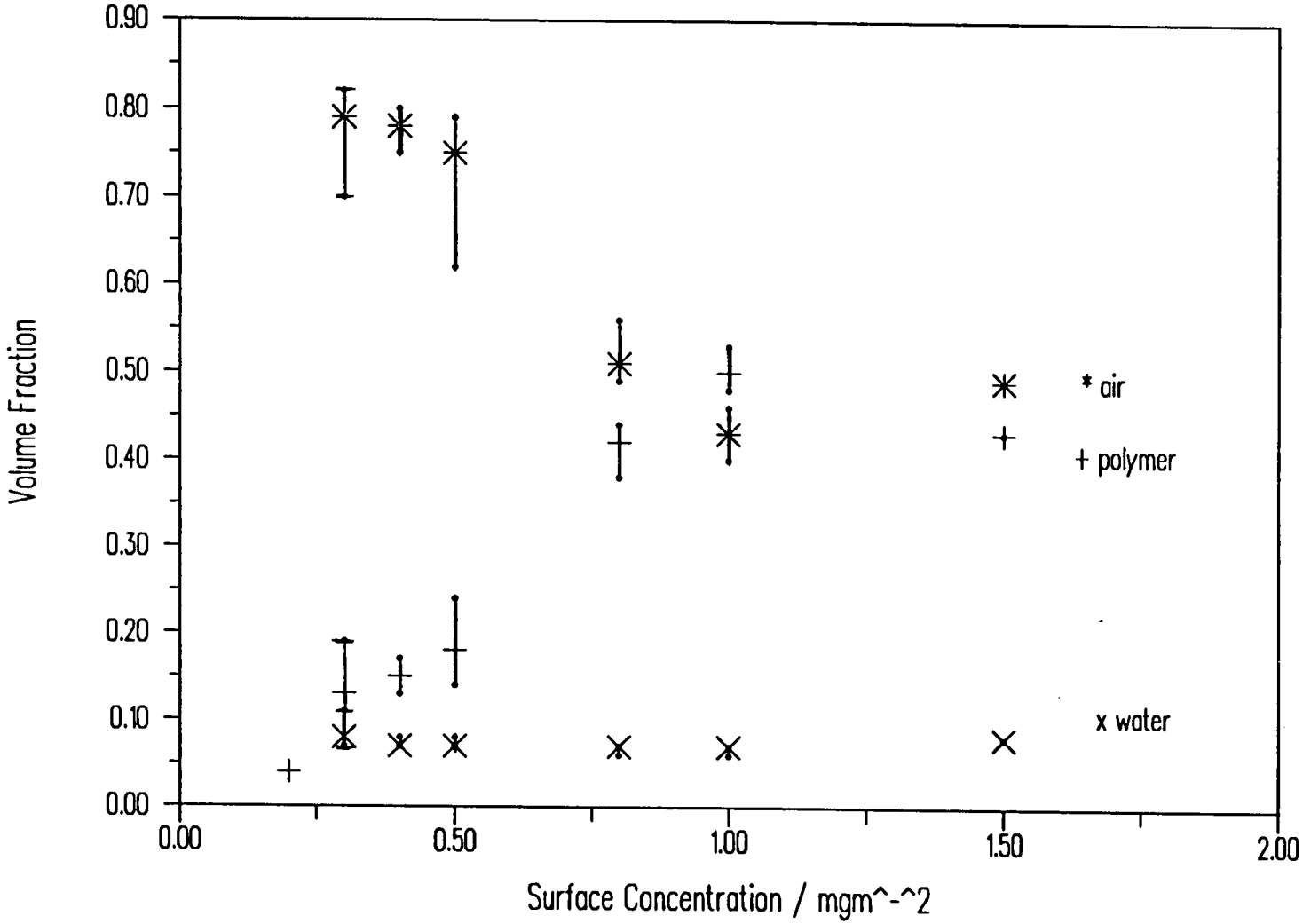

Figure 4.33 Variation in Layer Composition with Surface Concentration for iso-PMMA

polymer. Thus for the isotactic polymer, there is a significant amount of air in the layer even at the highest surface coverages. The volume fraction of water in the layer is low and virtually unchanging in all cases at around 7-8%.

From the product of the fitted thickness, d, and scattering length density, ρ, for the DPMMA/acmw contrast, where the polymer is the only material contributing to the signal, it is possible to calculate area per monomer (apm) values at a given surface concentration and hence derive apparent surface concentration values, Γ_a. These values are obtained by the simple formulae

$$\text{Area per monomer} = \Sigma b_i/\rho.d$$

and $$\Gamma_a = M_m/N_{av}.apm$$

where Σb_i = sum of the coherent scattering lengths of the constituent nuclei in the unit

M_m = molecular weight of unit

N_{av} = avogadro constant.

Applying these formulae to the data of table 4.6, the values in table 4.8 and figures 4.34-36 are obtained.

For SYNDIO and ATAPMMA the apparent surface concentration values, Γ_a, are generally about the same or slightly greater than the spread amount, Γ_s, but for ISOPMMA the values become significantly less, particularly at higher surface coverages. This can be seen clearly if Γ_a is plotted against Γ_s. For ISOPMMA the experimental values deviate from the $\Gamma_a = \Gamma_s$ diagonal. Evidently the fit obtained does not account for the total amount of polymer spread on the surface in this case. Given that PMMA is insoluble in water and is therefore unlikely to be lost to bulk, another explanation for this "missing" polymer must be found.

The neutron reflectivity is sensitive to all the syndiotactic polymer but seemingly not the isotactic. In addition, from surface pressure data, it is known that ISOPMMA is in good 2-D solvent conditions but SYNDIOPMMA is near collapse.

Tacticity	Γ/mg m^{-2}	ρ_d.d/Å^{-1}	a.p.m./Å^{2}molecule^{-1}	Γ_a/mg m^{-2}
SYNDIOTACTIC	0.2	9.6	102.3	0.18
	0.3	21.4	45.9	0.39
	0.4	25.0	39.3	0.46
	0.5	30.6	32.1	0.56
	0.6	39.0	25.2	0.71
	0.8	63.0	15.6	1.15
	1.0	77.2	12.7	1.41
	1.5	101.2	9.7	1.85
	2.0	104.4	9.4	1.91
ATACTIC	0.2	11.5	85.2	0.21
	0.5	34.9	28.2	0.64
	0.75	53.6	18.3	0.98
	1.0	67.7	14.5	1.23
	1.2	68.7	14.3	1.25
	1.7	70.6	13.9	1.29
	2.0	66.5	14.8	1.21
	2.1	89.4	11.0	1.63
	2.5	80.2	12.3	1.46
	3.5	96.4	10.2	1.76
	4.95	116.8	8.4	2.13
ISOTACTIC	0.3	12.8	76.7	0.23
	0.4	14.9	65.9	0.27
	0.5	15.0	65.5	0.27
	0.8	42.7	23.0	0.78
	1.0	47.9	20.5	0.87
	1.5	44.2	22.2	0.81

Table 4.8 Apparent Surface Coverages for PMMA

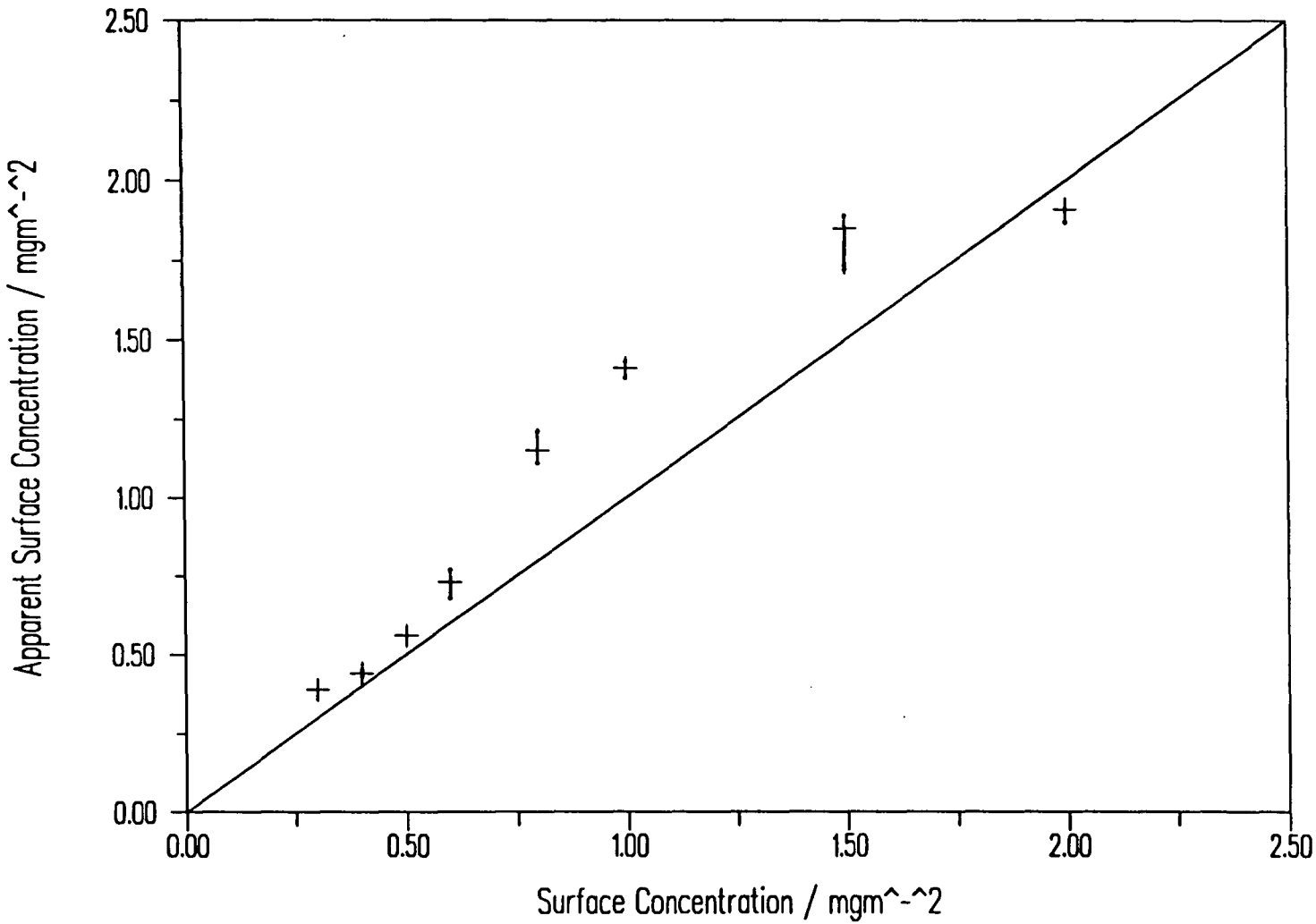

Figure 4.34 Apparent Surface Concentration against Dispensed Surface Concentration for syndio-PMMA

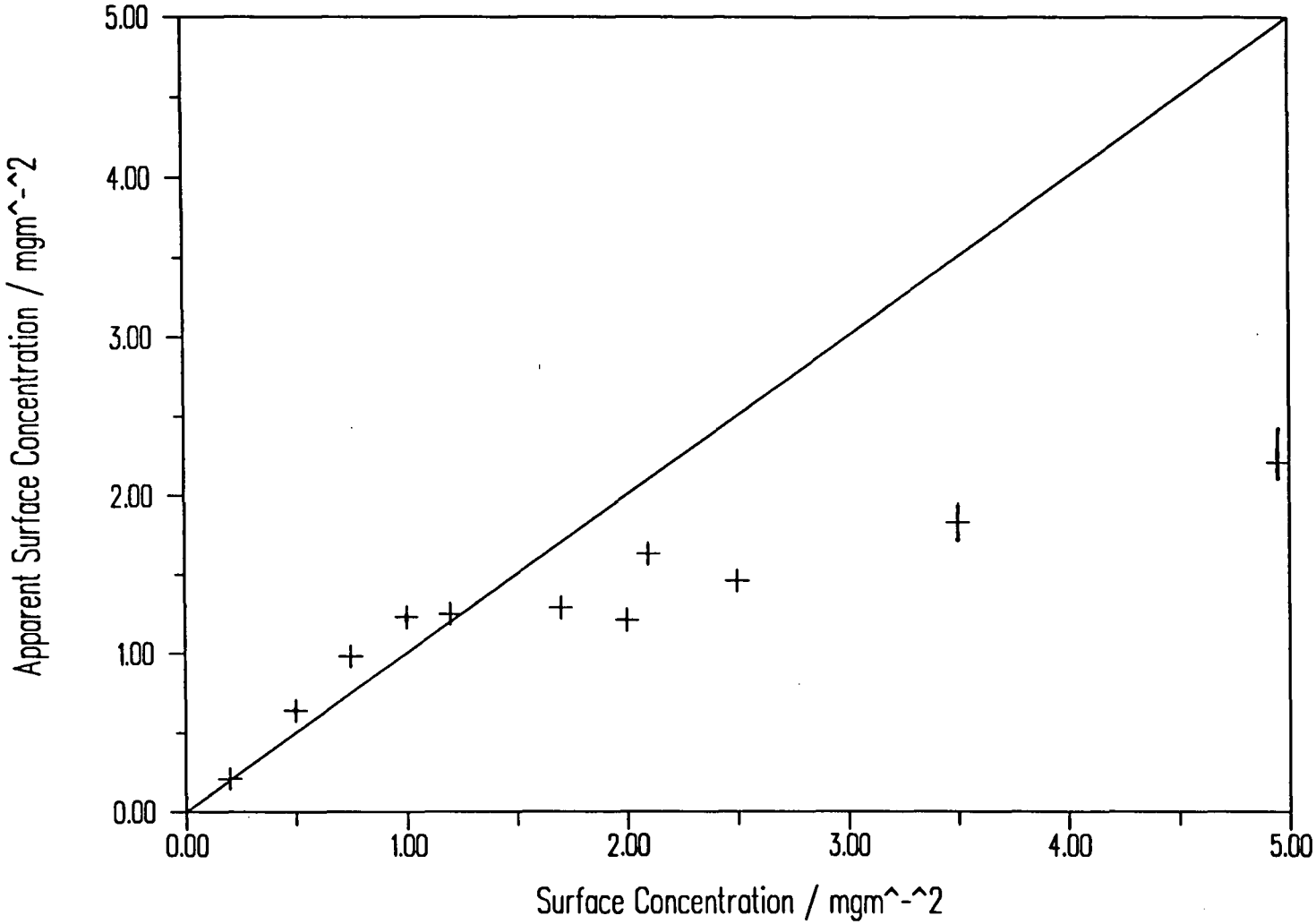

Figure 4.35 Apparent Surface Concentration against Dispensed Surface Concentration for ata-PMMA

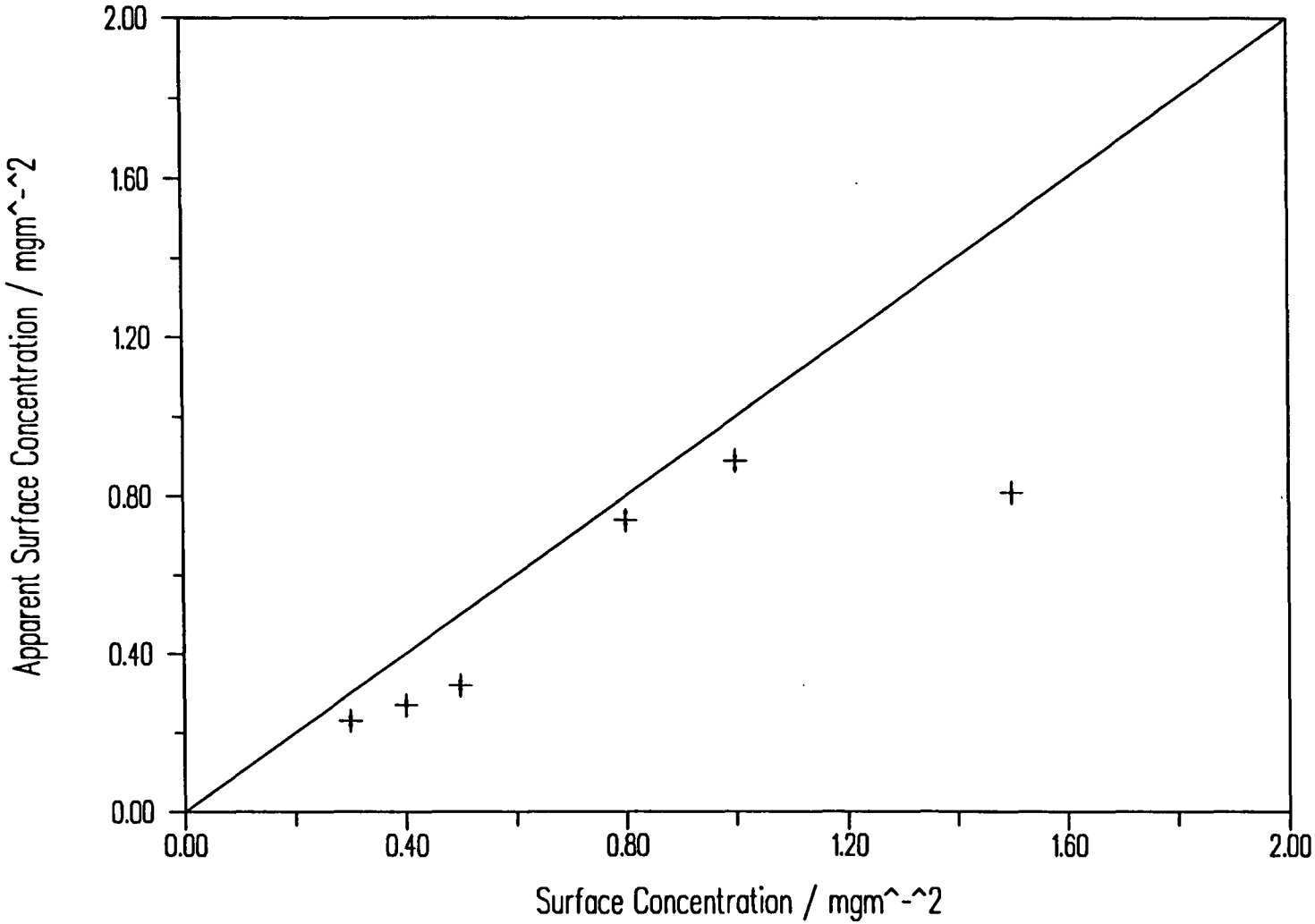

Figure 4.36 Apparent Surface Concentration against Dispensed Surface Concentration for iso-PMMA

One possible explanation for the observed behaviour then, might be that in order to minimise unfavourable subphase contacts, the syndiotactic chains exist in a dense configuration near to the interface whereas the isotactic polymer extends by looping and tailing into the subphase to maximise contacts. Presumably this looping is rather diffuse and therefore it is difficult to improve the fit and model by the introduction of a second layer, particularly for the hydrogenous polymer on D_2O where diffuse polymer effects would tend to be swamped by subphase signal. Additionally one might expect looping and tailing to occur on rather a long length scale, corresponding to a lower Q range than was experimentally available.

In an attempt to investigate this speculation, ISOPMMA has been studied at the same contrast conditions using the ILL instrument D17. Reflectivity profiles showing the effects of increasing surface concentration are illustrated in figures 4.37 and 4.38. It should be noted that the Q range studied is much lower and narrower than for CRISP. Each point on the profile represents an individually measured point at a single selected wavelength and angle, obtained by the ratio of the integrated peak reflected signal to the corresponding straight through unreflected beam. The data for which corresponding CRISP runs were carried out have been appended onto the higher Q data. Unfortunately due to limitations on instrument time only two sets of data for the D/acmw contrast, at 0.8 and 1.0 mgm^{-2}, and one for the H/D_2O, at $0.8mgm^{-2}$, were available for such treatment. The resulting reflectivity profiles in the range $0.01 < Q/Å^{-1} < 0.65$ are shown in figures 4.39 and 4.40.

Since there are so few data sets to work on and only one pair of profiles at both contrasts, it is difficult to assess the usefulness of this approach towards the development of an improved model. However applying the method previously used to obtain a residual scan for a single layer model, the values summarised in table 4.9 are obtained. The full Q range data are fitted by an almost identical set of values as

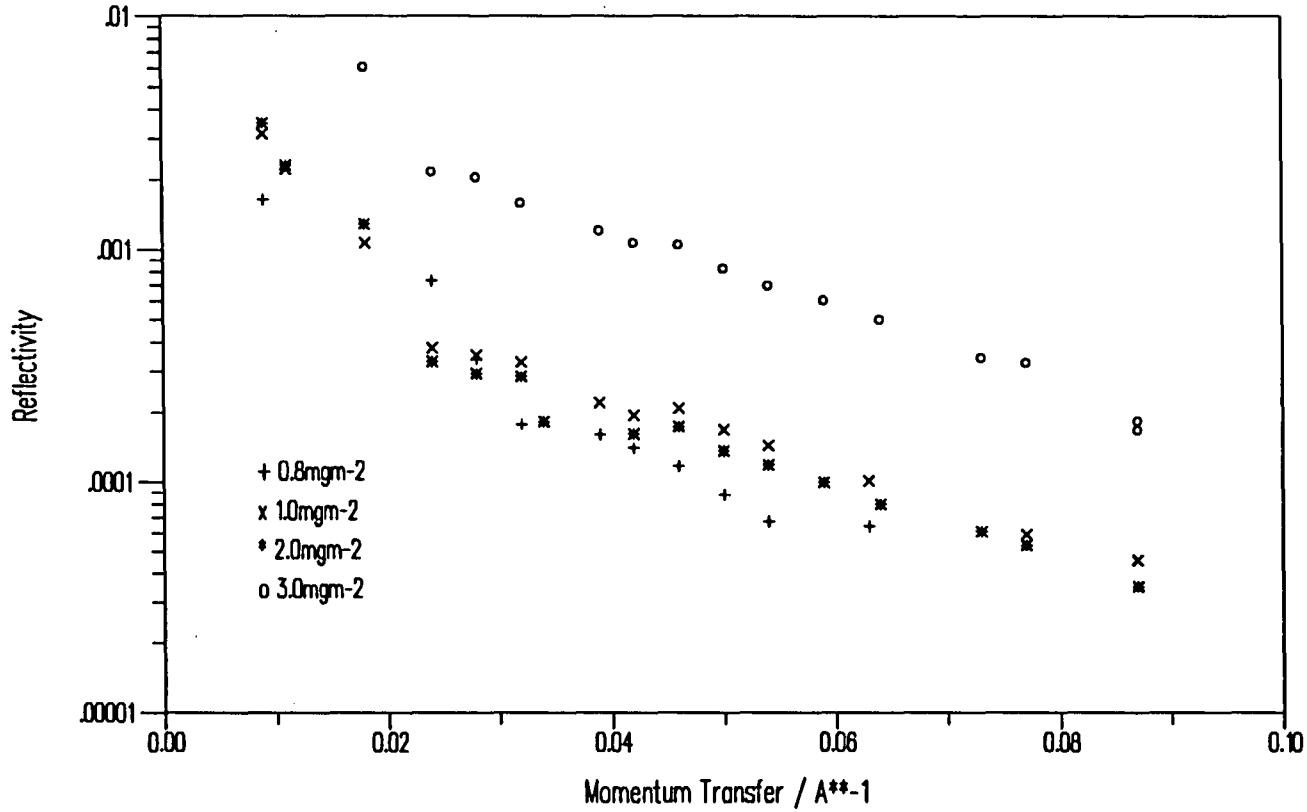

Figure 4.37 Neutron Reflectivity Profiles for ISODPMMA on acmw obtained on D17

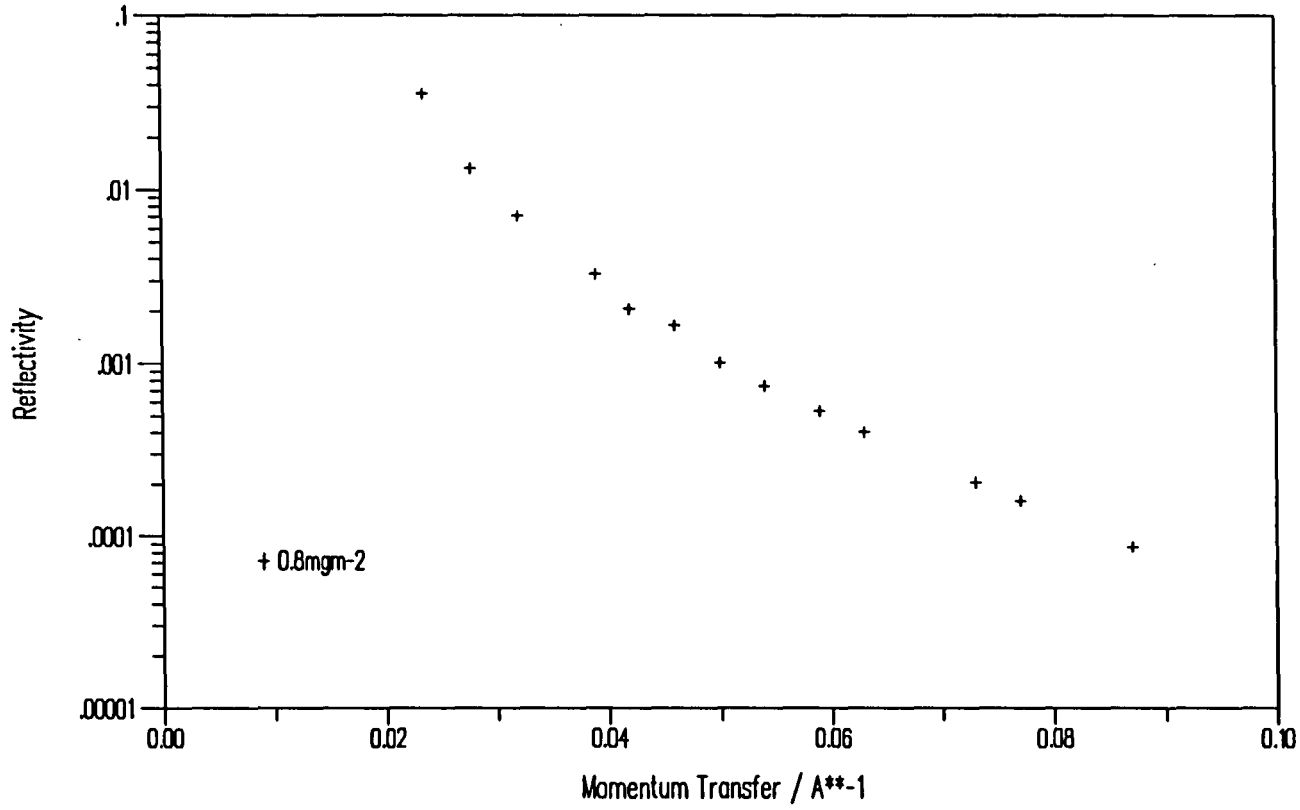

Figure 4.38 Neutron Reflectivity Profile for ISOHPMMA on D_2O obtained on D17

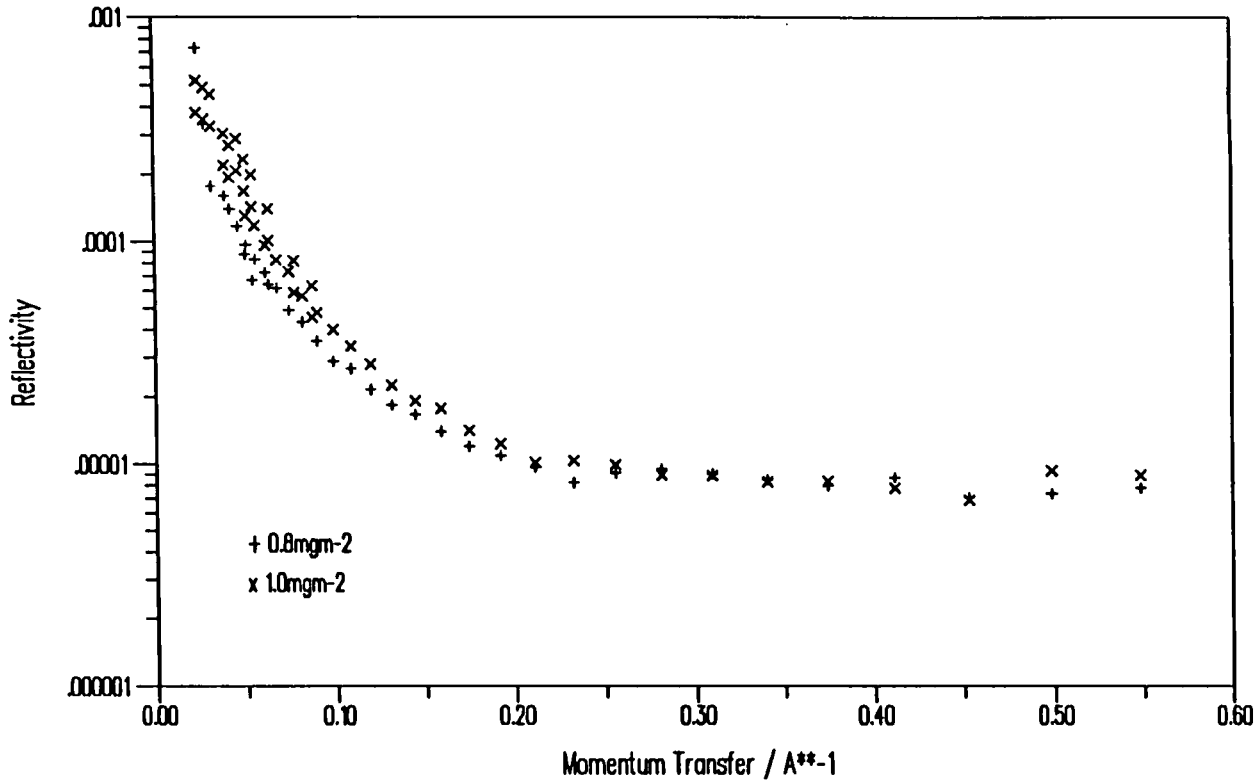

Figure 4.39 Combined Reflectivity Data obtained from D17 and CRISP for ISODPMMA on acmw

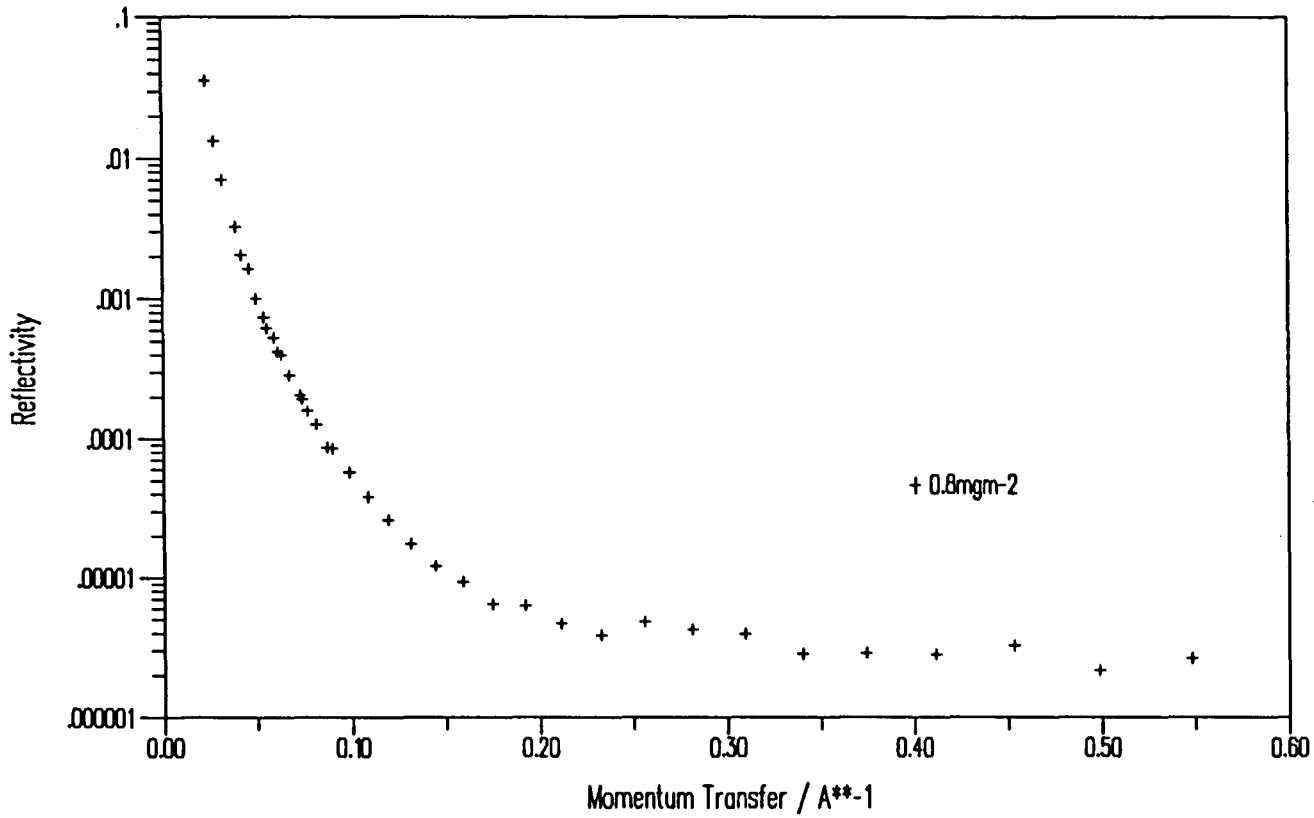

Figure 4.40 Combined Reflectivity Data obtained from D17 and CRISP for ISOHPMMA on D_2O

Γ/mgm^{-2}	d/acmw			H/D_2O		
	d/Å	$\rho/10^{-6}$Å^{-2}	res/10^{-2}	d/Å	$\rho/10^{-6}$Å^{-2}	res/10^{-2}
0.8	14	2.74	1.132	22	0.59	0.9408
1.0	13	3.53	0.8571	-	-	-

Table 4.9 Fitted Values from combined CRISP/D17 data for ISOPMMA

the CRISP data alone. However this is not particularly surprising as both surface concentrations are reasonably low and lie within the region where the apparent surface coverage obtained is more or less the same as the dispensed amount.

Comparison between Surface Pressure and Reflectometry Data

As a brief addendum to the observations made earlier concerning the surface pressure behaviour of SYNDIO and ISO PMMA, evidently the results of neutron reflectometry are generally consistent with the model of SYNDIOPMMA as a more condensed film than ISOPMMA, as reflected by the higher polymer content of the former film. The observed time dependence of the surface pressure must however be considered when dealing with reflectometry results. Given that significant surface pressure decays were noted for both tactic forms it should be stated clearly that the neutron reflectometry signals obtained showed absolutely no sign of any alteration over the 2-4 periods typically used to collect data. This then suggests that some form of film relaxation rather than desorption from the interface is responsible for the surface pressure loss, but the overall thickness and composition of the film at the resolution of the neutron experiment is maintained.

Neutron reflectometry measurements for ISOPMMA provide a possible explanation for the remarkable contrast in properties observed for SYNDIO and

ISOPMMA films held over a period of time whereby no pressure decay was observed for ISOPMMA held at $20mNm^{-1}$. From reflectometry ISOPMMA was observed to exist as a film of very constant thickness around 16Å and, although the polymer content of the film increased, even at high surface coverages the volume fraction of air in the film remained significant. One possible conformation which could explain this result is the isotactic PMMA helical coil, which has a diameter of around 13Å, and whose regular structure could account both for a large entrapped air content and an unwillingness to rearrange on the surface. It is speculated that the overall form of the ISOPMMA film at high surface concentrations would then be a series of crystalline regions separated by crystal defects in the form of amorphous loops or tails projecting into the subphase, due to favourable segment-subphase interactions, figure 4.41.

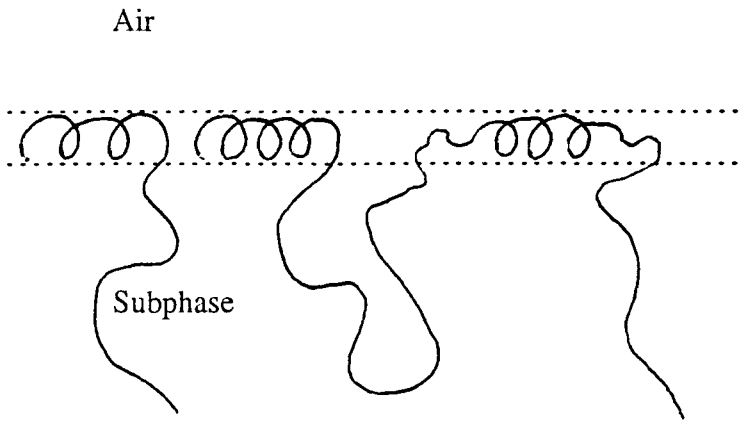

Figure 4.41 Speculative Model for ISOPMMA monolayer

4.3.1 Analysis of Reflectometry by the Kinematic Approximation

The analysis of reflectometry data has thus far been based on film parameters generated by least squares minimisation methods for the appropriate optical matrix calculations. The best fit profile generated in this case is an exact solution for the model employed and can be applied over an unrestricted momentum transfer range. Above very small Q values however the kinematic or first Born approximation described in Chapter 2 becomes valid and various kinematic formulae may be used to derive an understanding of the nature of the surface layer. Additionally the more straightforward relationships between the interfacial parameters of film thickness, scattering length density, air and substrate scattering length densities etc, make the kinematic method very valuable in anticipating any correlations of fitted parameters, and therefore determining the uniqueness of the solutions evaluated. Kinematic methods have therefore been used to refit the experimental reflectivity data from CRISP for SYNDIO- and ISOPMMA.

According to equation 2.34, for the special case where there is no contrast between the two bulk media separated by the interfacial region, such as is the case for the air/air contrast matched water interface, a plot of $\ln(R(Q).Q^2)$ against Q^2 should be a straight line of slope $-\sigma^2$ and intercept $\ln(16\pi^2m^2)$ where R(Q) has had the background signal subtracted, σ is the standard deviation of the rate of change of the scattering length density with respect to depth and m is the total surface excess scattering length density. In practice the region over which this linearity is observed is limited by the breakdown of the kinematic approximation at low Q (less than about $Q = 0.05\text{Å}^{-1}$) on the one hand, and the scatter in the data as the background is reached on the other (above about $Q = 0.2\text{Å}^{-1}$). Within these limits however it has been possible to fit the experimental data with the values summarised in table 4.10. Some typical fitted experimental data are shown in figures 4.42 and

4.43. The total scattering length density values obtained agree very well with those obtained from the products of the layer thickness and scattering length density values obtained by matrix calculation and shown in table 4.8. In addition, the thickness parameter σ may be seen to be directly related to the equivalent thickness values of table 4.8.

An important aspect of the neutron reflectometry technique is the ability to use contrast variation to provide simultaneous data sets in order to establish a unique solution for the film structure. Consideration of the relevant kinematic formulae give a useful demonstration of both the effectiveness and limitations of this technique. In order to determine an interfacial structure uniquely, it would be necessary to invert the reflectivity into the corresponding scattering length density profile. However it has been shown in Chapter 2 that even if the low Q and background limitations of the kinematic theory are neglected that it is impossible to invert R(Q) to $\rho_s(z)$ by the normalised Fourier Transform f(Q) of the surface inhomogeneity, as the relationships between the two are incomplete in the imaginary part of f(Q) and in its phase.

By use of equation 2.51 for the transform of the Patterson function of the gradient of $\rho(z)$, it is possible to bypass these difficulties somewhat, by considering the Patterson function for a two step profile in scattering length density where the film slab scattering length density, ρ_F, lies between the values of the two media, ρ_1 and ρ_2 (figure 2.4(a)). This is the case encountered for HPMMA on D_2O where medium 1 is air. As shown in Chapter 2, $|\rho'(Q)|^2$ may be generated by plotting the background subtracted reflectivity multiplied by $Q^4/16\pi^2$ against Q. This plot should be characterised by a sharp minimum of $(2\rho_d-\Delta\rho_p)^2$ at a Q value of π/d where d is the film thickness, and $\Delta\rho_p$ is the contrast of the system, equal to $\rho_2 - \rho_1$. Typical Patterson plots for SYNDIOHPMMA and ISOHPMMA on D_2O are illustrated in figures 4.44 and 4.45 and the parameters derived from their minima are listed in

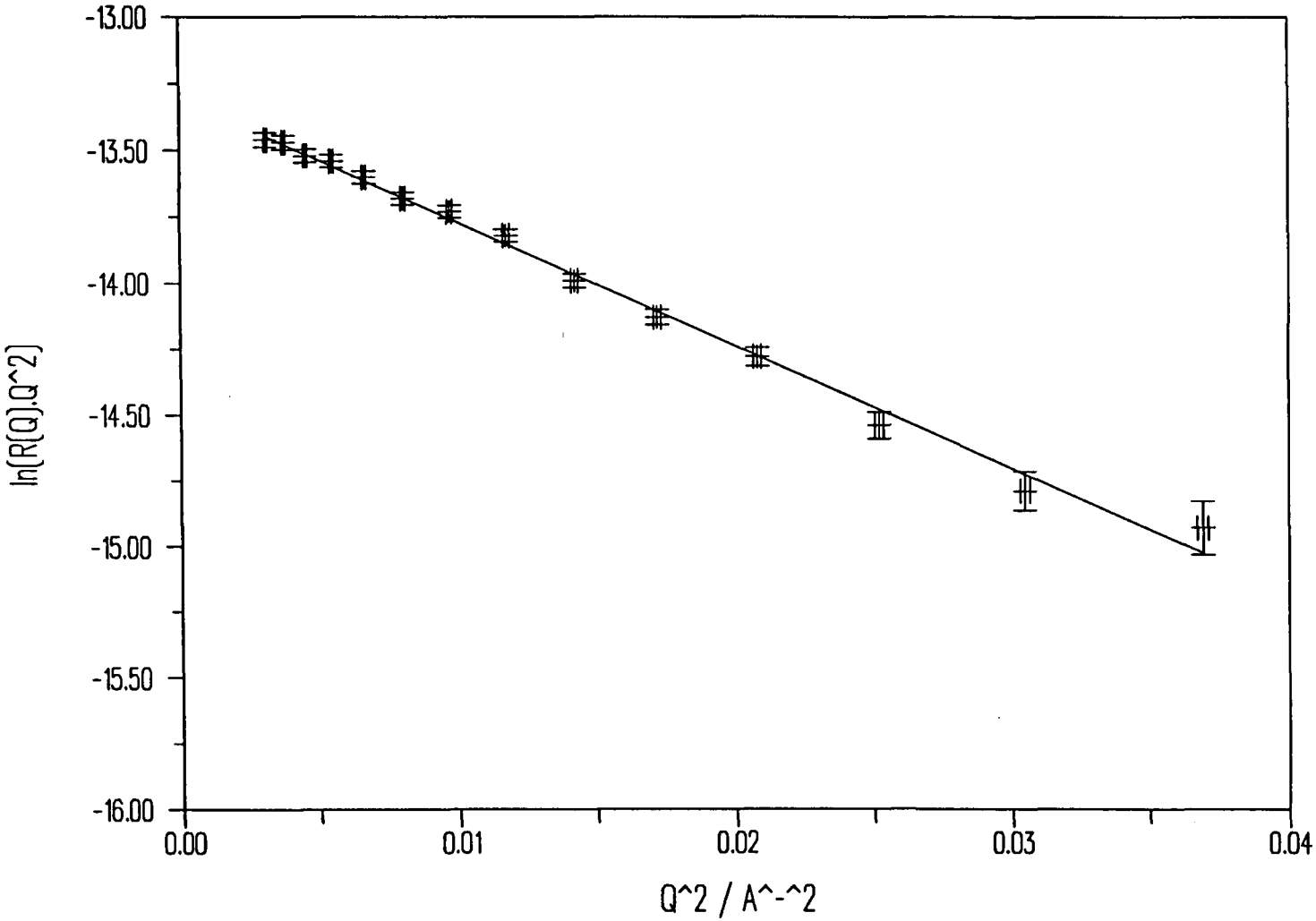

Figure 4.42 Plot of $\ln(R(Q).Q^2)$ v Q^2 for SYNDIODPMMA on acmw, $\Gamma = 1.5 mgm^{-2}$

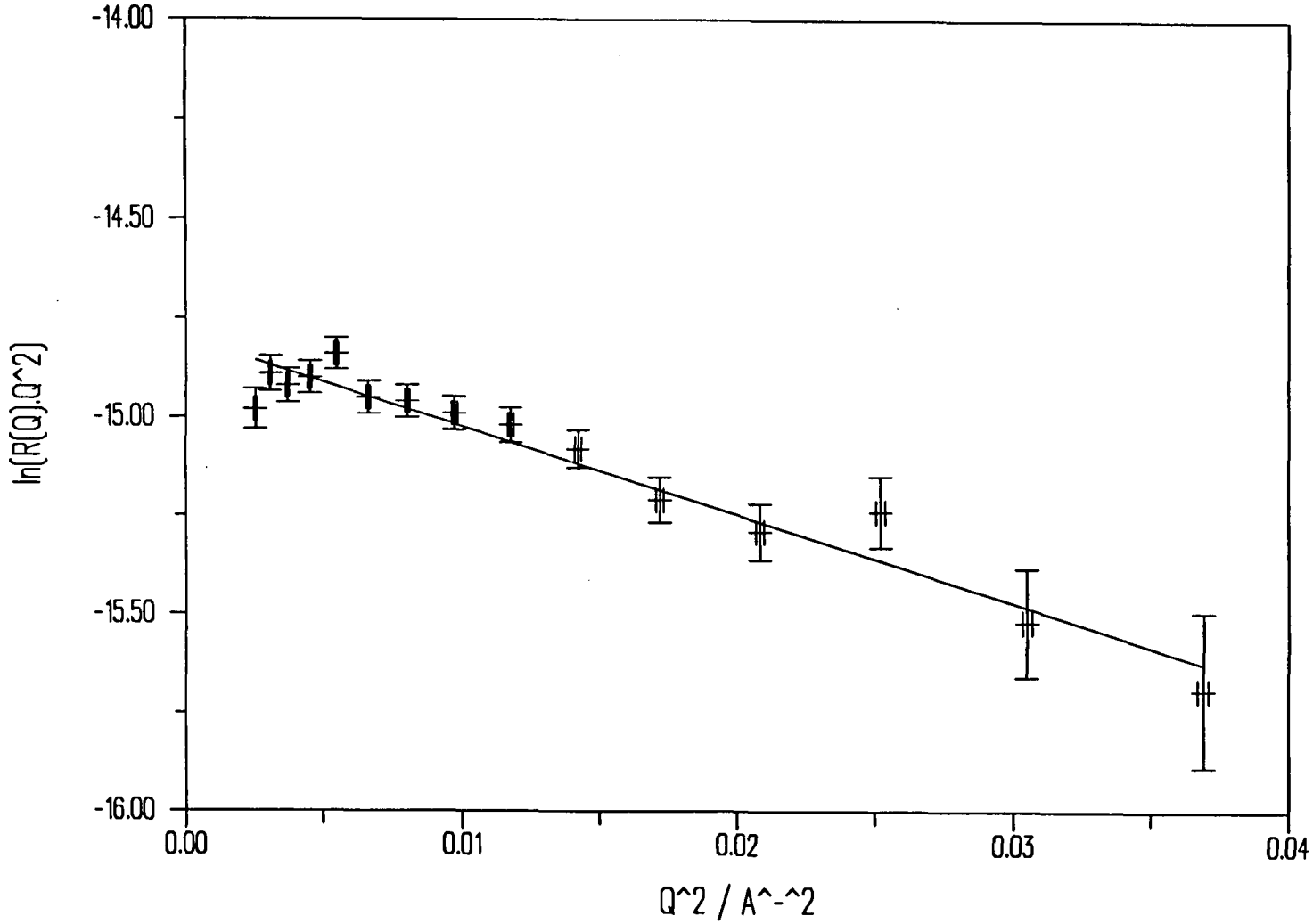

Figure 4.43 Plot of $\ln(R(Q).Q^2)$ v Q^2 for ISODPMMA on acmw, $\Gamma = 1.0 mgm^{-2}$

SYNDIODPMMA/acmw

Γ/mgm^{-2}	Intercept	Slope	m/10^{-6}Å^{-2}	σ
0.3	-16.4	-37.3	19.8	6.1
0.4	-16.2	-34.1	24.2	5.8
0.5	-15.7	-36.7	31.0	6.1
0.6	-15.3	-18.0	37.9	4.2
0.8	-14.3	-31.2	65.7	5.6
1.0	-13.9	-34.1	76.3	5.8
1.5	-13.3	-48.1	103.0	6.9
2.0	-13.2	-56.1	108.3	7.5

ISODPMMA/acmw

Γ/mgm^{-2}	Intercept	Slope	m/10^{-6}Å^{-2}	σ
0.3	-17.3	-51.2	13.9	7.2
0.4	-17.1	-49.3	15.4	7.0
0.5	-16.9	-24.2	17.0	4.9
0.8	-15.1	-23.2	41.9	4.8
1.0	-14.8	-22.3	48.6	4.7
1.5	-15.0	-22.1	44.0	4.7

Table 4.10 Results of Analysis of plots of $\ln(R(Q).Q^2)$ v Q^2 for PMMA

table 4.11

The experimental Patterson plots agree qualitatively with the predicted form. From the x co-ordinate of the minimum in the curve, layer thickness values are obtained which are rather similar to those of table 4.5 for hydrogenous polymer on D_2O. On the other hand the scattering length density values obtained from the depth of the minima appear to be very different from those obtained previously. This is a demonstration of the limitation of the neutron reflection technique under these particular contrast circumstances. According to equation 2.52 the minimum value of $R(Q).Q^4$ is $16\pi^2(2\rho_d-\Delta\rho_p)^2$ and it is the solutions for this term which are listed in table 4.11. However, noting that $\Delta\rho_p$ is simply the difference between the scattering

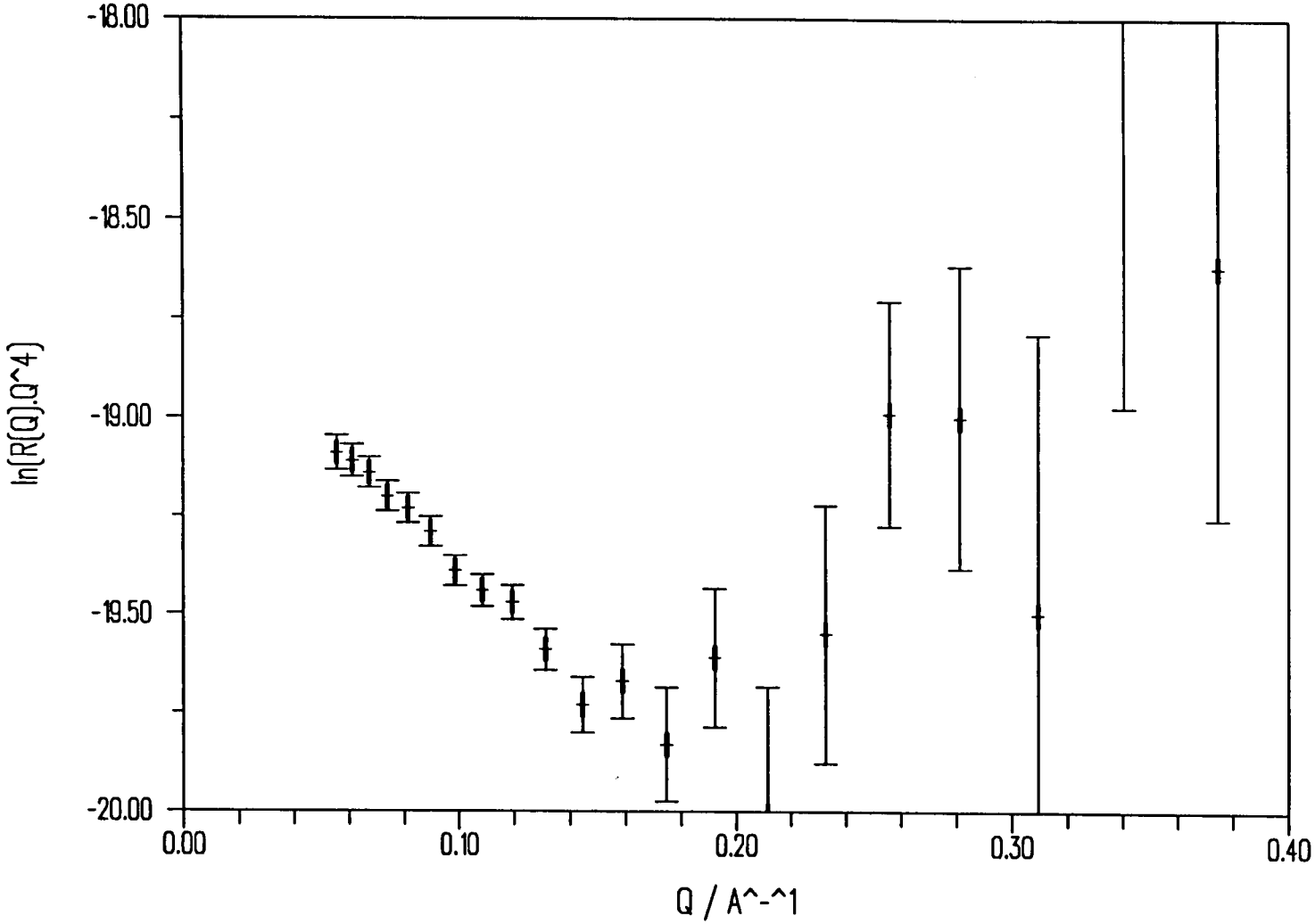

Figure 4.44 Plot of $\ln(R(Q).Q^4)$ v Q for SYNDIOHPMMA on D_2O, $\Gamma = 1.0 mgm^{-2}$

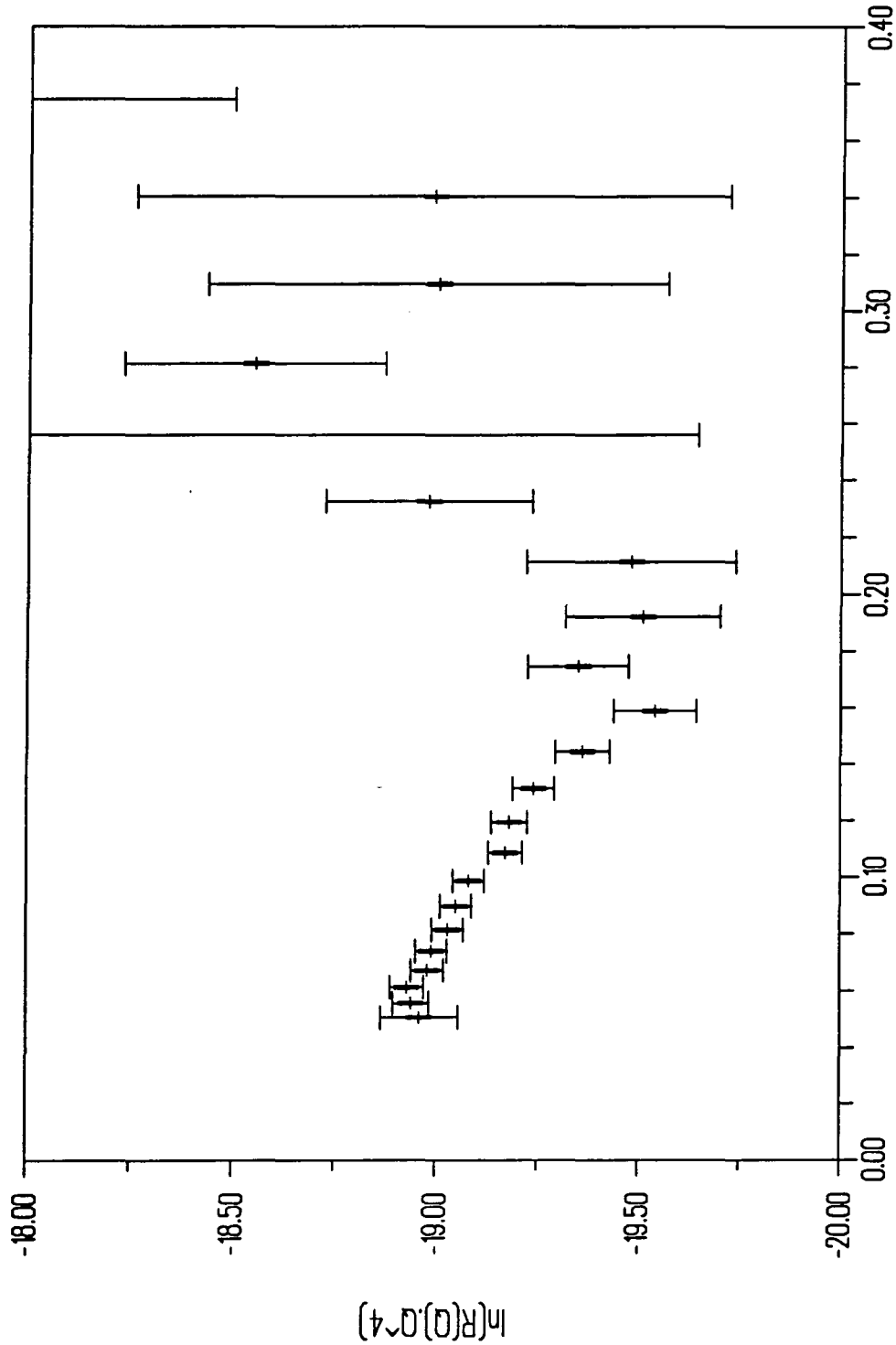

Figure 4.45 Plot of $\ln(R(Q).Q^4)$ v Q for ISOHPMMA on D_2O, $\Gamma = 1.0 mgm^{-2}$

SYNDIOHPMMA / D_2O

Γ/mgm^{-2}	x_{min}	y_{min}	d/Å	$\rho_d/10^{-6}$Å^{-2}	6.35-$\rho_d/10^{-6}$Å^{-2}
0.2	0.18	-19.4	17.5	5.61	0.74
0.4	0.15	-19.4	20.9	5.61	0.74
0.6	0.15	-19.5	20.9	5.49	0.86
0.8	0.16	-19.6	19.6	5.38	0.97
1.0	0.17	-19.8	18.5	5.17	1.18
1.5	0.18	-19.8	17.5	5.17	1.18
2.0	0.18	-19.9	17.5	5.07	1.28

ISOHPMMA / D_2O

Γ/mgm^{-2}	x_{min}	y_{min}	d/Å	$\rho_d/10^{-6}$Å^{-2}	6.35-$\rho_d/10^{-6}$Å^{-2}
0.3	0.17	-19.2	18.5	5.84	0.48
0.4	0.17	-19.2	18.5	5.87	0.48
0.5	0.17	-19.25	18.5	5.80	0.55
0.6	0.17	-19.3	18.5	5.74	0.61
0.8	0.17	-19.4	18.5	5.61	0.74
1.0	0.18	-19.5	17.5	5.49	0.86
1.5	0.18	-19.6	17.5	5.38	0.97

Table 4.11 Results of Analysis of plots of $\ln(R(Q).Q^4)$ v Q for HPMMA

length densities of the two bulk media it is easily seen that

$$2\rho_d-\Delta\rho_p = 2\rho_d - (\rho_2-\rho_1) = 2\rho_d - (\rho_s-\rho_a)$$

$$= 2\rho_d - \rho_s = 2(\rho_d-\rho_s) + \rho_s$$

$$= -1 \times (2(\rho_s-\rho_d) - \Delta\rho_p)$$

Therefore on squaring this term these two solutions are indistinguishable and an equally valid set of solutions with ρ_d equal to 6.35×10^{-6} minus the ρ_d values of table 4.11 exists. These values are found in the final column of table 4.11 and may be seen to agree fairly well with the data of table 4.5. In fact another two solutions exist which generate the same Patterson function but as these imply a negative film scattering length density they may be eliminated on the grounds of

being physically unrealistic.

In order to justify the choice of one of the two remaining possible solutions it is necessary to consider both contrast sets together. The two solutions represent two cases, one indicative of a high water uptake in the layer and the other a low uptake with polymer more or less floating on the subphase. The scattering length density values obtained from the D/acmw contrast indicate a dense film with a high polymer volume fraction and when one uses this value to solve with the first set of H/D_2O ρ_F values the result is large negative air volume fractions. For the second case, where a small water uptake is indicated the volume fraction values calculated are physically possible and are those of table 4.7. Therefore although strictly speaking a unique solution cannot be obtained by reflectometry for the layer thickness and composition, the use of multiple contrast can help to eliminate most possible solutions.

The Patterson plot can therefore be used as a means to estimate the layer thickness and scattering length density although in practice it is easier to obtain both d and ρ from other methods as there is often a considerable uncertainty in the exact position of the minimum in $R(Q).Q^4$.

4.3.2 Patchy Film Modelling

An alternative method has been used to account for the observed behaviour of PMMA films. There has been some conjecture as to whether poly(methyl methacrylate) spread on water forms a continuous monolayer or whether the film exists as dense patches of polymer floating on the subphase surrounded by voids of air. The previous homogeneous slab treatment indicated a layer containing only around 10% water, and the increase in polymer content was seen to correspond with the gradual exclusion of air. At low coverages in particular,

the high air content indicated by the fits might be described sensibly by a patchy system characterised by a fractional coverage of the surface.

As previously discussed in chapter 2, the methods of analysis based on the kinematic approximation provide a suitable method for the description of the reflection from a monolayer of patchy islands. For the special case of an interface with zero air-subphase contrast (eg deutero polymer on air contrast matched subphase) the best fit to the reflectivity data provides an uncorrelated value of the layer thickness (d) and values for the scattering length density of the film patches (ρ_F) and the fraction of the total surface covered (f) which are correlated by the product $\rho_F^2 f$ for infinitely large islands and $\rho_F^2 f^2$ for infinitely small islands. In order to determine ρ_F and f independently it is necessary to solve a second data set for the more general case where there is a non-zero air-subphase contrast, such as the hydrogenous polymer spread on D_2O. In this case a product of ρ_F and f do not factorise from the relevant kinematic expressions, and hence given the layer thickness as determined from the first contrast, it is possible to solve the two data sets together to determine the fractional coverage. If bulk scattering length density values (indicative of perfect polymer islands floating on the subphase surrounded by air voids) can be assumed, then it is possible to determine the island size ξ uniquely by finding the value of the island size factor $F(\xi)$ that gives the same fractional coverage on both contrasts.

This approach was used in an attempt to fit the experimental data for SYNDIO- and ISOPMMA, however on assuming bulk scattering length densities it proved impossible to fit both contrasts with physically viable values for the fractional coverage ($0 \leq f \leq 1$). In order to produce a simultaneous solution it was necessary to model the islands as a binary mixture of polymer and subphase and determine simultaneous scattering length density values for the two contrasts according to a weighted sum of the scattering length densities of these two

constituents according to their respective volume fractions in the mix. Introducing this additional unknown of composition means that it is no longer possible to determine the island size uniquely, however it is possible to determine solutions for the two limiting cases, namely infinitely small and infinitely large islands where $F(\xi)$ is defined as zero and unity respectively. The fitted values are listed in tables 4.12 and 4.13. These sets represent the extreme cases where a realistic solution is possible, and an infinite set of equivalent solutions exist for compositions between these limits where the island size varies from the very small to the very large.

SYNDIO - Large Islands

		D/acmw		H/D_2O							
Γ/mgm^{-2}	d/Å	$\rho/10^{-6}Å^{-2}$	$res/10^{-2}$	$\rho/10^{-6}Å^{-2}$	$res/10^{-2}$	ϕ_p	ϕ_s	f	f.ρd	apm/Å^2	Γ_a/mgm^{-2}
0.4	19	1.75	0.3787	4.72	0.5293	0.29	0.71	0.51	17.0	57.9	0.31
0.6	17	3.43	0.5326	3.24	1.268	0.57	0.43	0.45	26.2	37.4	0.48
0.8	18	4.70	0.4768	2.09	1.163	0.78	0.22	0.59	49.9	19.7	0.91
1.0	19	4.76	0.3907	2.04	0.5658	0.79	0.21	0.70	63.3	15.5	1.16
1.5	23	5.30	0.5688	1.55	1.255	0.88	0.12	0.73	89.0	11.0	1.62
2.0	23	5.18	0.5142	1.66	0.8280	0.86	0.14	0.77	91.7	10.7	1.66

SYNDIO - Small Islands

		D/acmw		H/D_2O							
Γ/mgm^{-2}	d/Å	$\rho/10^{-6}Å^{-2}$	$res/10^{-2}$	$\rho/10^{-6}Å^{-2}$	$res/10^{-2}$	ϕ_p	ϕ_s	f	f.ρd	apm/Å^2	Γ_a/mgm^{-2}
0.4	19	4.33	0.3787	2.43	0.5293	0.72	0.28	0.29	23.9	41.2	0.44
0.6	17	4.94	0.5326	1.88	1.268	0.82	0.18	0.42	35.3	27.8	0.64
0.8	18	5.42	0.4768	1.45	1.163	0.90	0.10	0.64	62.4	15.7	1.14
1.0	19	5.30	0.3907	1.55	0.5658	0.88	0.12	0.75	75.5	13.0	1.38
1.5	23	5.60	0.5688	1.28	1.255	0.93	0.07	0.81	104.3	9.4	1.91
2.0	23	5.48	0.5142	1.39	0.8280	0.91	0.09	0.82	103.4	9.5	1.89

Table 4.12 Results of Patchy Film Analysis for SYNDIOPMMA

ISO - Large Islands

		D/acmw		H/D_2O							
Γ/mgm^{-2}	d/Å	$\rho/10^{-6}Å^{-2}$	$res/10^{-2}$	$\rho/10^{-6}Å^{-2}$	$res/10^{-2}$	ϕ_p	ϕ_s	f	f.ρd	apm/Å^2	Γ_a/mgm^{-2}
0.3	11	1.32	0.4833	5.15	0.7865	0.22	0.78	0.71	10.3	95.3	0.19
0.4	14	1.57	0.4861	4.93	0.4488	0.26	0.74	0.45	9.9	99.2	0.18
0.5	12	2.20	0.6029	4.30	0.7830	0.37	0.63	0.41	10.8	90.7	0.20
0.8	15	4.03	0.4857	2.70	0.9769	0.67	0.33	0.44	26.6	36.9	0.49
1.0	15	4.51	0.5132	2.26	0.7072	0.75	0.25	0.50	33.8	29.1	0.62
1.5	17	3.97	0.7511	2.75	0.8004	0.66	0.34	0.43	29.0	33.8	0.53

ISO - Small Islands

		D/acmw		H/D_2O							
Γ/mgm^{-2}	d/Å	$\rho/10^{-6}Å^{-2}$	$res/10^{-2}$	$\rho/10^{-6}Å^{-2}$	$res/10^{-2}$	ϕ_p	ϕ_s	f	f.ρd	apm/Å^2	Γ_a/mgm^{-2}
0.3	11	1.32	0.4833	5.15	0.7865	0.22	0.78	0.71	10.3	95.3	0.19
0.4	14	1.57	0.4861	4.93	0.4488	0.26	0.74	0.45	9.9	99.2	0.18
0.5	12	2.20	0.6029	4.30	0.7830	0.37	0.63	0.41	10.8	90.7	0.20
0.8	15	4.03	0.4857	2.70	0.9769	0.67	0.33	0.44	26.6	36.9	0.49
1.0	15	4.51	0.5132	2.26	0.7072	0.75	0.25	0.50	33.8	29.1	0.62
1.5	17	3.97	0.7511	2.75	0.8004	0.66	0.34	0.43	29.0	33.8	0.53

Table 4.13 Results of Patchy Film Analysis for ISOPMMA

4.4 Ellipsometry

Ellipsometric data have been obtained for syndio and isotactic PMMA using the ellipsometer described in Chapter 3. For SYNDIOHPMMA, the experimentally determined values of the parameters $\delta\Delta$ and $\delta\psi$, representing the phase difference and amplitude attenuation, are shown in figures 4.46 and 4.47 for a complete compression / expansion cycle. The simultaneously recorded surface pressure is shown as a function of trough barrier position (proportional to the area per segment) in figure 4.48.

From figure 4.47, it is clear that there is no sensitivity in ψ to a change in the surface concentration, and hence it is only possible to estimate a film thickness by assuming a reasonable refractive index value for substitution into equations 1.33 and 1.34. Figure 4.49 shows a calculated thickness variation based on a film refractive index of 1.49, corresponding to a weighted average of the refractive indices of PMMA (1.502) and water (1.3390) at 436nm using a polymer volume fraction of 0.93.

Just as hysteresis is observed in the surface pressure isotherm so there is hysteresis in the observed phase difference for syndio PMMA, leading to a smaller layer thicknesses for equivalent barrier positions on expansion. Of course this simple approach takes no account of any possible compositional effects in the film and it is impossible to decouple the thickness / refractive index effect given insensitivity in amplitude attenuation.

It is possible however to make relative comparisons between the behaviour of syndio and iso PMMA by treatment of the equivalent ISOPMMA compression / expansion data, figures 4.50 and 4.51. Again no sensitivity in ψ was observed, due to the non-absorbing qualities of the substrate and film. Using the same assumed refractive index of 1.49 the thickness values shown in figure 4.52

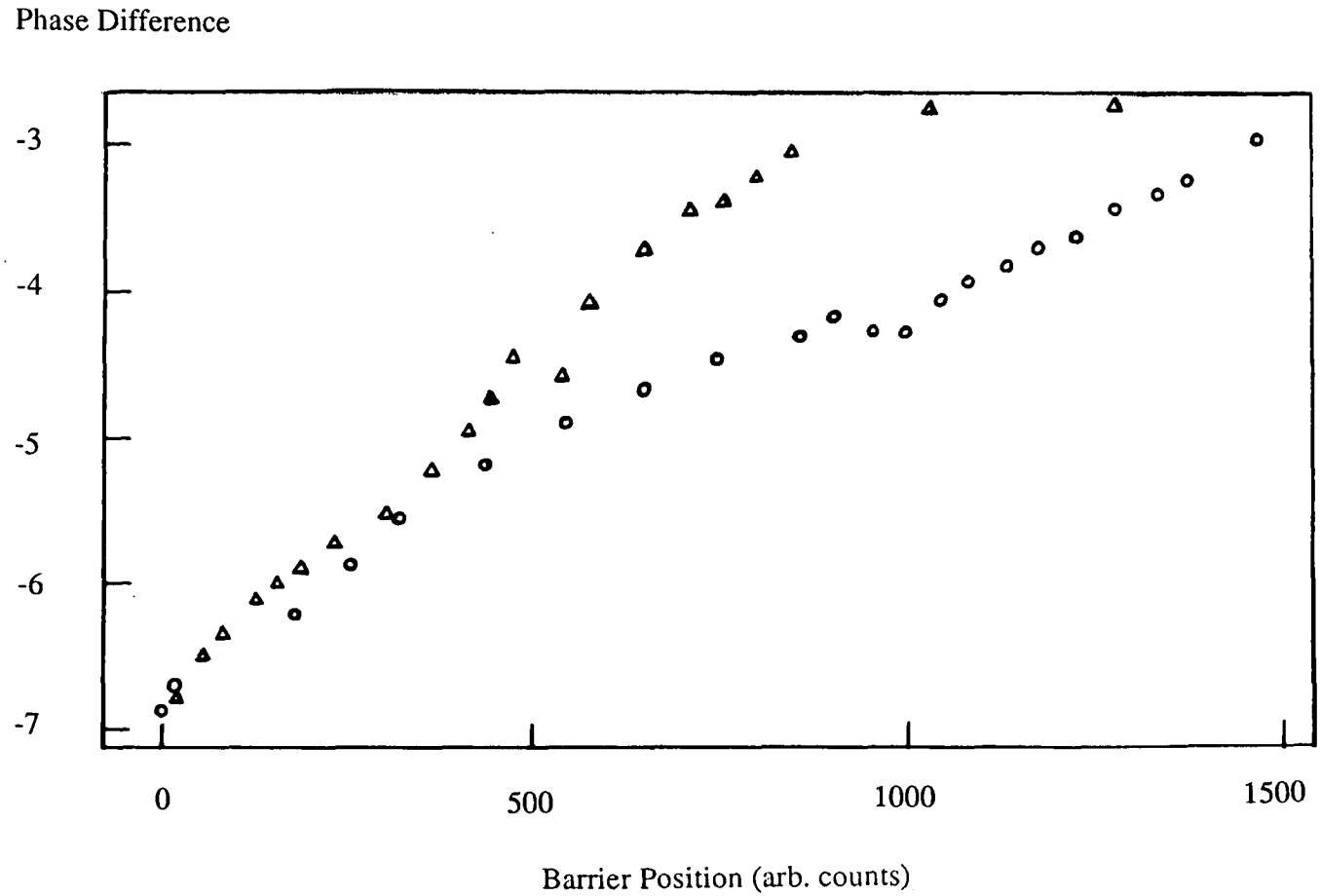

Figure 4.46 Phase Difference against Barrier Position for SYNDIOPMMA

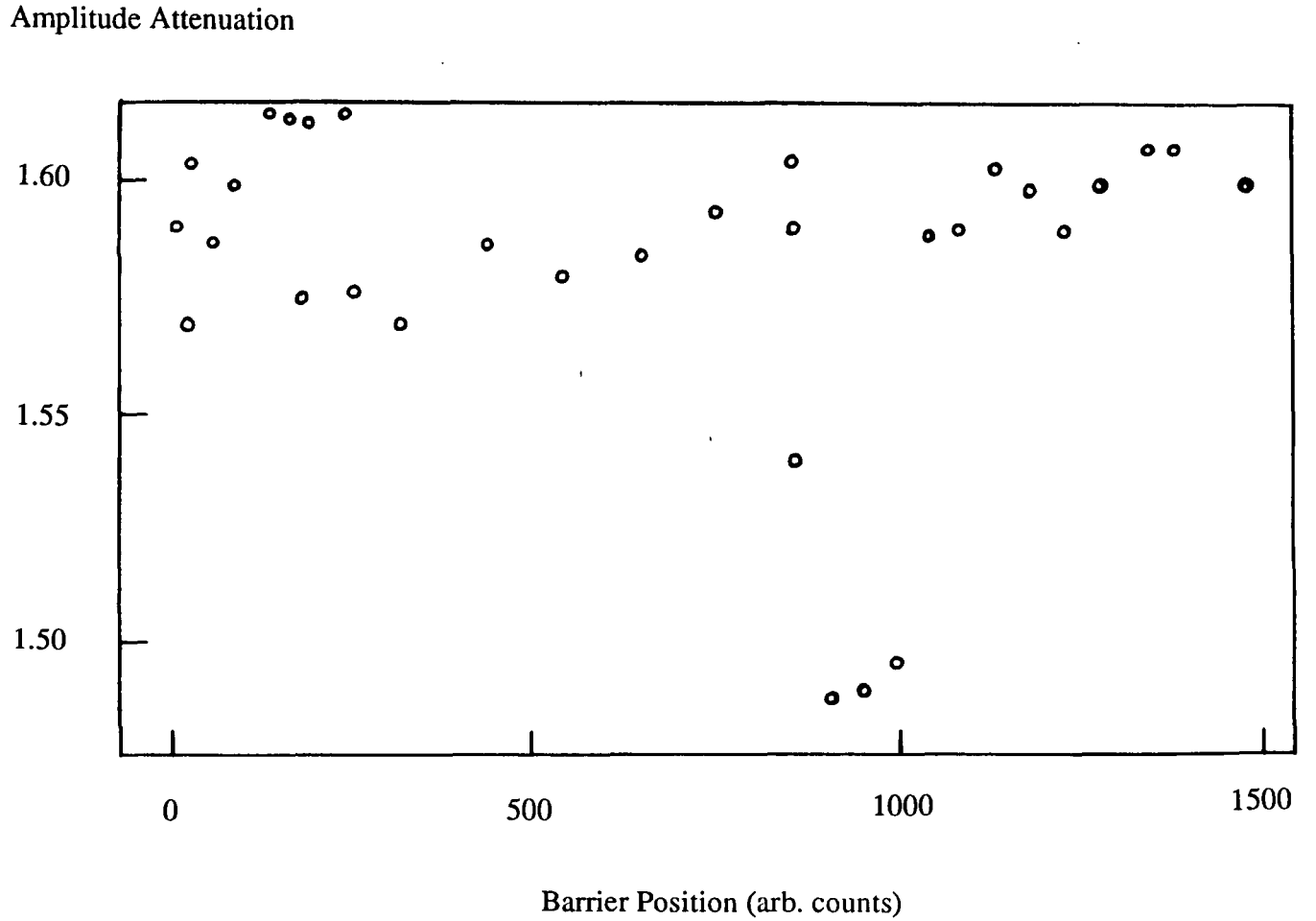

Figure 4.47 Amplitude Attenuation against Barrier Position for SYNDIOPMMA

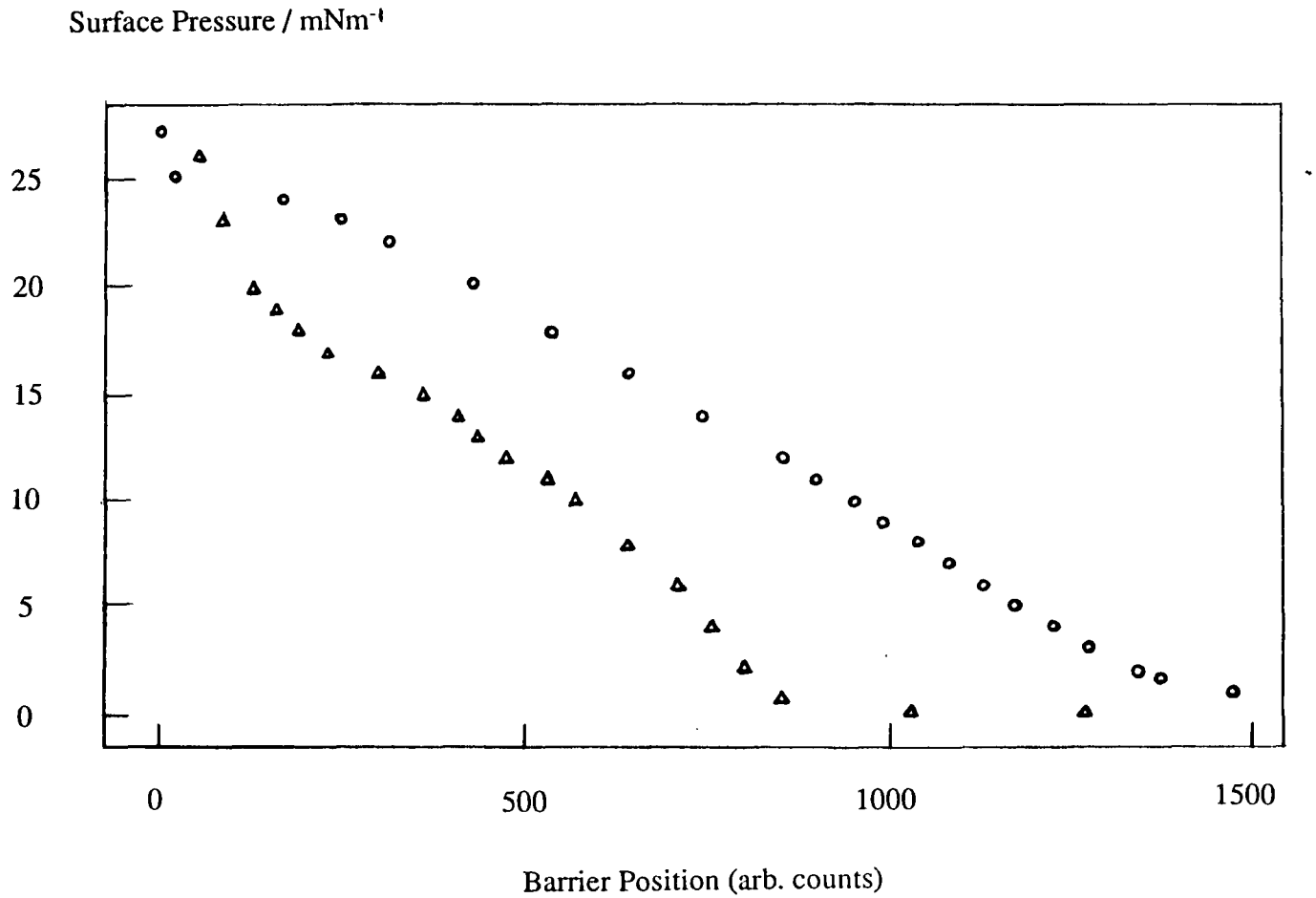

Figure 4.48 Surface Pressure against Barrier Position for SYNDIOPMMA

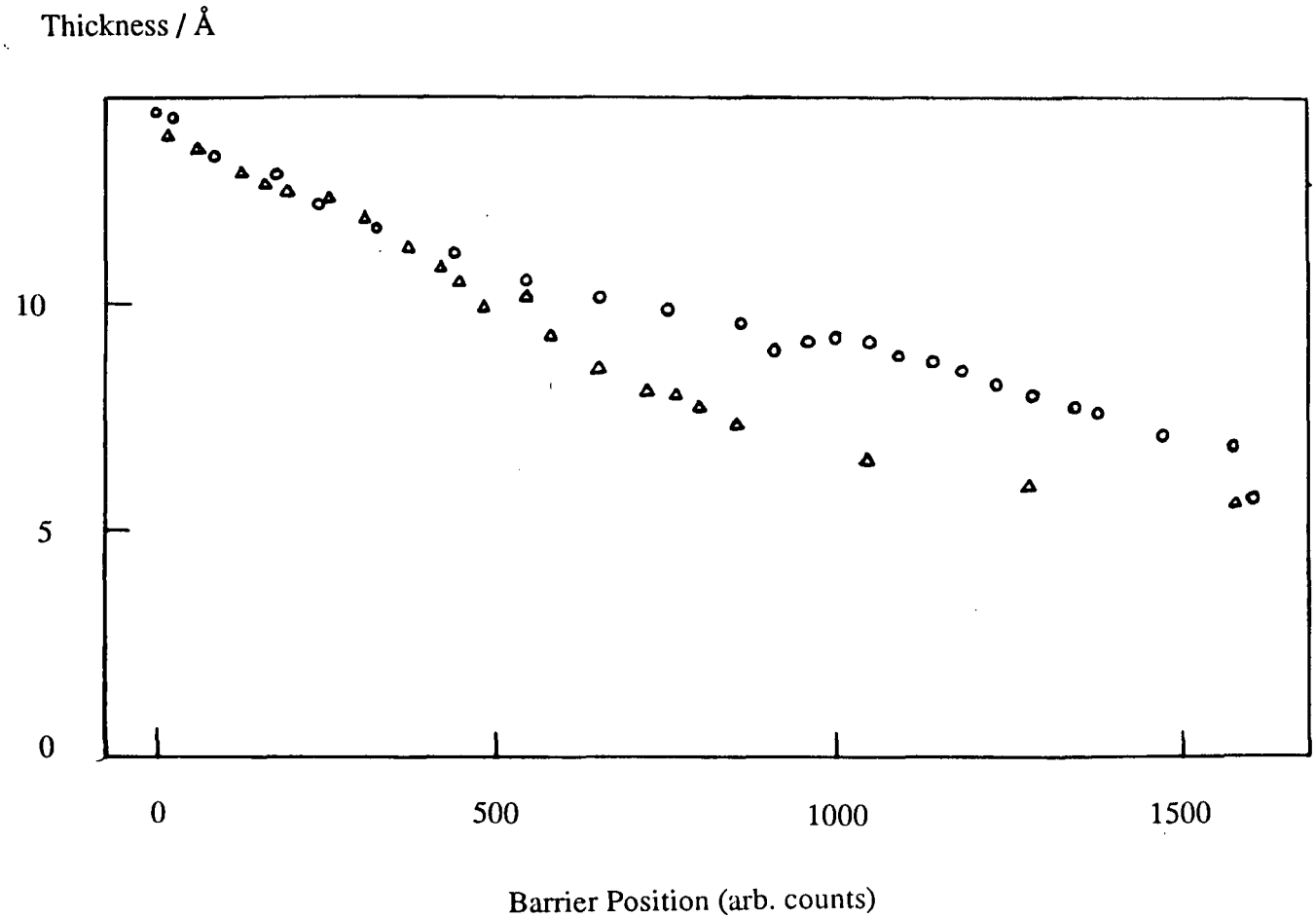

Figure 4.49 Layer Thickness against Barrier Position for SYNDIOPMMA

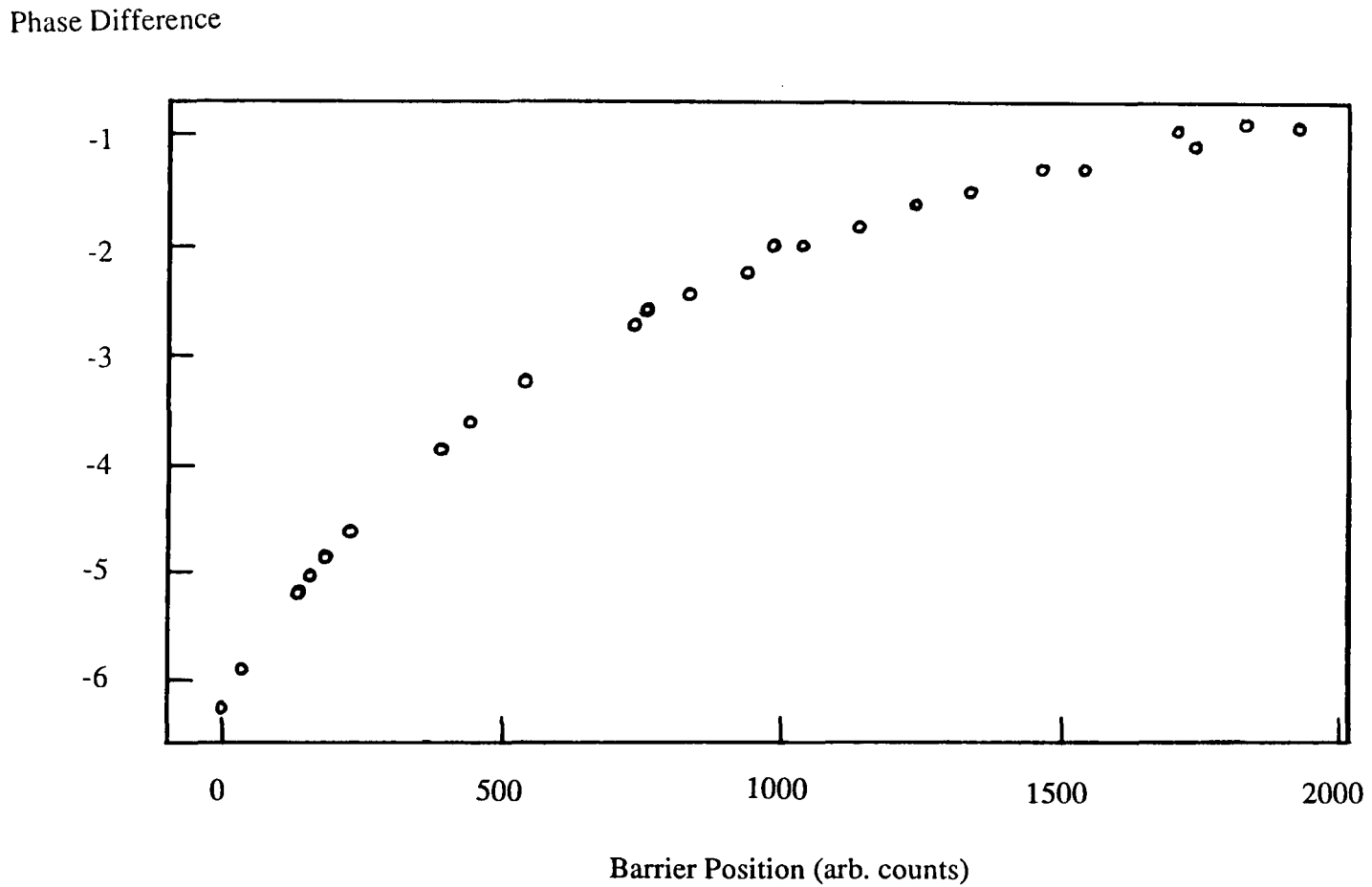

Figure 4.50 Phase Difference against Barrier Position for ISOPMMA

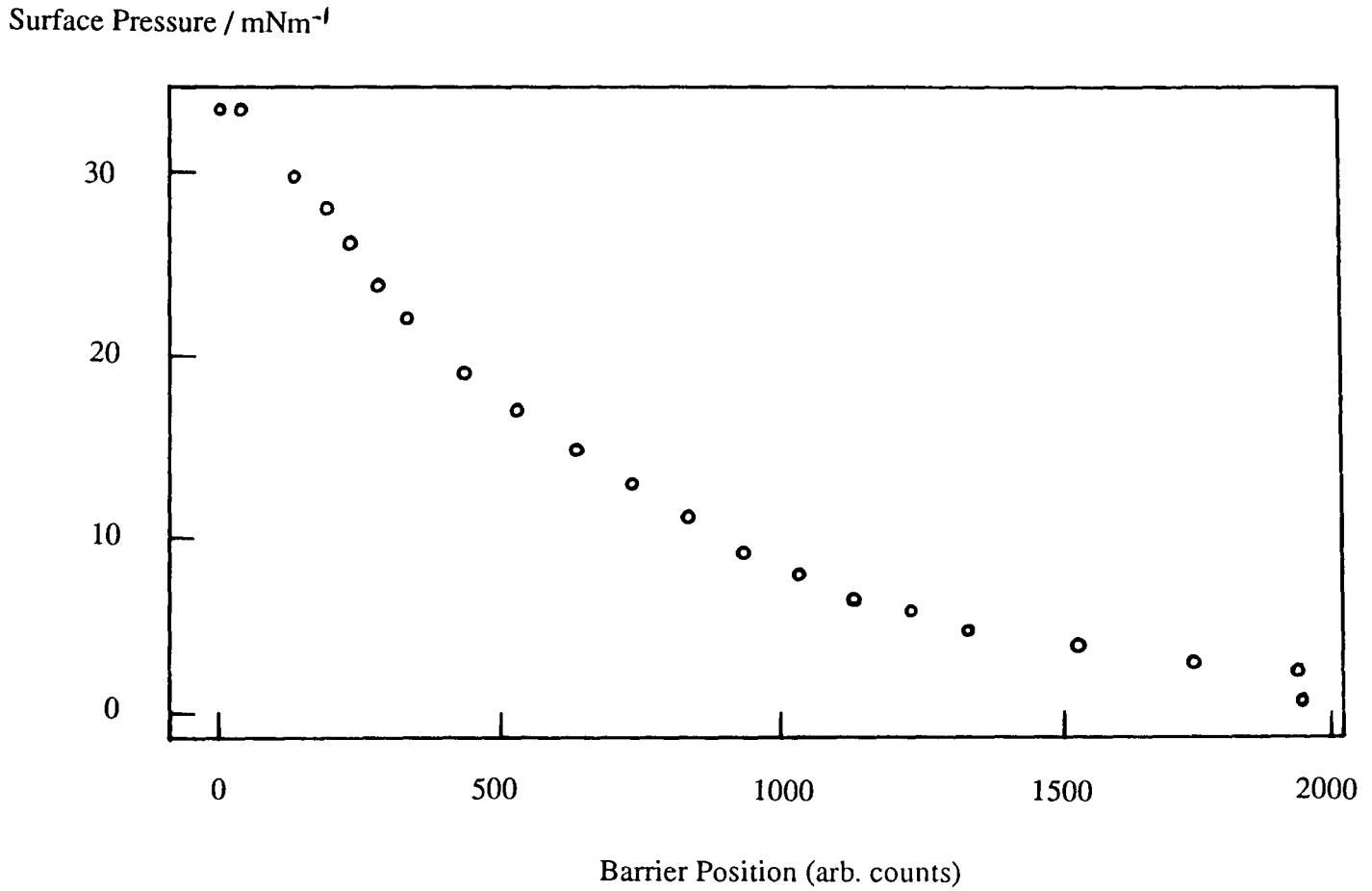

Figure 4.51 Surface Pressure against Barrier Position for ISOPMMA

were obtained. There was no hysteresis in the film properties and the layer thickness is rather less for iso PMMA than for the syndio at an equivalent concentration except for very high compressions, although in both cases the value at high areas per molecule is rather low to be realistic. This probably reflects the arbritrary selection of a refractive index value.

In the light of the information obtained from reflectometry, it might be more appropriate to treat the ellipsometry results with a varied refractive index, according to an estimate for the variation in film composition with surface concentration, in order to obtain a more realistic film thickness. In addition the refractive index value used clearly estimated the polymer content of the film, given the composition information obtained from reflectometry (which was only obtained in its final form after the analysis of the ellipsometry data). Unfortunately due to the fact that the analysis was dependent on software at the MPI-P, Mainz, it has not proved possible to reanalyse the results. Nevertheless it can be seen that, given a reasonable assumption of the film composition, ellipsometry can be used to obtain an estimate of the film thickness that is of the same order of that obtained independently by neutron reflectometry.

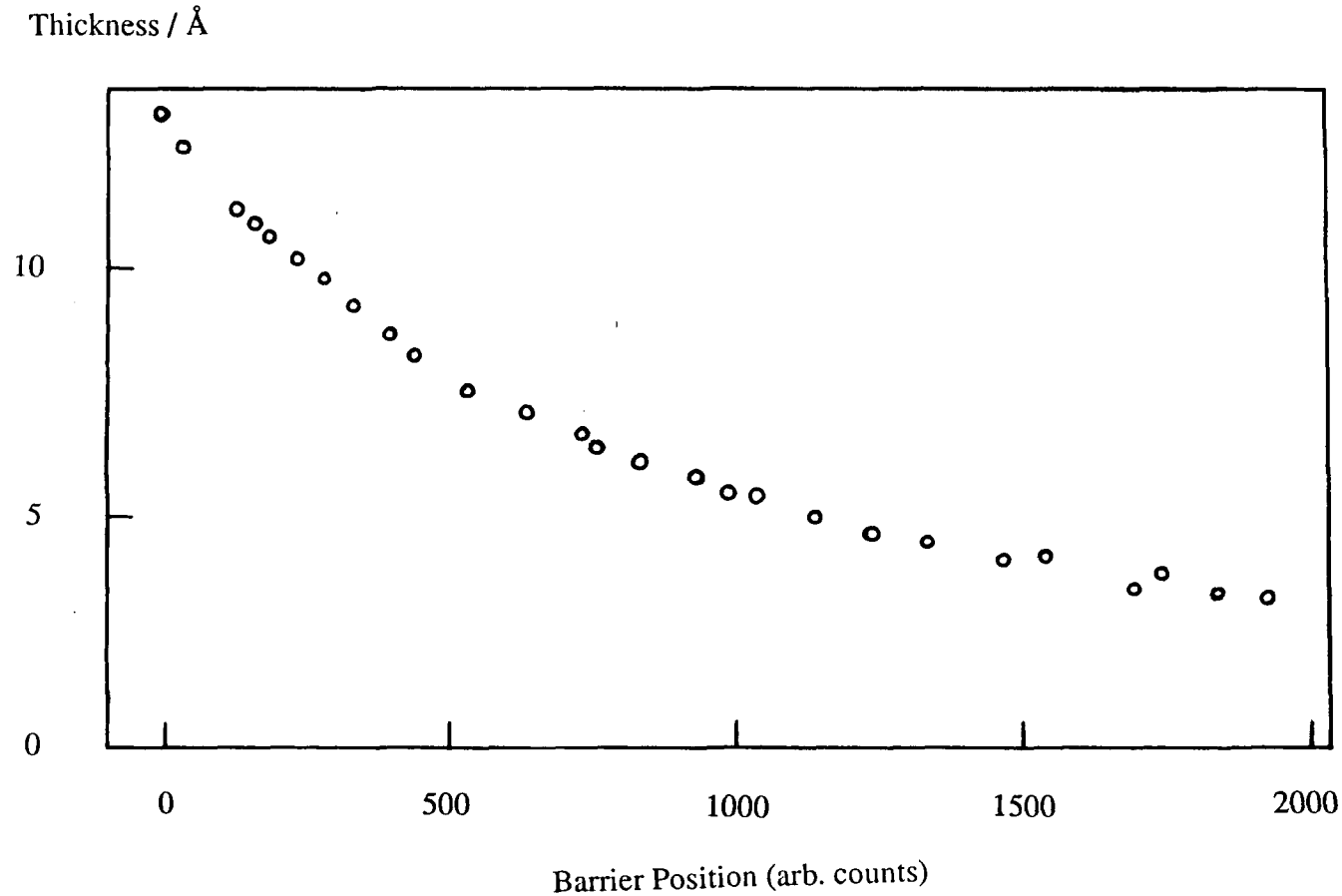

Figure 4.52 Layer Thickness against Barrier Position for ISOPMMA

4.5 Surface Quasi-Elastic Light Scattering

SQELS has been used to examine the viscoelastic properties of monolayers of syndiotactic and isotactic poly (methyl methacrylate), and to examine the free surface of water. The use of heterodyne mixing has enabled the collection of suitable data within times as short as a few tens of seconds. By use of non-linear fitting methods, values have been obtained for the propogation frequency and damping rate of the experimental correlation function over a range of surface wavenumbers for water.

For syndio and isotactic PMMA, a single wavenumber value has been used to obtain correlation data. Film viscoelastic parameters have been derived both by fitting the full form of a doubly exponentially damped cosine function to the experimental data, and by the so called direct data analysis or Fourier transform route.

4.5.1 SQELS from Water

Before studying polymer monolayers, surface light scattering was used to examine the propogation of capillary ripples on the surface of clean water, in order to determine the surface wavenumbers corresponding to the scattered light coincident with each diffraction order at the pinhole of the photomultiplier tube. The first three, smallest angle spots were omitted to avoid flare associated with edge effects at the neutral density filter, and the high q limit was determined by the drop off in the scattered intensity with scattering angle. By non-linear least squares fitting of an appropriate doubly exponentially damped cosine function (equation 1.61) to the experimental data, values were obtained for the propagation frequency and wave damping for each run. Fitted data of typical quality are shown in figure 4.53. In

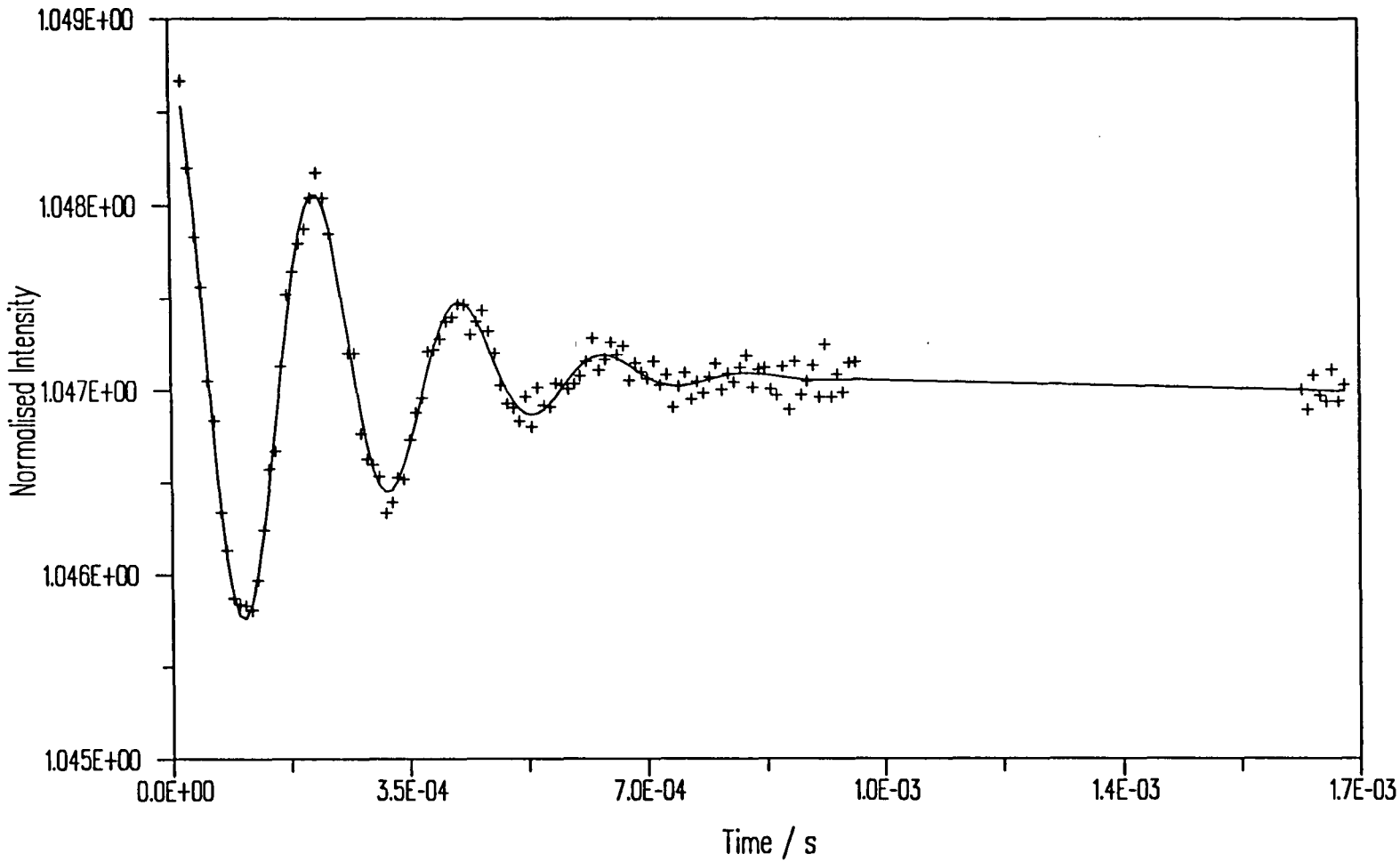

Figure 4.53 Typical fitted correlation function. The illustration is for a SYNDIOPMMA monolayer on water at a surface pressure of 1.75mgm^{-2} and a surface wavenumber of 294cm^{-1}

addition it is possible to determine the relative intensities of the reference (I_r) and scattered (I_s) light giving rise to the heterodyne beat pattern. Values for water over a range of diffraction orders are summarised in table 4.14 and figures 4.54-4.56, where errors are estimated from the standard deviation of the average of ten repeated measurements.

Order	I_r/I_s	$I_s/10^{-4}$	ω_o/s^{-1}	Γ/s^{-1}	q/cm^{-1}(from ω_o)	q/cm^{-1}(from Γ)
4	4114	9.165	41407	1905	286	306
5	5228	6.677	53596	2352	340	340
6	131156	4.787	66762	3365	394	407
7	8667	4.284	70335	3416	408	410
8	106844	6.505	85004	4910	463	491

Table 4.14 Estimation of q from SQELS on water

As the diffraction order is increased the propagation frequency decreases and the wave damping increases, both in a more or less linear fashion. Using the appropriate approximation formulae, equations 1.45 and 1.46, it is possible to use the values of ω_0 and Γ to estimate the surface wavenumber corresponding to each diffraction spot as shown in the final columns of table 4.14.

These values are seen to vary in a linear fashion with the diffraction order, the wavenumber obtained from the damping being marginally higher than the value estimated from the frequency. This may be due to slightly insufficient scattered intensity leading to an overestimate of the damping, but given the reproducibility of the data, this is not a major error. From the relative uncertainties on the measurement of ω_0 and Γ, the value obtained from ω_0 is the more reliable value and it is that value that is employed henceforth.

The scattered intensity falls off with increasing scattering angle (spot

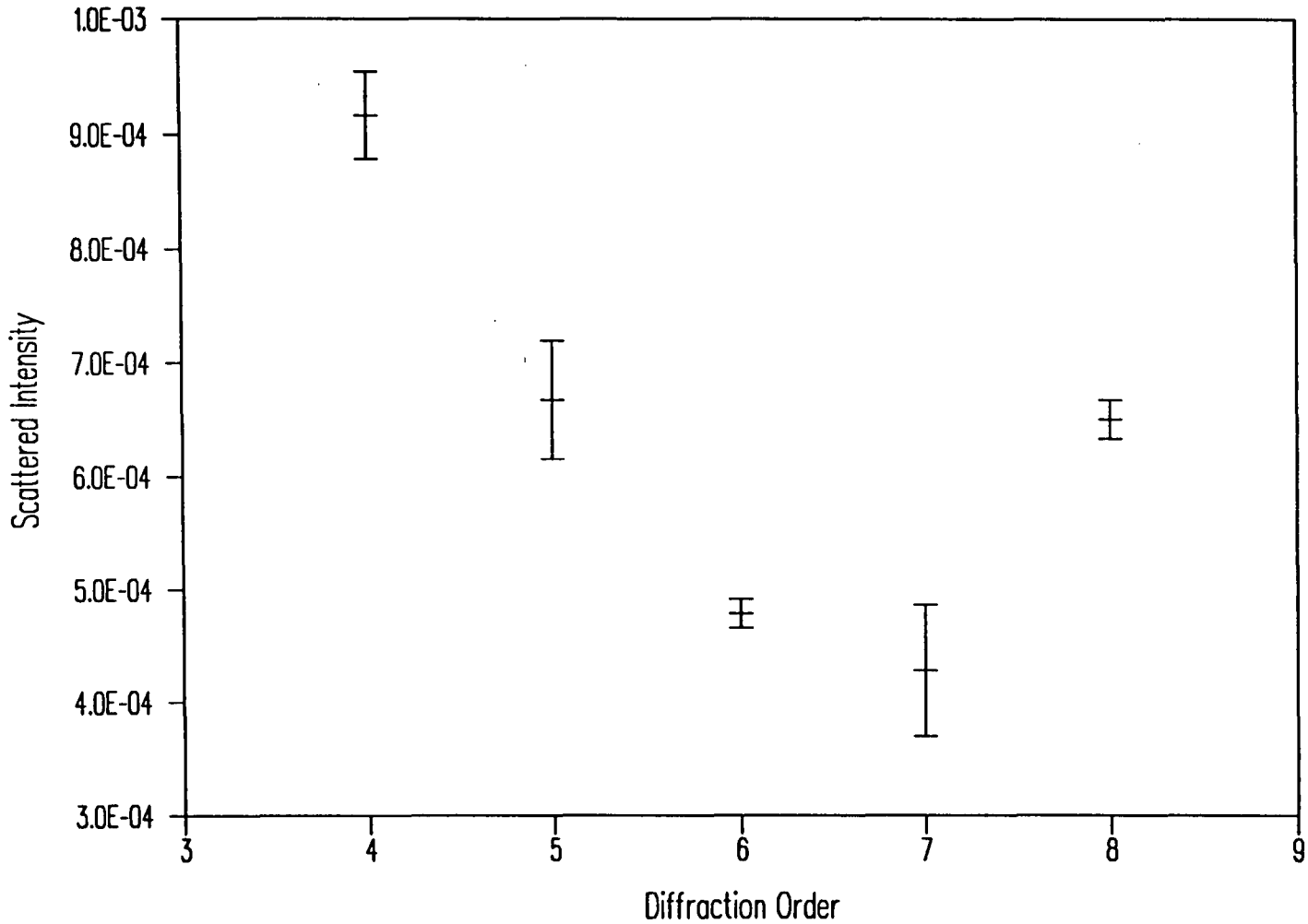

Figure 4.54 Scattered Intensity against Diffraction Order from SQELS of water

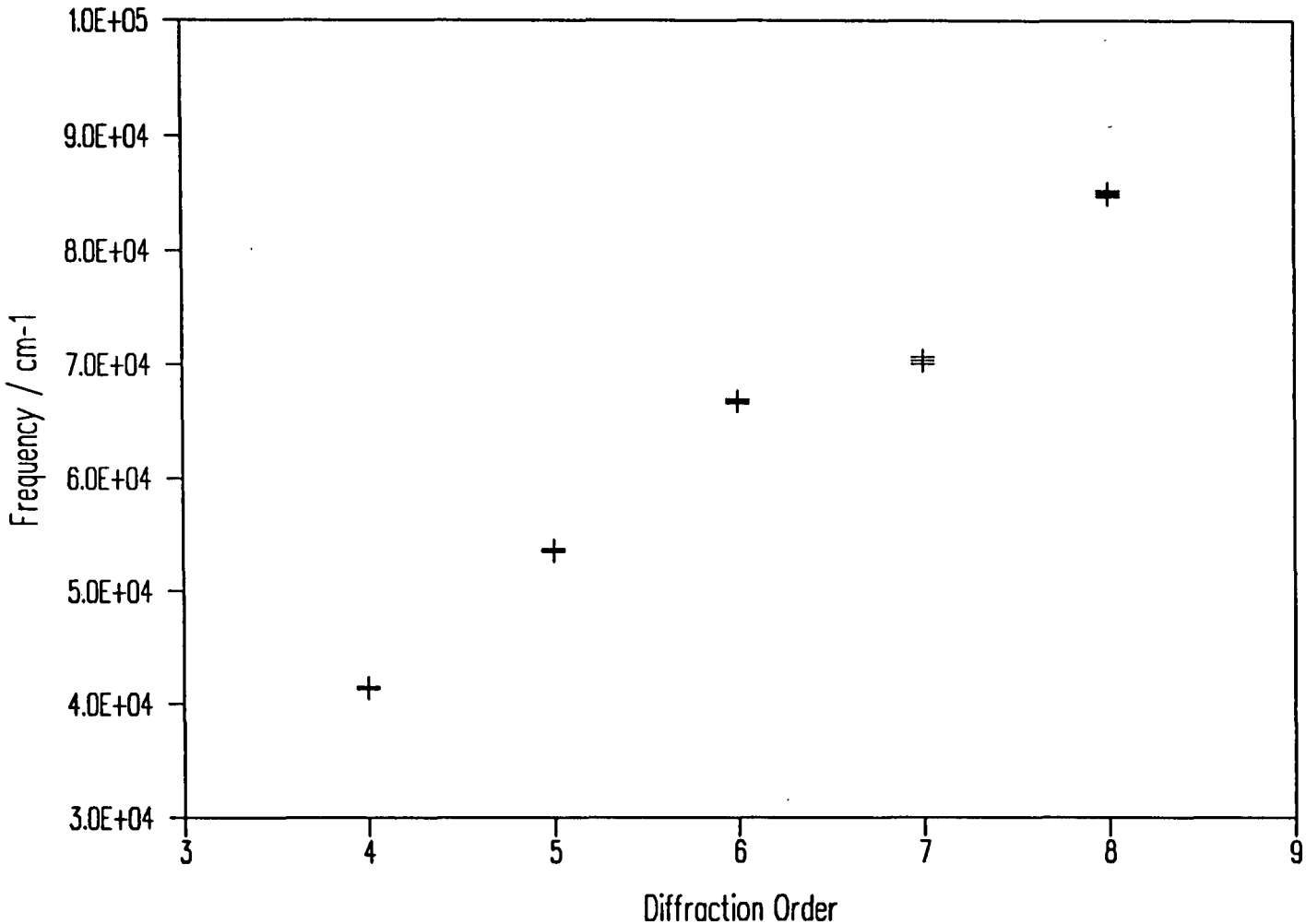

Figure 4.55 Propogation Frequency against Diffraction Order from SQELS of H_2O

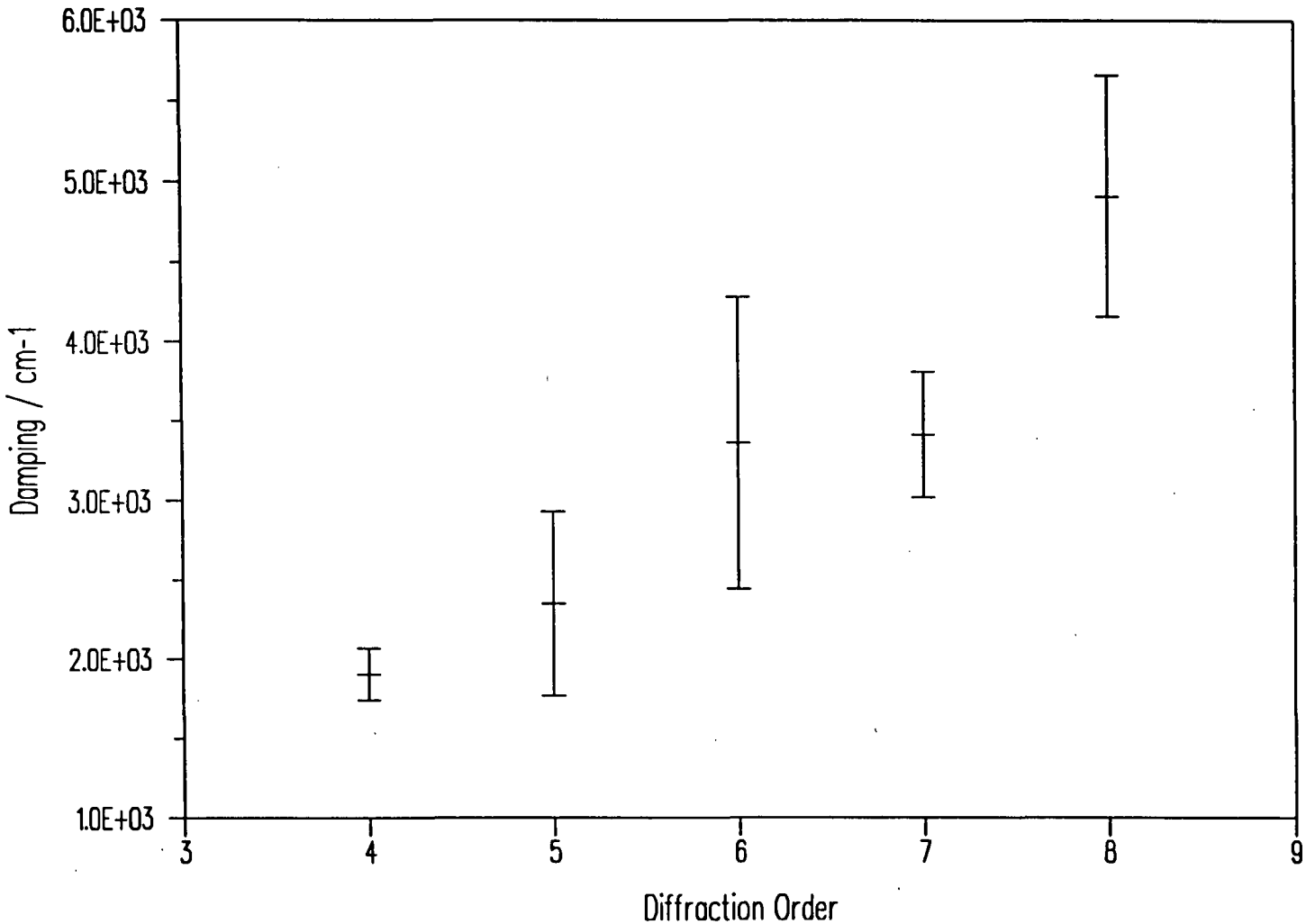

Figure 4.56 Wave Damping against Diffraction Order for SQELS from Water

number), and so the data acquisition time was greater for higher diffraction orders. For the fourth order for example, reasonable data could be collected in under one minute, while at the eighth order a time of around five minutes per run was required. It was decided therefore to use the fourth diffraction spot as a convenient point at which to measure the surface viscoelastic properties of poly(methyl methacrylate) monolayers.

4.5.2 SQELS from PMMA Monolayers

Correlation functions have been obtained for SQELS from monolayers of syndiotactic and isotactic PMMA spread on water as a function of the surface concentration of polymer. Measurements were made during compression of the films at room temperature (298K), and for each surface concentration at which the film was held, five repeated correlation functions were recorded. The fitted values quoted are averages of five repeated measurements.

Concentrating on SYNDIOPMMA firstly, from the best fitted form of equation 1.61, the values of the ratio of the reference to scattered intensity, the scattered intensity, the propagation frequency, and the wave damping as a function of surface concentration shown in figures 4.57-4.60.

The scattered intensity is seen to rise considerably with surface concentration and this was accompanied by a noticeable increase in the ease of data acquisition, enabling run times of as little as twenty seconds to be used for moderately high surface concentrations.

The wave damping and propogation rate are observed to decrease with increasing coverage apart from very low surface concentrations when there appears to be a slight rise in the parameters for the film covered surface over those of the free liquid. These results may be usefully re-presented as a function of the

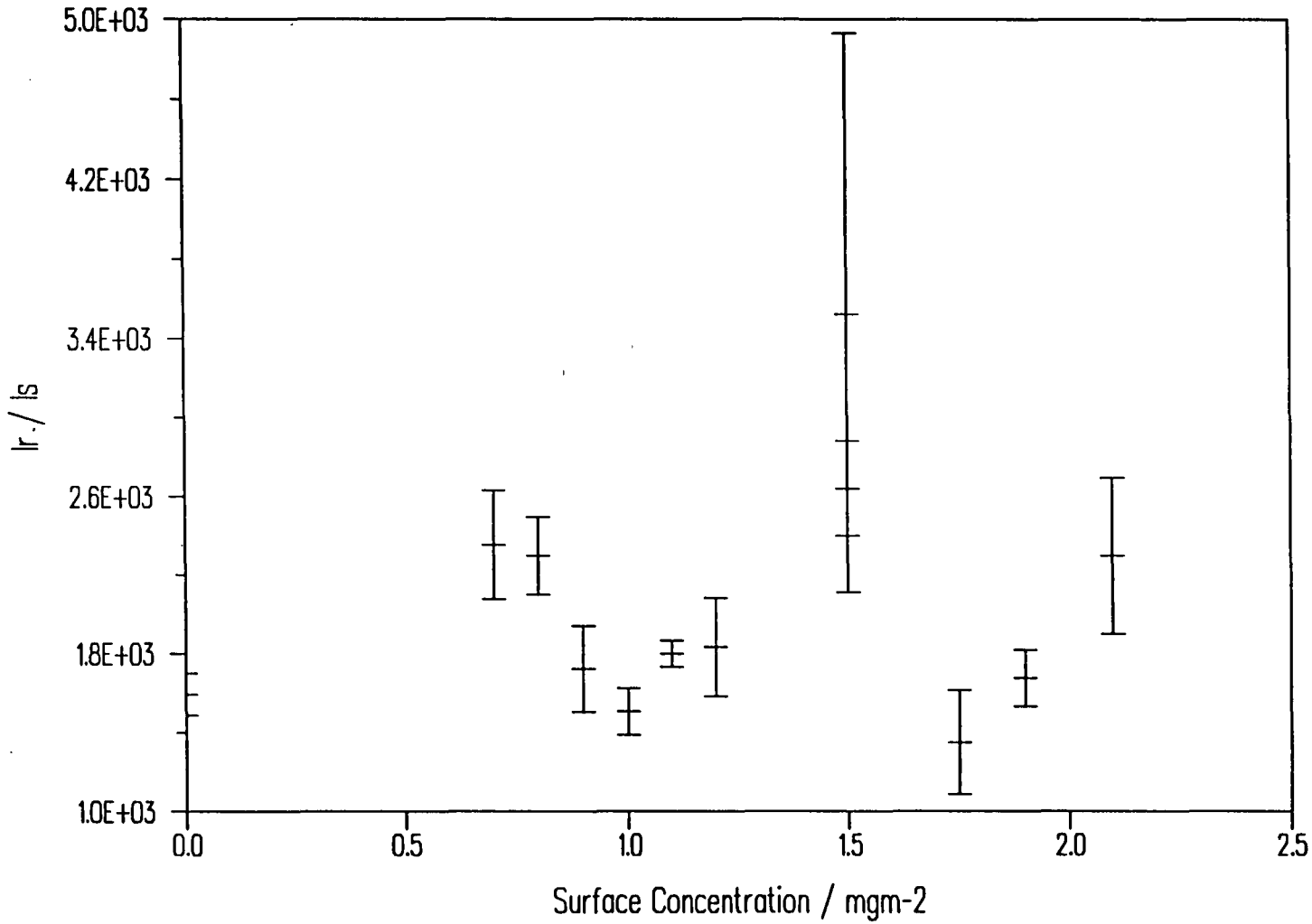

Figure 4.57 Ratio of Reference to Scattered Intensities against Surface Concentration for SYNDIOPMMA

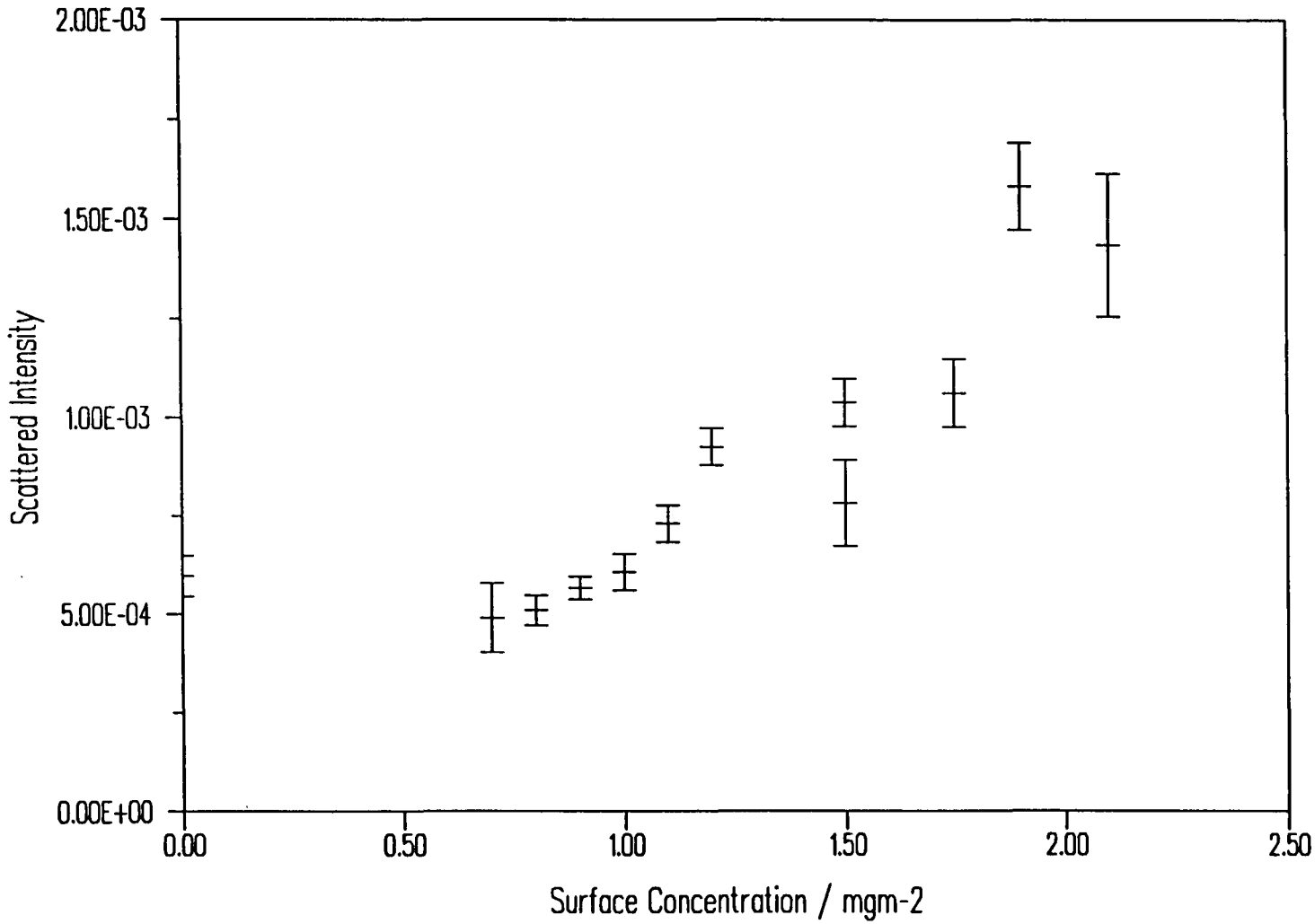

Figure 4.58 Scattered Intensity against Surface Concentration for SYNDIOPMMA

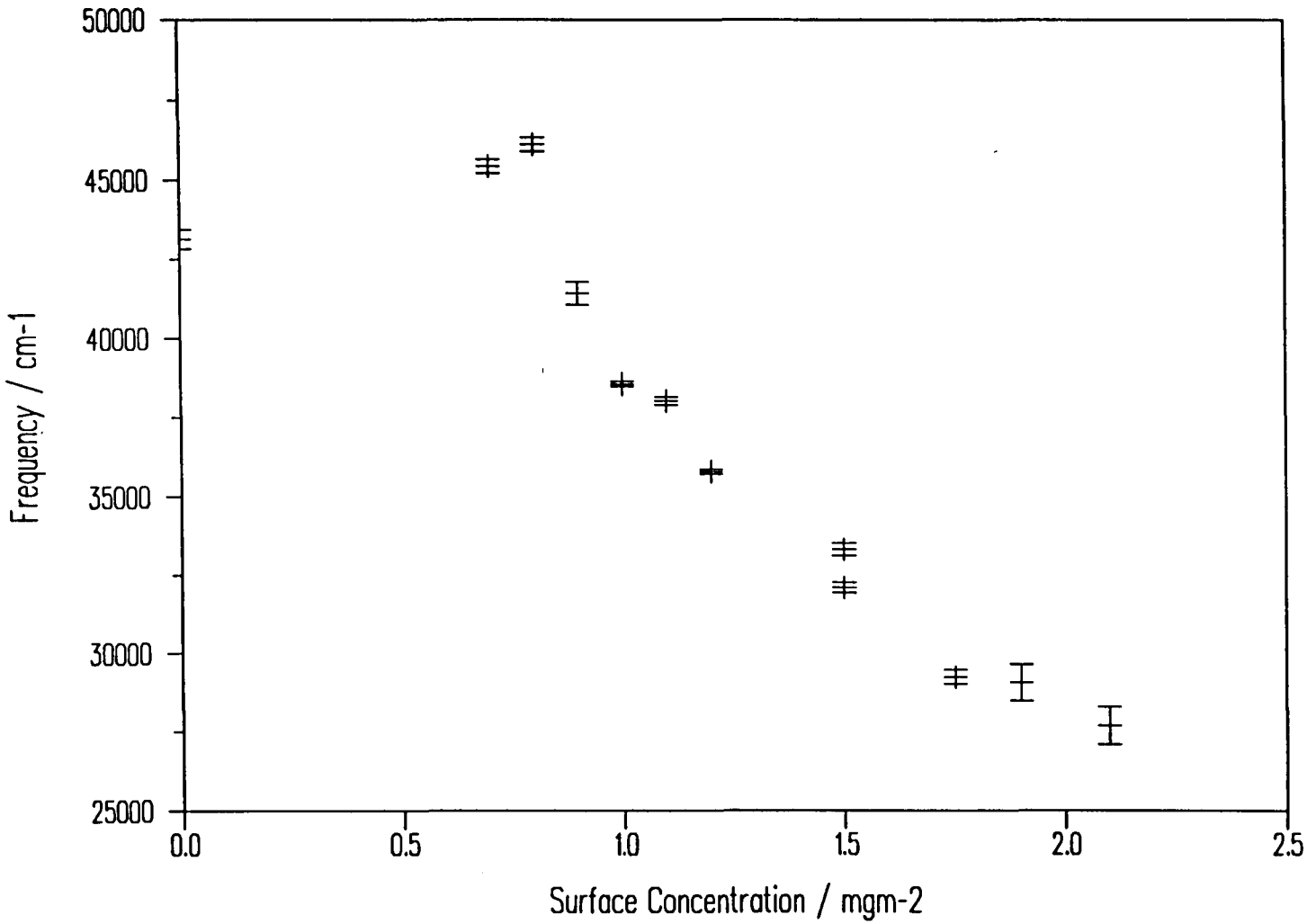

Figure 4.59 Propogation Frequency against Surface Concentration for SYNDIOPMMA

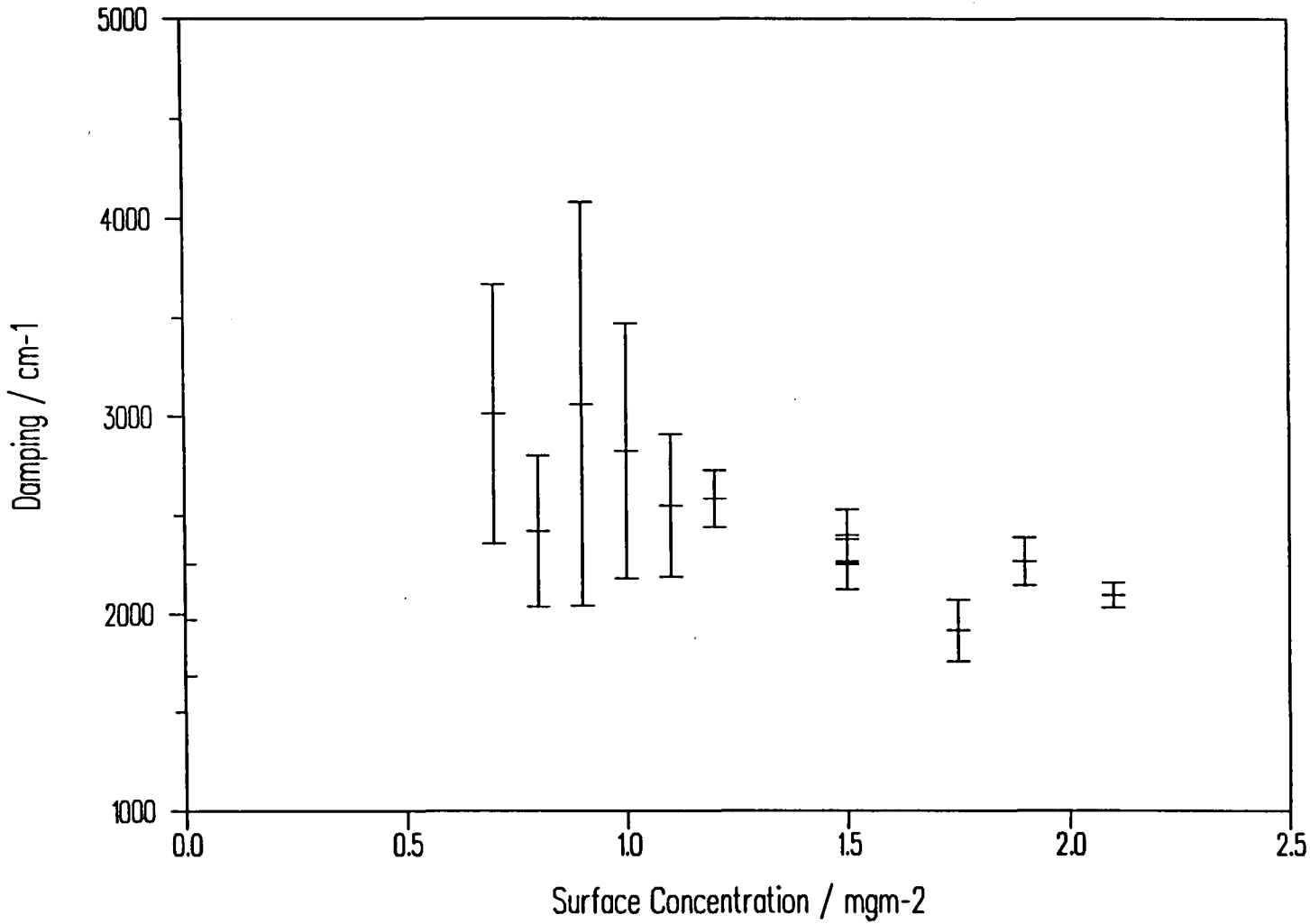

Figure 4.60 Wave Damping against Surface Concentration for SYNDIOPMMA

simultaneously measured surface pressure of the film, figures 4.61 and 4.62.

Turning to ISOPMMA, the fitted values of I_r/I_s, I_s, ω_o, and Γ are shown in figures 4.63-4.66. Considering the values of the I_r/I_s ratio and the scattered intensity firstly, it is apparent that these values are of the order of one hundred times greater and less respectively than their equivalents for SYNDIOPMMA. The reason for this is instrumental in origin rather than being associated with the nature of the spread films. It has been found that the heterodyne effect was very sensitive to the alignment and focussing of the various optical components in the apparatus, and even very slight changes in the set-up led to the loss of optimum performance. The I_r/I_s values are indicative of rather insufficient heterodyne mixing and this was reflected in the difficulty associated with the collection of suitable data at the time when the ISOPMMA monolayer was studied. Consequently rather larger run times were required to acquire even moderately acceptable correlation functions. Nevertheless it was still possible to obtain the frequency and damping values shown in figures 4.65 and 4.66.

One consquence of the rather poor quality of the data obtained was to increase the uncertainty in the values of ω_o and Γ. However the propogation frequency was still fitted with reasonable reproducibility, and a similar trend in the frequency shift to that observed for SYNDIOPMMA was obtained. The damping appears to rise through a maximum and then decrease slightly, but in this case the errors are increased considerably, and no definite trend can be determined. By plotting ω_o and Γ as a function of surface pressure, figures 4.67 and 4.68, an almost linear plot is obtained for the variation of the propogation frequency.

By substitution of the appropriate values of ω_o and Γ into the dispersion equation it is possible to calculate corresponding values for the film viscoelastic moduli, γ_o, γ', ϵ_o, and ϵ'. The uncertainty in these values is determined to a large extent by the sensitivity of the dispersion equation to each modulus, and also by the

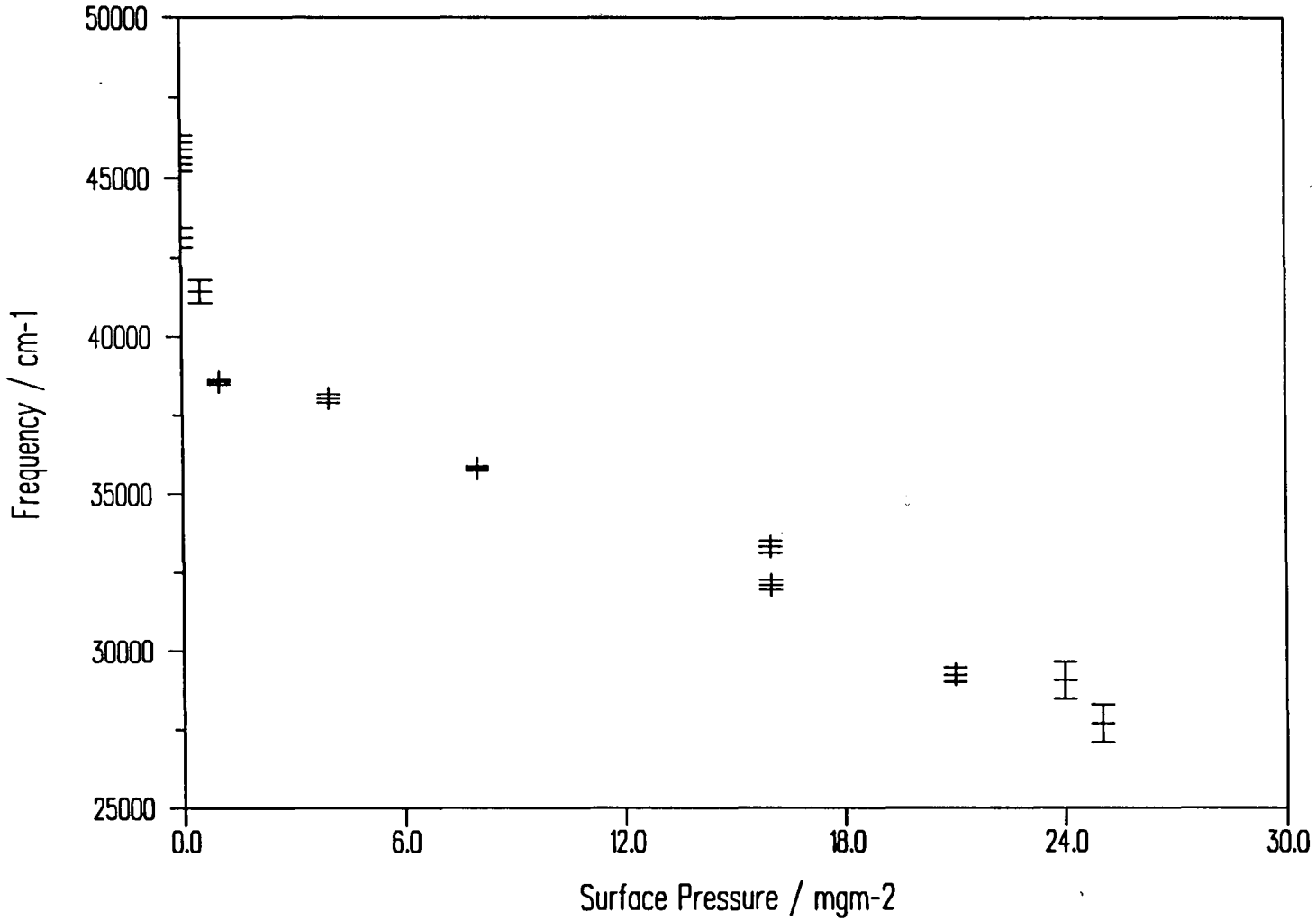

Figure 4.61 Propogation Frequency against Surface Pressure for SYNDIOPMMA

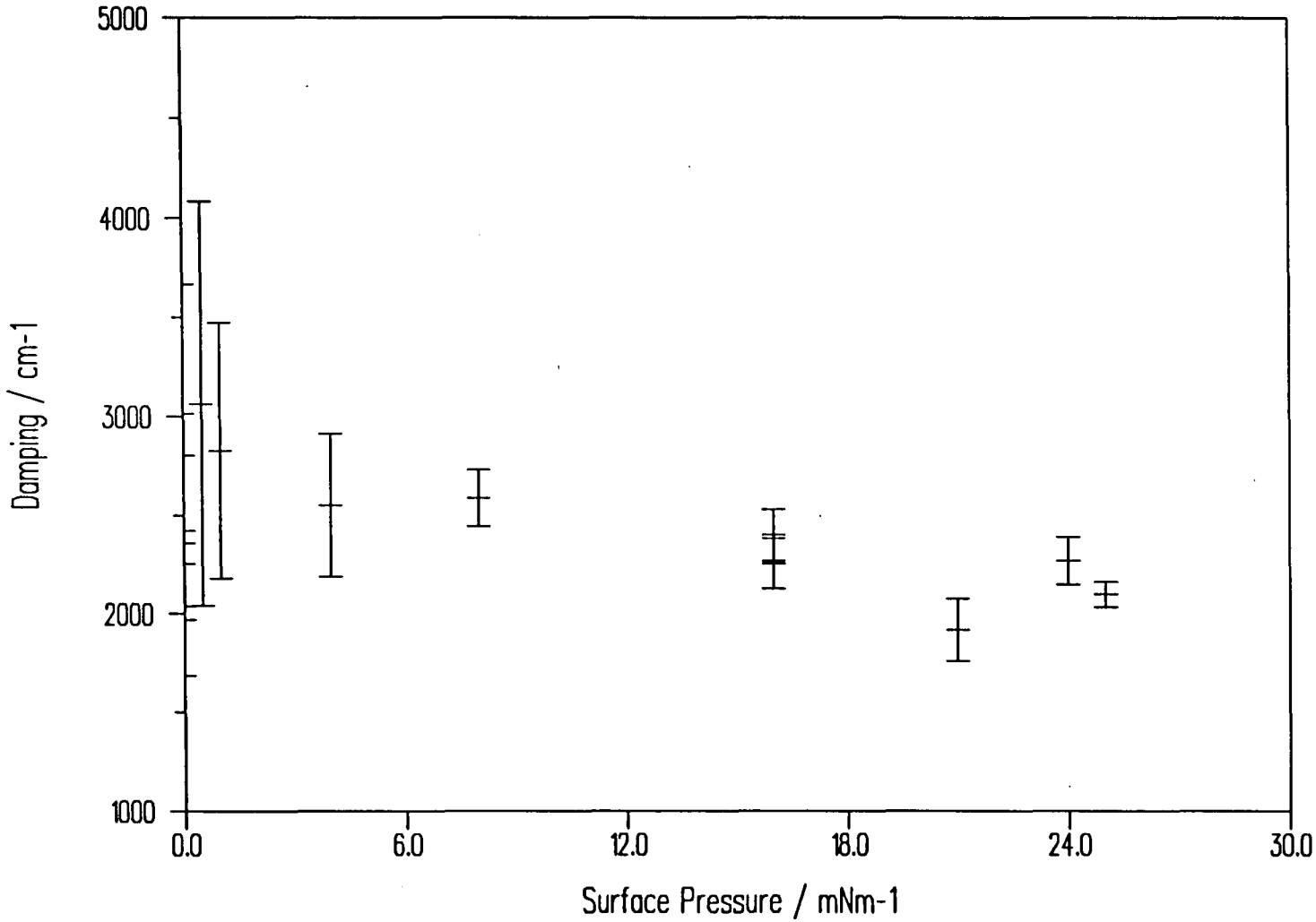

Figure 4.62 Wave Damping against Surface Pressure for SYNDIOPMMA

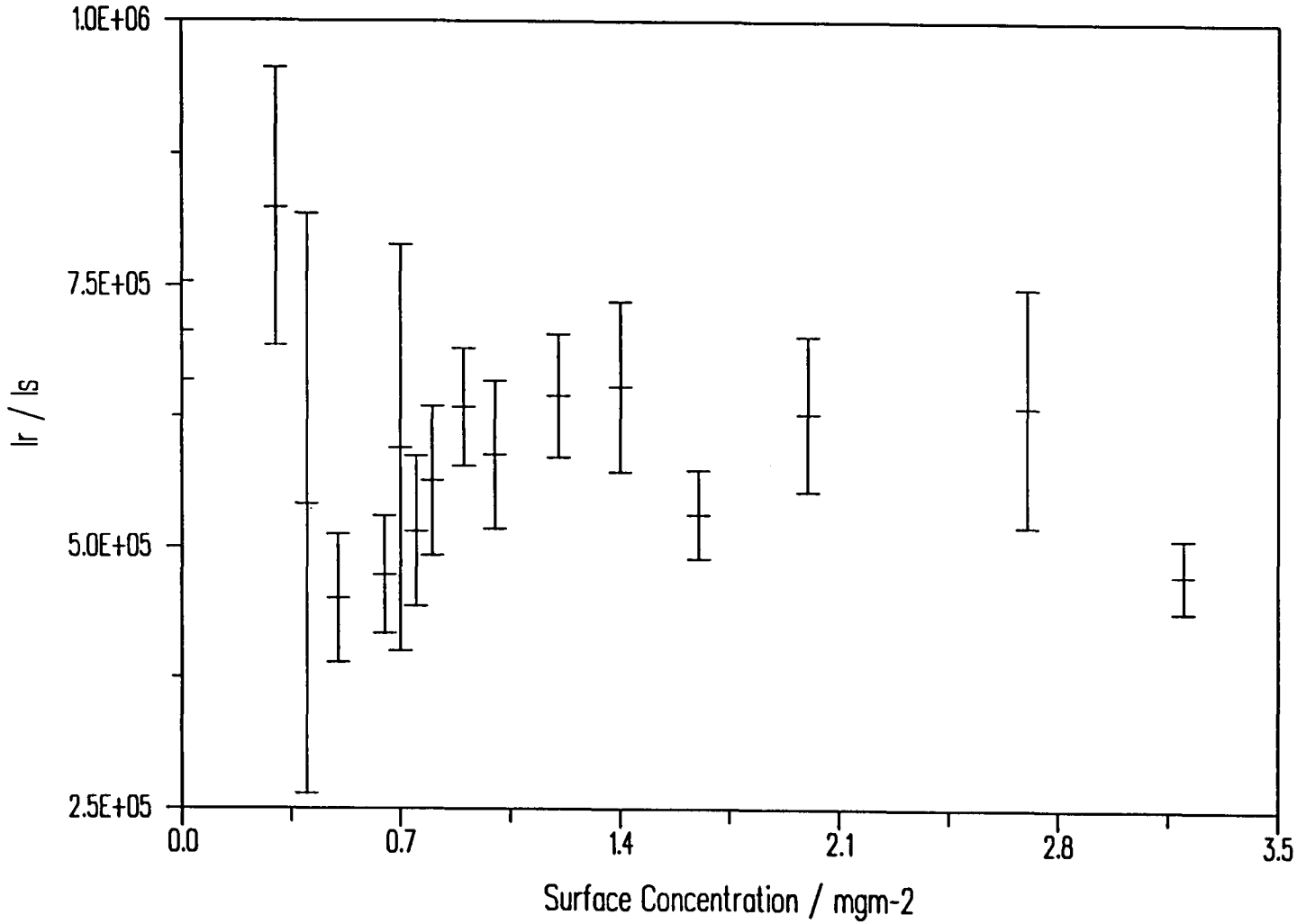

Figure 4.63 Ratio of Reference to Scattered Intensities against Surface Concentration for ISOPMMA

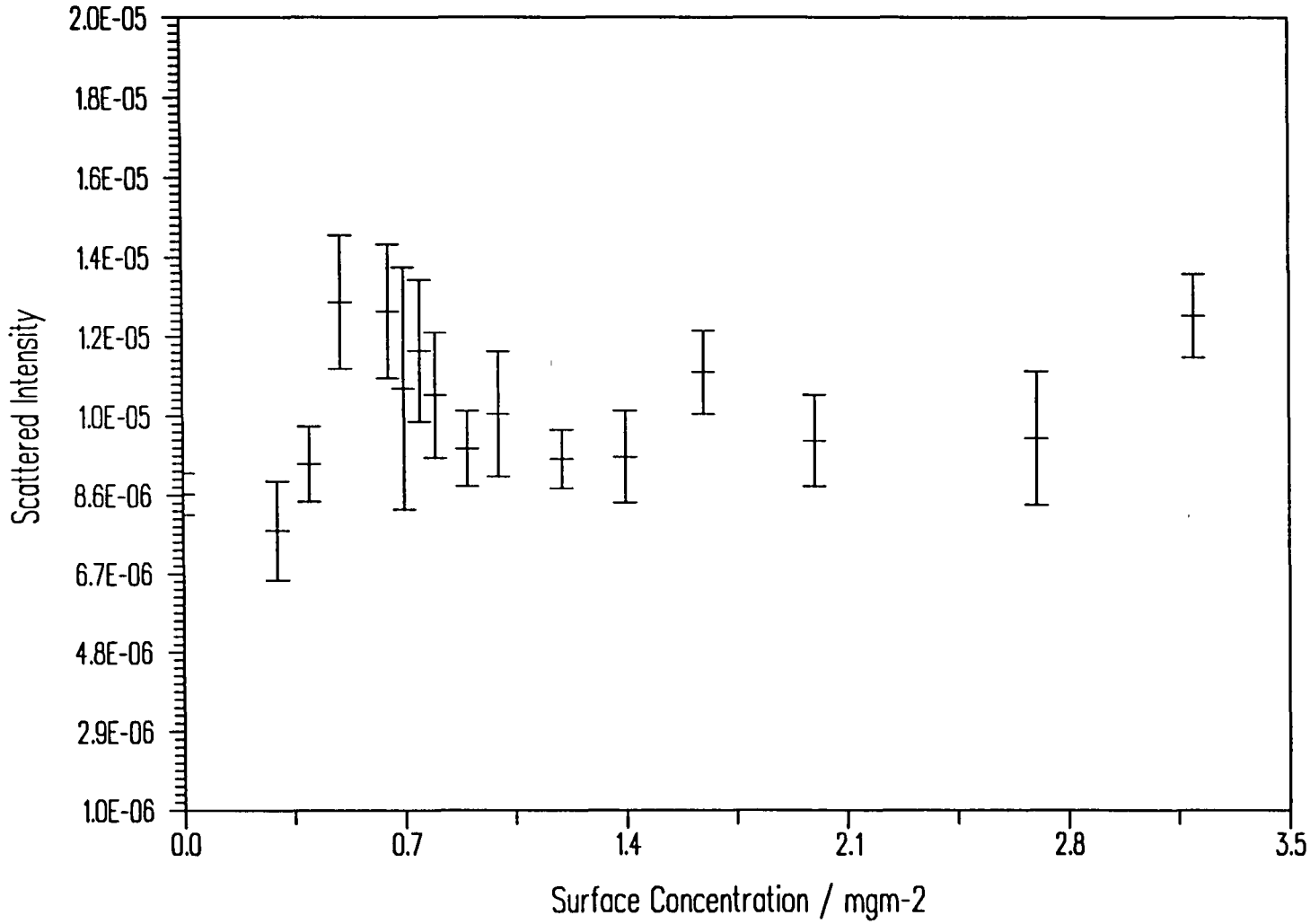

Figure 4.64 Scattered Intensity against Surface Concentration for ISOPMMA

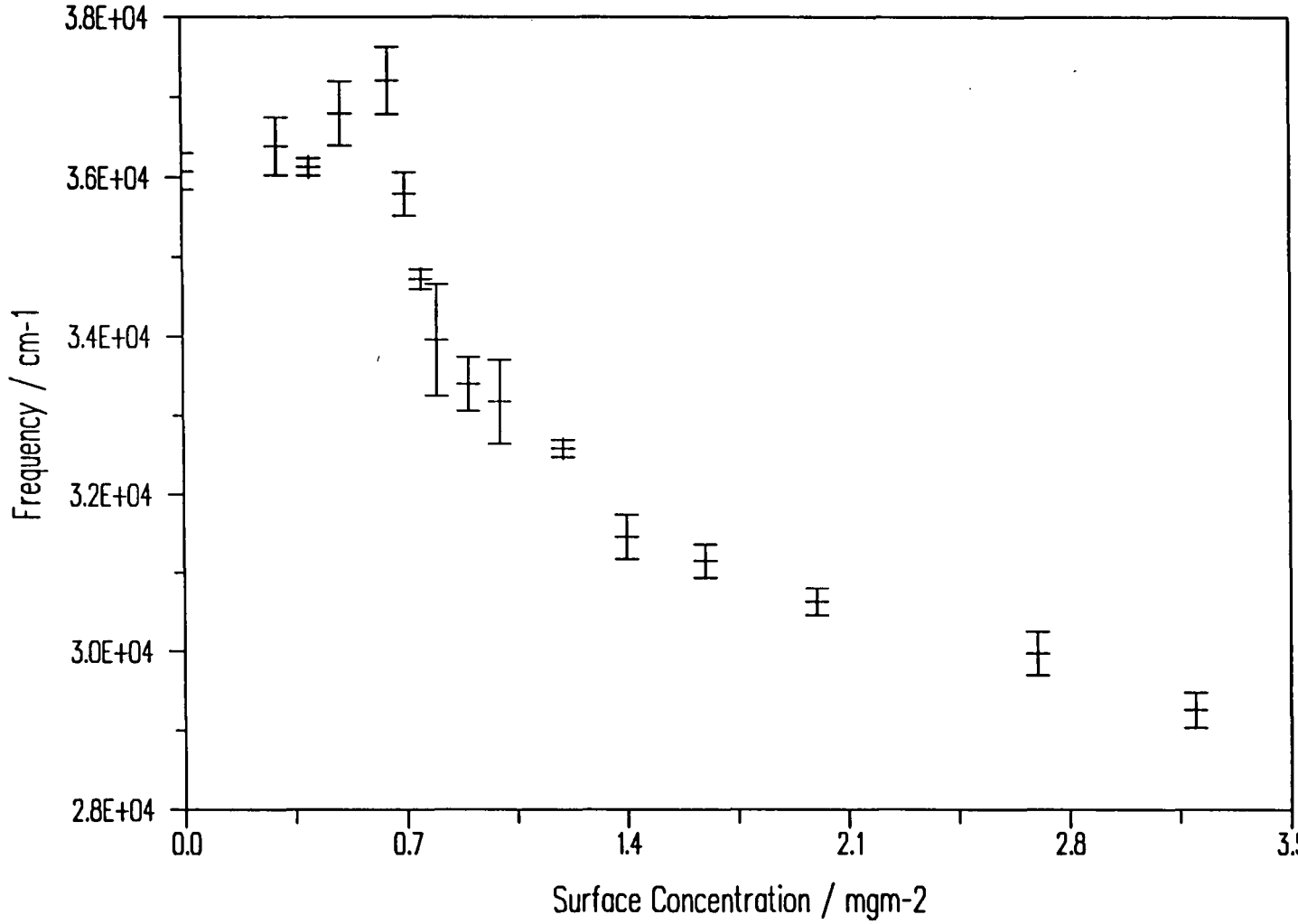

Figure 4.65 Propogation Frequency against Surface Concentration for ISOPMMA

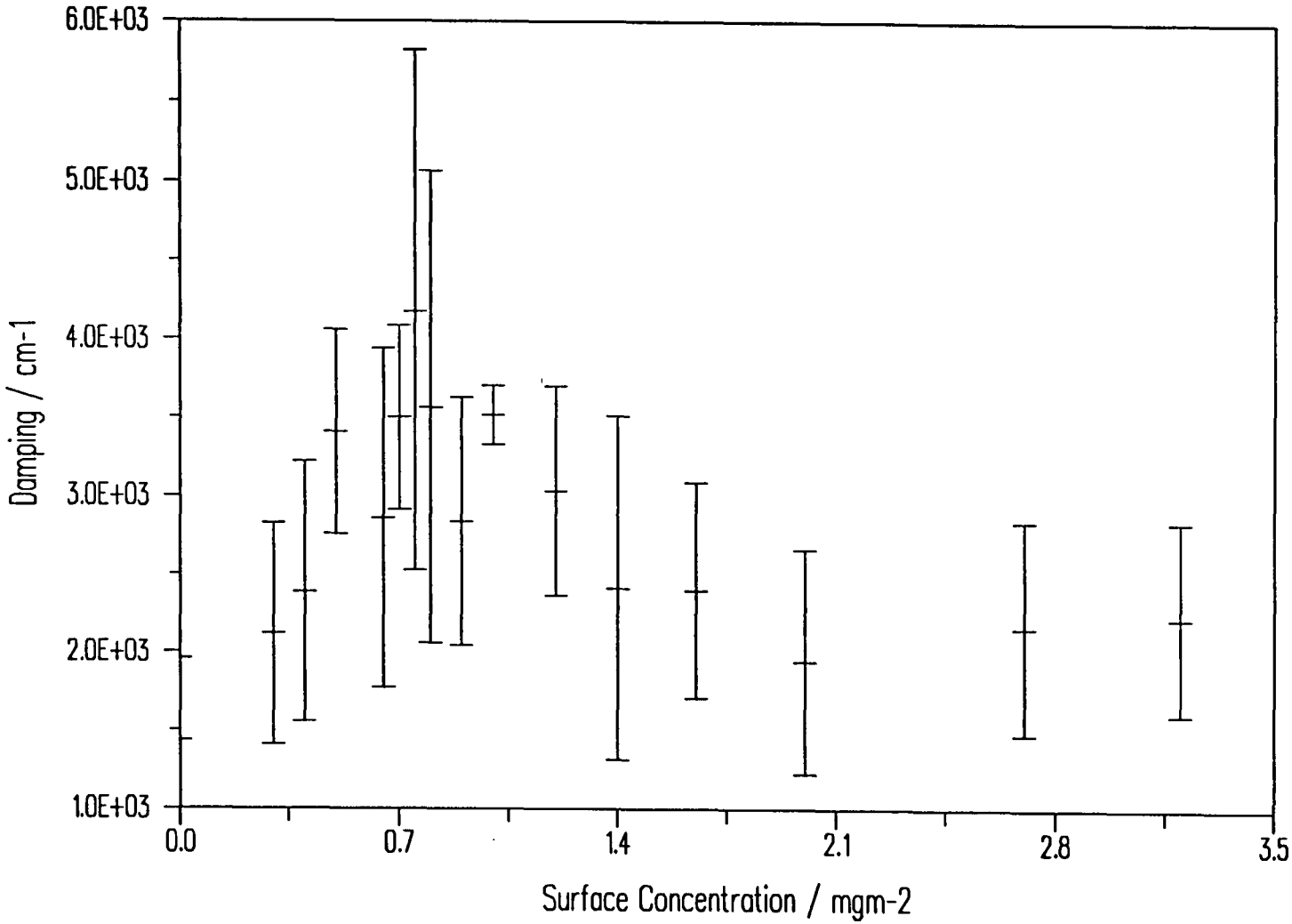

Figure 4.66 Wave Damping against Surface Concentration for ISOPMMA

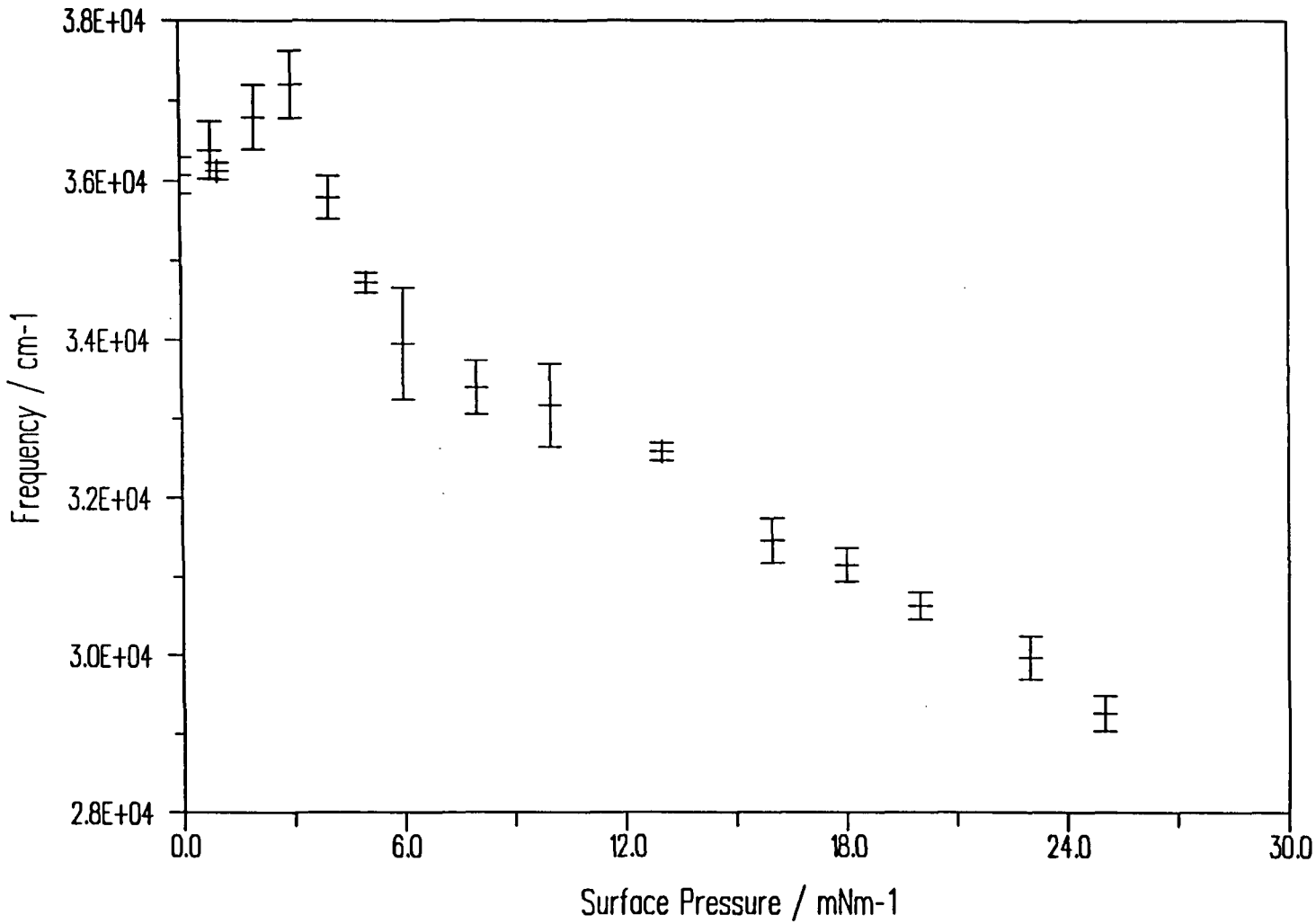

Figure 4.67 Propogation Frequency against Surface Pressure for ISOPMMA

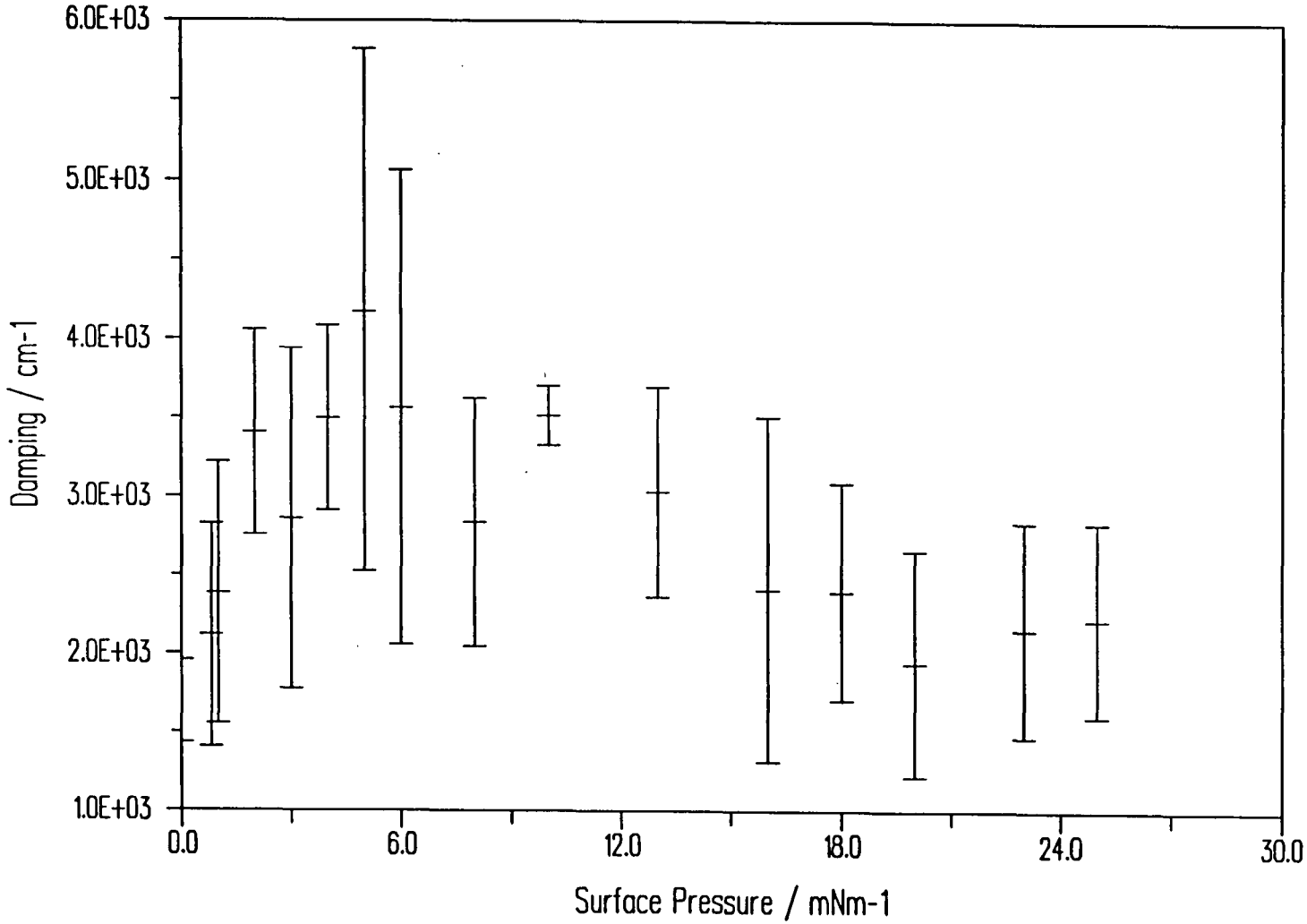

Figure 4.68 Wave Damping against Surface Pressure for ISOPMMA

quality of the experimental data. As previously mentioned the data for ISOPMMA is much poorer than for SYNDIOPMMA due to instrumental problems and so it has only proved possible to fit values for all four moduli for SYNDIOPMMA. For ISOPMMA only the surface tension was reliably fitted. All values are summarised in figures 4.69-4.73, where errors are estimated by the standard deviation in the results of five repeated experiments.

For the isotactic polymer the SQELS data is in good agreement with the Wilhelmy plate measured surface. For SYNDIOPMMA however, at low surface coverage the surface tension is apparently greater than the surface tension of clean water! This would indicate a negative surface pressure and is consistent with an experimental observation made during recording of SYNDIOPMMA isotherms. When spreading this film onto a clean water subphase with zero surface pressure, a depression to a slightly negative surface pressure was often seen. This depression was removed by arbritary rezeroing (as has presumably been done so by other workers with the same material) but given that SQELS appears to confirm the effect future studies may have to take this into consideration. Certainly it would be of interest to obtain more data at low surface coverages in order to elucidate this effect which presumably is due to some sort of intermolecular cohesive force. Earnshaw and Winch reported similar data for a pentadecanoic acid monolayer, for which laser light scattering estimated a slightly negative surface pressure at a point where the classically measured pressure was zero[5].

Direct Data Analysis

The data interpretation method used so far relies on the non-linear least squares fitting of the correlation function $G(\tau)$ to the measured correlation signal. From the fitted values of ω_0 and Γ, the dispersion equation may be employed to

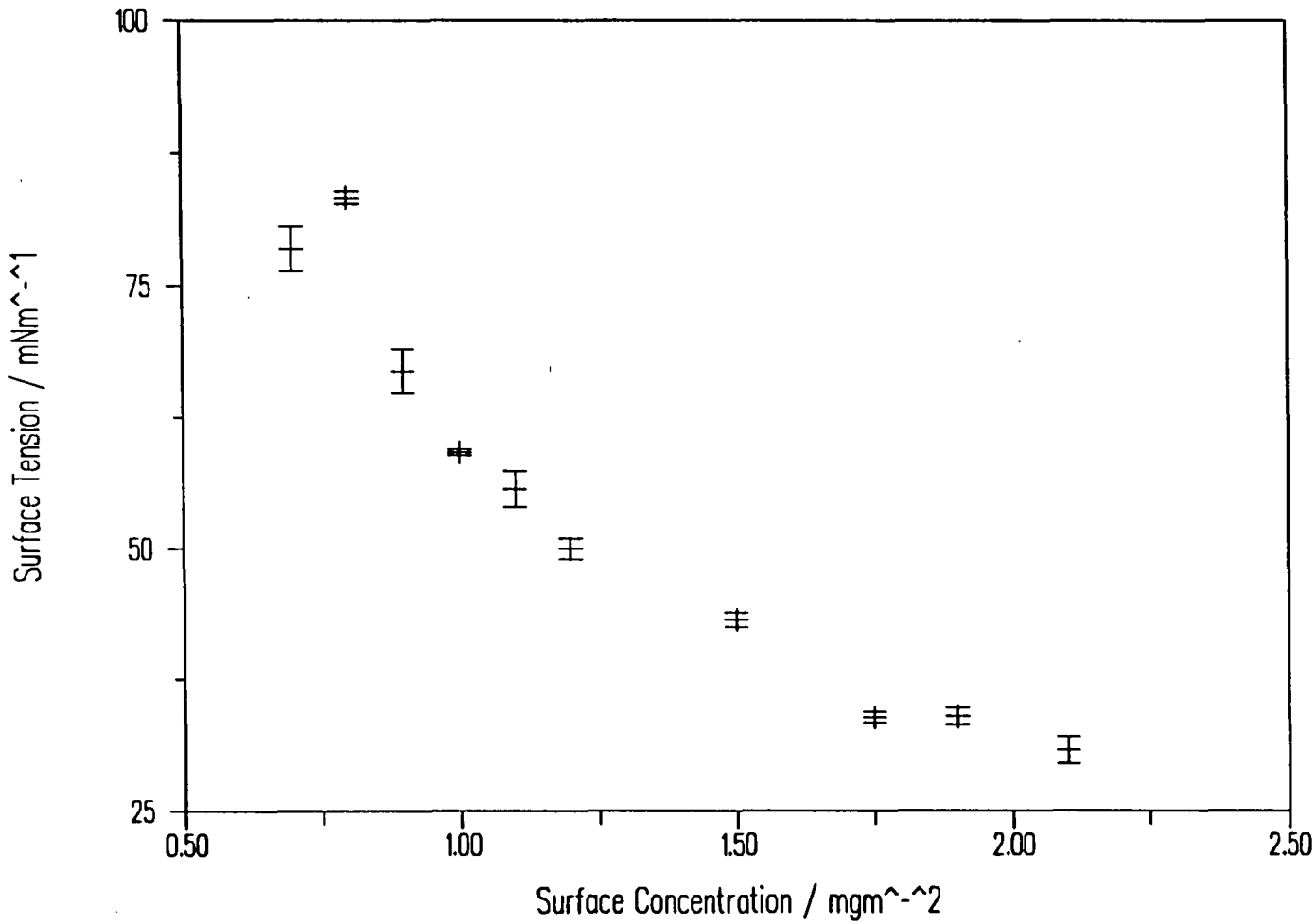

Figure 4.69 Surface Tension (estimated from SQELS) against Surface Concentration for SYNDIOPMMA

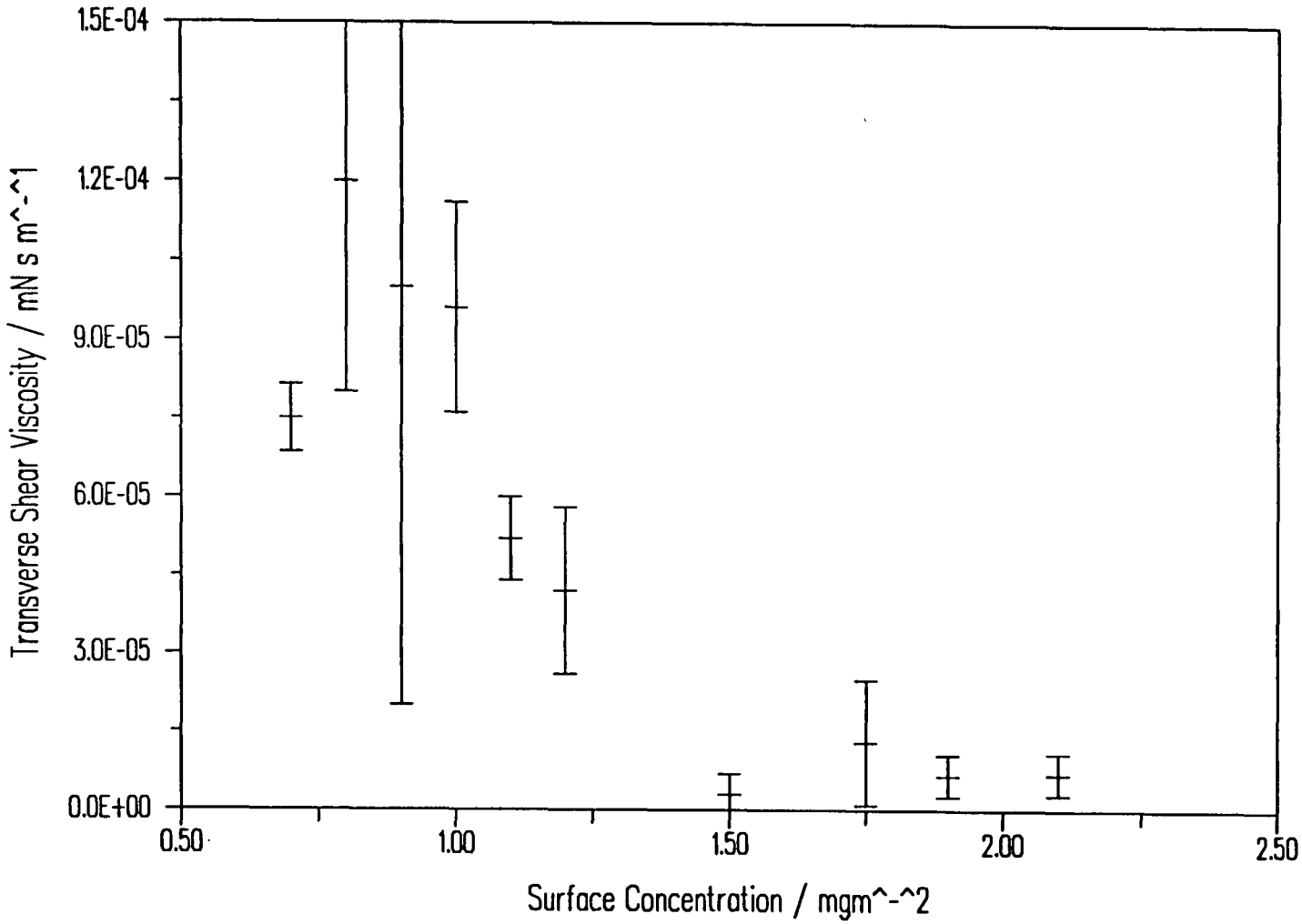

Figure 4.70 Surface Transverse Shear Viscosity against Surface Concentration for SYNDIOPMMA

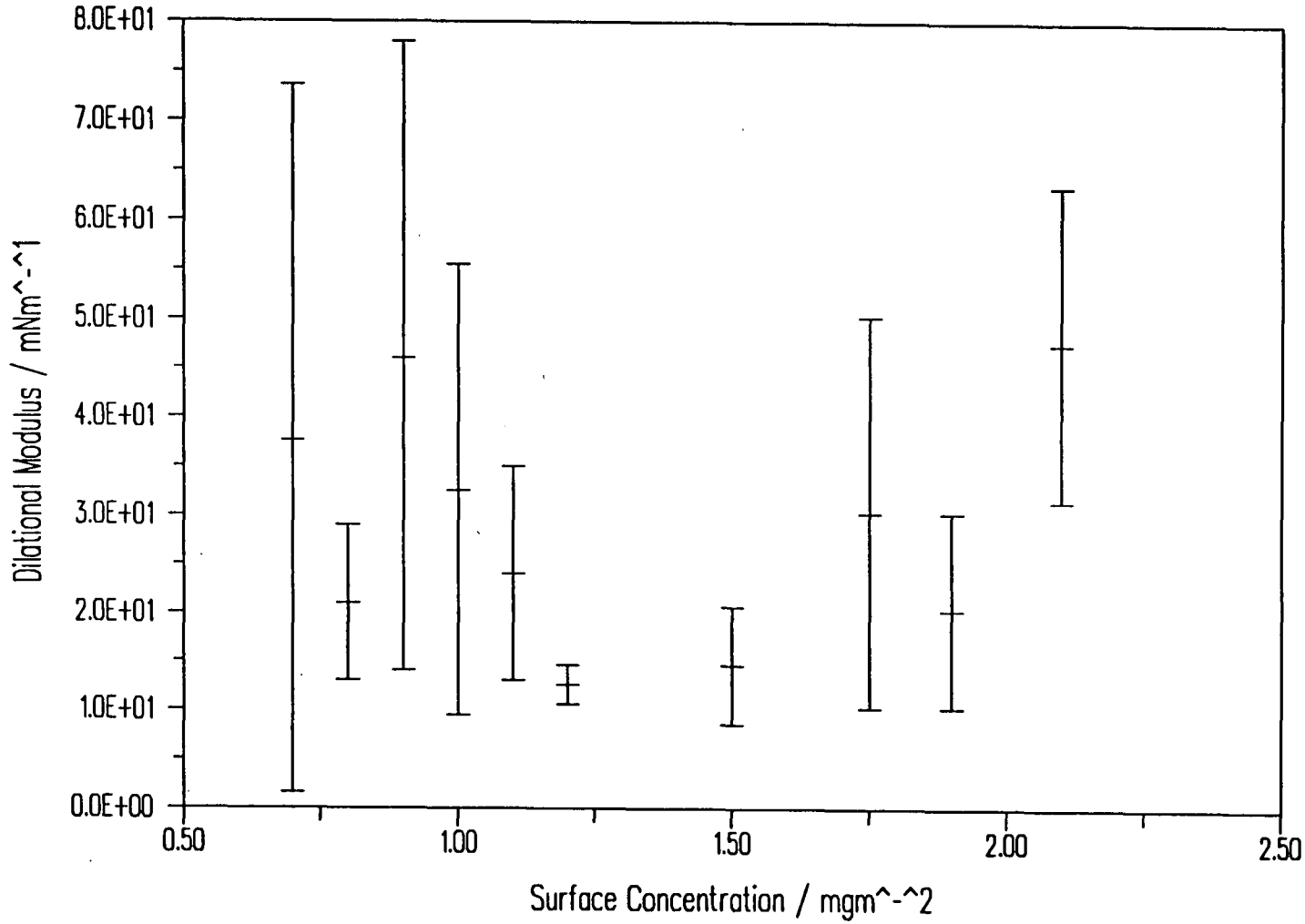

Figure 4.71 Surface Dilational Modulus against Surface Concentration for SYNDIOPMMA

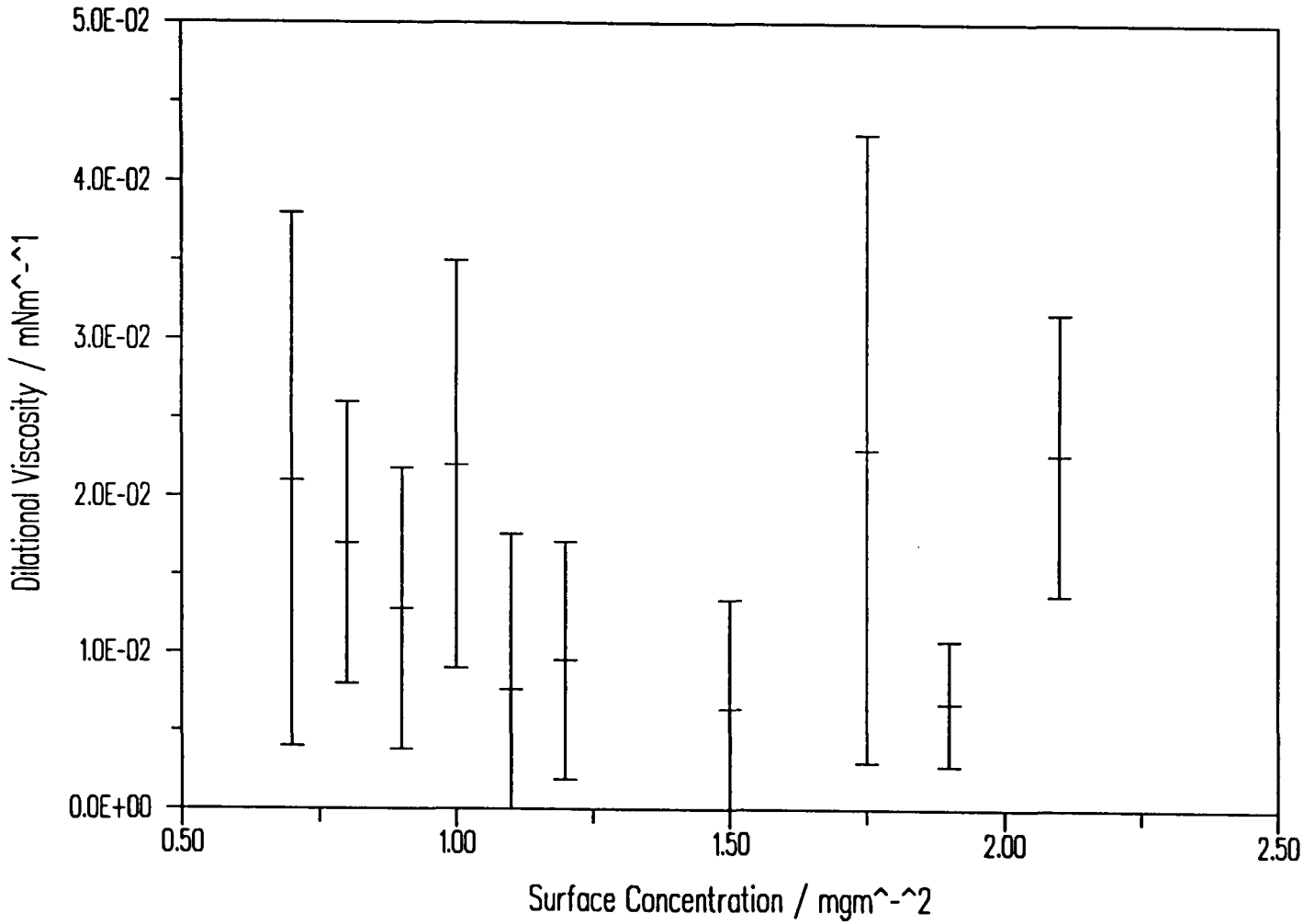

Figure 4.72 Surface Dilational Viscosity against Surface Concentration for SYNDIOPMMA

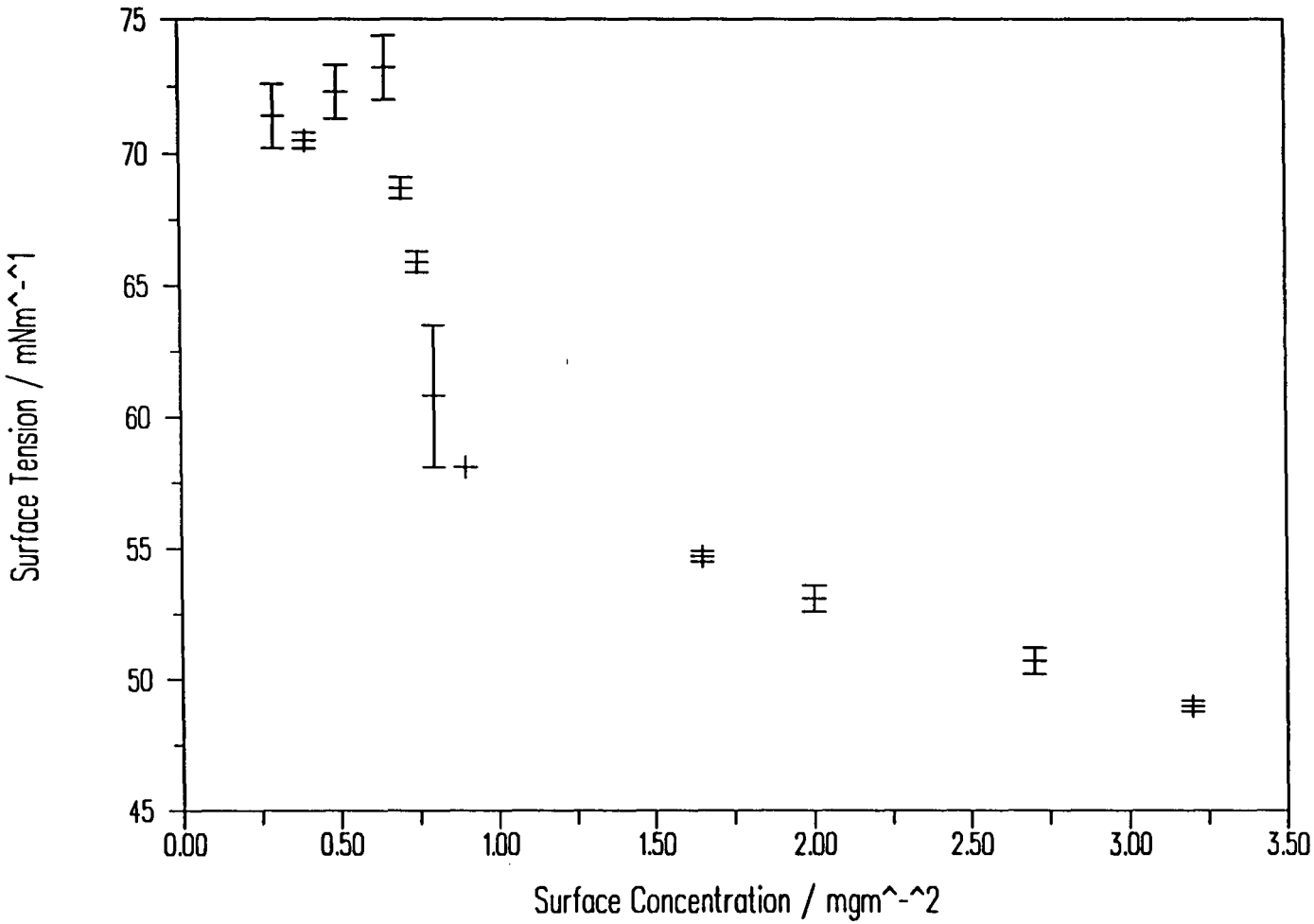

Figure 4.73 Surface Tension against Surface Concentration for ISOPMMA

estimate values for the film viscoelastic parameters. Indeed it is possible to estimate the surface tension as above, but only by the fortunate fact the the form of the dispersion equation makes it predominantly sensitive to the value of γ_o. The other three parameters become increasingly less well defined and in general the use of two measured experimental variables to determine four required parameters cannot be successfully carried out.

In order to get around this difficulty an alternative method of data analysis has been employed. Instead of fitting the mathematical form of the measured correlation function to the experimental data, a Fourier transformation routine has been used to calculate a correlation function from the power spectrum generated by a given set of film viscoelastic parameters in the dispersion equation. By altering the values of the four film parameters least squares minimisation has been used to directly fit their values to the experimental data. Figures 4.74-4.78 summarise the film parameters so obtained using the experimental data of the previous section, with the five replicated experiments appended onto one another to improve statistics. Note that in this case errors are estimated statistically from the sensitivity of the fit to the variation of each individual parameter.

The strong dependence of the signal on surface tension is reflected in the very small errors on the data of figures 4.74 and 4.78, the most notable feature again being the anomalous low surface concentration increase in surface tension for SYNDIOPMMA. In figure 4.75 a decreasing trend in transverse shear viscosity is clearly discernible for SYNDIOPMMA. Earnshaw has noted such a trend at moderate surface concentrations for other monolayers to be proceeded by an apparent initial sharp increase at low coverages[5,6]. The range of the present data does not extend to a sufficiently low coverage to confirm this for the case of PMMA, but this provides another compelling reason for further attention to this area.

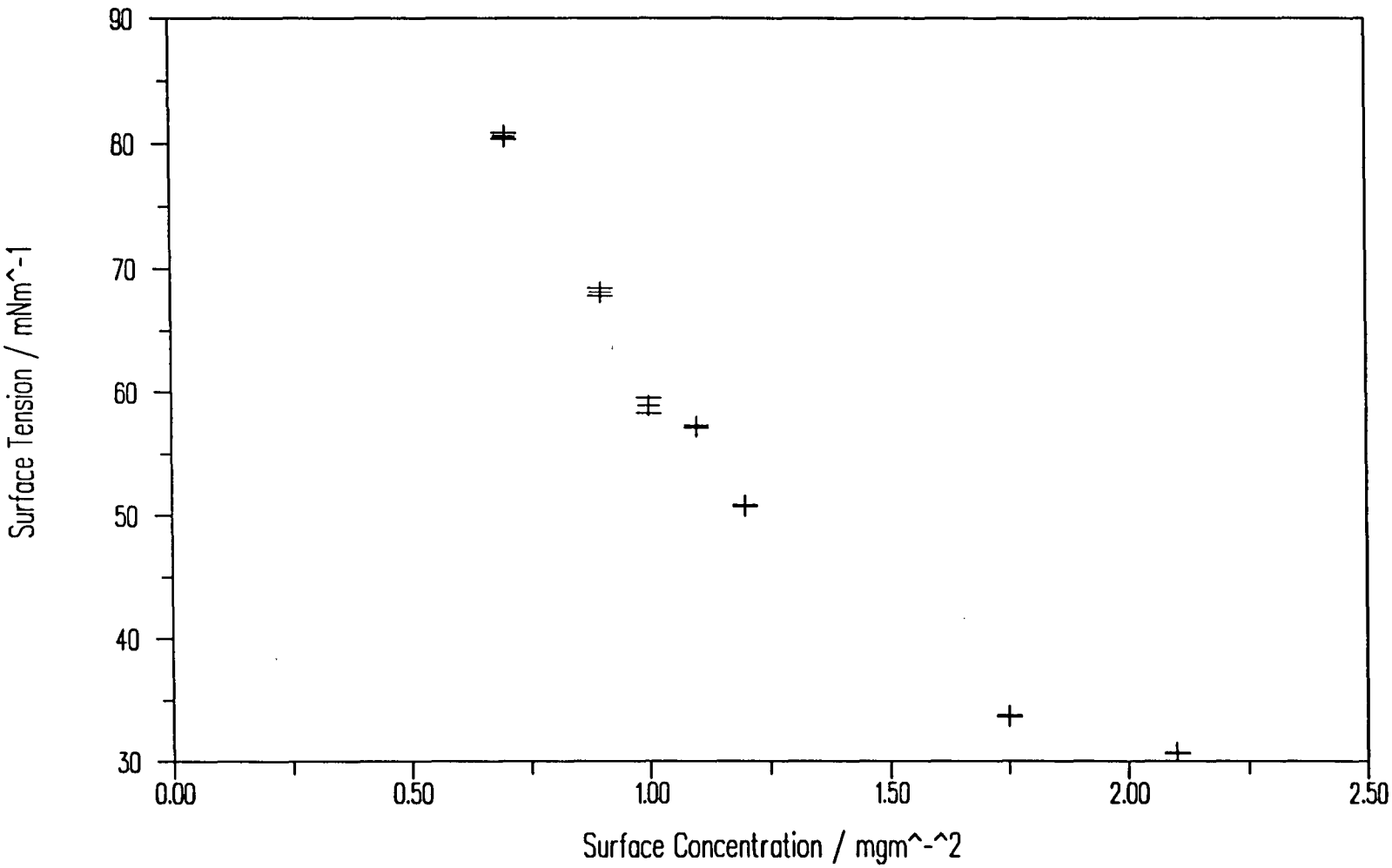

Figure 4.74 Surface Tension (estimated from appended runs) v Surface Concentration for SYNDIOHPMMA

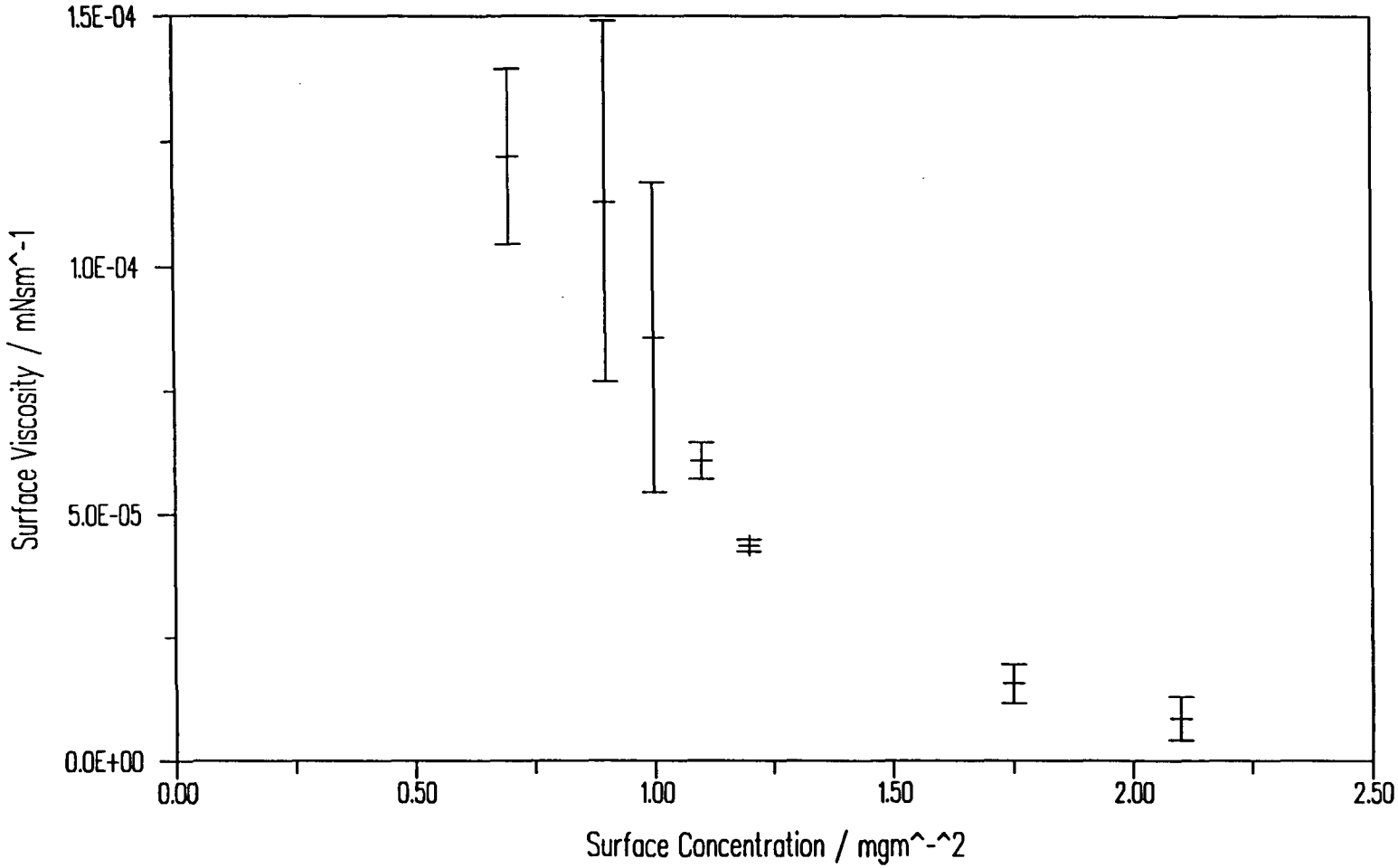

Figure 4.75 Surface Transverse Viscosity (from appended runs) v Surface Concentration for SYNDIOHPMMA

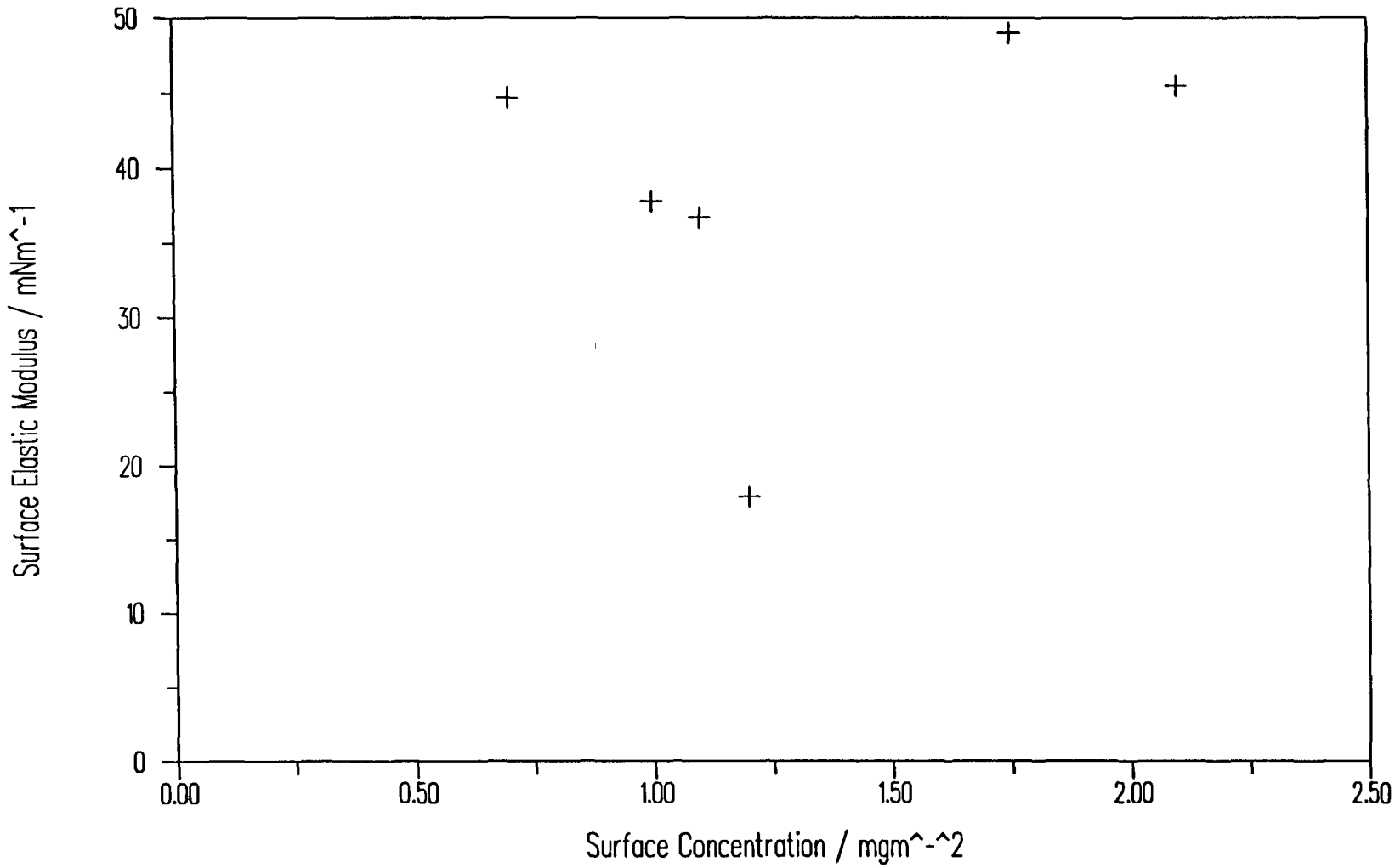

Figure 4.76 Surface Elastic Modulus (appended data) v Surface Concentration for SYNDIOHPMMA

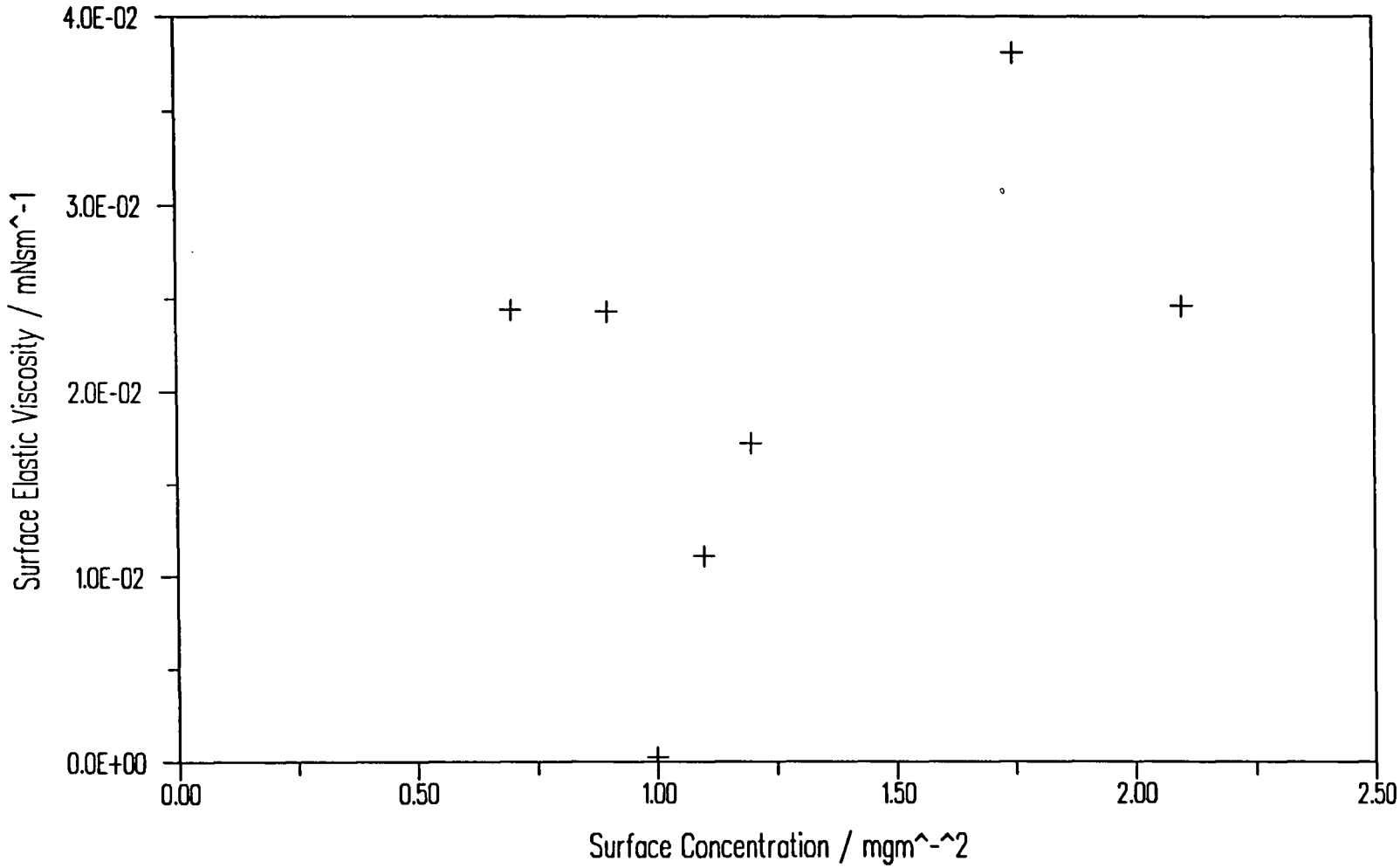

Figure 4.77 Surface Elastic Modulus (appended data) v Surface Concentration for SYNDIOHPMMA

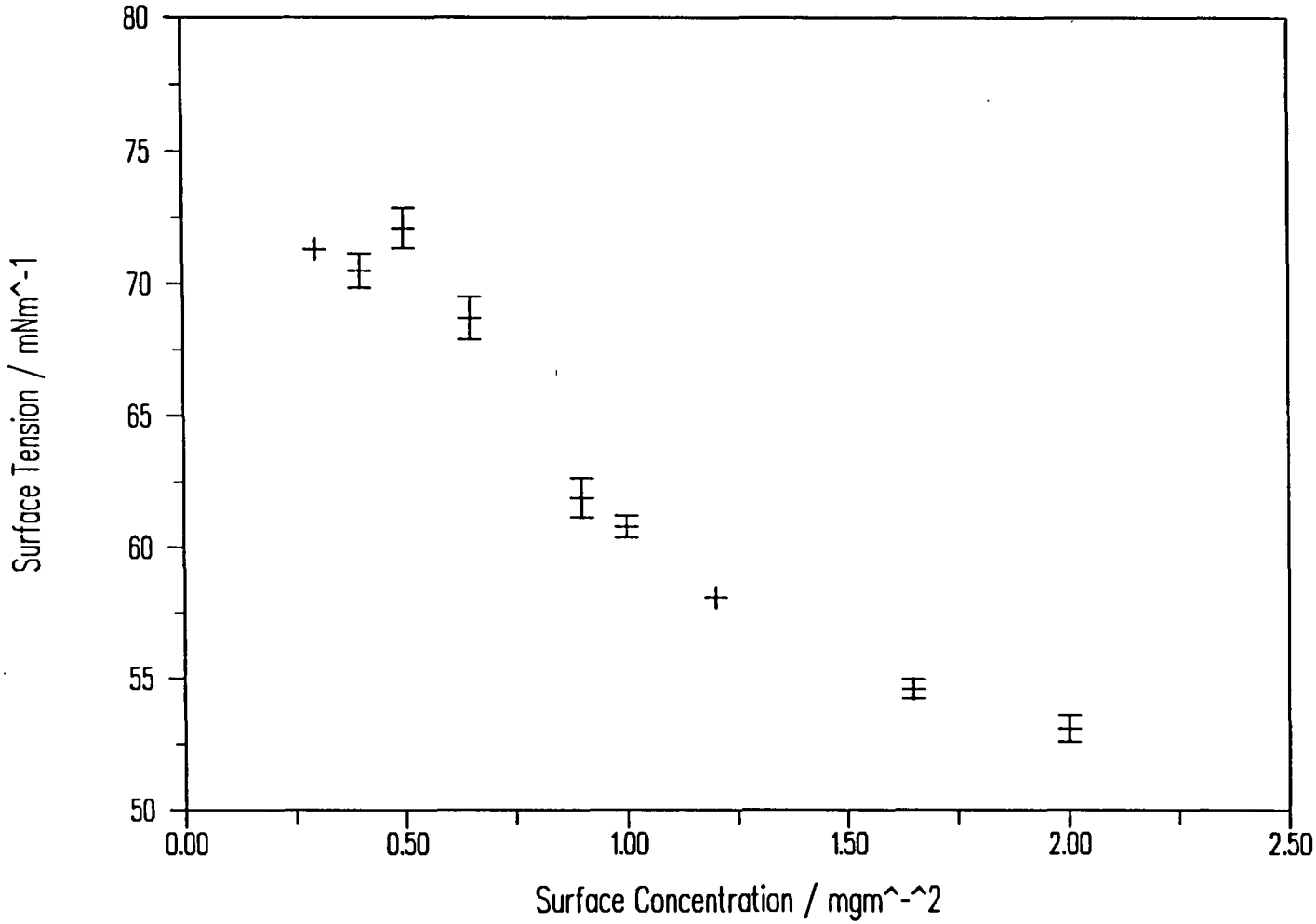

Figure 4.78 Surface Tension (appended data) v Surface Concentration for ISOHPMMA

The data of figures 4.76 and 4.77 clearly demonstrate that at the present level of data quality it has not been possible to reliably fit values to the surface transverse viscosity and surface elastic modulus even for SYNDIOPMMA. Error bars have been omitted from these plots but are of a greater order than the data values, and no attempt will be made to ascribe any meaning to the data values. Thus it has not been possible to compare the dependence of the dynamically measured film elasticity with the statically measured Gibb's elasticity, defined as $\Gamma.d\pi/d\Gamma$, where Γ is the surface concentration and π is the classically measured surface pressure. The dependence of this function on Γ for SYNDIO and ISOPMMA are shown in figures 4.79 and 4.80, where a maximum turning point may be seen in each case.

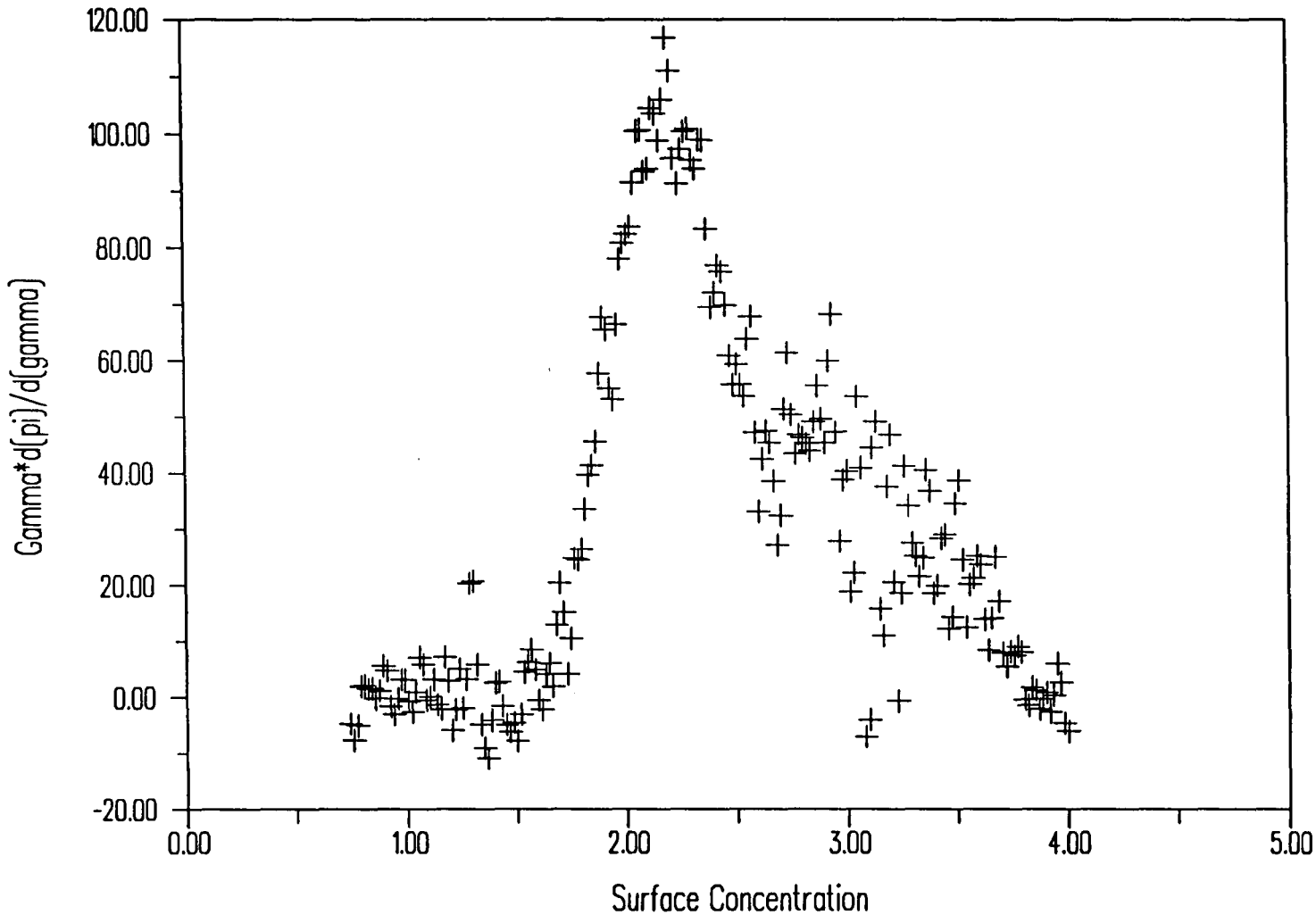

Figure 4.79 Gibbs Static Elasticity v Surface Concentration for SYNDIOHPMMA

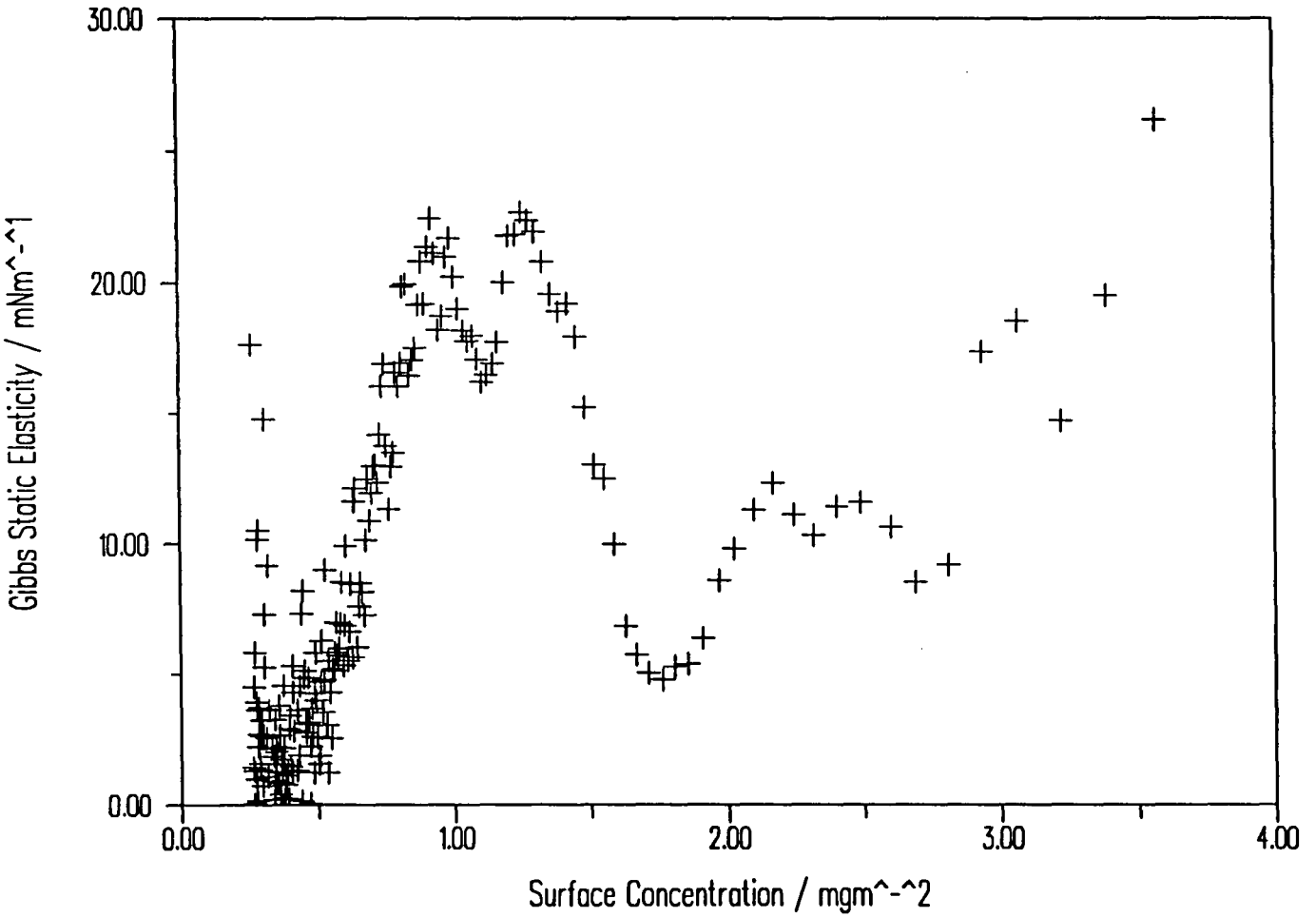

Figure 4.80 Gibbs Static Elasticity v Surface Concentration for ISOHPMMA

References

1. Jaffe, J., Berliner, C., Lambert, M., *J. Chem. Phys.*, **64**, 499, 1967.

2. Williot, J.P., Berliner, C., Ruysschaert, J.M., Jaffe, J., *Eur. Poly. J.*, **7**, 1295, 1971.

3. Vilanove, R., Poupinet, D., Rondelez, F., *Macromolecules*, **21**, 2880, 1988.

4. Kato, T., *Langmuir*, 6, 870, 1990.

5. Earnshaw, J.C., Winch, P.J., *J. Phys.: Condens. Matter*, **2**, 8499, 1990.

6. Earnshaw, J.C., McGivern, R.C., Winch, P.J., *J. Phys. France*, **49**, 1271, 1988.

CHAPTER 5 - POLY(ETHYLENE OXIDE)

Summary

A matched pair of poly (ethylene oxide), samples, one protonated and the other deuterated, have been synthesised by high vacuum anionic methods and characterised for molecular weight by gel permeation chromatography. The results of examination of spread monolayers of these polymers by surface pressure, neutron reflection and ellipsometry techniques are reported.

Classically defined as liquid expanded in type, on scaling law type treatment the surface pressure isotherm of PEO yields a characteristic exponent indicative of good two dimensional solvent conditions with favourable segment - subphase interactions. Neutron reflectometry characterised the film as being much more diffuse and associated with the subphase than was the case for PMMA. Low Q reflectometry data was collected in order to try to characterise the film further. Ellipsometry provided further evidence for the expanded nature of the PEO film, as there was much less contrast and hence sensitivity in the experimental parameters than for other samples studied.

5.1 Synthesis and Characterisation

The methods of high vacuum anionic synthesis described in Chapter 3 were employed to prepare samples of hydrogenous and deuterated poly (ethylene oxide). The weight average molecular weights of these polymers were determined by light scattering, by interpolation of the appropriate Zimm plot to zero concentration, for example Figure 5.1. From the interception on the y-axis the molecular weight values in Table 5.1 were obtained.

Polymer	Intercept	M_w
HPEO	1422	39800
DPEO	1575	35600

Table 5.1 Weight Average Molecular Weights for PEO, estimated from light scattering

Gel permeation chromatography using water as the system solvent was used to obtain estimates for the number and weight average molecular weights of the PEO samples. These values and polydispersity indices are summarised in table 5.2.

Polymer	M_n	M_w	M_w / M_n
HPEO	25800	41000	1.59
DPEO	21600	44000	2.04

Table 5.2 Molecular Weights for PEO, estimated from gel permeation chromatography

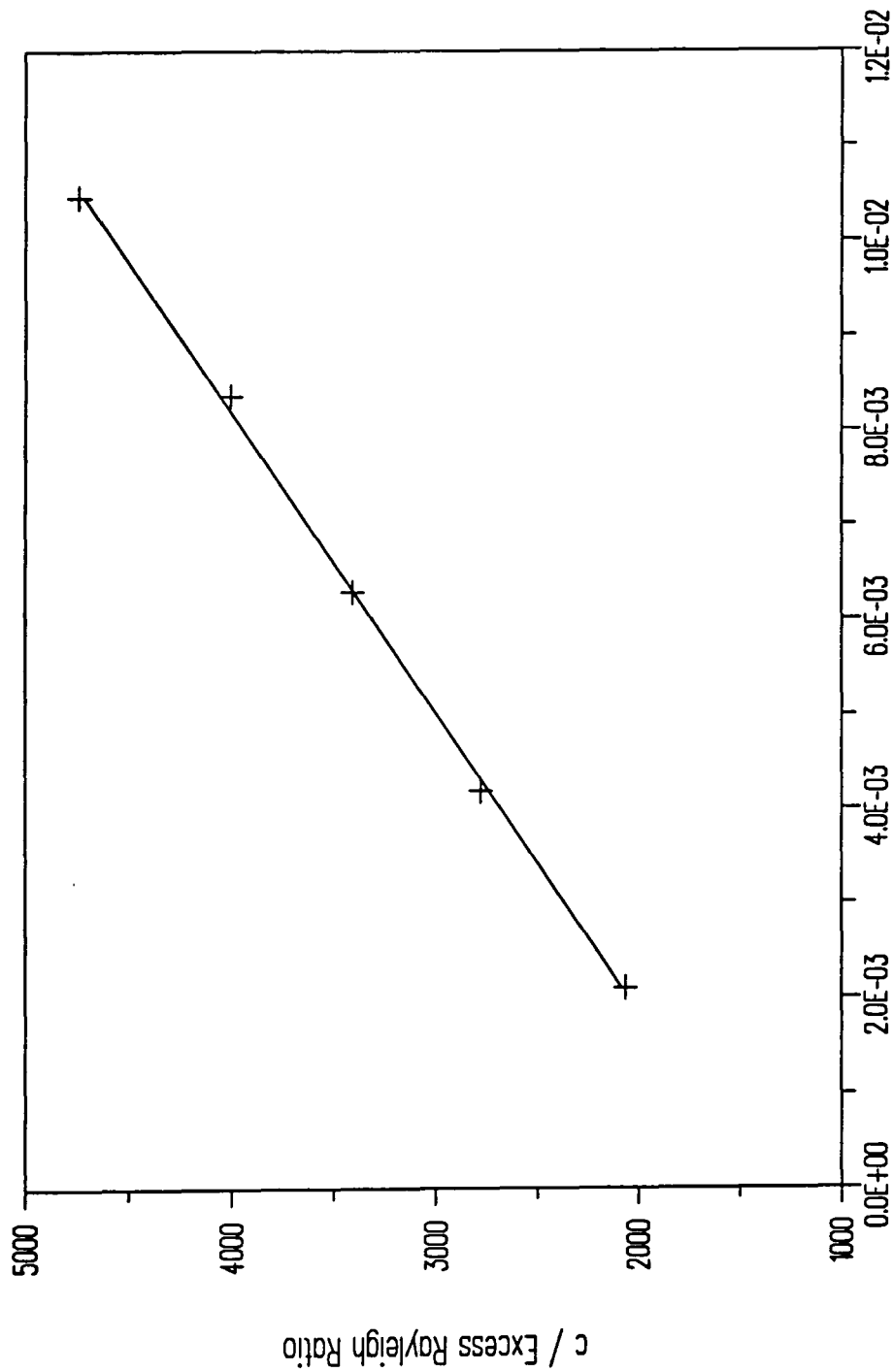

Figure 5.1 Zimm Plot for HPEO in chloroform

5.2 Surface Pressure - Concentration Isotherm Studies

Surface pressure - concentration isotherms have been obtained for HPEO and DPEO at 25°C, figures 5.2 and 5.3. The isotherms were found to be very similar for hydrogenous and deuterated PEO and the reproducibility was excellent provided suitable care was taken in the preparation of the surface. However the plateau region in the isotherm of DPEO occurred at a slightly lower surface pressure, $9mNm^{-2}$, than for HPEO, which gave the classically accepted value of $10mNm^{-2}$.

Considering the isotherm of HPEO, the shape of the isotherm is very different in many ways to those described in the last chapter for poly (methyl methacrylate) and is classically defined as liquid expanded in type. The surface pressure is of much smaller magnitude, with a plateau value of around 10 mN m^{-1} reached at a surface concentration of around 0.6 mg m^{-2} and the surface pressure onset occurs at a much lower surface concentration. Indeed at even the lowest surface concentrations for which data were recorded there is a small but finite surface pressure measurable. When the rapidly rising part of the surface pressure variation is extrapolated back to zero pressure a limiting area per segment of $43Å^2$ is obtained. The very large area per segment suggests that PEO chains at the interface adopt a much more expanded configuration than PMMA as segments exert an influence on one another while still far apart.

The data of figures 5.2 and 5.3 are presented on a double logarithmic scale in the semi-dilute regime in figures 5.4 and 5.5. Linear plots with slope y = 2.91 and 2.90 for HPEO and DPEO respectively are obtained. These correspond to a value of 0.76 for the critical scaling exponent v. The value is unambiguously that for a film in good solvent conditions which has been widely predicted as 0.77. This is indicative of favourable segment - solvent interactions, suggesting again that the

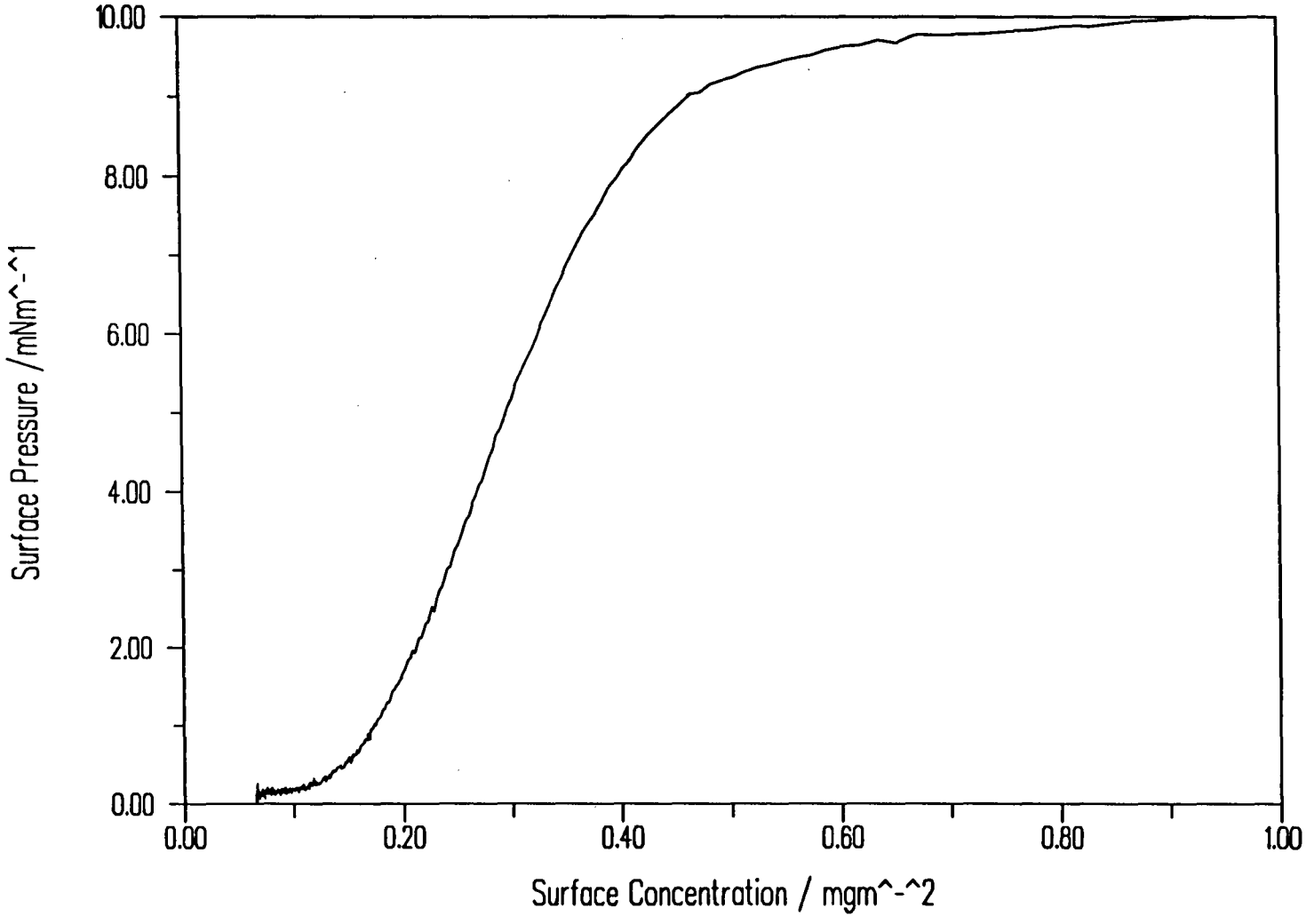

Figure 5.2 Surface Pressure - Surface Concentration Isotherm for HPEO

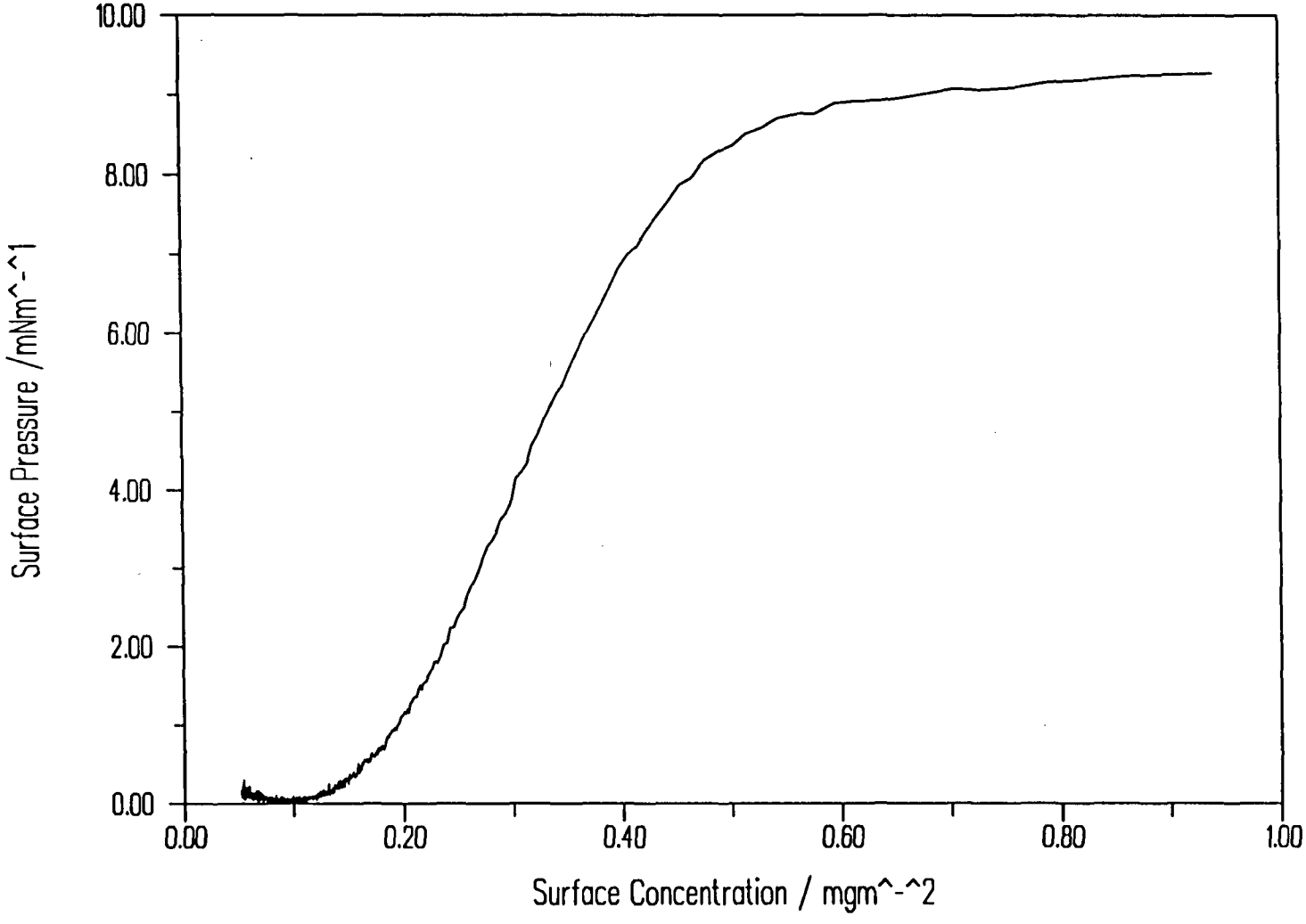

Figure 5.3 Surface Pressure - Surface Concentration Isotherm for DPEO

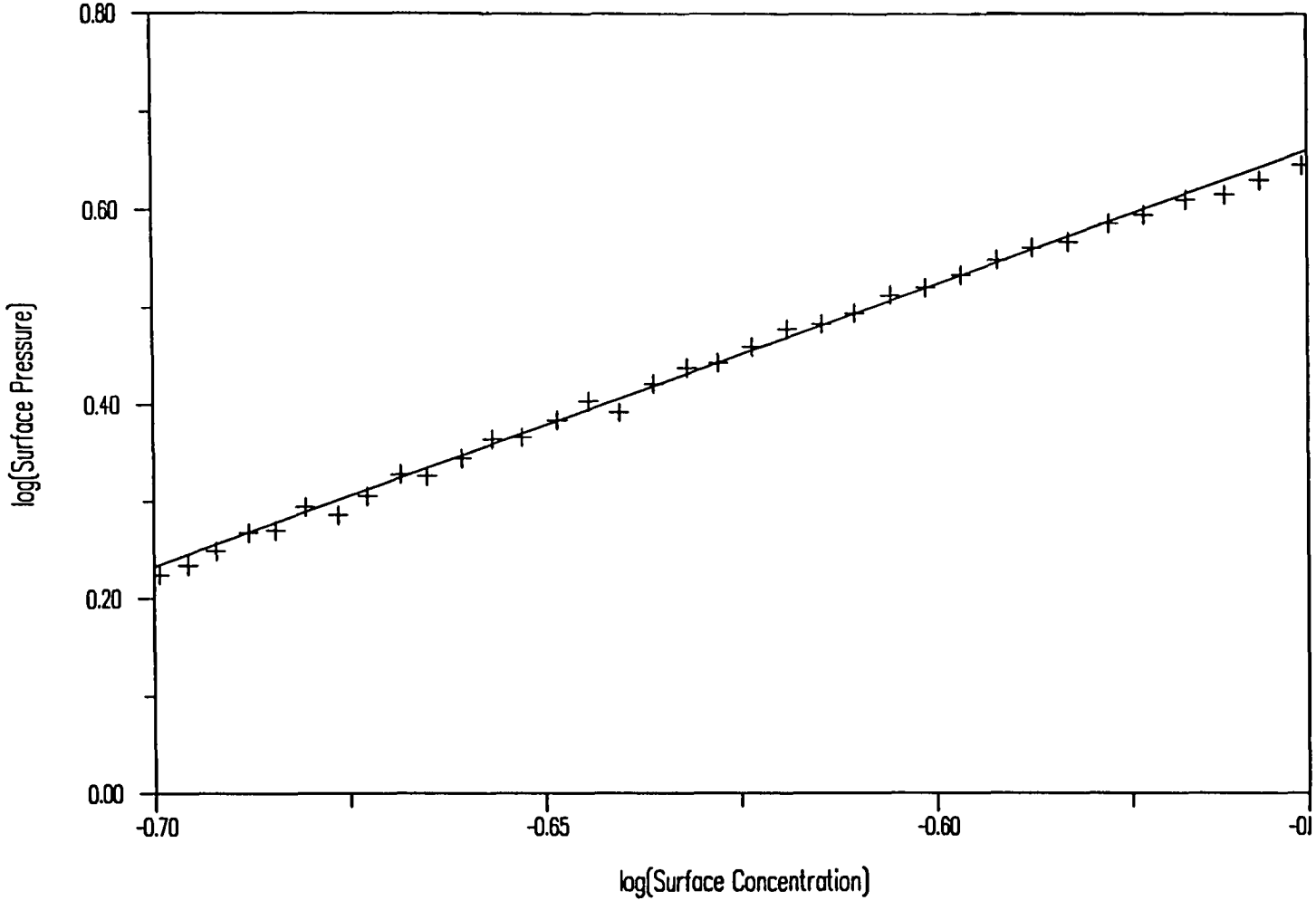

Figure 5.4 Double Logarithmic Plot of Surface Pressure -Surface Concentration Data for HPEO

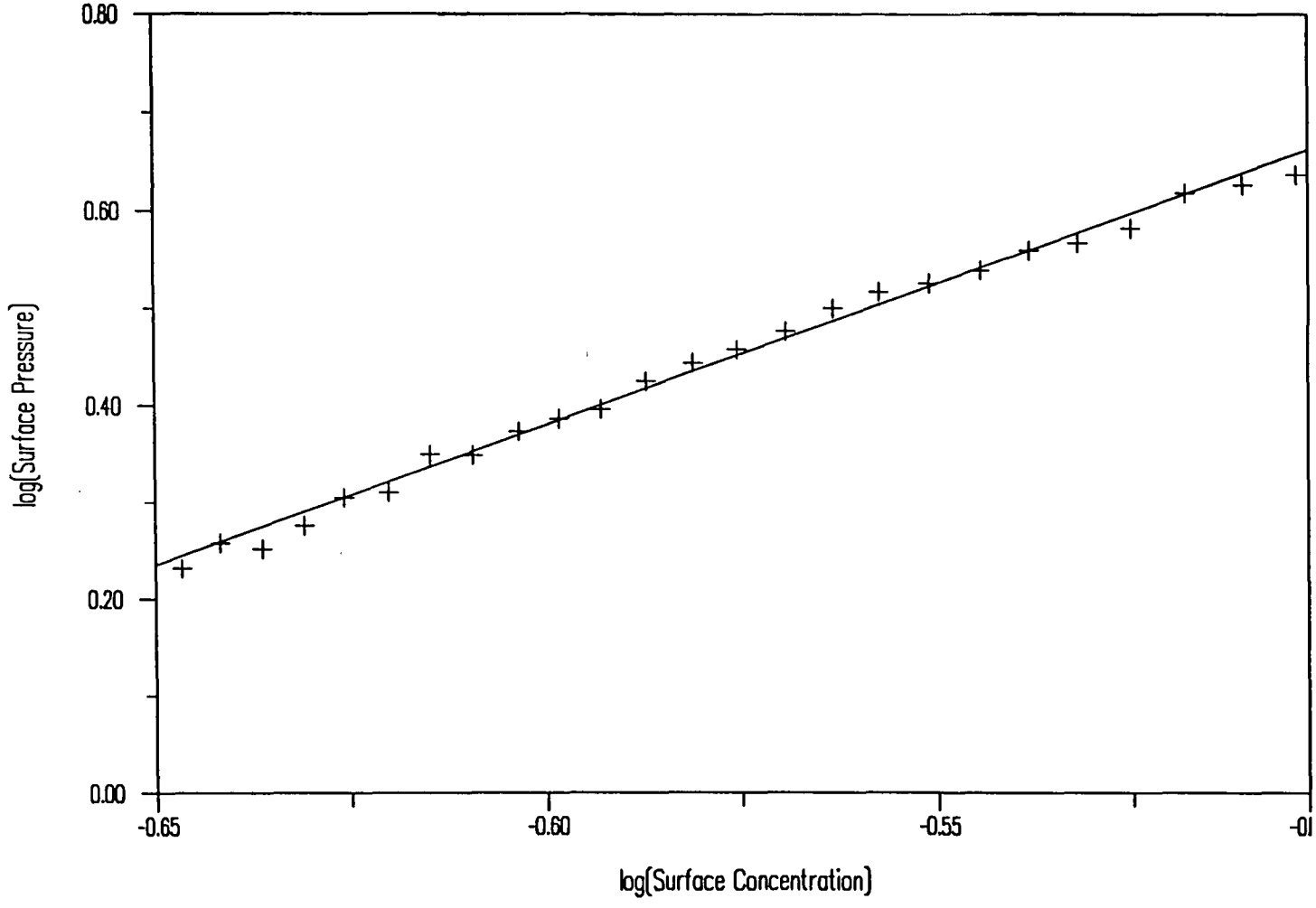

Figure 5.5 Double Logarithmic Plot of Surface Pressure - Surface Concentration Data for DPEO

chains are likely to favour as expanded a form as possible in order to maximise such interactions. Further support for such a picture of the PEO film is obtained by examination of the dilute regime by equation of state plotting, figures 5.6 and 5.7. The slope of the plot of π/Γ v Γ is positive in this case, corresponding to a positive two dimensional second virial coefficient for the segment - solvent interaction. As previously discussed for PMMA it has not been possible to produce any meaningful extrapolation of this data to zero concentration in order to obtain a molecular weight value or numerical value of the second virial coefficient.

5.2.1 Kinetic and Hysteresis Effects in PEO Monolayers

The surface pressure isotherms reported thus far have been exclusively compression isotherms, that is after initial spreading and a delay of approximately ten minutes to ensure evaporation of the solvent and expansion of the film to cover the available area, the surface pressure is recorded as the film is compressed slowly by bringing the trough barriers together. Given that PEO is bulk soluble in water some questions must arise as to the stability of PEO monolayers over a period of time when spread on water. To try and elucidate this matter PEO monolayers have been subjected to compression and expansion cycles to various limiting surface and concentrations and the degree of hysteresis (difference between successive compression and expansion isotherms) observed.

Compression-expansion cycle isotherms for HPEO compressed to 0.8, 0.6, 0.4, and 0.3 mgm^{-2} are shown in figures 5.8 to 5.11. The hysteresis is seen to depend upon the surface pressure/concentration to which the film is compressed. At $\Gamma = 0.8$ mgm^{-2} there is a large effect and on subsequent repetition of the cycle there is further hysteresis whereas at $\Gamma = 0.4$ mgm^{-2} the effect is much smaller. At lower compressions such as $\Gamma = 0.3$ mgm^{-2} there is no hysteresis at all suggesting that the

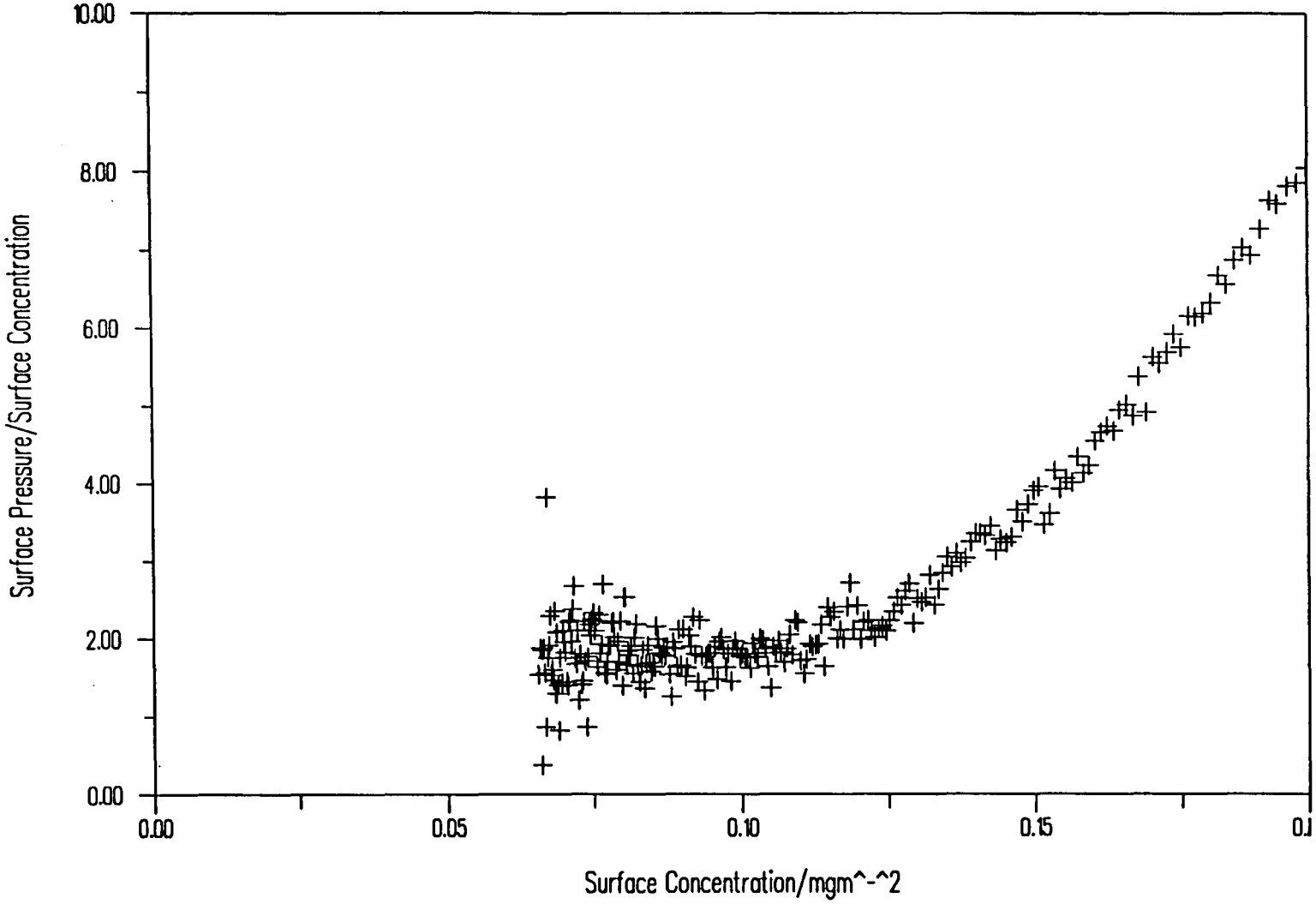

Figure 5.6 Surface Pressure/Surface Concentration v Surface Concentration for HPEO

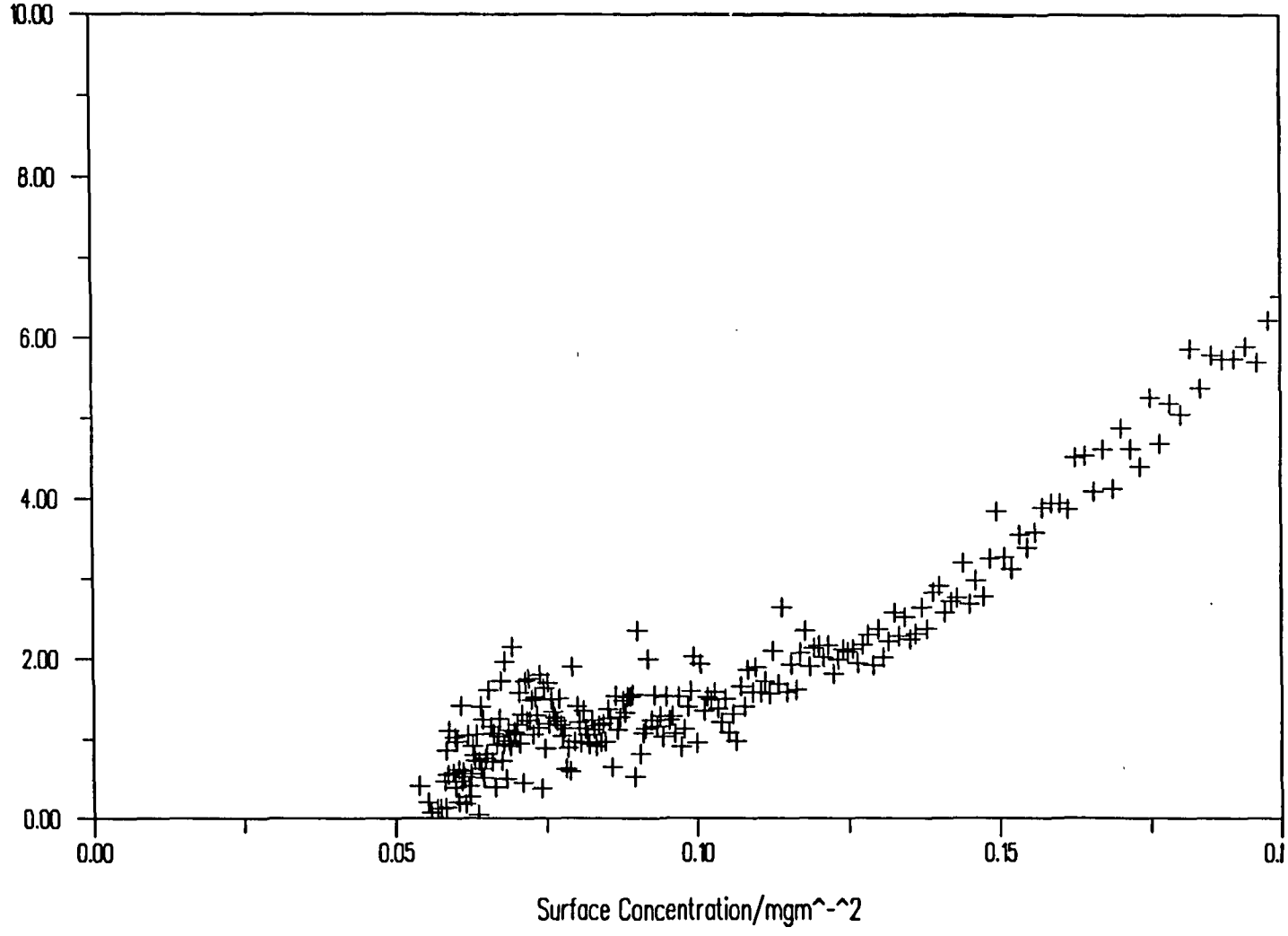

Figure 5.7 Surface Pressure/Surface Concentration v Surface Concentration for DPEO

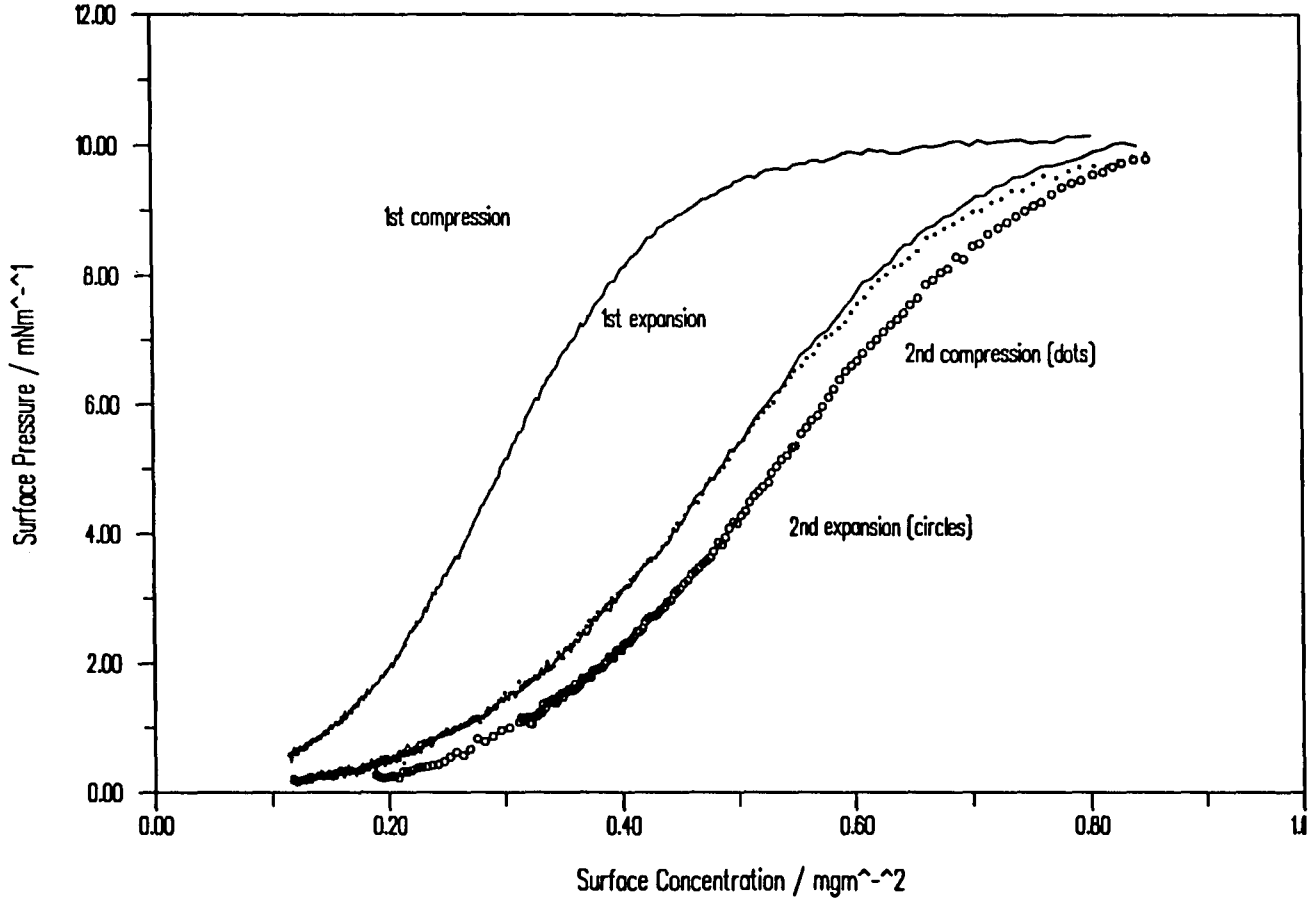

Figure 5.8 Compression - Expansion Surface Pressure Cycles for HPEO from $\Gamma = 0.8 mgm^{-2}$

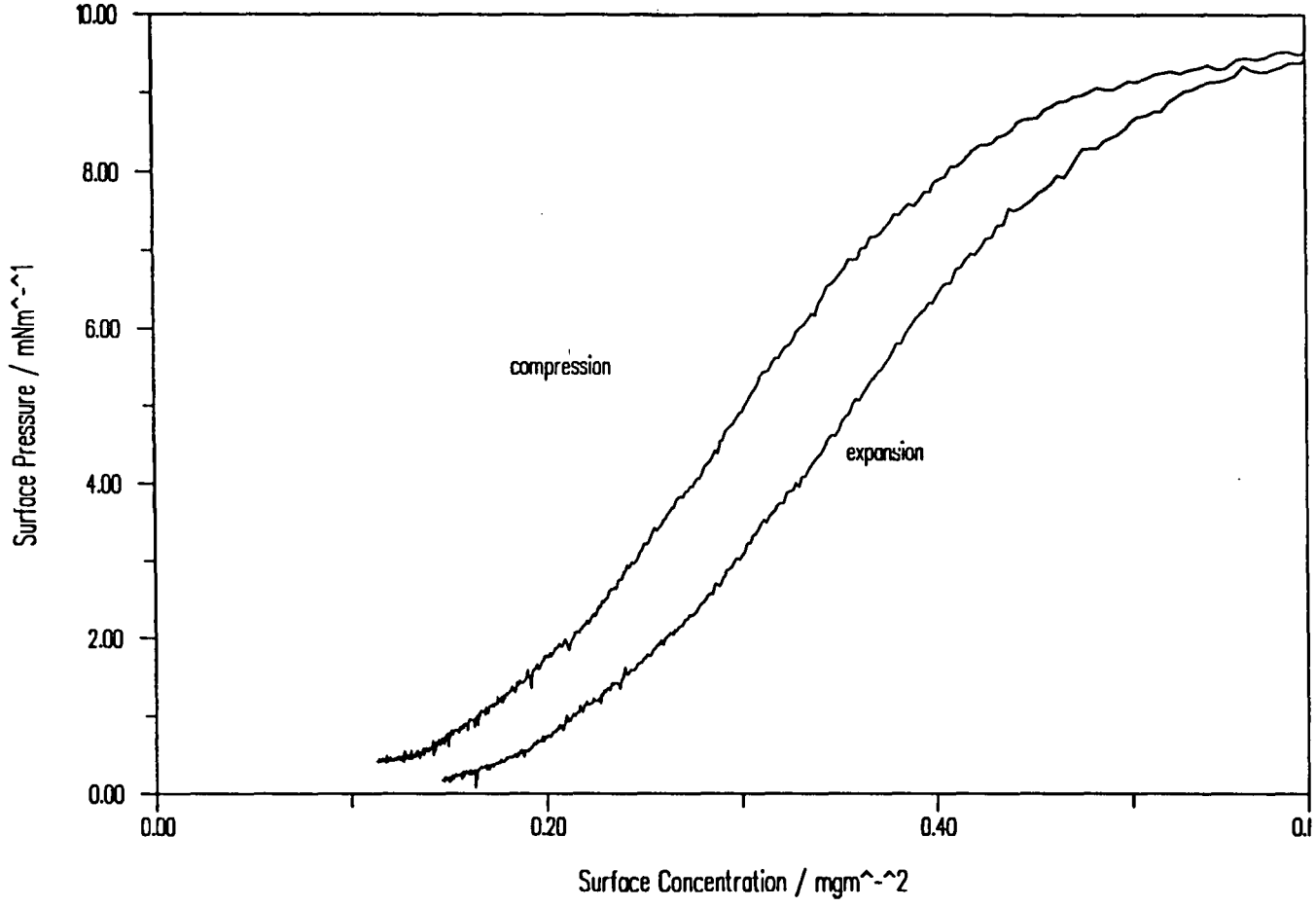

Figure 5.9 Compression - Expansion Surface Pressure Cycle for HPEO from $\Gamma = 0.6 mgm^{-2}$

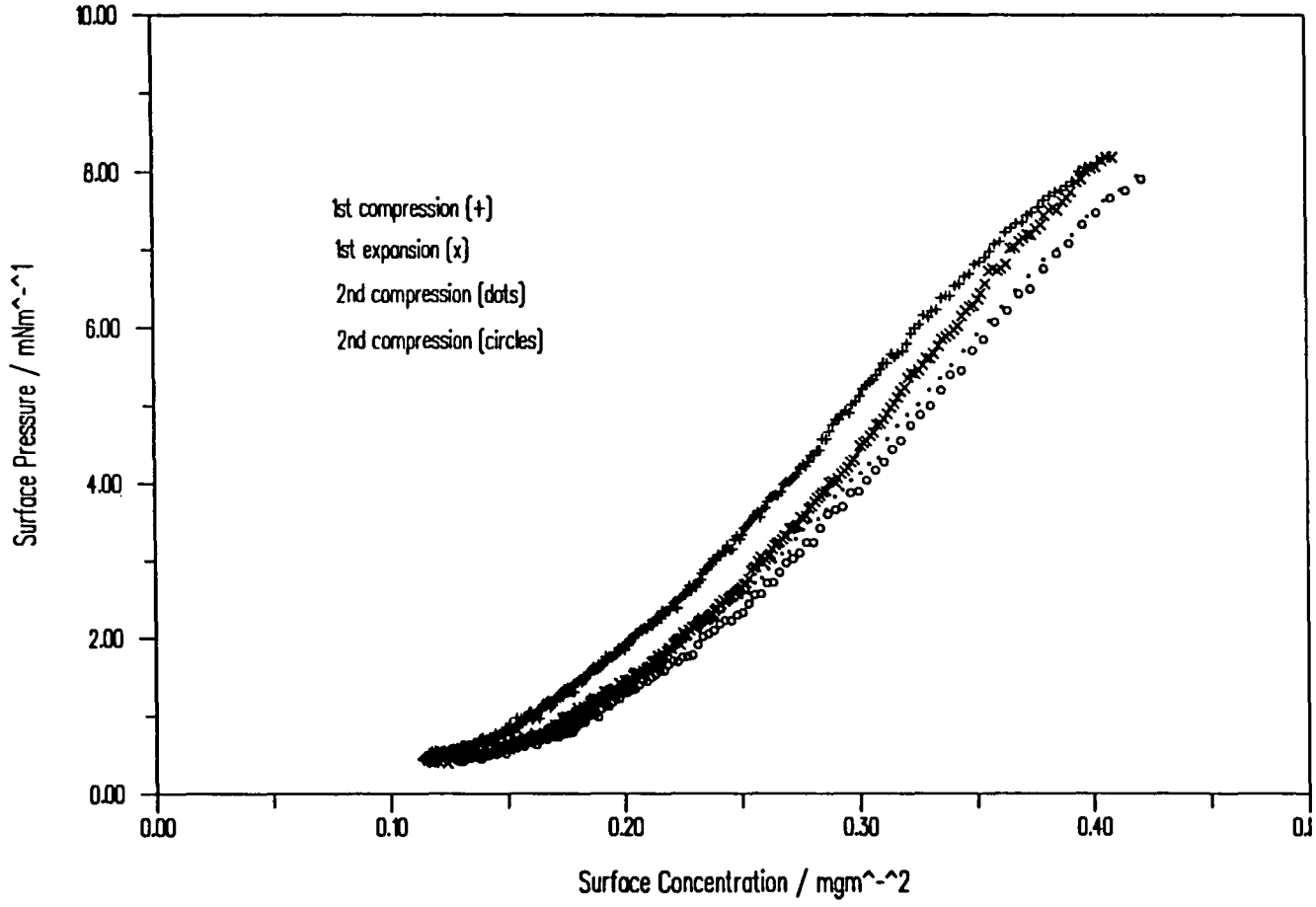

Figure 5.10 Compression - Expansion Surface Pressure Cycles for HPEO from $\Gamma = 0.4 mgm^{-2}$

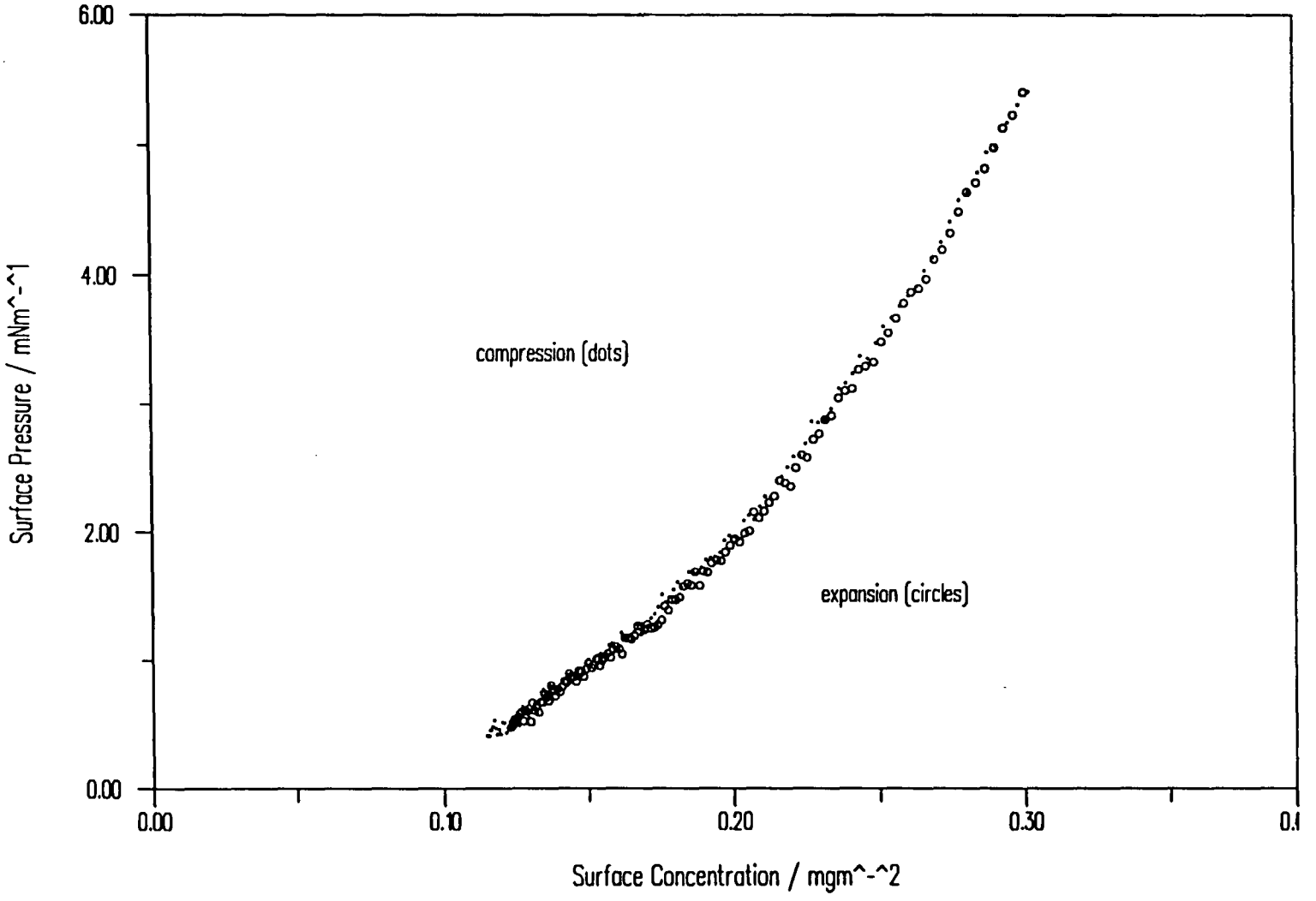

Figure 5.11 Compression - Expansion Surface Pressure Cycle for HPEO from $\Gamma = 0.3 mgm^{-2}$

effect may be associated in some way with the change in the slope of the compression isotherm between Γ = 0.3 and 0.4 mgm^{-2}. The hysteresis effect is such that at a given surface concentration there is a lower expansion surface pressure than measured on compression. This suggests either a larger area per segment becoming available by some dipping or relaxation mechanism or else loss of material by dissolution over the time scale of the measurement.

The surface pressure of compressed HPEO monolayers was studied as a function of time by carrying out a normal compression isotherm to a given surface concentration and then recording the surface pressure with time as the barriers were held still. Figure 5.12 shows superimposed data for surface concentrations held at Γ = 0.8, 0.6, 0.4, 0.3, and 0.2 mgm^{-2} over periods of time ranging from one to three hours.

At the highest surface concentration there is a dramatic time dependence in the surface pressure which decays aways in a function of approximately Gaussian appearance. The same shape is evident at Γ = 0.6 mgm^{-2} although the rate of decay appears to be considerably reduced given the relatively small difference in the starting t = 0 surface pressure. At intermediate surface concentrations the decay shape seems to change slightly to a more exponential form and the rate of decay is reduced again. Finally at Γ = 0.2 mgm^{-2} there is virtually no decay in the surface pressure and it would appear that at large time values the other curves are tending to drop towards this limit in the surface pressure.

It would appear therefore that there are considerable time dependent effects in PEO monolayers which cannot be explained solely in terms of overshoot arguments concerning the rate of compression of the film. Either dramatic rearrangements of film structure which result in a lower surface pressure are occurring or there is loss of up to 75% of the film material to bulk solution over the period of one to three hours. These observations will be reconsidered together with

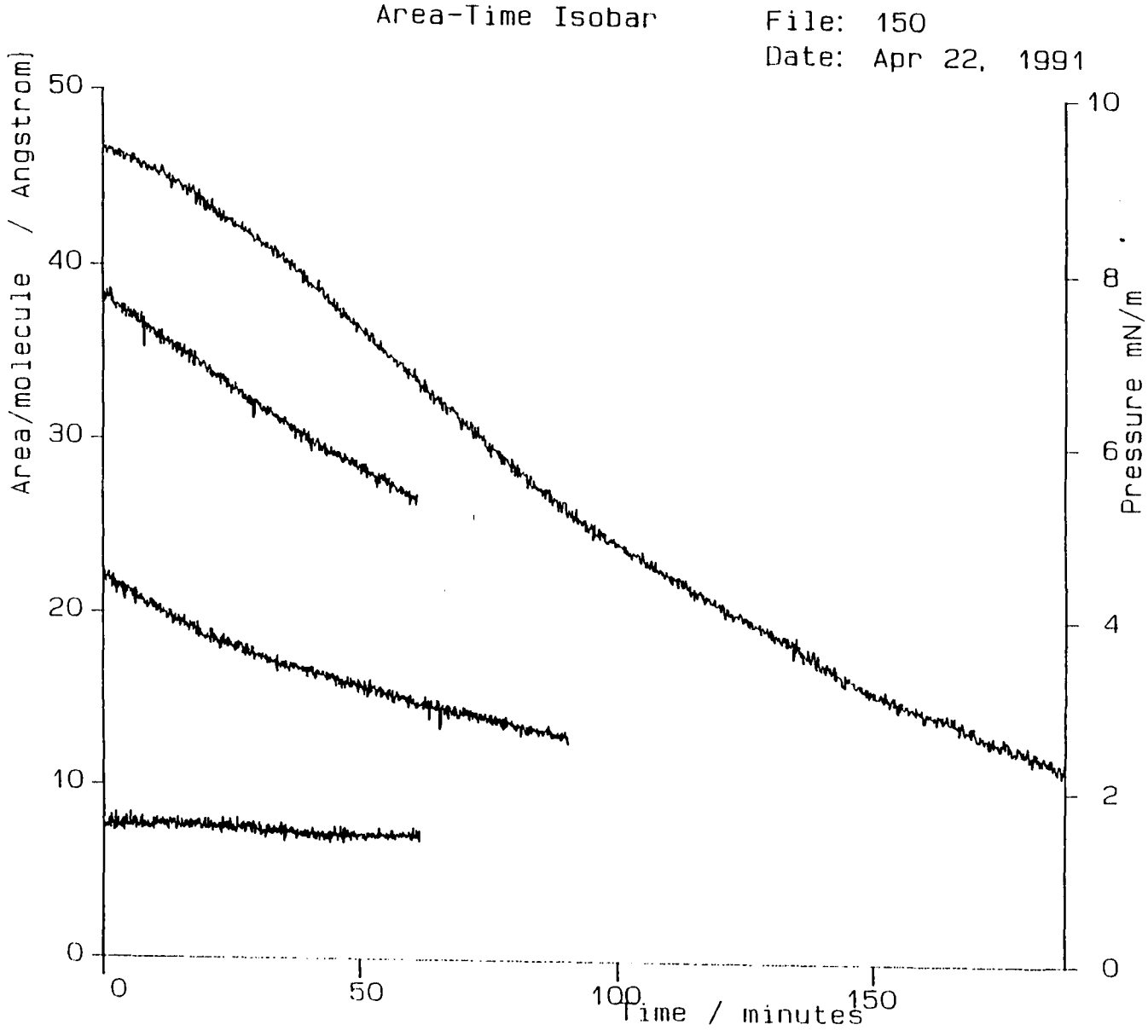

Figure 5.12 Surface Pressure as a function of time for PEO monolayers held at various surface concentrations

neutron reflectivity data.

5.3 Neutron Reflectometry

Neutron reflectometry studies on monolayers of PEO were carried out exclusively on CRISP. Given that surface pressure measurements indicated that it was likely that the polymer was present in some sort of expanded configuration at the interface, reflectivity data was recorded over the Q range $0.01 \leq Q/Å^{-1} \leq 0.65$ in order to provide sensitivity to long range effects. This was achieved by carrying out identical experiments at three different incident beam angles to provide three individual profiles with overlapping Q values such that when combined they provided one reflectivity profile. Studies were carried out at two contrasts, DPEO on air contrast matched water, and HPEO on D_2O.

The experimentally determined profiles for a series of surface concentrations in the range 0.2 - 0.8 mg m^{-2} are shown in figures 5.13 and 5.14. For the case of the deuterated polymer on air contrast matched water there is an increase in the measured reflectivity with increasing surface concentration, and conversely for the hydrogenous film on D_2O the subphase reflectivity signal is depressed somewhat by the addition of polymer. It should be noted however that the magnitude of these effects is rather smaller than for poly(methyl methacrylate). It is noticeable that for the deutero polymer on air contrast matched water there is a rather steep initial decay in reflectivity, indicative of a rather thick layer.

Applying a similar rational to data fitting as previously employed for PMMA a single layer residual scan has been used as the initial basis of calculation. The fitted values so obtained are summarised in table 5.3. The layer thickness and scattering length densities based on these fits are listed in table 5.4 and figures 5.15 and 5.16. Corresponding volume fraction composition and apparent surface coverage values are shown in table 5.5 and figures 5.17 and 5.18.

It is evident from these figures that the model fails to describe the

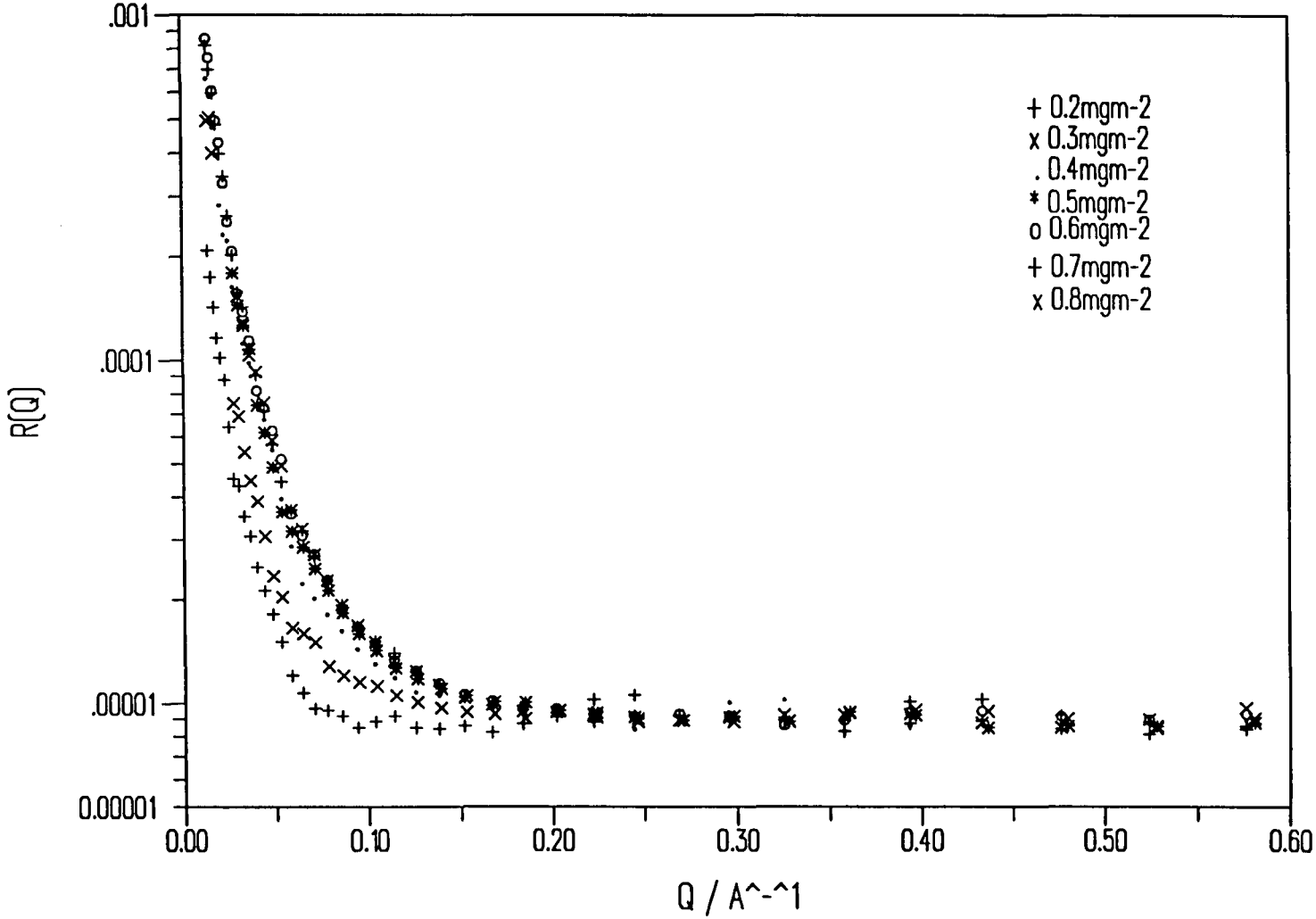

Figure 5.13 Neutron Reflectivity Profiles for DPEO on air contrast matched water

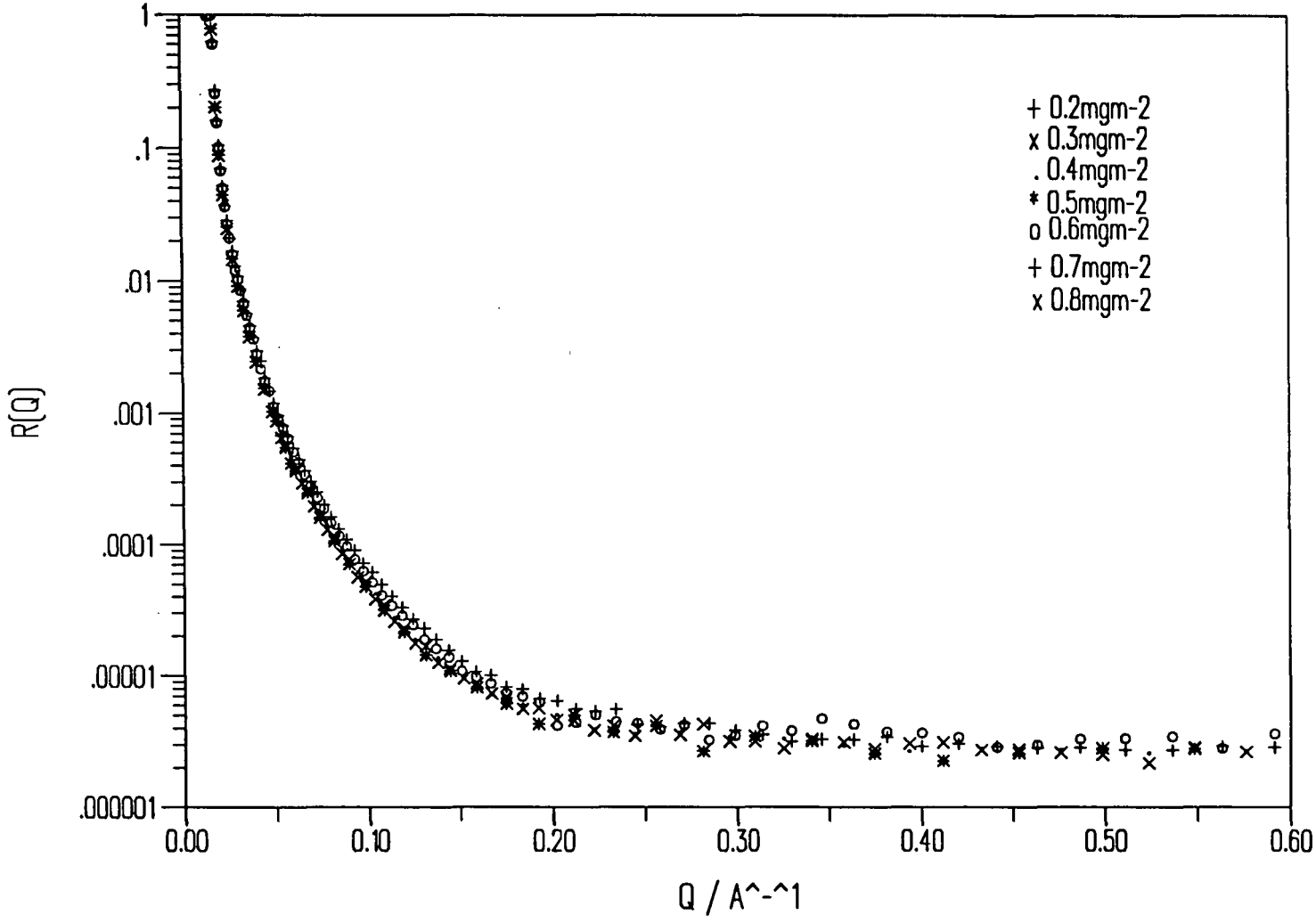

Figure 5.14 Neutron Reflectivity Profiles for HPEO on D2O

Γ/mg m^{-2}	D/acmw			H/D_2O		
	d/Å	$\rho/10^{-6}$Å^{-2}	res/10^{-2}	d/Å	$\rho/10^{-6}$Å^{-2}	res/10^{-2}
0.2	62	0.26	0.3838	17	6.08	0.4626
0.3	37	0.50	0.4464	22	5.60	0.7210
0.4	37	0.77	0.5689	21	5.53	0.8923
0.5	29	0.96	0.5480	21	5.41	0.8595
0.6	32	0.98	0.5452	17	5.69	0.5952
0.7	30	1.04	0.6444	-	-	-
0.8	24	1.15	0.4924	21	5.42	1.083

Table 5.3 Single Slab Model Fitted Parameters for PEO on water

Γ/mg m^{-2}	D/acmw			H/D_2O	
	d/Å	$\rho/10^{-6}$Å^{-2}	res/10^{-2}	$\rho/10^{-6}$Å^{-2}	res/10^{-2}
0.2	40	0.37	0.7728	6.17	0.5421
0.3	30	0.59	0.4936	5.74	1.126
0.4	29	0.94	0.7201	5.63	1.040
0.5	25	1.08	0.5857	5.49	1.032
0.6	25	1.26	0.7329	5.91	0.7023
0.8	23	1.20	0.5020	5.42	1.071

Table 5.4 Single Slab Model Fitted Parameters for PEO on water - residual optima

system very satisfactorily. There is an extremely large difference between the positions of the residual minima for the two contrasts at the same surface concentration, particularly at low coverages, and the back calculated values of the surface concentration are a slight overestimate at low coverages and an underestimate at higher coverages.

In the light of information gained about the structure of solution surface

Γ/mg m^{-2}	Volume Fraction			ρ.d/10^{-6}Å^{-1}	a.p.m./Å^{2}monomer^{-1}	Γ_a/mgm^{-2}
	polymer	water	air			
0.2	0.06	0.97	-0.03	14.8	30.9	0.26
0.3	0.09	0.90	0.01	17.7	25.9	0.31
0.4	0.15	0.87	-0.02	27.3	16.8	0.47
0.5	0.17	0.85	-0.02	27.0	17.0	0.47
0.6	0.20	0.91	-0.11	31.5	14.5	0.55
0.7	0.16	-	-	31.2	14.7	0.54
0.8	0.19	0.84	-0.03	27.6	16.6	0.48

Table 5.5 Layer Composition and Apparent Coverage Variation for PEO on water

excess adsorbed poly(ethylene oxide) from neutron reflectometry[1], an attempt was made to fit the data with a two layer model constraining the first layer thickness and density by the best single layer fit values. However no sensible fit was possible by this route for which a better fit (according to the residual value) was obtained.

Consequently a third strategy was adopted. Arbitrarily fixing the first layer thickness d_1, the three parameters ρ_1, d_2 and ρ_2 were allowed to float from reasonably estimated values. By a similar residual scan process to that used for the single layer model, optimum values for the four model parameters were obtained for both contrasts. d_1 was the preferred variable to scan as it was found that the shape of the residual minimum curve was slightly steeper when scanning d_1 than d_2. In addition, carrying out similar scans from fixed values for the other parameters in turn, the minima in these fits were found to converge on the same solutions obtained by the method just outlined, suggesting that a consistent solution was reached for each minimisation route.

It was found that the quality of the fit was more sensitive to moving the model further from the best fit values for DPEO/acmw than those for HPEO/D_2O,

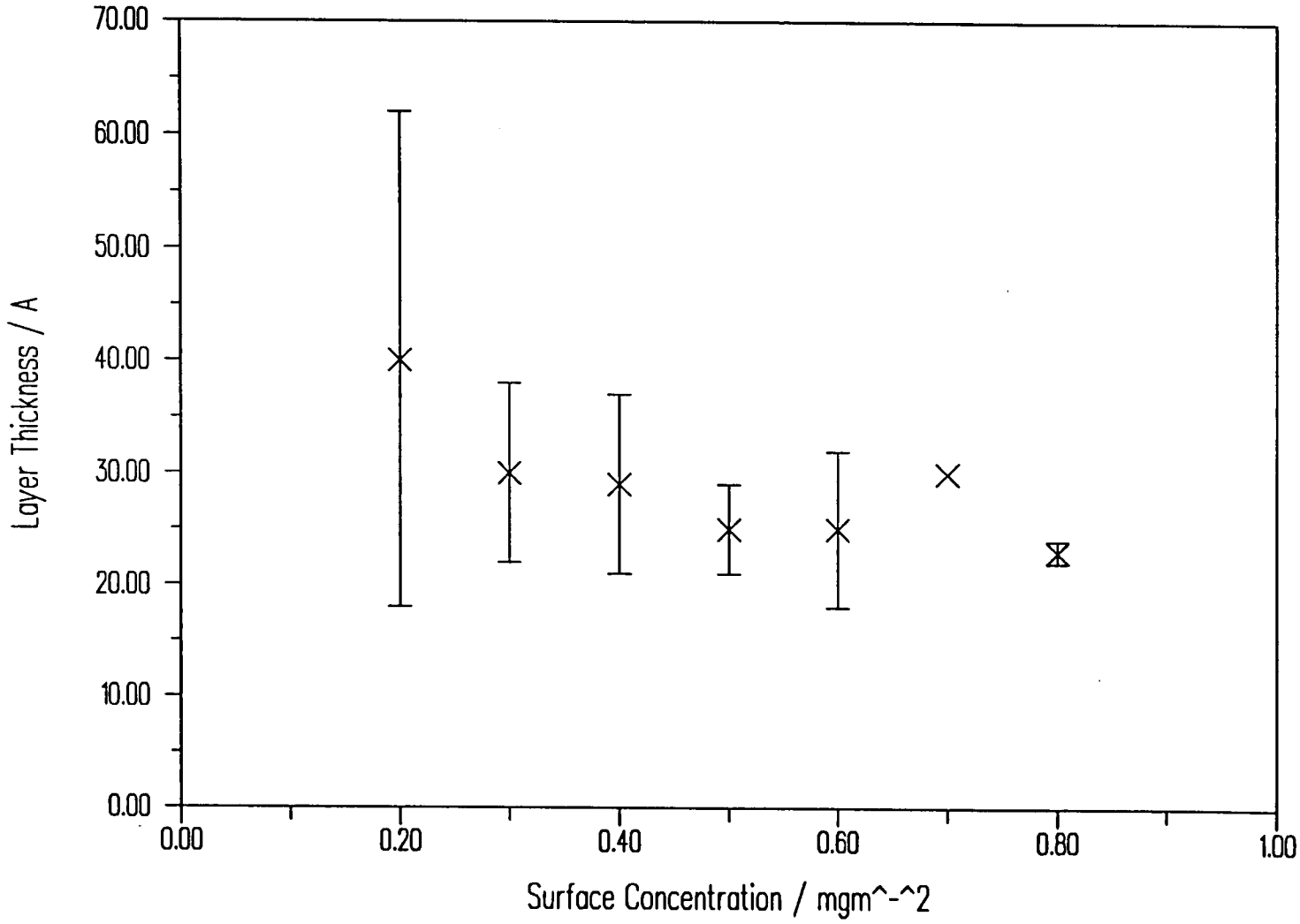

Figure 5.15 Variation of Layer Thickness with Surface Concentration for PEO on water

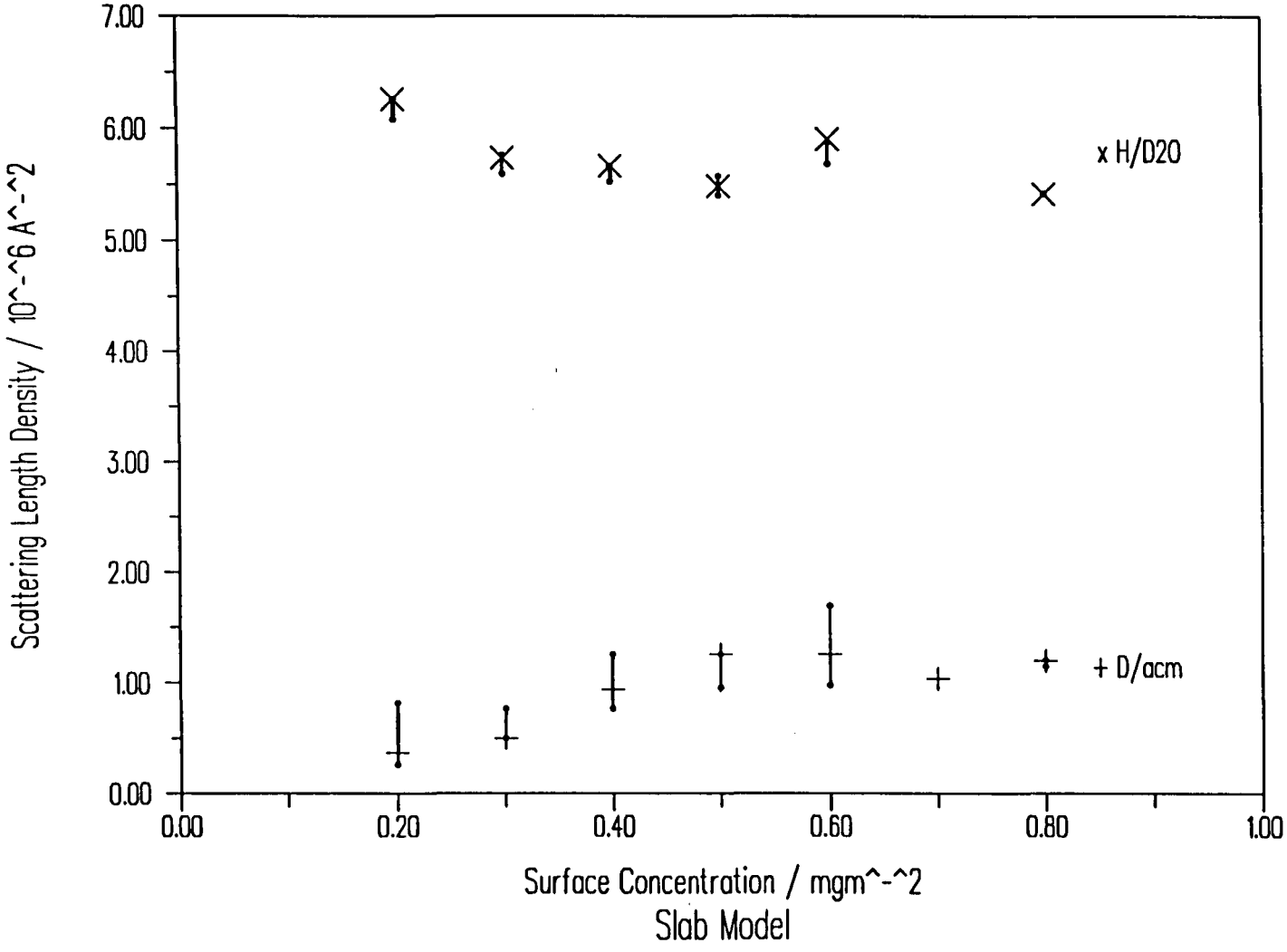

Figure 5.16 Variation of Scattering Length Density with Surface Concentration for PEO

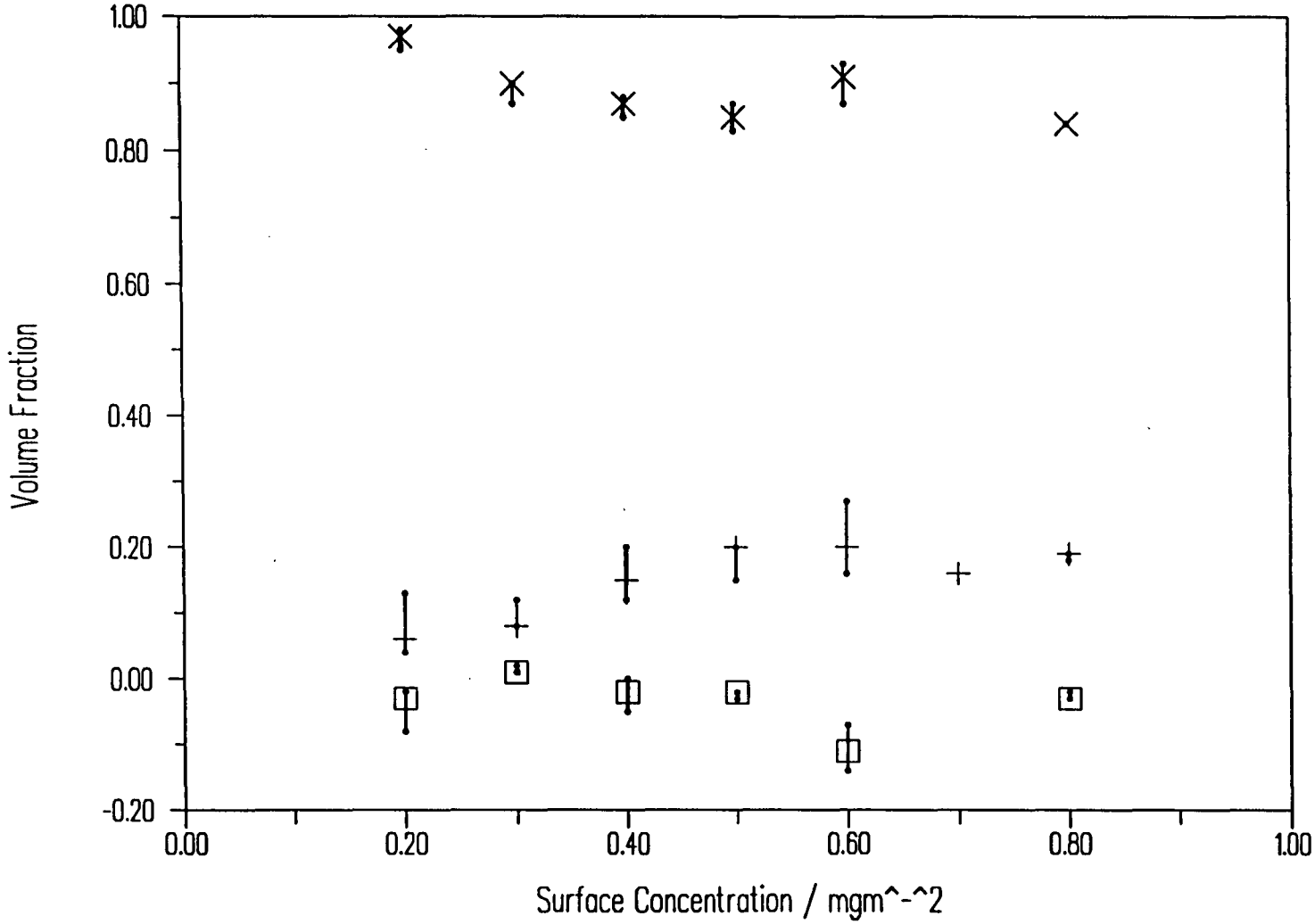

Figure 5.17 Variation in Layer Composition with Surface Concentration for PEO on water

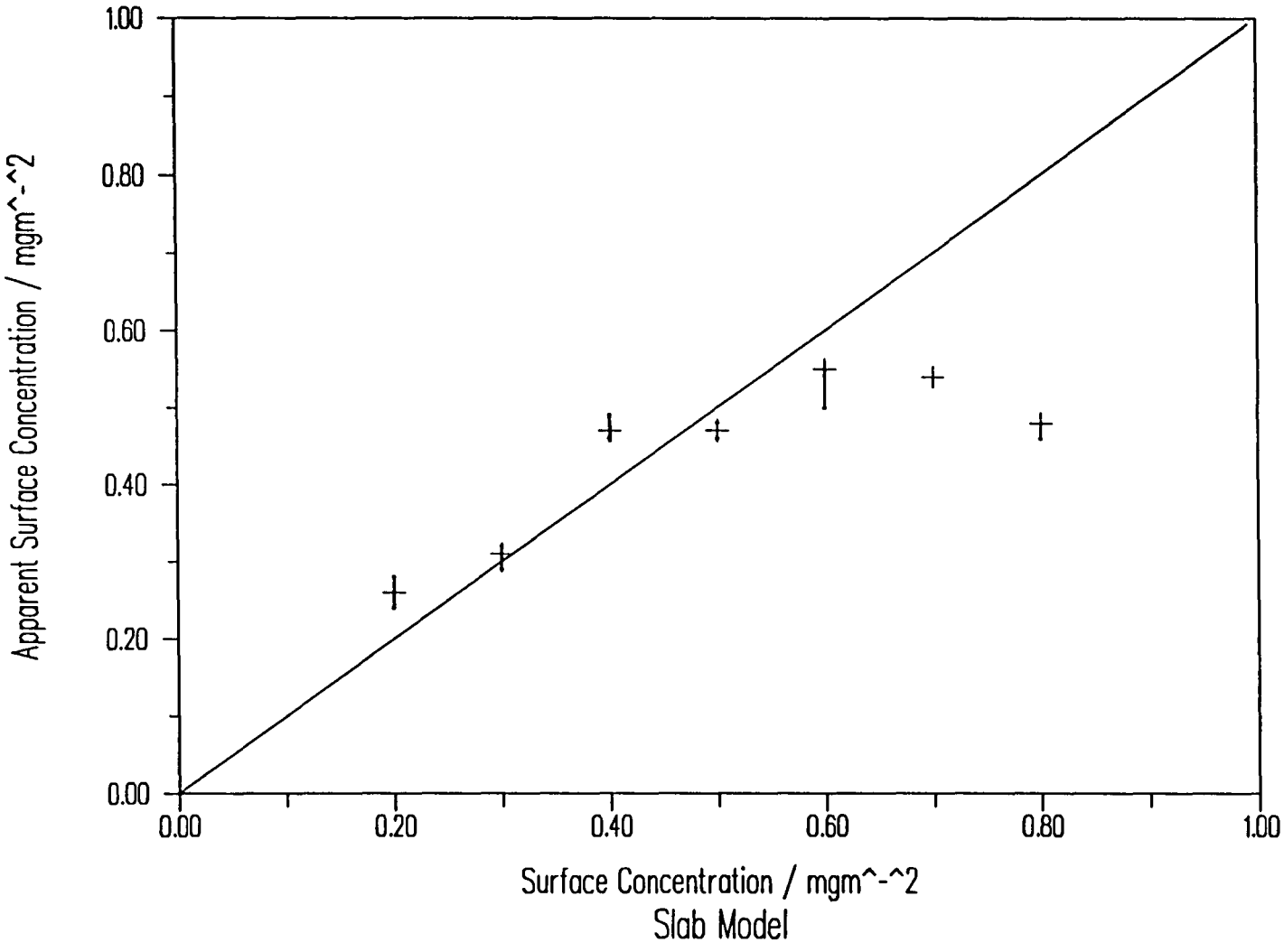

Figure 5.18 Apparent Surface Concentration against Dispensed Surface Concentration for PEO on water

and hence those layer thicknesses were selected as the optimum fitted values. The final two layer model parameters are summarised in tables 5.6 and 5.7. Figures 5.19-24 show the trends in the two layer fitted values. The uncertainty in the layer thicknesses is probably of the order of the scatter in the values and may be seen to be fairly large for the lower layer in particular. Similarly the scattering length densities obtained are subject to some uncertainty due to the coupling of layer thickness and density. However the values of tables 5.6 and 5.7 provide reasonable estimates within the limit of the measurement.

A final approach to data fitting was adopted in which instead of using a slab model for the film, an attempt was made to use a physically more realistic model by treating the film as a scattering length density gradient from the air film interface to the bulk subphase scattering length density value. Two such diffuse gradient models were used, namely a Gaussian (normal) distribution and an exponential decay. The diffuse gradients were generated by splitting the thickness of the film into twenty incremental slab layers. The decay was characterised in each case by the scattering length density of a nominal "top" layer at the air - film side, (the value of ρ decaying in a Gaussian or exponential fashion from this value to that of the bulk subphase) and by a "characteristic length", conceptually the equivalent of the slab thickness in the simpler model.

The characteristic length was defined for the Gaussian decay to be that distance equivalent to two standard deviations of the distribution (corresponding to 95% of the total integral of the distribution) and for the exponential decay as twice that distance from the air - film interface by which the value of the scattering length density had fallen to 1/e of its original value. These definitions were chosen to provide characteristic lengths for each distribution which were roughly comparable in terms of the depth at which the scattering length density had reached a value which was essentially that of the subphase.

Γ/mg m^{-2}			D/acmw			H/D_2O		
	d_1/Å	d_2/Å	$\rho_1/10^{-6}$Å^{-1}	$\rho_2/10^{-6}$Å^{-1}	residual/10^{-2}	$\rho_1/10^{-6}$Å^{-1}	$\rho_2/10^{-6}$Å^{-1}	residual/10^{-2}
0.2	17	47	0.20	0.27	0.3825	6.08	6.30	0.4564
0.3	24	49	0.69	0.08	0.2765	5.59	6.19	0.7084
0.4	22	35	1.07	0.17	0.4290	5.43	6.10	0.9219
0.5	24	55	1.13	0.09	0.3373	5.41	6.15	0.9058
0.6	23	43	1.23	0.12	0.2951	5.84	6.28	0.6619
0.7	24	48	1.19	0.10	0.3333	-	-	-
0.8	-	-	-	-	-	-	-	-

Table 5.6 Two Layer Fitted Parameters for PEO on water

Γ/mg m^{-2}	Volume Fractions (Layer 1)			Volume Fractions (Layer 2)			$\Sigma\rho.d/10^{-6}$Å^{-1}	a.p.m. / Å^2 monomer^{-1}	Γ_a/mgm^{-2}
	polymer	water	air	polymer	water	air			
0.2	0.03	0.95	0.02	0.04	0.99	-0.03	16.1	28.5	0.28
0.3	0.11	-	-	0.01	-	-	20.5	22.4	0.36
0.4	0.17	0.84	-0.01	0.03	0.96	0.01	29.5	15.5	0.51
0.5	0.18	-	-	0.01	-	-	32.1	14.3	0.56
0.6	0.19	0.90	-0.09	0.02	0.99	-0.01	33.5	13.7	0.58
0.7	0.19	-	-	0.02	-	-	33.4	13.7	0.58
0.8	-	-	-	-	-	-	-	-	-

Table 5.7 Volume Fraction and Apparent Surface Coverage values for PEO on water - two layer model

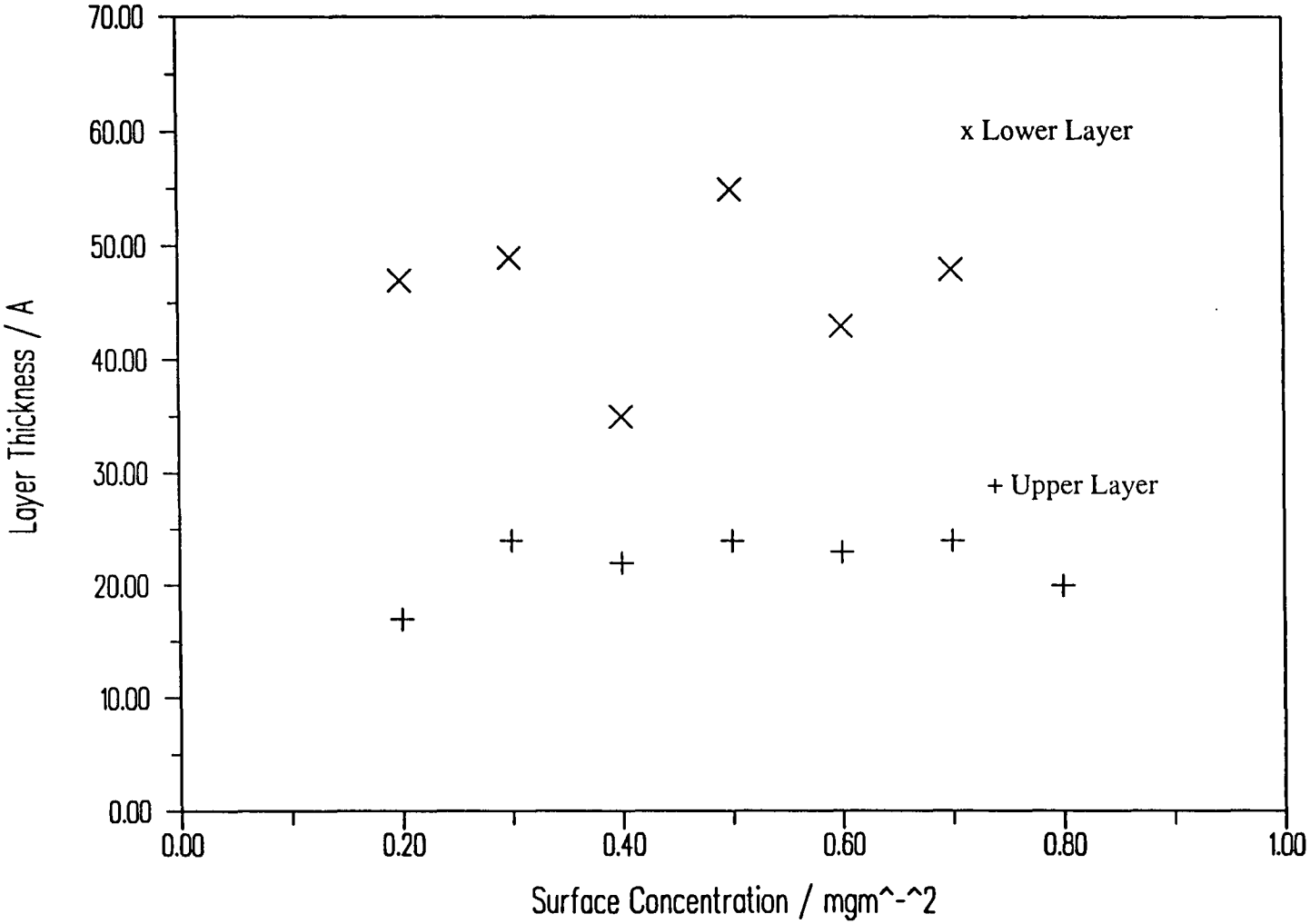

Figure 5.19 Layer Thicknesses v Surface Concentration for PEO on water, two layer model

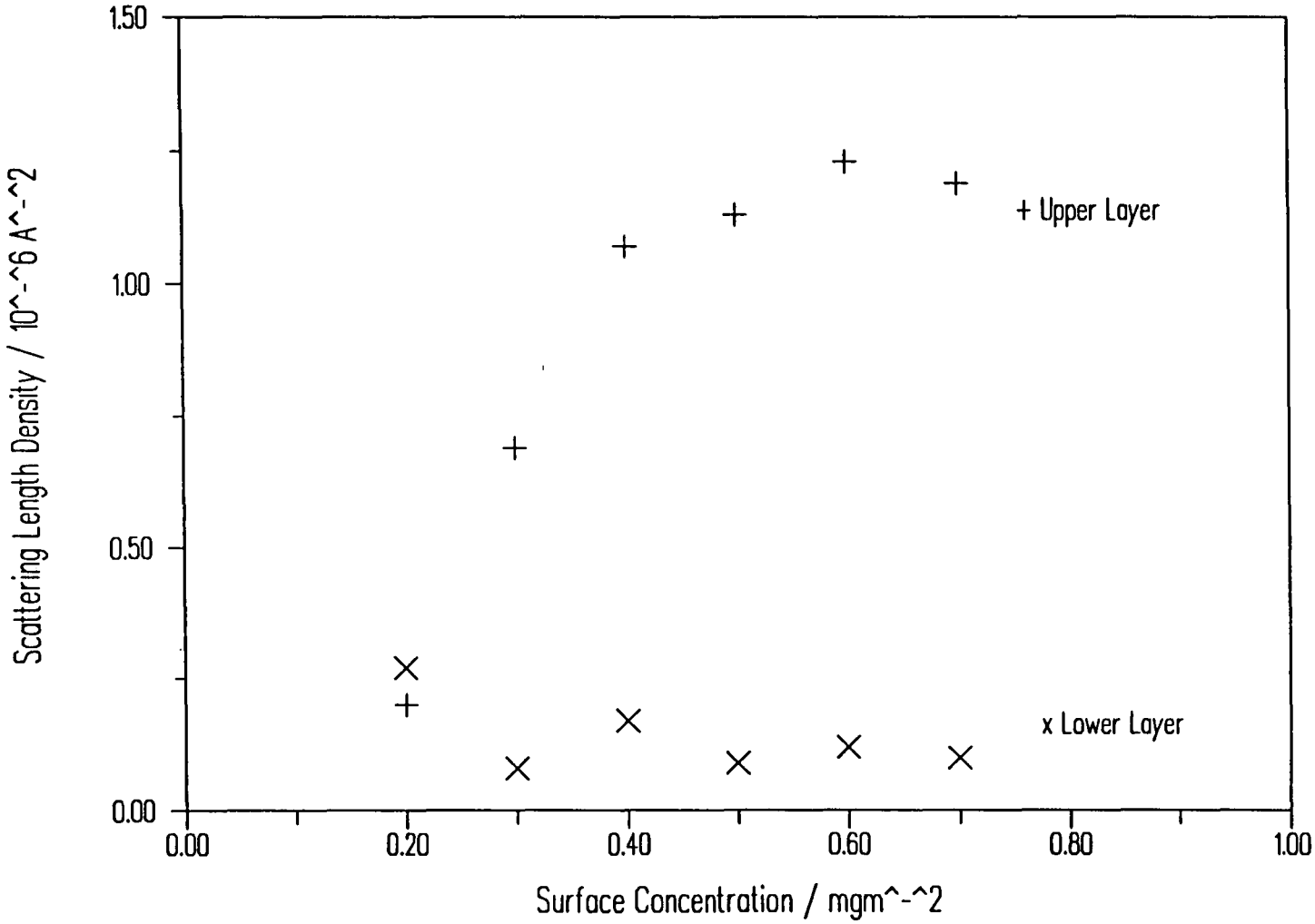

Figure 5.20 Scattering Length Density v Surface Concentration for DPEO on acmw, two layer model

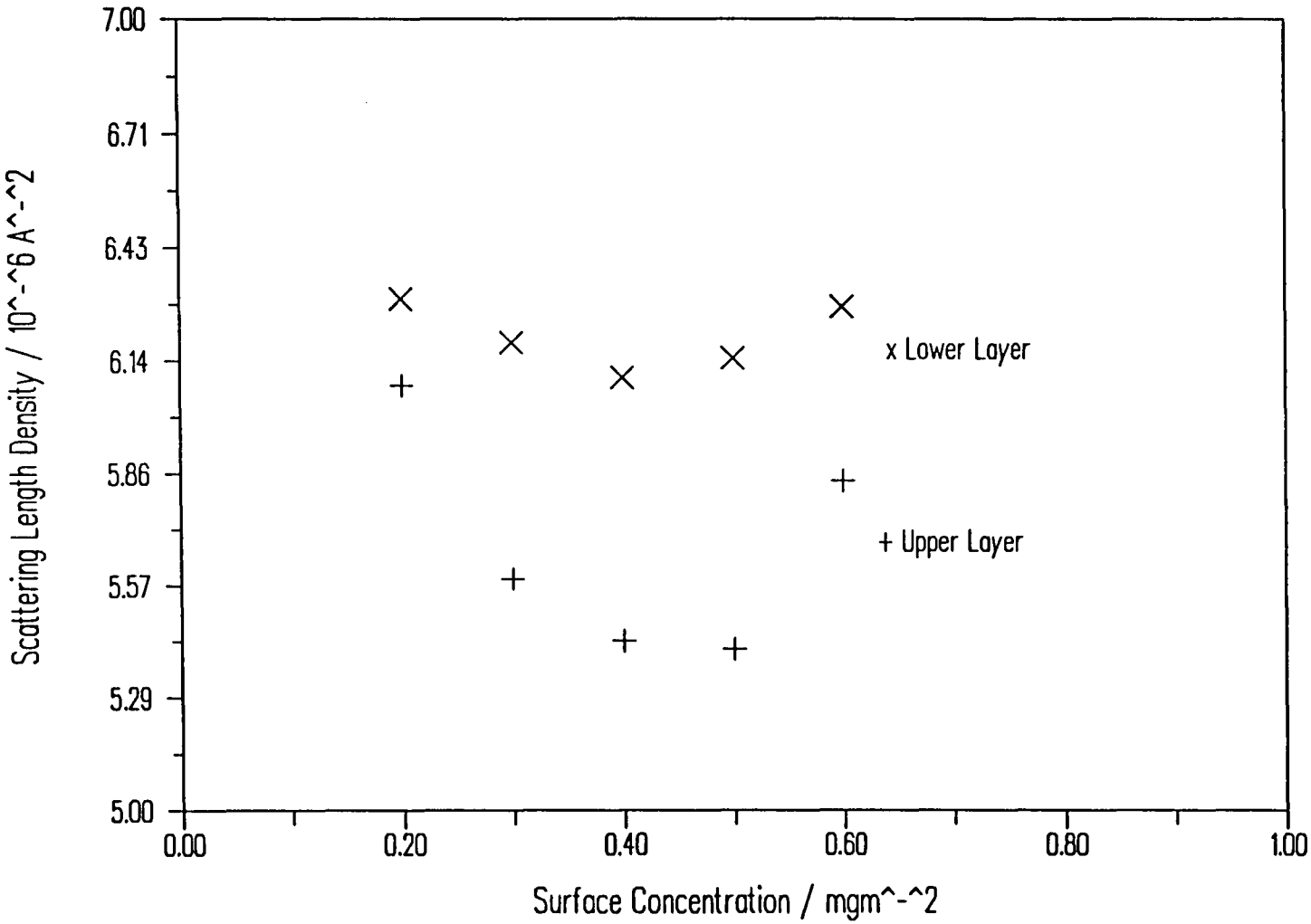

Figure 5.21 Scattering Length Density v Surface Concentration for HPEO on D_2O, two layer model

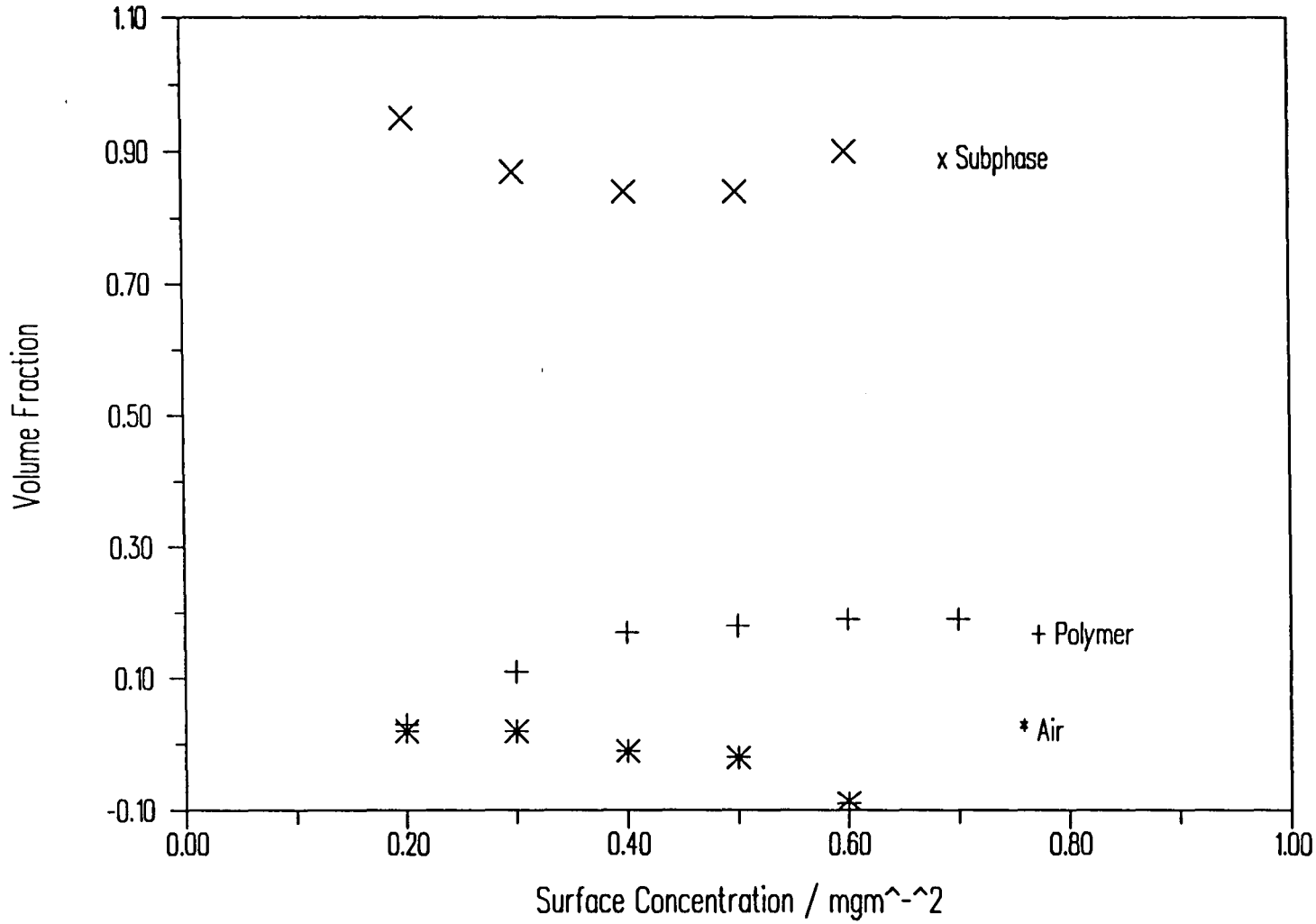

Figure 5.22 Upper Film composition v Surface Concentration for PEO on water, two layer model

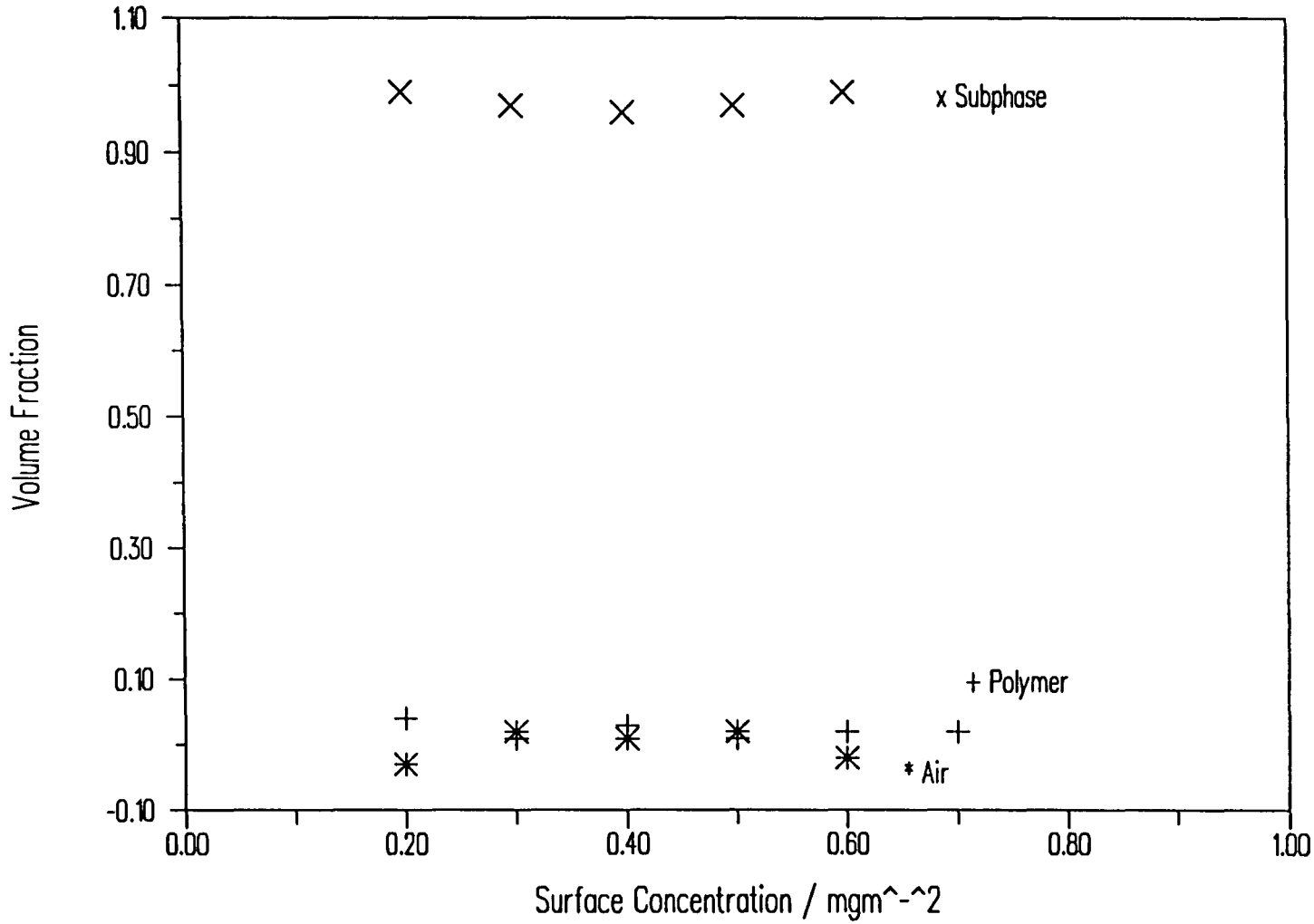

Figure 5.23 Lower Layer Composition v Surface Concentration for PEO on water, two layer model

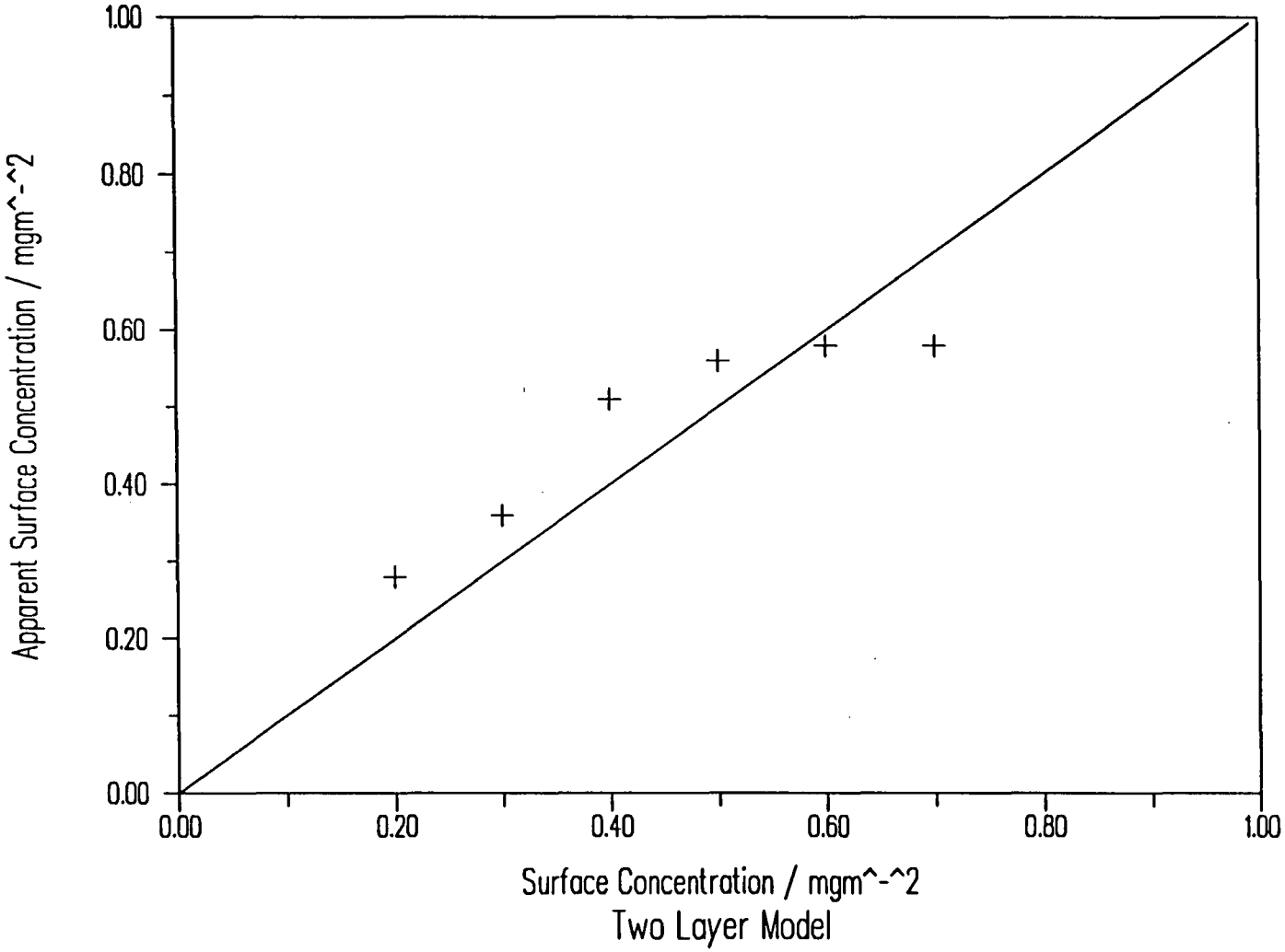

Figure 5.24 Apparent Surface Concentration v Dispensed Surface Concentration for PEO on water, two layer model

The form of diffuse scattering length density profile used for an n incremental layer model was

$$\rho(i) = \rho(1).expon + \rho(n + 1).(1 - expon)$$

where $\rho(i)$ = scattering length density of i^{th} layer, and the subphase corresponds to the $n+1^{th}$ layer. The incremental step length s is given by

$$s = d_{char}.(e/n)$$

where e = 2.71828 and d_{char} is the characteristic length of the profile.

For an exponential profile, the modifying term expon is given by

$$expon = \exp(1.5 - i) \times e/0.5n$$

while for a gaussian profile

$$expon = \exp(-x^2/2(d_{char}/2)^2)$$

where $x = s \times (i - 1.5)$.

Example density profiles for both contrasts, generated using these forms, are illustrated in figure 5.25. The Gaussian and exponential functions shown have the same initial scattering length density values and characteristic lengths to give some idea of how the values obtained on fitting compare to one another.

Residual scanning as a function of d_{char} while floating ρ_1 established stable residual minima for DPEO/acmw for both decay functions, and the characteristic length values so obtained were used successfully to fit the scattering length densities for HPEO/D_2O at equivalent surface concentrations. It was found that neither the addition of a thin slab to the best fit model of either type nor the addition of a diffuse decay to the best fit single slab model led to an improvement in the quality of the fit. In the latter case the general effect was to decrease both ρ_1 and d_{char} and increase the residual, and it was also found that the solutions tended to reduce to physically impossible values (eg negative characteristic lengths) for a top layer thickness greater than about 10 or 15 Å, without passing through a residual minimum.

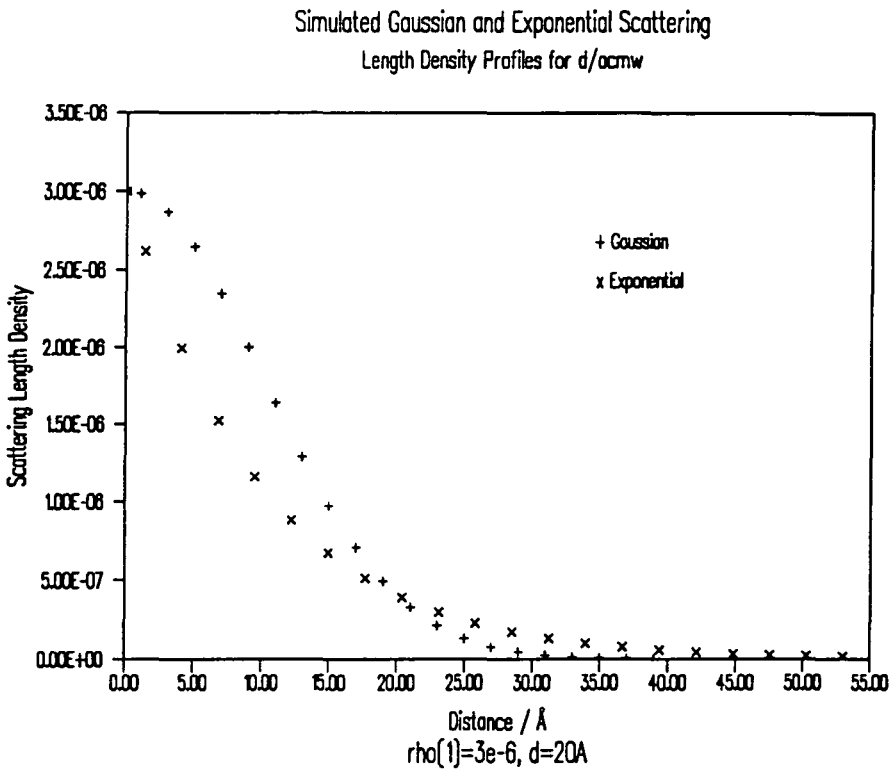

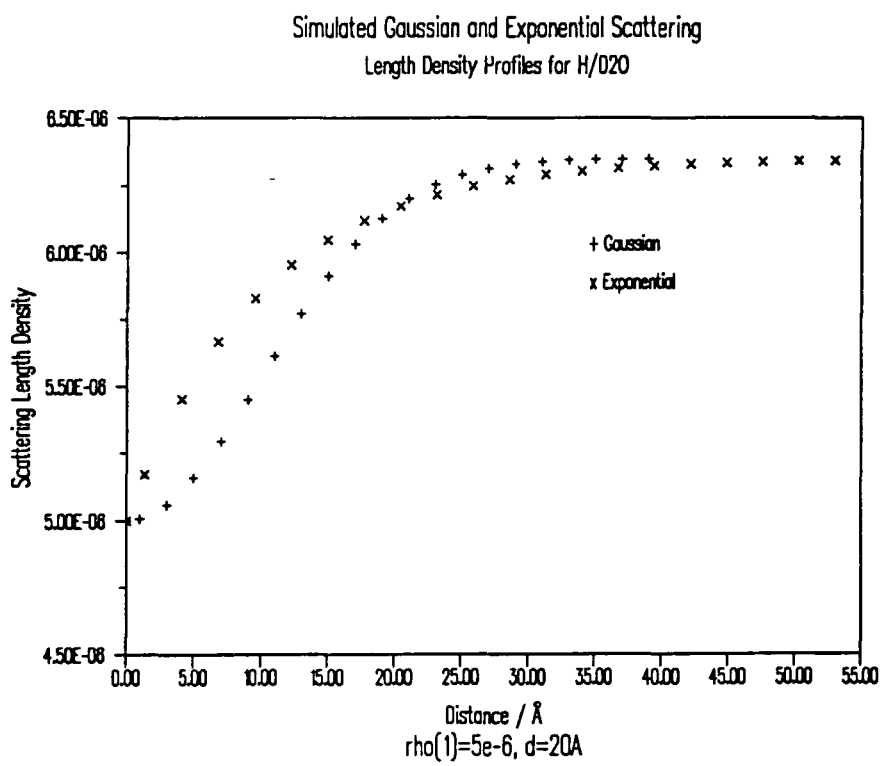

Figure 5.25 Example Scattering Length Density Profiles for Diffuse Models

From the value of the respective scattering length densities and incremental thicknesses it is possible to calculate,

a) the variation in polymer, air and subphase volume fractions as a function of depth from the interface, and

b) the total back calculated surface excess from the sum of the incremental $\rho_i.d_i$ products obtained from the DPEO/acmw contrast.

These values are summarised in tables 5.8-10, where d refers to the characteristic dimension of the distribution and ρ (and therefore derived quantities such as volume fractions) refer to the values fitted for the uppermost layer of the distribution. Layer thickness, scattering length density, composition and apparent surface concentration variations are illustrated in figures 5.26-5.33.

It is necessary to try and evaluate the four fitted models for PEO in terms of the quality of the fits, the parameters obtained from the fits and the physical reality of the models employed. Comparing the data of tables 5.3-10 it is apparent that in all of these categories the simple single slab model is least successful. The residual values to the best fits are rather higher than for the other three cases, there is no great agreement in the back calculated surface coverages and a simple slab is not as appropriate a model for PEO, which is water soluble and appears to form a diffuse film, as it was for insoluble, condensed PMMA films. In the case of the other three models the situation is rather less clear. None of the three generates the best fits exclusively, but the two layer model seems to give considerably lower residuals in the majority of cases. It did however fail to provide a physically sensible fit at the highest surface coverage of $0.8 mgm^{-2}$. There is some improvement in the calculated surface coverages but none of the models removes the large disagreement between Γ and Γ_a at large surface concentrations. Given that the best quality fits to the experimental data were obtained by a two layer model it seems reasonable to adopt this as a working description of the diffuse PEO surface film.

Gaussian

Γ/mg m^{-2}	D/acmw			H/D_2O		
	d/Å	ρ/10^{-6}Å^{-2}	res/10^{-2}	d/Å	ρ/10^{-6}Å^{-2}	res/10^{-2}
0.2	67	0.40	0.4274	17	5.86	0.4614
0.3	41	0.74	0.3863	34	5.40	0.8060
0.4	41	1.13	0.4780	41	5.38	0.8227
0.5	32	1.42	0.4745	31	5.08	0.7793
0.6	36	1.43	0.4337	21	5.38	0.6148
0.7	35	1.45	0.4657	-	-	-
0.8	26	1.72	0.4956	48	5.24	0.8876

Exponential

Γ/mg m^{-2}	D/acmw			H/D_2O		
	d/Å	ρ/10^{-6}Å^{-2}	res/10^{-2}	d/Å	ρ/10^{-6}Å^{-2}	res/10^{-2}
0.2	51	0.67	0.5136	11	5.18	0.4612
0.3	33	1.22	0.3206	49	5.14	0.8410
0.4	31	1.93	0.4347	111	5.33	0.6748
0.5	25	2.38	0.3992	34	4.51	0.7785
0.6	28	2.37	0.3262	20	4.82	0.6256
0.7	26	2.50	0.3732	-	-	-
0.8	17	3.31	0.5216	119	5.15	0.7017

Table 5.8 Residual Mimimum fitted Parameters for diffuse models of PEO on water

In the light of the observed hysteresis and time dependent decay in the surface pressure of PEO monlayers some concern must be expressed over this discrepency and over the neutron reflection measurement which take on average two to three hours to record. Given that there seems to be a rather large alteration in the state of the monolayer over that period of time at moderate to large surface concentrations it is difficult to define what layer thickness and density is being recorded by the reflection experiment. Presumably some sort of average structure

Gaussian

Γ/mg m^{-2}	D/acmw			H/D_2O	
	d/Å	ρ/10^{-6}Å^{-2}	res/10^{-2}	ρ/10^{-6}Å^{-2}	res/10^{-2}
0.2	42	0.57	0.7561	6.12	0.4886
0.3	38	0.78	0.3947	5.38	0.9360
0.4	41	1.13	0.4780	5.38	0.8227
0.5	31	1.46	0.4760	5.08	0.7793
0.6	28	1.76	0.5796	5.59	0.6320
0.8	37	1.28	0.7864	5.13	0.9056

Exponential

Γ/mg m^{-2}	D/acmw			H/D_2O	
	d/Å	ρ/10^{-6}Å^{-2}	res/10^{-2}	ρ/10^{-6}Å^{-2}	res/10^{-2}
0.2	31	0.99	0.7479	5.91	0.4716
0.3	41	1.06	0.3692	5.04	0.8458
0.4	71	1.11	1.442	5.18	0.6925
0.5	29	2.13	0.4264	4.32	0.7952
0.6	24	2.69	0.3846	5.05	0.6283
0.8	78	1.12	2.515	4.99	0.7142

Figure 5.9 Residual optimum values for diffuse models of PEO on water

over the period of measurement might result, however two important observations must be made.

Firstly the surface pressure decay would suggest that, if material is lost from the film to bulk, that about 75% of the spread material was disappearing from the surface before a limiting surface pressure was reached. The discrepency in the back calculated surface coverage from neutron reflection does indeed suggest a limit, but of around Γ = 0.6mgm^{-2}, much higher than the value of around Γ =

Gaussian

Γ/mg m^{-2}	Volume Fraction			ρ.d/10^{-6}Å^{-1}	a.p.m./Å^{2}monomer^{-1}	Γ_a/mgm^{-2}
	polymer	water	air			
0.2	0.09	0.96	-0.05	15.0	30.5	0.26
0.3	0.12	0.84	0.04	18.6	24.7	0.32
0.4	0.18	0.83	-0.01	29.0	15.8	0.51
0.5	0.23	0.78	-0.01	28.4	16.2	0.49
0.6	0.28	0.86	-0.14	30.9	14.8	0.54
0.7	0.12	-	-	31.8	14.4	0.55
0.8	0.20	0.79	0.01	29.7	15.4	0.52

Exponential

Γ/mg m^{-2}	Volume Fraction			ρ.d/10^{-6}Å^{-1}	a.p.m./Å^{2}monomer^{-1}	Γ_a/mgm^{-2}
	polymer	water	air			
0.2	0.16	0.92	-0.08	15.2	30.1	0.27
0.3	0.17	0.78	0.05	21.6	21.2	0.38
0.4	0.18	0.80	0.02	39.1	11.7	0.68
0.5	0.34	0.65	0.01	30.7	14.9	0.53
0.6	0.43	0.76	-0.19	32.0	14.3	0.56
0.7	0.40	-	-	32.3	14.2	0.56
0.8	0.18	0.77	0.05	43.4	10.6	0.75

Table 5.10 Volume Fraction and Apparent Surface Coverages obtained from diffuse model fitting

0.2mgm^{-2} suggested by surface pressure decay.

Secondly, if significant loss of material took place over the period of the reflection experiment, then one would have expected to observe a visible shift in the measured reflectivity with time, particularly for DPEO/acmw. However during neutron reflectometry measurements no time drift of the measured reflectivity was observed at any surface concentration. A reflectometry experiment was carried out on CRISP to investigate this point using PEO spread on a 0.4M solution of aqueous

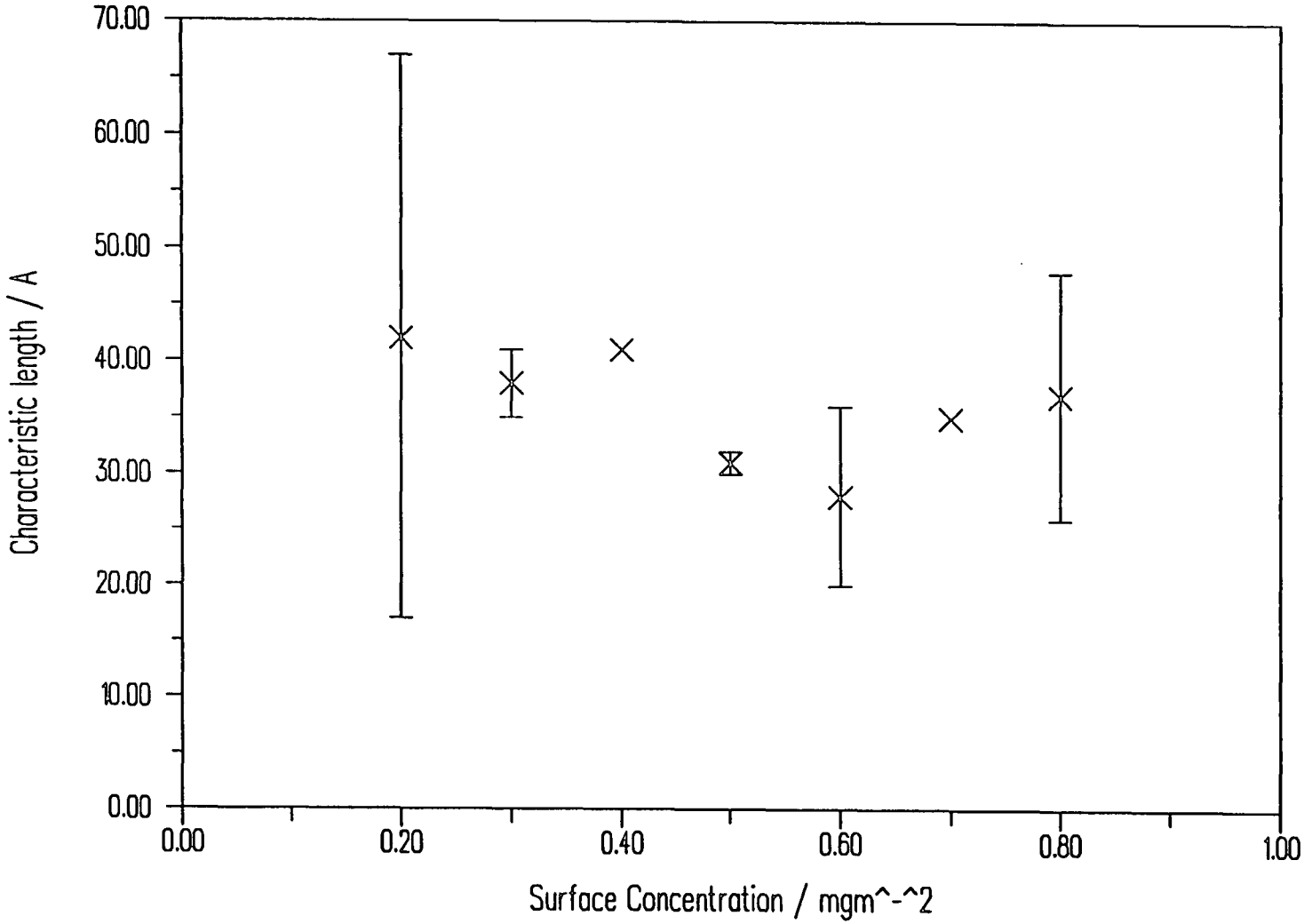

Figure 5.26 Characteristic Length v Surface Concentration for PEO on water - Gaussian Model

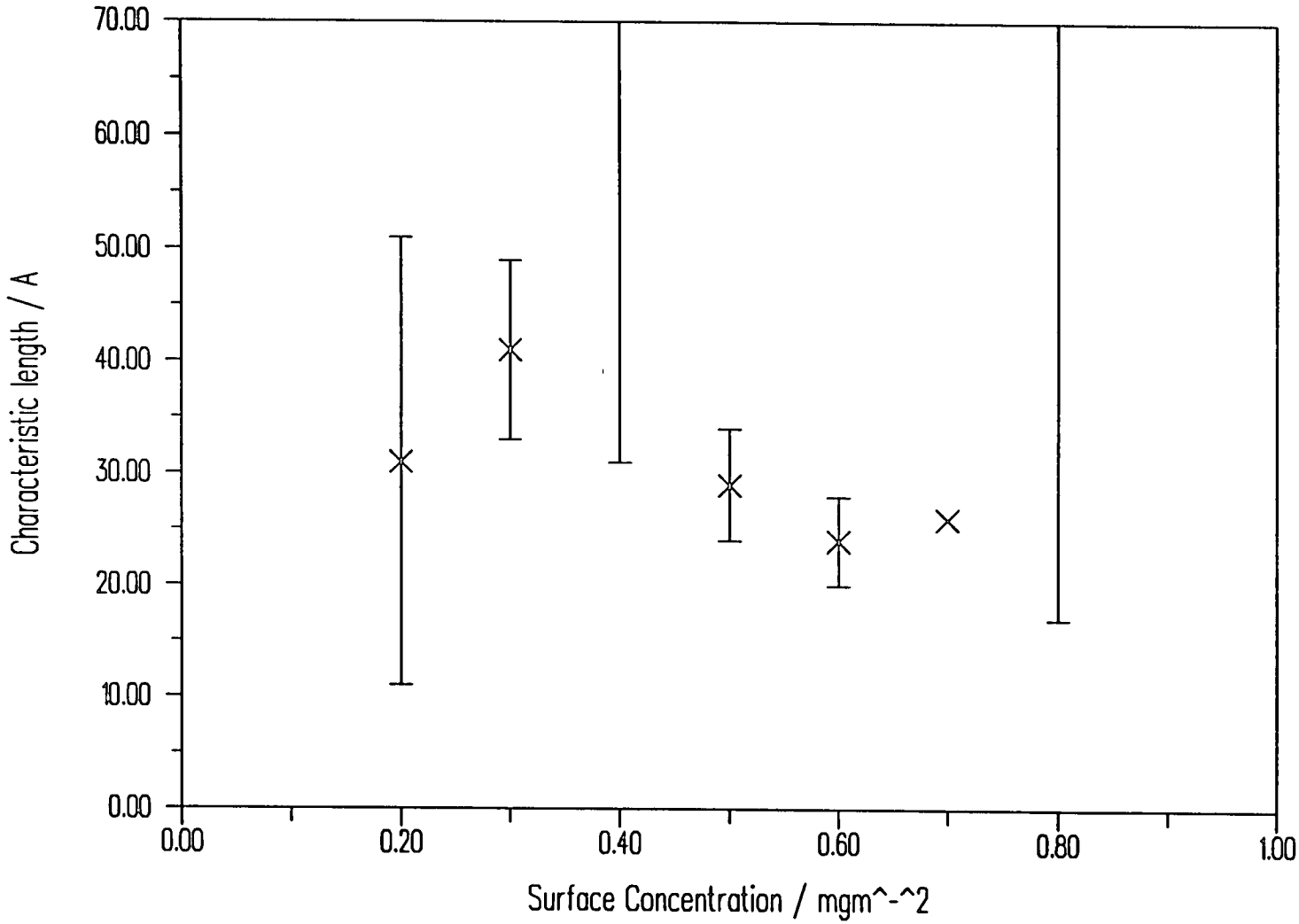

Figure 5.27 Characteristic Length v Surface Concentration for PEO on water - Exponential Model

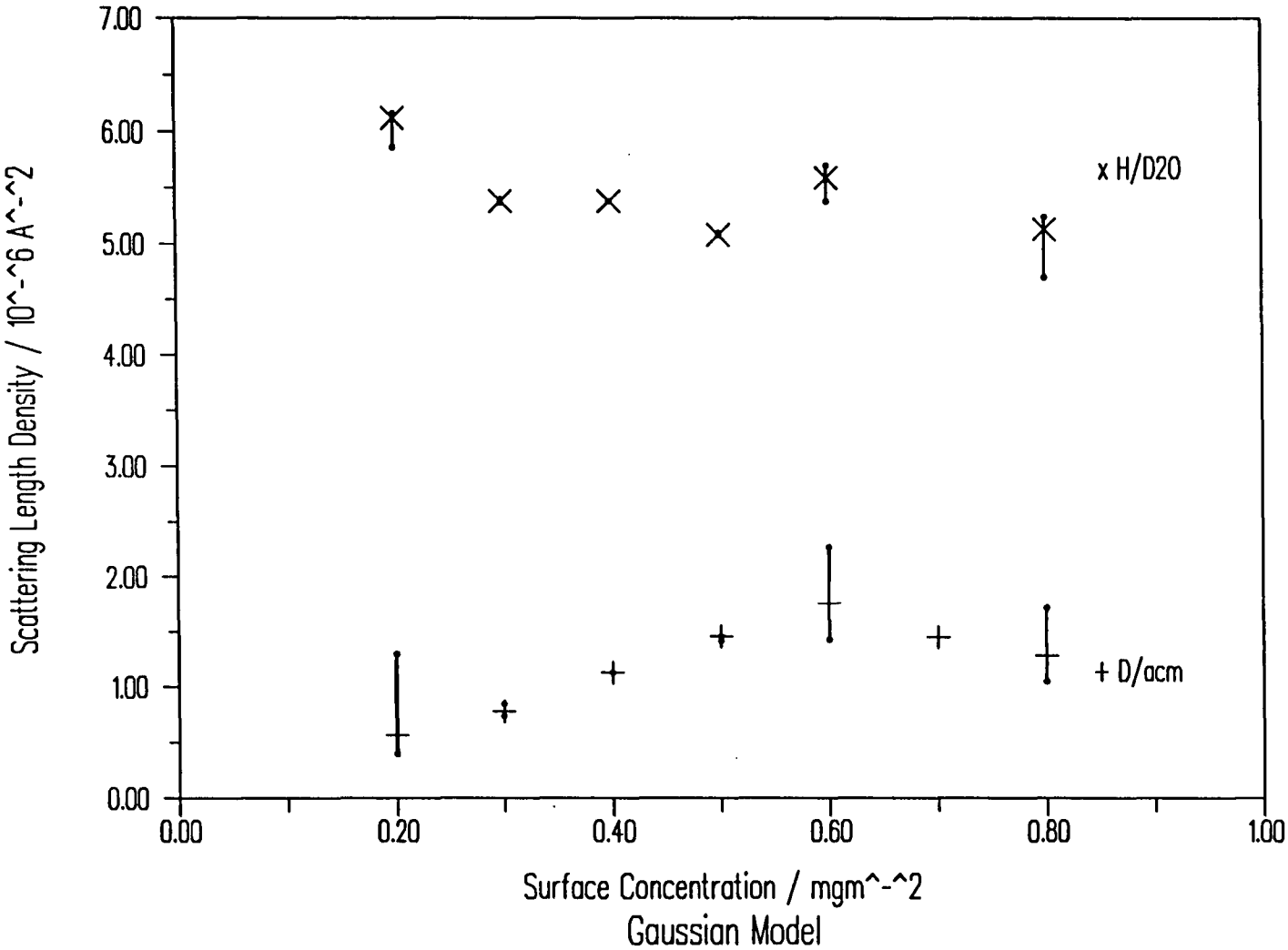

Figure 5.28 Variation of Topmost layer scattering length density for PEO on water - Gaussian Model

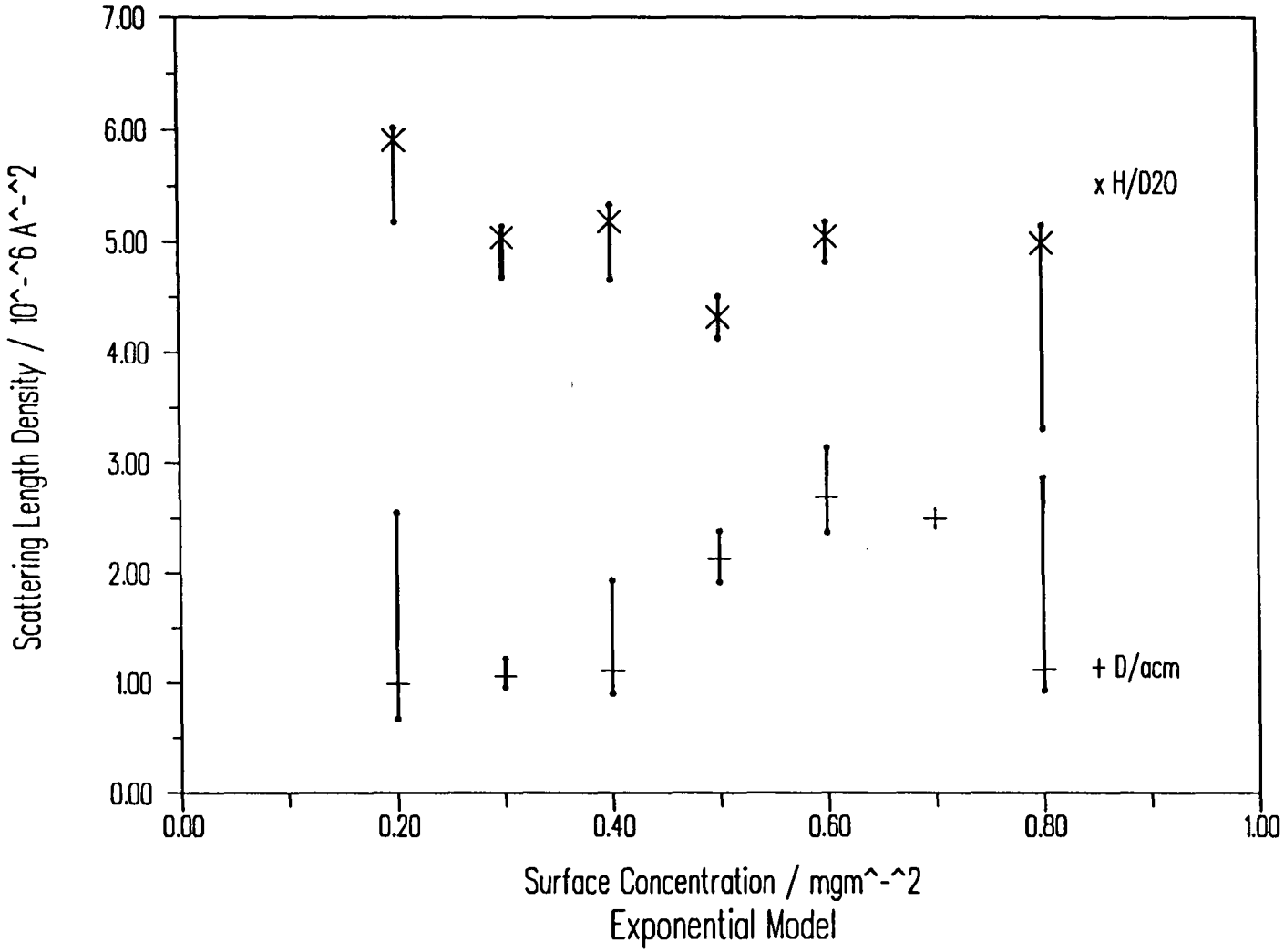

Figure 5.29 Variation of topmost layer scattering length density for PEO on water - Exponential Model

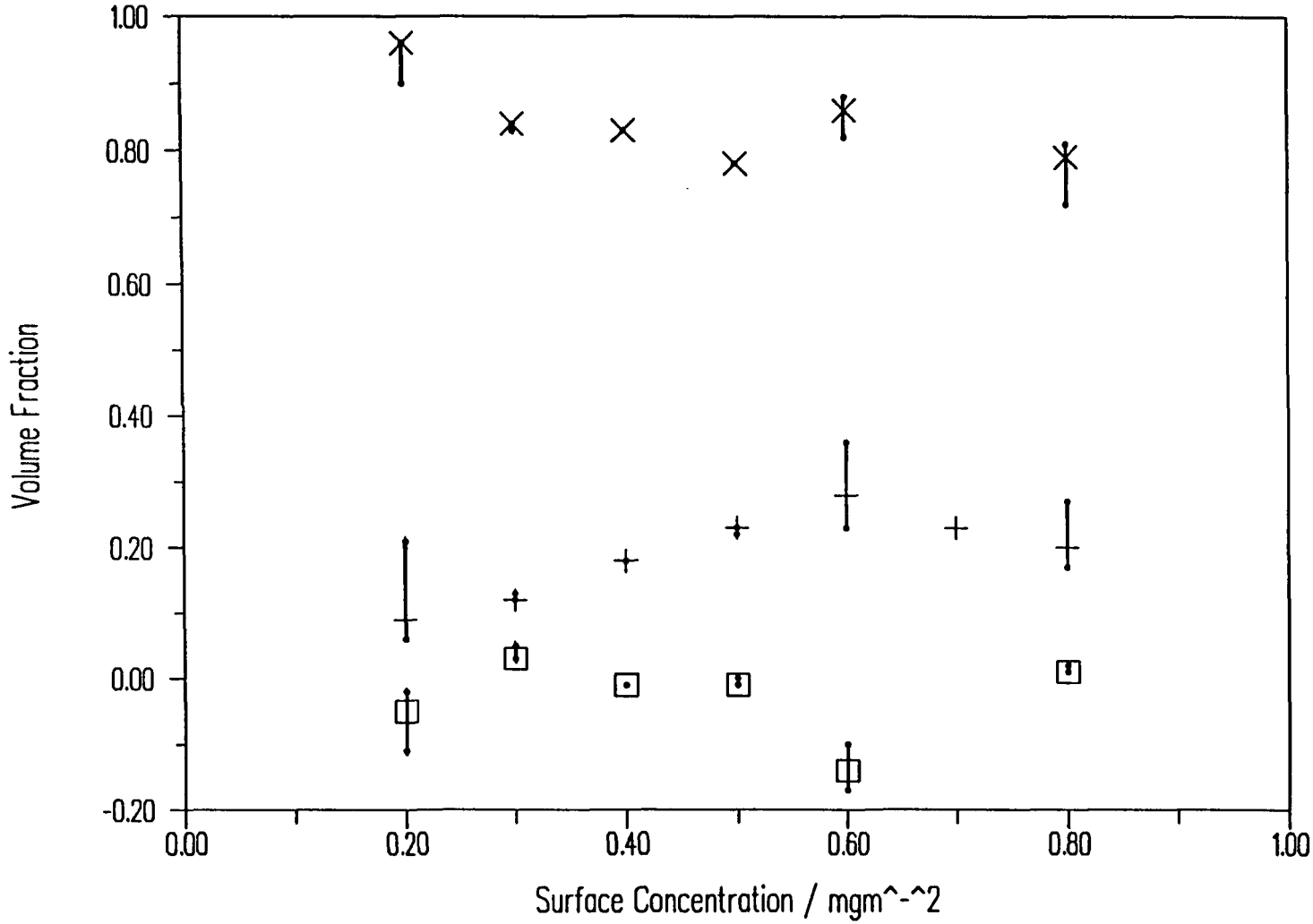

Figure 5.30 Variation in topmost layer composition for PEO on water - Gaussian Model

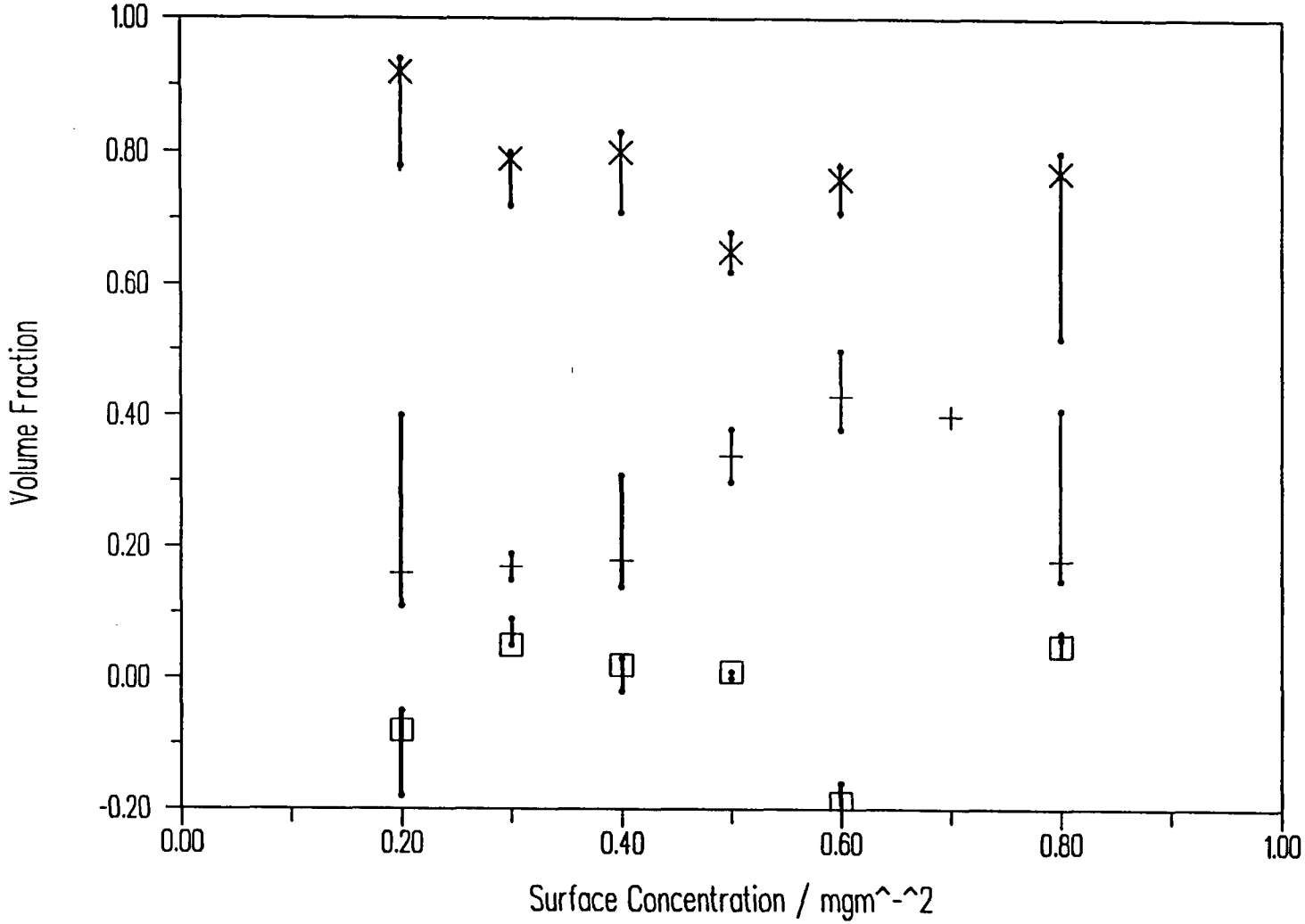

Figure 5.31 Variation in Topmost layer Composition for PEO on water - Exponential Model

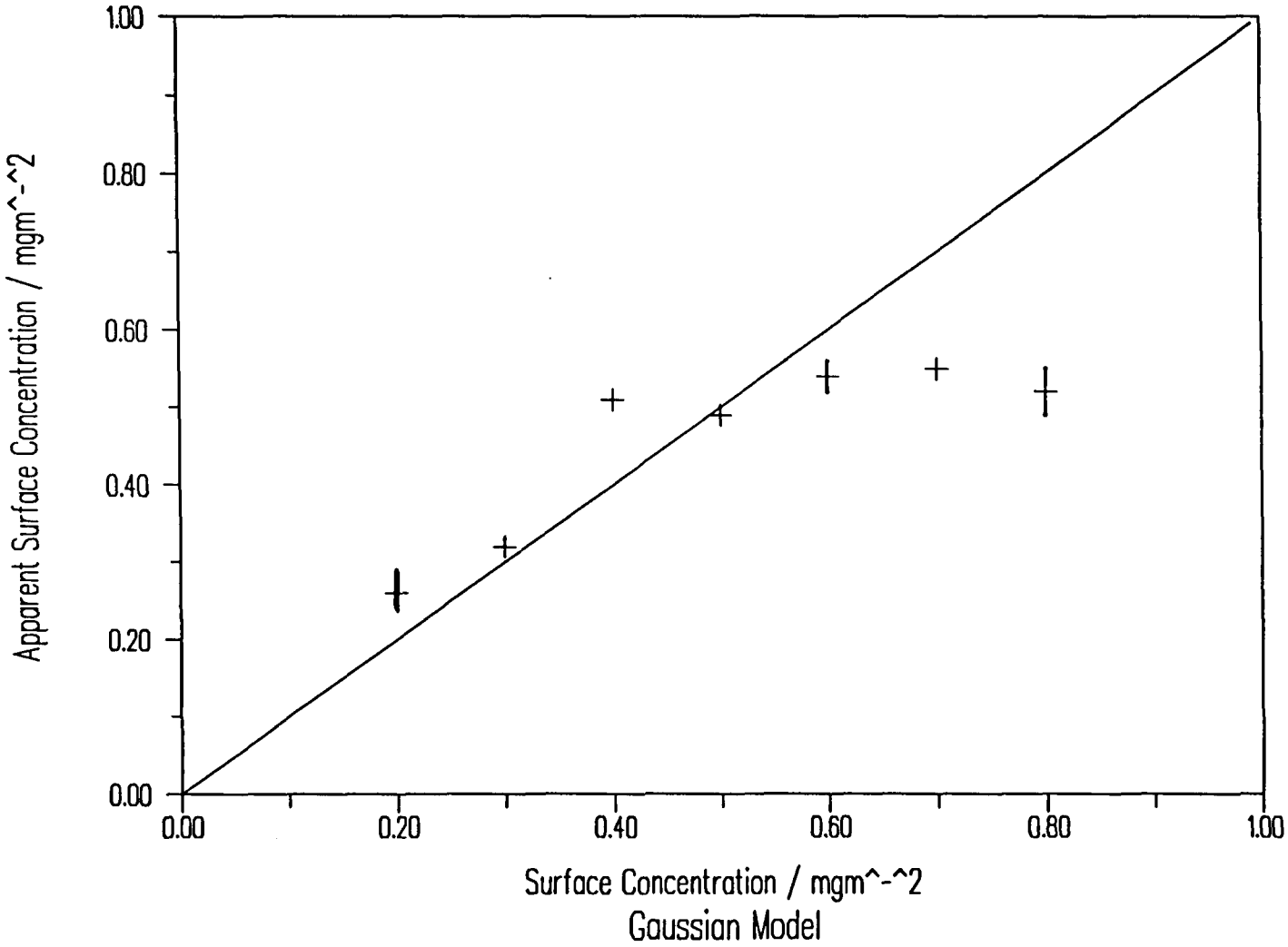

Figure 5.32 Apparent Surface coverage v Dispensed Surface Concentration for PEO on water - Gaussian Model

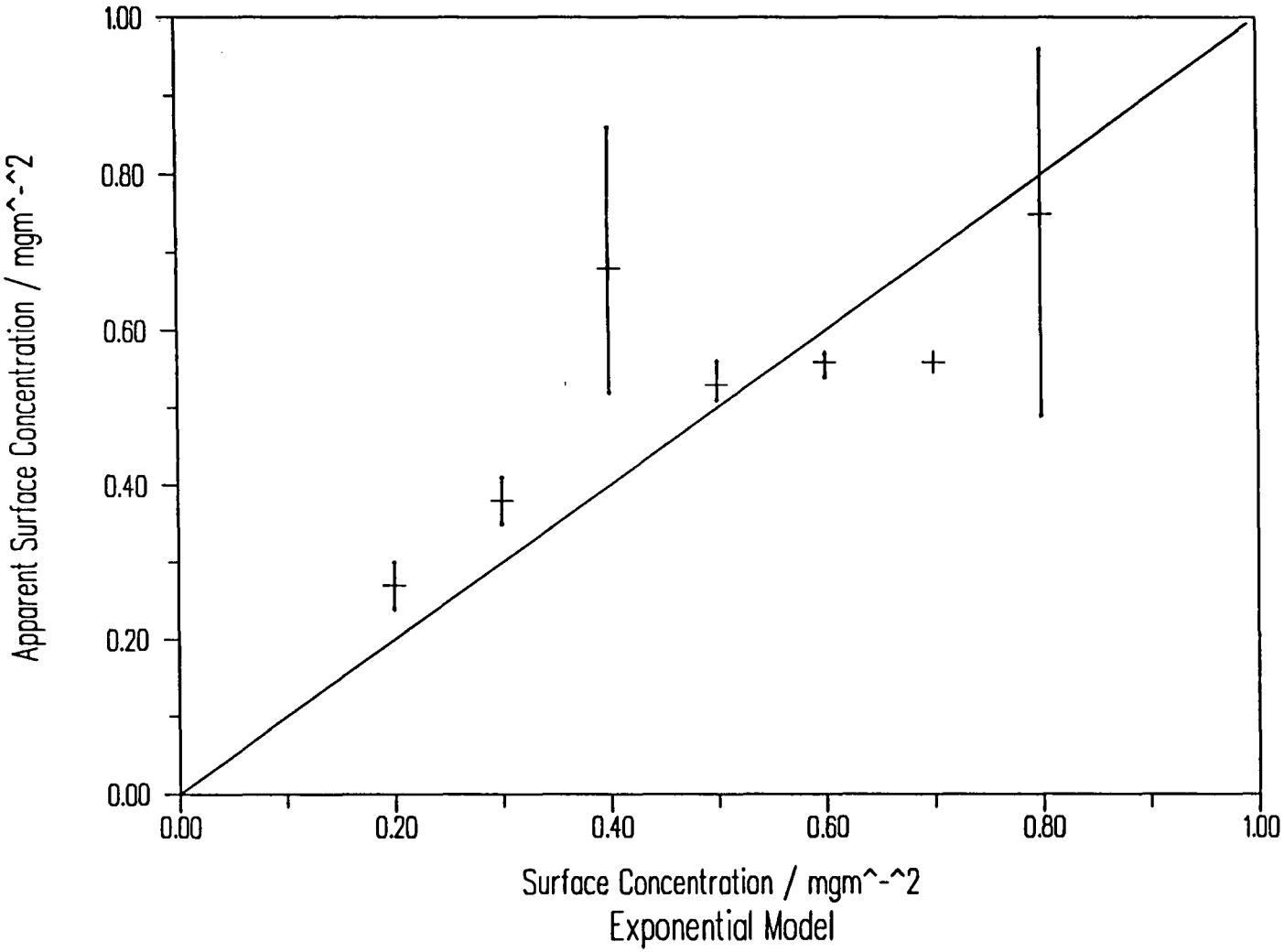

Figure 5.33 Apparent Surface Coverage v Dispensed Surface Concentration for PEO on water - Exponential Model

$MgSO_4$, and over an eight hour period a succession of profiles recorded over half an hour each at a surface coverage of $0.8mgm^{-2}$ were observed to be virtually identical.

5.3.1 Application of the Kinematic Approximation

The use of kinematic formulae enables some further observations about the behaviour of PEO films to be made. As previously discussed for the case of poly (methyl methacrylate), a Patterson analysis may be made by plotting the background subtracted reflectivity multiplied by the scattering vector to the fourth power against the scattering vector. A sharp minimum in the Patterson plot is predicted at a Q value equal to π/d, where d is the thickness of a single sharp edged film at the interface. An example of a Patterson plot for HPEO on D_2O is shown in figure 5.34.

The minimum in $R.Q^4$ is much less sharp than was the case for PMMA, indicating a less sharply defined film thickness. From the minima at various surface concentrations the thickness values shown in table 5.11 and figure 5.35 were obtained.

Comparing the Patterson function for the D/acmw situation, for example figure 5.36, the plot is seen to show qualitative agreement with the theory at low Q values, where the value of $R.Q^4$ rises from a virtually zero value. At higher Q values the error values associated with background subtraction tend to swamp the minimum position in $R.Q^4$, however the point at which the plot levels off is seen to be in approximate agreement with the value obtained from the Patterson plot for $HPEO/D_2O$.

A Guinier plot of $\ln(R.Q^2)$ against Q^2 for DPEO/acmw at moderate Q values should be a straight line with slope related to σ, the second moment of the scattering length density distribution at the interface. The zero Q intercept of this plot is related to the total scattering length density over z space, m. An example plot

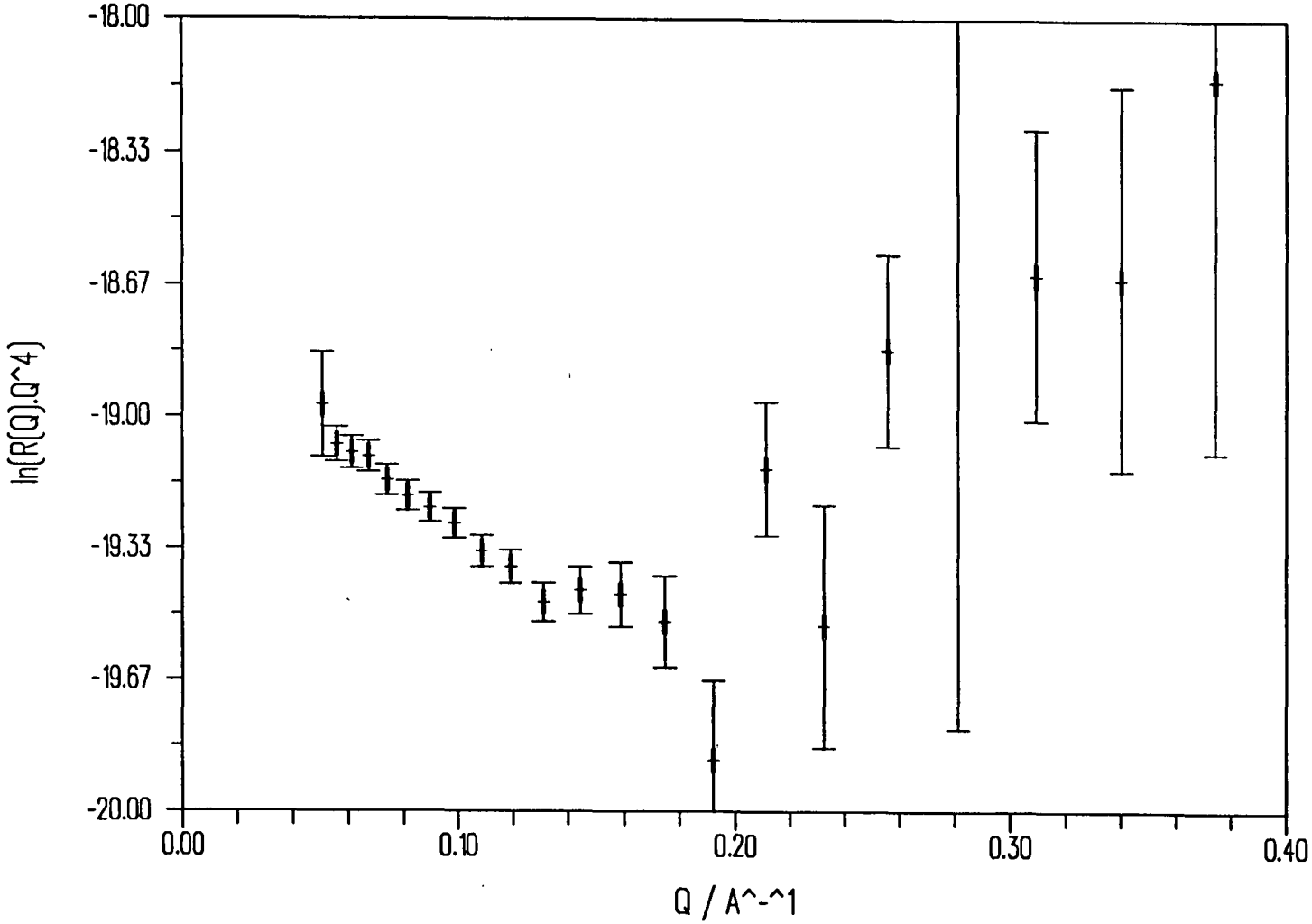

Figure 5.34 Patterson Plot for HPEO / D_2O, Surface Concentration = 0.5mgm^{-2}

Γ/mgm^{-2}	x_{min}	y_{min}	d/Å	$\rho_F/10^{-6}$Å^{-2}
0.2	0.17	-19.2	18.5	5.94
0.3	0.15	-19.4	20.9	5.61
0.4	0.17	-19.5	18.5	5.49
0.5	0.18	-19.5	17.5	5.49
0.6	0.18	-19.4	17.5	5.61
0.8	0.22	-19.6	14.4	5.38

Table 5.11 Results of Analysis of Patterson Functions for HPEO on D_2O

is shown in figure 5.37 and values of m and σ are tabulated in table 5.12. By assuming a Gaussian distribution, for which σ corresponds to d divided by $\sqrt{12}$, a layer thickness may be estimated. These values are shown in the final column of table 5.12 and in figure 5.37. These values are clearly very different from those obtained by Patterson analysis, being thicker, particularly at low surface concentrations.

In order to account for this difference, one must note that, while the Patterson function is valid for a single step scattering length density profile, the Guinier plot is valid for a continuous scattering length density gradient. It will therefore be particularly sensitive to any diffuse region in the interfacial structure unlike the Patterson function which will respond to any denser, more step-like profile. Noting also that the layer thickness for the Patterson analysis is of the order of the upper layer thickness obtained by two layer matrix modelling, and the Guinier plot thickness is rather more like the lower two layer model thickness, it is suggested that the kinematic analysis for PEO spread on water supports the diffuse two layer structure already proposed.

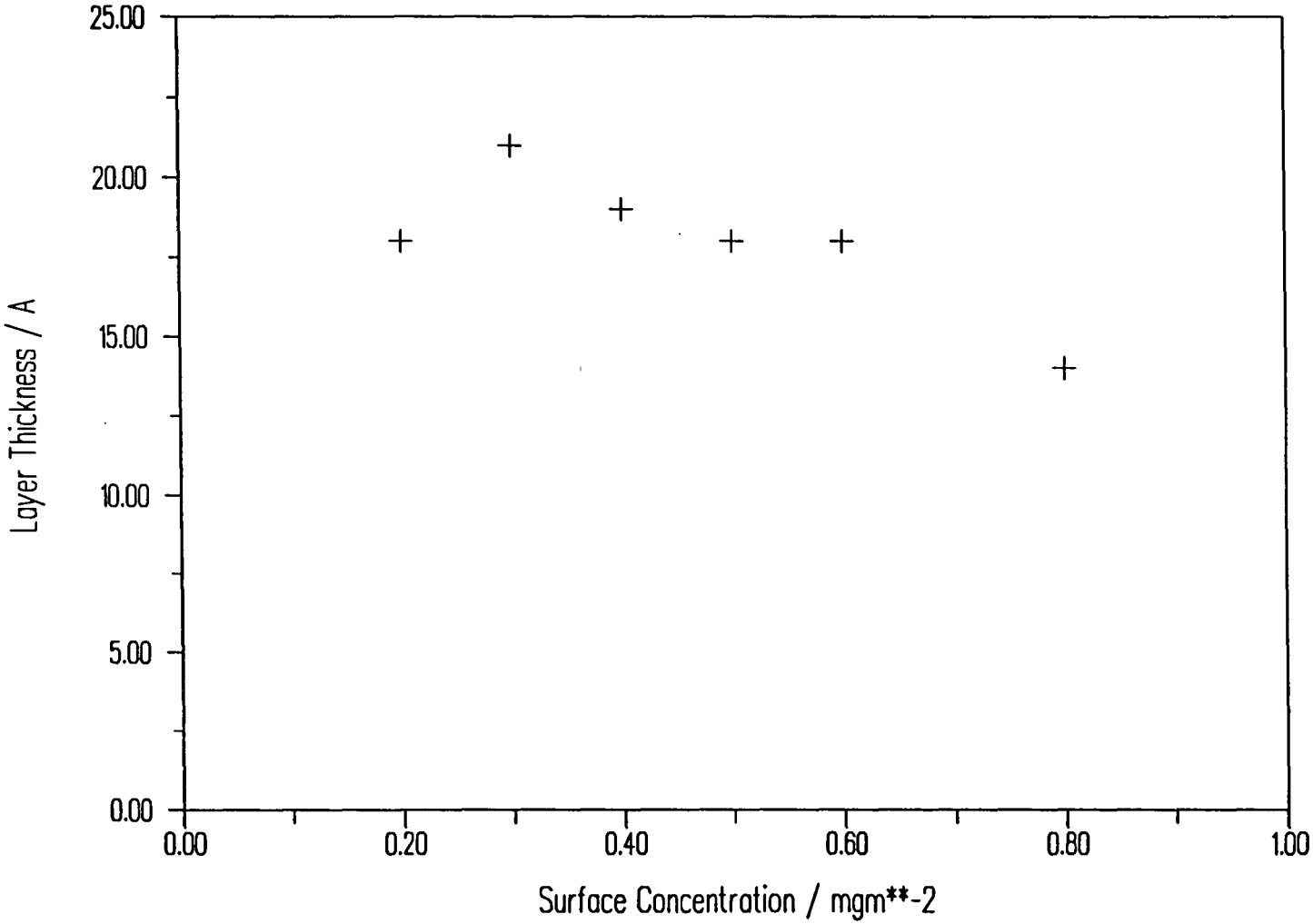

Figure 5.35 Layer Thickness obtained from Patterson Function Analysis for PEO on water

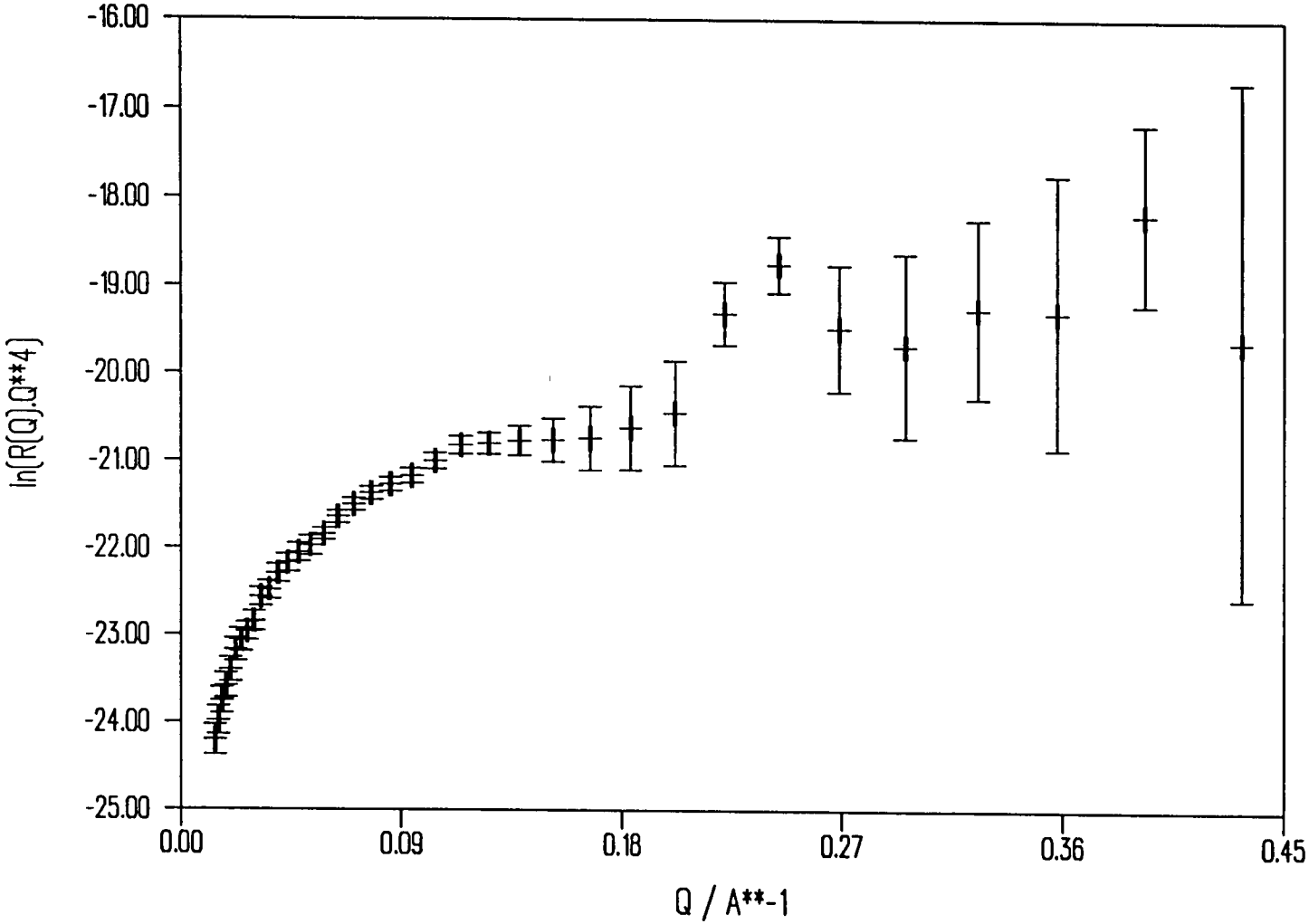

Figure 5.36 Patterson Plot for DPEO / acmw, surface concentration = 0.7mgm^{-2}

Γ/mgm^{-2}	Intercept	Slope	m/10^{-6}Å^{-2}	σ	d
0.2	-17.0	-326.9	16.2	18.1	62.7
0.3	-16.5	-95.2	20.8	9.8	33.9
0.4	-16.4	-42.1	21.9	6.5	22.5
0.5	-16.1	-45.2	25.4	6.7	23.2
0.6	-16.0	-53.5	26.7	7.3	25.3
0.7	-16.0	-44.0	26.7	6.6	22.9
0.8	-15.9	-59.6	28.1	7.7	26.7

Table 5.12 Results of Analysis of Guinier plots for DPEO on acmw

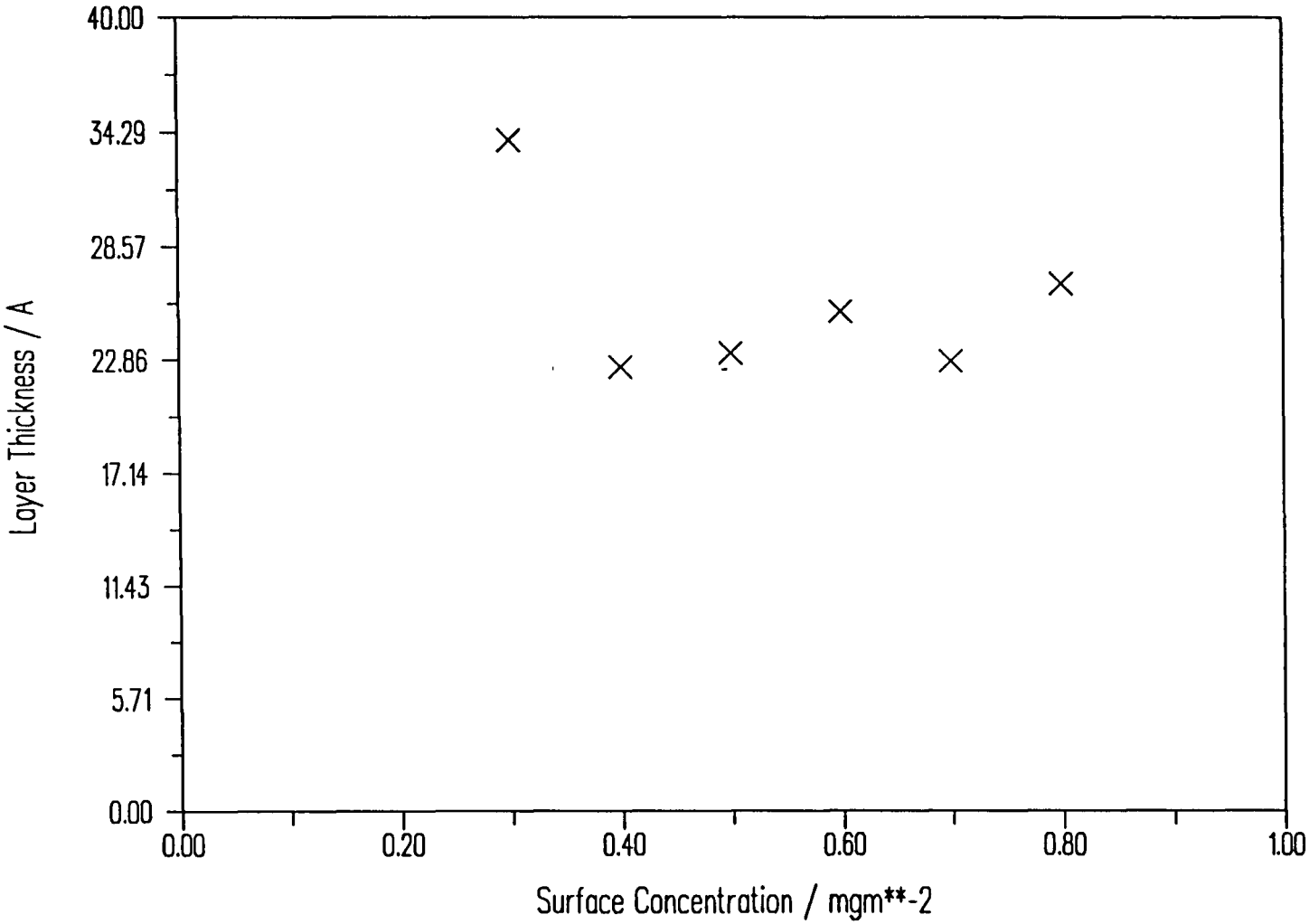

Figure 5.37 Layer Thickness obtained from Guinier Plot analysis for PEO on water

5.4 Monolayers of PEO on Salt Subphases

In addition to studying PEO monolayers spread on pure water the case of PEO spread on aqueous subphases containing various concentrations of magnesium sulphate has been considered, using the same PEO samples as in the pure water experiments. Surface pressure - concentration isotherms have been recorded at salt concentrations approaching and including bulk theta solvent conditions, and two salt concentrations have been employed in neutron reflectometry experiments.

5.4.1 Surface Pressure - Concentration Studies

Surface pressure - concentration isotherms are presented for HPEO spread on aqueous solutions of magnesium sulphate at room temperature (298K) with salt concentrations of 0.4,0.6, and 0.8M, and for a salt concentration of 0.39M at 315K, corresponding to an accepted theta solvent condition for bulk PEO solution[2], figures 5.38. The data of figure 5.2 for PEO on pure water are superimposed for comparison. Increasing the salt concentration is seen to slightly increase the slope of the rapidly rising portion of the isotherm, and to cause the plateau on the isotherm to become less horizontal, rising above the salt free isotherm plateau value of $10mNm^{-1}$. The limiting area per monomer unit, obtained by linear extrapolation of the surface pressure to the concentration axis was reduced slightly by the addition of salt to the subphase, table 5.13.

The critical scaling exponent ν derived from the slope of the double logarithmic plots of semi-dilute regime surface pressure data is also affected by the addition of electrolyte to the subphase. These values are shown in table 5.14. As the value of the slope y increases, the scaling exponent value is depressed from that

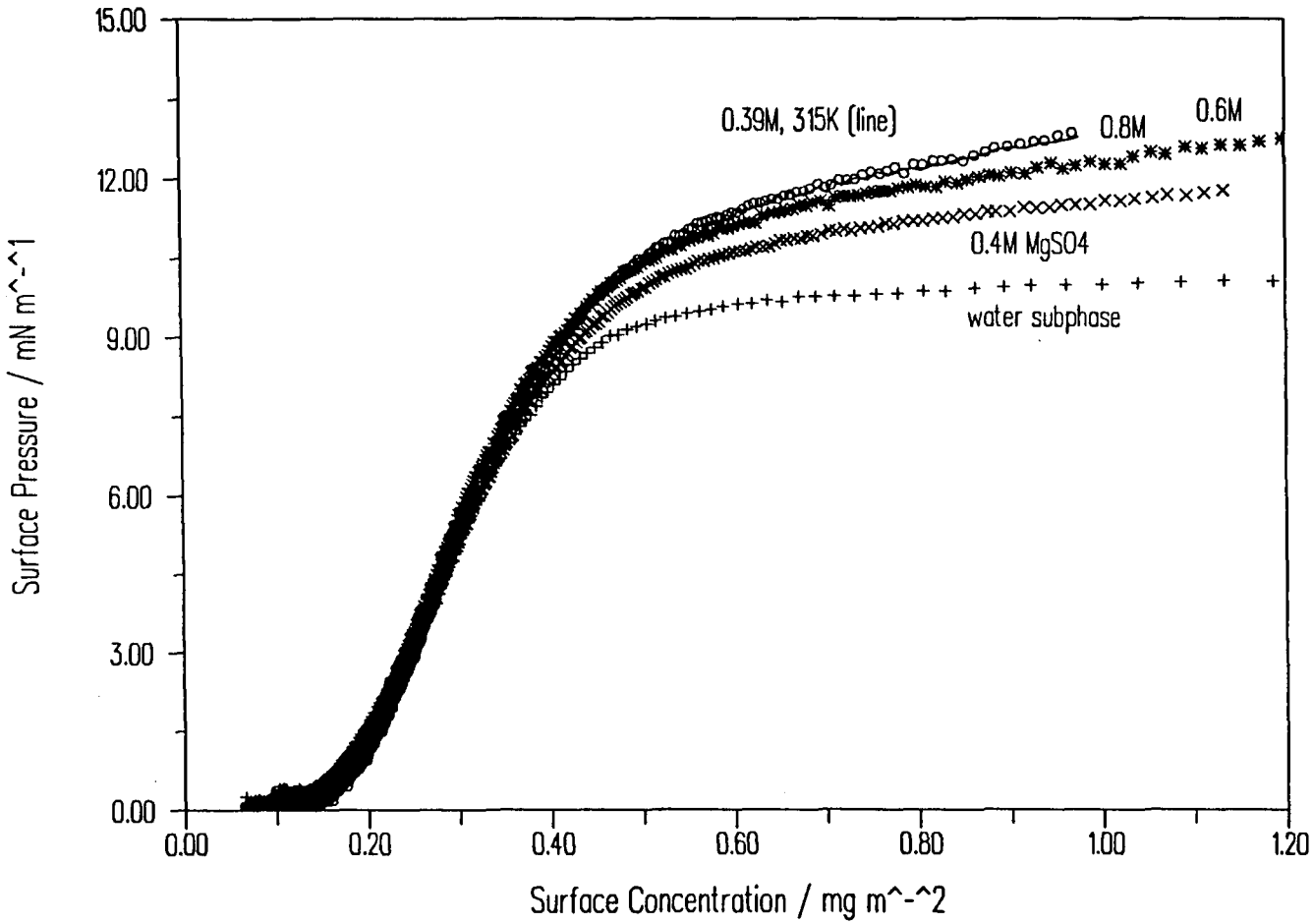

Figure 5.38 Effect of the addition of magnesium sulphate to the shape of the surface pressure isotherm of poly (ethylene oxide)

Conditions	Γ_{lim}	apm_{lim}
pure water	0.17	43
0.4M $MgSO_4$	0.18	41
0.6M $MgSO_4$	0.18	41
0.8M $MgSO_4$	0.19	38
0.39MMgSO_4, 315K	0.19	38

Table 5.13 Limiting areas per monomer unit for PEO on $MgSO_4$ subphases

Conditions	Slope	ν
Pure water	2.91	0.76
0.4M $MgSO_4$	4.37	0.65
0.6M $MgSO_4$	4.84	0.63
0.8M $MgSO_4$	5.57	0.61
0.39M $MgSO_4$, 315K	4.78	0.63

Table 5.14 Critical Scaling Exponents for PEO on salt subphases

obtained in good 2-D solution conditions (ν = 0.77 as for PEO on water). The addition of more salt to the subphase is seen to reduce the scaling exponent value, but as the salt concentration is increased a law of diminishing return on the amount of salt added is observed. Comparing the differences between the isotherms at salt concentrations of 0.4 and 0.6M, and 0.6M and 0.8M for example, the change in the isotherm is much greater in the former than the latter case. Finally, the isotherm obtained at room temperature and with a salt concentration of 0.8M is seen to be very similar in appearance to that obtained for a monolayer spread on the bulk theta solvent.

A final comparison between the various isotherms may be made by an

equation of state plot in the dilute regime, where a positive initial slope is anticipated for good 2-D solution conditions. Equation of state plots of the ratio of the surface pressure to the surface concentration against the surface concentration are shown for the four salt concentrations in figures 5.39-42. There is indeed a positive slope at the two lower room temperature salt concentrations, but at 0.8M $MgSO_4$ and with bulk theta conditions, there is an initial negative dip before a positive gradient is achieved. This is at odds with the results of scaling law plotting in the semi-dilute region, which implies that, although the scaling exponent is depressed by the addition of salt, it is never reduced to as low as 0.56, the approximate value for theta conditions. A negative slope in the dilute region equation of state plot implies less than theta, near collapse conditions and hence a scaling exponent of between 0.5-0.55. However, the similarity between the isotherms at room temperature and 0.8M and bulk theta conditions is again striking.

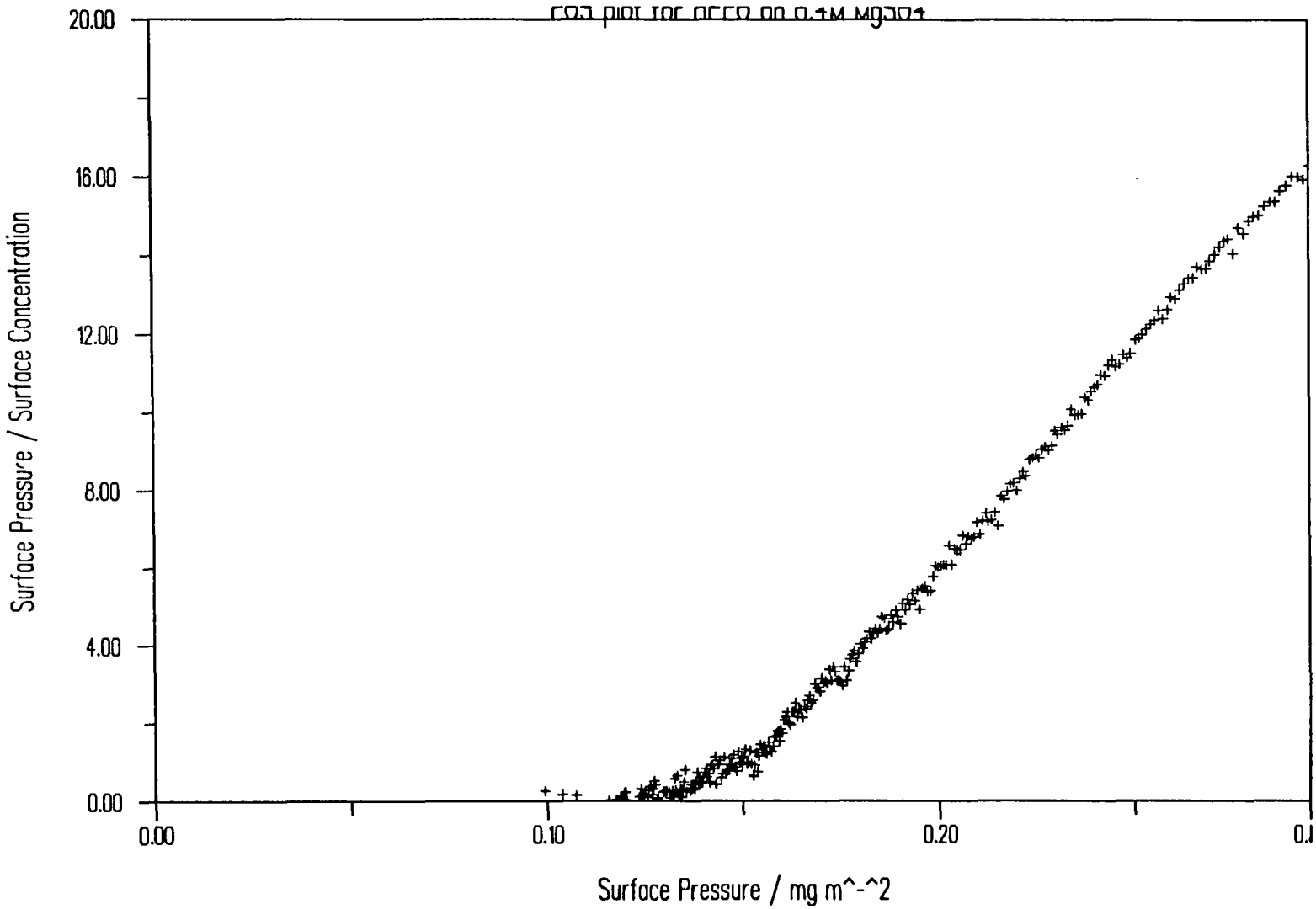

Figure 5.39 Surface Pressure / Surface Concentration v Surface Concentration for HPEO on 0.4M $MgSO_4$

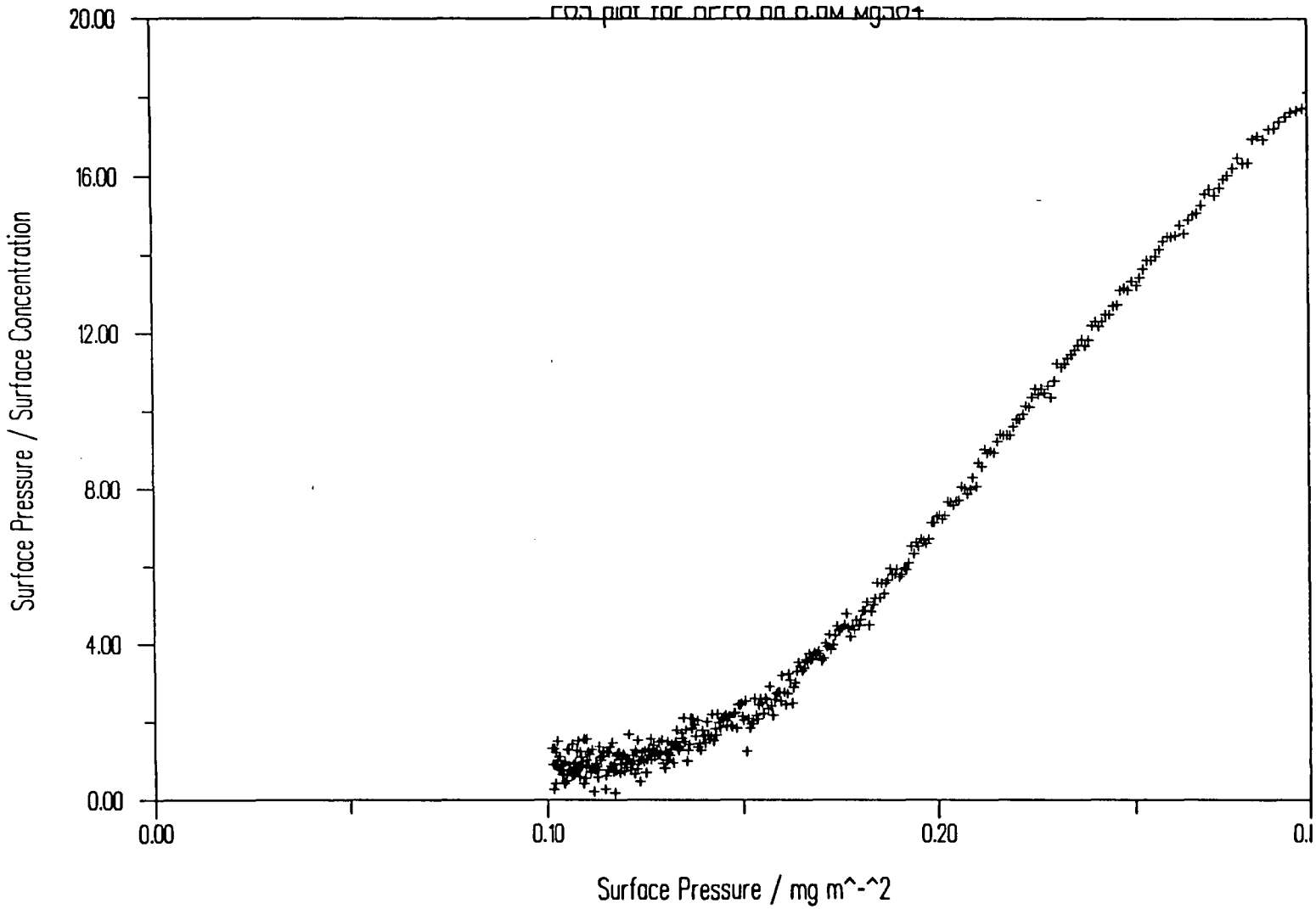

Figure 5.40 Surface Pressure / Surface Concentration v Surface Concentration for HPEO on 0.6M $MgSO_4$

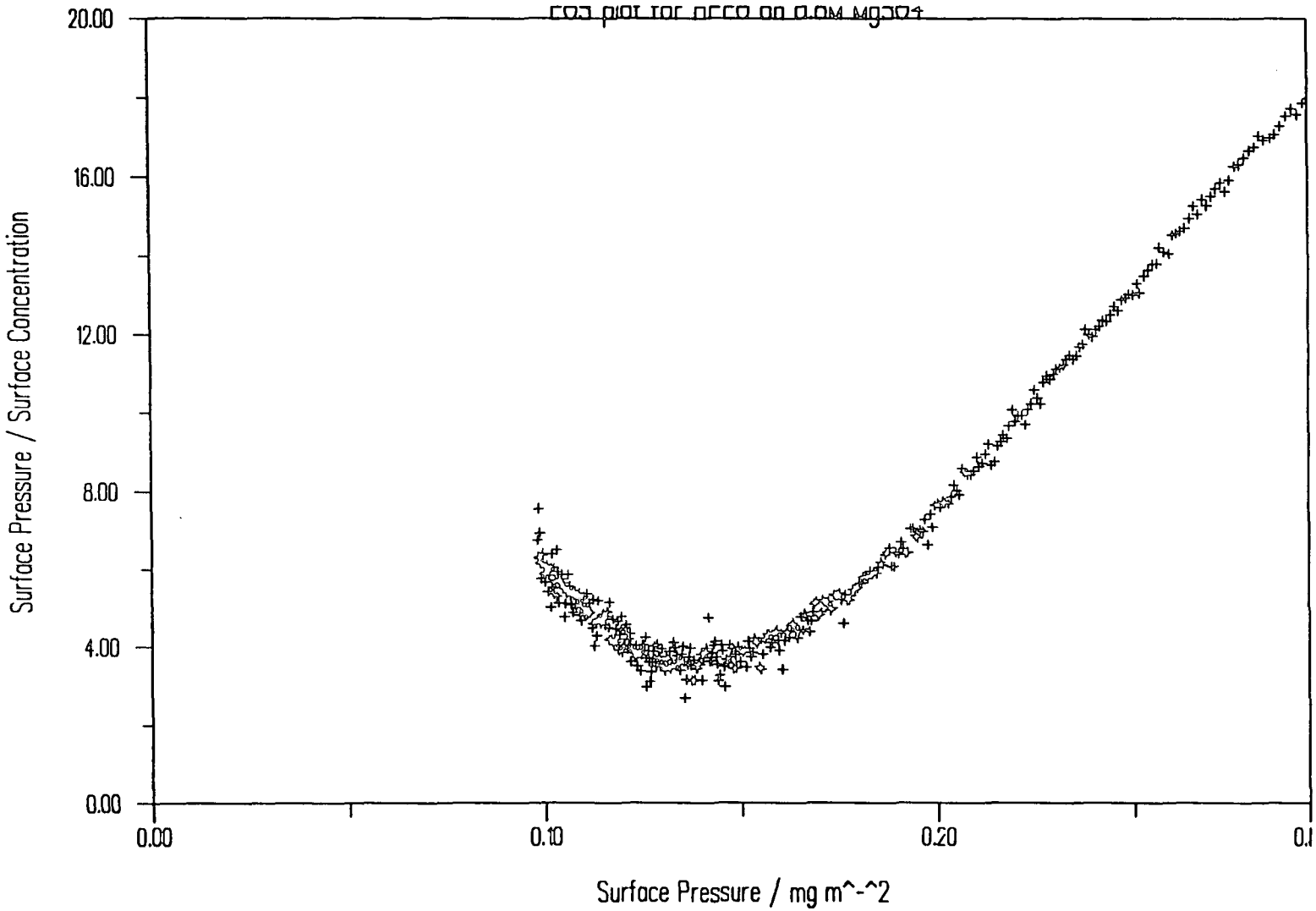

Figure 5.41 Surface Pressure / Surface Concentration v Surface Concentration for HPEO on 0.8M $MgSO_4$

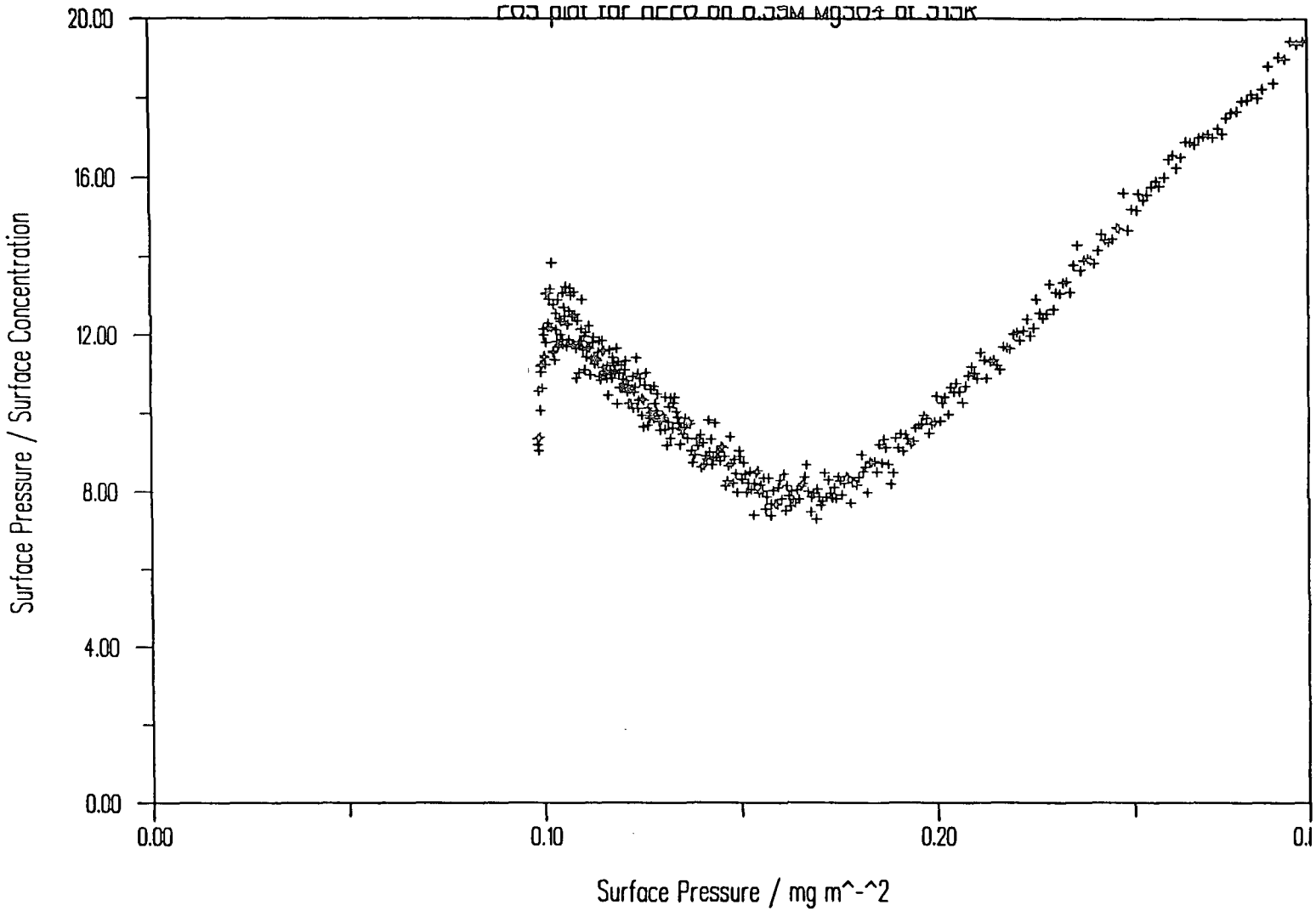

Figure 5.42 Surface Pressure / Surface Concentration v Surface Concentration for HPEO on 0.39 M $MgSO_4$

5.4.2 Neutron Reflectometry

Neutron reflectometry was used to study how and if the surface pressure effects just detailed were reflected in the film structures. Concerns over the possibility of subphase evaporation and the fact that the neutron reflection trough employed had no means of enabling high temperature thermostatting meant that it was impractical to study monolayers spread on the bulk theta solvent system, however it was decided to use two salt concentrations at room temperature, these being 0.4M and 0.8M respectively, the former having given an isotherm slightly changed from the pure water case, and the latter being rather similar to the bulk theta case. As for PEO on water, CRISP was employed in multi-angle mode giving a momentum transfer range of 0.01-0.65$Å^{-1}$.

Reflectivity profiles for DPEO on salt subphases made up in air contrast matched water and HPEO on D_2O salt solutions were recorded at identical surface concentrations to those used for PEO on pure water. These were fitted in a similar fashion to the pure water data using four models; a single slab, a double layer, and gaussian and exponential decays.

Comparing the general trends in the fitted values for the layer thickness and scattering length densities for any of the models with the data for PEO on pure water reported earlier, one can see that in general for a given surface concentration the film spread on a salt subphase is best modelled by a much thinner layer with a more dense packing of polymer in it. Perhaps unexpectedly, the films spread on 0.8M $MgSO_4$ are if anything slightly thicker than those on 0.4M, but they are also modelled as being more dense in polymer.

Of the three models exhaustively applied to the data, namely single film, gaussian and exponential decays, no one model is obviously superior to the others. At low coverages the single film model appears to be most successful in terms of

residual to fit, but as the surface concentration is increased the gaussian or the exponential model seems to be more favoured, perhaps suggesting that there is still some ability for the film to loop into the subphase on compression, although not to such an extent as was the case for the pure water subphase.

A full two layer analysis across both contrasts was not achieved, but tables 5.33 and 5.34 give best fitted values to the D/acmw data which give very low residuals indeed. The film thinning on salt addition is reflected in the collapse of d_1, the upper film thickness, in this case, but forcing these layer thicknesses onto the fit for H/D_2O data did not produce a successful fit. One might expect that the second layer thickness would be the one to collapse on addition of salt and it is possible that the fits obtained were launched from misleading initial estimates. However attempts to locate an equivalent solution with reversed layer thicknesses were unsuccessful.

Γ/mg m^{-2}	D/acmw			H/D_2O		
	d/Å	$\rho/10^{-6}$Å^{-2}	res/10^{-2}	d/Å	$\rho/10^{-6}$Å^{-2}	res/10^{-2}
0.2	7	2.00	0.4728	19	5.31	0.5202
0.3	11	1.75	0.3653	20	5.23	0.7208
0.4	11	2.33	0.4090	19	4.97	1.162
0.5	17	1.75	0.5891	20	5.10	0.9195
0.6	22	1.47	0.5128	19	4.93	0.5522
0.7	24	1.35	0.4801	19	4.92	0.6334
0.8	24	1.16	0.5588	20	4.97	0.6850

Table 5.15 Single Slab Model Fitted Parameters for PEO on 0.4M $MgSO_4$

Γ/mg m^{-2}	D/acmw			H/D_2O	
	d/Å	$\rho/10^{-6}$Å^{-2}	res/10^{-2}	$\rho/10^{-6}$Å^{-2}	res/10^{-2}
0.2	13	1.09	0.4831	4.80	0.5728
0.3	16	1.22	0.3925	4.96	0.7597
0.4	15	1.76	0.4008	4.65	1.208
0.5	19	1.56	0.6037	4.94	0.9028
0.6	21	1.53	0.5182	5.05	0.5808
0.7	22	1.47	0.4850	5.08	0.6977
0.8	22	1.25	0.5662	5.07	0.7118

Table 5.16 Single Slab Model Fitted Parameters for PEO on 0.4M $MgSO_4$ residual optima

Γ/mg m^{-2}	Volume Fraction			ρ.d/10^{-6}Å^{-1}	a.p.m./Å^{2}monomer^{-1}	Γ_a/mgm^{-2}
	polymer	water	air			
0.2	0.17	0.74	0.09	14.2	32.3	0.25
0.3	0.19	0.76	0.05	19.5	23.5	0.34
0.4	0.28	0.71	0.01	26.4	17.3	0.46
0.5	0.25	0.76	-0.01	29.6	15.5	0.52
0.6	0.24	0.77	-0.01	32.1	14.3	0.56
0.7	0.23	0.78	-0.01	32.3	14.2	0.56
0.8	0.20	0.78	0.02	27.5	16.7	0.48

Table 5.17 Single Slab Composition and Apparent Coverage for PEO on 0.4M $MgSO_4$

Γ/mg m^{-2}	D/acmw			H/D_2O		
	d/Å	$\rho/10^{-6}$Å^{-2}	res/10^{-2}	d/Å	$\rho/10^{-6}$Å^{-2}	res/10^{-2}
0.2	9	2.50	0.4178	24	4.77	0.4602
0.3	13	2.39	0.3560	31	4.86	0.6532
0.4	12	3.44	0.3910	69	5.08	1.089
0.5	19	2.53	0.5277	31	4.57	0.8224
0.6	25	2.10	0.4162	26	4.32	0.4766
0.7	25	2.10	0.3934	26	4.31	0.5728
0.8	26	1.73	0.4637	31	4.52	0.6308

Table 5.18 Gaussian Model Fitted Parameters for PEO on 0.4M $MgSO_4$

Γ/mg m^{-2}	D/acmw			H/D_2O	
	d/Å	$\rho/10^{-6}$Å^{-2}	res/10^{-2}	$\rho/10^{-6}$Å^{-2}	res/10^{-2}
0.2	17	1.35	0.4884	4.01	0.5173
0.3	22	1.46	0.4496	4.42	0.7075
0.4	41	1.17	1.234	4.87	1.092
0.5	25	1.99	0.5918	4.25	0.8492
0.6	26	2.04	0.4206	4.32	0.4766
0.7	26	2.03	0.3943	4.31	0.5728
0.8	28	1.63	0.4740	4.42	0.6360

Table 5.19 Gaussian Model Fitted Parameters for PEO on 0.4M $MgSO_4$, residual optima

Γ/mg m^{-2}	Volume Fraction			$\rho.d/10^{-6}$Å^{-1}	a.p.m./Å^{2}monomer^{-1}	Γ_a/mgm^{-2}
	polymer	water	air			
0.2	0.21	0.61	0.18	14.4	31.9	0.25
0.3	0.23	0.68	0.09	20.1	22.8	0.35
0.4	0.19	0.75	0.06	30.1	15.2	0.52
0.5	0.31	0.64	0.05	31.2	14.7	0.54
0.6	0.32	0.65	0.03	33.2	13.8	0.58
0.7	0.32	0.65	0.03	33.1	13.9	0.58
0.8	0.26	0.67	0.07	28.6	16.0	0.50

Table 5.20 Gaussian Model Composition and Apparent Coverage for PEO on 0.4M $MgSO_4$

Γ/mg m^{-2}	D/acmw			H/D_2O		
	d/Å	$\rho/10^{-6}$Å^{-2}	res/10^{-2}	d/Å	$\rho/10^{-6}$Å^{-2}	res/10^{-2}
0.2	8	3.57	0.4704	23	3.78	0.4269
0.3	10	3.94	0.3436	39	4.35	0.5864
0.4	9	5.84	0.3677	120	4.82	0.9150
0.5	15	4.13	0.4559	40	3.98	0.7356
0.6	19	3.56	0.3074	26	3.12	0.4380
0.7	19	3.55	0.3167	25	2.99	0.5472
0.8	20	2.90	0.3559	34	3.72	0.5728

Table 5.21 Exponential Model Fitted Parameters for PEO on 0.4M $MgSO_4$

Γ/mg m^{-2}	D/acmw			H/D_2O	
	d/Å	$\rho/10^{-6}$Å^{-2}	res/10^{-2}	$\rho/10^{-6}$Å^{-2}	res/10^{-2}
0.2	16	1.85	0.4919	2.39	0.4599
0.3	25	1.73	0.6637	3.60	0.6230
0.4	65	1.24	1.972	4.49	0.9310
0.5	28	2.76	1.102	3.26	0.7574
0.6	23	3.04	0.3787	2.68	0.4469
0.7	22	3.15	0.3516	2.48	0.5561
0.8	27	2.29	0.4966	3.18	0.5903

Table 5.22 Exponential Model Fitted Parameters for PEO on 0.4M $MgSO_4$, residual optima

Γ/mg m^{-2}	Volume Fraction			$\rho.d/10^{-6}$Å^{-1}	a.p.m./Å^{2}monomer^{-1}	Γ_a/mgm^{-2}
	polymer	water	air			
0.2	0.29	0.35	0.36	14.7	31.2	0.26
0.3	0.27	0.54	0.19	21.5	21.3	0.37
0.4	0.20	0.69	0.11	40.0	11.6	0.70
0.5	0.44	0.47	0.09	38.4	11.9	0.67
0.6	0.48	0.38	0.14	34.7	13.2	0.60
0.7	0.50	0.35	0.15	34.4	13.3	0.60
0.8	0.36	0.47	0.17	30.7	14.9	0.53

Table 5.23 Exponential Model Composition and Apparent Coverage for PEO on 0.4M $MgSO_4$

Γ/mg m^{-2}	D/acmw			H/D_2O		
	d/Å	$\rho/10^{-6}$Å^{-2}	res/10^{-2}	d/Å	$\rho/10^{-6}$Å^{-2}	res/10^{-2}
0.2	10	1.65	0.4214	20	5.76	0.4308
0.3	9	2.37	0.2910	22	5.69	0.3830
0.4	15	2.15	0.4723	20	5.48	0.4790
0.5	16	2.04	0.5114	20	5.49	0.4578
0.6	26	1.46	0.7295	21	5.29	0.4946
0.7	25	1.65	0.8065	23	5.30	0.4587
0.8	26	1.46	0.7295	21	5.27	0.3769

Table 5.24 Single Slab Model Fitted Parameters for PEO on 0.8M $MgSO_4$

Γ/mg m^{-2}	D/acmw			H/D_2O	
	d/Å	$\rho/10^{-6}$Å^{-2}	res/10^{-2}	$\rho/10^{-6}$Å^{-2}	res/10^{-2}
0.2	15	1.13	0.4587	5.65	0.5151
0.3	16	1.37	0.4391	5.55	0.4971
0.4	17	1.91	0.4838	5.39	0.5264
0.5	18	1.84	0.5254	5.42	0.4752
0.6	23	1.61	0.7567	5.37	0.5209
0.7	24	1.70	0.8618	5.33	0.4737
0.8	24	1.64	0.7611	5.38	0.4505

Table 5.25 Single Slab Model Fitted Parameters for PEO on 0.8M $MgSO_4$, residual optima

Γ/mg m^{-2}	Volume Fraction			$\rho.d/10^{-6}$Å^{-1}	a.p.m./Å^{2}monomer^{-1}	Γ_a/mgm^{-2}
	polymer	water	air			
0.2	0.18	0.87	-0.05	17.0	26.9	0.30
0.3	0.22	0.85	-0.07	21.9	20.9	0.38
0.4	0.30	0.82	-0.12	32.5	14.1	0.57
0.5	0.29	0.83	-0.12	33.1	13.8	0.58
0.6	0.25	0.82	-0.07	37.0	12.4	0.64
0.7	0.27	0.82	-0.09	40.8	11.2	0.71
0.8	0.26	0.82	-0.08	41.8	11.0	0.72

Table 5.26 Single Slab Composition and Apparent Coverage for PEO on 0.8M $MgSO_4$

Γ/mg m^{-2}	D/acmw			H/D_2O		
	d/Å	$\rho/10^{-6}$Å^{-2}	res/10^{-2}	d/Å	$\rho/10^{-6}$Å^{-2}	res/10^{-2}
0.2	10	2.62	0.4217	25	5.53	0.4972
0.3	8	4.27	0.2887	29	5.44	0.4589
0.4	17	3.06	0.4143	25	5.12	0.5821
0.5	18	2.94	0.4496	26	5.16	0.5142
0.6	30	2.07	0.5825	29	4.94	0.6204
0.7	29	2.33	0.7019	32	4.94	0.5760
0.8	31	2.26	0.8240	28	4.86	0.5017

Figure 5.27 Gaussian Model Fitted Parameters for PEO on 0.8M $MgSO_4$

Γ/mg m^{-2}	D/acmw			H/D_2O	
	d/Å	$\rho/10^{-6}$Å^{-2}	res/10^{-2}	$\rho/10^{-6}$Å^{-2}	res/10^{-2}
0.2	17	1.58	0.4582	5.23	0.5492
0.3	19	1.87	0.5185	5.13	0.5404
0.4	21	2.54	0.4712	4.93	0.6026
0.5	22	2.47	0.5086	4.99	0.5714
0.6	29	2.13	0.5841	4.94	0.6204
0.7	31	2.21	0.7139	4.91	0.5770
0.8	30	2.32	0.8267	4.93	0.5062

Table 5.28 Gaussian Model Fitted Parameters for PEO on 0.8M $MgSO_4$, residual optima

Γ/mg m^{-2}	Volume Fraction			ρ.d/10^{-6}Å^{-1}	a.p.m./Å^{2}monomer^{-1}	Γ_a/mgm^{-2}
	polymer	water	air			
0.2	0.25	0.80	-0.05	16.8	27.2	0.29
0.3	0.30	0.77	-0.07	22.3	20.6	0.39
0.4	0.40	0.74	-0.14	33.4	13.7	0.58
0.5	0.39	0.75	-0.14	34.1	13.5	0.59
0.6	0.34	0.75	-0.09	38.7	11.8	0.67
0.7	0.35	0.74	-0.09	42.9	10.7	0.75
0.8	0.37	0.74	-0.11	43.6	10.5	0.76

Table 5.29 Gaussian Model Composition and Apparent Coverage for PEO on 0.8M $MgSO_4$

Γ/mg m^{-2}	D/acmw			H/D_2O		
	d/Å	$\rho/10^{-6}$Å^{-2}	res/10^{-2}	d/Å	$\rho/10^{-6}$Å^{-2}	res/10^{-2}
0.2	7	4.74	0.4219	22	5.02	0.5432
0.3	6	7.21	0.2919	31	5.07	0.4898
0.4	13	5.12	0.3510	22	4.32	0.6408
0.5	13	5.19	0.3825	24	4.47	0.6096
0.6	24	3.37	0.4135	28	4.18	0.6938
0.7	23	3.82	0.5220	34	4.32	0.6398
0.8	26	3.56	0.6243	26	3.96	0.5892

Table 5.30 Exponential Model Fitted Parameters for PEO on 0.8M $MgSO_4$

Γ/mg m^{-2}	Volume Fraction			$\rho.d/10^{-6}$Å^{-1}	a.p.m./Å^{2}monomer^{-1}	Γ_a/mgm^{-2}
	polymer	water	air			
0.2	0.39	0.64	-0.03	17.0	26.9	0.30
0.3	0.41	0.66	-0.07	23.0	20.0	0.40
0.4	0.64	0.53	-0.17	34.3	13.4	0.60
0.5	0.62	0.55	-0.17	35.0	13.1	0.61
0.6	0.50	0.59	-0.09	40.9	11.2	0.71
0.7	0.52	0.56	-0.08	45.9	10.0	0.80
0.8	0.56	0.57	-0.13	45.9	10.0	0.80

Table 5.31 Exponential Model Composition and Apparent Coverage for PEO on 0.8M $MgSO_4$

Γ/mg m^{-2}	D/acmw			H/D_2O	
	d/Å	$\rho/10^{-6}$Å^{-2}	res/10^{-2}	$\rho/10^{-6}$Å^{-2}	res/10^{-2}
0.2	14	2.45	0.4730	4.29	0.5583
0.3	18	2.57	0.7201	4.41	0.5367
0.4	17	4.06	0.4608	3.72	0.6548
0.5	18	3.92	0.5042	3.87	0.6279
0.6	26	3.17	0.4215	4.04	0.6950
0.7	28	3.30	0.5884	3.88	0.6558
0.8	26	3.56	0.6243	3.96	0.5892

Table 5.32 Exponential Model Fitted Parameters for PEO on 0.8M $MgSO_4$, residual optima

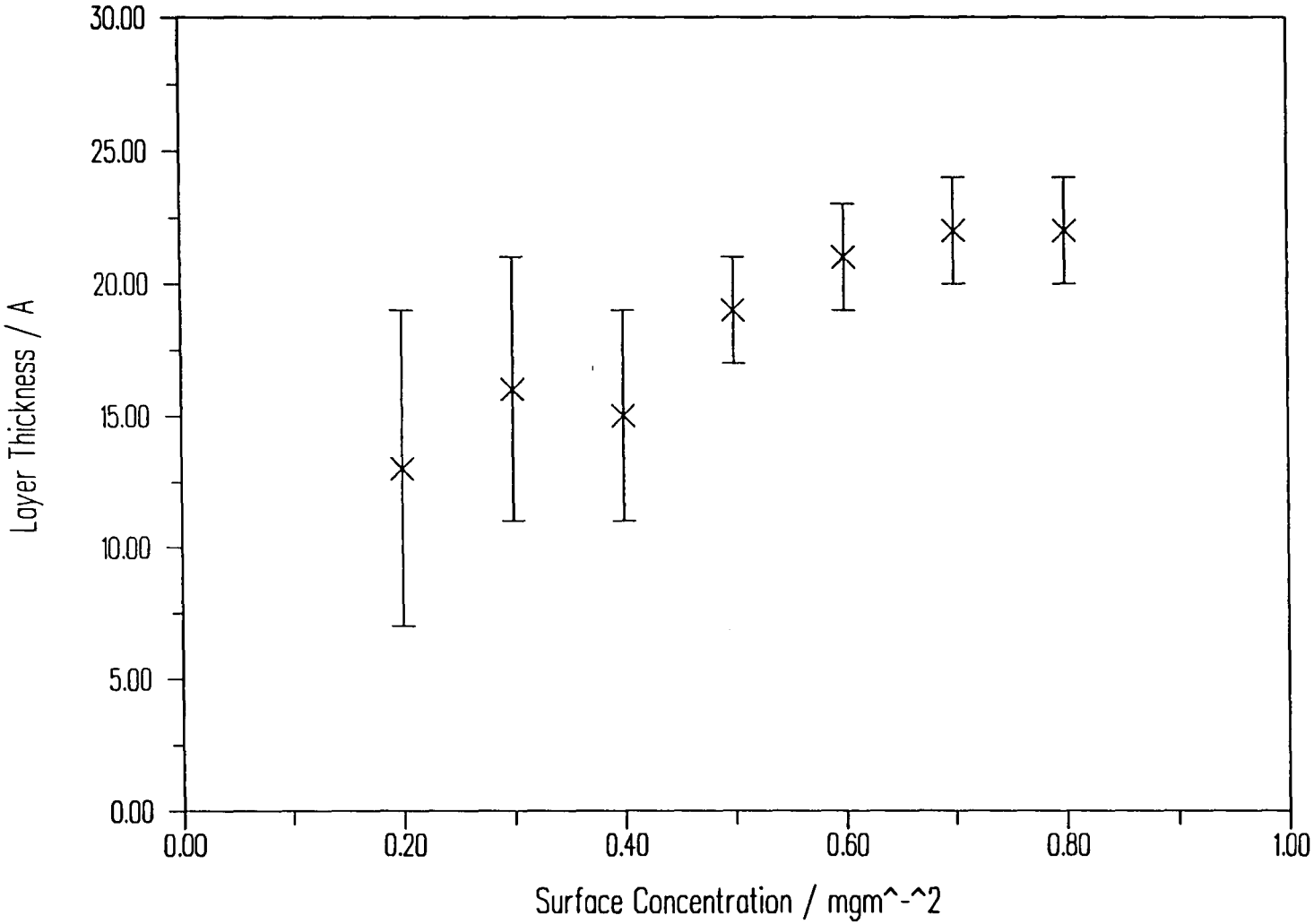

Figure 5.43 Variation of Layer Thickness with Surface Concentration for PEO on 0.4M $MgSO_4$ Slab Model

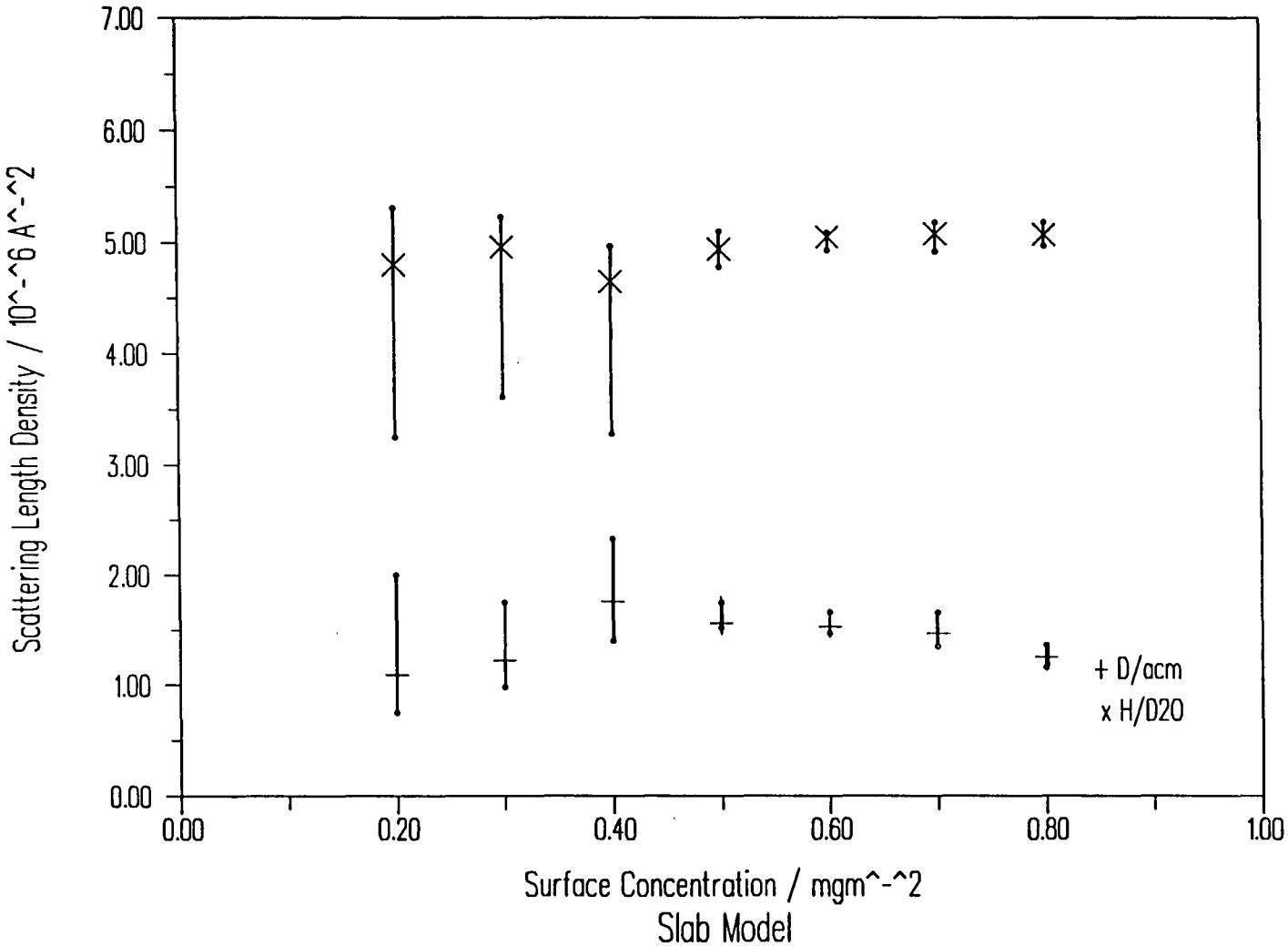

Figure 5.44 Variation of Scattering Length Density for PEO on 0.4M $MgSO_4$

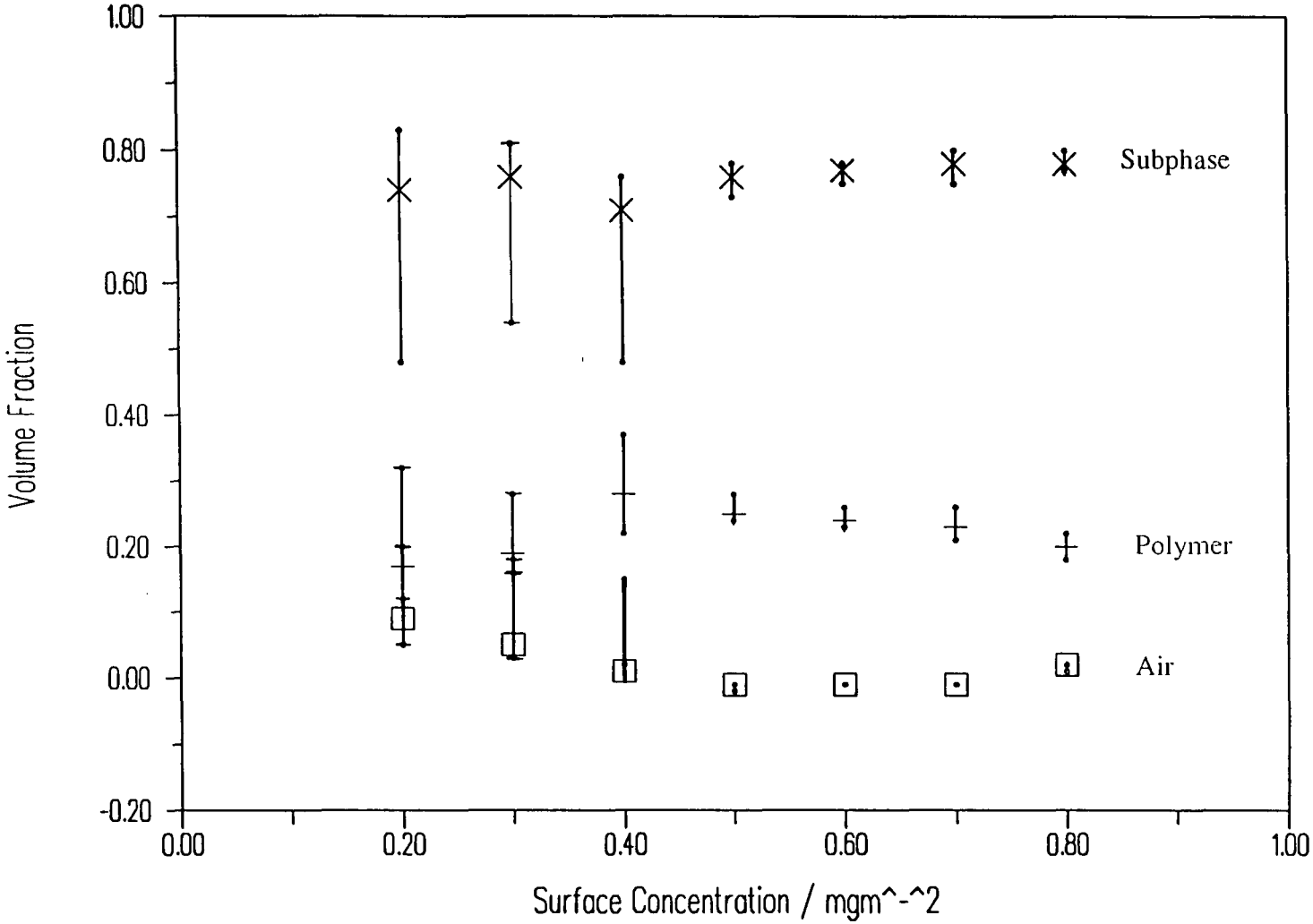

Figure 5.45 Variation of Layer Composition for PEO on 0.4M $MgSO_4$

Slab Model

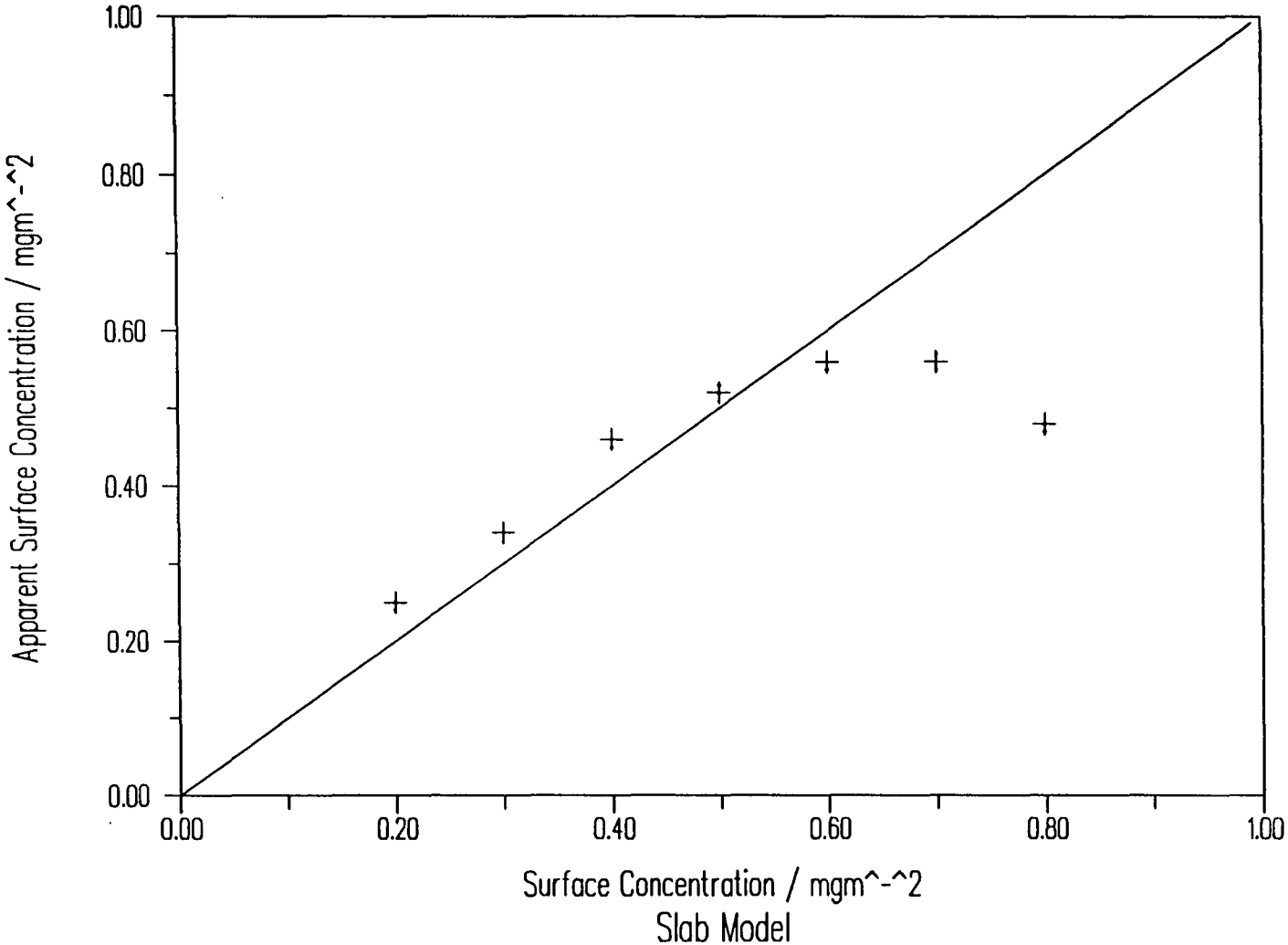

Figure 5.46 Variation of Apparent Surface Coverage for PEO on 0.4M $MgSO_4$

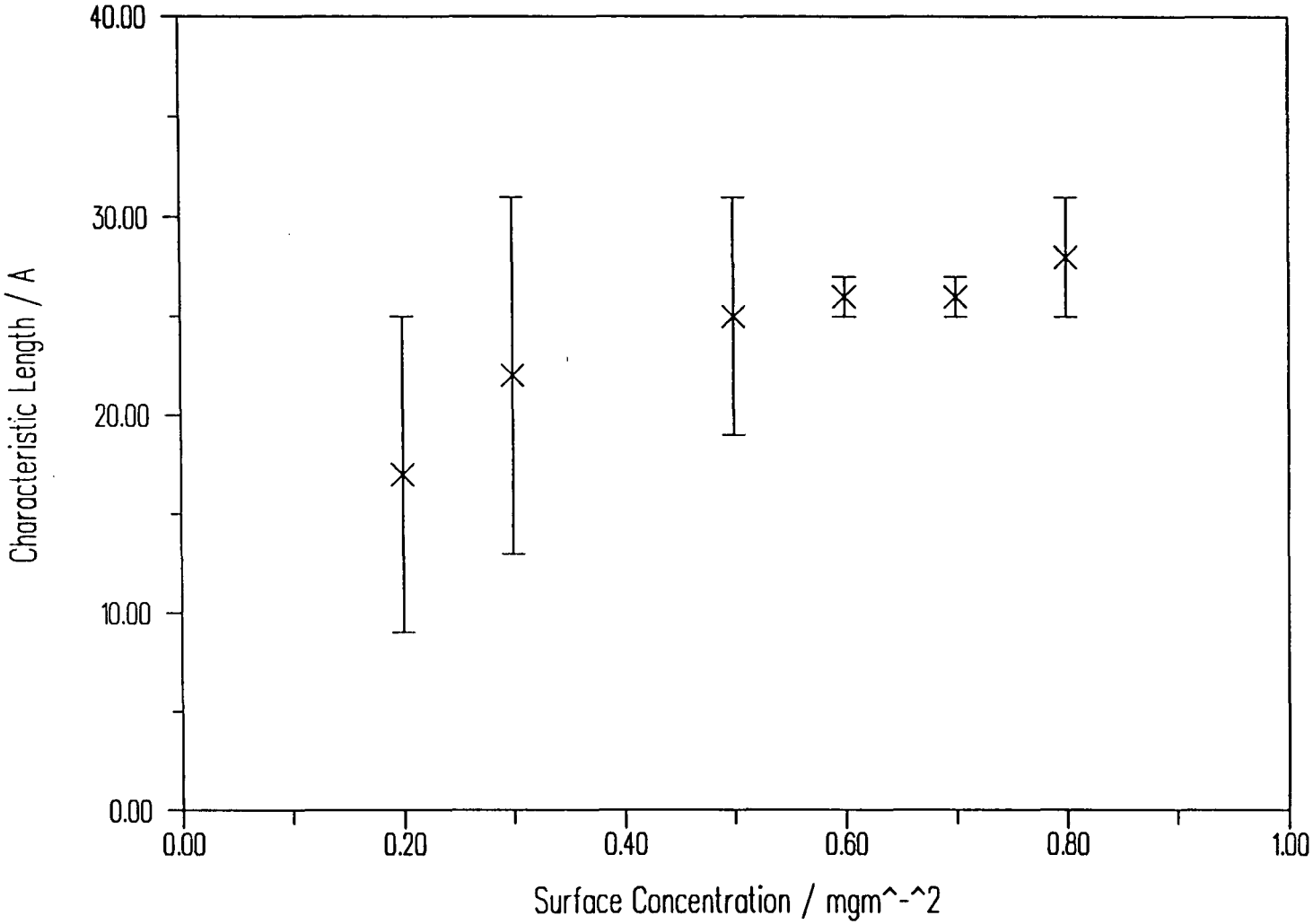

Figure 5.47 Variation of Layer Characteristic Length for PEO on 0.4M $MgSO_4$

Gaussian Model

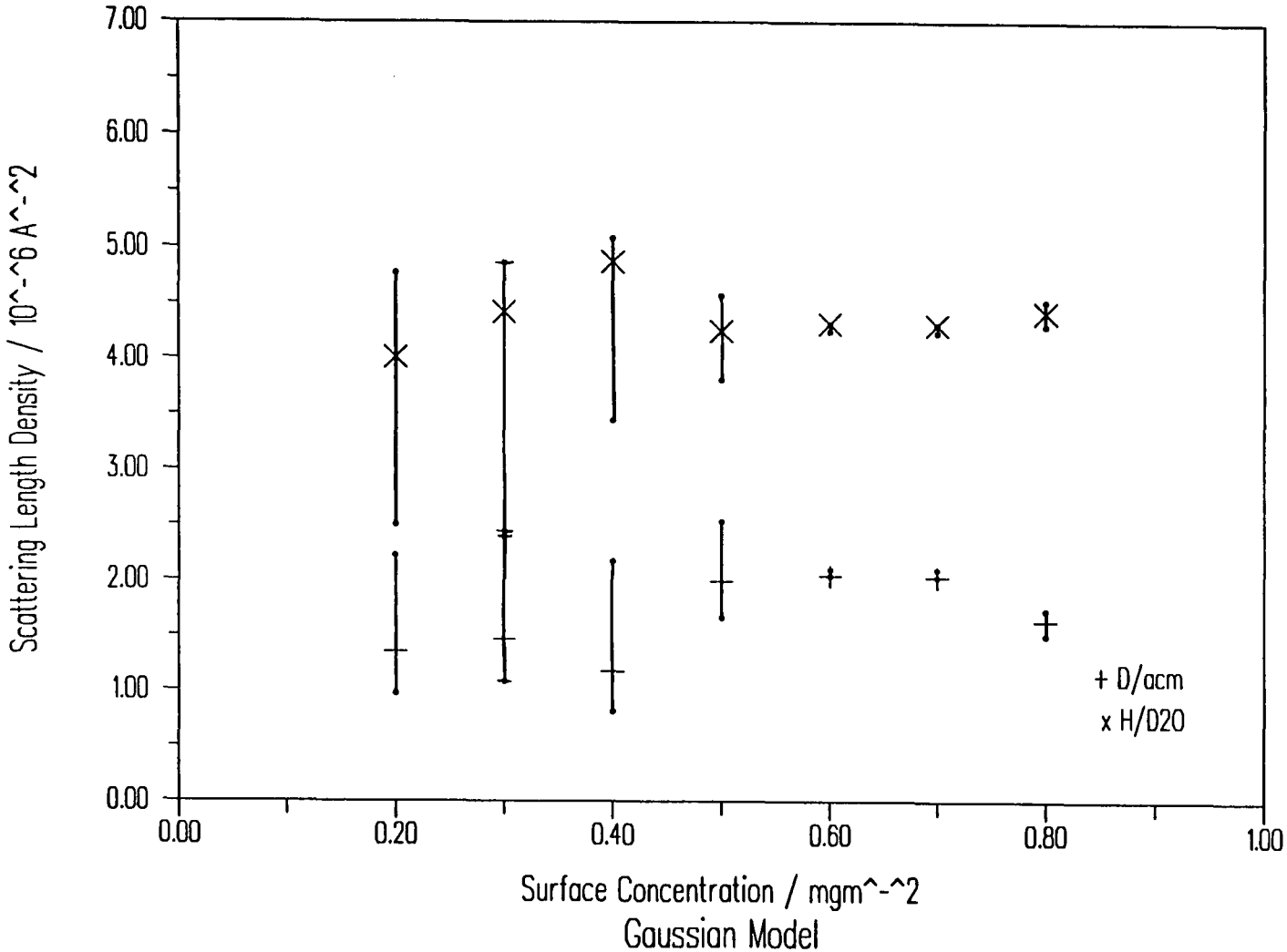

Figure 5.48 Variation of Topmost Layer Scattering Length Density in a Gaussian Distribution for PEO on 0.4M $MgSO_4$

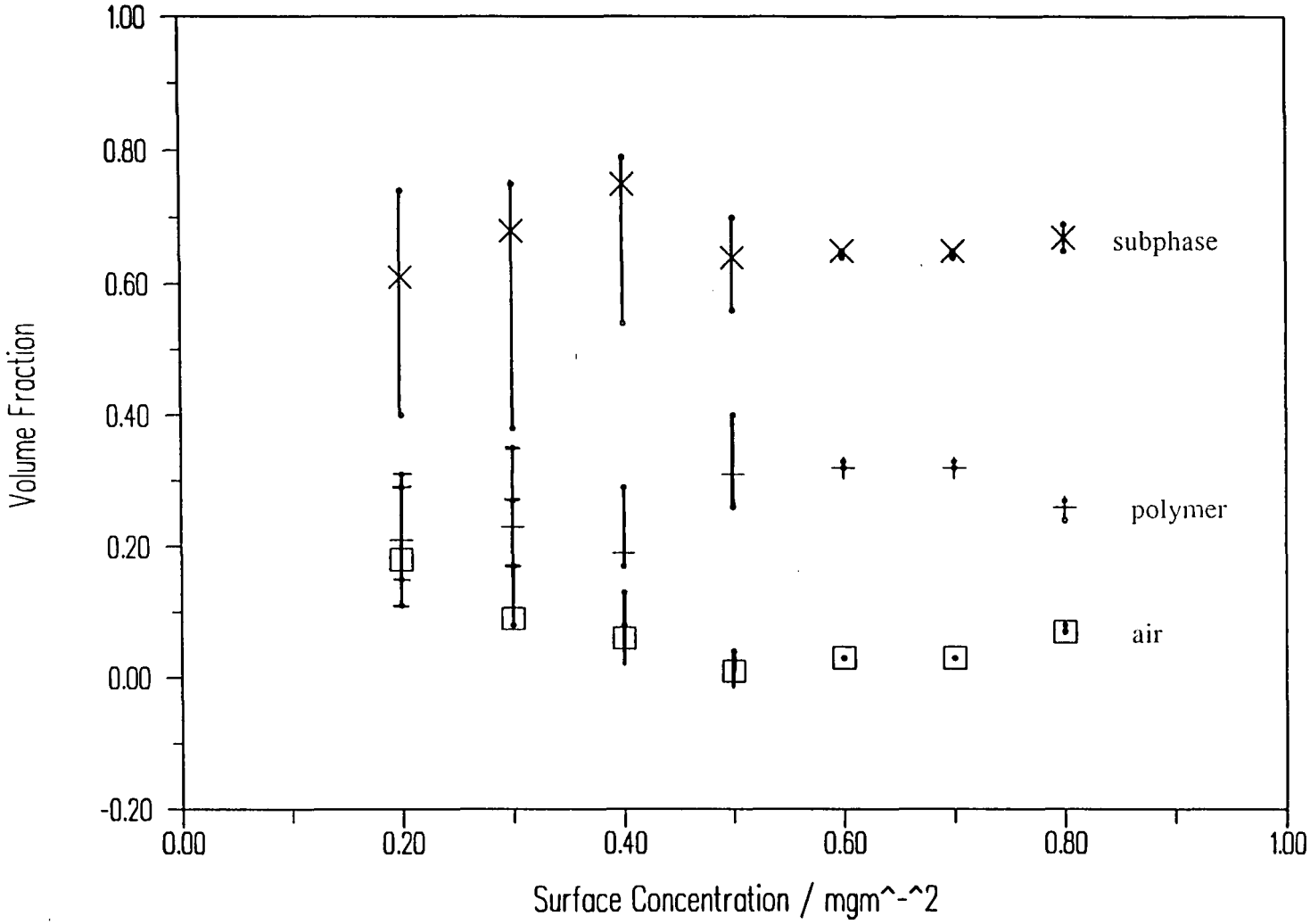

Figure 5.49 Variation in Composition for the Topmost Layer of a Gaussian Distribution for PEO on 0.4M $MgSO_4$

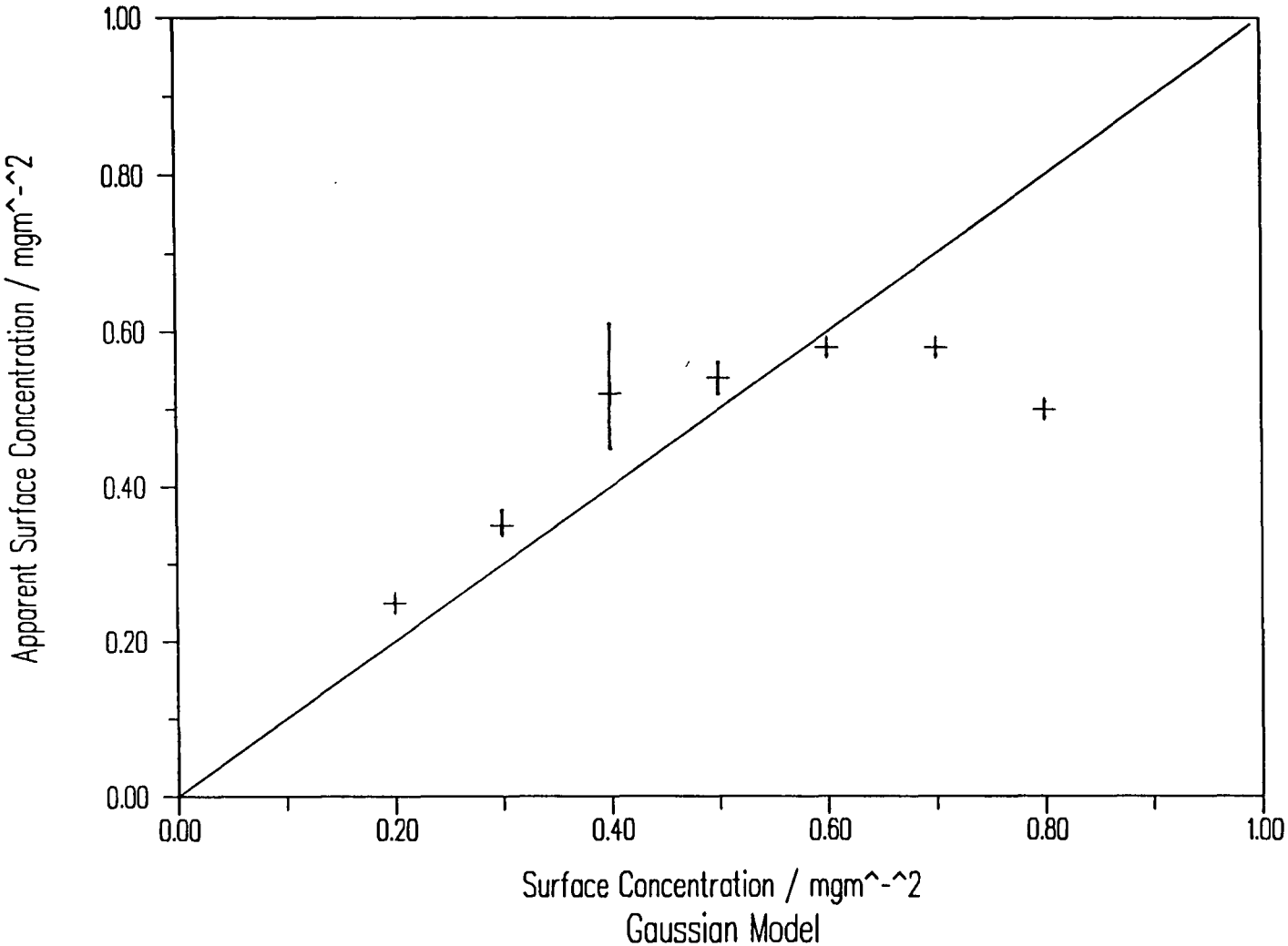

Figure 5.50 Variation of Apparent Surface Coverage for PEO on 0.4M $MgSO_4$

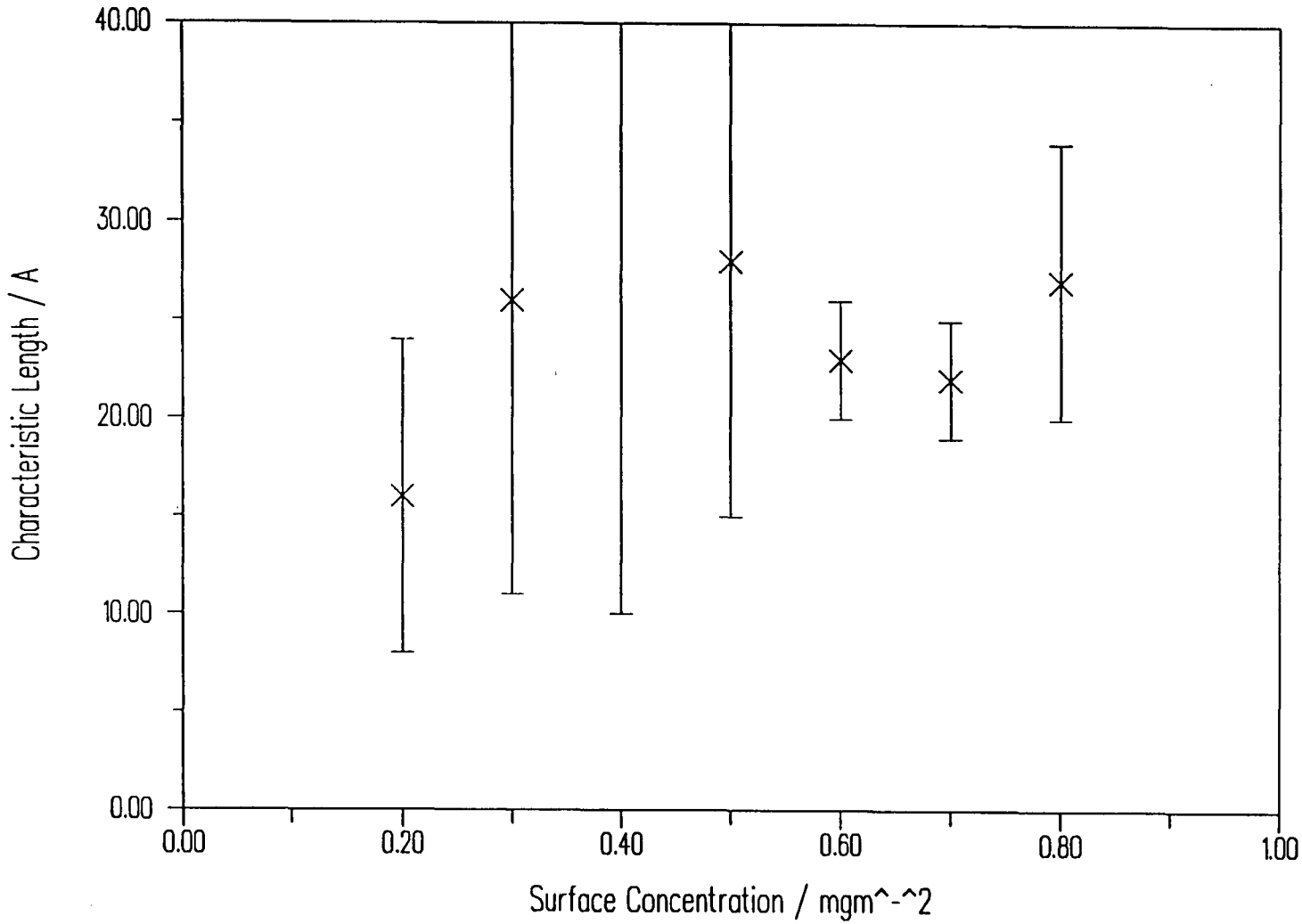

Figure 5.51 Variation of Layer Characteristic length for PEO on 0.4M $MgSO_4$

Exponential Model

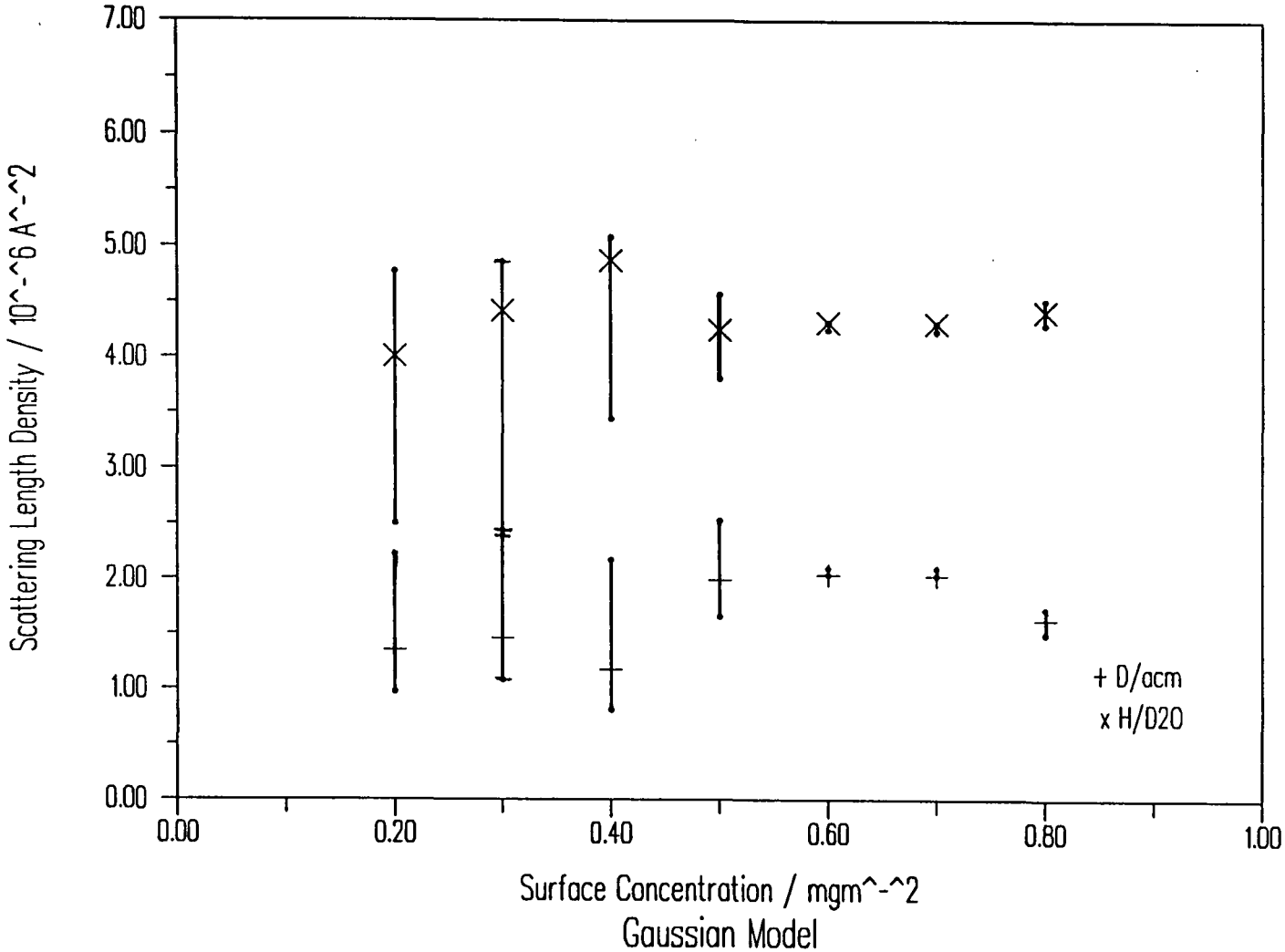

Figure 5.52 Variation of Scattering length Density for PEO on 0.4M $MgSO_4$

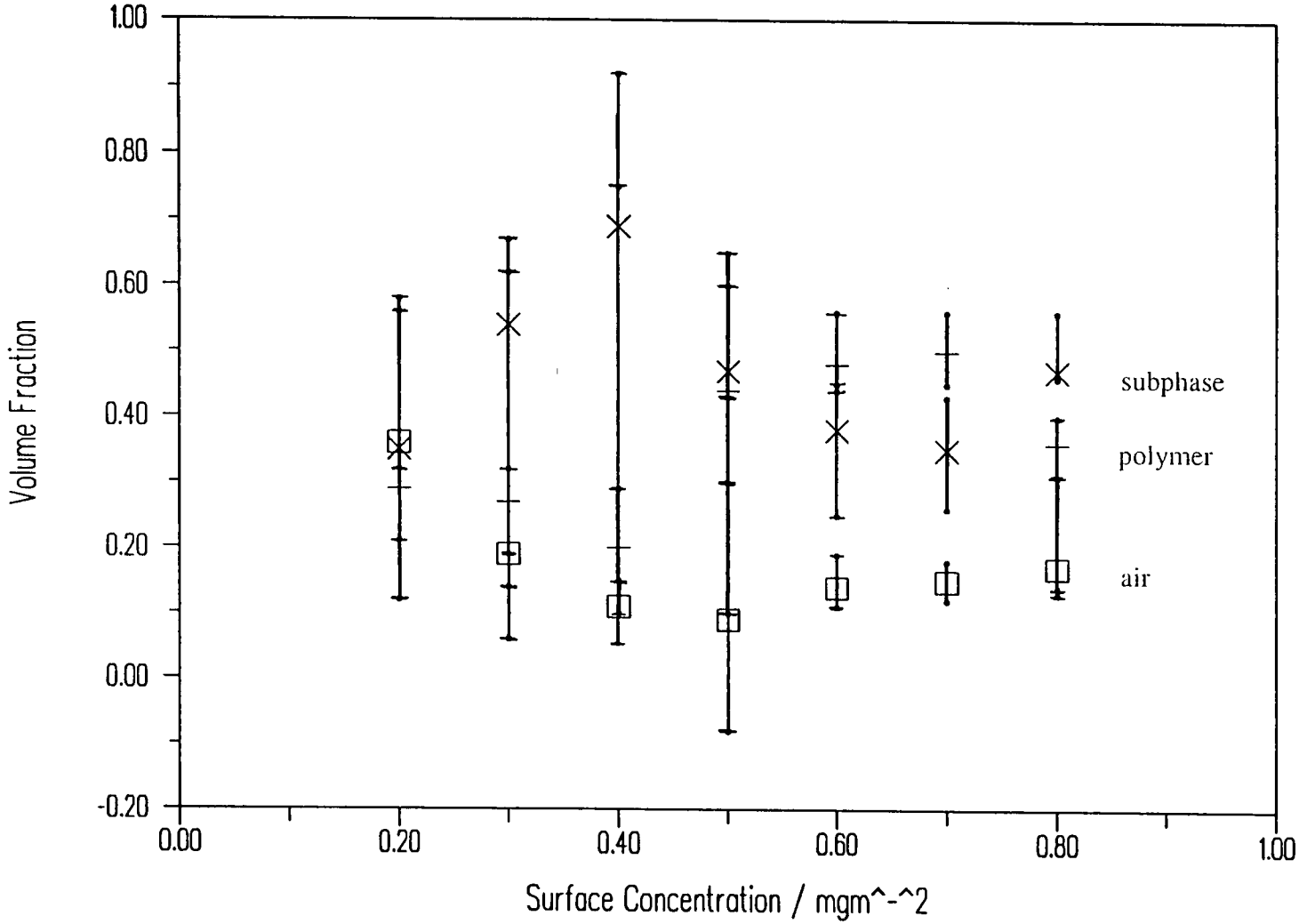

Figure 5.53 Variation of Topmost Layer Composition for an Exponential Distribution

PEO on 0.4M $MgSO_4$

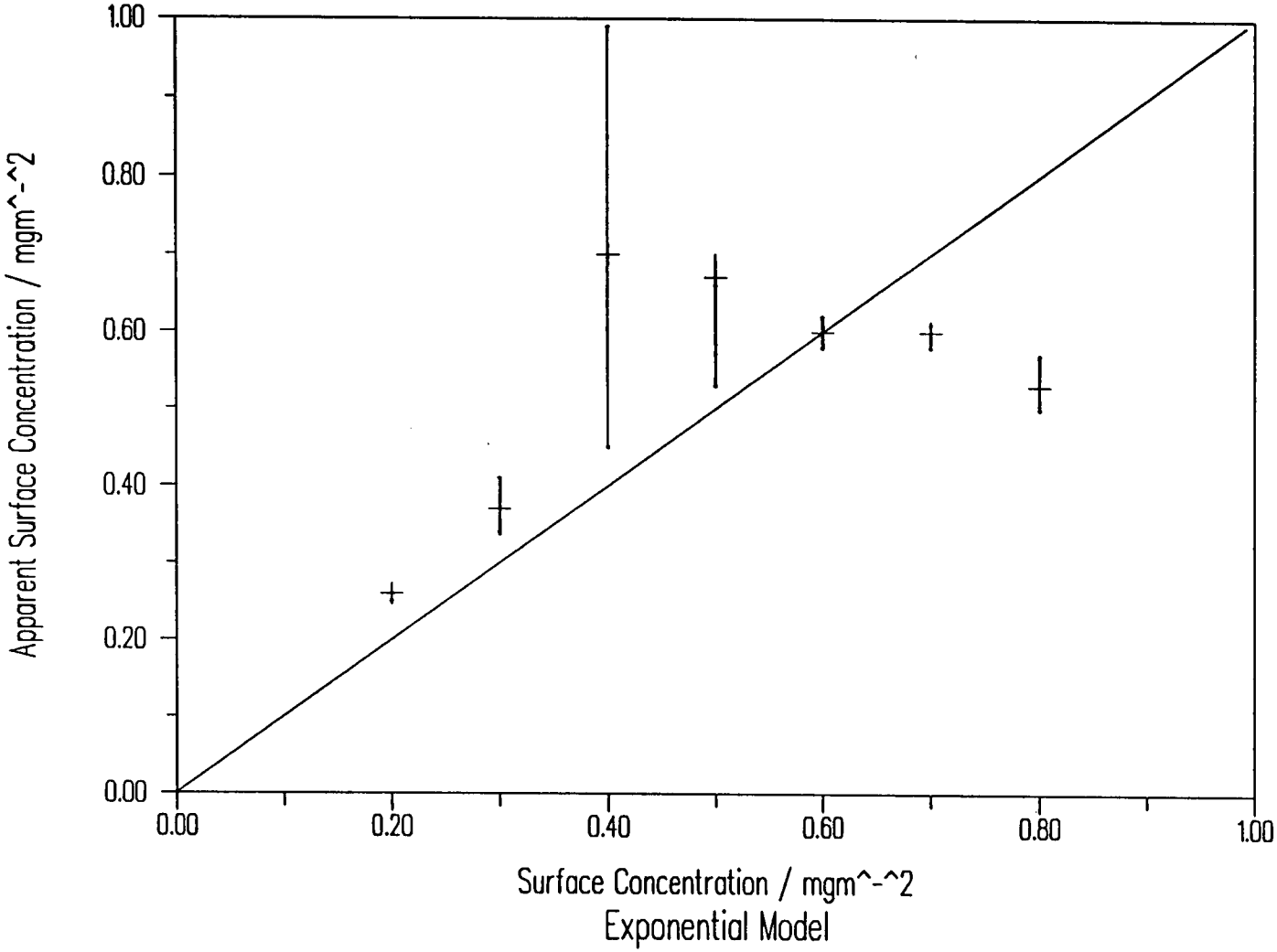

Figure 5.54 Variation of Apparent Surface Coverage for PEO on 0.4M $MgSO_4$

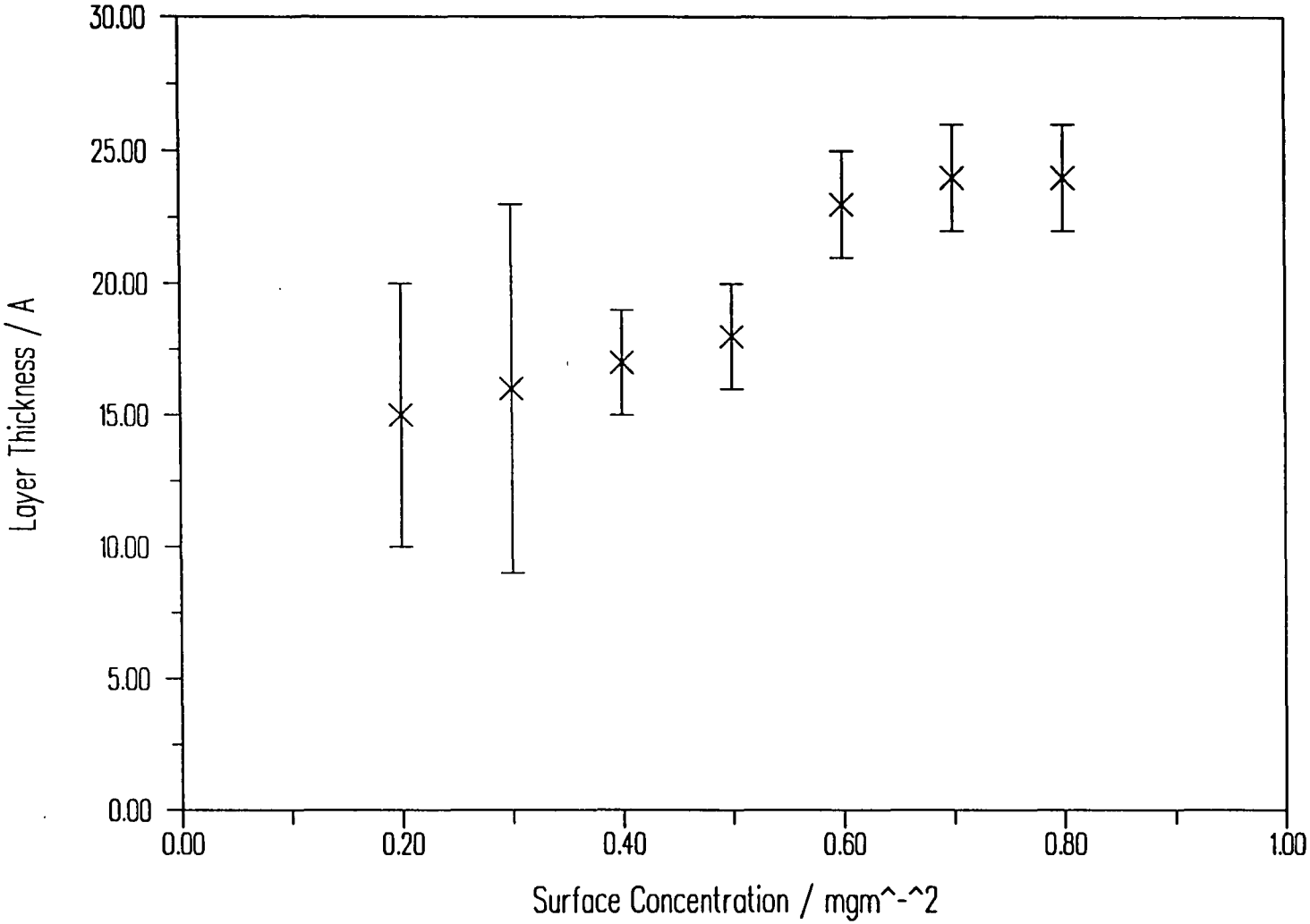

Figure 5.55 Variation of Layer Thickness for PEO on 0.8M $MgSO_4$

Slab Model

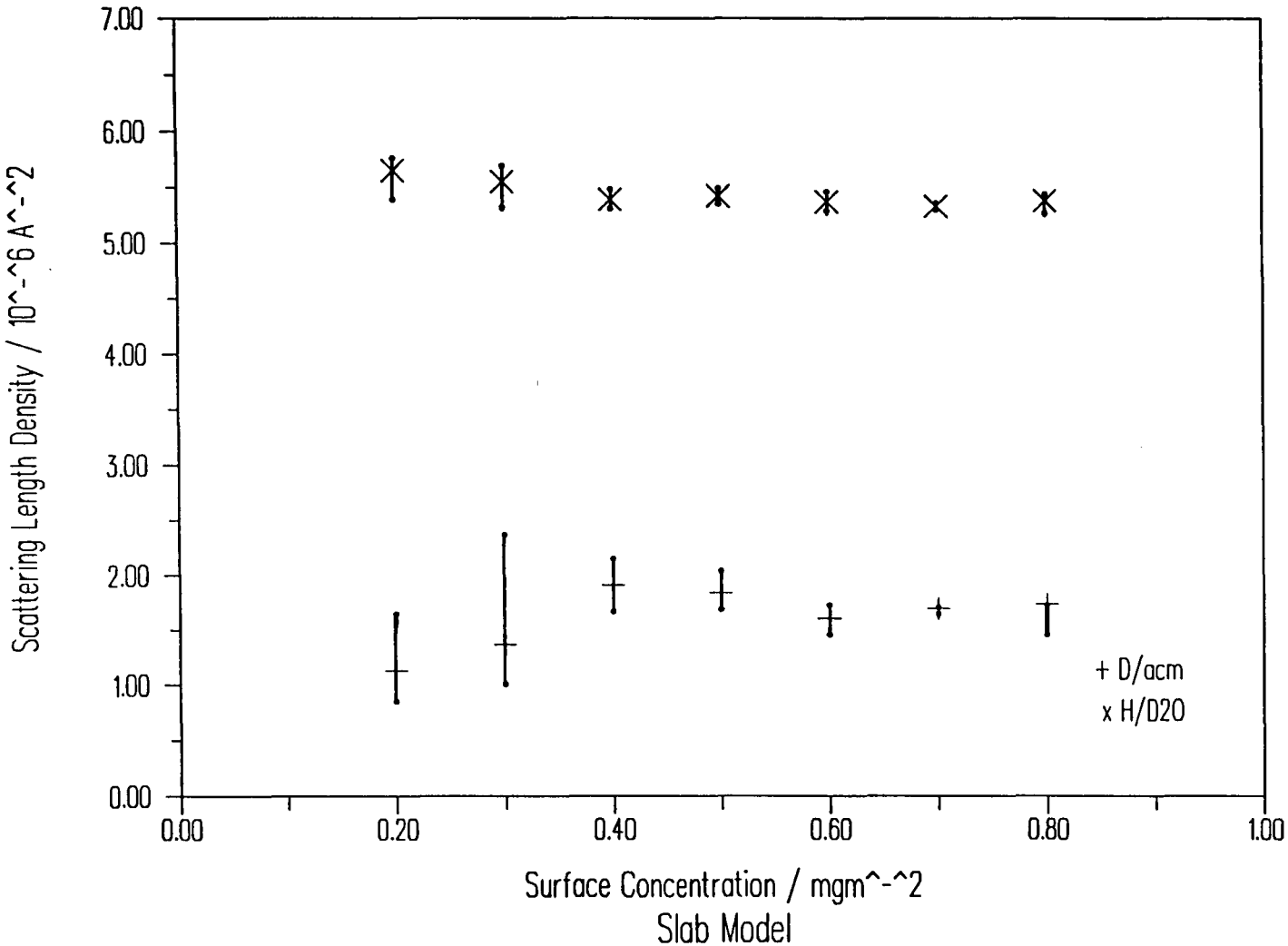

Figure 5.56 Variation of Scattering length Density for PEO on 0.8M $MgSO_4$

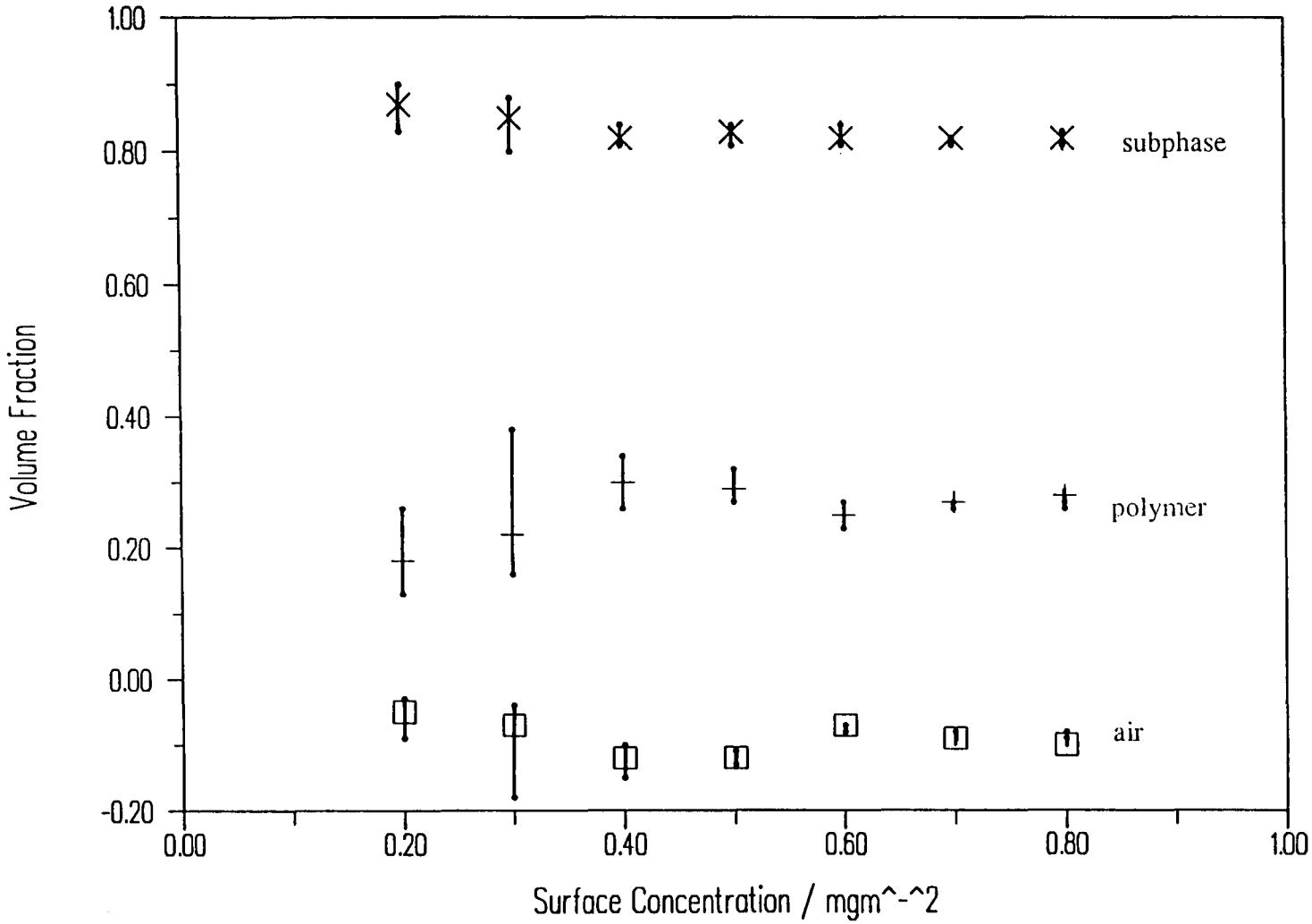

Figure 5.57 Variation of Film Composition for PEO on 0.8M $MgSO_4$

Slab Model

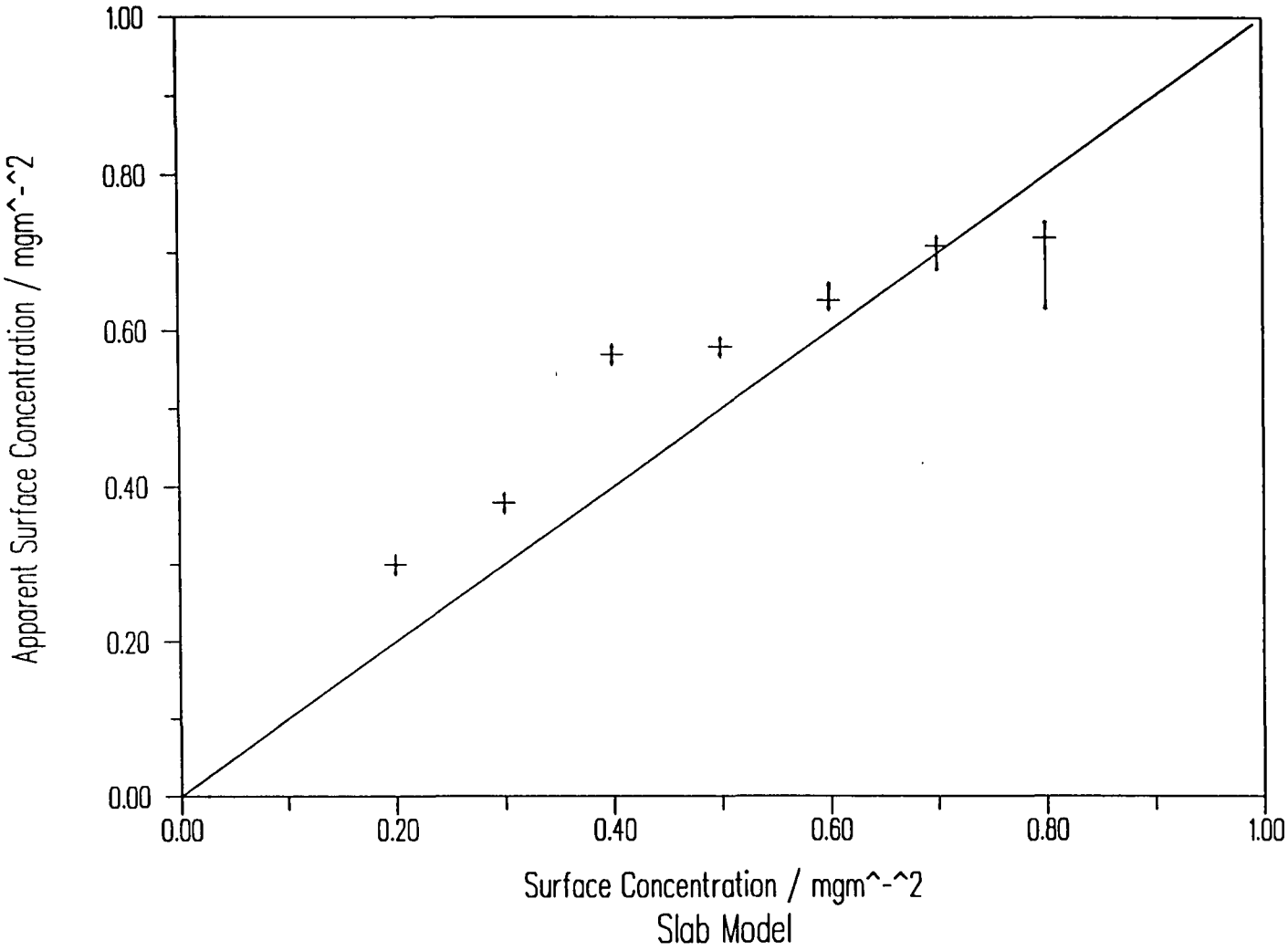

Figure 5.58 Variation of Apparent Surface Concentration for PEO on 0.8M $MgSO_4$

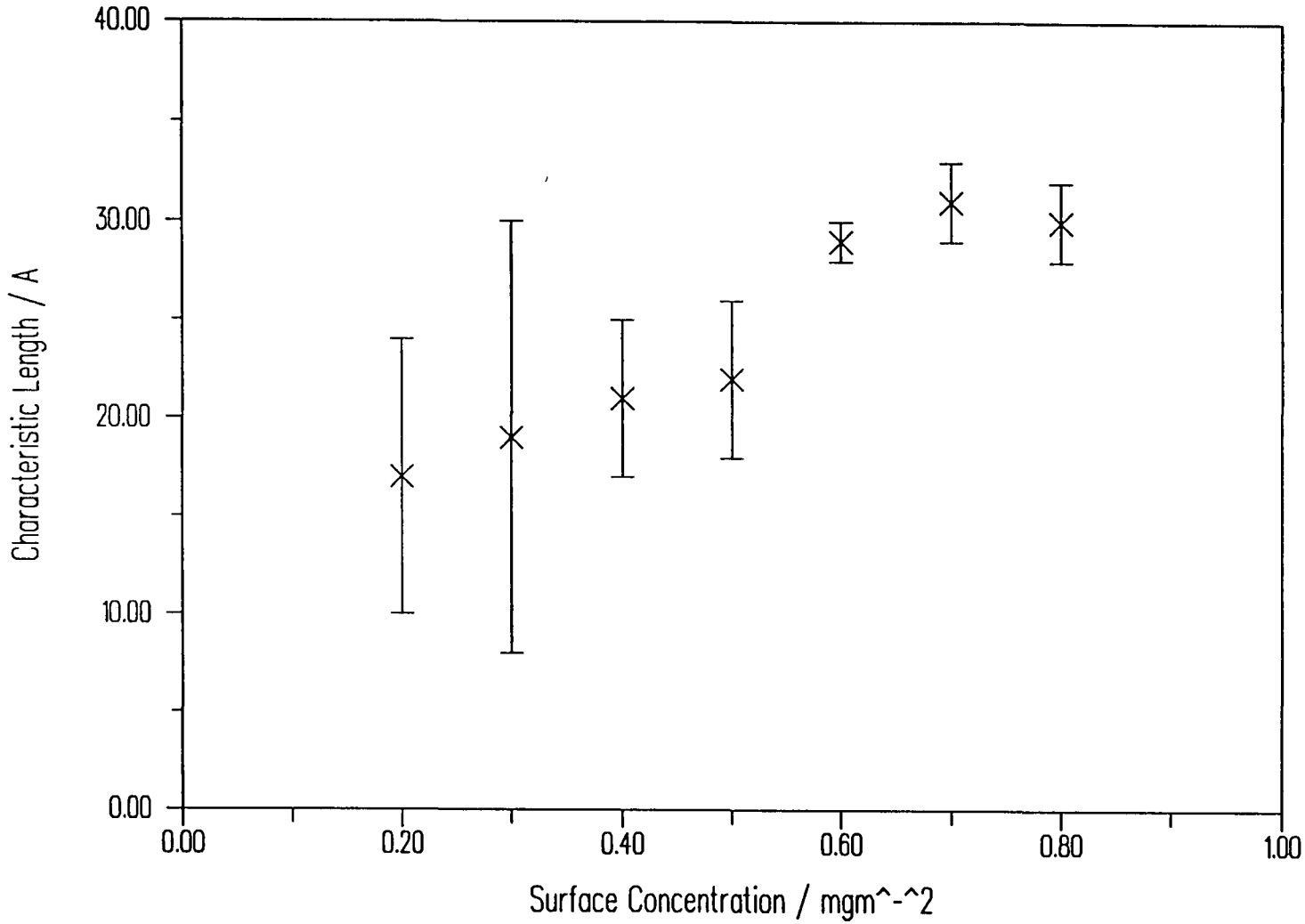

Figure 5.59 Variation in Layer Characteristic Length for PEO on 0.8M $MgSO_4$

Gaussian Model

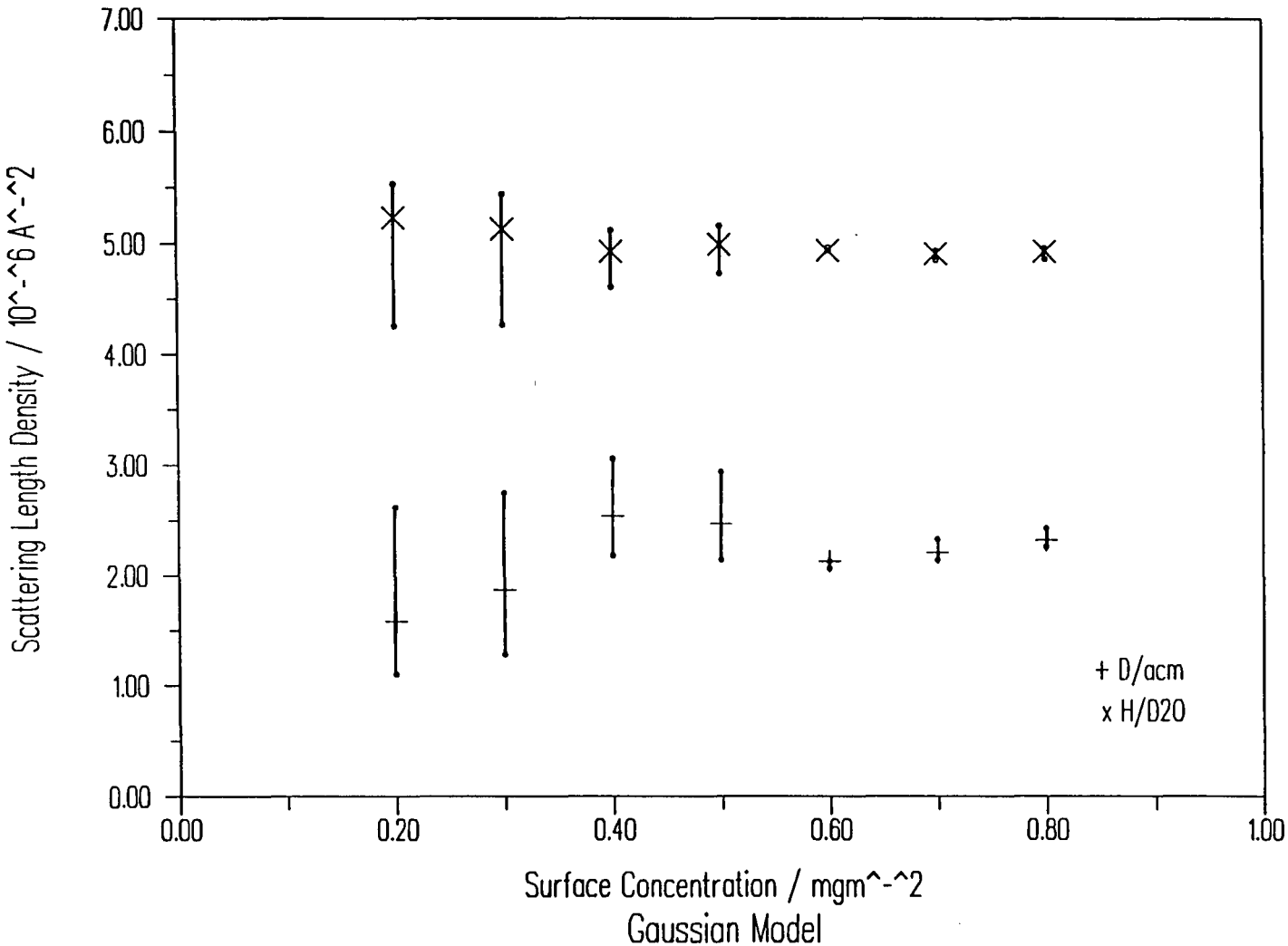

Figure 5.60 Variation in Topmost Layer Scattering length Density for PEO on 0.8M $MgSO_4$

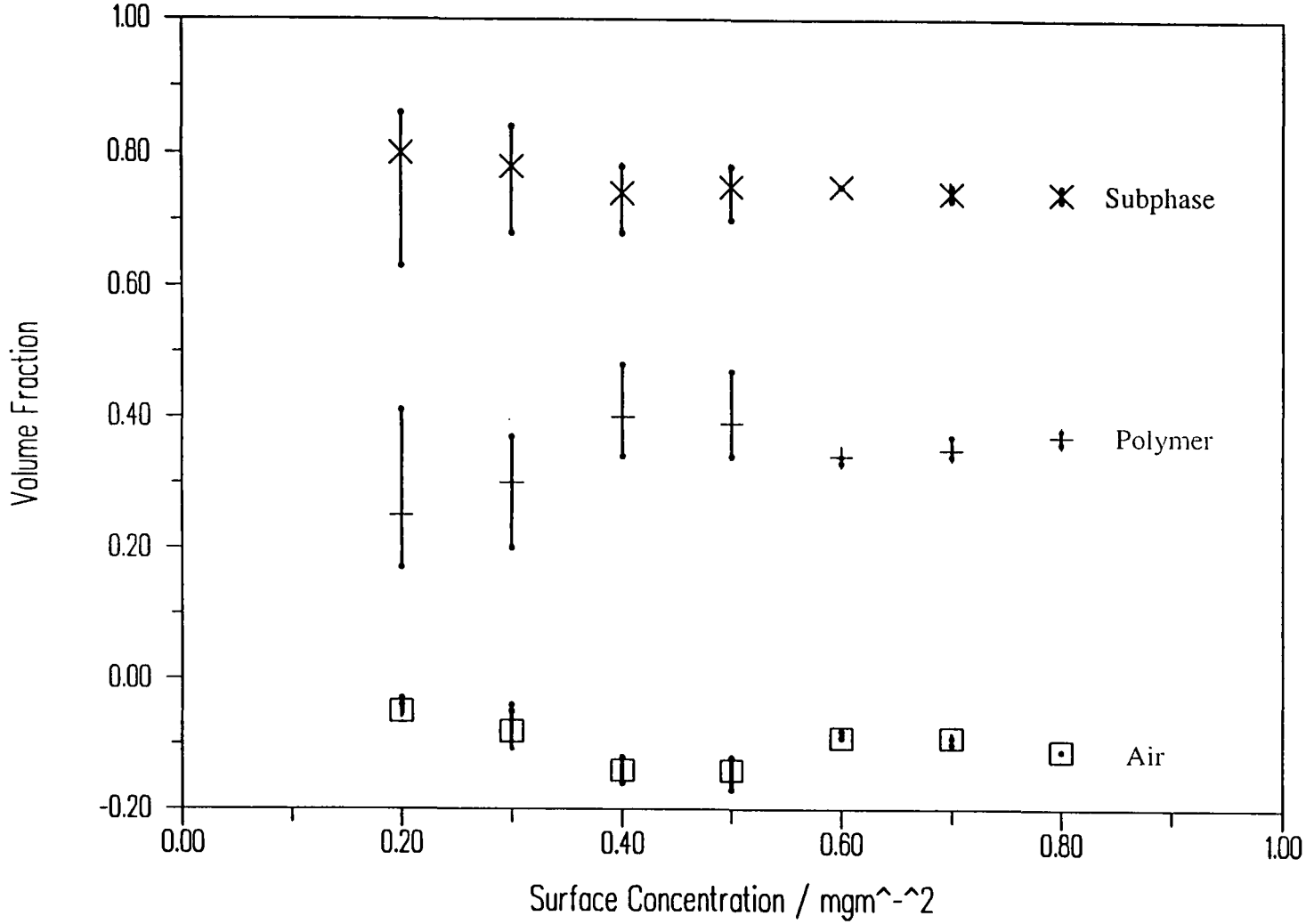

Figure 5.61 Variation in Topmost Layer Composition for PEO on 0.8M $MgSO_4$

Gaussian Model

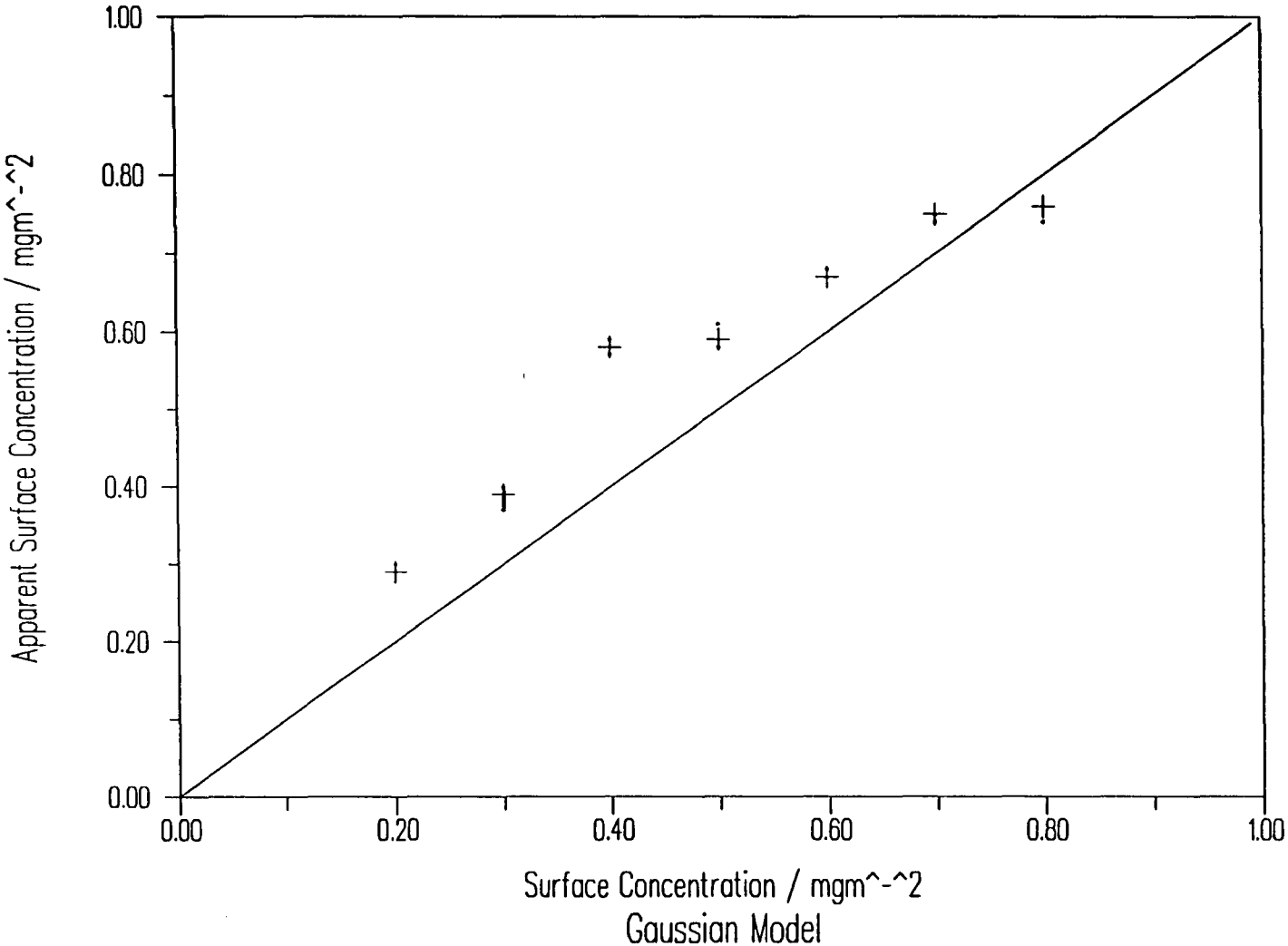

Figure 5.62 Variation of Apparent Surface Coverage for PEO on 0.8M $MgSO_4$

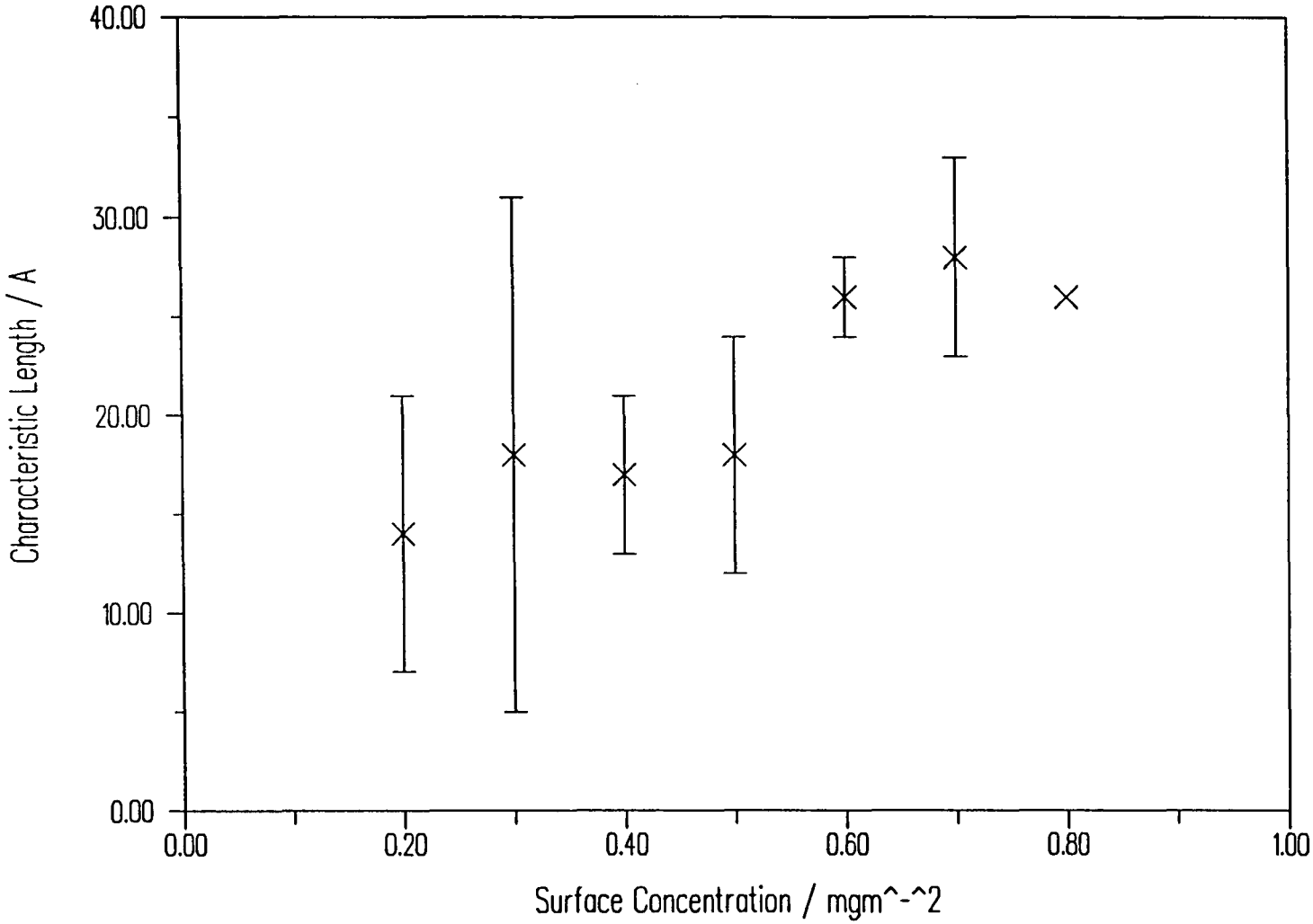

Figure 5.63 Variation of Characteristic Length for PEO on 0.8M $MgSO_4$

Exponential Model

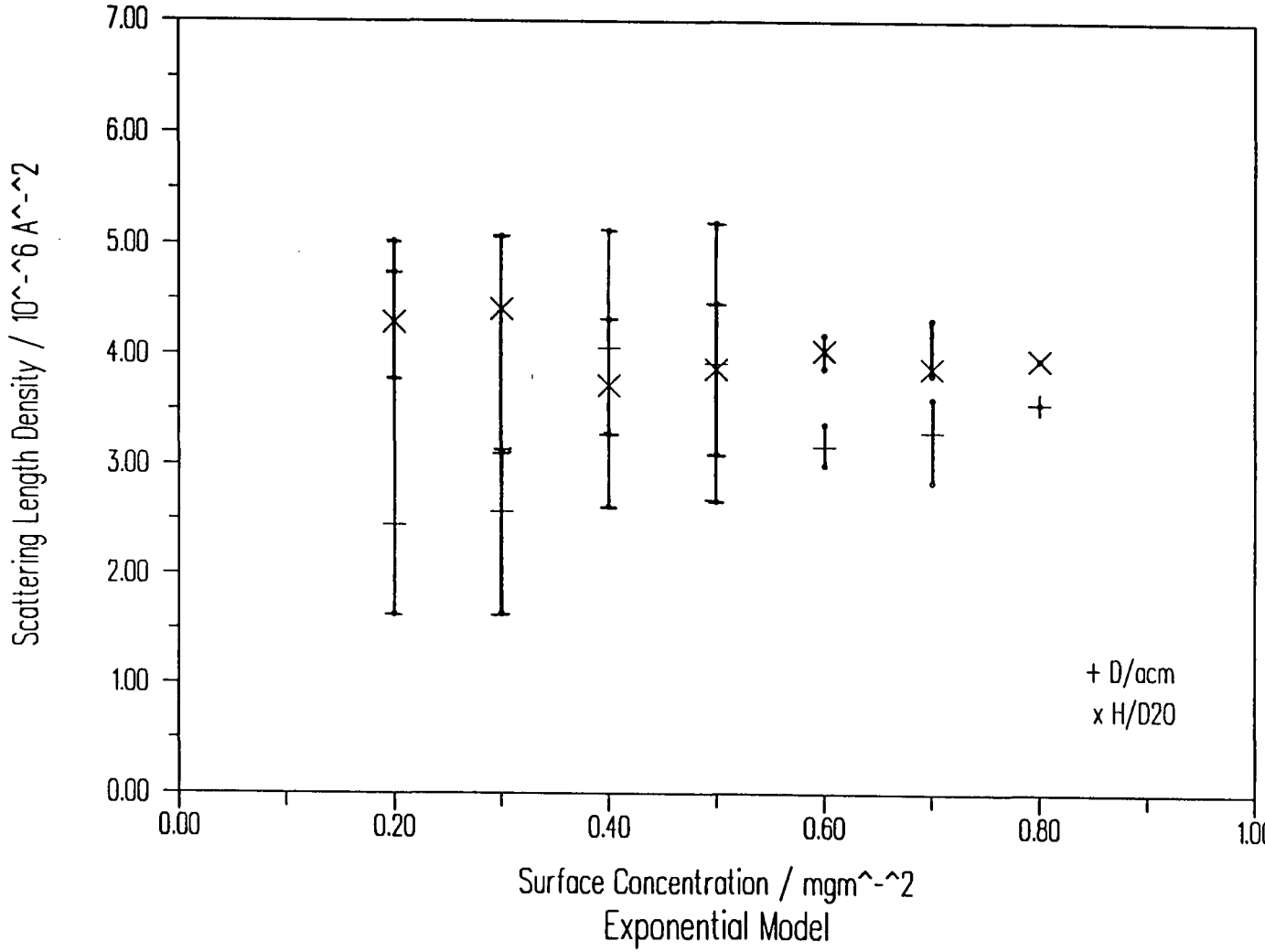

Figure 5.64 Variation in Topmost Layer Scattering length Density for PEO on 0.8M $MgSO_4$

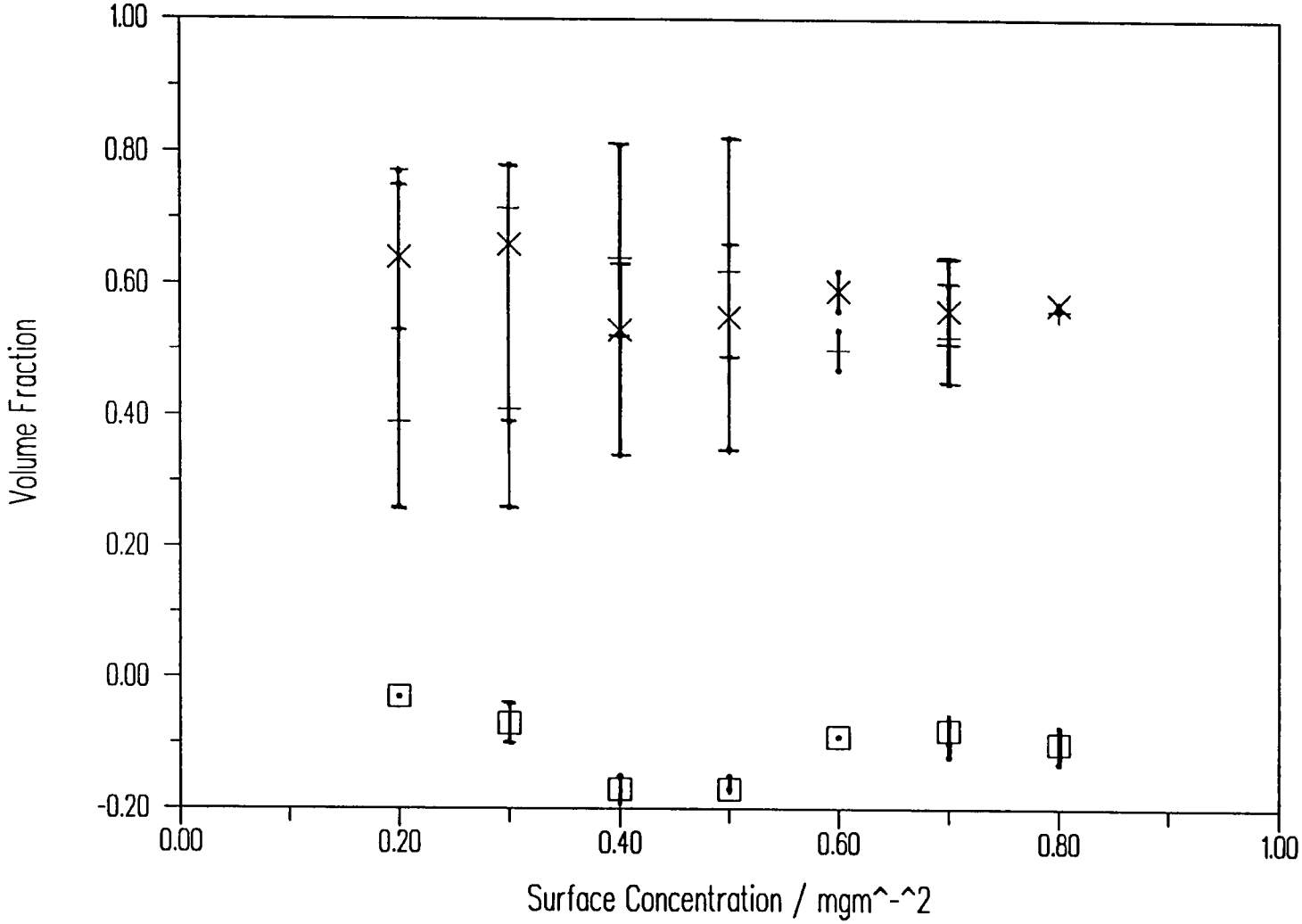

Figure 5.65 Variation in Topmost Layer Composition for PEO on 0.8M $MgSO_4$

Exponential Model

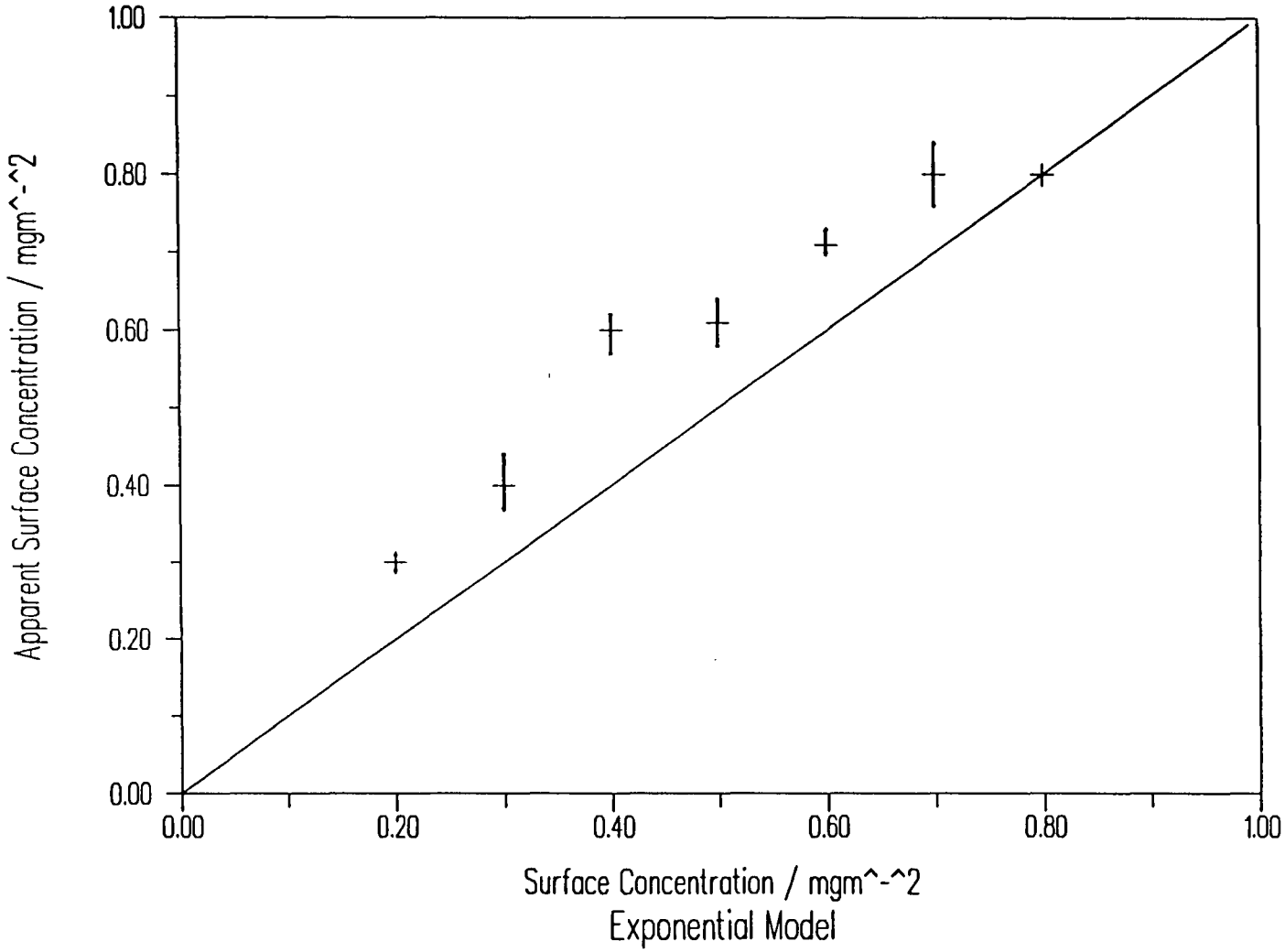

Figure 5.66 Variation in Apparent Surface Coverage for PEO on 0.8M $MgSO_4$

Γ/mg m^{-2}	d_1/Å	d_2/Å	$\rho_1/10^{-6}$Å^{-1}	$\rho_2/10^{-6}$Å^{-1}	residual/10^{-2}
0.2	-	-	-	-	-
0.3	4	45	4.42	0.59	0.2192
0.4	4	29	5.69	0.14	0.2545
0.5	-	-	-	-	-
0.6	9	29	2.85	0.28	0.1803
0.7	9	25	2.74	0.35	0.2611
0.8	9	30	2.40	0.25	0.2784

Table 5.33 Two Layer Fitted Parameters for DPEO on 0.4M $MgSO_4$ in acmw

Γ/mg m^{-2}	d_1/Å	d_2/Å	$\rho_1/10^{-6}$Å^{-1}	$\rho_2/10^{-6}$Å^{-1}	residual/10^{-2}
0.2	-	-	-	-	-
0.3	-	-	-	-	-
0.4	5	23	5.20	0.31	0.2196
0.5	5	24	5.23	0.33	0.2600
0.6	5	36	5.48	0.36	0.3699
0.7	6	33	4.82	0.46	0.3059
0.8	7	37	4.29	0.44	0.4576

Table 5.34 Two Layer Fitted parameters for DPEO on 0.8M $MgSO_4$ in acmw

Analysis by the Kinematic Approximation

In the same way that the kinematic approximate method was applied to the reflectometry data for PEO on water, Patterson and Guinier plots have been obtained for PEO on $MgSO_4$ subphases. From the minima in the Patterson functions, the d_{sharp} values in figures 5.67 and 5.68 have been estimated. From the slope and intercept of the appropriate Guinier plots values of m and σ tabulated in tables 5.37 and 5.38 were obtained corresponding to the d_{diff} values for a Gaussian scattering length density distribution shown in figures 5.69 and 5.70. It is very noticeable that

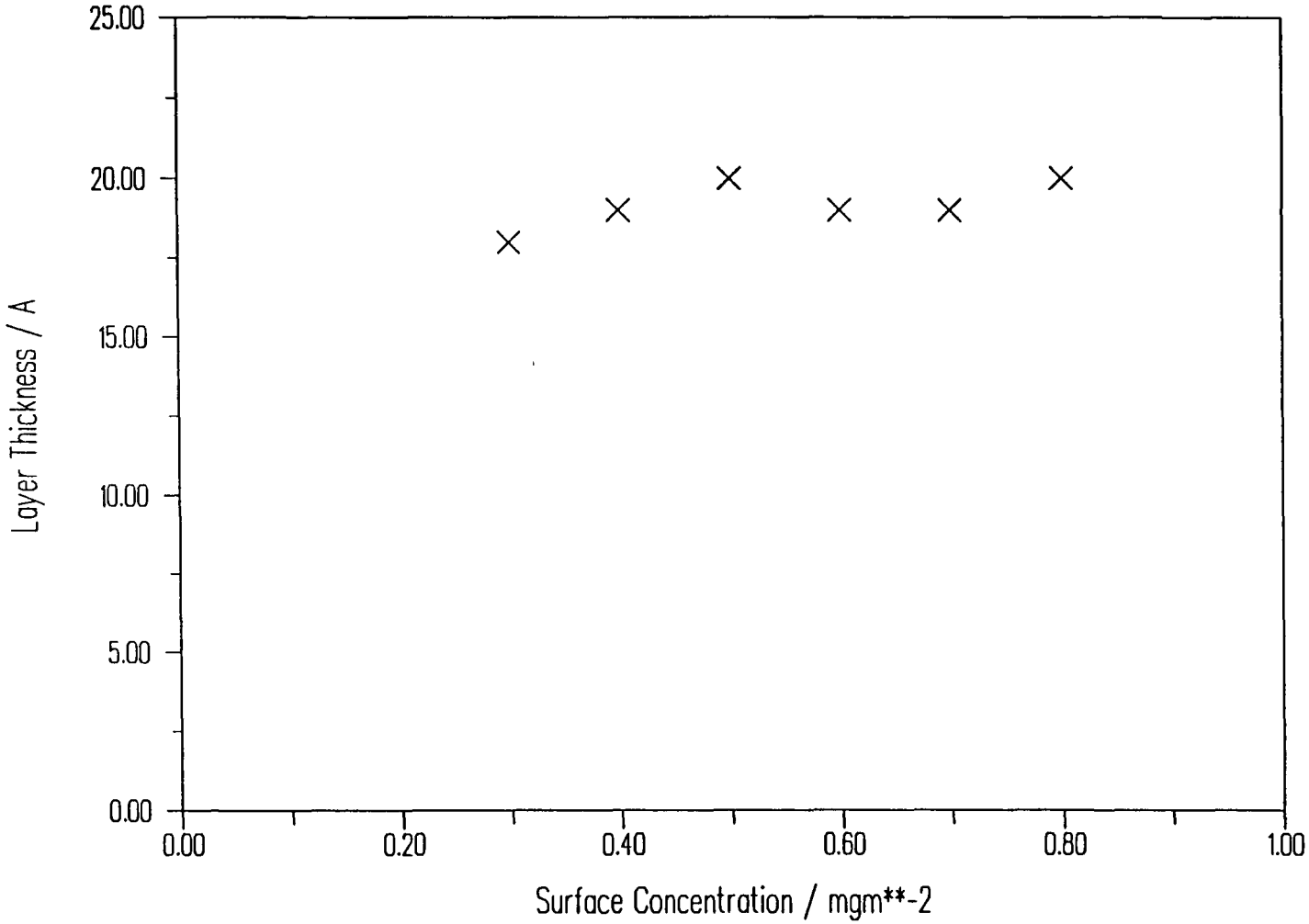

Figure 5.67 Layer Thickness obtained from Patterson plots for PEO on 0.4M $MgSO_4$

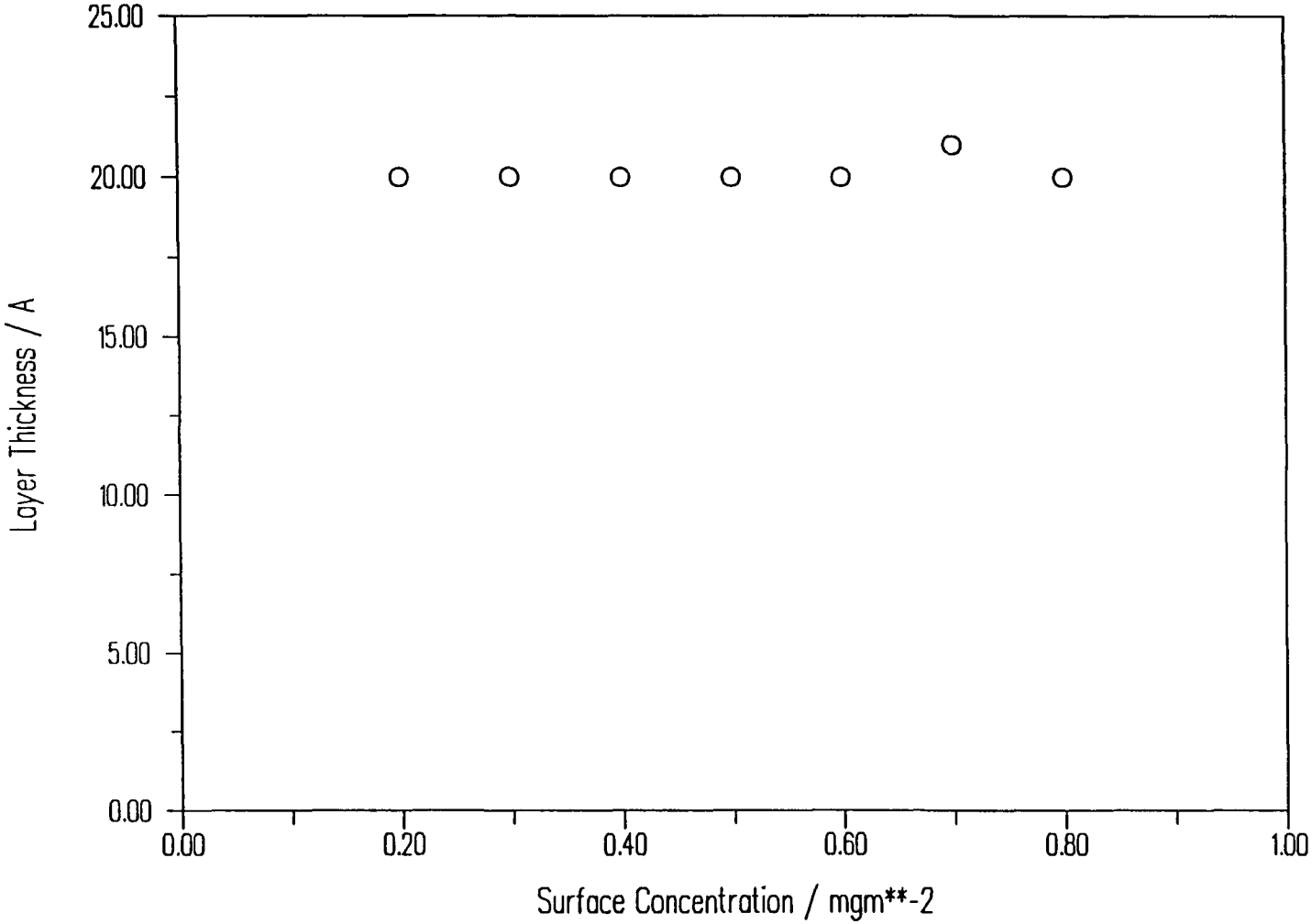

Figure 5.68 Layer Thickness obtained from Patterson plots for PEO on 0.8M $MgSO_4$

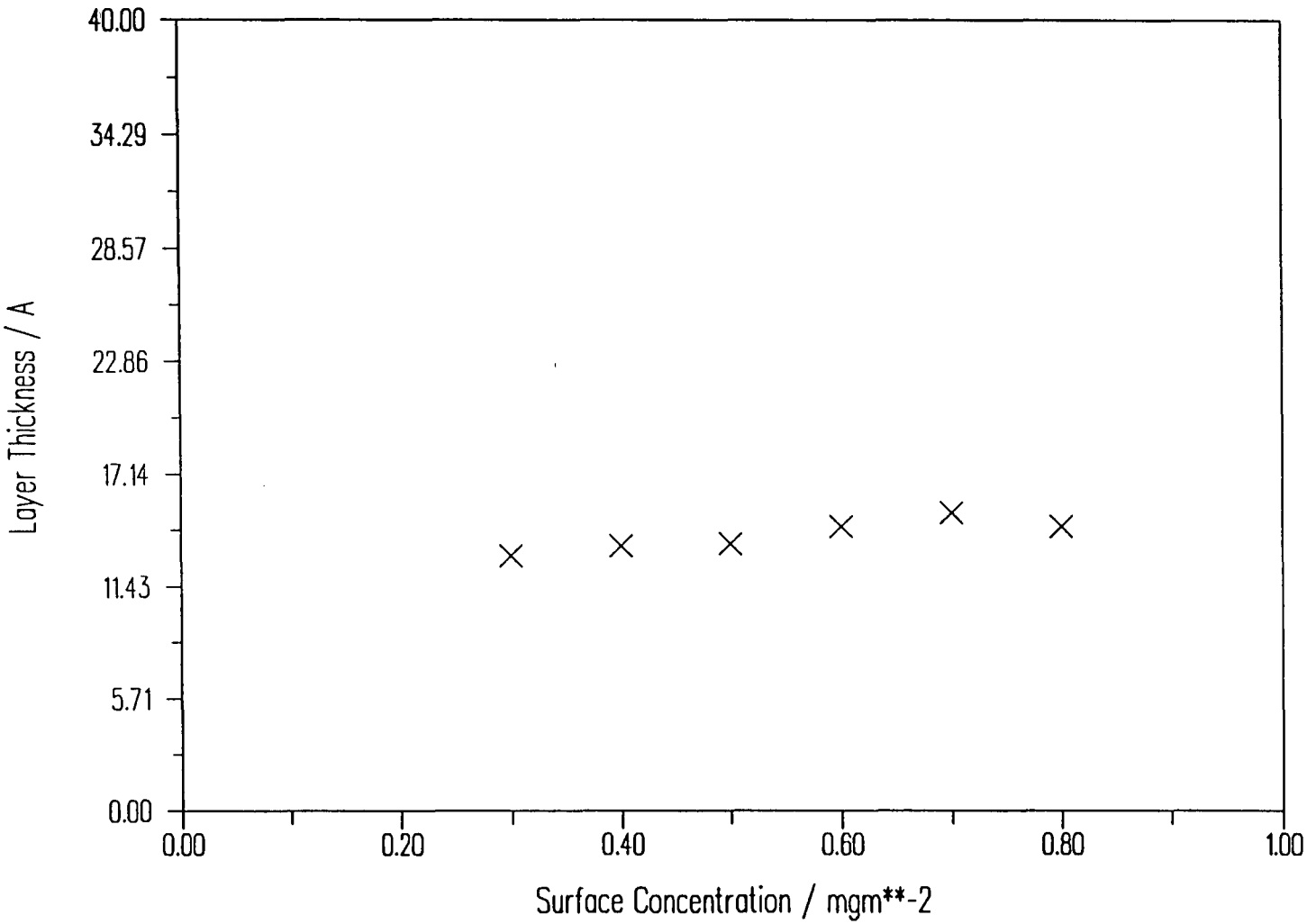

Figure 5.69 Layer Thickness obtained from Guinier plots for PEO on $0.4MgSO_4$

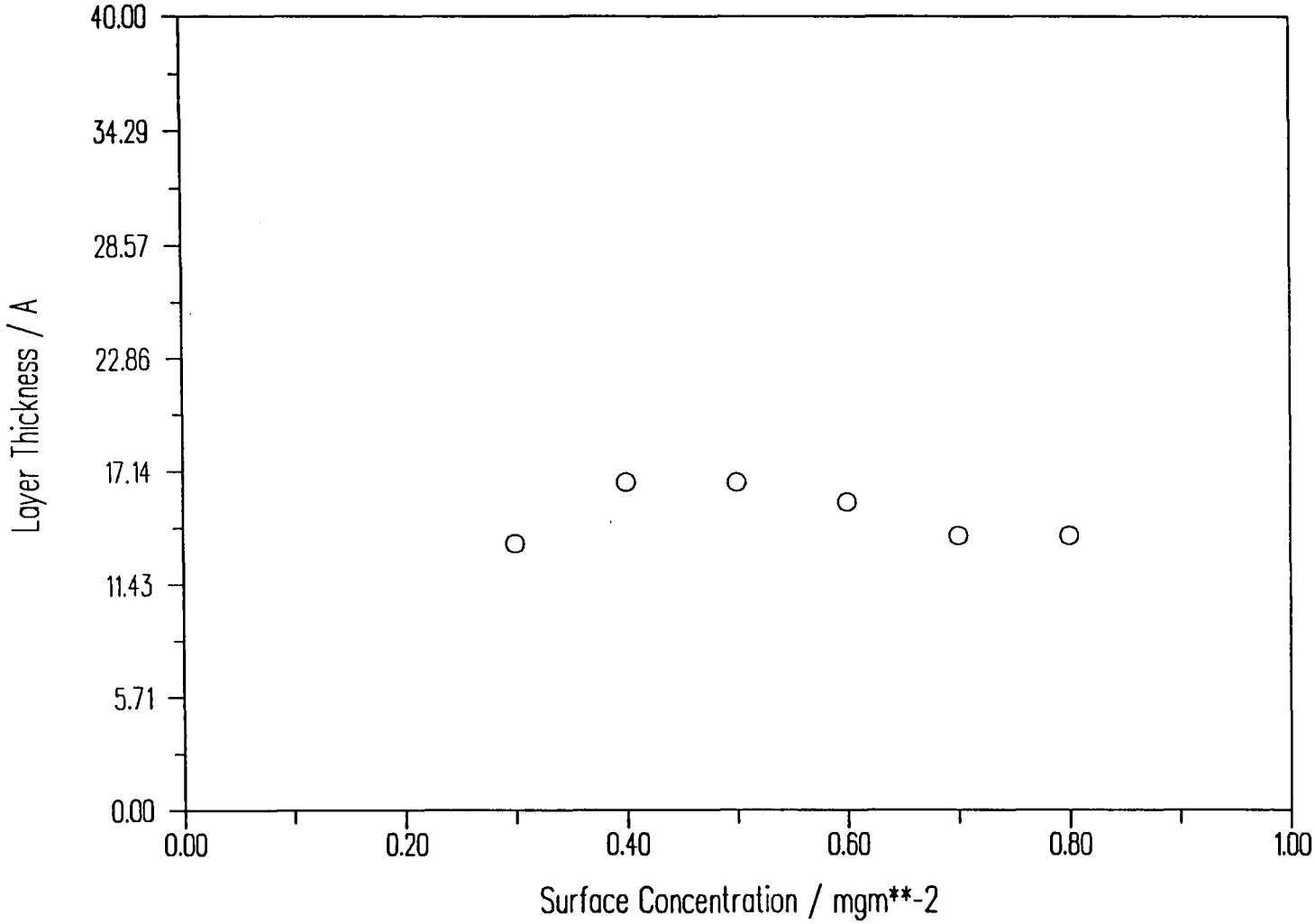

Figure 5.70 Layer Thickness obtained from Guinier plots for PEO on 0.8M $MgSO_4$

the d_{diff} values are very much reduced from those obtained for PEO on pure water, while the d_{sharp} values obtained from the Patterson plots remain fairly similar to those obtained from the pure water subphase experiments.

5.5 Ellipsometry

Ellipsometry has been used to examine PEO when spread as a monolayer on pure water. As previously discussed for the case of poly (methyl methacrylate), the lack of refractive index contrast in air-liquid interface experiments leads to a lack of sensitivity in one of the experimental parameters (the amplitude attenuation) and hence no unique calculation of both film thickness and refractive index is possible.

The variation of the phase retardation, $\Delta\delta$ with the trough barrier position is shown in figure 5.71. The equivalent surface pressure plot is shown in figure 5.72. By assuming a constant refractive index in the film of 1.45, the thickness variation shown in figure 5.73 is obtained.

The thickness values in this case are very much lower than those estimated from ellipsometry for PMMA, and also much smaller than those estimated from neutron reflectometry for PEO. Indeed these thickness values are around the size or smaller than the cross-section of the wan der Waal's radii of the constituent atoms in the ethylene oxide monomer unit.

These differences arise mainly from the simple approach used to analyse ellipsometry data. One major difficulty is the correct choice of a reasonable estimate for the film refractive index. In this case the value of 1.45 was used, corresponding to a polymer volume fraction in the film of approximately 0.96 (the refractive indices of PEO and water are 1.455 and 1.339 respectively). From neutron reflectometry however it has been determined that the polymer volume fraction in PEO monolayers is of the order of 0.1 - 0.2. Using a polymer volume fraction of 0.2 for example, a refractive index of 1.36 is obtained, which would lead to correspondingly higher layer thicknesses when substituted into the relevant optical expressions.

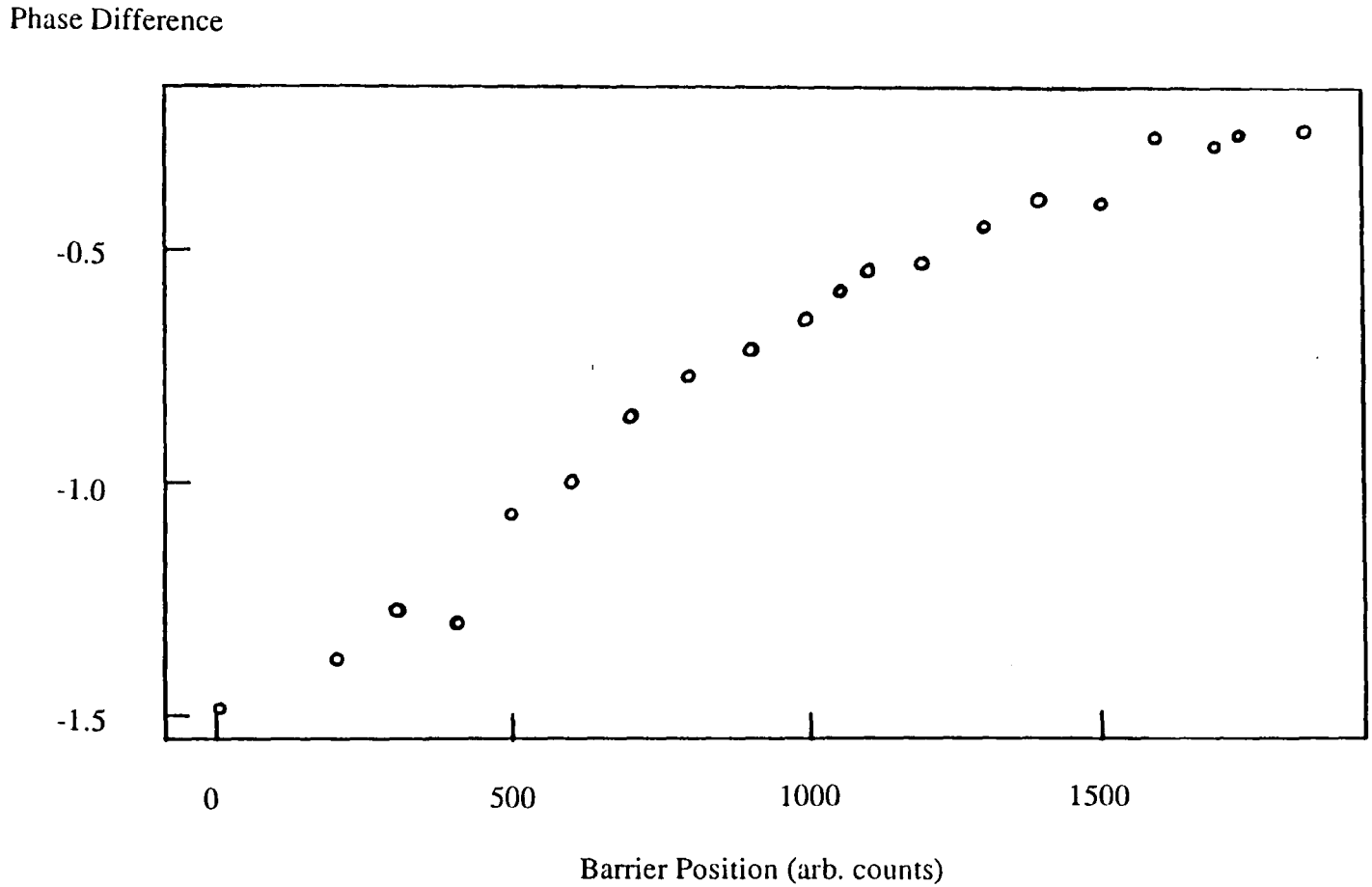

Figure 5.71 Phase Difference against Barrier Position for PEO

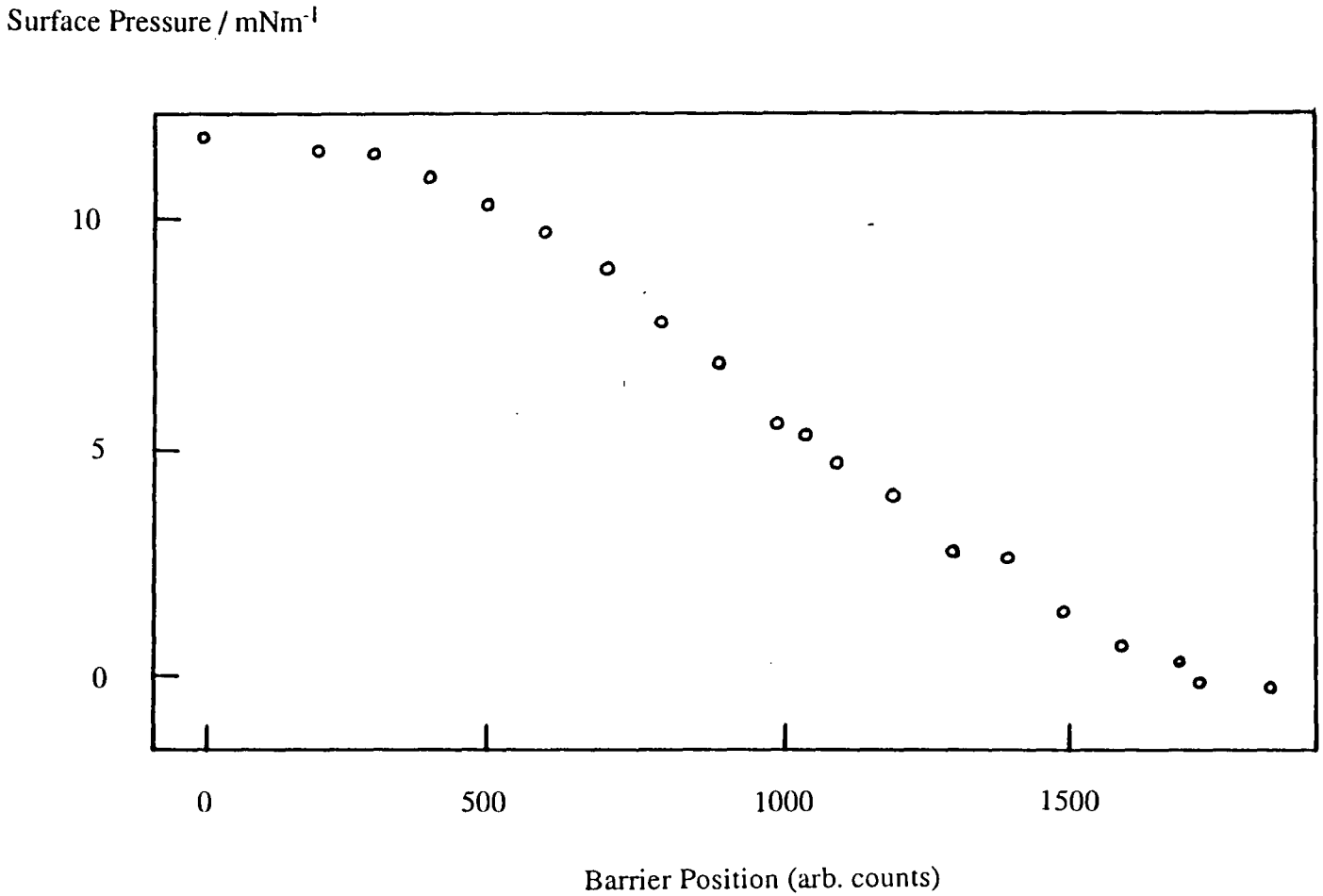

Figure 5.72 Surface Pressure against Barrier Position for PEO

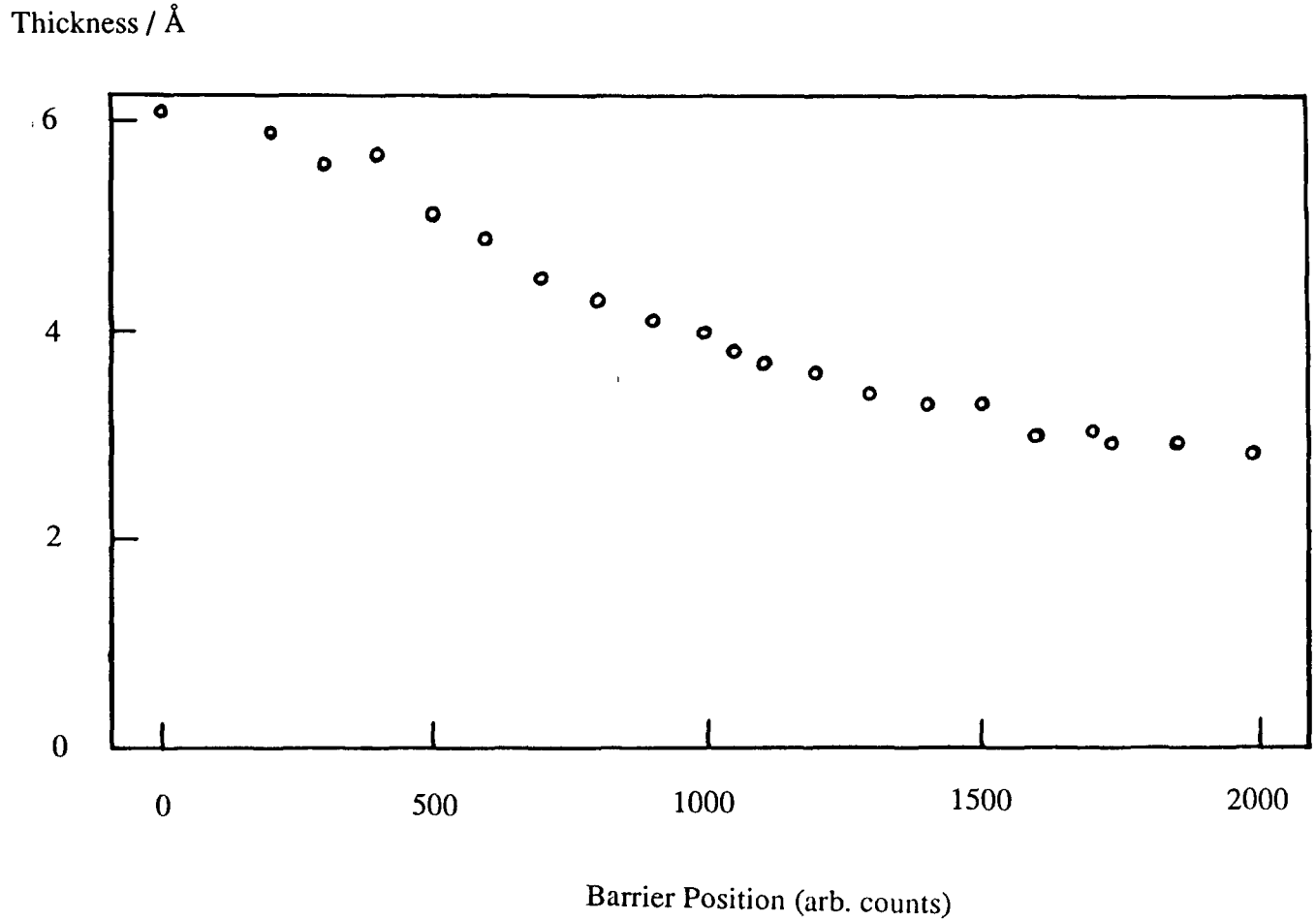

Figure 5.73 Film thickness against Barrier Position for PEO

Additionally from the information obtained by reflectometry, the appropriateness of a single film model for the description of PEO films is questionable. However the extension of the formulae describing ellipsometric phenomena to the case of diffuse interfacial forms is not readily achieved. A model based on a patchy layer of pure polymer islands surrounded by air voids has been suggested but the appropriateness of this model for the highly diffuse and hydrophilic PEO film seems dubious.

The very thin layer thickness obtained for a roughly equivalent refractive index to that used in PMMA analysis supports the notion that the PEO film is very much more diffuse in polymer than a PMMA film. This is also reflected in the magnitude of the phase retardation effect which is much smaller than was the case for poly (methyl methacrylate) at a similar surface concentration.

References

1. Rennie, A.R. Crawford, R.J., Lee, E.M., Thomas, R.K., Crowley, T.L., Roberts, S., Qureshi, M.S., Richards, R.W., *Macromolecules*, **22**, 3466, 1989.

2. *Polymer Handbook*, Brandrup, J., Immergut, E.H., eds., Wiley - Interscience, 3rd Ed., New York, 1989.

CHAPTER 6 - POLY (METHYL METHACRYLATE - 4-VINYL PYRIDINE) DIBLOCK COPOLYMERS

Summary

The synthesis of diblock copolymers of poly (methyl methacrylate) and poly (4-vinyl pyridine) is described. A description of the conversion of these products to partially polyelectrolyte materials by alkylation with ethyl bromide and the methods used to characterise both sets of materials chemically are given.

Surface pressure measurements have been used to characterise the thermodynamic state of PMMA4VP and PMMA4VPQ monolayers, suitable precautions having been taken to ensure that the polymer was deposited in a simple non-aggregated form from solution. PMMA4VPQ partial polyelectrolytes were found to form a rather more expanded film at the surface than their uncharged counterparts (as classically defined), but the critical scaling exponents obtained for the quaternised material was 0.53 - 0.55, near the value expected for a theta system. PMMA4VP gave a value of 0.60 - 0.65, intermediate between those of theta and good solvent behaviour.

6.1 Synthesis and Characterisation

High vacuum anionic synthesis was used as previously described to prepare PMMA-4VP diblock copolymers with hydrogenous and deuterated PMMA blocks. Molecular weight analysis of these polymers by gel permeation chromatography gave the results set out in table 6.1.

Polymer	M_n	M_w	M_w / M_n
HPMMA4VP	521500	2146000	4.1
DPMMA4VP	503000	1470000	2.9

Table 6.1 Molecular Weight Characteristics of PMMA4VP copolymers

The samples have rather broad molecular weight distributions and the measured chromatograms contained much noise in the measured signal indicating that they there were poorly dissolved in the system solvent, THF. This was thought to be due primarily to difficulties associated with introducing the second monomer, methyl methacrylate to the living 4VP solution in the reaction flask.

Microanalysis may be used conveniently to assess the composition of the diblock copolymer by using the single nitrogen atom of the 4-vinyl pyridine ring as a criterion for its proportion in the polymer. Microanalysis results are summarised in table 6.2.

Another method of estimating the relative proportions of the two blocks in the polymer is to make use of the UV-visible absorption at 358nm associated with the pyridine ring of 4-vinyl pyridine. Table 6.3 presents concentration corrected relative absorbances for both diblock copolymers and the equivalent absorptions for a homo poly(4-vinyl pyridine). By ratioing the absorption for the block copolymer to that for the homopolymer, the 4-vinyl pyridine equivalent in the copolymer is

Polymer	Weight			Mole Ratio				
	%C	%H	%N	C	H	N	PMMA	P4VP
HPMMA4VP	61.99	7.29	3.18	5.17	7.29	0.23	0.76	0.24
DPMMA4VP	54.72	6.65	1.78	4.56	6.65	0.13	0.85	0.15

Table 6.2 Analysis of PMMA4VP copolymers by Microanalysis

Polymer	Relative Absorption / cm^2g^{-1}	%4VP
HPMMA4VP	7885	17
DPMMA4VP	6071	13
4VP (homo)	47778	-

Table 6.3 Analysis of PMMA4VP copolymers by UV-visible Absorption Spectroscopy

obtained.

From the combination of information from microanalysis and UV-visible spectroscopy the composition of HPMMA4VP may be estimated as approximately 80:20 PMMA/4VP, and DPMMA4VP as 85:15 PMMA/4VP.

Copolymers with partially polyelectrolyte character have been prepared by quaternisation of PMMA4VP copolymers with ethyl bromide. Four combinations of the two diblock copolymers above and hydrogenous and deuterated ethyl bromide have been used to prepare the polymers HPMMA4VPQH (abbreviated further to HH), HPMMA4VPQD (HD), DPMMA4VPQH (DH), and DPMMA4VPQD (DD). Bromine elemental analysis provides a convenient route to demonstrate the completeness of the quaternisation reaction, Table 6.4, the experimentally obtained values being very close to the theoretically expected amounts in all cases except

one, where a large excess bromine content may possibly have been caused by residual reactant impurity.

Polymer	% Br	%Br(theor)
HPMMA4VPQH	13.16	13.3
HPMMA4VPQD	14.25	13.2
DPMMA4VPQH	15.51	9.7
DPMMA4VPQD	9.57	9.6

Table 6.4 Bromine Elemental Analysis of PMMA4VPQ copolymers

6.2 Surface Pressure - Concentration Isotherm Studies

6.2.1 HPMMA4VP Copolymers

Surface pressure - surface concentration isotherms for HPMMA4VP and DPMMA4VP are presented in figures 6.1 and 6.2. The shape of the isotherms is that of a liquid condensed type monolayer, with a relatively large limiting surface concentration of approximately $1mgm^{-2}$. This corresponds to a limiting area per segment of $18Å^2$. The surface pressure onset however is rather gradual, starting from a surface concentration of only $0.5mgm^{-2}$. In the semi-dilute regime a steep, steady rise in surface pressure is observed, but this rise is not as steep as in, for example, an atactic-PMMA monolayer.

The reproducibility of the surface pressure data for these materials was found to be rather poor, particularly at high surface concentrations. This was thought to be due to the sensitivity of the polymer to the presence of acidic gases absorbed into the subphase from the air above the interface. By the use of an inert atmosphere (nitrogen blanket over the liquid surface) it was possible to minimise the dissolution of carbon dioxide in the subphase and the associated reduction in subphase pH. Isotherms recorded under these conditions were much more consistent, indicating considerable sensitivity of PMMA4VP copolymers to subphase pH conditions. This observation was also valid for PMMA4VPQ polyelectrolyte films.

From the slopes of double logarithmically plotted semi-dilute regime surface pressure data, figures 6.3 and 6.4, the scaling exponent values of $\nu = 0.65$ (slope $y = 4.3$) and $\nu = 0.60$ ($y = 5.9$) were obtained for HPMMA4VP and DPMMA4VP respectively. The difference in these values is a reflection of the dependence of ν on y, which is very sensitive to changes in y when $y \leq 6$. Scaling exponent values in the range of 0.6 to 0.65 are intermediate between those of

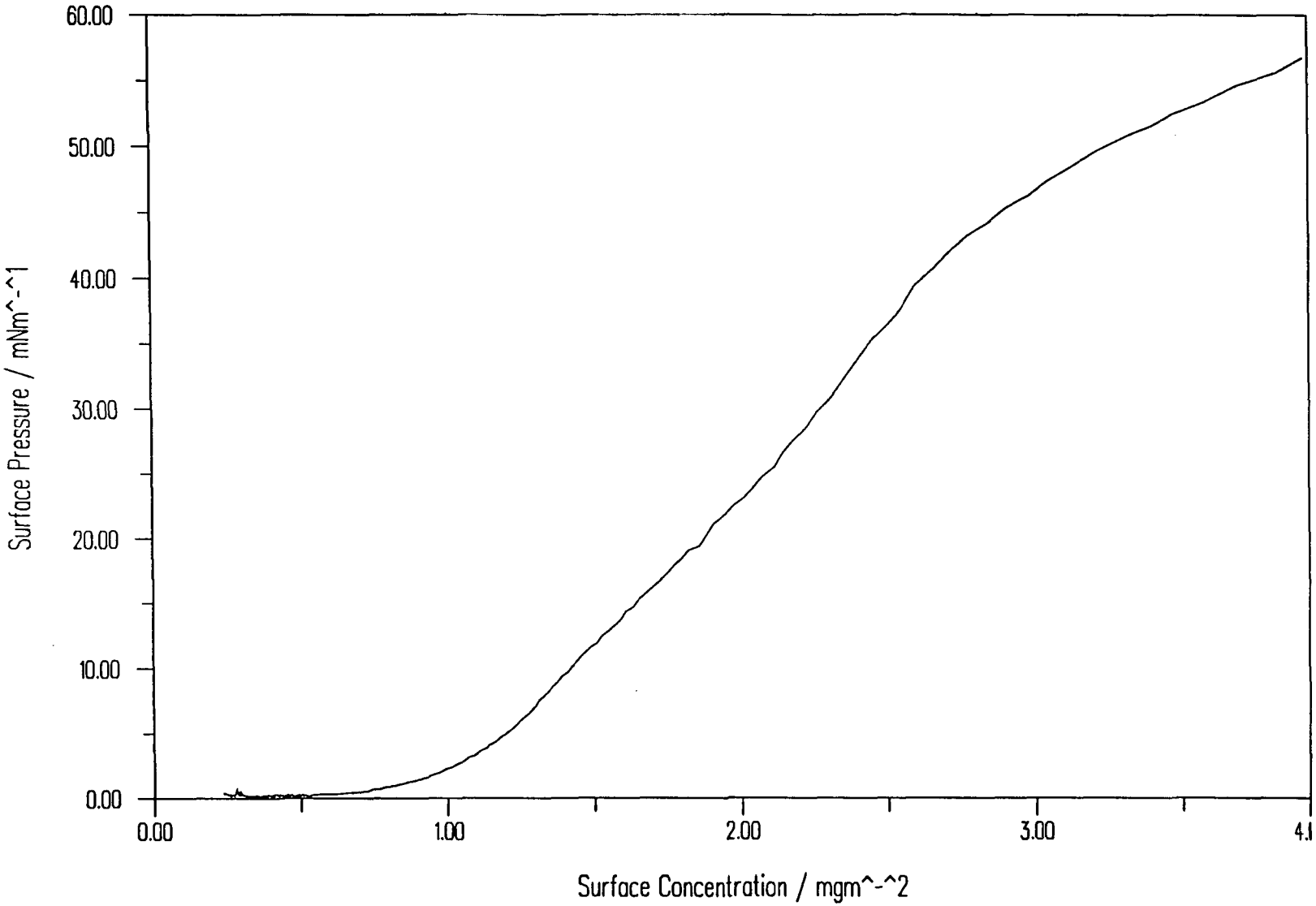

Figure 6.1 Surface Pressure against Surface Concentration for HPMMA4VP on water

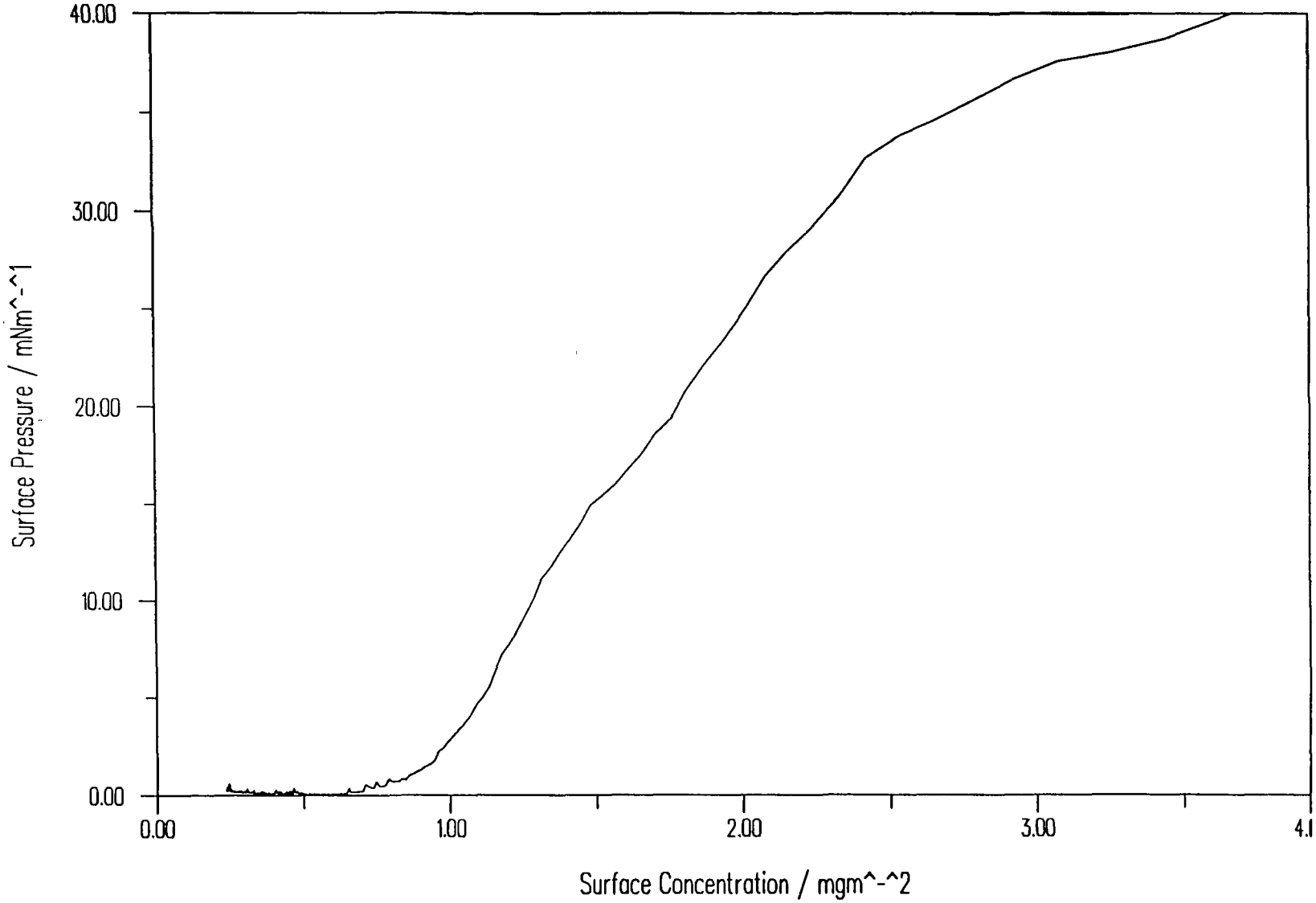

Figure 6.2 Surface Pressure against Surface Concentration for DPMMA4VP on water

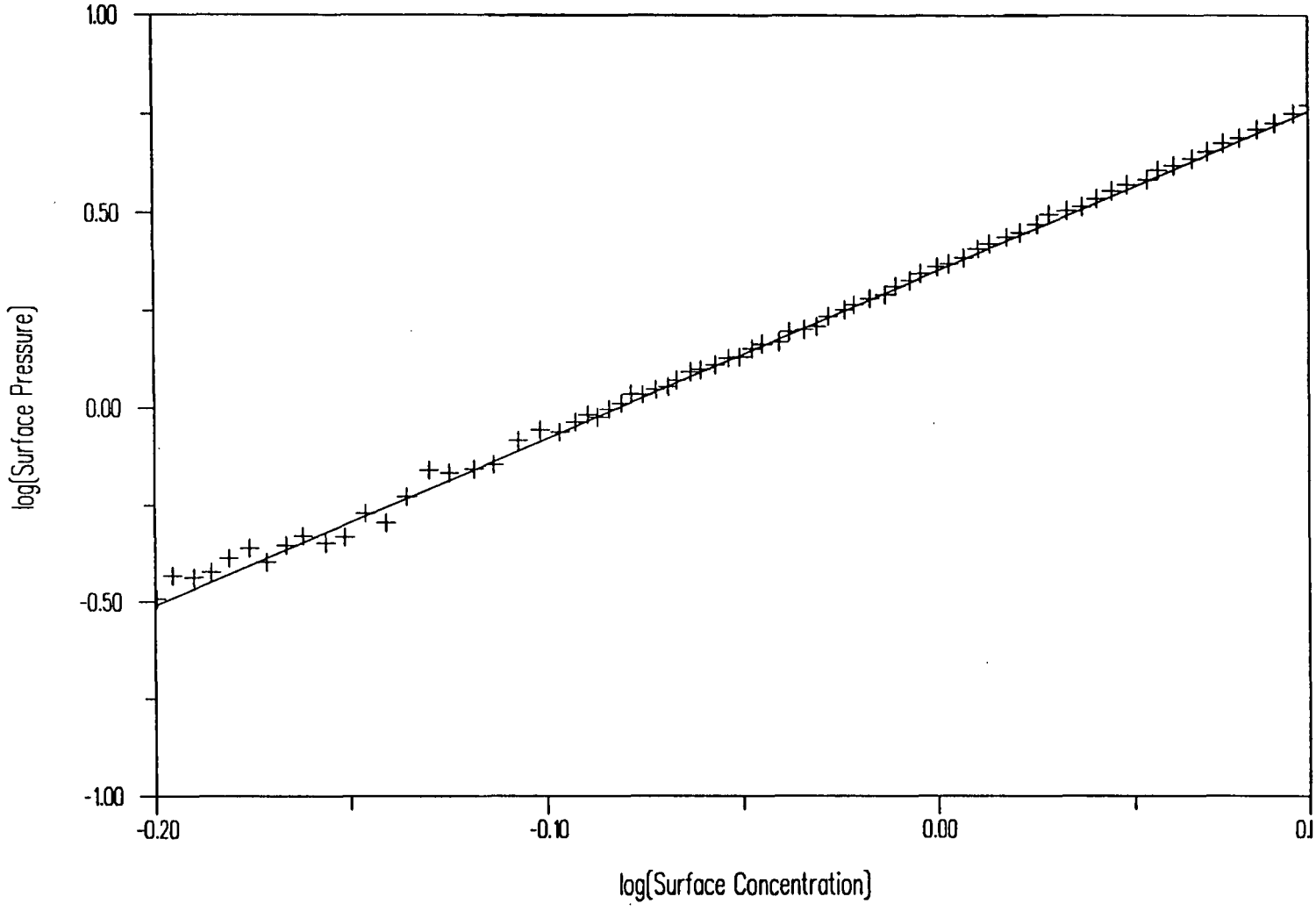

Figure 6.3 Double Logarithmic Plot of Surface Pressure Isotherm for HPMMA4VP on water

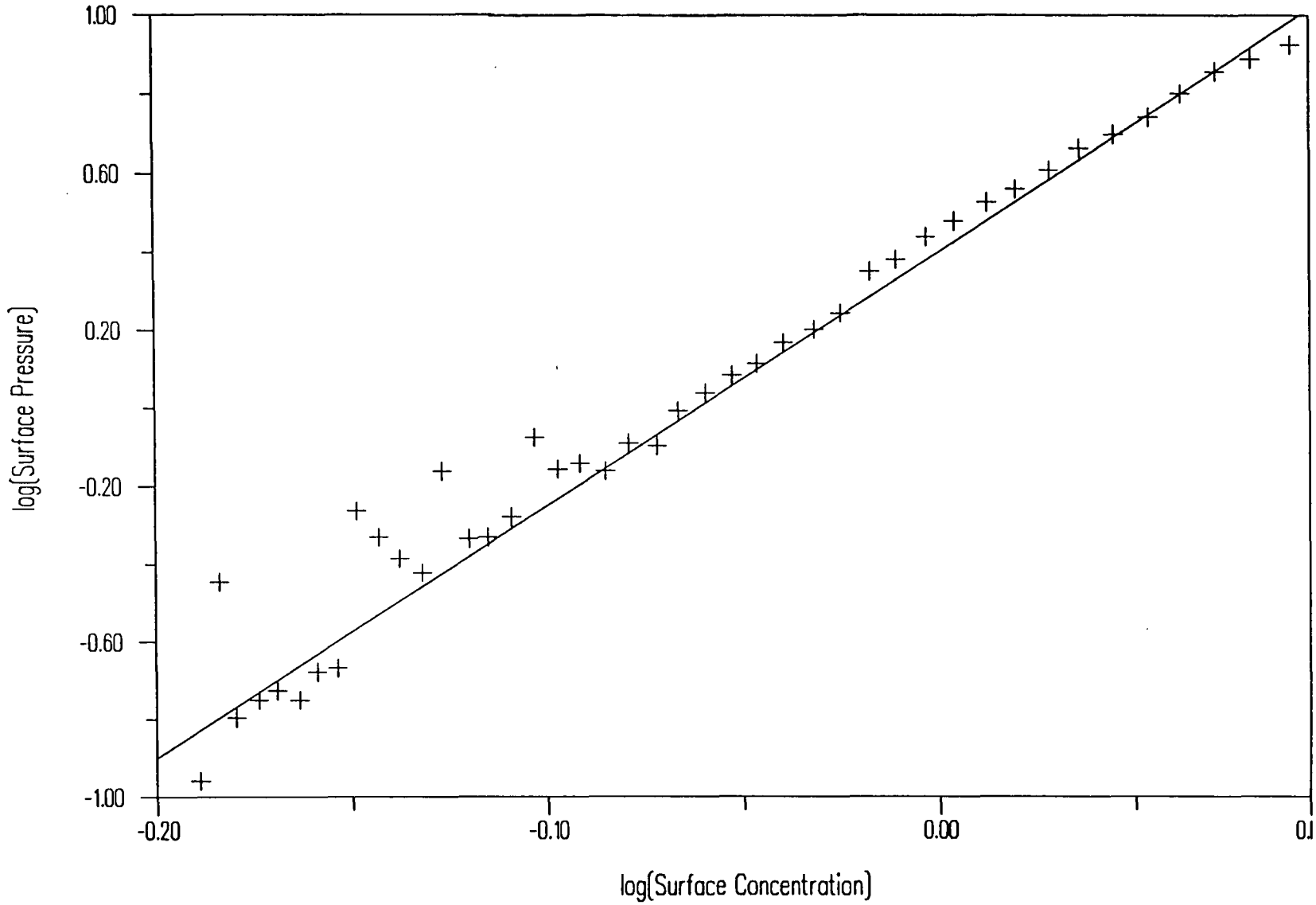

Figure 6.4 Double Logarithmic Plot of Surface Pressure Isotherm for DPMMA4VP on water

monolayers in the theta condition ($\nu \approx 0.56$) and those in good 2-D solvent conditions ($\nu = 0.77$). From equation of state plots, figures 6.5 and 6.6, there appears to be a very slightly negative initial slope at low surface concentrations, indicative of poor solvent conditions, but no definite trend is easily seen.

6.2.2 PMMA4VPQ Copolymers

For the purpose of spreading Langmuir films, it is important that the polymer is spread from a well dissolved, dissociated state. For all the other systems described in this thesis, chloroform provides a good solvent for preparing spreading solutions. Solutions of quaternised PMMA4VPQ copolymers in chloroform however were observed to be slightly cloudy, giving rise to suspicion as to whether the polymer was fully dissociated as single chains or aggregated in micelles.

In order to investigate this question, particle size analysis on dilute solutions of HPMMA4VPQ(H) in chloroform, and in an 80/20 v/v mixture of chloroform and methanol was carried out by quasi - elastic light scattering. From the average of ten repeated experiments a particle size of 159±1.7nm was obtained for the chloroform solution, while the mixed solvent value was 37±18nm. The uncertainty in this latter value was due to the relatively low intensity of excess scattering from the mixed solvent solution, which was typically a factor of 50 less than for the cloudy chloroform solution. From these values it is clearly seen that the amphiphilic polymer is associated into aggregates of micellar dimensions when dissolved in chloroform, but when dissolved in the mixed solvent a particle size is obtained which is of the order of the value expected for isolated single coils.

Surface pressure - surface concentration isotherms for PMMA4VPQ copolymers spread from the mixed chloroform / methanol mixture are shown in figures 6.7 - 6.10. By comparison with figures 6.1 and 6.2 for the unquaternised

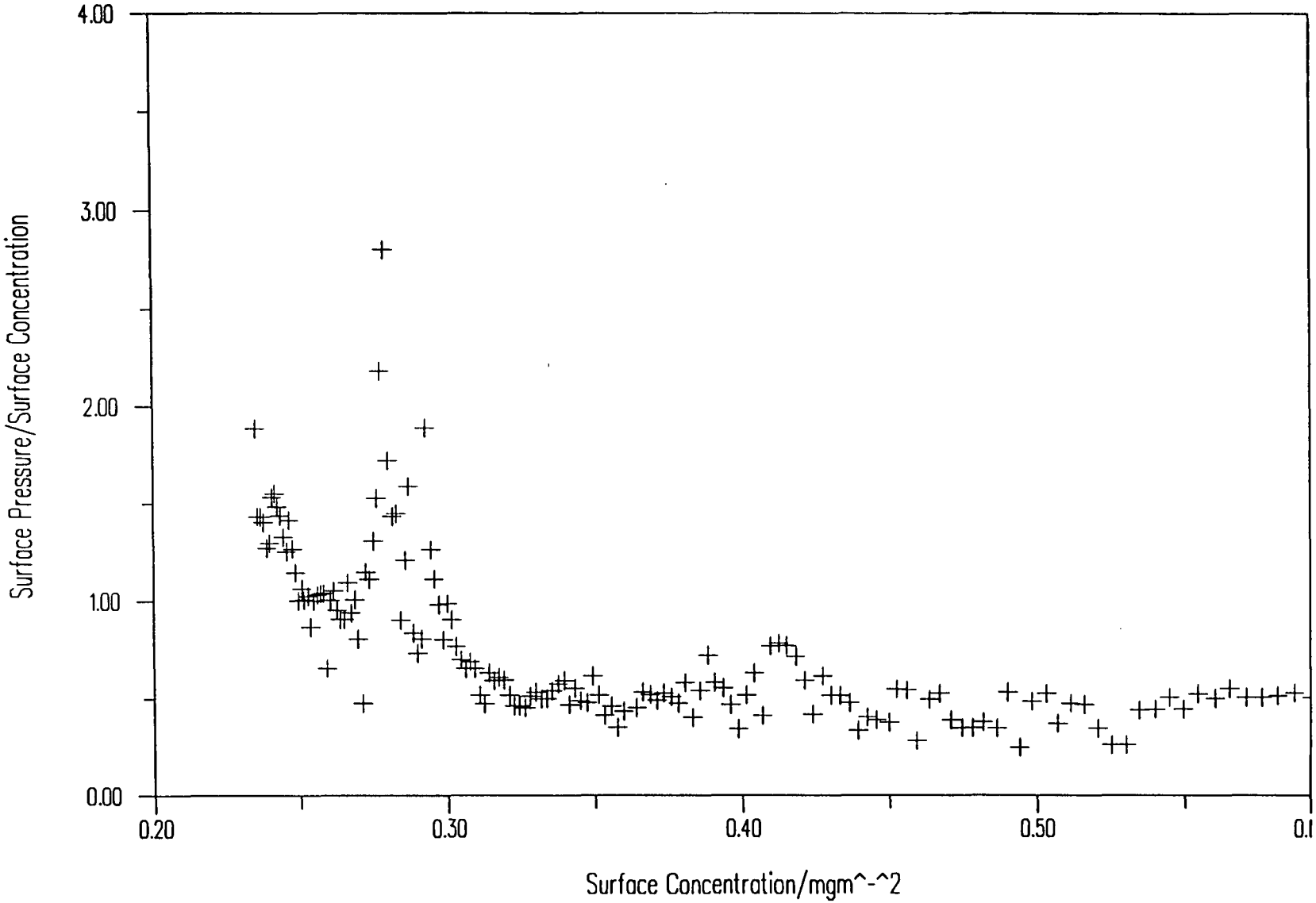

Figure 6.5 Surface Pressure / Surface Concentration v Surface Concentration for HPMMA4VP

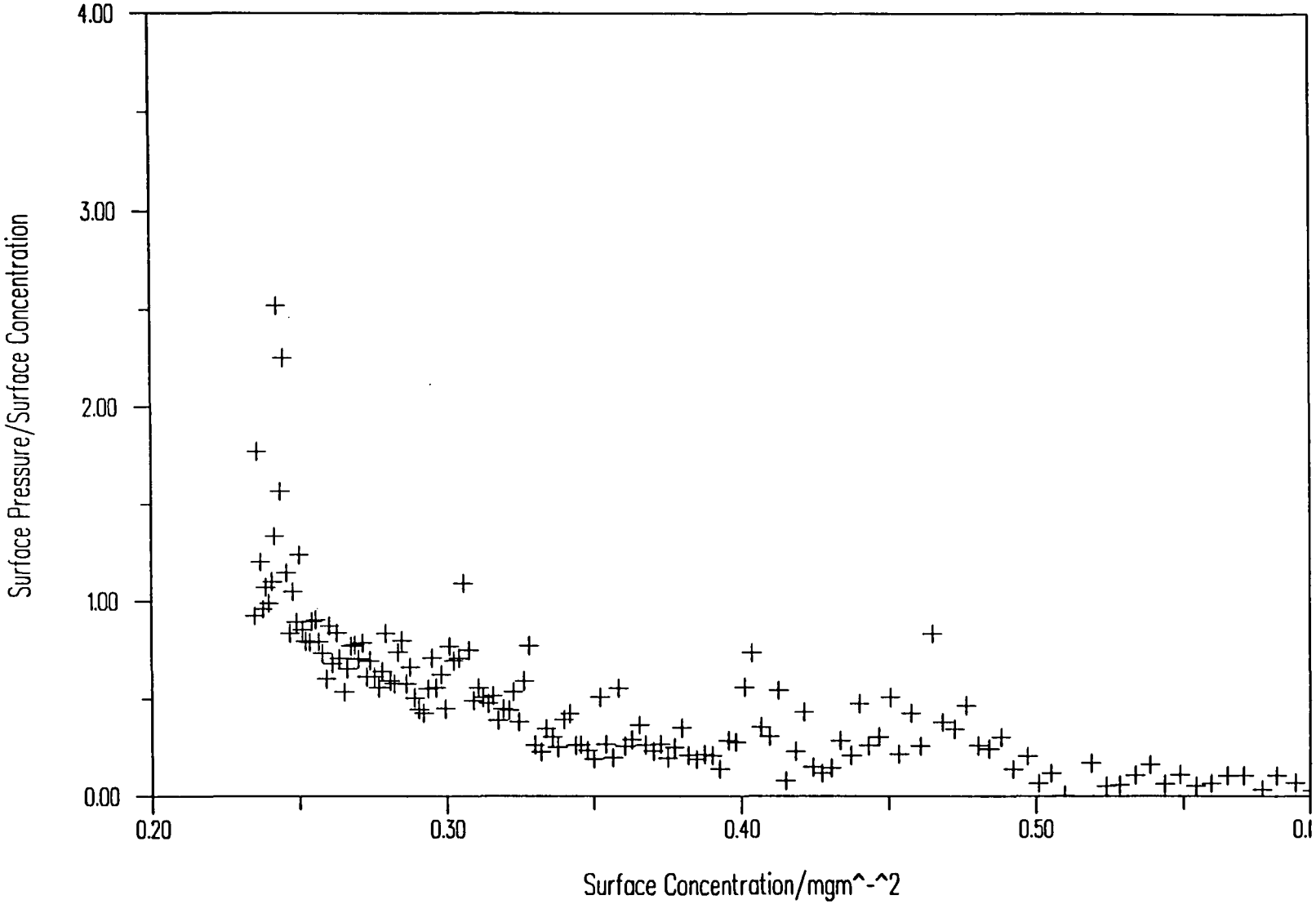

Figure 6.6 Surface Pressure /Surface Concentration v Surface Concentration for DPMMA4VP

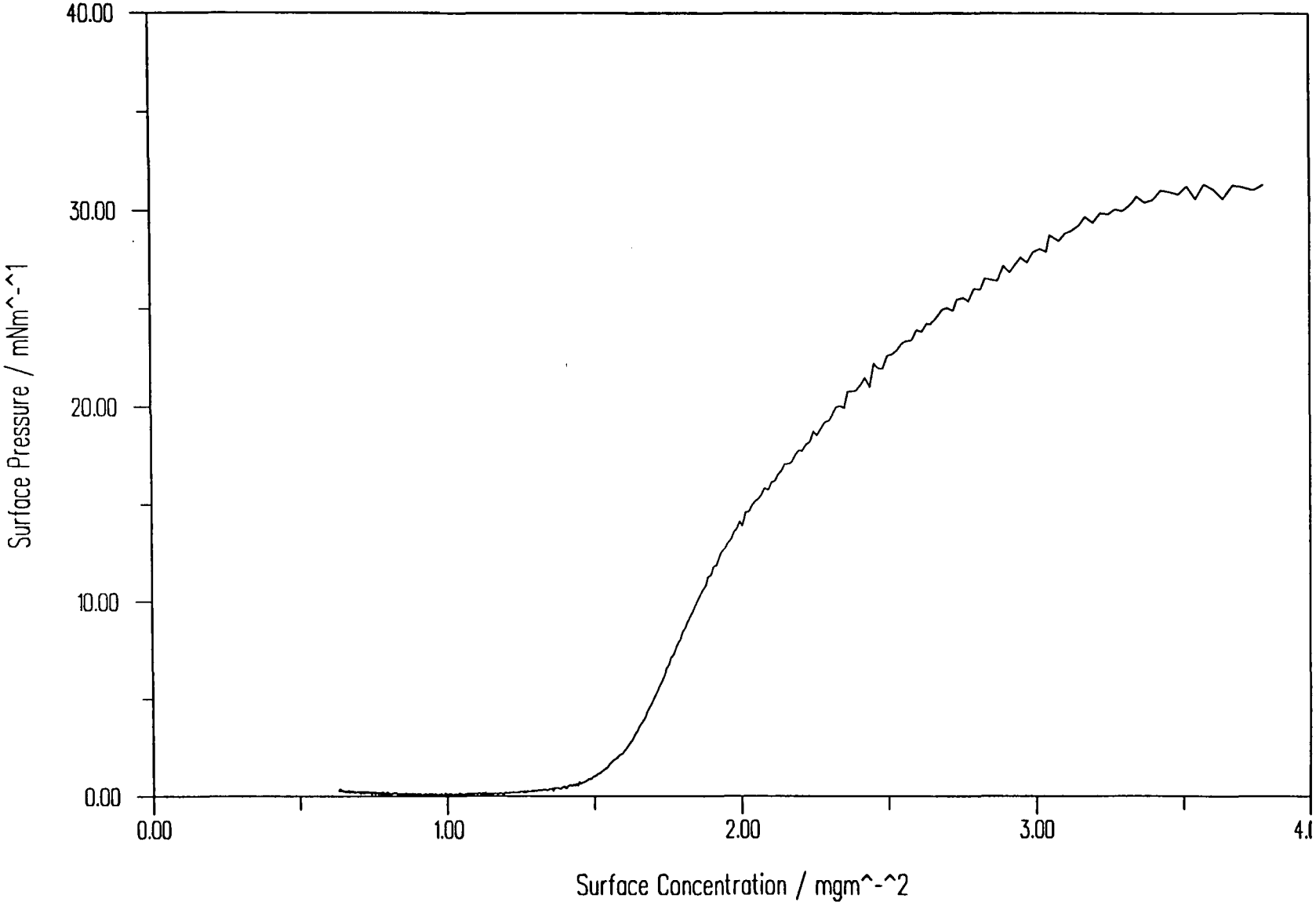

Figure 6.7 Surface Pressure - Surface Concentration Isotherm for HPMMA4VPQ(H) on water

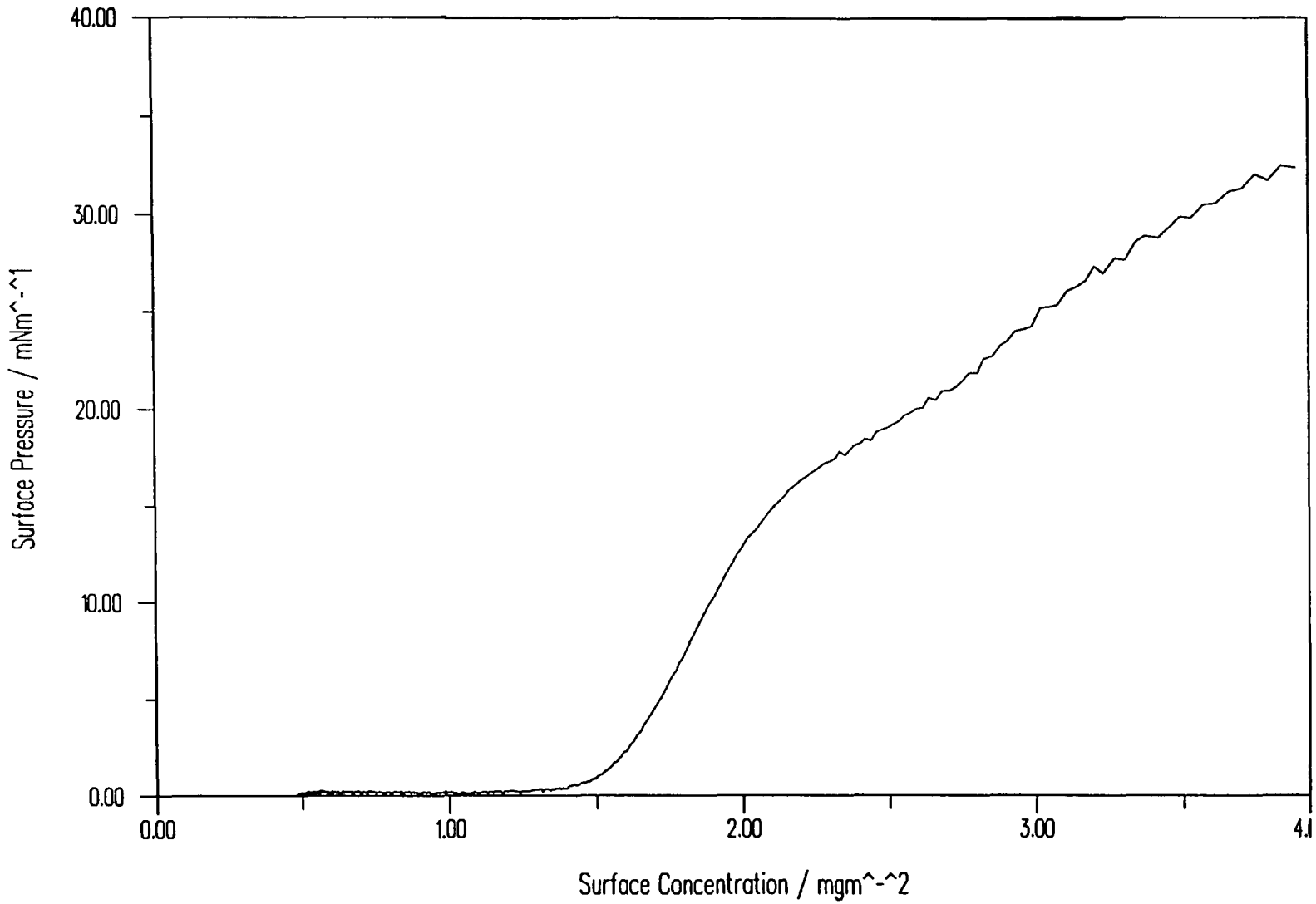

Figure 6.8 Surface Pressure - Surface Concentration Isotherm for HPMMA4VPQ(D) on water

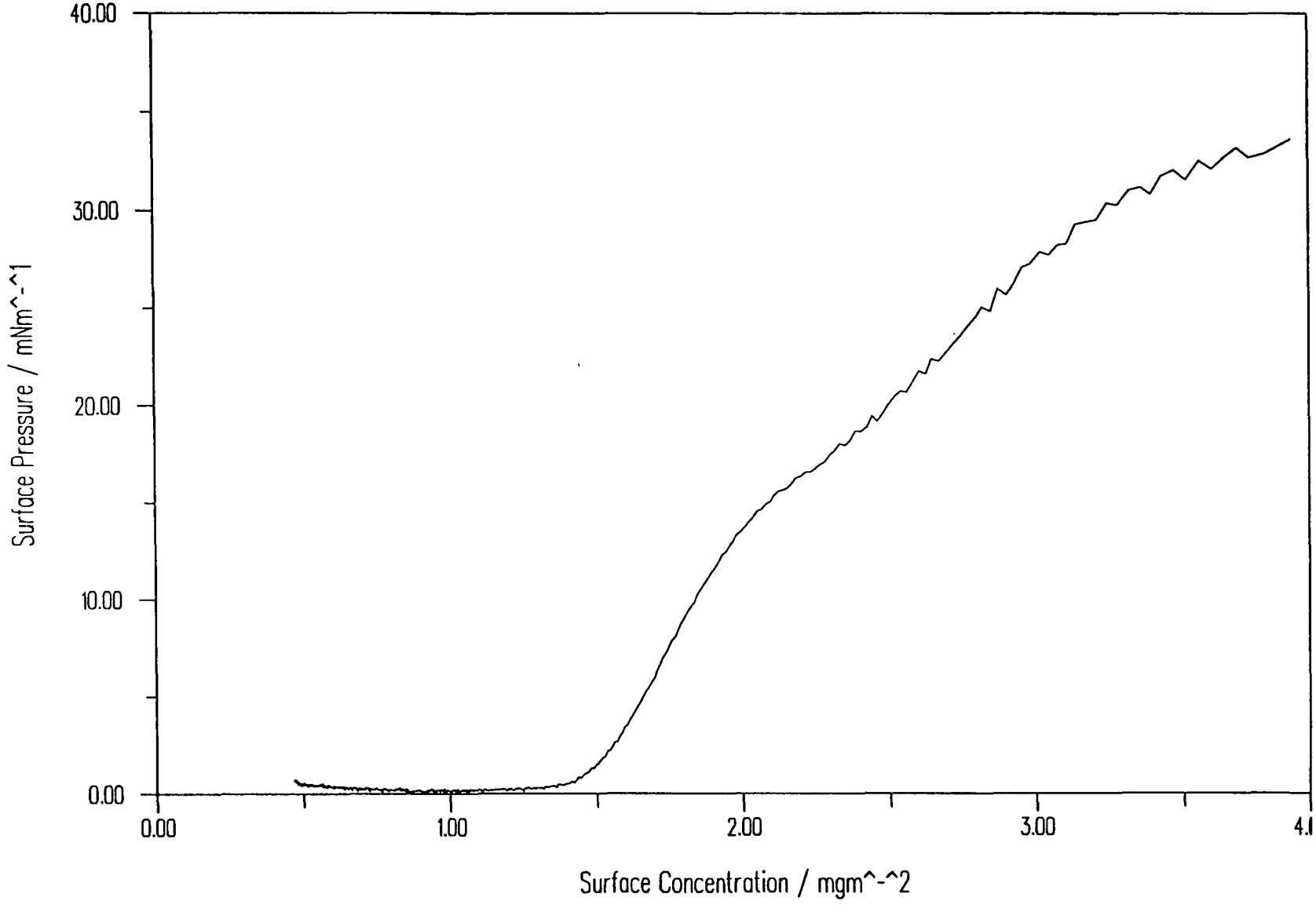

Figure 6.9 Surface Pressure - Surface Concentration Isotherm for DPMMA4VPQ(H) on water

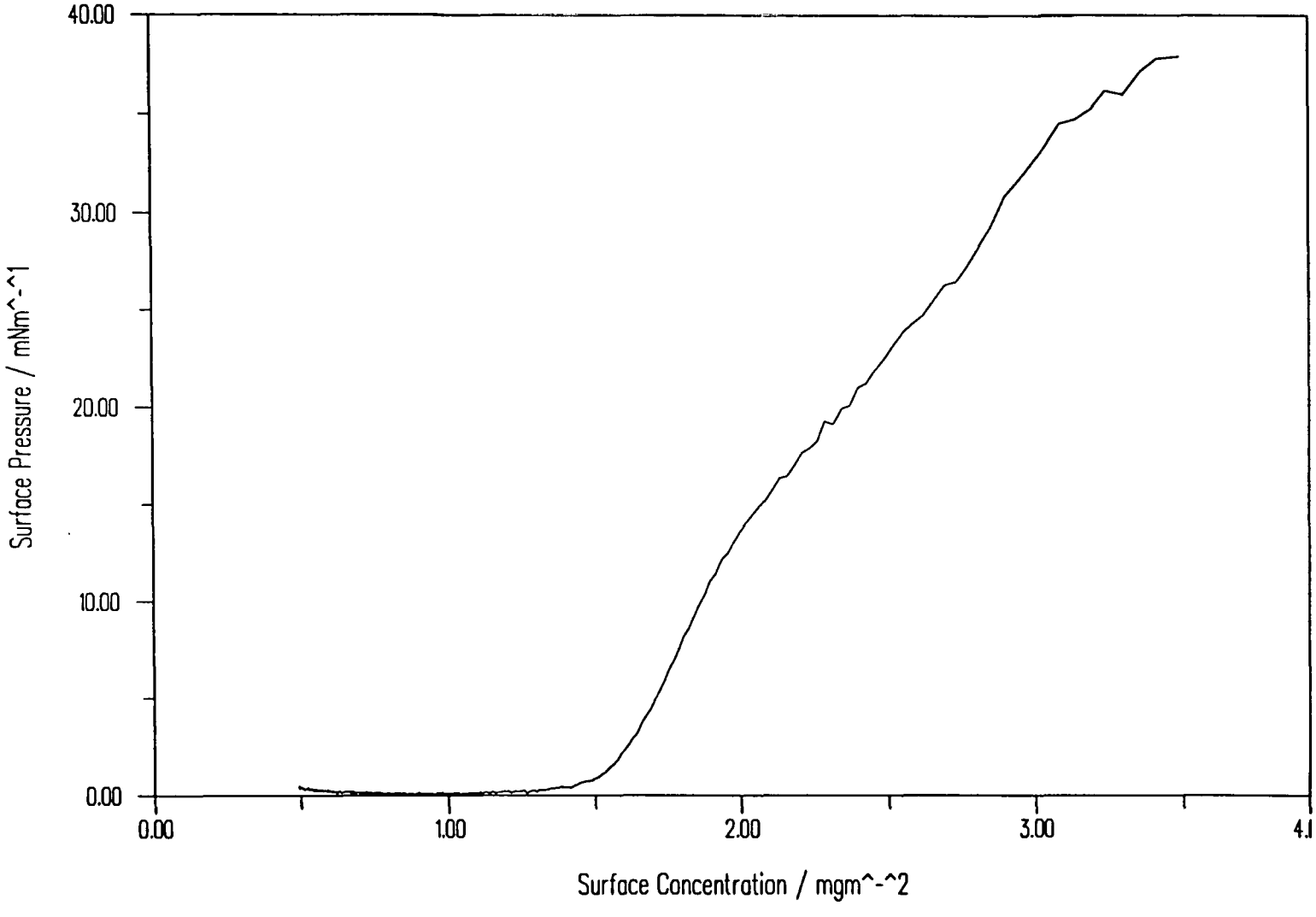

Figure 6.10 Surface Pressure - Surface Concentration Isotherm for DPMMA4VP(Q)D

material it may be seen immediately that the quaternised polymer films have a much larger surface concentration of pressure onset and limiting area per segment, around $\Gamma = 1.2 mgm^{-2}$ and $A_{lim} = 11 - 12$ Å^2 respectively. The limiting area values for each material are shown in table 6.5.

Polymer	Γ_{lim}/mgm^{-2}	$A_{lim}/Å^2unit^{-1}$	Γ^*/mgm^{-2}	$\Gamma^{**}/mgmm^{-2}$	y	v
HH	1.54	11	1.41	1.78	12.3	0.54
HD	1.55	11	1.41	1.78	12.0	0.54
DH	1.50	12	1.35	1.70	13.0	0.55
DD	1.55	12	1.41	1.78	12.9	0.53

Table 6.5 Analysis of Surface Pressure Isotherms for PMMA4VPQ Monolayers

As was the case for unquaternised PMMA4VP polymers, the high pressure data was rather irreproducible, but a common feature of the isotherms was the presence of a point of inflection at around $2mgm^{-2}$, at a surface pressure of around 15 - $20mNm^{-1}$.

From the scaling law double logarithmic plots, eg. figure 6.11, scaling exponent values tabulated on the right hand side of table 6.5 were obtained. The values are much lower than those of the unquaternised material, the typical value of 0.54 being around the order associated with theta or just less than theta conditions. This is reflected in the equation of state plot, figure 6.12, which has a clearly negative initial slope, indicative of a negative two dimensional second virial coefficient. This behaviour was observed for all four polymers.

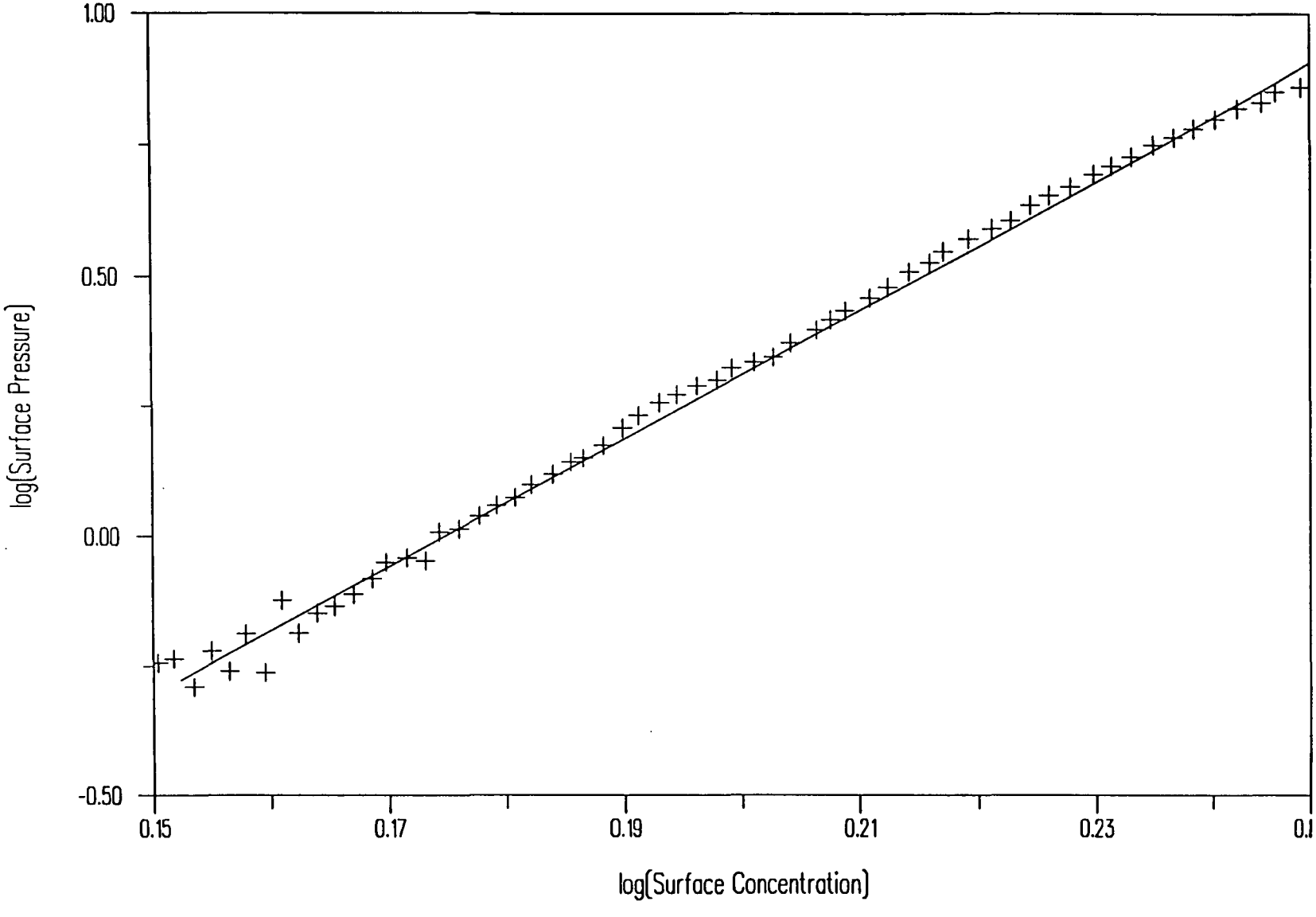

Figure 6.11 Double Logaritmic Plot of Surface Pressure - Surface Concentration Data for HPMMA4VPQ(H)

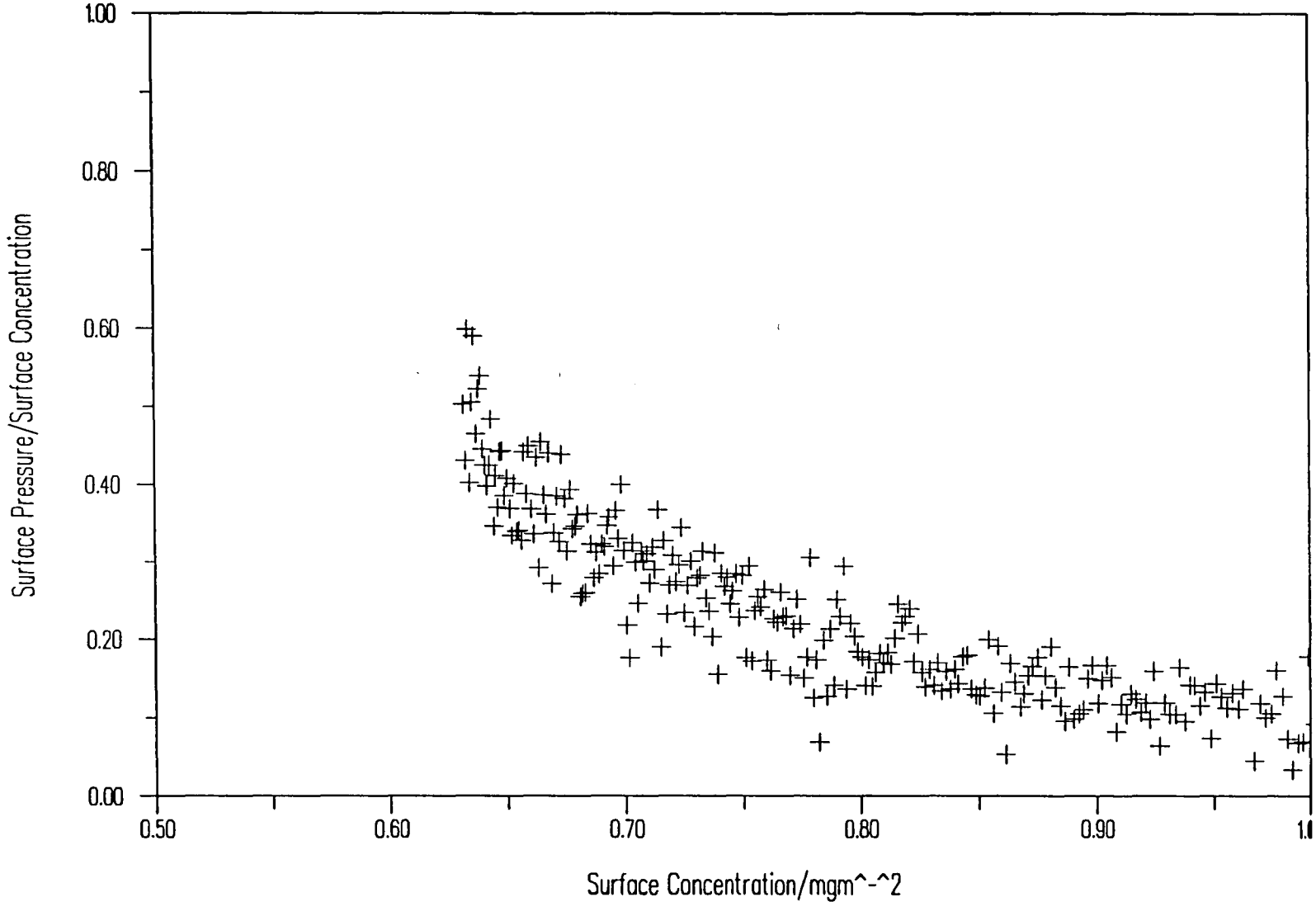

Figure 6.12 Surface Pressure / Surface Concentration v Surface Concentration for HPMMA4VPQ(H)

6.3 Neutron Reflectometry

6.3.1 PMMA4VP

Neutron reflectivity profiles for DPMMA4VP on air contrast matched water and HPMMA4VP on D_2O are shown in figures 6.13 and 6.14. The general trends in the profiles are rather like those seen for PMMA. The D/acmw contrast gives a rise in reflectivity for a given momentum transfer with rising surface concentration, although the profiles become closer together at higher concentrations. For the H/D_2O contrast there is considerable depression of the reflectivity indicative of a condensed film structure like PMMA's, rather than a subphase expanded film like PEO.

A single film modelling approach has been applied to PMMA4VP monolayers, the best fitted values being summarised in table 6.6, and the optimum values in table 6.7.The position of the residual minima for both contrasts at a given surface concentration are very close together giving low errors on the optimum thickness values. From the optimum scattering length density values, volume fractions may be estimated by approximating "average" scattering length density values for the hydrogenous and deuterated polymers of $\rho_H = 0.96\times10^{-6}Å^{-2}$ and $\rho_D = 5.32\times10^{-6}Å^{-2}$, these values being calculated from the scattering length densities of the two monomer components in the polymer and weighted according to the relative block sizes. The composition variation is shown in table 6.8, along with derived apparent surface concentration values.

PMMA4VP may be seen to exist as a very dense film with a similar thickness to that observed for syndiotactic poly (methyl methacrylate). The variation of the film thickness is relatively small with surface concentration, but the polymer volume fraction increases to around 0.8 at high surface concentrations.

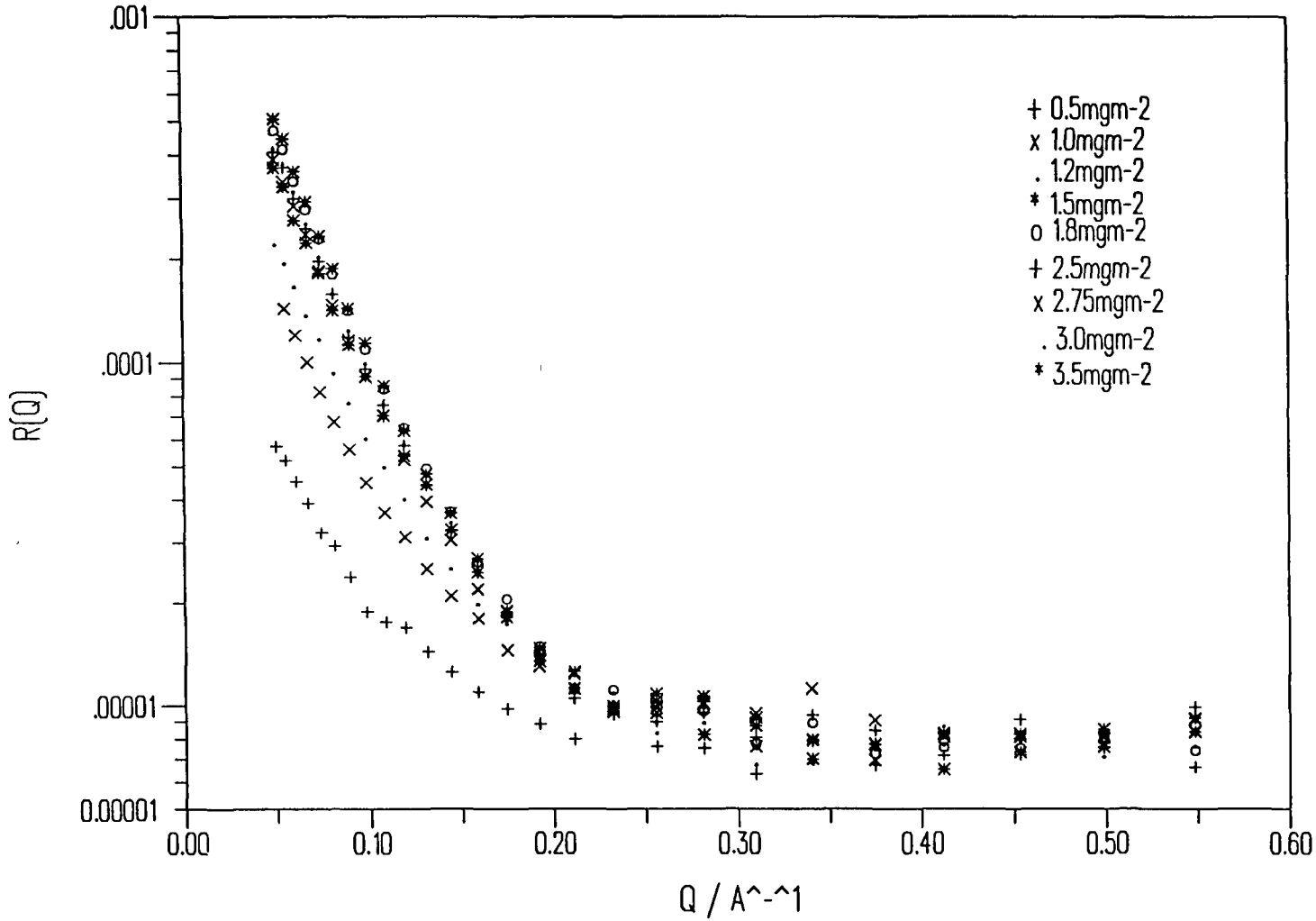

Figure 6.13 Neutron Reflectivity Profiles for DPMMA4VP on acmw

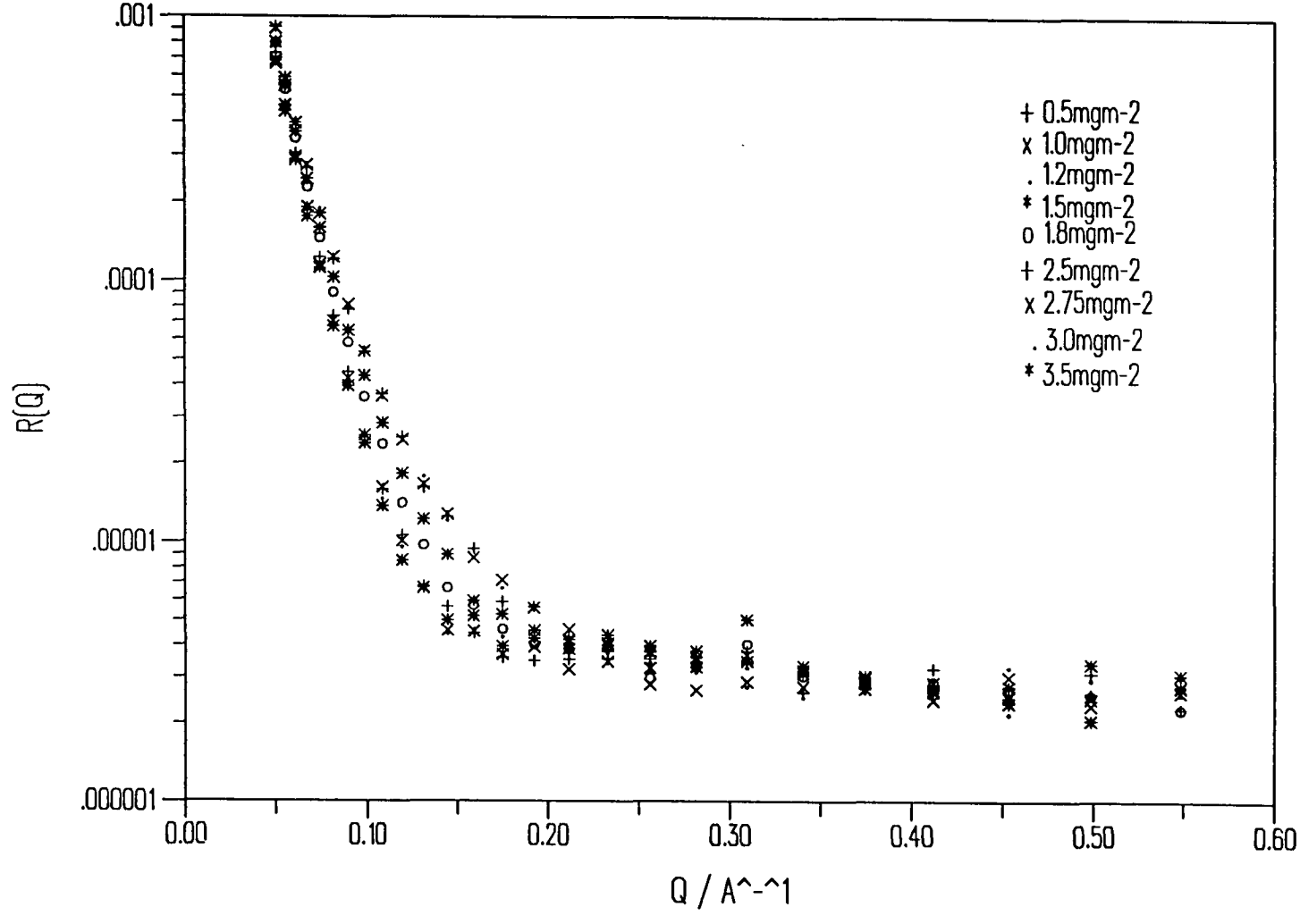

Figure 6.14 Neutron Reflectivity Profiles for HPMMA4VP on D_2O

Γ/mg m^{-2}	D/acmw			H/D_2O		
	d/Å	ρ/10^{-6}Å^{-2}	res/10^{-2}	d/Å	ρ/10^{-6}Å^{-2}	res/10^{-2}
0.5	15	2.05	0.6441	17	1.84	0.6676
1.0	17	3.14	0.5865	16	3.29	0.6114
1.2	17	3.72	0.5076	17	3.72	0.5076
1.5	19	4.29	0.6303	19	4.29	0.6303
1.8	21	4.49	0.6524	20	4.61	0.6596
2.5	21	4.17	0.8268	20	4.28	0.8941
2.75	21	4.04	1.072	21	4.04	1.072
3.0	22	4.11	0.7029	22	4.11	0.7029
3.5	23	4.29	0.6313	23	4.29	0.6313

Table 6.6 Single Slab Model Residual Minima for PMMA4VP on water

Γ/mg m^{-2}	D/acmw			H/D_2O	
	d/Å	ρ/10^{-6}Å^{-2}	res/10^{-2}	ρ/10^{-6}Å^{-2}	res/10^{-2}
0.5	16	1.94	0.6502	0.88	0.6977
1.0	16.5	3.18	0.6044	0.85	0.7014
1.2	17	3.72	0.5076	0.79	0.6955
1.5	19	4.29	0.6303	1.40	0.6757
1.8	20.5	4.55	0.6442	1.56	0.7180
2.5	20.5	4.23	0.8524	2.18	0.9877
2.75	21	4.04	1.072	2.06	0.6261
3.0	22	4.11	0.7029	2.13	1.110
3..5	23	4.29	0.6313	1.97	1.149

Table 6.7 Single Slab Model Optimum Fitted Parameters for PMMA4VP on water

At low and moderate surface concentrations the apparent surface concentration is in excellent agreement with the dispensed amount. It is only at high surface concentrations (around 2.5mgm^{-2}) that a systematic discrepancy becomes obvious, with apparent surface concentrations deviating below the linear diagonal. This is again similar to the behaviour of syndiotactic PMMA.

In general the good agreement of the residual minimum thicknesses for

Γ/mg m^{-2}	Volume Fraction			ρ.d/10^{-6}Å^{-1}	a.p.m./Å^{2}monomer^{-1}	Γ_a/mgm^{-2}
	polymer	water	air			
0.5	0.36	0.08	0.56	31.0	28.4	0.63
1.0	0.60	0.04	0.36	52.5	16.7	1.07
1.2	0.70	0.02	0.28	63.2	13.9	1.29
1.5	0.81	0.10	0.09	81.5	10.8	1.65
1.8	0.86	0.12	0.02	93.3	9.4	1.90
2.5	0.80	0.22	-0.02	86.7	10.1	1.77
2.75	0.76	0.21	0.03	84.8	10.4	1.72
3.0	0.77	0.21	0.02	90.4	9.7	1.84
3.5	0.81	0.19	0.00	98.9	8.9	2.01

Table 6.8 Layer Composition and Apparent Surface Coverage Variation for PMMA4VP on water

both contrasts, the apparent and dispensed surface concentrations, and the reasonably low residual values suggest that a single film model is a reasonable description of the PMMA4VP monolayer, and efforts to improve on it by an additional layer were not successful, using the criterion of an improvement in the residual of the fit to the experimental data.

Kinematic Analysis

The kinematic formulae of section 2.2 have been applied to reflectivity from PMMA4VP monolayers. A typical Guinier plot of $\ln(R(Q)^2.Q^2)$ v Q^2 for DPMMA4VP on air contrast matched water is shown in figure 6.15. From the slope and intercept of the linear portion of this plot, determined by the low Q breakdown of kinematic theory and high Q experimental background, the values in table 6.9 were obtained.

The layer thicknesses obtained from the Guinier plots are in broad agreement with the values obtained from a single film matrix model, although at low

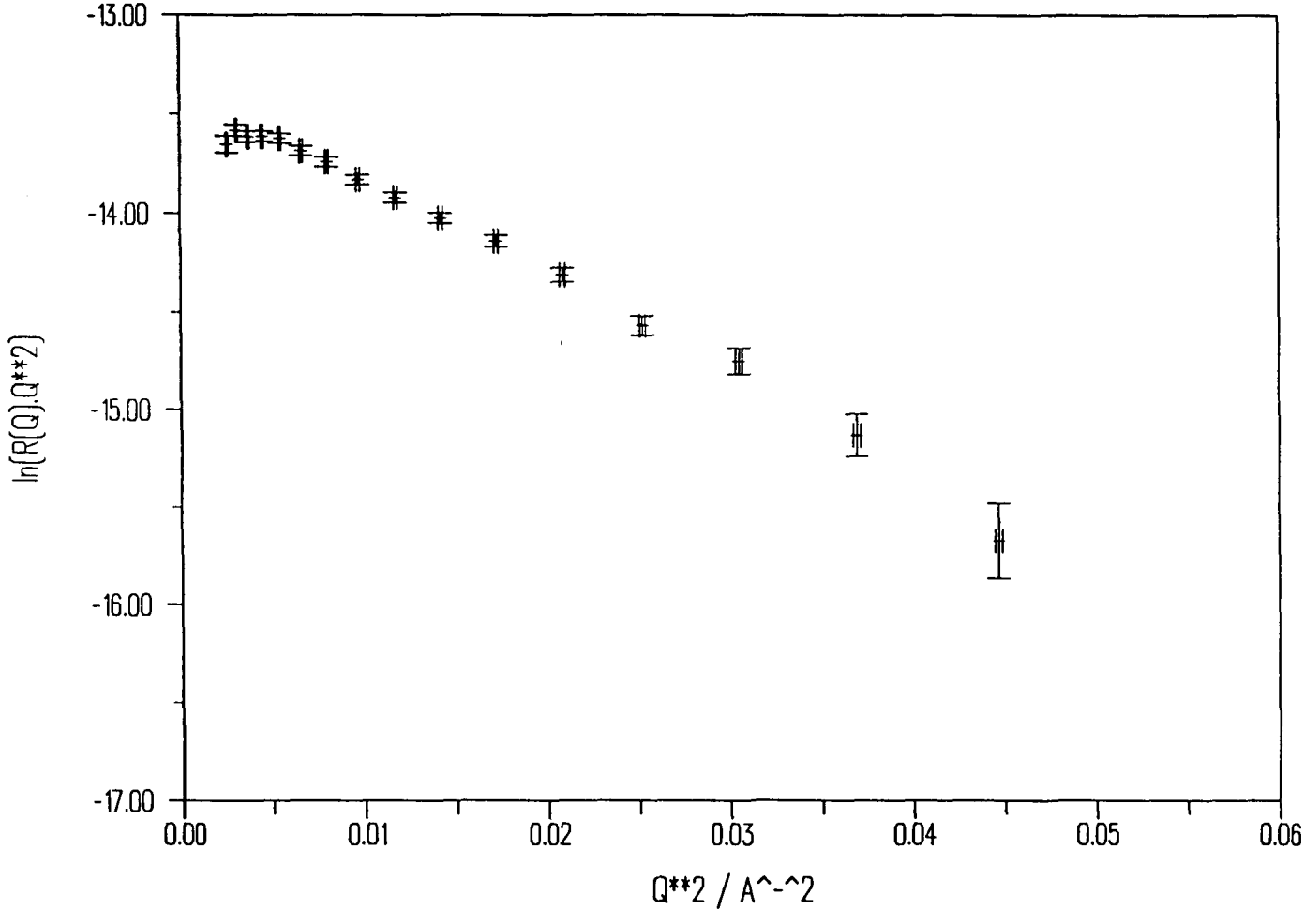

Figure 6.15 Guinier Plot for DPMMA4VP on acmw, surface concentration = 1.8mgm^{-2}

Γ/mgm^{-2}	Intercept	Slope	m/10^{-6}Å^{-2}	σ	d
0.5	-15.7	-24.4	31.0	4.9	17.0
1.0	-14.6	-28.8	53.8	5.4	18.7
1.2	-14.3	-25.5	62.5	5.1	17.7
1.5	-13.7	-39.6	84.3	6.3	21.8
1.8	-13.4	-47.7	98.0	6.9	23.9
2.5	-13.5	-48.3	93.2	6.9	23.9
2.75	-13.6	-45.2	88.6	6.7	23.2
3.0	-13.5	-48.1	93.2	6.9	23.9
3.5	-13.3	-59.4	103.0	7.7	26.7

Table 6.9 Results of Analysis of Guinier plots for DPMMA4VP on acmw

coverages the values are slightly higher than the matrix model values and at the highest coverage the Guinier plot gives a slightly higher thickness, possibly explained by some diffuse projection from the film into the subphase.

Patterson plots for HPMMA4VP on D_2O and DPMMA4VP on air contrast matched water are shown in figures 6.16 and 6.17. In each case a minimum is observed at the characteristic π/d point. It is very striking that the minima in both types of plot are well defined, indicating a relatively dense, slab-like layer. The thickness values obtained for a single film are shown in table 6.10.

The values are essentially similar for both contrasts, and similar to those previously obtained from other methods, except at surface concentrations of 2.5mgm^{-2} and above, where the H/D_2O contrast values increase but the D/acmw values remain approximately constant. This may be due to background truncation of the high Q data for the D/acmw contrast or possibly a reflection of greater sensitivity in the former contrast to diffuse polymer projection into the subphase.

In summary then, both optical matrix and kinematic treatments of the reflectometry data for PMMA4VP copolymers seem to suggest that the film is

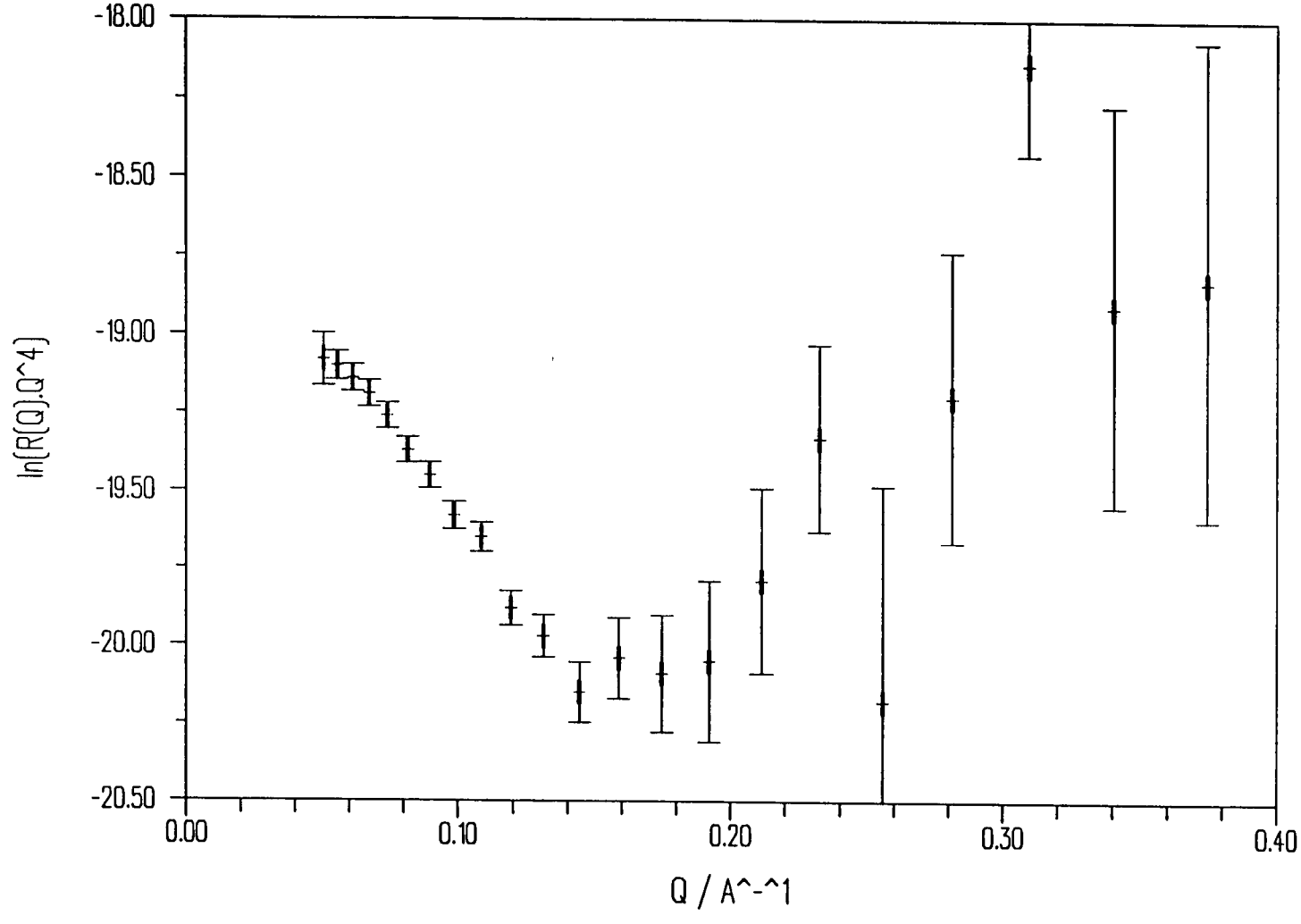

Figure 6.16 Patterson Plot for HPMMA4VP on D_2O, surface concentration = 1.8mgm^{-2}

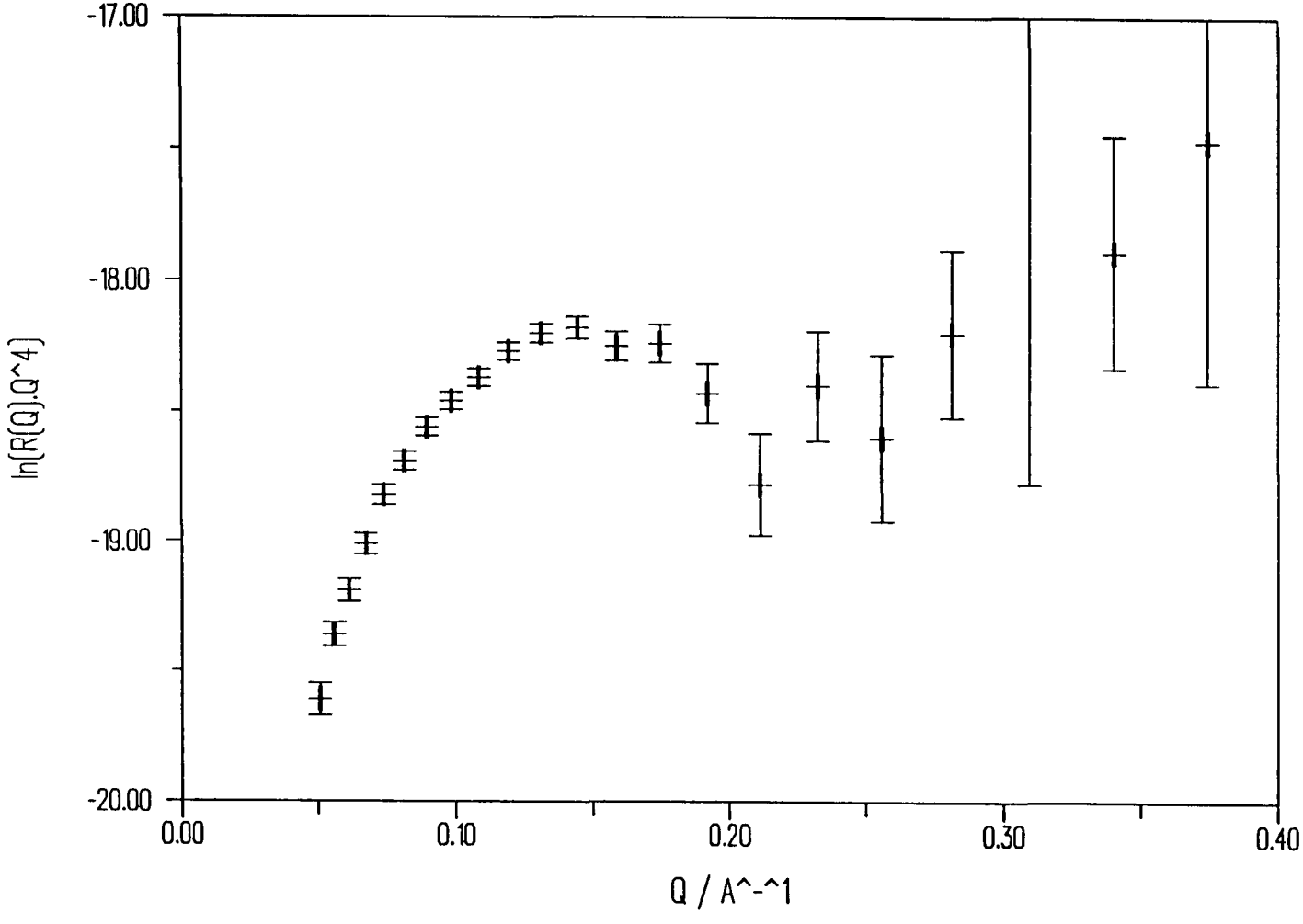

Figure 6.17 Patterson Plot for DPMMA4VP on acmw, Surface Concentration = 1.8mgm^{-2}

	H/D_2O				D/acmw	
Γ/mgm^{-2}	x_{min}	y_{min}	d/Å	$\rho_F/10^{-6}Å^{-2}$	x_{min}	d/Å
0.5	0.23	-19.5	14	0.86	0.20	16
1.0	0.23	-19.4	14	0.67	0.23	14
1.2	0.20	-19.3	17	0.61	0.25	13
1.5	0.18	-20.0	18	1.37	0.20	16
1.8	0.17	-20.1	19	1.46	0.21	15
2.5	0.17	-20.8	19	1.93	0.25	13
2.75	0.15	-20.9	21	2.02	0.22	14
3.0	0.14	-20.9	22	2.02	0.22	14
3.5	0.13	-20.7	24	1.90	0.23	14

Table 6.10 Results of Analysis of Patterson Functions for PMMA4VP on water

essentially a single simple film, except possibly at very large surface coverages. Two reasons may be given to account for this. Possibly the scattering length density of (hydrogenous) 4VP segments is insufficient to show up in the case of these segments projecting into the subphase. On the other hand, it is likely that preferential desorption of 4VP segments from the interface is not taking place for the unquaternised polymer. Although poly-4VP might be expected to display a slightly greater affinity for the aqueous subphase than PMMA, it is by no means the readily water soluble material of its polyelectrolyte quaternised form. The structural effects of the inclusion of a dissociated, water soluble poly-4VPQ block will be considered in the next section.

6.3.2 PMMA4VPQ Copolymers

Neutron reflectivity profiles for DPMMA4VPQ(D) on air contrast

matched water (DD/acmw) and HPMMA4VPQ(H) on D_2O (HH/D_2O) over a range of surface concentrations are shown in figures 6.18 and 6.19. By comparison with the reflectivity profiles for the unquaternised material, figures 6.13 and 6.14, the same general features of a condensed monolayer are observed. However on attempting to fit a single layer model of the type used successfully for PMMA4VP, differences between the two cases become apparent. Residual minimum values for a smooth edged, single layer model at both contrasts are shown in table 6.11, and optimum values in table 6.12.

The residual minimum positions for the two contrasts are rather further apart for the quaternised monolayers than for the unquaternised (which gave excellent agreement) but the most notable difference is in the quality of the best fitted functions, as reflected by the residual values. For the quaternised films these are generally higher than acceptable for a good fit to the data, and at higher surface concentrations in particular, the fitted line is a very poor match indeed for the experimental data (cf data at Γ = 3.0 mgm^{-2}). For the lowest surface concentration data it was not possible to fit physically sensible values for the D/acmw contrast. The reason for this is not apparent but may be associated with the small amount of deuterated material at the surface leading to an unreliable measurement.

A dramatic improvement in the quality of the fitted data may be achieved by the use of a two layer model, using the strategy of fitting previously described in the studies of PMMA monolayers. The results of such an analysis are shown in table 6.13.

A plausible explanation for the apparent two layer nature of the PMMA4VPQ monolayer is the solubilisation of hydrophilic poly (4-vinyl ethylpyridinium) segments in the subphase while poly (methyl methacrylate) segments remain attached more closely to the surface, in a fashion similar to their homopolymer monolayers. Such a segregation would lead to an effective decrease of

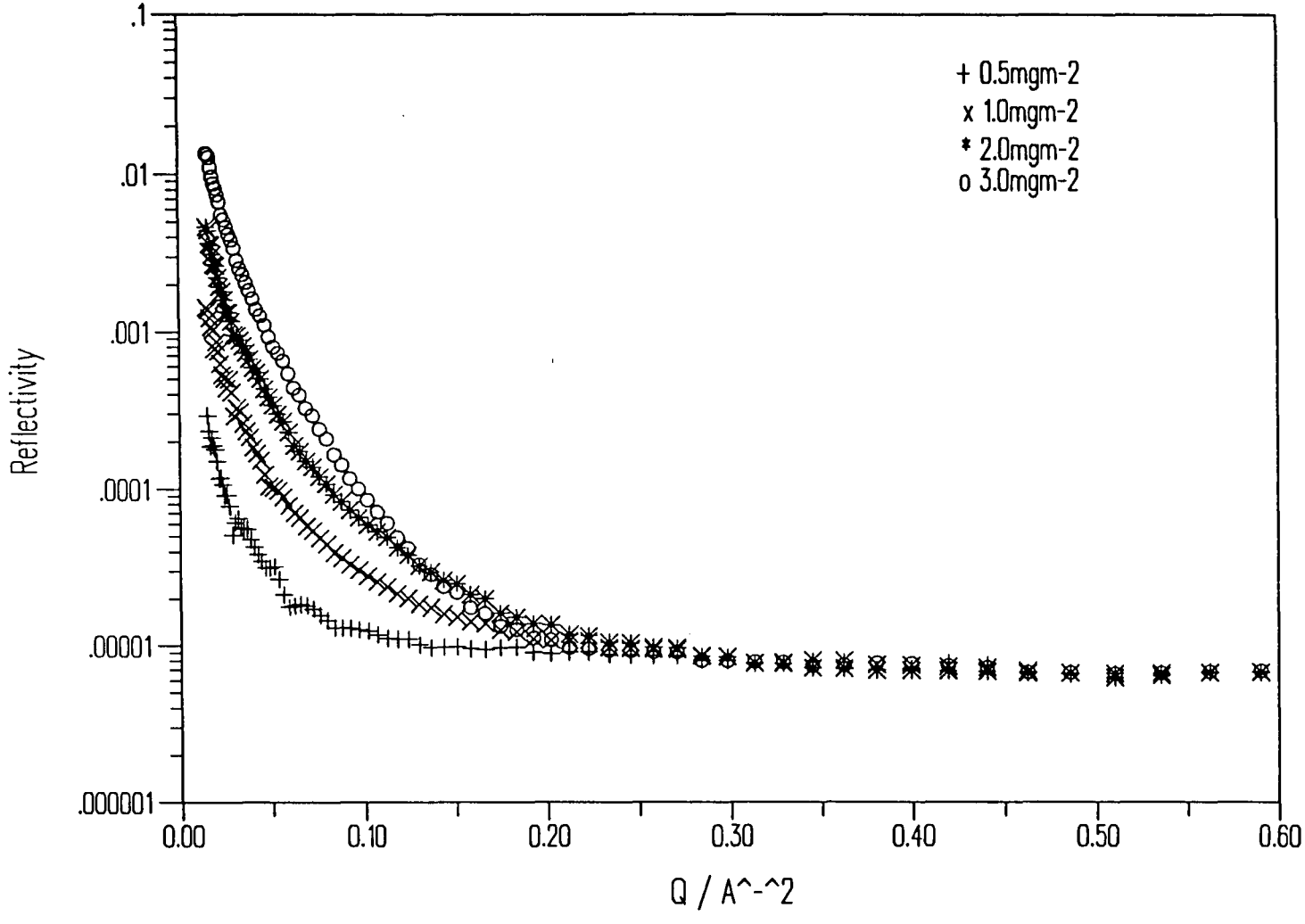

Figure 6.18 Neutron Reflectivity Profiles for DPMMA4VPQ(D) on water obtained using CRISP

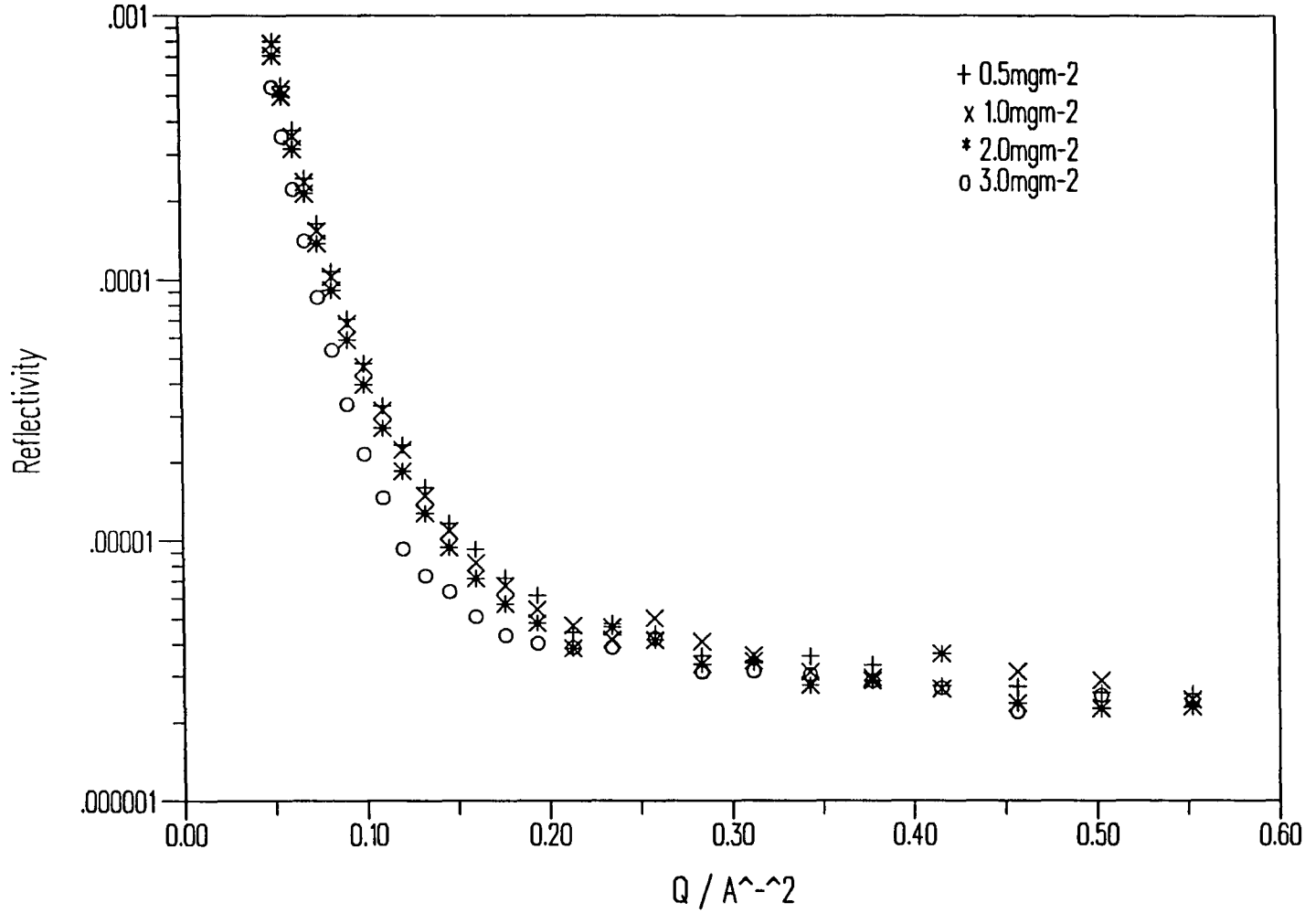

Figure 6.19 Neutron Reflectometry Profiles for HPMMA4VPQ(H) on D_2O obtained using CRISP

Γ/mg m^{-2}	D/acmw			H/D_2O		
	d/Å	$\rho/10^{-6}$Å^{-2}	res/10^{-2}	d/Å	$\rho/10^{-6}$Å^{-2}	res/10^{-2}
0.5	-	-	-	24	0.72	0.8789
1.0	14	3.09	0.4764	23	0.83	0.8309
2.0	19	3.98	0.6497	22	1.13	1.048
3.0	32	4.20	1.041	25	1.83	1.633

Table 6.11 Single Slab Model Residual Minima for PMMA4VPQ on water

Γ/mg m^{-2}	D/acmw			H/D_2O	
	d/Å	$\rho/10^{-6}$Å^{-2}	res/10^{-2}	$\rho/10^{-6}$Å^{-2}	res/10^{-2}
0.5	-	-	-	-	-
1.0	18	2.47	0.5561	0.90	1.105
2.0	21	3.71	0.6940	1.15	1.069
3.0	28	4.49	1.1186	1.78	1.875

Table 6.12 Single Slab Model Optimum Fitted Parameters for PMMA4VPQ on water

Γ/mg m^{-2}			D/acmw			H/D_2O		
	d_1/Å	d_2/Å	$\rho_1/10^{-6}$Å^{-1}	$\rho_2/10^{-6}$Å^{-1}	resid/10^{-2}	$\rho_1/10^{-6}$Å^{-1}	$\rho_2/10^{-6}$Å^{-1}	resid/10^{-2}
0.5	-	-	-	-	-	-	-	-
1.0	9	34	4.38	0.19	0.2924	0.64	5.82	1.37
2.0	14	23	4.78	0.60	0.2962	0.31	5.46	1.010
3.0	23	23	4.77	1.47	0.4859	0.94	5.45	1.303

Table 6.13 Two Layer Fitted Parameters for PMMA4VPQ on water

segment density at the interface, accounting for the much higher surface concentration of surface pressure onset observed in the surface pressure isotherm of PMMA4VPQ copolymers.

In order to confirm the structure of the PMMA4VPQ film it would be desirable to investigate different contrast conditions, and in particular the case of a block copolymer of hydrogenous poly (methyl methacrylate) with deuterated poly (4-vinyl pyridine) on a low scattering length density subphase. Unfortunately deuterated 4-vinyl pyridine monomer was not available and these experiments have not been attempted.

Some limited work was carried out using an HPMMA4VPQ(D) copolymer on air contrast matched water (where of course the bracketted D refers to deuterated ethyl bromide, not 4-vinyl pyridine). This however met with little success, apparently due to the combination of the small amount of deuterated material in the polymer and its diffuse distribution in the film.

With the proposed two layer model in mind, and given the lack of complementary information from different contrasts to uniquely determine the distribution of the two polymer types at the interface, it is not possible to calculate compositional variation of the PMMA4VPQ film. From the fitted scattering length densities it appears that the upper layer has relatively constant segment concentration whereas the lower layer becomes more concentrated in polymer (probably 4VPQ segments) as surface concentration is increased.

Kinematic Analysis

Kinematic analysis of the reflectometry data for PMMA4VPQ copolymers has been carried out in a similar fashion to that employed for previous systems. An example of a Guinier plot for the DD copolymer on air contrast

matched water is shown in figure 6.20, and from the full set of plots the parameters in table 6.15 were obtained. A large increase in the thickness obtained is seen at a surface concentration of $3mgm^{-2}$, consistent with the notion that more hydrophilic portions of the polymer chain may project into the subphase.

Patterson functions obtained at both contrast conditions studied are shown in figures 6.21 and 6.22. Relevant quantities derived from the plots are shown in table 6.16. From the plots it can be seen that in this particular case the minima in the Patterson plots are very shallow and that it is not at all easy to determine the minimum position with great accuracy. In the case of the DD/acmw contrast the minimum is smoothed to such an extent that it is only definitely discernible at the highest surface concentration studied, and the layer thickness obtained in this case is rather less than that obtained from the from the HH/D_2O contrast. This and the fact that the minima are rather less sharply defined than for the unquaternised films are further evidence for the extension of 4VPQ segments into the subphase, as the Patterson function is generated for a single film bounded by two sharp steps in scattering length density.

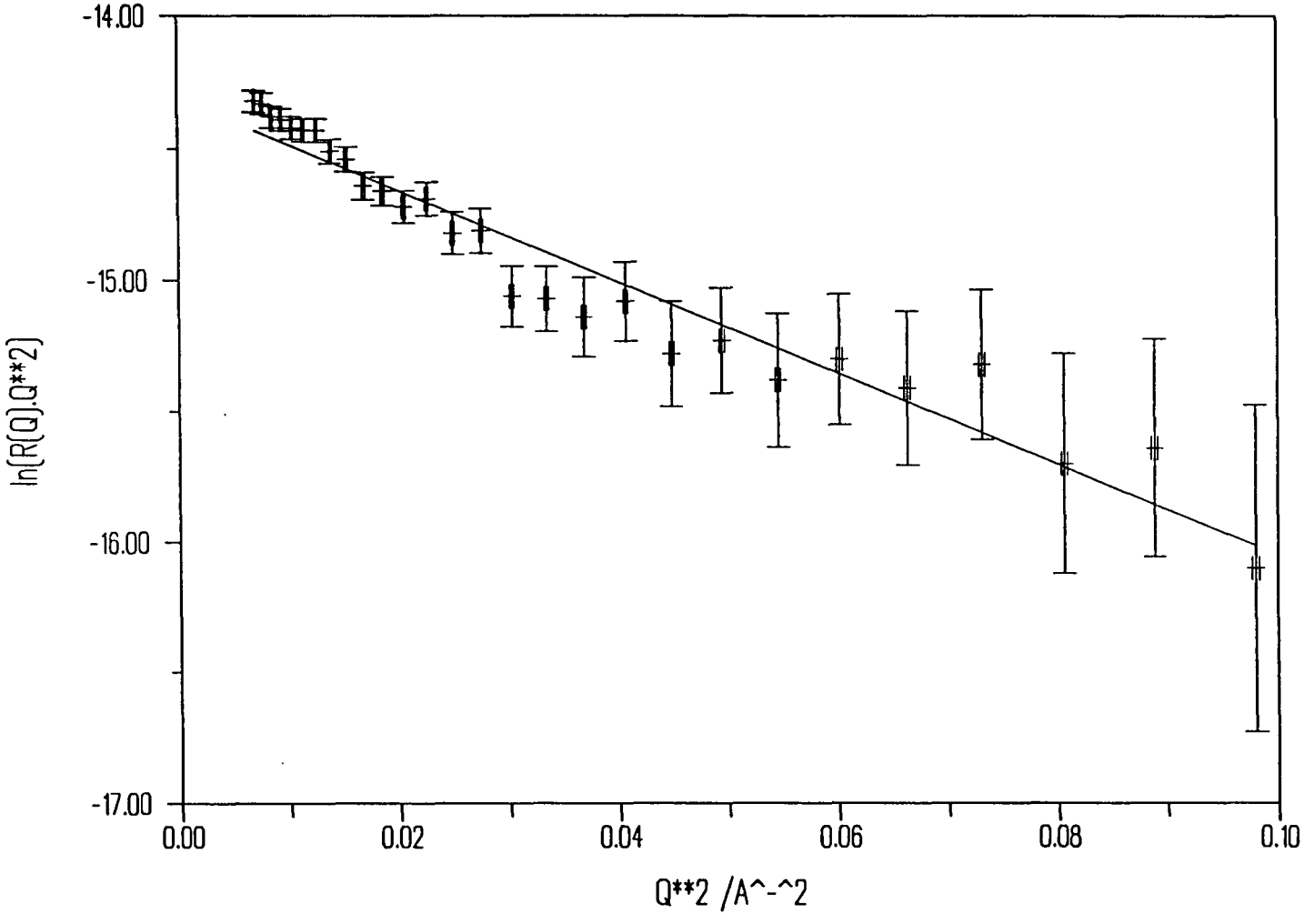

Figure 6.20 Guinier Plot for DPMMA4VPQ(D) on water, surface concentration = 2.0mgm^{-2}

Γ/mgm^{-2}	Intercept	Slope	m/10^{-6}Å^{-2}	σ	d
1.0	-15.1	-14.8	41.9	3.8	13.2
2.0	-14.3	-17.4	62.5	4.2	14.5
3.0	-13.2	-76.0	108.3	8.7	30.1

Table 6.15 Results of Analysis of Guinier plots for DPMMA4VPQ(D) on acmw

	HH/D_2O				DD/acmw	
Γ/mgm^{-2}	x_{min}	y_{min}	d/Å	ρ_F/10^{-6}Å^{-2}	x_{min}	d/Å
0.5	0.15	-19.3	20.9	0.61	-	-
1.0	0.15	-19.5	20.9	0.86	-	-
2.0	0.15	-19.7	20.9	1.08	-	-
3.0	0.12	-20.4	26.2	1.70	0.18	17.5

Table 6.16 Results of Analysis of Patterson Functions for PMMA4VPQ

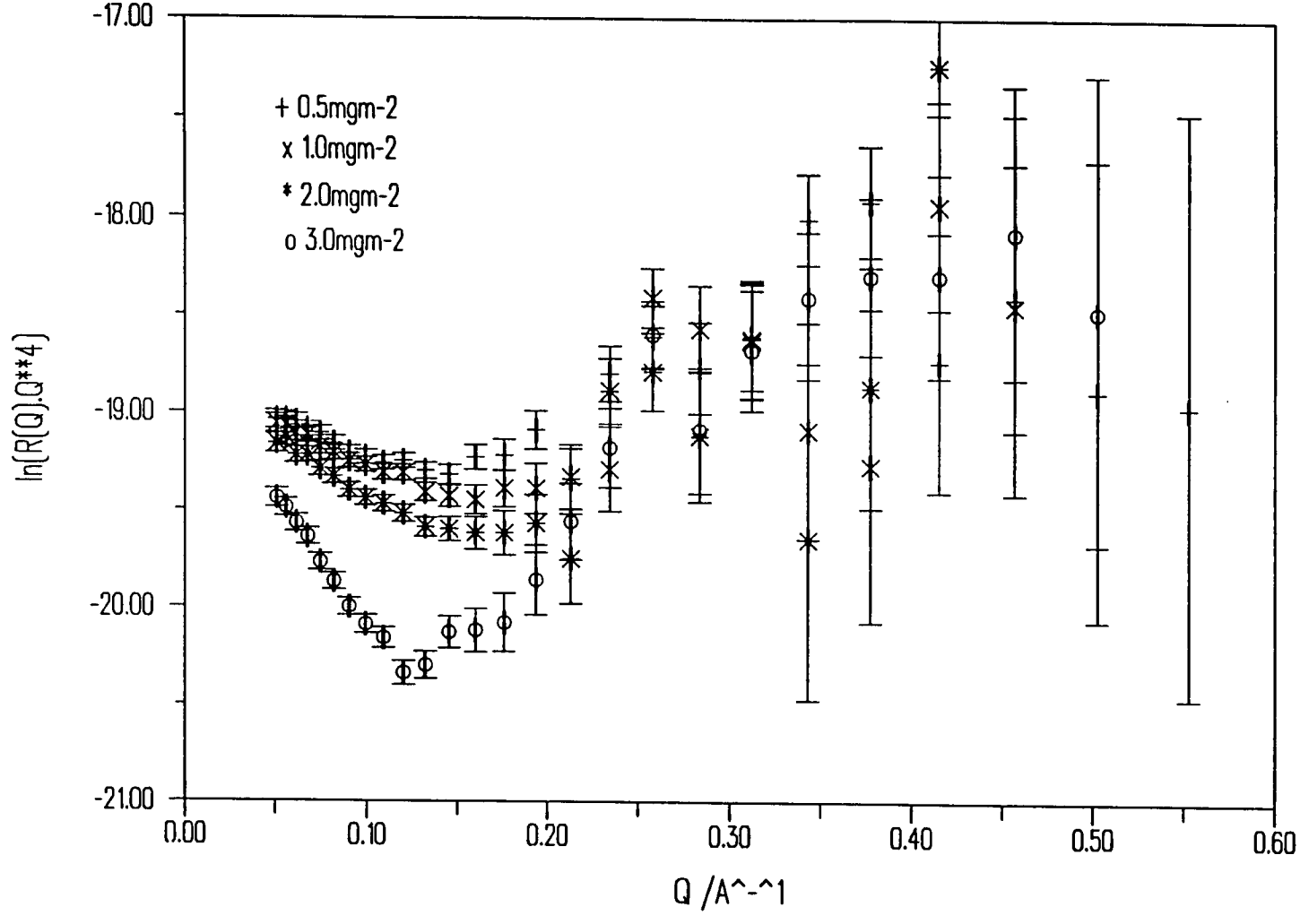

Figure 6.21 Patterson Plots for HPMMA4VPQ(H) on D_2O

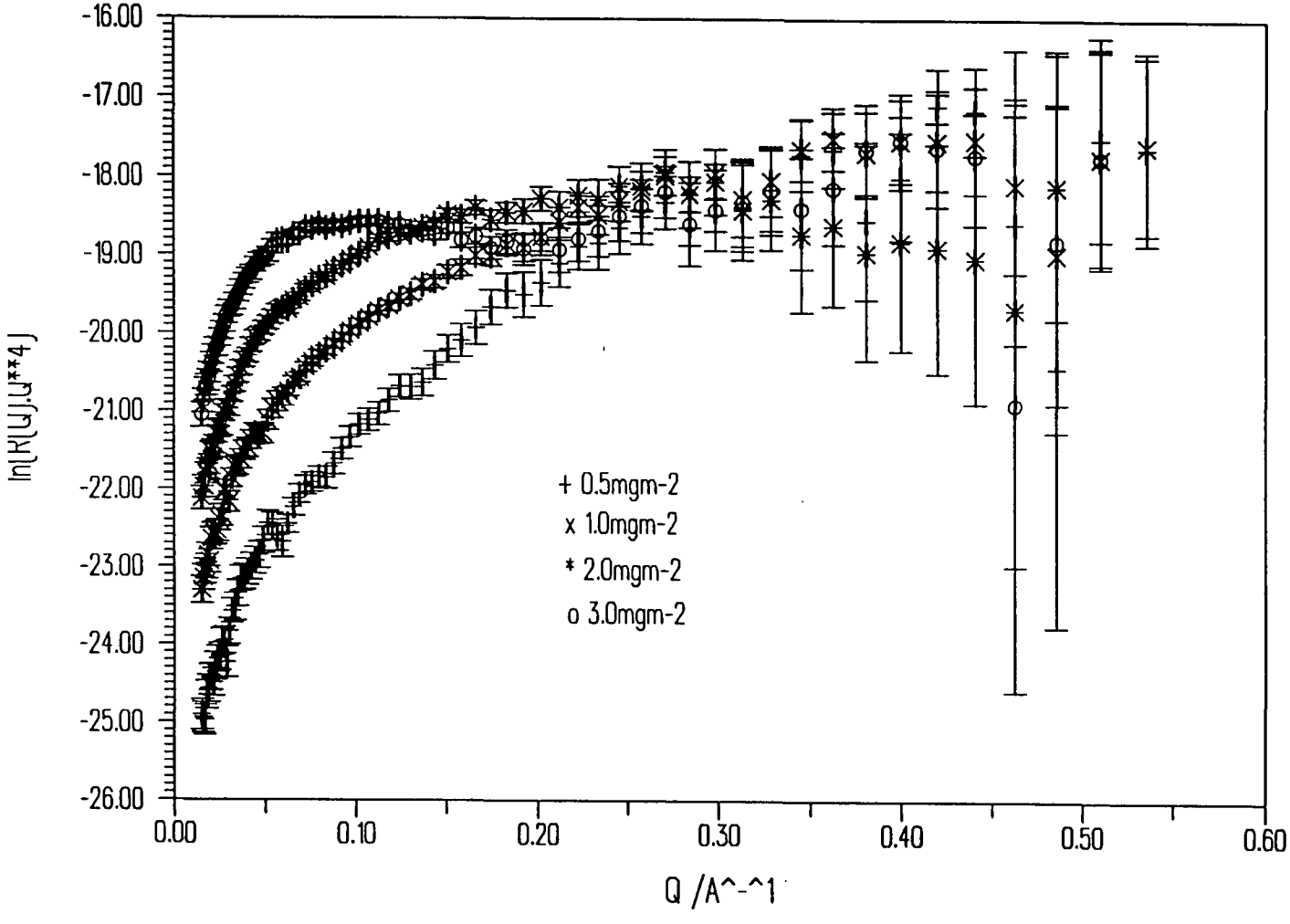

Figure 6.22 Patterson Plots for DPMMA4VPQ(D) on acmw

6.4 Ellipsometry

Unquaternised PMMA4VP copolymer has been studied by ellipsometry during a barrier compression/expansion cycle. Plots of phase retardation and surface pressure as a function of barrier position are shown in figures 6.23 and 6.24. As usual no sensitivity in amplitude attenuation was observed and consequently an intermediate refractive index of 1.48 was used to estimate the layer thickness. The thickness values so obtained are shown in figure 6.25.

On comparison with the trends observed for PMMA and PEO (sections 4.4 and 5.5), PMMA4VP is seen to be much more like the former. The film thickness rises from a rather low value of about 7Å to around 21Å. Of course no account is taken of compositional effects leading to an alteration in the refractive index. However it can be seen that, with the possible exception of low surface concentrations, a realistic layer thickness can be obtained using a refractive index corresponding approximately to a polymer volume fraction of around 0.9. This is in agreement with the results obtained from neutron reflectometry, which suggested PMMA4VP existed as a dense, well defined single film.

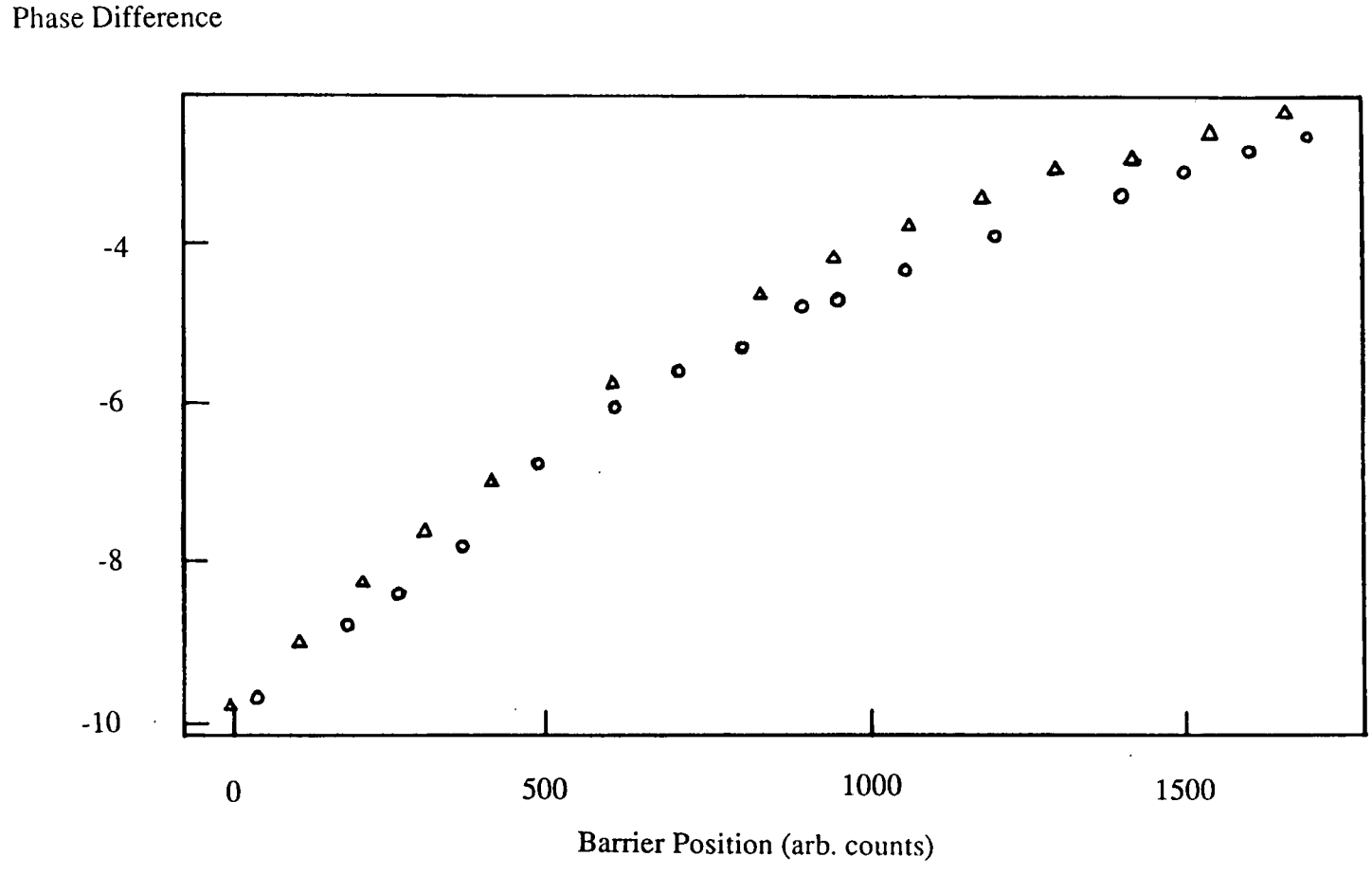

Figure 6.23 Phase Retardation v Barrier Position for PMMA4VP

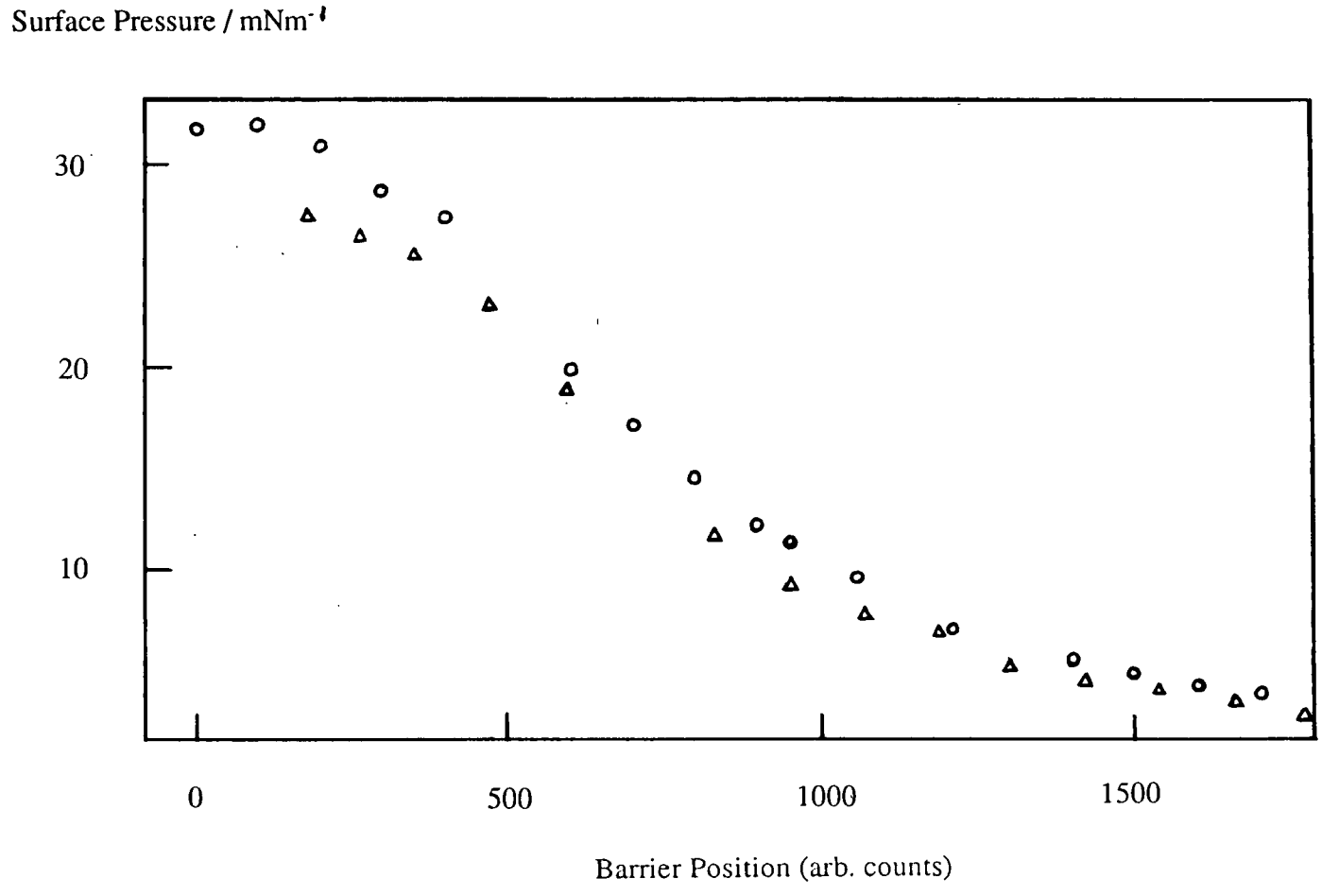

Figure 6.24 Surface Pressure v Barrier Position for PMMA4VP

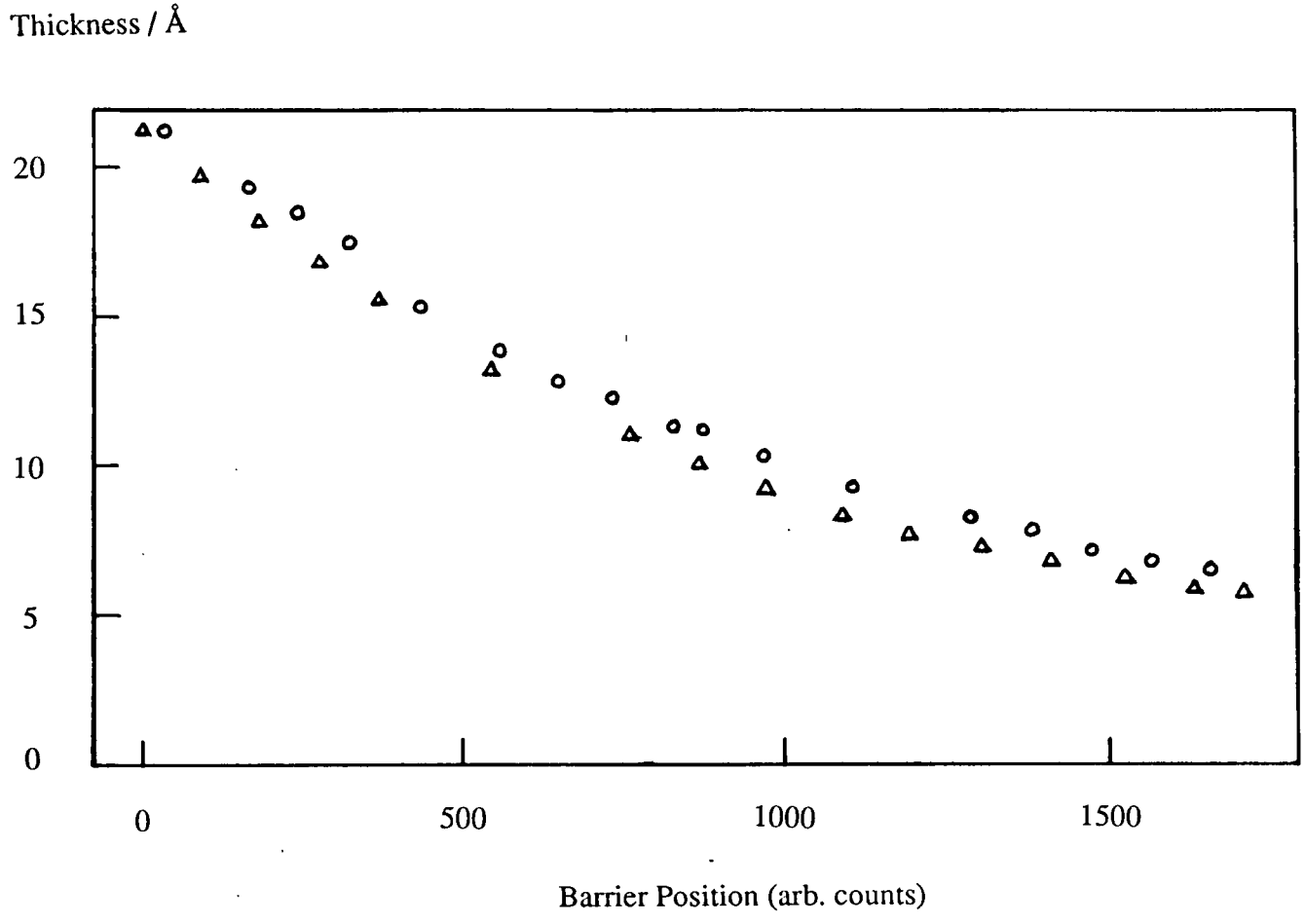

Figure 6.25 Film Thickness v Barrier Position for PMMA4VP

CHAPTER 7 - CONCLUSIONS

In conclusion, it is useful to briefly highlight some of the main points of similarity and difference to have emerged between the various materials examined during this study.

A major objective of this project was to examine the relationship between the thermodynamic nature of polymer monolayers as observed by surface pressure studies and their structure as observed by neutron reflectometry. In this regard, the usefulness of the latter technique has been demonstrated clearly. Monolayers of PMMA of various stereotacticity have been shown to have very different structure and composition as well as thermodynamic properties. Within the resolution of the technique a systematic modelling procedure has been applied to the reflectometry data to assess these changes and give a measure of the errors involved. Additionally evidence has been obtained of the existence of a two dimensional surface crystallisation phenomenon for isotactic PMMA monolayers, a result independently supported in a publication released shortly after the initial submission date of this thesis.[1,2]

The thermodynamic evidence describing PEO as a highly expanded monolayer has been supported by structural information obtained from reflectometry and ellipsometry. In this case the film is best modelled as a diffuse thick film. The use of various methods for the description of diffuse films in matrix calculations has been compared and the usefulness of the kinematic expressions for structural elucidation has been demonstrated. Structural and thermodynamic effects on the PEO films caused by the addition of electrolyte to the subphase have been examined in tandem for the first time, and again the various models employed have been considered critically.

Finally PMMA4VP copolymers and partially polyelectrolyte

PMMA4VPQ copolymers have been examined. In the uncharged form the film has been shown to behave as thin monolayer rather in the fashion of syndiotactic PMMA. In the quaternised form however neutron reflectometry results indicate a rather different behaviour, possibly indicative of tailing hydrophilic segments, a result which might explain the anomalous surface pressure behaviour of these films. Unlike previous studies, in this case no additional electrostatic contribution to the surface pressure has been observed, indeed there appears to be a lesser surface pressure at any given surface concentration. This may be due to either segment redistribution away from the interface (in the form of looping and tailing PVPQ blocks) or a counterion bridging mechanism leading to greater lateral cohesion in the film.

It is perhaps worthwhile to point out, and reassuring for anyone wishing to apply two dimensional theories to Langmuir films, that in all of the cases mentioned above neutron reflectometry consistently indicated layer thicknesses that were much less than one might predict for the three dimensional radius of gyration of any of the sample materials. This dimension is of importance as a widely accepted transition point between two and three dimensional behaviour.

The sensitivity of surface quasi-elastic light scattering to the presence of polymer monolayers has been graphically demonstrated for the case of PMMA, and results obtained may be related to information obtained from the classical surface pressure measurement. Clearly much work remains to be done in the optimization of the SQELS technique, but it is equally clear that the development of such a technique and the possible growth of the study of non-specularly reflected scatter in neutron experiments represent major opportunities for an increased understanding of polymer monolayers and many other surface structures.

References

1. Brinkhuis, R.H.G., Schouten, A.J., *Macromolecules*, **24**, 1487, 1991.

2. Brinkhuis, R.H.G., Schouten, A.J., *Macromolecules*, **24**, 1496, 1991.

REVISED VERSION

UNIVERSITY OF DURHAM

Board of Studies in Chemistry

COLLOQUIA, LECTURES AND SEMINARS GIVEN BY INVITED SPEAKERS 1ST AUGUST 1990 TO 31ST JULY 1991

ALDER, Dr. B.J. (Lawrence Livermore Labs., California) — 15th January, 1991
Hydrogen in all its Glory

BELL†, Prof. T. (SUNY, Stoney Brook, U.S.A.) — 14th November, 1990*
Functional Molecular Architecture and Molecular Recognition

BOCHMANN†, Dr. M. (University of East Anglia) — 24th October, 1990
Synthesis, Reactions and Catalytic Activity of Cationic Titanium Alkyls

BRIMBLE, Dr. M.A. (Massey University, New Zealand) — 29th July, 1991
Synthetic Studies Towards the Antibiotic Griseusin-A

BROOKHART, Prof. M.S. (University of N. Carolina) — 20th June, 1991
Olefin Polymerizations, Oligomerizations and Dimerizations Using Electrophilic Late Transition Metal Catalysts

BROWN, Dr. J. (Oxford University) — 28th February, 1991*
Can Chemistry Provide Catalysts Superior to Enzymes?

BUSHBY†, Dr. R. (Leeds University) — 6th February, 1991*
Biradicals and Organic Magnets

COWLEY, Prof. A.H. (University of Texas) — 13th December, 1990
New Organometallic Routes to Electronic Materials

CROUT, Prof. D. (Warwick University) — 29th November, 1990
Enzymes in Organic Synthesis

DOBSON†, Dr. C.M. (Oxford University) — 6th March, 1991
NMR Studies of Dynamics in Molecular Crystals

GERRARD†, Dr. D. (British Petroleum) — 7th November, 1990*
Raman Spectroscopy for Industrial Analysis

HUDLICKY, Prof. T. (Virginia Polytechnic Institute) — 25th April, 1991
Biocatalysis and Symmetry Based Approaches to the Efficient Synthesis of Complex Natural Products

JACKSON†, Dr. R. (Newcastle University) — 31st October, 1990
New Synthetic Methods: α-Amino Acids and Small Rings

KOCOVSKY†, Dr. P. (Uppsala University) — 6th November, 1990*
Stereo-Controlled Reactions Mediated by Transition and Non-Transition Metals

LACEY, Dr. D. (Hull University) — 31st January, 1991 *
Liquid Crystals

LOGAN, Dr. N. (Nottingham University) — 1st November, 1990
Rocket Propellants

MACDONALD, Dr. W.A. (ICI Wilton) — 11th October, 1990 *
Materials for the Space Age

MARKAM, Dr. J. (ICI Pharmaceuticals) — 7th March, 1991
DNA Fingerprinting

PETTY, Dr. M.C. (Durham University) — 14th February, 1991 *
Molecular Electronics

PRINGLE†, Dr. P.G. (Bristol University) — 5th December, 1990
Metal Complexes with Functionalised Phosphines

PRITCHARD, Prof. J. (Queen Mary & Westfield College, London University) — 21st November, 1990
Copper Surfaces and Catalysts

SADLER, Dr. P.J. (Birkbeck College London) — 24th January, 1991
Design of Inorganic Drugs: Precious Metals, Hypertension + HIV

SARRE, Dr. P. (Nottingham University) — 17th January, 1991
Comet Chemistry

SCHROCK, Prof. R.R. (Massachusetts Institute of Technology) — 24th April, 1991 *
Metal-ligand Multiple Bonds and Metathesis Initiators

SCOTT, Dr. S.K. (Leeds University) — 8th November, 1990
Clocks, Oscillations and Chaos

SHAW†, Prof. B.L. (Leeds University) — 20th February, 1991
Syntheses with Coordinated, Unsaturated Phosphine Ligands

SINN†, Prof. E. (Hull University) — 30th January, 1991
Coupling of Little Electrons in Big Molecules. Implications for the Active Sites of (Metalloproteins and other) Macromolecules

SOULEN†, Prof. R. (South Western University, Texas) — 26th October, 1990
Preparation and Reactions of Bicycloalkenes

WHITAKER†, Dr. B.J. (Leeds University) — 28th November, 1990
Two-Dimensional Velocity Imaging of State-Selected Reaction Products

† Invited specifically for the postgraduate training programme.

UNIVERSITY OF DURHAM

Board of Studies in Chemistry

COLLOQUIA, LECTURES AND SEMINARS GIVEN BY INVITED SPEAKERS 1ST AUGUST 1989 TO 31ST JULY 1990

BADYAL, Dr. J.P.S. (Durham University) — 1st November, 1989 *
Breakthoughs in Heterogeneous Catalysis

BECHER, Dr. J. (Odense University) — 13th November, 1989
Synthesis of New Macrocylic Systems using Heterocyclic Building Blocks

BERCAW, Prof. J.E. (California Institute of Technology) — 10th November, 1989 *
Synthetic and Mechanistic Approaches to Ziegler–natta Polymerization of Olefins

BLEASDALE, Dr. C. (Newcastle University) — 21st February, 1990
The Mode of Action of some Anti–tumour Agents

BOWMAN, Prof. J.M. (Emory University) — 23rd March, 1990
Fitting Experiment with Theory in Ar–OH

BUTLER, Dr. A. (St. Andrews University) — 7th December, 1989
The Discovery of Penicillin: Facts and Fancies

CHEETHAM, Dr. A.K. (Oxford University) — 8th March, 1990 *
Chemistry of Zeolite Cages

CLARK, Prof. D.T. (ICI Wilton) — 22nd February, 1990
Spatially Resolved Chemistry (using Natures's Paradigm in the Advanced Materials Arena)

COLE–HAMILTON, Prof. D.J. (St. Andrews University) — 29th November, 1989 *
New Polymers from Homogeneous Catalysis

CROMBIE, Prof. L. (Nottingham University) — 15th February, 1990
The Chemistry of Cannabis and Khat

DYER, Dr. U. (Glaxo) — 31st January, 1990
Synthesis and Conformation of C–Glycosides

FLORIANI, Prof. C. (University of Lausanne, Switzerland) — 25th October, 1989
Molecular Aggregates – A Bridge between homogeneous and Heterogeneous Systems

GERMAN, Prof. L.S. (USSR Academy of Sciences – Moscow) — 9th July, 1990
New Syntheses in Fluoroaliphatic Chemistry: Recent Advances in the Chemistry of Fluorinated Oxiranes

GRAHAM, Dr. D. (B.P. Reserch Centre) — 4th December, 1989 *
How Proteins Absorb to Interfaces

GREENWOOD, Prof. N.N. (University of Leeds) — 9th November, 1989
Novel Cluster Geometries in Metalloborane Chemistry

HOLLOWAY, Prof. J.H. (University of Leicester) — 1st February, 1990
Noble Gas Chemistry

HUGHES, Dr. M.N. (King's College, London) — 30th November, 1989
A Bug's Eye View of the Periodic Table

HUISGEN, Prof. R. (Universität München) — 15th December, 1989
Recent Mechanistic Studies of [2+2] Additions

KLINOWSKI, Dr. J. (Cambridge University) — 13th December 1989*
Solid State NMR Studies of Zeolite Catalysts

LANCASTER, Rev. R. (Kimbolton Fireworks) — 8th February, 1990
Fireworks – Principles and Practice

LUNAZZI, Prof. L. (University of Bologna) — 12th February, 1990
Application of Dynamic NMR to the Study of Conformational Enantiomerism

PALMER, Dr. F. (Nottingham University) — 17th October, 1989
Thunder and Lightning

PARKER, Dr. D. (Durham University) — 16th November, 1989*
Macrocycles, Drugs and Rock 'n' roll

PERUTZ, Dr. R.N. (York University) — 24th January, 1990
Plotting the Course of C–H Activations with Organometallics

PLATONOV, Prof. V.E. (USSR Academy of Sciences – Novosibirsk) — 9th July, 1990
Polyfluoroindanes: Synthesis and Transformation

POWELL, Dr. R.L. (ICI) — 6th December, 1989
The Development of CFC Replacements

POWIS, Dr. I. (Nottingham University) — 21st March, 1990
Spinning off in a huff: Photodissociation of Methyl Iodide

ROZHKOV, Prof. I.N. (USSR Academy of Sciences – Moscow) — 9th July, 1990
Reactivity of Perfluoroalkyl Bromides

STODDART, Dr. J.F. (Sheffield University) — 1st March, 1990*
Molecular Lego

SUTTON, Prof. D. (Simon Fraser University, Vancouver B.C.) — 14th February, 1990
Synthesis and Applications of Dinitrogen and Diazo Compounds of Rhenium and Iridium

THOMAS, Dr. R.K. (Oxford University) — 28th February, 1990*
Neutron Reflectometry from Surfaces

THOMPSON, Dr. D.P. (Newcastle University) — 7th February, 1990
The role of Nitrogen in Extending Silicate Crystal Chemistry

APPENDIX B - RESEARCH CONFERENCES ATTENDED DURING PERIOD OF STUDY

ESF Discussion Workshop on Interfaces and Reflectivity, 8-10th June 1989, Max Planck Institut für Polymerforschung, Mainz, Germany*.

Structural Evaluation of Polymers, Macro Group UK, 10-11th April 1990, University of Strathclyde, Glasgow*.

33rd IUPAC International Symposium on Macromolecules, 8th-13th July 1990, Montreal, Canada*.

Neutron Scattering 1990, SERC UK Neutron Beam Users Community Meeting, 11th-12th September 1990, Churchill Hall, University of Bristol*.

Neutron Reflectivity at Interfaces, Neutron Scattering Group, 13th-14th September 1990, University of Bristol.

Macro Group UK Meeting, 26th-28th March 1991, University of Bristol.

Polymer Surfaces and Interfaces II, International Symposium, 22nd-26th July 1991, Durham.

Speciality Polymers '91, Supramolecular Aspects of Polymer Synthesis and Polymer Structure, 30th September - 2nd October 1991, Max Planck Institut für Polymerforschung, Mainz, Germany*.

* Denotes presentation by the author